Deriving Planetary Surface Characteristics from Orbiting Laser Altimeter Pulse-Widths on: Mars, the Moon, and Earth

William David Poole

Thesis submitted for the degree of Doctor of Philosophy

2015

Mullard Space Science Laboratory
Department of Space and Climate Physics
University College London

I, William David Poole confirm that the work presented in this thesis is my own. Where information has been derived from other sources, I confirm that this has been indicated in the thesis.

Signature _____

Abstract

A set of equations linking the time-spread of a laser altimeter echo-profile, commonly known as the pulse-width, to the variance of topography within the pulse-footprint are tested by comparing pulse-width data to surface characteristics measured from high-resolution Digital Terrain Models. The research is motivated by the advent of high-resolution Digital Terrain Models over Mars, which enables the calibration of Mars Orbiter Laser Altimeter pulse-widths, and evolves to include lunar and terrestrial data in an attempt to validate the theory and develop new methods.

Analysis of Mars Orbiter Laser Altimeter pulse-width data reveals mixed results. Over homogeneously rough terrain, at kilometre-scales, these pulse-widths show some correlation to surface characteristics, once poor pulse data has been removed. However, where roughness is highly variable over short baselines, little correlation is observed, which is attributed to a mix of georeferencing errors and instrument methods.

In a similar study, Lunar Orbiter Laser Altimeter pulse-widths are shown to produce only poor correlations with surface characteristics over local study sites. Instead, the observed correlations differ from orbit to orbit, with the majority of those used appearing to contain poor quality pulse-width data - attributed to the instrument methods - and only 14 % revealing correlations similar, or better, than observed over Mars.

Finally, an examination of the relationship between footprint-scale surface characteristics and pulse-width estimates derived from smoothed Ice, Cloud, and land Elevation Satellite echo-profiles enables different pulse-width thresholds to be tested. Here, pulse-widths measured using a 10 % Peak Energy threshold are shown to produce greater correlations than those observed using the Mars Orbiter Laser Altimeter and the Lunar Orbiter Laser Altimeter data, which use a Full Width Half Maximum threshold.

To conclude, pulse-widths can show strong correlations to surface roughness and slope within the pulse-footprint. However the assumption that detrended surface roughness can be derived by applying a slope contribution effect is shown to be unfounded. The principal recommendation is for future instruments to use a full echo-profile in estimating pulse-width values at a 10 % Peak Energy threshold, providing both efficient noise removal and a better correlated dataset.

Contents

List of Figures

List of Tables

ABBREVIATIONS

AATE Adaptive Automatic Terrain Extraction
ALSC Adaptive Least Squares Correlation
ASPRS American Society for Photogrammetry and Remote Sensing
ASTER Advanced Spaceborne Thermal Emission and Reflection
ATM Airborne Topographic Mapper

BELA BepiColombo Laser Altimeter

CCD Charge Coupled Device
CDI Course-Deviation Indicator
CPR Circular Polarisation Ratio
CRISM Compact Reconnaissance Imaging Spectrometer for Mars
CTX Context Camera

DLR Deutsches Zentrum für Luft- und Raumfahrt
German Aerospace Center
DTM Digital Terrain Model
See Glossary Entry: Digital Terrain Model

ESA European Space Agency
ESP Extended Science Phase

FOV Field Of View
FTP File Transfer Protocol
FWHM Full Width Half Maximum

GALA Ganymede Laser Altimeter
GCM General Circulation Model
GDEM Global Digital Elevation Model
GIS Geographical Information System
See Glossary Entry: Geographic Information System
GLAH Geoscience Laser Altimeter HDF5 format data

GLAS Geoscience Laser Altimeter System

GLD100 Global Lunar Digital Terrain Model 100 m topographic model

GPFMS Global Positioning Flight Management System

GPS Global Positioning Systems

HDF5 Hierarchical Data Format 5

HiRISE High Resolution Imaging Science Experiment

HRSC High Resolution Stereo Camera

IAU International Astronomical Union

ICESat Ice, Cloud, and land Elevation Satellite

ILS Instrument Landing System

IMU Inertial Measuring Units

INS Inertial Navigation Systems

IQR Inter-Quartile-Range

ISIS3 Integrated Software for Imagers and Spectrometers Version 3

JUICE JUpiter ICy moons Explorer

LALT Laser Altimeter, on-board SELenological and ENgineering Explorer "KAGUYA" (SELENE) (above)

LEND Lunar Exploration Neutron Detector

LOLA Lunar Orbiter Laser Altimeter

LPA Laser Profile Array

LPNS Lunar Prospector Neutron Spectrometer

LRO Lunar Reconnaissance Orbiter

LROC Lunar Reconnaissance Orbiter Camera

LROC-NAC Lunar Reconnaissance Orbiter Camera - Narrow Angle Camera

LROC-WAC Lunar Reconnaissance Orbiter Camera - Wide Angle Camera

MARSIS Mars Advanced Radar for Subsurface and Ionosphere Sounding

MATLAB MATrix LABoratory
See Glossary Entry: MATLAB

MDIM Mars Digital Image Mosaic

MEGDR Mission Experiment Gridded Data Record

MER Mars Exploration Rover

MESSENGER	MErcury Surface, Space ENvironment, GEochemistry, and Ranging
MEX	Mars Express
MGS	Mars Global Surveyor
MLA	Mercury Laser Altimeter
MOC	Mars Orbiter Camera
MOLA	Mars Orbiter Laser Altimeter
MPO	Mercury Planetary Orbiter
MRO	Mars Reconnaissance Orbiter
MSL	Mars Science Laboratory
MST	Multi-Sensor Triangulation
NASA	National Aeronautics and Space Administration
NEAR-Shoemaker	Near Earth Asteroid Rendezvous - Shoemaker
NGATE	Next-Generation Automatic Terrain Extraction
NIR	Near-infrared
PDS	Planetary Data System URL: http://pds.nasa.gov
PEDR	Precision Experiment Data Record
PNR	Permanently Shadowed Region
PSP	Primary Science Phase
RMS	Root-Mean-Square
ROI	Region-Of-Interest
SAR	Synthetic Aperture Radar
SELENE	SELenological and ENgineering Explorer "KAGUYA"
SHARAD	Mars SHAllow RADar sounder
SLA	Shuttle Laser Altimeter
SNR	Signal to Noise Ratio See Glossary Entry: Signal-to-Noise Ratio
SOCET SET®	SOftCopy Exploitation Toolkit See Glossary Entry: SOCET SET®
SPICE	Spacecraft and Planetary ephemerides, Instrument C-matrix and Event kernels
SSD	Sum-of-Squared Differences
TES	Thermal Emission Spectrometer
THEMIS	THermal EMission Imaging System
TOF	Time-Of-Flight

USA United States of America

USGS United States Geological Survey

WGS 84 World Geodetic System 1984
See Glossary Entry: World Geodetic System 84

GLOSSARY

Absolute Slope A measure of surface roughness, defined on Page 78 as

$$s_{abs} = \frac{1}{\Delta x}\left\{\frac{1}{n}\sum_{i=1}^{n}\left|z\left(x_i\right) - z\left(x_i + \Delta x\right)\right|\right\}$$

Aerodynamic Roughness Length A parameter used to measure the mean wind speed at the surface, equivalent to the height at which the log of the wind speed is 0, and related to the roughness of terrain

Aerographic A coordinate system used to define points on the surface of Mars

Aeroid The equipotential surface of Mars, derived from MOLA data

ArcMap Part of the ArcGIS Geographic Information System processing suite used to map and process data throughout this work, versions 10.0 and 10.1 are used in this work

Autocorrelation Length A measure of surface roughness, which explores the correlation of terrain which itself, defined on Page 79 as

$$C\left(\Delta x\right) = \frac{1}{\xi^2}\left[\frac{1}{n-1}\sum_{i=1}^{n} z\left(x_i\right) z\left(x_i + \Delta x\right)\right]$$

Baseline The scale, i.e. size of the window or profile, across which surface roughness is measured, can also be defined as the distance between camera positions
See Symbol List: b_c

Beam Divergence The spreading out of the laser beam due to diffraction effects after it has passed through the aperture, which causes an increase in the pulse-footprint with distance, and a gaussian distribution of energy across the footprint

Breakpoint The scale at which the Hurst exponent breaks, and thought to be an indicator of scale at which competing processes change

Detrend A process that removes the effect of background slope from elevation and surface roughness estimates

Digital Terrain Model Gridded elevation model of terrain, where each point has a point in x, y, and z. Other forms are digital surface model and digital elevation model. DTM is used here as this work focuses on bare terrain, i.e. devoid of vegetation and other objects on the surface

Effective Slope Deviation A measure of surface roughness, defined on Page 78 as

$$s_{eff} = \frac{\xi}{C} = \frac{1}{C}\left[\frac{1}{n-1}\sum_{i=1}^{n}\left(z\left(x_i\right)-\bar{z}\right)^2\right]^{\frac{1}{2}}$$

Foehn Winds A dry downslope wind that warms adiabatically as it descends. Unlike katabatic winds, these winds were cool through adiabatic cooling by orographic lifting, depositing precipitation on the windward side, and descending as warm dry air on the lee side

Geary's C A method of measuring surface roughness, similar to autocorrelation length, defined on Page 80 as

$$I_C = \frac{n-1}{2W}\cdot\frac{\sum_i\sum_j w_{ij}\left(z_i-z_j\right)^2}{\sum_i\left(z_i-\bar{z}\right)^2}$$

Geographic A coordinate system used to define points on the surface of Earth

Geographic Information System Software used to map and process geographic data

Geoid A surface defining the equipotential surface on Earth, and is the shape of the surface would take if the Earth was covered entirely by water

Hurst Exponent A measure of the scaling of terrain when data forms one or more linear lines-of-best-fit on a variogram, defined below

Inter-Quartile Range A measure of the distribution of a sample, here used as a measure of surface roughness

Katabatic Winds A downslope wind caused by radiational cooling of air at a topographic high, increasing in density and falling under gravitational forces, downslope, warming adiabatically as it does so.

Laser Altimeter Instrument to derive terrain elevation from laser ranging, here it is defined as an orbiting lidar instrument

Lidar An laser ranging instrument, which comes in many forms and uses. In this work it is defined as a non orbiting laser ranging instrument. The name is a portmanteau of *LIght* and *raDAR* (http://www.oed.com), also written as LiDAR and LIDAR, but is often assumed to be an acronym of "Light Detection and Radar", or "Laser Imaging, Detection and Ranging".

Mars Dichotomy Describes the sharp difference between the north and south of Mars. The north appears as low, smooth terrain, whist the south, in sharp contrast, is higher in elevation and much rougher.

MATLAB Numerical software produced by Mathworks, and used extensively to process the numerical data in this work
See Acronym List: MATLAB

Median Differential Slope A method of measuring surface roughness, defined on Page 79 as

$$s_d = \frac{z_{\frac{\Delta x}{2}} - z_{\frac{-\Delta x}{2}}}{\Delta x} - \frac{z_{\Delta x} - z_{-\Delta x}}{2\Delta x}$$

Moran's I A method of measuring surface roughness, similar to autocorrelation length, defined on Page 79 as

$$I = \frac{n}{\sum_i \sum_j w_{ij}} \frac{\sum_i \sum_i w_{ij} (z_i - \bar{z}) (z_j - \bar{z})}{\sum_i (z_i - \bar{z})^2}$$

Parallax The apparent change in position of an object when viewed at different angles

Planetocentric A coordinate system where latitude is measured as the angle between the equatorial plane and the vertical point on the surface, with a line drawn from the surface to the centre of mass of the body

Planetographic A coordinate system where latitude is measured as the angle between the equatorial plane and the vertical point on the surface, with a line drawn perpendicular from the surface to the equatorial plane of the body

Pulse The pulse of photons output from a laser, with the distribution of photons output as approximately as a Gaussian distribution

Pulse Broadening Broadening of the original transmitted pulse due to receiver response time, beam curvature, and terrain effects

Pulse-Footprint The spatial extent of a laser pulse upon the target surface, usually defined as when the energy drops to 1/e or $1/e^2$

Pulse-Rate Number of pulses per second from a laser instrument

Pulse-Width The time-spread of the received backscatter from a laser altimeter pulse

Range The maximum difference in elevations within a given baseline

Reference Frame A solution which defines from observational data the specific numerical location of given points in the reference system [*LRO Project and LGCWG*, 2008]

Reference Height A reference surface from which topographic elevation is measured, often simply defined as a sphere or ellipsoid, or, more complex, as an equipotential surfaces such as geoid, selenoid, or aeroid

Reference System A system that includes some definition of a physical environment, specific terminology, and associated theories that form an idealised model for defining positions on a particular body [*LRO Project and LGCWG*, 2008]

RMS Beam Curvature Effect The Root-Mean-Square of the beam curvature effect

RMS Deviation A measure of surface roughness, defined on Page 77 as

$$\nu(\Delta x) = \left\{ \frac{1}{n} \sum_{i=1}^{n} [z(x_i) - z(x_i + \Delta x)]^2 \right\}^{\frac{1}{2}}$$

RMS Height A measurement of surface roughness, defined on Page 77 as

$$\xi = \left[\frac{1}{n-1} \sum_{i=1}^{n} (z(x_i) - \bar{z})^2 \right]^{\frac{1}{2}}$$

RMS of the Terrain within the Pulse-Footprint The Root-Mean-Square of the terrain effect on the final received pulse-width

RMS Received Optical Pulse-Width The Root-Mean-Square of the total received optical pulse-width by a laser altimeter

RMS Receiver Impulse Response The Root-Mean-Square of the receiver impulse response

RMS Slope A measure of surface roughness, defined on Page 78 as

$$s_{rms} = \frac{\nu(\Delta x)}{\Delta x} = \frac{1}{\Delta x} \left\{ \frac{1}{n} \sum_{i=1}^{n} [z(x_i) - z(x_i + \Delta x)]^2 \right\}^{\frac{1}{2}}$$

RMS Transmitted Pulse-Width The Root-Mean-Square of the transmitted pulse-width

Sastrugi Long wind eroded features that occur on ice sheets that can be used to infer prevailing wind direction

Selenographic A coordinate system used to define points on the surface of the Moon

Selenoid A surface defining the equipotential surface of the Moon

Shapefile A file containing point or polygonal data, containing georeferenced data that can be projected along with raster datasets

Signal-to-Noise Ratio A measure of the desired signal to the noise level within a dataset

Slope The slope of a surface with respect to the horizontal

SOCET SET® Software to produce digital terrain models from both HiRISE and LROC-NAC stereo-pairs. See Acronym Entry: SOftCopy Exploitation Toolkit (SOCET SET®)

Stereo-Photogrammetry A method of producing a 3-dimensional model of an object from two or more overlapping images

Surface Roughness A measure of the vertical exaggerations across a horizontal plane or profile, at a defined baseline

Topex/Poseidon An Earth reference system defined as an equatorial radius of 6 378 136.300 000 m, and a polar radius of 6 356 751.600 563 m

World Geodetic System 84 An Earth reference system defined as an equatorial radius of 6 378 137.000 000 m, and a polar radius of 6 356 752.314 245 m

GREEK SYMBOLS

α	Extinction coefficient
γ	Laser beam divergence
ζ	The Gouy phase shift
η	Lidar optical efficiency
θ	Surface slope
θ_c	Planetocentric latitude
θ_g	Planetographic latitude
λ	Wavelength
λ_L	Laser wavelength
μ	Mean of Gaussian Distribution
ν	RMS, or Allen, deviation of elevation
ν_0	RMS deviation calculated at unit scale Δx_0
ν	Wave frequency
ρ	Surface reflectivity
ξ	RMS height
ξ_0	Unit scale of surface roughness measurement
σ	Standard deviation of Gaussian distribution
σ_b	RMS Beam curvature pulse-width
σ_f	RMS System pulse-width
σ_r	RMS Received pulse-width
σ_ξ	RMS Roughness pulse-width
σ_s	RMS Slope pulse-width
σ_t	RMS Terrain pulse-width
σ_x	RMS Transmitted pulse-width
ϕ_r	Intensity of received pulse
ϕ_t	Intensity of transmitted pulse
τ	Opacity
χ	Distance from μ

Roman Symbols

a	Equatorial radius
a_G	Amplitude of Gaussian distribution
A	Area of footprint
A_D	Device constant of laser degradation
A_R	Area of a laser ranging receiver telescope
b	Polar radius
b_c	Baseline length between camera positions
B	Volume backscatter coefficient
c	Speed of light
C	Autocorrelation length
E	Photon energy
E_0	Energy transmitted from a laser altimeter
E_a	Laser activation energy in eV
E_{eff}	Lidar system efficiency
f	Focal length
G	Geometrical form factor
h	Planck's constant
h_c	Height of camera
h_i	Height at point i
h_j	Height at point j
h_p	Height at point p
Δh	Difference in height between point h_i and h_j
H	Hurst exponent
i	Imaginary number, where $i^2 = -1$
I	Moran's I
I_C	Geary's C
I_L	Intensity at angle, θ, from nadir
k	Boltzman's constant
k_n	The wavenumber, as is given by $k_n = 2\pi/\lambda$
M	Atmospheric transmission
n	Number of points

N_B	Background radiation noise photon count
N_L	Number of transmitted photons detected
N_S	Expected number of photons detected
p_i	Parallax at point i
p_j	Parallax at point j
Δp	Difference in parallax between p_i and p_j
P_L	Laser power
P_C	Probability that a scattered photon is collected by the receiver telescope
P_S	Probability that a transmitted photon is scattered
q_0	The minimum spot radius
q	The beam spot radius
r	Range in elevation points
r_a	Radial distance from the centre of the beam
r_c	Radius of curvature
R	Distance between laser and target surface
R_a	Arithmetic Average
ΔR	Range bin
R_z	The Rayleigh range
s_a	Absolute slope
s_c	Curvature
s_e	Effective slope
s_d	Median differential slope
s_r	RMS slope
s_{r0}	RMS slope calculated at unit scale Δx_0
SS_{res}	Sum of squares of residuals
SS_{tot}	Total sum of squares
t	Time-of-flight for a laser pulse
Δt	Time bin
T	Absolute temperature in Kelvin
T_{Light}	Atmospheric transmittance
T_{Total}	Total atmospheric transmittance
w_{ij}	Element of a matrix of spatial weights
W	Sum of all w_{ij}
x	Horizontal component of point on the surface of an ellipse
x_0	Unit scale
Δx	Spacing between elevation points
Δx_0	Difference in unit scale
X_b	Hurst exponent break-point scale
y	Vertical component of point on the surface of an ellipse

$\bar{z}$	Mean elevation for all z within a window
$z(x_i)$	Elevation at point x_i
z_0	Aerodynamic Roughness Length

Acknowledgements

Firstly, I would like to thank Felix Ng, my supervisor during my time at the University of Sheffield's Geography department. He sparked my interest in exploring the features within the Residual South Polar Cap of Mars, which led me to pursuing a PhD in planetary science.

Secondly, I would like to thank my supervisors during my PhD. Prof. Jan-Peter Muller not only set up the project, but has also encouraged me to be a valuable member of the planetary science community. Sanjeev, my second supervisor, has offered great advice, particularly when interpreting surface images. Finally, I would like to thank Peter Grindrod: an excellent scientist with a great career ahead him and will no doubt make an excellent supervisor to many PhD students over the coming years. Thank you all for helping me understand what a PhD is about, and supporting me in my first steps in research.

I would also like to thank all my friends and family for steering me through life.

Last but not least, Rachel, thank you for all the happy moments, and putting up with me during my PhD (and the rest of the time!).

"*I am not young enough to know everything*"

J M Barrie (1860-1937)

The Admirable Crichton, Act I

1

INTRODUCTION

1.1 MOTIVATION

A comprehensive understanding of surface roughness and slope across a variety of baselines enables quantitative comparisons of the relative age, magnitude, and type of geological processes acting to shape a planetary surface, whilst estimates at small baselines can also be used to help identify candidate landing and roving sites [*Kreslavsky and Head*, 1999, 2000; *Kreslavsky et al.*, 2013; *Rosenburg et al.*, 2011; *Smith et al.*, 2010b]. With this in mind, a science goal of the Mars Orbiter Laser Altimeter (MOLA) instrument was to characterise the surface at ∼100 m-scales using the time-spread of the echo-profile, commonly known as the pulse-width, and a set of theoretically derived equations developed by *Gardner* [1992], which relate the pulse-width to the variance of terrain within the pulse-footprint (Figures 1.1a and 1.1b) [*Anderson*, 2003; *Neumann et al.*, 2003a; *Smith et al.*, 2001]. The work in this thesis compares these pulse-widths to surface characteristics from high-resolution Digital Terrain Models (DTMs) to address the fact that the true relationship between these properties has not been extensively explored [*Aharonson et al.*, 1998; *Anderson*, 2003; *Kim and Muller*, 2008; *Kim and Park*, 2011; *Saiger et al.*, 2007; *Smith et al.*, 2001]. In further testing of the theory, laser altimeter pulse-width data from the Moon and Earth are explored in an attempt to validate and develop methods for future laser altimeter instruments [*Hussmann et al.*, 2013; *Schenk et al.*, 2004; *Schutz et al.*, 2005; *Smith et al.*, 2010a,b; *Robinson et al.*, 2010; *Thomas et al.*, 2007; *Tran et al.*, 2010].

The equations governing the relationship between the pulse-widths and the surface characteristics - a term used throughout this thesis to refer to surface roughness and slope - within the pulse-footprint are described in detail in Chapter 2, but the basic principle is that variation of elevations within the pulse-footprint cause broadening of the echo-profile compared to the transmitted pulse [*Gardner*, 1992]. The advantage to using such datasets is that, in addition to providing a global elevation model, laser altimeter data could be used to quantitatively characterise global terrain at smaller baselines than can be derived from along-track elevation profiles, albeit with sometimes large inter-orbit spacing [*Aharonson et al.*, 1998; *Garvin et al.*, 1999; *Kreslavsky and Head*, 1999, 2000; *Neumann et al.*, 2003a; *Smith et al.*, 2001]. MOLA operated in an era before

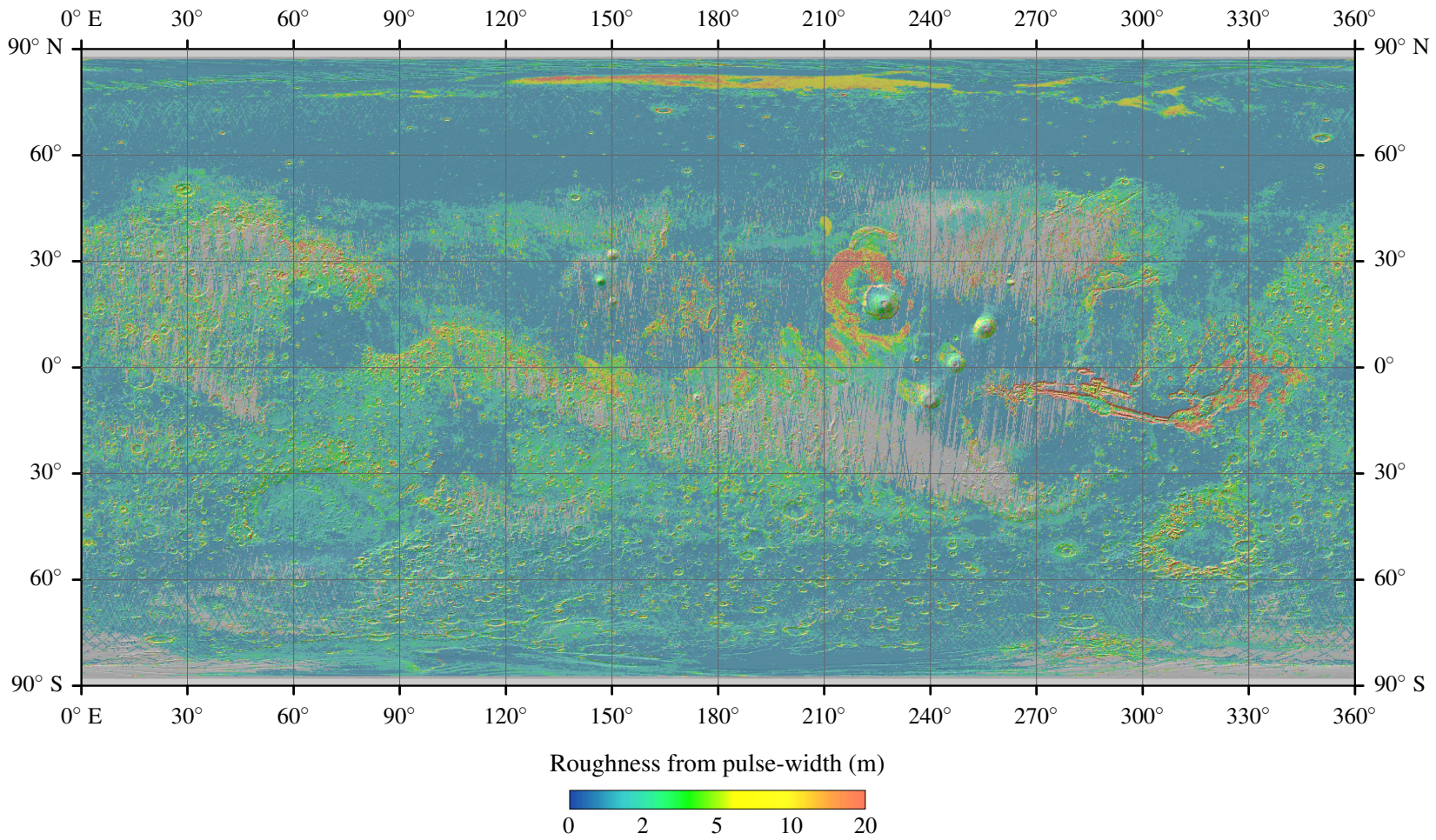

Figure 1.1a: Map of Mars surface roughness from MOLA pulse-widths using data from *Neumann et al.* [2003a]. Poor data has been removed from the original dataset to produce this map, and the original MOLA pulse-footprint baseline was revised from 170 m [*Smith et al.*, 2001] to 75 m [*Neumann et al.*, 2003a]. Grey terrain depicts regions where there is no data.

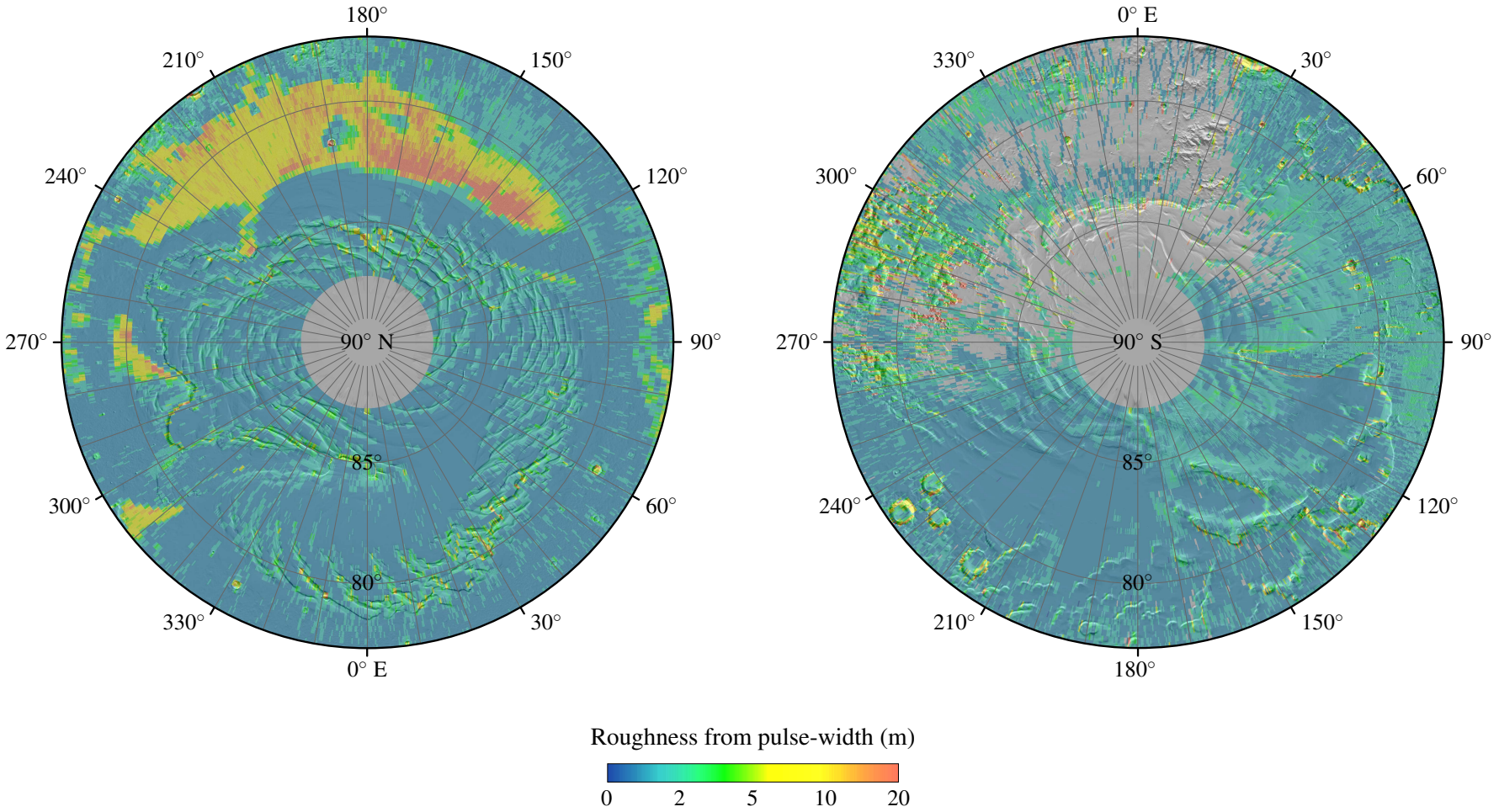

Figure 1.1b: Map of Mars polar surface roughness from MOLA pulse-widths using data from *Neumann et al.* [2003a]. Poor data has been removed from the original dataset to produce this map, and the original MOLA pulse-footprint baseline was revised from 170 m [*Smith et al.*, 2001] to 75 m [*Neumann et al.*, 2003a]. Grey terrain depicts regions where there is no data.

extensive high-resolution DTMs were available over Martian terrain, meaning that calibration with ground data was not possible [*Smith et al.*, 2001]. The advent of such data from the High Resolution Imaging Science Experiment (HiRISE), from which DTMs with 1 m pixel^{-1} post spacing can be produced, as well an extensive mapping phase for the Mars Science Laboratory (MSL) landing site selection process, means that pulse-widths can be compared to accurate estimates of surface characteristics at a wide variety of baselines ($\geq$10 m) to determine their responsiveness to underlying terrain, taking into account the different estimates of pulse-footprints and the distribution of energy across the pulse-footprint [*Aharonson et al.*, 1998; *Garvin et al.*, 1999; *Kim and Muller*, 2008, 2009; *Kim and Park*, 2011; *Kim et al.*, 2013; *Kirk et al.*, 2008; *Kim and Muller*, 2009; *McEwen et al.*, 2007; *Neumann et al.*, 2003a; *Shepard et al.*, 2001; *Smith et al.*, 2001]. The overall aim being to calibrate a pre-existing, but underused, global dataset for future use, which, in addition to landing and roving site selection, could further our understanding of Martian climate and climate history by improving upon current estimates of aerodynamic roughness length for Mars General Circulation Models (GCMs), and develop our knowledge of Martian geology on global scales, rather than the smaller Region's-Of-Interest (ROIs) explored in image data [*Golombek et al.*, 2012a; *Heavens et al.*, 2008; *Kreslavsky and Head*, 1999, 2000; *Kreslavsky et al.*, 2013].

More recently, the Lunar Orbiter Laser Altimeter (LOLA) and the Ice, Cloud, and land Elevation Satellite (ICESat) have recorded echo-pulse information to aid in the identification of candidate lunar landing sites and further our understanding of the spatial distribution and temporal changes of surface characteristics of ice sheets, sea-ice, and sea surfaces, respectively [*Schutz et al.*, 2005; *Smith et al.*, 2010b; *Zwally et al.*, 2002]. Like MOLA, both pulse-width datasets can be calibrated using high-resolution elevation data, from which surface characteristics at a range of baselines can be derived for comparison to these pulse-widths [*Csatho et al.*, 2005; *Mattson et al.*, 2012; *Tran et al.*, 2010]. LOLA employs similar methods to those used by MOLA, but improved co-registration between pulse-width and DTM datasets provides better conditions for testing of the theory [*Mattson et al.*, 2012; *Smith et al.*, 2010b; *Tran et al.*, 2010]. ICESat, which failed in 2009, recorded the full echo-profile within the dataset, which enables new methods of pulse-width estimates using different thresholds to be developed, with the aim of finding improved correlations between these data, as well as a range of terrain types and atmospheric conditions to highlight the criteria under which the theory fails [*Csatho et al.*, 2005; *Schutz et al.*, 2005; *Zwally et al.*, 2002].

A lack of familiarity of these pulse-width datasets, as well as deep interest in the recent influx of more easily interpretable high-resolution image data from planetary surfaces, could be why these datasets are often overlooked [*Gardner*, 1992; *Smith et al.*, 2001]. This original research attempts to validate the methods of estimating surface characteristics, focussing on surface roughness and slope, from planetary laser altimeter pulse-widths through comparison with high-resolution DTMs over extensive areas of Mars, the Moon, and Earth to prove the usefulness of such data. Doing so could unlock the potential of these global datasets, one of which (ICESat) has a multiyear time-series, and improve the methods for future laser altimeters to survey the Earth's ice sheets and barely explored planetary terrains [*Abdalati et al.*, 2010; *Hussmann et al.*, 2013; *Thomas et al.*, 2007].

1.2 AIMS AND OBJECTIVES

The universal aim of this research is

- To investigate the relationship between space-borne laser altimeter pulse-widths and surface characteristics within the pulse-footprint.

The research has the following objectives

- To compare laser altimeter pulse-width data to surface characteristics measured from high-resolution DTMs over the same area, in effect, calibrating the pulse-width data.
- To use a variety of surface characteristics and identify the best correlations.
- To determine if planetary surface roughness and slope can be derived from space-borne planetary laser altimeters pulse-widths, as proposed by *Gardner* [1992], and if so, the baseline at which these surface characteristics best correlate.
- To determine if detrended surface roughness, i.e. roughness from slope, can be derived from laser altimeter pulse-width data by applying a simple slope-correction to pulse-width values, as proposed by *Neumann et al.* [2003a].
- To develop new methods of estimating pulse-width based on different thresholds, rather than the Full Width Half Maximum (FWHM) proposed by *Gardner* [1992] and employed by MOLA and LOLA, that produce improved correlations between pulse-widths and surface characteristics.
- To test different pulse selection criteria, based on different atmospheric conditions and terrain characteristics, to identify where the theory works most effectively or fails.
- To determine the effect of energy distribution across the pulse-footprint by applying a weighting when calculating the surface characteristics.

The thesis comprises of three individual projects exploring pulse-width data over Mars, the Moon, and Earth, which are presented in Chapters 3 to 5 respectively. The order of the chapters coincides with the chronological order in which the projects were established. As a result, additional aims and objectives are created for individual projects as the investigation evolves, which aim to address issues raised in the preceding chapter(s).

1.3 OUTLINE OF THESIS

An introduction to the theory used in this thesis is presented in Chapter 2, which is composed of three topics. The first addresses laser ranging, with an overview of the theoretical components to laser altimeter pulse-widths, atmospheric effects on pulse-width broadening due to clouds and scattering, and an explanation of the causes of beam divergence and the resulting energy distribution

across the pulse-footprint. Section 2.2 introduces the techniques and the relative merits of stereo-photogrammetry and scanning lidar, both of which are used to produce the high-resolution DTMs from which surface characteristics are derived in this work; concluding with an introduction to coordinate systems and reference surfaces. Finally, Section 2.3 presents a synopsis of the surface characteristics used in this work, including how surface roughness and slope are derived from elevation data. The scaling nature of terrain is introduced, followed by a discussion on detrending elevation data and how to produce an effective measure of surface roughness, and the details that should be reported.

Chapters 3 to 5 contain the individual projects comparing laser altimeter pulse-widths from MOLA, LOLA, and ICESat to surface characteristics from high-resolution DTM data over Mars, the Moon, and Earth respectively. Each chapter contains (1) a literature review of relevant surface roughness and slope research, (2) a description of the instruments and datasets used in the comparison, (3) a description of the chapter specific methods, (4) a description of the study sites, (5) a presentation of the results, (6) a discussion, and (7) concluding remarks from the chapter.

The closing chapter presents the overarching conclusions from the three science chapters, outlines the originality and contributions the work in this thesis makes to science, and, finally, proposes ideas for future projects related to laser altimeter pulse-width data, using current and future datasets, and exploring how laboratory studies could improve our understanding of pulse-surface interactions over planetary surfaces.

2

Literature Review

This chapter introduces the background theory and literature used for the work in this thesis, and is divided into three sections addressing laser ranging, DTMs and surface characteristics. A specific review of planetary surface roughness and slope, as well as a description of the laser altimeter and DTM source instruments is provided in the appropriate science chapter (Chapters 3 to 5).

Section 2.1 outlines (1) the theory of laser ranging and deriving surface characteristics from the time-spread of the backscatter (laser altimeter pulse-widths), (2) the effects of atmospheric scattering and clouds on laser altimeter pulses and echo-profiles, and (3) how energy is distributed across the transmitted pulse-footprint due to beam divergence effects.

Section 2.2 describes the theory and relative merits concerning the derivation of DTMs from stereo-photogrammetry, including a brief description of the different families of stereo-matching algorithms, and scanning lidar, both of which are used to derive surface characteristics for the calibration of the pulse-width datasets in this work. A synopsis of the different reference surfaces and a description of the coordinate system transformation used in Chapter 5 are presented.

Finally, Section 2.3 presents (1) a review of the different methods of estimating 1- and 2-dimensional surface roughness and slope from elevation data, (2) a description of the scaling nature of terrain, and (3) a discussion of how and why elevation data may be detrended. The section concludes by outlining how an effective measure of surface roughness is produced and reported to best enable results to be correctly interpreted and replicated.

2.1 LASER ALTIMETRY

2.1.1 INTRODUCTION

Laser ranging uses photon Time-Of-Flight (TOF) measurements to determine the range to a target surface at scales from millimetres to thousands of kilometres, for a variety of applications including: manufacturing, the military, and surveying [*Bender et al.*, 1973; *Siegman*, 1986]. The basic principles of laser ranging, which is employed by planetary laser altimeters and remote sensing lidar to produce a 3-dimensional map of underlying terrains, are introduced here [*Csatho et al.*, 2005; *Siegman*, 1986; *Smith et al.*, 2001, 2010a,b]. For clarity, in this work, the term *laser altimeter* refers to an orbiting laser altimeter instrument used by instruments such as the Mars Orbiter Laser Altimeter (MOLA), the Lunar Orbiter Laser Altimeter (LOLA), and the Ice, Cloud, and land Elevation Satellite (ICESat) to make along-track elevation measurements, whilst *lidar* refers to the airborne scanning laser altimeters used to make dense elevation models, as discussed in Section 2.2.3 [*Schutz et al.*, 2005; *Smith et al.*, 2001, 2010a,b]. The following sections outline: the basic principles of laser ranging, how surface characteristics may be related to surface characteristics, and the atmospheric and divergence effects that affect the quality and shape of echo-profiles.

2.1.2 LASER RANGING

One approach to laser ranging is to count the number of wavelengths between an instrument and a target surface using a continuous laser beam and comparing the transmitted and received phase shift [*Shan and Toth*, 2009]. To accurately measure this phase shift, a modulation signal is superimposed on the transmitted signal: the wavelength of a laser is typically $\sim$1 mm and therefore too small for mapping applications [*Shan and Toth*, 2009]. The wavelength, λ, of the modulation signal can be changed to find the total number of integer wavelengths within the round-trip-travel-distance, and a known period, which can be used with the phase shift to determine the range by

$$R = \frac{k_n \lambda + \Delta\lambda}{2}, \qquad [2.1]$$

where R is the range, k_n is the wavenumber, and $\Delta\lambda$ is the wavelength shift.

The most common approach to laser ranging is to use the photon TOF [*Shan and Toth*, 2009]. This method is employed by the laser altimeters and lidar instruments that produce data used in this thesis [*Csatho et al.*, 2005; *Schutz et al.*, 2005; *Smith et al.*, 2001, 2010a]. The basic principle is to measure the TOF, t, for a pulse of photons to make the round-trip from a laser to the target surface, from which it is reflected, and back again, where it is collected by the receiver telescope and recorded. Using this approach, the range, R, is determined by

$$R = \frac{ct}{2}, \qquad [2.2]$$

where c is the speed of light. The distance is halved as the TOF measures the round-trip-travel-time

of a pulse, which is twice the distance between the laser altimeter and the target surface. This method of laser ranging also enables the profile, or pulse-width of the echo-pulse, to be recorded, from which the surface characteristics can theoretically be inferred [*Gardner*, 1992].

The MOLA, LOLA, and ICESat laser altimeters are diode pumped Q-switched Nd:YAG or Cr:Nd:YAG lasers that operate at 1064 nm wavelength [*Schutz*, 2001; *Smith et al.*, 2001, 2010b]. The energy, E, per photon is related to frequency, ν, and wavelength by

$$E = h\nu = \frac{hc}{\lambda} = 1.86 \times 10^{-19}\ \text{J}\ \ (\lambda = 1064\ \text{nm}), \qquad [2.3]$$

where h is Planck's constant[1]. Q-switching produces a pulse of photons with a higher peak power than can be achieved by a continuous wave, whilst Nd:YAG and Cr:Nd:YAG refers to the lasing mediums, neodymium-doped yttrium aluminium garnet (Nd:$Y_3Al_5O_{12}$) and chromium and neodymium-doped yttrium aluminium garnet (Cr:Nd:$Y_3Al_5O_{12}$) respectively [*Siegman*, 1986]. *Ott et al.* [2006] show that laser altimeters have a typical electrical to optical conversion efficiency of $\leq$3 %, whilst one must also be aware of the relatively low return signal compared to the transmitted pulse, with many photons scattered by the target surface or, in the case of Mars and Earth, by the atmosphere. The temporal energy profile of the transmitted pulse is approximately Gaussian, also known as a normal distribution, whilst the cross-section energy intensity also varies similarly across the pulse-footprint, as discussed in Section 2.1.5. A more complete description of different laser types is presented in *Siegman* [1986].

Employing laser altimeters on non-repeat, near-polar-orbiting spacecraft, like Mars Global Surveyor (MGS) and Lunar Reconnaissance Orbiter (LRO), enables global Digital Terrain Models (DTMs) to be generated by accumulating elevation data along orbit tracks (Figure 2.1) [*Smith et al.*, 1999, 2001, 2010a,b]. High pulse-rates will reduce along-track spacing, but is limited by the available power and the pulse TOF (1 ms at 300 km orbit), however inter-orbit spacings are typically much larger, with elevation values typically interpolated to form a continuous data product. Figure 2.1 shows the planned orbits over a large region of Mars for the MOLA instrument and an example subset over Eberswalde Crater showing heavily interpolated inter-orbit areas that appear smooth. Global DTMs, such as this, can be used for geological, geophysical, and atmospheric circulation studies of planetary bodies, furthering our understanding of surface formation and evolutionary processes [*Smith et al.*, 1999, 2001, 2010a,b]. Increasing the number of unique orbits and ensuring a long mission lifetime reduces the average inter-orbit spacing and increases the global point density for a more accurate global DTM, whilst cross-correlating elevation values at orbit cross-over locations helps validate and correct data as the mission progresses, safeguarding data quality and consistency.

Laser altimeters have also been used to produce global DTMs of Mercury and 433 Eros, on the MErcury Surface, Space ENvironment, GEochemistry, and Ranging (MESSENGER) mission to Mercury and the Near Earth Asteroid Rendezvous - Shoemaker (NEAR-Shoemaker) mission, respectively [*Cavanaugh et al.*, 2007; *Cheng et al.*, 1998; *Cole et al.*, 1997; *Solomon et al.*, 2001;

[1] Planck's constant, h, is $6.626\,069\,57 \times 10^{-34}$ m^2 kg s^{-1}

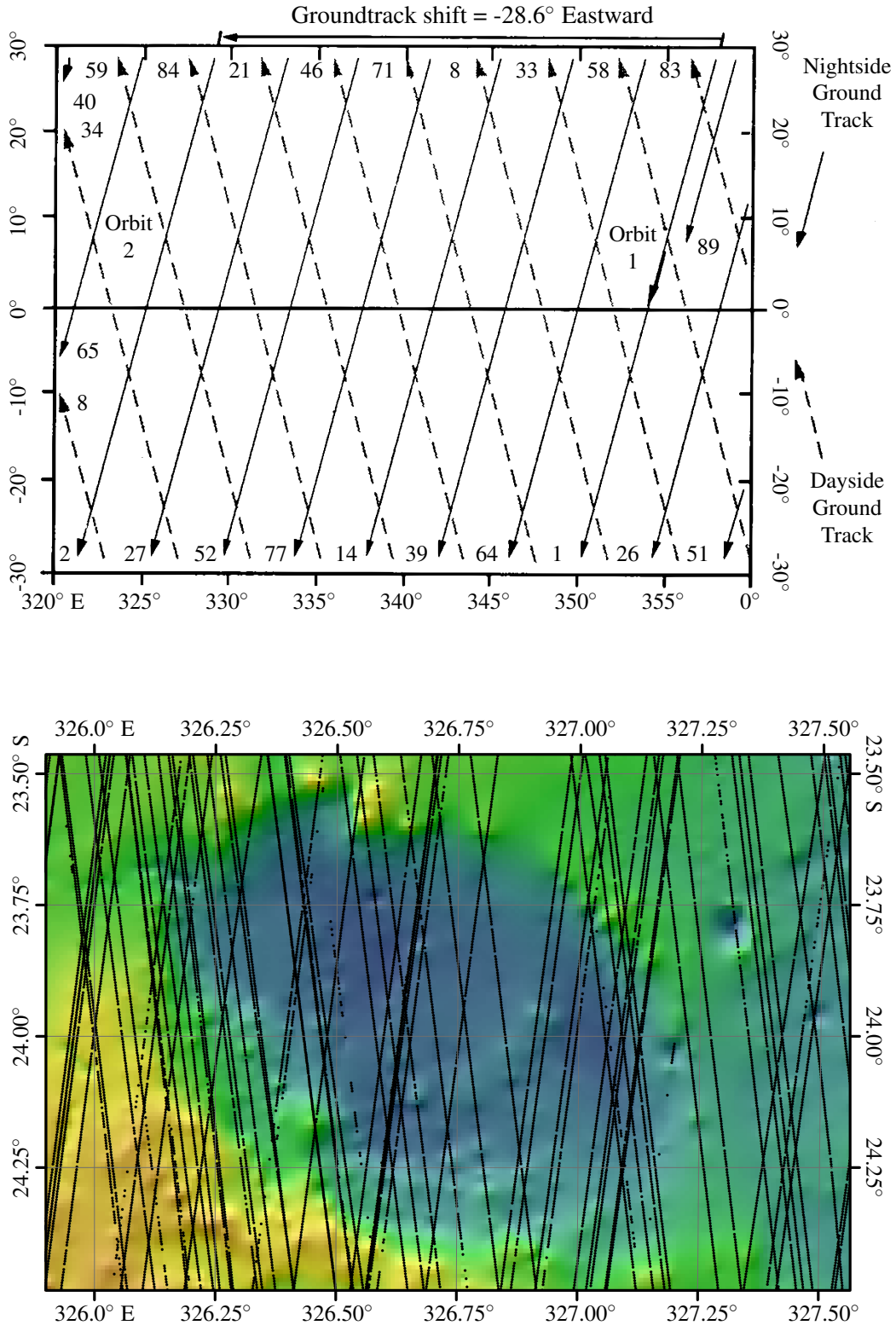

Figure 2.1: Schematic (top) and map (bottom) of MOLA track spacing, showing some of the planned and actual orbit tracks, and resulting elevation data over Eberswalde Crater. Dayside tracks pass south to north towards the north west, whilst nightside tracks pass north to south towards the south west, image reproduced from *Malin Space Science Systems* [No Date.]. As non-repeat laser altimeter instruments complete more orbits, inter-orbit spacing is reduced. The Eberswalde Crater regions shows the track spacing with the resulting DTM; inter-orbit regions are interpolated and appear smooth.

Zuber et al., 2008]. Although these missions have produced valid range data for their respective target bodies, data from these missions are not used in this work. In the case of the MESSENGER mission, high-resolution DTMs ($\sim$1 m) are not available over the surface, meaning that there is not the extensive high-resolution topographic surface information to which to calibrate the pulse-widths [*Solomon et al.*, 2001]. For the NEAR-Shoemaker mission, pulse-widths are not available within the data record [*Cheng et al.*, 1998].

The degradation and ultimate failure of lasers are significant defects of lasers. Lasers are particularly susceptible to temperature, such that their time-to-failure can be given by Arrhenius's equation [*Epperlein*, 2013]

$$= A_D e^{E_a/kT} \qquad [2.4]$$

where A_D is the device constant in time, E_a is the activation energy of the device in eV, k is Boltzman's constant, and T is the absolute temperature in Kelvin. Other modes of decay and failure include (1) active region degradation, whereby chemical changes occur in the lasing medium, (2) electrode degradation; electrostatic discharge, (3) thermal fatigue, (4) diode bar darkening, and (5) catastrophic optical damage [*Epperlein*, 2013; *Ott et al.*, 2006]. Laser degradation is inevitable, but can be mitigated by careful operating procedures, paying particular attention to operating temperatures, or fitting multiple lasers [*Epperlein*, 2013; *Schutz et al.*, 2005; *Shan and Toth*, 2009; *Smith et al.*, 2010a,b; *Zwally et al.*, 2002].

In addition to elevation data, laser altimeter and lidar can provide information on vegetation density and structure, as in *Fujii and Fukuchi* [2005] and *Harding and Carabajal* [2005], by using recorded pulse profiles. Forest canopy and ground-returns form distinct features within the profile, which enable the vertical distribution of vegetation above the ground to be determined [*Harding and Carabajal*, 2005]. Furthermore, ground-returns can be used to produce *bare-earth* terrain models (i.e. DTMs), from which vegetation volume can be estimated and terrain beneath canopies, that cannot be penetrated using stereo-photogrammetry, can be explored [*Harding and Carabajal*, 2005; *Lillesand et al.*, 2008; *Shan and Toth*, 2009].

2.1.3 DERIVING SURFACE PROPERTIES FROM LASER ALTIMETER PULSE-WIDTHS

Gardner [1992] proposes the received pulse-width, defined as the time-spread of the received echo, to be related to the transmitted pulse-width, receiver response time, beam curvature effect, and terrain effects by

$$\sigma_r^2 = \sigma_x^2 + \sigma_f^2 + \sigma_b^2 + \sigma_t^2, \qquad [2.5]$$

where σ_r is the RMS received optical pulse-width, σ_x is the RMS transmitted pulse-width, σ_f is the RMS receiver impulse response, σ_b is the RMS beam curvature effect, and σ_t is RMS of the terrain within the pulse-footprint. The theory is used to infer the surface roughness of planetary terrain from orbiting laser altimeter data, where pulse-footprints are typically metres to tens of metres in diameter [*Aharonson et al.*, 1998; *Garvin et al.*, 1998; *Neumann et al.*, 2003a, 2009; *Schutz et al.*, 2005; *Smith et al.*, 2001, 2010b]. Testing the theory by comparing the terrain contribution, σ_t,

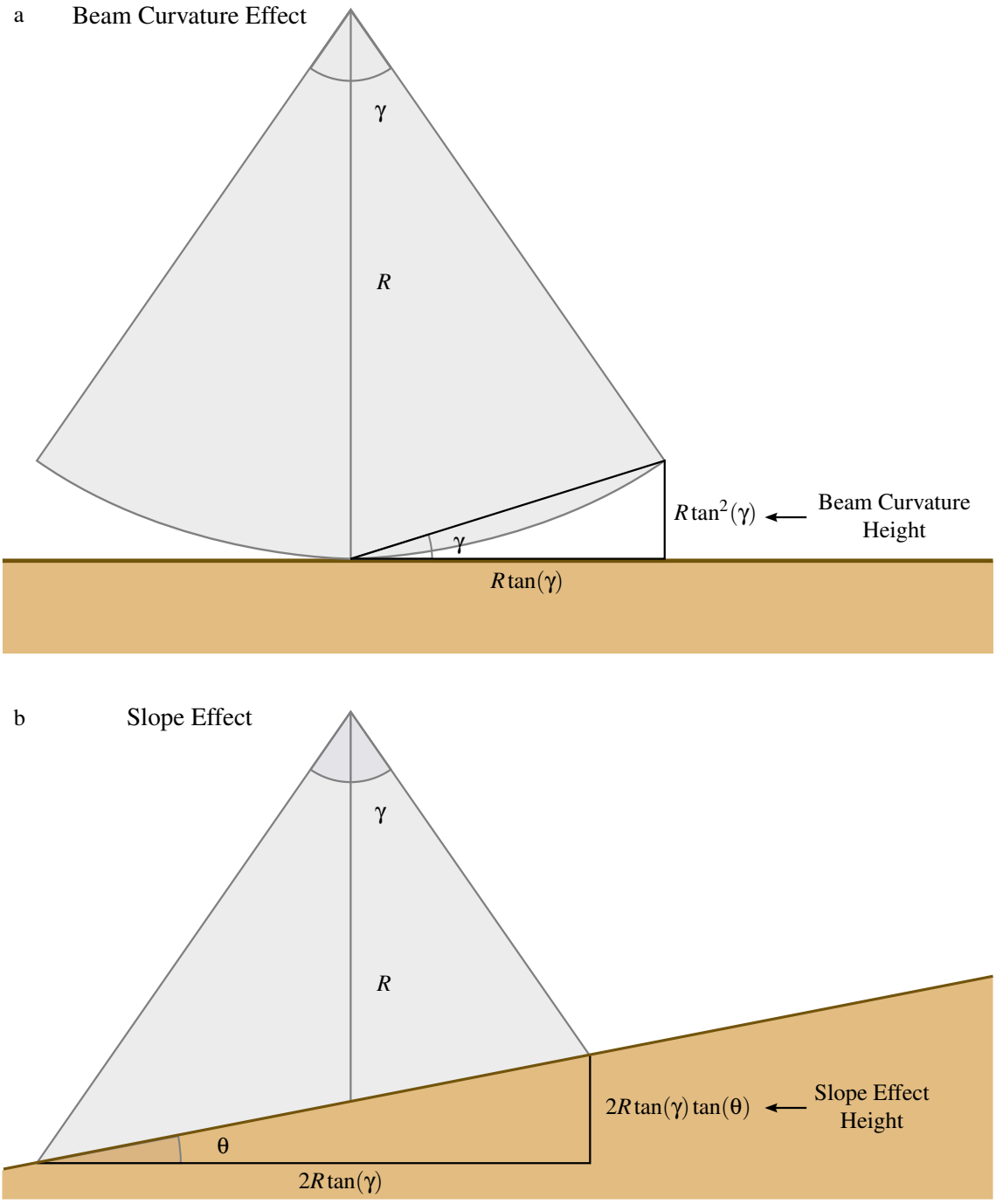

Figure 2.2: Schematics of how beam curvature (a) and slope-correction (b) effects to the final received pulse-width are derived using trigonometry and Equation 2.2, resulting in Equations 2.6 to 2.7. Beam curvature effects are caused by beam divergence as the transmitted pulse moves away from the aperture. As the pulse-front travels at the same velocity this results in a curved wavefront in cross-section view (a), meaning that different parts of the pulse-front reach the target surface at different times as the outer edges of the beam must travel furthest. Slope-correction effects, which are simplified, also arise from beam divergence effects and assumes the highest point within the pulse-footprint is at one edge of the pulse-footprint and the lowest point at the other (b). Curvature and divergence effects are shown heavily exaggerated.

derived by accounting for the effects of σ_x, σ_f, and σ_b, to estimates of surface characteristics from high-resolution DTMs forms the backbone of the work in this thesis [*Harding and Carabajal*, 2005; *Neumann et al.*, 2003a; *Smith et al.*, 2001, 2010b].

RMS transmitted pulse-width and RMS receiver impulse response are related to instrument setup and the performance of the instrument electronics, but RMS beam curvature effect and RMS of the terrain within the pulse-footprint are governed by instrument optics, pointing angles, and terrain, such that

$$\sigma_b^2 = \frac{4R^2}{c^2}\tan^4(\gamma), \tag{2.6}$$

$$\begin{aligned}\sigma_t^2 &= \sigma_s^2 + \sigma_\xi^2 \\ &= \frac{4R^2}{c^2}[\tan^2(\gamma)\tan^2(\theta)] + \sigma_\xi^2,\end{aligned} \tag{2.7}$$

where γ is the beam divergence, σ_s is the effect due to slope, σ_ξ is the effect due to surface roughness, and θ is the slope of the surface orthogonal to laser pulse direction [*Neumann et al.*, 2003a]. Figure 2.2 shows how σ_b and σ_s, in Equations 2.6 and 2.7, are derived using trigonometry and Equation 2.2. In addition to the original theory outlined by *Gardner* [1992], the slope-correction effect is tested against detrended surface roughness, i.e. roughness from slope, to explore whether the assumption applied in *Neumann et al.* [2003a] upholds in real-world situations.

Figure 2.3 shows four schematics depicting the effects that different terrain morphology has on the received pulse-width. Smooth, gently undulating terrain has a weak effect on pulse broadening due to the relatively small variations in topography across the pulse-footprint, whilst smooth sloping terrain, and rough features both have a much greater effect on pulse broadening. Finally, rough, sloping terrain has the greatest pulse broadening effect as it combines both elements of Equation 2.7. Using the assumption introduced above, the background slope shown in this final schematic can be removed, and the resulting detrended surface roughness tested against the roughness contribution to pulse-width, especially where the slope is consistent across the pulse-footprint.

The RMS received optical pulse-width is best derived from the a full echo-profile of the received pulse. Failing that, different thresholds of received energy intensity can be employed to determine the pulse-width and overcome issues with noise detected by the receiver [*Abshire et al.*, 2000; *Neumann*, 2001; *Smith et al.*, 2001]. Additionally, the pulse-width timing mechanism must have sufficient timing resolution to produce accurate estimates of pulse-width that can be used to determine fine-scale differences in terrain elevations. For example, timing bins of 1 ns are used by ICESat and MOLA, which result in a theoretical elevation accuracy of 15 cm, using Equation 2.2, and is thought to be capable of detecting surface roughness as small as 1 m [*Schutz et al.*, 2005; *Smith et al.*, 2001].

Pulse-width broadening is dominated by the contribution from terrain. Using ICESat as an example

$$\sigma_r = 150.00 \text{ ns},$$

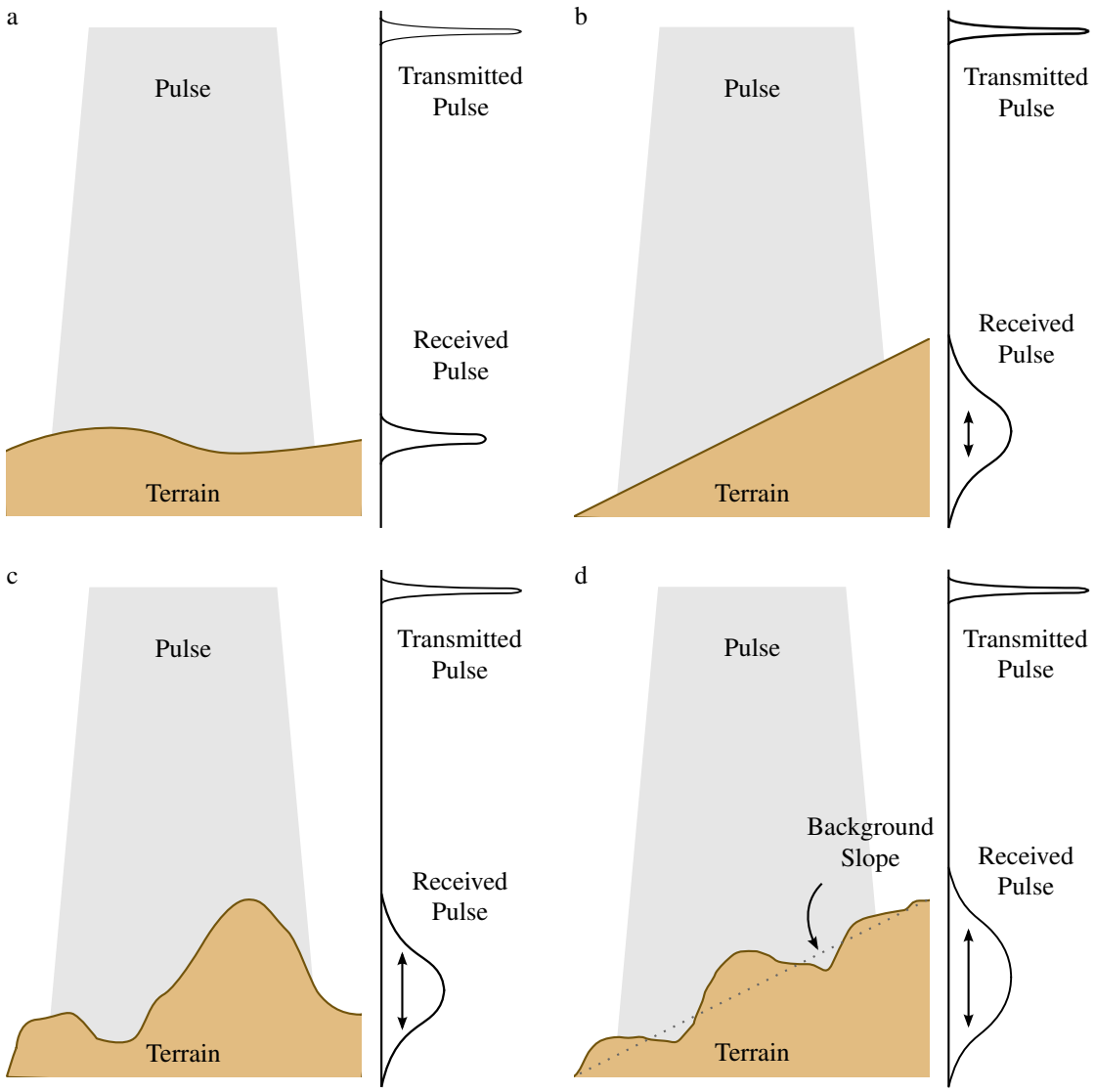

Figure 2.3: Schematic depicting the effects of surface roughness and slope within the pulse-footprint on the received pulse-width. (a) Gently undulating terrain results in a mild broadening of the σ_r compared to the transmitted pulse. (b) Smooth sloping terrain and (c) rough terrain result in a wider broadening, and (d) rough, sloping terrain causes the greatest pulse-width broadening. The pulse cross-section is shown in grey and the terrain in orange.

$$\sigma_x = 6.00 \text{ ns},$$
$$\sigma_f = 1.70 \text{ ns},$$
$$\sigma_b = 0.02 \text{ ns},$$
$$\sigma_t = 149.87 \text{ ns}.$$

On top of this, the final signal is subject to noise in the form of: (1) photon and speckle noise, (2) multiplication noise by the detector, (3) detector thermal noise, (4) and quantisation noise [*Gardner*, 1992]. The result will be natural variation within the return signal, which could result in a less than perfect correlation with surface characteristics within the pulse-footprint.

2.1.4 ATMOSPHERIC EFFECTS ON A LASER PULSE

As a laser pulse or beam propagates through an atmosphere it is attenuated as light is scattered by molecules, aerosols, and clouds. This effect is prevalent on both Mars, which has a thin atmosphere (0.6 kPa) containing clouds and dust, and Earth, which has a much thicker atmosphere and greater cloud cover and density (101.3 kPa). Scattering acts to broaden the pulse-width both by shortening the path-length, as photons are reflected back towards the detector before reaching the target surface, and increasing the path-length of photons that do reach the target surface, but are affected by single- and multiple-forward-scattering events (Figure 2.4). Although useful for measuring the cloud and aerosol distribution within an atmosphere from laser altimeters and lidar pulses, which can be used in weather forecasting and climate modelling, these effects impact negatively when the pulse-widths are to be used as an estimate of surface characteristics within the pulse-footprint. If the magnitude of these effects is known, the pulse-widths can be corrected, otherwise it is best to remove these pulses from the dataset [*Neumann et al.*, 2003a,b].

Figure 2.5 shows a schematic of pulse-width broadening for a single pass through a column of the atmosphere with three distinct cloud layers, from *Hogan* [2006]. The cloud layers are modelled

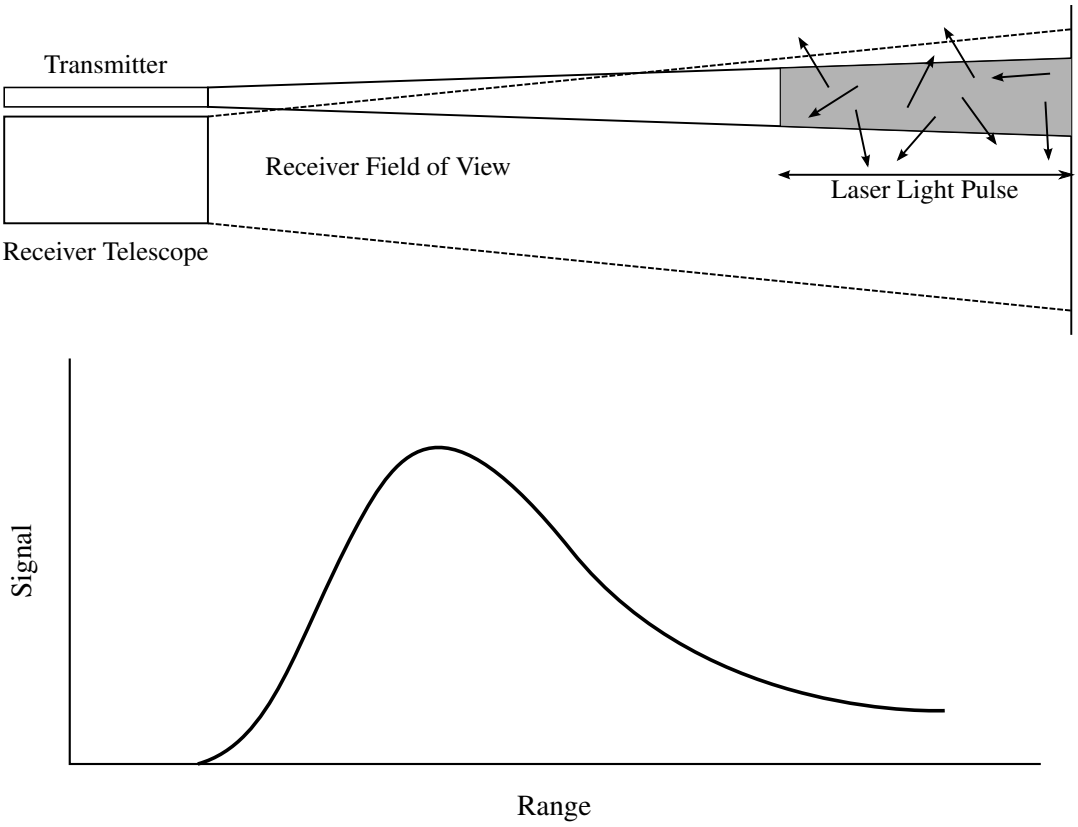

Figure 2.4: Schematic depicting atmospheric scattering of photons within a laser pulse and the resulting broadening of the received echo-profile. Photons scattered back towards the receiver have a shorter path-length than those reflected from the target surface, whilst photons that experience single- and multiple-forward-scattering have an increased path length, which cause the long-tailed distribution. Image reproduced from *National Oceanic and Atmospheric Administration* [No Date.a].

as infinitely thin and have an opacity, τ, of 0.69, such that: half the photons at *any* cloud layer pass through without being scattered; a quarter are forward-scattered to the next layer; and the remaining quarter are scattered away from the detector Field Of View (FOV), neglecting the small fraction that may be backscattered towards the detector. This is because

$$\tau = \ln\left[\frac{\phi_r}{\phi_t}\right] \qquad [2.8]$$

$$\therefore \ \frac{\phi_r}{\phi_t} = \exp^{\tau} = 2 \ (\tau = 0.69), \qquad [2.9]$$

where ϕ_r and ϕ_t are the received and transmitted intensities, respectively. The distributions at the top of the figure represent the effect on the pulse-profile at the ground. The figure shows single- and multiple-scattering events to have a significant effect on pulse-width, however, the measurable effect may be much smaller in real world situations where clouds are not infinitely thin, and background radiation and detector noise affects the echo-profile. For ICESat, multiple-scattering can increase photon path-length by tens of centimetres compared to ground-returns, a difference which is important considering the satellite's principal science goal is to observe changes in ice sheet elevation, and sea ice volume and extent [*Duda et al.*, 2001].

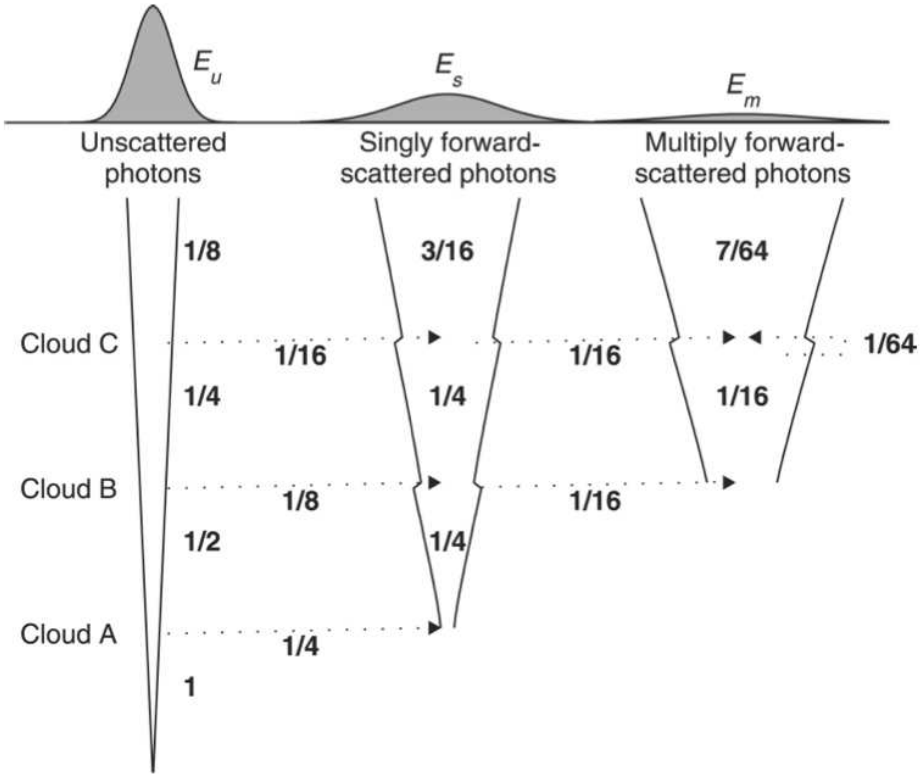

Figure 2.5: Schematic representing the proportion of energy in laser pulse passing through a column of atmosphere unscattered and forward-scattered from three infinitely thin cloud layers that each have an opacity of 0.69, from *Hogan* [2006]. The plots represent the resulting energy profile from unscattered, single-scattered, and multiple-scattered light after one pass through the atmosphere. Scattering not only acts to broaden the pulse-width, but reduces the intensity of light compared to the unscattered profile.

Light extinction refers to those photons that are scattered away from the FOV of the detector and those absorbed by molecules in the atmosphere. In reality, most of the transmitted pulse is lost in this way, which reduces the intensity of the return signal. Using Operation 2A of the ICESat mission, the mean transmitted energy over the study site used in Chapter 5 is 0.07 J, whilst the equivalent mean received energy is 1.21×10^{-14} J. This translates to a transmitted pulse of 3.76×10^{17} photons and a return of 65×10^{3} photons, which will further affect the quality of the return signal. The lidar equation attempts to relate the total number of received photon counts, N_S, to the total transmitted laser photon counts, N_L, by

$$N_S(\lambda, R) = N_L(\lambda_L) . P_{\text{Scatter}} . P_{\text{Collected}} . T_{\text{Total}} . E_{\text{eff}} + N_B \Delta t, \quad [2.10]$$

where P_S is the probability of a photon being scattered, P_C is the probability of a scattered photon being collected by the receiver telescope, T_{Total} is the total transmitted light transmission during laser pulse propagation, E_{eff} is the laser system efficiency, N_B is the background noise count, and Δt is the time bin [*Fujii and Fukuchi*, 2005].

Each of the components in Equation 2.10 can be generalised by the following set of equations

$$N_L = \left[\frac{P_L(\lambda_L)\, \Delta t}{h \nu_L} \right], \quad [2.11]$$

$$P_{\text{Scatter}} = \left[B(\lambda, \lambda_L, R)\, \Delta R \right], \quad [2.12]$$

$$P_{\text{Collected}} = \left[\frac{A}{R^2} \right], \quad [2.13]$$

$$T_{\text{Total}} = \left[T_{Light}(\lambda_L, R)\, T_{Light}(\lambda, R) \right], \quad [2.14]$$

$$= \exp\left[-\left(\int_0^R \alpha(\lambda_L, R)\, dR + \int_0^R \alpha(\lambda, R)\, dR \right) \right], \quad [2.15]$$

$$= \exp\left[-2 \int_0^R \alpha(\lambda, R')\, dR' \right] \rightarrow \text{ when } \lambda = \lambda_L, \quad [2.16]$$

$$E_{\text{Efficiency}} = \left[\eta(\lambda, \lambda_L)\, G(R) \right]. \quad [2.17]$$

In these equations: P_L is the laser power; λ_L is the laser wavelength; B is the volume backscatter coefficient; ΔR is the range bin; A is the area of the footprint; T_{Light} is the atmospheric transmittance at λ_L or another λ; α is the extinction coefficient; η is the optical efficiency of the system; and G is the geometric form factor.

This is a general form of the lidar equation, which is used for remote sensing of the lower atmosphere, and assumes only elastic scattering where there is no change in wavelength of the light, as in Equation 2.16. Other forms of the lidar equation exist for different lidar types, such as aerosol, differential absorption, and Raman lidar, which are used for exploring aerosol distributions, reflectance and gas concentrations, and atmospheric light extinction and water vapour distribution, respectively [*Fujii and Fukuchi*, 2005].

In an atmosphere, both elastic and inelastic scattering from atoms, molecules, and particles can affect photons within a pulse. Rayleigh and Mie scattering are forms of elastic scattering, whereby

the kinetic energy of a photon and incident molecule, or particle, is conserved. Scattered photon energy may only change as a result of Doppler effects, caused by the relative velocity of these atoms and molecules along the photon travel direction. Rayleigh scattering occurs when the scattering particle is much smaller than the wavelength of the light, which here is $\sim$1 µm, with atoms typically on the order of 10^{-10} m (1 Å). Rayleigh scattering intensity is proportional to λ^{-4} and therefore has a strong dependence on the wavelength of incident light, whereby shorter wavelengths are scattered more readily than longer ones, and the energy scattered isotropically. Mie scattering however, occurs when a photon encounters a particle of similar size to its wavelength. In this case the energy is not distributed isotropically, instead it is preferentially forward-scattered, an effect that is enhanced with increasing particle size. Finally, inelastic scattering of laser pulses refers to Raman scattering, whereby the total kinetic energy of the photon and scattering particle is not conserved, here the atomic states of the particle or molecule are changed, and the scattered photon has a different wavelength to that emitted from the laser.

2.1.5 BEAM DIVERGENCE AND ENERGY DISTRIBUTION

The cross-section of the transmitted pulse increases with distance from the laser aperture, an effect called beam divergence that is caused by diffraction. Diffraction is the spreading out of wave-fronts as they pass by an object or through an aperture, and can be described by the Huygens Principle, which states that every point on a wavefront can be considered a source of secondary wavelets [*Feynman et al.*, 2006, Lectures: 26 and 30]. These wavelets experience both constructive

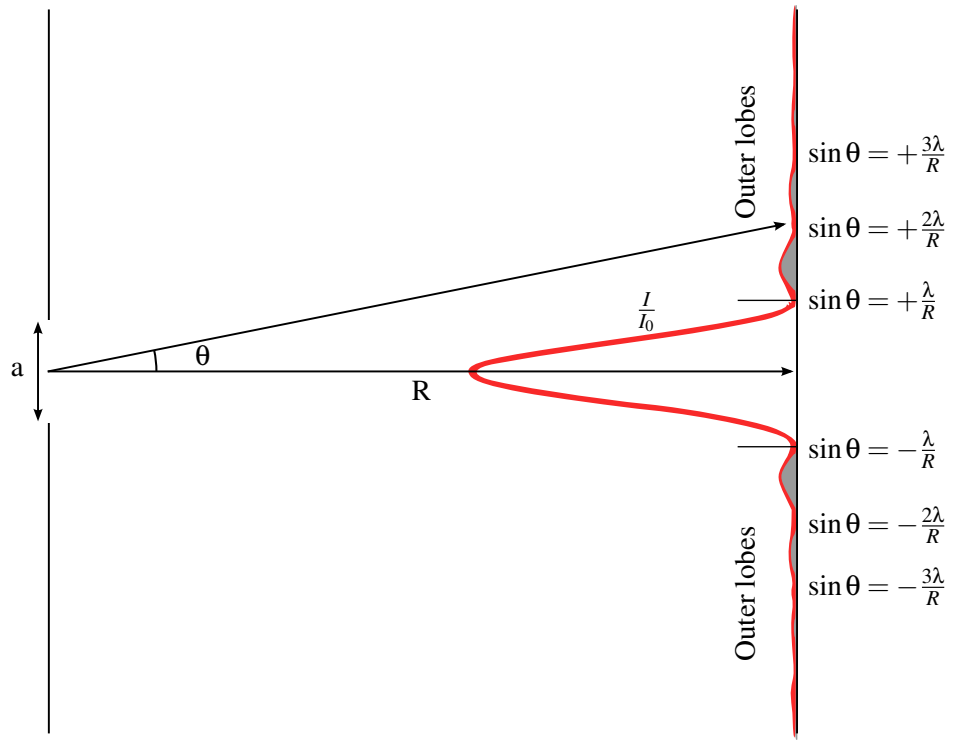

Figure 2.6: Schematic of the diffraction pattern of light passing through a single slit. Regions of constructive and destructive interference are shown, but only the central peak is considered significant, whilst the energy within the outer lobes is considered negligible.

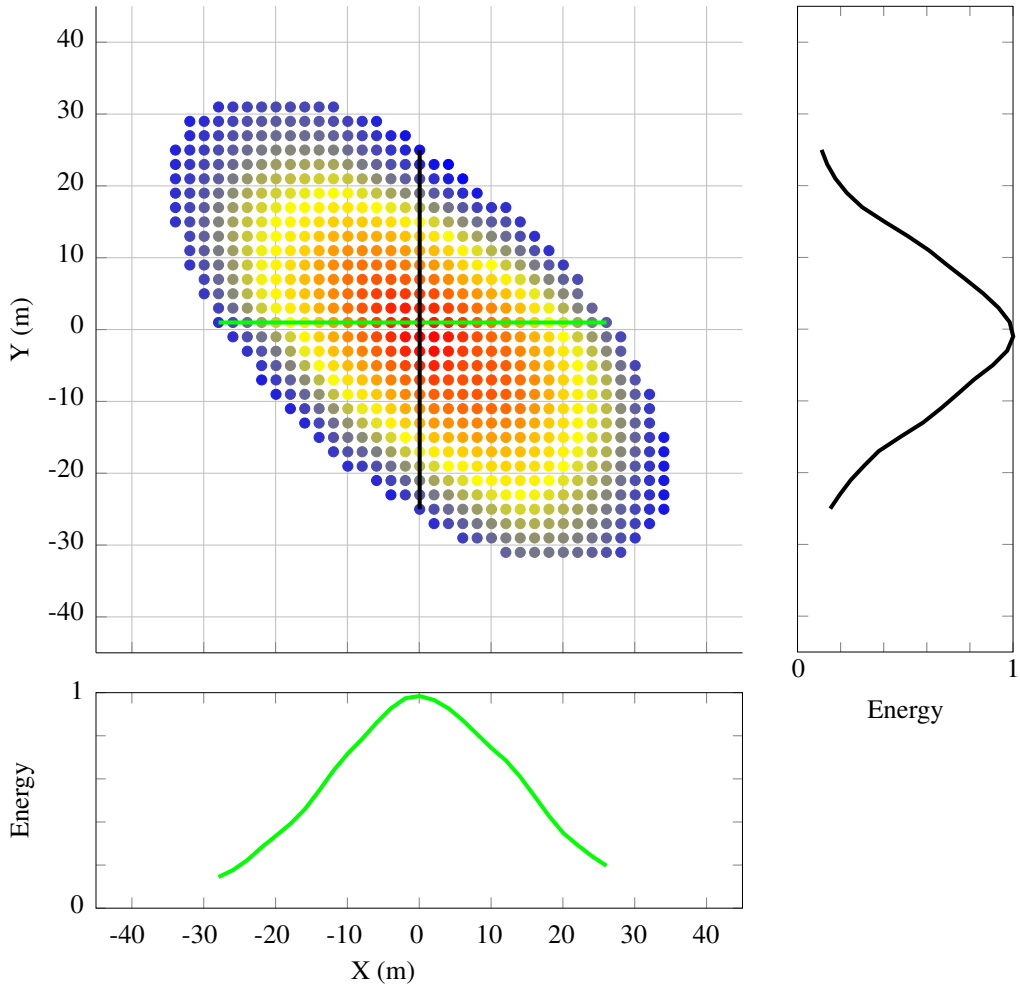

Figure 2.7: Plots of transmitted energy distribution across an example ICESat pulse and energy profiles across the pulse in the horizontal and vertical axes. Red shows peak energy, and blue shows the e^{-2} peak energy, which is chosen as the cutoff threshold for the ICESat pulse-footprint extent, other instruments may use e^{-1} [*Harding and Carabajal*, 2005]. Transects in green and black show the energy distribution across the pulse, with the energy shown relative to peak energy at the centre of the pulse.

and destructive interference to form a diffraction pattern on the target surface, as in Figure 2.6. In single-slit diffraction, which applies to the transmission of laser beams, the interference pattern appears as a central region of high intensity surrounded by rings, or lobes, of much lower intensity (Figure 2.6). As laser beam divergence is small, a paraxial approximation can be applied, meaning the cross-sectional energy distribution can be assumed to be Gaussian and only the 0^{th} order constructive interference pattern, shown as the central high-intensity region in Figure 2.6, is assumed to be significant [*Siegman*, 1986]. It is this 0^{th} order constructive interference pattern that is given as the pulse-footprint.

The central spot diameter, q, of the beam at a distance, R, from the laser can be calculated from the beam-waist, q_0, Rayleigh range, R_z, and the wavelength of the transmitted light by

$$q(R) = q_0 \sqrt{1 + \left(\frac{R}{R_z}\right)^2}. \qquad [2.18]$$

The beam-waist is defined as the narrowest width of the beam, whilst the Rayleigh range is the distance required for the beam diameter to double in diameter from the beam-waist [*Svelto*, 2010, p 131- 161], and is given as

$$R_z = \frac{\pi q_o^2}{\lambda}. \qquad [2.19]$$

These equations can be used to calculate the expected pulse-footprint at a particular orbiting height.

The energy distribution across the pulse-footprint due to divergence effects is given by

$$E_{ra} = E_0 \frac{q_0}{q(R)} \exp\left(\frac{-r_a^2}{q(R^2)} - ik_n R - ik_n \frac{r_a^2}{2r_c(z)} + i\zeta(z)\right), \qquad [2.20]$$

where E_0 is the transmitter energy, i is the imaginary number ($i = \sqrt{-1}$), r_a is the distance from the centre of the pulse-footprint, r_c is the radius of curvature, and ζ is the Gouy phase shift, an additional contribution that applies only to Gaussian beams [*Svelto*, 2010, p 131- 161]. In practise, this causes an effect known as *hot-spotting*, which describes the concentration of energy (and therefore photons) towards the centre of the pulse-footprint [*Siegman*, 1986]. Figure 2.7 shows the distribution within a typical ICESat pulse-footprint, relative to peak energy found at the centre of the pulse: the elliptical pulse-footprint is generated by the laser pointing geometry. This energy distribution pattern suggests the resulting echo-profile will be more representative of the terrain in the central region of the pulse-footprint, shown in red, than terrain near the edge of the pulse-footprint. The profile plots to the right and bottom of Figure 2.7 show the energy profile to be approximately Gaussian along transects shown in the main plot, relative to the peak energy. This energy distribution can be accounted for when calculating surface characteristics, provided a high enough DTM resolution, within the pulse-footprint by applying a weighting. More commonly, it is assumed that only the terrain within the central half of the pulse-footprint contributes to the σ_r, where up to 90 % of the energy is thought to be concentrated [*Kreslavsky et al.*, 2013; *Smith et al.*, 2001, 2010a,b; *Neumann et al.*, 2003a].

2.1.6 REFLECTED ENERGY DISTRIBUTION

The final factor to be aware of regarding laser altimeter elevation and pulse-width measurements is the distribution of reflected energy from a target surface. Natural terrains are typically considered Lambertian, or diffuse, surfaces, such that incident energy is reflected almost isotropically from the surface, whilst wet surfaces cause specular reflection [*Acharya and Ray*, 2005; *Brenner et al.*, 2011; *Gardner*, 1992; *Kwok et al.*, 2006, 2007; *Shan and Toth*, 2009]. The intensity of light reflected from Lambertian surfaces, I_L, appears approximately similar across a wide range of viewing angles, following Lambert's cosine law for an ideal diffuse reflector [*Acharya and Ray*, 2005, Page: 20]

$$I_L = E_0 A \cos(\theta). \qquad [2.21]$$

Specular surfaces on the other hand, reflect light perfectly at an angle equal, but opposite to the angle of incidence with respect to nadir (Figure 2.8). In practice, no surfaces are perfectly Lambertian or

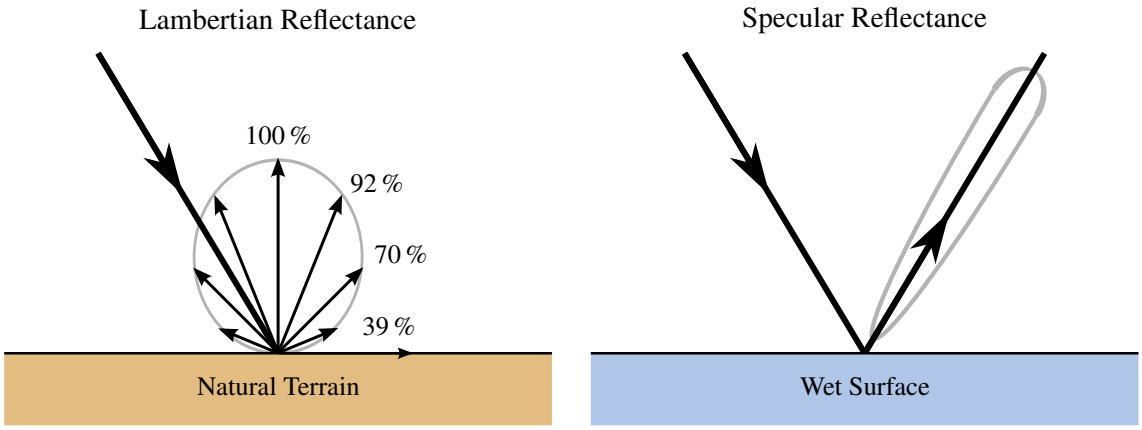

Figure 2.8: Schematic of Lambertian and Specular reflectance from typical terrain and wet surfaces, respectively. Reflectance from Lambertian surfaces appears at similar intensities for most viewing angles, whilst specular surfaces perfectly reflect incident light. The Lambertian schematic shows the relative intensity compared to light reflected at nadir for 22.5°, 45° and 67.5° (from top to bottom) viewing angles; whilst the grey region in the specular reflectance schematic depicts the more typical distribution of reflected light due to small roughness features, such as waves, upon a specular surface. Most surfaces exhibit both of these behaviours, but at different proportions.

specular, instead surfaces exhibit properties of both, with the relative magnitude of each component dependent on surface composition and roughness [*Acharya and Ray*, 2005, Page: 20].

A result of these reflection behaviours is that off-nadir viewing angles of laser altimeter and lidar systems on specular surfaces may result in energy being reflected away from the instrument FOV. Over Lambertian surfaces a significant proportion of the transmitted energy will be lost relative to the received energy, even at nadir angles; the advantage being that the received energy will remain similar over a range of viewing angles [*Brenner et al.*, 2011; *Gardner*, 1992; *Kwok et al.*, 2006, 2007; *Shan and Toth*, 2009]. The received energy of a transmitted pulse over a Lambertian surface can be approximated to [*Shan and Toth*, 2009]

$$E_R = \rho \frac{M^2 A_R}{2\pi R^2} E_0, \qquad [2.22]$$

where ρ is the surface reflectivity, M is the atmospheric transmission, and A_R is the area of the receiver telescope. For an orbiting laser altimeter at 300 km, with a 1 m receiver telescope and a transmitted pulse energy of 50 mJ, the received energy is $\sim 2.22 \times 10^{-14}$ J, assuming an atmospheric transmission factor of 0.8 and a surface reflectivity of 0.5, typical for bare-earth terrains, a result that is similar to the ICESat example above.

In this thesis, most of the study sites are bare-earth terrains, which can be assumed to be Lambertian surfaces. Only in Chapter 5, where approximately two-thirds of the pulses used are over icy terrain, could specular reflection cause complications. However, even over icy surfaces, specular reflection is only considered to occur over very smooth waters, grease ice, and smooth ice types in open leads in sea ice. The ICESat data used in Chapter 5 are taken over ice sheets and glacial terrains, which are typically rough and therefore can still be considered as Lambertian surfaces [*Brenner et al.*, 2011; *Gardner*, 1992; *Kwok et al.*, 2006, 2007].

2.1.7 MEASURING SURFACE ROUGHNESS IN INDUSTRY USING LASERS

Lasers are also used for measuring fine-scale (0.01 µm to 10 µm) surface roughness of manufactured surfaces. Here, two techniques are typically applied [*Laser Check*, 2015; *Olympus*].

One method uses a small footprint laser moving across a surface, measuring continuously so that it produces a profile of the surface in much the same way a laser altimeter produces an elevation profile of a planets surface, as shown in Figure 2.9. This method is an adaption of the profile method, which typically uses a solid contact with the surface using a stylus, which moves up and down with the surface as the stylus is dragged across, to produce a profile. From this profile surface roughness can then be calculated. The advantages to using a laser are that (1) the surface is not damaged in the process, (2) the profiles can be made in 2-dimensions as well as along single profiles, and (3) the laser footprint can be made much smaller (0.2 µm) than the tip of the stylus (2 µm to 10 µm), enabling much finer scale surface roughness to be measured [*Olympus*].

Another method uses the intensity of laser scatter to determine the roughness of a surface, as shown in Figure 2.9 [*Laser Check*, 2015]. Here, a laser pulse is focussed onto the surface, where it is reflected. Some of this reflected light will be specularly reflected, as discussed above, resulting in a peak intensity opposite to the angle of incidence. However, much of the light from a rough surface will be scattered at different angles, as in Lambertian reflection. Software is then used to relate the intensity of scattered light at different angles to the surface roughness of the material [*Laser Check*, 2015]. The advantage to this method is that it can be applied at single points across a surface, rather than having to be calculated using profiles, and that it can be completed very quickly, in fractions of a second.

In industry, surface roughness is typically calculated using the arithmetic average, R_a, which is given as

$$R_a = \frac{1}{n}\sum_{i=1}^{n}\left(z(x_i) - \bar{z}\right), \qquad [2.23]$$

where n is the number of points, $z(x_i)$ is the elevation at point x_i, and $\bar{z}$ is the mean profile elevation.

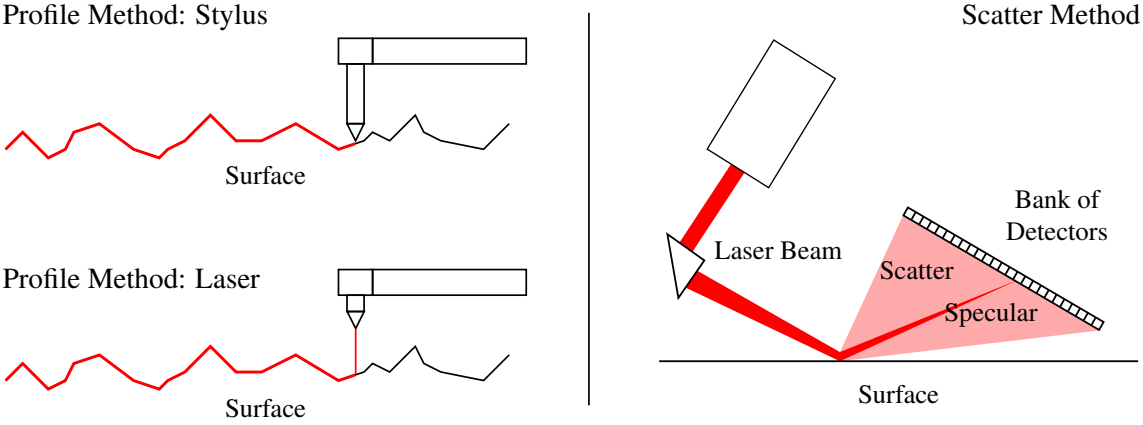

Figure 2.9: Schematic showing two methods of measuring surface roughness in manufacturing. Left: how surface roughness is calculated along profiles, with the top schematic showing a solid contact with a stylus and the below, showing non-contact, laser, method [*Olympus*]. Right: a schematic of how surface roughness is measured using laser scattering [*Laser Check*, 2015].

2.2 DIGITAL TERRAIN MODELS

2.2.1 INTRODUCTION

This section describes the background theory regarding how the DTMs used in this thesis are produced using stereo-photogrammetry and airborne scanning lidar, and concludes with an introduction to reference surfaces and the coordinate system transformation used in Chapter 5. Like the preceding section, descriptions of the instruments are found in the appropriate science chapters.

2.2.2 STEREO-PHOTOGRAMMETRY

Stereo-photogrammetry uses two or more overlapping images, taken at different viewing angles, to produce 3-dimensional models of surfaces or objects within an image-set. It is used here to produce the DTMs used in Chapters 3 and 4, but can also be used in computer vision, manufacturing, and surveying.

2.2.2.1 DERIVING HEIGHTS

The underlying principle is to use the apparent change in position, known as the parallax, of corresponding points in stereo-images to measure the range, with points closer to the camera positions having a greater parallax. A schematic of how surface elevation is derived from ideal geometry is shown in Figure 2.10, from which the following equations are derived

$$h_j = h_c - \frac{b_c f}{p_j}, \tag{2.24}$$

$$= \frac{h_c.P_j}{b_c + P_j}, \tag{2.25}$$

where h_p is the height of the point above the reference surface, h_c is the height of the camera above the reference surface, p_j is the parallax at point j, b_c is the distance between the cameras, known as the base, f is the focal length of the cameras, and P_j is the reference surface parallax [*Lillesand et al.*, 2008]. The parallax is

$$p_j = x_j^1 + x_j^2, \tag{2.26}$$

where x_j^1 and x_j^2 are the position of point j in each image, as shown in Figure 2.10.

More commonly, the relative heights, Δh, between two points is required, given as [*Lillesand et al.*, 2008]

$$\begin{aligned} \Delta h &= h_i - h_j, \\ &= \frac{(h_c - h_j)\,\Delta p}{p_j + \Delta p}, \end{aligned} \tag{2.27}$$

where h_i and h_j are the heights at point i and j respectively, p_j is the parallax at point j, and Δp is the difference between p_j and p_i, the parallax at point i (Figure 2.10).

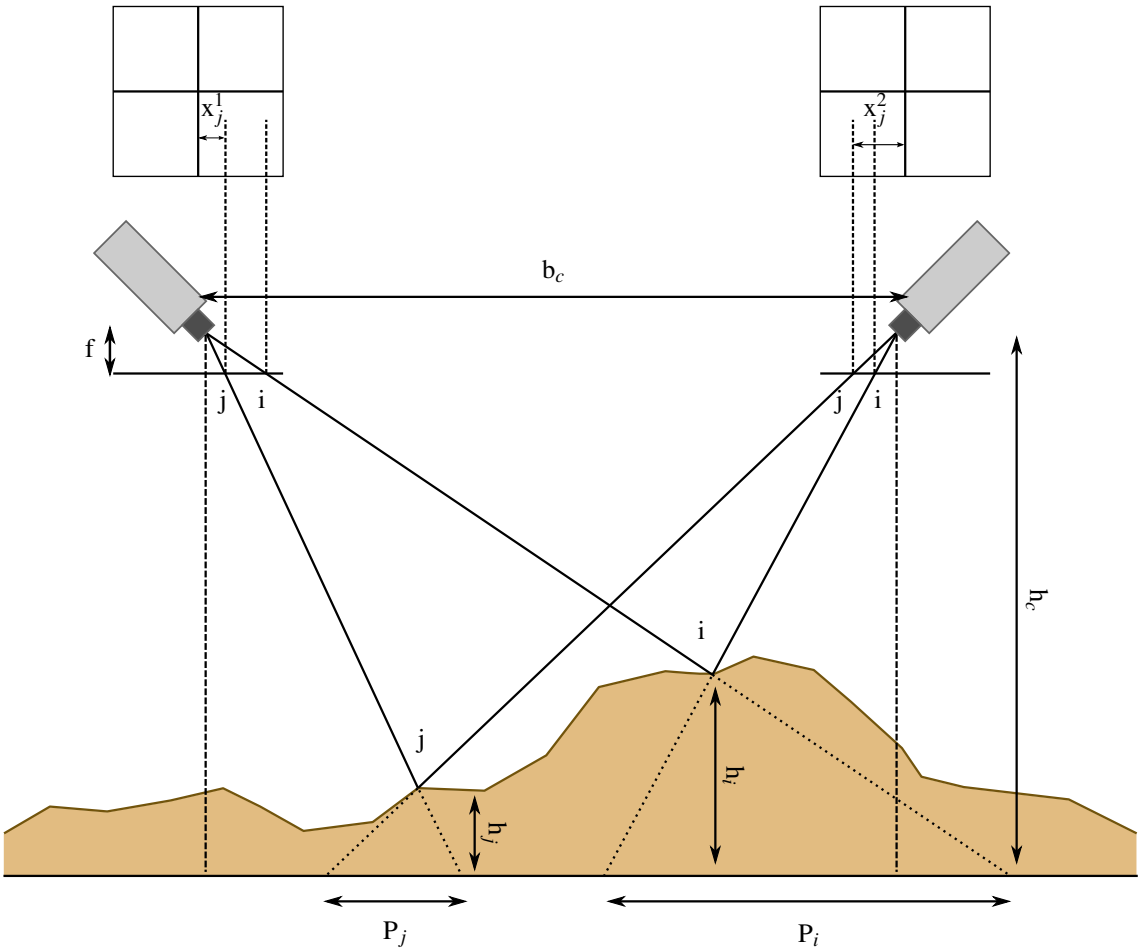

Figure 2.10: Schematic showing how the parallax equations, Equations 2.24 and 2.26, are derived from similar triangles in stereo-imagery [*Lillesand et al.*, 2008]. Image frames are shown at the top with the apparent position of point *j* shown. Heights are measured above a reference surface.

A factor that affects the quality of the resulting height estimates is the base-to-height ratio. *Hasegawa et al.* [2000] observe a base-to-height ratio between 0.5 and 1.0 produces good quality DTMs. To determine elevation accuracy, h_{acc}, this ratio is multiplied by the stereo-matching accuracy, M_{acc}, such that [*Seiz et al.*, 2007]

$$h_{acc} = \frac{h_c M_{acc}}{b_c}. \qquad [2.28]$$

Using the characteristics of High Resolution Imaging Science Experiment (HiRISE), described in Chapter 3, as an example, the resulting DTMs have a height accuracy of $\geq$0.14 m, assuming: 0.25 m pixel^{-1} images, M_{acc} of 0.2 pixels, h_c of 300 km, and a stereo-angle of 20°, resulting in a base-to-height ratio of 0.3 to 0.4 [*Kirk et al.*, 2008].

In terrain mapping, these heights are measured relative to a reference height so the resulting DTMs can be placed in a 3-dimensionally defined position. Further refinements to DTM elevation values can be made by bundle adjustment, whereby the DTM is rotated and shifted in 3-axes and 3-dimensions to *best-fit* a lower resolution elevation basemap [*Gwinner et al.*, 2009]. Different methods can be employed to determine the best-fit, but a common method is to minimises the mean

difference in elevations [*Gwinner et al.*, 2009; *Kim and Muller*, 2009].

Finally, orthorectified images are produced using the original images and the DTM. Orthorectification corrects images for camera pointing angles and variations in terrain across the images, producing an image with consistent horizontal scale [*Lillesand et al.*, 2008]. A consistent scale across the image means these images create excellent basemaps, to which other data can be co-registered.

2.2.2.2 MATCHING ALGORITHMS

To produce a continuous dataset, the parallax, which is known as the disparity in computer vision, is calculated for each set of corresponding points found in stereo-images. These pairs of points are found by stereo-matching algorithms, which fall into one of three broad groups: feature-, local-, or global-based matching, depending upon their methods.

Feature matching algorithms attempt to find matching features in image-pairs, such as corners, edges, points, defined by sharp changes in contrast or colour. The images must be preprocessed to identify features by applying different operators, such as edge detectors. These features are then compared to features in the corresponding image to identify common, matching features. The parallax is found for each point in the matched features and interpolation is applied to estimate parallax values for regions between matching features. Typically, feature matching is less affected by image noise than local and global matching processes, described below, which depend on pixel intensity values [*Zhang et al.*, 2006].

Local matching algorithms, or window-based approaches, attempt to find corresponding points by matching a small window of pixels in one image to a moving window of pixels in another. As described in *Scharstein and Szeliski* [2002], local matching algorithms usually employ three distinct stages in the production of a disparity map: (1) matching cost computation, (2) cost aggregation, and (3) disparity computation. In (1), a metric, such as the squared difference of intensity values in the Sum-of-Squared Differences (SSD) algorithm, is compared in a reference image window to the moving window. This metric is applied at different disparities, defined by a disparity-range, and the results are assessed in the aggregation step, which often acts to smooth the aggregation costs, typically by averaging or summing, over a finite window [*Scharstein and Szeliski*, 2002]. Finally, the disparity is computed, for the SSD algorithm, this is the minimal aggregated value for each pixel in the overlapping image region.

Global matching algorithms attempt to apply a matching cost computation over the entire image, rather than localised windows, and typically skip the aggregation stage [*Scharstein and Szeliski*, 2002]. Here, the aim is to find the minimum cost for the sum of a data and smoothness function, the latter is used to ensure consistency across the dataset and is often applied by looking at neighbouring pixel disparities, whilst the data function is similar to that applied in the local matching techniques [*Scharstein and Szeliski*, 2002].

Each of these broad methods has advantages and disadvantages compared to the others, such as accuracy, computational time, and ease of use [*Scharstein and Szeliski*, 2002]. A full discussion on

the comparison between different stereo-matching algorithms is beyond the scope of this thesis, but a comparison is presented in *Scharstein and Szeliski* [2002]. Instead, the remainder of this section will focus on the algorithms used in this thesis.

The Context Camera (CTX), HiRISE, and Lunar Reconnaissance Orbiter Camera - Narrow Angle Camera (LROC-NAC) DTMs used in Chapters 3 and 4 are produced in SOftCopy Exploitation Toolkit (SOCET SET®) and use a combination of edge (feature) matching and local matching to produce a dense disparity map suitable for a range of terrains [*DeVenecia et al.*, 2007]. This strategy, termed Next-Generation Automatic Terrain Extraction (NGATE), is a development to the Adaptive Automatic Terrain Extraction (AATE) local matching algorithm that adaptively changes window sizes depending on local signal variation [*DeVenecia et al.*, 2007; *Zhang and Miller*, 1997; *Zhang et al.*, 2006]. In their work on adaptive window sizing, *Okutomi and Kanade* [1992] state two points to consider when using local matching

1. ...the variation of the signal within the window must be large enough, relative to the noise, that the SSD values exhibit a clear and sharp minimum at the correct disparity.

2. ...the variation of the disparity within the window, which must be small enough that signals of corresponding positions are duly compared.

A balance must be found between these two considerations, as increasing window sizes typically increases both the signal variation and the likelihood of points with different disparities being included within a window. Adaptive window sizing tries to find such a balance and has been shown to improve the elevation accuracy over difficult to match terrains [*Zhang et al.*, 2006].

In local based matching, discontinuities, such as roofs, are difficult to match as in practise they are linear features rather than areas. The NGATE strategy accounts for this by applying a feature based algorithm to the images to identify these features [*DeVenecia et al.*, 2007; *Zhang et al.*, 2006]. An iterative matching approach is applied whereby local matching is applied to regions between identified features, reducing the need for interpolation, and incorporated in such as a way as to assist the feature matching algorithms, and vice-versa [*DeVenecia et al.*, 2007; *Zhang et al.*, 2006].

Competing methods, such as those by *Kim and Muller* [2009], *Kim et al.* [2013] and others, have been applied to produce CTX, HiRISE, and High Resolution Stereo Camera (HRSC) DTMs, but are not used here [*Ivanov and Lorre*, 2002]. These algorithms apply the Adaptive Least Squares Correlation (ALSC) matcher from *Gruen and Baltsavias* [1986], with *Ivanov and Lorre* [2002] also employing a preliminary matcher from *Zitnick and Kanade* [2000] to produce a set of dense seed points for the ALSC matcher to use with a region-growing strategy starting from highest quality corresponding points from the preliminary matcher [*Otto and Chau*, 1989]. *Kim and Muller* [2009] and *Kim et al.* [2013] use iterative local matching, whereby matching is completed at successively smaller window sizes to produce more refined results that use matching points with the least noise. Data from larger windows are used as base data, which is used in the event that results from smaller window sizes produce pixel-to-pixel slopes of 45°.

Finally, the HRSC DTMs, which are used in Chapter 3, use a local matching scheme based on cross-correlation and least-squares sub-pixel adjustment [*Gwinner et al.*, 2009].

2.2.2.3 CHALLENGES OF STEREO-PHOTOGRAMMETRY

Greenfeld [1991] presents a useful outline of the problems that can affect stereo-matching quality, which affect all three stereo-matching groups. The problems relating to the type of terrains used in this thesis are shown in Table 2.1. To reduce some of these effects in terrain mapping, stereo-images should be acquired with minimum differences in time or season to minimise variation in atmospheric and lighting conditions that cause significant changes in image appearance in computer vision. Other challenges may be unavoidable, such as the geometric and textural problems highlighted in Table 2.1. Only by employing a more advanced and potentially more computationally expensive matching algorithm, may these effects be reduced.

Furthermore, high-resolution pushbroom imagers, such as CTX, HiRISE, and LROC-NAC used in Chapters 3 and 4, often suffer problems associated with camera geometry and methods [*Kim and Muller*, 2009; *Kirk et al.*, 2008]. For example, HiRISE images are composed of 20 individual strips from overlapping Charge Coupled Devices (CCDs) that must be stitched together to form a single image, whilst *jitter*, high frequency spacecraft oscillations, causes image distortions that must be corrected for in preprocessing [*Kim and Muller*, 2009; *Kim et al.*, 2013; *Kirk et al.*, 2008]. This jitter effect is less pronounced on CTX and LROC-NAC that operate at a lower resolution and altitude respectively.

Any of the effects in Table 2.1 can impact negatively on matching quality. Poorly matched regions can appear as pits and spikes due to sharp differences in elevation between neighbouring pixels, or heavily interpolated terrain where there are few or no matching points. These interpolated regions rely on neighbouring positive matches from which to estimate elevation, and typically occur over smooth terrains lacking in features or signal variation. The pits and spikes can be removed during blunder detection by applying a simple smoothing filter, such as applying a threshold for the variation within a window or maximum slope between neighbouring pixels, but large expanses of interpolated terrain should be masked out if reliable terrain information is vital to the study, as it is here [*Kim and Muller*, 2009; *Kirk et al.*, 2008]. More sophisticated blunder detection relies on increasing the redundancies in the matching points. This is applied in the NGATE strategy by computing the parallax of a pixel using at least two methods, with the more reliable result, or the result most similar to neighbourhood pixels, being chosen. NGATE also performs back matching, whereby the reference image and moving window image are swapped, thereby doubling the matching redundancy [*Zhang et al.*, 2006].

Stereo-matching can be very computationally expensive, which is especially dependent on the algorithm employed [*Scharstein and Szeliski*, 2002]. Rather than search for corresponding points across an entire image, it is often possible to place constraints on the maximum disparities that are likely to occur through some prior knowledge of camera pointing geometry and scene information, such as a low resolution DTM over the Region-Of-Interest (ROI) in terrain mapping. For example, in a 1000 pixel $\times$ 1000 pixel overlapping stereo region, the number of cost computations for each point is reduced from $\sim 10^6$ computations to 100, if it is known that the maximum disparity in the images, or in that region of the images, is $\leq$10 pixels.

Table 2.1: An outline of the relevant problems that can affect stereo-matching quality for images over bare-earth terrains, from *Greenfeld* [1991].

Problem	Issues
Photometric	Resolution due to atmospheric conditions and the camera's optics quality (especially in the comer of the image frame). The corresponding images will have different sharpness (a low pass filtering effect on one image only).
	Reflectance such as sparkling of water bodies.
	Illumination. Effect of the sun's angle and strength of illumination due to partial cloudiness.
	Foreshortened effect. Elements smaller than pixel size which change the value of the sampled gray level.
	Digital camera radiometric calibration differences (integration time, gray level range definition, exposure setting, etc.).
	Digital camera noise during image digitization.
Geometric	Relief displacement and occluded areas.
	Projective deformation.
	Scale variation due to changes in the distance between the camera and the recorded object.
	Base to height ratio. The smaller this ratio, the less the effect of geometric distortions; however, the height determination is weakened and vice versa.
Textural	Existence of distinguishable structures. Featureless surfaces such as ice sheets, sand, and man-made objects such as runways are extremely difficult to match (if possible at all).
	Repetitive texture such as roofs, marked parking lots, ploughed fields, etc.
	Hanging surfaces such as multi-level highway intersections.
	Ambiguous levels such as tree tops and the ground below them. - Thin objects, which are one pixel wide, may be represented differently in the pixel grid (stair case effect).

To further reduce the computation time in stereo-matching, the matching problem can be reduced to a 1-dimensional search along epipolar lines, as defined in Figure 2.11, produced through epipolar-rectification, also known as epipolar-resampling. Here, images are projecting into a common image plane, often the projection plane of one of the images, by rotating an image to align features, and stretching an image to match pixel sizes. Using the example above, whereby the elevation constraints reduce the search for each corresponding point to 10 pixels, the potential number of cost computations reduces from 100 to 10. Two methods are used to find a suitable epipolarity model: (1) use precise knowledge of camera location and orientation, and a suitable camera/sensor model, to apply a transform to project the images into a common plane; (2) use image correspondence [*Wang et al.*, 2011]. For pushbroom cameras, such as the HiRISE and LROC-NAC, epipolar curves, rather than lines are produced [*Kim*, 2000].

Erroneous stereo-matches can be identified by studying the distribution of the magnitudes of

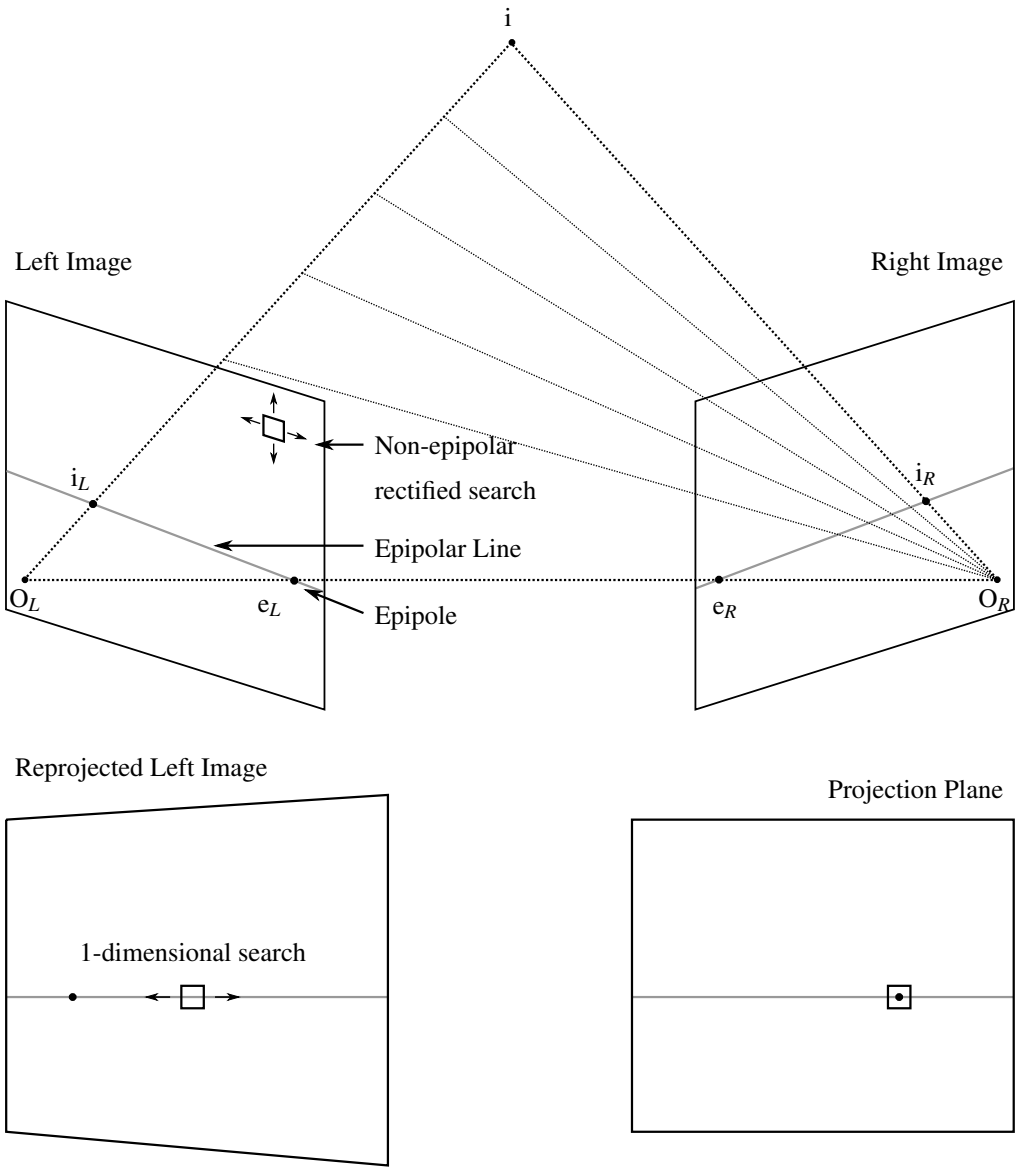

Figure 2.11: A schematic of epipolar rectification of stereo-pairs. Rather than searching for matching points in the entire image, which can be many millions of pixels, images can be projected into a common frame such that the search is reduced to a 1-dimensional problem, searching along the epipolar plane. This plane is defined by lines drawn between the centre of the projections in the left and right images, O_L and O_R, and point i.

the matching vectors produced by plotting stereo-images adjacently. Vectors of positive matches will generally appear similar in direction and path length, whilst negative matches may vary in direction and path lengths, dependent upon the disparity constraints. Another method is to use the Root-Mean-Square (RMS)-error from a previous elevation model used as a basemap, setting a threshold to determine the maximum allowed difference between the new DTM and the basemap, above which one can safely assume to be an erroneous value [*Scharstein and Szeliski*, 2002].

Finally, there is a limit to the resolution of the resulting DTMs, which are typically produced at between 3 to 4 times the resolution of the original images (i.e. original HiRISE images are 0.25 m pixel^{-1} and resulting DTMs are at 1 m pixel^{-1}). This is related to the size of objects capable

of being resolved in imagery, which is typically 3 pixels to 4 pixels across [*Kirk et al.*, 2008; *Gwinner et al.*, 2010; *McEwen et al.*, 2007, 2010].

2.2.3 LIDAR

Like laser altimeters, lidar instruments use photon TOF measurements to determine the range to an object or surface, as described in Section 2.1.2. This section focusses on the characteristics of airborne lidar instruments used in high-resolution terrain mapping, such as the Airborne Topographic Mapper (ATM), which is used in Chapter 5 [*Shan and Toth*, 2009].

2.2.3.1 LIDAR SYSTEMS

Airborne lidar systems typically use pulsed Nd:YAG lasers, similarly to laser altimeter systems, as these produce 1064 nm wavelength light, which is not attenuated by absorption in the atmosphere [*Shan and Toth*, 2009]. Recording the echo-profile enables the aerosol and vegetation distribution to be derived, but can also be used in the processing stage to identify the true ground return for a more accurate range measurement [*Fujii and Fukuchi*, 2005; *Shan and Toth*, 2009]. The recording of the full echo-profile is facilitated by the fact that large amounts of data can be

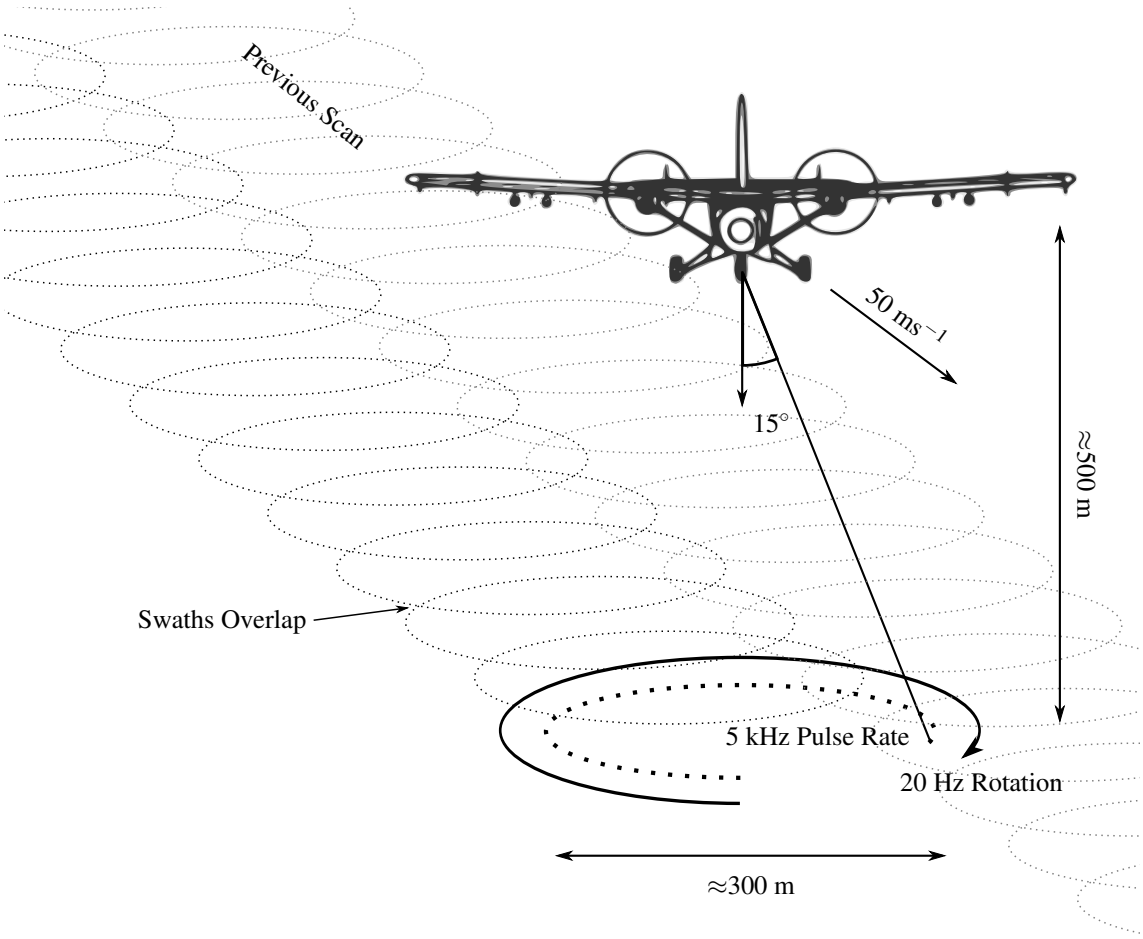

Figure 2.12: Schematic of ATM data collection, showing the direction of travel, overlapping swathes, and rotational scanning of the instrument.

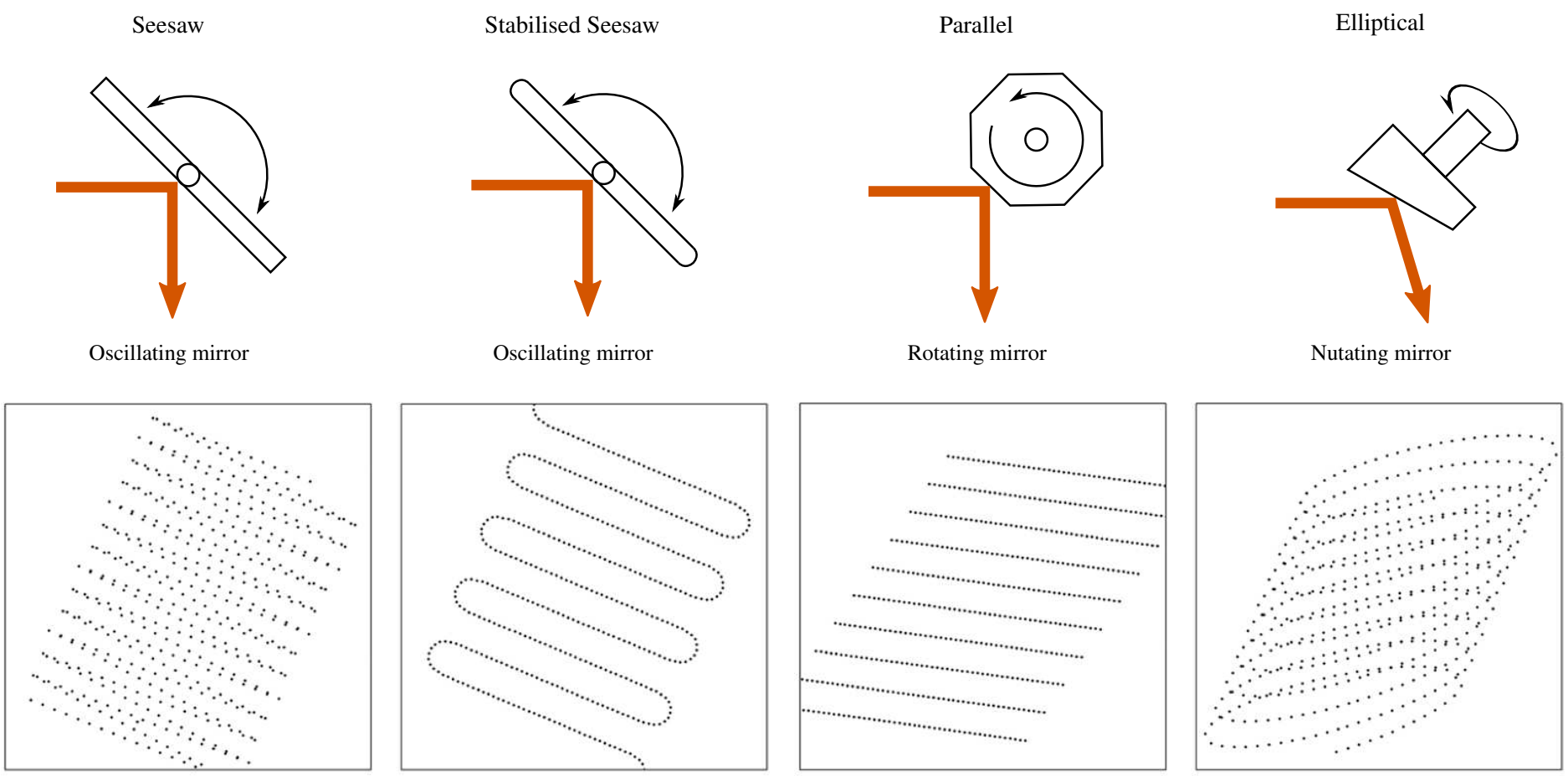

Figure 2.13: Schematic of the different scanning patterns from scanning lidar, modified from *Brenner* [2006] and *Gatziolis and Andersen* [2008]. These scanning methods are designed to increase the spatial coverage of data along each flight path by using oscillating or rotating mirrors.

stored without the need for transmission, as is the case for planetary laser altimeters. Fine-scale mapping is conducted at altitudes of 100's of metres and wider scale mapping at several kilometres, with DTMs typically produced from parallel or overlapping flight paths [*Shan and Toth*, 2009]. The smaller ranging distances allow lidar to operate using smaller pulse energies and receiver telescopes compared to space-borne systems, whilst also enabling higher pulse-rates due to the reduced photon TOF (1.67×10^{-6} s at 500 m as in Figure 2.13), which can produce a denser dataset [*Shan and Toth*, 2009].

To fully utilise the greater pulse-rates, lidar systems often use scanning techniques to divert pulses across a swathe, thereby increasing the spatial extent of data retrieved from each flight path [*Fujii and Fukuchi*, 2005; *Shan and Toth*, 2009]. High-speed scanning mechanisms typically use two mirrors to make rapid changes to the beam direction in 2-dimensions [*Shan and Toth*, 2009]. Examples of different swathe patterns, such as elliptical, parallel, and seesaw, are presented in Figure 2.12 and Figure 2.13. With the exception of the parallel swathe pattern, these patterns produce a dense irregularly spaced point cloud, which can then be converted to raster datasets [*Fujii and Fukuchi*, 2005; *Gatziolis and Andersen*, 2008]. The ATM, used in Chapter 5, employs an elliptical scanning pattern, which is produced by circular rotation of the laser beam and the forward motion of the aircraft (Figure 2.12). Swathe width is dependent on instrument altitude and the scanning angle, but is typically on the order of 100's of metres for instruments conducting high-resolution mapping [*Csatho et al.*, 2005; *Shan and Toth*, 2009]. Flying at lower altitudes, narrowing the scanning angle, and decreasing the flight speed increases the data density but may increase time - the first two reduce the swathe width - and cost for collecting data. Lower altitudes also results in a smaller pulse-footprint ($\sim$1 m), which produces more accurate elevation measurements due to lower topographic variation within the pulse-footprint [*Shan and Toth*, 2009].

On-board Global Positioning Systems (GPS), Inertial Measuring Units (IMU), and Inertial Navigation Systems (INS) ensure centimetre accuracy for geolocation and altitude of the lidar instrument, which results in a highly precise, well geolocated 3-dimension model of the surface [*Csatho et al.*, 2005]. Using ground based differential GPS systems at the mapping location can further improve the geolocation and elevation accuracy of the instrument and the resulting DTM [*Shan and Toth*, 2009]. Higher timing resolution receivers, compared to orbiting laser altimeters, improve the accuracy of range measurements. The RMS-error for data from lidar is typically 15 cm using the ranges described above, which is better than the accuracy derived from orbiting instrument stereo-pairs [*Liu*, 2008; *Shan and Toth*, 2009]. However, poor data is a common occurrence, with some pulses reporting anomalously high terrain as a result of strong atmospheric backscatter triggering the receiver; these data can be removed during blunder detection using methods described above, such as a median filter, to the data [*Csatho et al.*, 2005; *Liu*, 2008; *Meng et al.*, 2010; *Shan and Toth*, 2009]. Interpolation methods are then used to fill data gaps and produce a continuous dataset from the irregular point cloud. Systematic errors are more complex, such as ensuring consistent elevations across overlapping flight paths and correcting errors that may arise through bundle adjustment, described above [*Csatho et al.*, 2005].

2.2.3.2 COMPARING LIDAR AND STEREO-PHOTOGRAMMETRY

A commonly assumed disadvantage to using lidar technology for high-resolution mapping is the financial cost compared to stereo-photogrammetry [*Gatziolis and Andersen*, 2008; *Shan and Toth*, 2009; *Thompson and Maune*, 2002; *Toth and Grejner-Brzezinska*, 2000]. In fact, when elevation post spacings of $\leq$0.66 m (0.44 m^2 $pixel^{-1}$) are required, lidar becomes a cost-effective method of deriving elevation data, whilst for spacings $\geq$1.66 m (2.76 m^2 $pixel^{-1}$), stereo-photogrammetry offers a cheaper alternative: the cross-over point occurs at some point between and depends on the surveying region and technology [*Thompson and Maune*, 2002].

DTM accuracy from lidar is less dependent on the instrument range, whereas the accuracy is inversely proportional to instrument altitude for stereo-photogrammetry. Instead, lidar DTM accuracy is more dependent on the instrument timing resolution, instrument setup, and weather conditions: optically thick cloud and fog causes scattering that may be recorded as a surface. In general, lidar improves the regularity of data points, reducing the need for interpolation over large areas. However, aerial stereo-photogrammetry typically produces more data points due to higher pixel density compared to lidar points, the drawback being that stereo-matched pixels may not be evenly distributed across a ROI, such as over smooth, featureless terrain [*Scharstein and Szeliski*, 2002]. For both dataset types, applying smoothing filters across the data can reduce the visual impact of errors in a dataset [*Scharstein and Szeliski*, 2002]. In practice this also introduces errors to pixel values that were otherwise correct [*Scharstein and Szeliski*, 2002].

Lidar data acquisition times are longer when producing datasets of similar density and extent due to the smaller swathe widths and, therefore, more flightpaths: lidar and stereo-photogrammetry typically have similar FOV ($\sim$40°), but lidar must operate at a lower altitude [*Leberl et al.*, 2010; *Baltsavias*, 1999]. The advantage of lidar is that only one fly-over is required per swathe and data can be acquired both day and night. Additionally, lidar can produce accurate bare-earth terrain models over vegetated terrain as some of the lidar signal penetrates through gaps in a forest canopy [*Toth and Grejner-Brzezinska*, 2000].

During quality control, stereo-images can be used to manually identify errors in the DTM and map breaklines in the terrain, such as ridgelines [*Liu*, 2008; *Thompson and Maune*, 2002]. Feature matching algorithms, as described above, can use sharp changes in contrast to identify the precise location of such features, which can also be used to co-register the data. Despite recent gains in breakline detection from lidar point clouds, discussed in *Liu* [2008], the fact remains that the precise location of breakline features will be missing in lidar data unless a very high pulse rate is used [*Thompson and Maune*, 2002].

Efficiently reducing the enormous volume of data produced during a lidar campaign to a useable, regularly spaced, and quickly accessible dataset presents another challenge to lidar, with the original data containing irregularly spaced echo-profiles, with over-sampling in some areas [*Gatziolis and Andersen*, 2008; *Liu*, 2008]. Challenges also apply to the different methods of poor data removal, especially where it can be difficult to correctly identify ground returns over vegetated terrains [*Csatho et al.*, 2005; *Liu*, 2008]. As lidar is a relatively new technology, there are

fewer standards regarding the production and accuracy reporting of data, leading to the American Society for Photogrammetry and Remote Sensing (ASPRS) drawing up guidelines to improve consistency and enable comparison [*American Society for Photogrammetry and Remote Sensing Lidar Committee*, 2004a,b; *Liu*, 2008].

Finally, it is suggested that laboratory calibration of lidar systems must be conducted at a much higher rate than stereo-imaging systems, every 500 hrs compared to 3 yrs, whilst calibration should also be completed for each flight campaign [*Thompson and Maune*, 2002].

2.2.4 REFERENCE SURFACES

Geographic, aerographic, and selenographic refers to the reference frames of Earth, Mars, and the Moon respectively. These reference frames are defined as a solution for the location of data within a reference system, which attempts to define the physical environment, and a model for defining the positions on a planetary body [*LRO Project and LGCWG*, 2008]. DTM and laser altimeter elevations are measured relative to a reference surface, shown schematically in Figure 2.14, which can vary in complexity from a spherical or elliptical model of the planet to an equipotential surface.

The simplest model is a sphere, however, few planetary bodies are this kind, so a more realistic model is an ellipsoid, defined by three axes, which accounts for the equatorial bulge caused by rotation of a large rotating body about a central axis. Reference spheres and ellipsoids are used as a basis for coordinate systems, with longitude measured in degrees from an arbitrary point on the surface, known as the meridian, and the latitude in degrees from the equator [*Snyder*, 1987]. For a spherical coordinate system, measuring the latitude is simplified by the fact the equatorial and polar radii are the same, and thus the system defaults to a planetocentric coordinate system, whereby latitude is measured from the centre of the body (Figure 2.14). Two options are available for ellipsoidal bodies: planetocentric or planetographic, the latter is defined as the angle between a line perpendicular from the surface and the equatorial plane (Figure 2.14) [*Snyder*, 1987].

Unfortunately, modelling a surface as a sphere or ellipse fails to account for the change in gravitational potential across a planetary body due to the spin of a planet and changes in density across a surface (Figure 2.14) [*Fowler*, 2005; *Snyder*, 1987]. These effects are accounted for in an equipotential surface, which correlates to the shape a planetary body would take if it was covered entirely by water, assuming no changes in water density and no currents, as every point has the same scalar potential [*Fowler*, 2005; *Snyder*, 1987]. On Earth the equipotential surface is known as the geoid, whilst on the Moon and Mars the surface is known as the selenoid and aeroid respectively. This surface may show only small deviations from an ellipsoid, such as the geoid which deviates 85 m to −106 m from a commonly used ellipsoid, but is preferred when measuring topography, particularly when modelling water flow [*Fowler*, 2005].

The commonly used parameters for Mars, the Moon, and Earth are presented in Table 2.2, whilst specific coordinate systems and reference surfaces used by data in this work are discussed in the relevant science chapters in Section 3.5 (Mars), Section 4.5 (the Moon), and Section 5.6 (Earth).

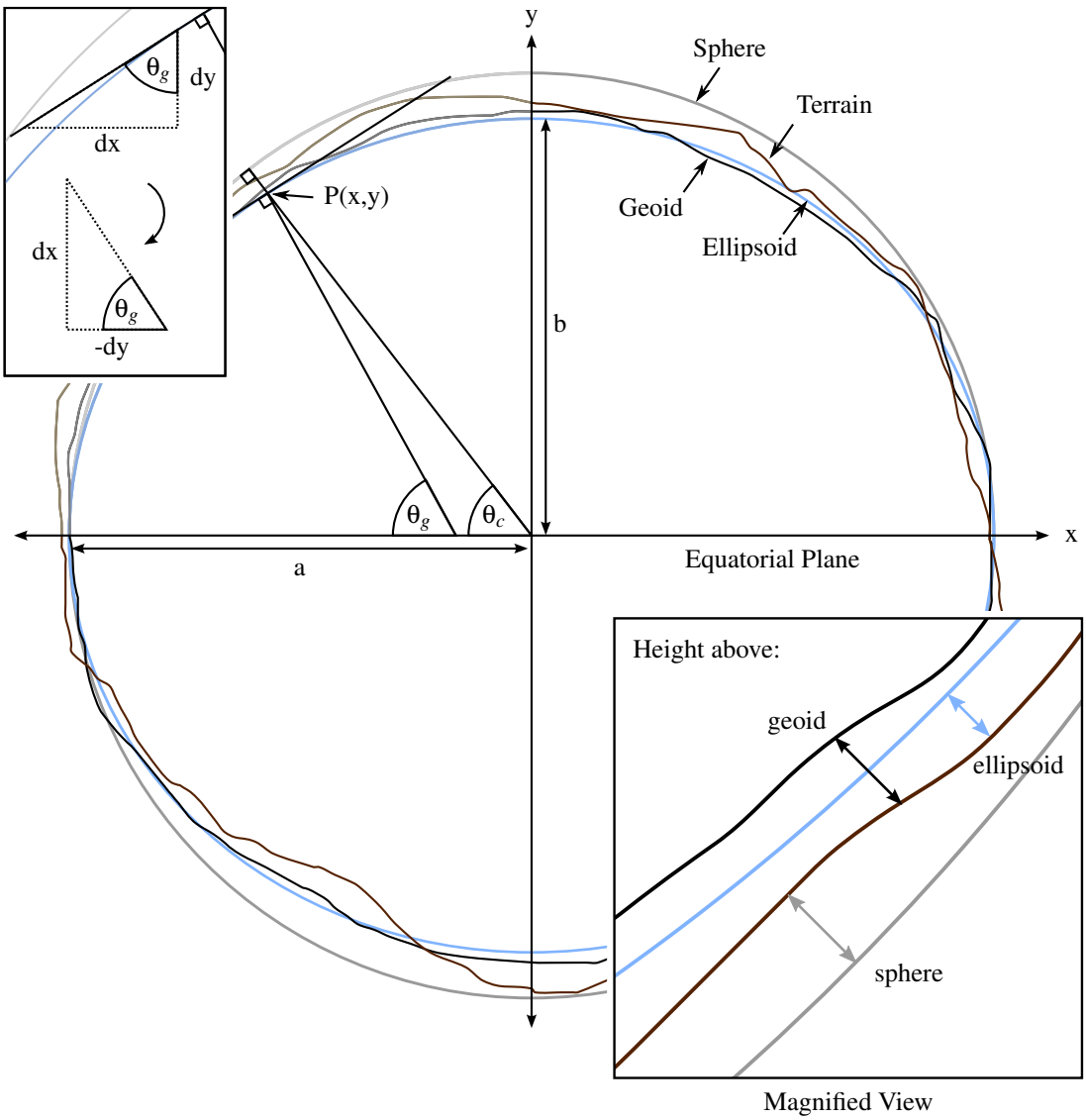

Figure 2.14: Schematic describing different reference surfaces and latitude measurements, adapted from *Rossi* [2008]. θ_c and θ_g are the planetocentric (sphere) and planetographic (ellipsoid) latitudes, respectively. a and b are the equatorial and polar radii of an ellipse, respectively.

Table 2.2: Common planetary mapping parameters for the three planets discussed in this work [*Grayzeck*, 2013; *Bennett et al.*, 2011].

Planet	Mean Radius (km)	Equatorial Radius (km)	Polar Radius (km)	Standard
Mars	3389.50 ± 0.20	3396.19 ± 0.10	3376.20 ± 0.10	IAU2000
Moon	1737.4 ± 0.1	1737.4 ± 0.1	1737.4 ± 0.1	IAU2000
Earth	6371.0	6378.1370	6356.7523	WGS84
Earth	6371.0	6378.1363	6356.7516	TOPEX

2.2.5 COORDINATE SYSTEM TRANSFORMATIONS

Geospatial data often needs to be converted from one coordinate system to another. However, converting between coordinate systems is not an exact process and instead requires mathematical approximations. This section discusses the conversion between different planetary geographic coordinate systems used in Chapter 5, based on *Haran* [2004] and *Meeus* [1991]. Conversions between different projection systems is not discussed here, as a thorough description of the most commonly used projection systems are discussed in *Snyder* [1987].

To derive the equation to convert between planetocentric, θ_c, and planetographic latitude, θ_g, for heights on the surface of an ellipse, one must first use the equation for an ellipse

$$1 = \frac{x^2}{a^2} + \frac{y^2}{b^2}, \tag{2.29}$$

$$x^2 = a^2 - \frac{a^2}{b^2} y^2, \tag{2.30}$$

$$\therefore \ \tan(\theta_g) = -\frac{dx}{dy} = \frac{y}{x}\frac{a^2}{b^2} = \frac{a^2}{b^2}\tan(\theta_c), \tag{2.31}$$

where x and y are points on the surface of an ellipse, and a and b are the equatorial and polar radius, respectively (Figure 2.14) [*Meeus*, 1991].

An iterative process using the Newton-Raphson method to find improved approximations of a function is used to convert ICESat latitude data from the TOPEX/Poseidon reference ellipse to the World Geodetic System 1984 (WGS 84) ellipse, as in *Haran* [2004]. This is repeated until the change in distance on the surface of an ellipse, δ, is small (10^{-12} m) [*Haran*, 2004; *Ligas and Banasik*, 2011; *Meeus*, 1991]. From the equations above

$$\theta_2 = \arctan\left(\frac{a_2}{b_2}\tan(u_2)\right), \tag{2.32}$$

$$u_2 = u_{2,p} - \delta, \tag{2.33}$$

$$\delta = \frac{f(u_2)}{f'(u_2)}. \tag{2.34}$$

Here, $u_{2,p}$ is the value of u_2 for the previous loop, and

$$u_1 = \arctan\left(\frac{b_1}{a_1}\tan(\theta_1)\right), \tag{2.35}$$

$$u_2 = \arctan\left(\frac{b_2}{a_2}\tan(\theta_2)\right). \tag{2.36}$$

If θ_1 is less than or equal to 45°

$$f(\theta_1 \leq 45) = \left(b_2^2 - a_2^2\right) * \sin(u_2) + a_2 * (a_1\cos(u_1) + h_1\cos(\theta_1)) * \tan(u_2) - b_2 a_1\cos(u_1) + h_1\cos(\theta_1) = 0, \tag{2.37}$$

$$f'(\theta_1 \leq 45) = \left(b_2^2 - a_2^2\right) * \cos(u_2) + a_2\frac{a_1\cos(u_1) + h_1\cos(\theta_1)}{\cos^2(u_2)} = 0, \tag{2.38}$$

if θ_1 is greater than 45°

$$f(\theta_1 > 45) = \left(a_2^2 - b_2^2\right) * \cos(u_2) + b_2 * \frac{(a_1 \cos(u_1) + h_1 \cos(\theta_1))}{\tan(u_2)} - a_2 * (a_1 \cos(u_1) + h_1 \cos(\theta_1)) = 0, \quad [2.39]$$

$$f'(\theta_1 > 45) = -\left(\left(a_2^2 - b_2^2\right) * \sin(u_2) + b_2 * \frac{b_1 \sin(u_1) + h_1 \sin(\theta_1)}{\sin^2(u_2)}\right) = 0. \quad [2.40]$$

To find the height above the new ellipsoid, h_2, after the new latitude has been found, one can use the following equations
if θ_1 is less than or equal to 45°

$$h_2(\theta_1 \leq 45) = \frac{(a_1 * \cos(u_1) + h_1 * \cos(\theta_1)) - a_2 * \cos(u_2)}{\cos(\theta_2)}, \quad [2.41]$$

if θ_1 is greater than 45°

$$h_2(\theta_1 > 45) = \frac{(b_1 * \sin(u_1) + (h_1 * \sin(\theta_1))) - a_2 * \sin(u_2)}{\sin(\theta_2)}. \quad [2.42]$$

However, near the poles and the equator, where

$$\theta_2 \approx \theta_1, \quad [2.43]$$

$$h_2(\text{Equator}) = h_1 + a_1 - a_2, \quad [2.44]$$

$$h_2(\text{Pole}) = h_1 + b_1 - b_2. \quad [2.45]$$

Using different methods to convert between coordinate systems produces only small deviations from the results using the method above, as the maximum shift when converting from TOPEX/POSEIDON ellipsoid to the WGS 84 ellipsoid is <1 m, even at ±45° N, where the maximum shift occurs [*Ligas and Banasik*, 2011; *National Snow and Ice Data Center*, 2014a]. The main differences between the different methods of conversion are the number of iterations required to derive the new latitudes, and the computational time required to do so, neither of which are issues for this work due to the relatively low number of ICESat data points (∼36 000) to which the transformation is applied [*Ligas and Banasik*, 2011].

2.3 ESTIMATING SURFACE ROUGHNESS AND SLOPE

2.3.1 INTRODUCTION

The work in this thesis tests the relationship between laser altimeter pulse-widths and variation of terrain, described by surface roughness and slope, within the pulse-footprint, as proposed by *Gardner* [1982] in Equations 2.5 to 2.7. Surface roughness and slope provide useful methods in quantitative geology, a field that has been improved by the digitisation of maps, enabling ever more complex methods to analyse, classify, and compare terrains to further our understanding of the type

and relative strength of the formation and evolution processes that shape a surface [*Wood*, 1996]. However, neither slope nor surface roughness have an absolute scientific definition, with methods depending on the field of study, data source, and personal preference [*Shepard et al.*, 2001]. This section describes the different methods of measuring surface roughness and slope that are relevant to the work in this thesis, along with terrain scaling, and methods of detrending data. The section concludes by outlining the best practices of defining and reporting these terrain variations.

2.3.2 METHODS OF CALCULATING SURFACE ROUGHNESS

In this work, surface roughness is defined as

> A measure of the height variations across a horizontal plane or profile, at a defined baseline.

This definition is adapted from that given in *Shepard et al.* [2001], adding the the final phrase - *at a defined baseline* - to stress the fact that surface roughness is a dynamic value that, typically, varies depending on the baseline at which it is measured. For correct interpretation and verification of a result, the baseline should always be reported. Static measures of surface roughness typically appear when surface roughness is derived from radar or optical scattering models, where the baseline is fixed, and, unfortunately, this trend continues in other works, where it is possible to measure surface roughness at a variety of baselines [*Shepard et al.*, 2001].

The different methods of calculating the height variations along 1- (profile) and 2-dimensional (gridded) elevation datasets are discussed below, using the review by *Shepard et al.* [2001]. Their review, along with *Kreslavsky et al.* [2013], is used here, and in Section 2.3.8, which outlines how surface roughness should be reported.

2.3.2.1 SURFACE ROUGHNESS FROM ELEVATION ESTIMATES

The most common method of calculating surface roughness is the RMS height [*Shepard et al.*, 2001], ξ, given as

$$\xi = \left[\frac{1}{n-1} \sum_{i=1}^{n} \left(z(x_i) - \bar{z} \right)^2 \right]^{\frac{1}{2}}. \qquad [2.46]$$

The RMS deviation, or Allen deviation of elevation, ν, is the RMS difference in elevation between points separated by Δx, and is given by

$$\nu(\Delta x) = \left\{ \frac{1}{n} \sum_{i=1}^{n} \left[z(x_i) - z(x_i + \Delta x) \right]^2 \right\}^{\frac{1}{2}}. \qquad [2.47]$$

Both the RMS height and RMS deviation scale with the size of the baseline at which they are measured, which is described in Section 2.3.5 below.

The Inter-Quartile-Range (IQR) can also be used to measure the terrain distribution, which is defined as the difference between the upper and lower quartiles, and may also be referred to as the

mid-spread of the distribution. *Kreslavsky et al.* [2013] consider this to be more stable than the methods presented above, as it is not influenced by anomalously high or low topography.

Finally, the simplest method is to use the range, r, of elevations within a baseline. Typically the maximum difference in elevation within a baseline is used, but different thresholds can be applied, such as 10 %, 14 % (e^{-2}), 37 % (e^{-1}), or 90 % values of the maximum range, which will reduce the effects of anomalously high or low terrain, as discussed above.

2.3.2.2 SURFACE ROUGHNESS FROM SLOPE ESTIMATES

Slope can also be used as a representation of surface roughness, where it is commonly reported in degrees [*Shepard et al.*, 2001]. This is not to be confused with slope, which measures the slope of the surface over a baseline. Instead, it is a measure of the distribution of slope across a baseline, or measures slope from a background slope, as in the case for Equation 2.51.

The RMS slope, s_r, of a profile is represented as

$$s_{rms} = \frac{\nu(\Delta x)}{\Delta x} = \frac{1}{\Delta x}\left\{\frac{1}{n}\sum_{i=1}^{n}\left[z(x_i) - z(x_i + \Delta x)\right]^2\right\}^{\frac{1}{2}}. \qquad [2.48]$$

Like the RMS deviation, the RMS slope is also dependent on the step size, Δx. This method can be considered a poor representation of surface roughness, as outlying points within a long-tailed frequency distribution will bias the RMS slope towards a higher value [*Shepard et al.*, 2001; *Rosenburg et al.*, 2011]. The RMS slope is ideally used when the distribution is Gaussian, which, unfortunately, is not the typical distribution of natural terrains [*Aharonson et al.*, 2001]. To overcome this, the absolute slope value can be used (Equation 2.50).

The effective slope, s_e, is commonly used in radar-scattering models and is given by

$$s_{eff} = \frac{\xi}{C} = \frac{1}{C}\left[\frac{1}{n-1}\sum_{i=1}^{n}\left(z(x_i) - \bar{z}\right)^2\right]^{\frac{1}{2}}, \qquad [2.49]$$

where C is the autocorrelation length, described below. This method can also be referred to as the RMS slope, and may be considered a poor measure of surface roughness as it depends on two other measures of surface roughness, RMS height and the autocorrelation length. In this way, two surfaces that appear very different when using other measures of surface roughness can appear very similar, if the RMS height and autocorrelation length scale appropriately [*Shepard et al.*, 2001].

The absolute slope along a profile, s_a, is given as

$$s_{abs} = \frac{1}{\Delta x}\left\{\frac{1}{n}\sum_{i=1}^{n}\left|z(x_i) - z(x_i + \Delta x)\right|\right\}. \qquad [2.50]$$

This value helps in reducing the effect of a few high, or erroneous, values that may distort the data when viewed using RMS slope alone [*Shepard et al.*, 2001].

The methods described above are susceptible to long-tailed distributions of slope, which will affect the resulting surface roughness values, but may not be representative of the terrain. *Kreslavsky*

and Head [1999, 2000] present data using the median differential slope, s_d, given by

$$s_d = \frac{z_{\frac{\Delta x}{2}} - z_{\frac{-\Delta x}{2}}}{\Delta x} - \frac{z_{\Delta x} - z_{-\Delta x}}{2\Delta x}, \quad [2.51]$$

to measure the distribution of slopes from laser altimeter profile data. Here, $z_{\frac{\Delta x}{2}}$ and $z_{\frac{-\Delta x}{2}}$ are the z values at half a baseline ahead and behind the cell, and $z_{\Delta x}$ and $z_{\Delta x}$ are the z values at one baseline ahead and behind the cell for which surface roughness is being calculated, respectively. This method incorporates some detrending of the data, discussed in more detail in Section 2.3.6, by removing large baseline slopes from the data without enhancing effects from high slope values that may be present along a profile, or within a window.

Finally, *Kreslavsky et al.* [2013] develop a method for deriving surface roughness over the lunar surface using the curvature, s_c, of terrain along LOLA profiles, where s_c is given as

$$s_c = \frac{z_{\frac{\Delta x}{2}} - z_{\frac{-\Delta x}{2}}}{\Delta x^2}. \quad [2.52]$$

The results are downsampled to 8 pixels degree^{-1}, and the IQR of s_c values are found within each pixel. The surface roughness maps are produced by finding the relative values compared to a typical value for the lunar highlands. The aim is to produce a stable roughness map that enables intuitive comparisons of terrain across the lunar surface.

2.3.2.3 AUTOCORRELATION

The autocorrelation length, C, is a measure of how a surface repeats itself across a defined scale [*Shepard et al.*, 2001], and can be written as

$$C(\Delta x) = \frac{1}{\xi^2}\left[\frac{1}{n-1}\sum_{i=1}^{n} z(x_i)\, z(x_i + \Delta x)\right]. \quad [2.53]$$

The autocorrelation function is normalised covariance between the profile and itself when offset by a step, Δx. This means that the autocorrelation is equal to 1 when Δx is equal to 0, meaning that a profile, of length $n-1$, is perfectly correlated with itself [*Orosei et al.*, 2003]. The autocorrelation length is defined as the distance required to reduce the normalised correlation value to e^{-1} ($\sim$37 %) [*Shepard et al.*, 2001]. Large correlation lengths are generally seen in smooth surfaces, whereas rough surfaces have low correlation lengths [*Shepard et al.*, 2001]. White noise has an autocorrelation length of 0, whilst a straight line has an autocorrelation length of 1.

For estimating autocorrelation length in 2- and 3-dimensions, Moran's I can be used as a measure of spatial autocorrelation, which returns a value between −1 and 1, where again 1 means perfect correlation, 0 represents a random spatial process, and −1 represents spatial diffusion. Moran's I, I, is defined as:

$$I = \frac{n}{\sum_i \sum_j w_{ij}} \frac{\sum_i \sum_i w_{ij}\,(z_i - \bar{z})\,(z_j - \bar{z})}{\sum_i (z_i - \bar{z})^2}, \quad [2.54]$$

where n is the number of spatial units indexed by i and j, and w_{ij} is an element of a matrix of spatial weights. Moran's I looks at global autocorrelation, and is therefore less sensitive to local spatial autocorrelation.

Geary's C, I_C, is better suited for studying local autocorrelation. Rather than ranging from −1 to 1, Geary's C ranges from 0 to 2, where 0 means perfect dispersion, 0 is no autocorrelation, and 2 is perfectly correlated. It is given as

$$I_C = \frac{n-1}{2W} \cdot \frac{\sum_i \sum_j w_{ij} (z_i - z_j)^2}{\sum_i (z_i - \bar{z})^2}, \quad [2.55]$$

where W is the sum of all w_{ij}.

2.3.3 METHODS OF CALCULATING SLOPE

Slope has also been used to explore differences in the magnitude and type of geological processes, and refers to the slope of a surface relative to the horizontal [*Rosenburg et al.*, 2011; *Shepard et al.*, 2001]. Slope could be included in the definition given for surface roughness above, as it is a measure of the height variations across a surface, however, unlike surface roughness, it is dependent on the order of the height elements within a baseline. The different methods used to measure slope in this thesis are described below.

On a unit scale level along a 1-dimensional profile, slope is measured as the gradient of a line between neighbouring points. At larger baselines, slope can be measured either by: (1) the gradient of a line fitted to the two end points within the baseline; (2) fitting a line-of-best-fit to the data within the baseline; (3) the mean unit-scale slope estimates across a baseline. These methods will provide very different results, especially if the terrain is not a smooth continuous slope, which will each be susceptible to different baseline slopes along the profile.

In two dimensions calculating slope can be more difficult. ArcMap calculates slope in two dimensions as the maximum rate of change between a cell and its eight neighbours by [*Environmental Systems Research Institute*, 2012]

$$\frac{dz}{dx} = \frac{(c+2f+i)-(a+2d+g)}{8 \times pixelsize}, \quad [2.56]$$

$$\frac{dz}{dy} = \frac{(g+2h+i)-(a+2b+c)}{8 \times pixelsize}, \quad [2.57]$$

$$\theta = \frac{180}{\pi} \tan^{-1} \left(\sqrt{\left(\frac{dz}{dx}\right)^2 + \left(\frac{dz}{dy}\right)^2} \right). \quad [2.58]$$

The values for a to i are shown with an example in Figure 2.15. This can be applied to slopes at different baselines by either resampling the DTM data to the desired baseline before calculating the slope, or finding the mean slope, calculated at the original DTM resolution, within a baseline. In preliminary work for Section 3.8, it was shown that these methods produce very similar results. The resulting slope value using the example DTM values in Figure 2.15 is 75.26°, if the pixel size is 5 m.

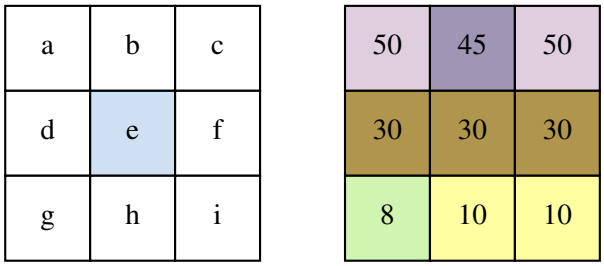

Figure 2.15: Schematic and example DTM patch used to calculate the slope in ArcMap using Equations 2.56 to 2.58. These equations calculate slope for pixel *e*. If any pixel values are missing, they are assigned the value of *e*.

Another method, used particularly with ICESat data in Chapter 5, calculates slope as the maximum slope of a plane fitted to elevation data extracted from within laser altimeter pulse-footprints. This method is considered more accurate as it uses all elevation points within a window and can produce slope estimates at different baselines using the full resolution data, and detrended surface roughness. The equation to calculate the maximum slope, derived from the equation for a plane, is given as

$$z = ax + by + c, \tag{2.59}$$

$$\theta = \frac{180}{\pi} \tan^{-1}\left(\sqrt{a^2 + b^2}\right). \tag{2.60}$$

Using this method slope is effectively calculated at a baseline equal to the width of the elevation data used to produce the plane. The resulting slope value using the example DTM values in Figure 2.15 is 75.62°, assuming the same pixel size as above.

Beyond this, aspect, curvature, and convexity can also provide statistical information about a surface, but as these values cannot be determined from laser altimeter pulse-widths they are not discussed here [*Wood*, 1996, Chapter 4].

2.3.4 TERRESTRIAL EXAMPLES OF ROUGHNESS

To give a context to the expected surface roughness values, Figures 2.16a to 2.16d show schematics and a table of the mean, maximum, and minimum surface roughness, as measured using RMS height, for four example terrains observed on Earth. Figure 2.16a shows a smooth (5°) sloping plane, dotted with few rocks and boulders. Figure 2.16b shows a rough (5°) sloping terrain, modelled on the terrain used in *Shepard et al.* [2001], who use an elevation profile along a lava field to explore how different measures of surface roughness respond to the terrain. Here, the boulders are much larger and more closely spaced. Figure 2.16c shows a series of linear, equally spaced dunes (5 m), all of equal height (10 m) and length (65 m). Figure 2.16d shows a schematic of a sea cliff face, similar to those found on the south coast of the UK. The sea is modelled as a smooth surface, with a gently (3°) sloping beach, landslide deposit material at the base of a 100 m high cliff, and a gently sloping cliff top (3°).

The data in the tables beneath each schematic give an indication as to how RMS height responds to each of the terrains at different baselines. The surface roughness values are produced across 11 different baselines between 2 m to 500 m, which are similar to those used in Chapter 3. Figure 2.16a produces the lowest mean surface roughness values until the 250 m baseline data, above which

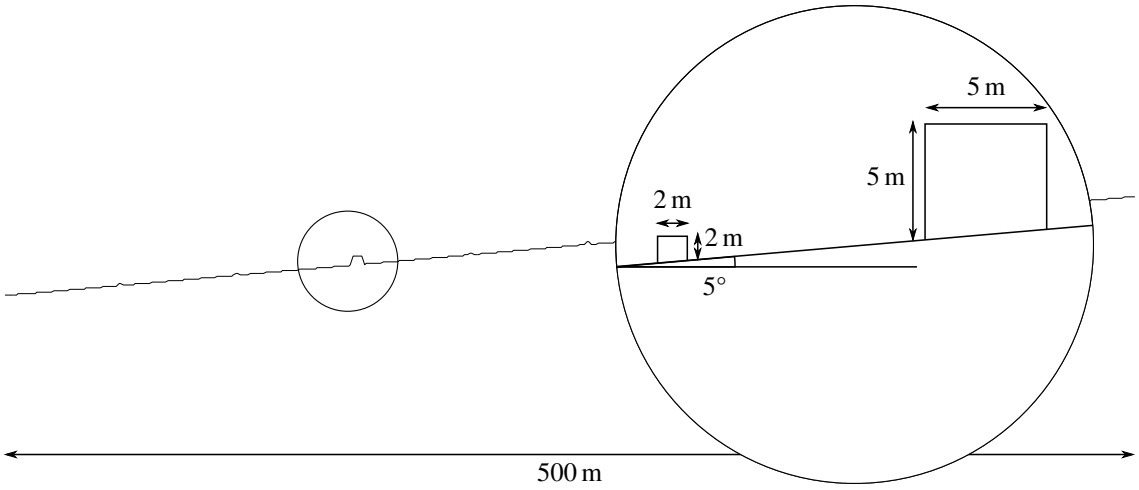

Value	2 m	5 m	7 m	10 m	15 m	25 m	50 m	75 m	100 m	250 m	500 m
Mean	0.11	0.25	0.33	0.42	0.57	0.83	1.43	2.03	2.64	6.37	12.69
Max	2.89	2.29	2.26	2.25	2.20	2.06	2.12	2.47	2.96	6.47	12.69
Min	0.00	0.00	0.19	0.26	0.33	0.57	1.20	1.75	2.36	6.27	12.69

Figure 2.16a: Terrestrial example of roughness over a smooth, sloping plane, dotted with some rocks and boulders. The table shows the mean, maximum, and minimum roughness values observed along the profile.

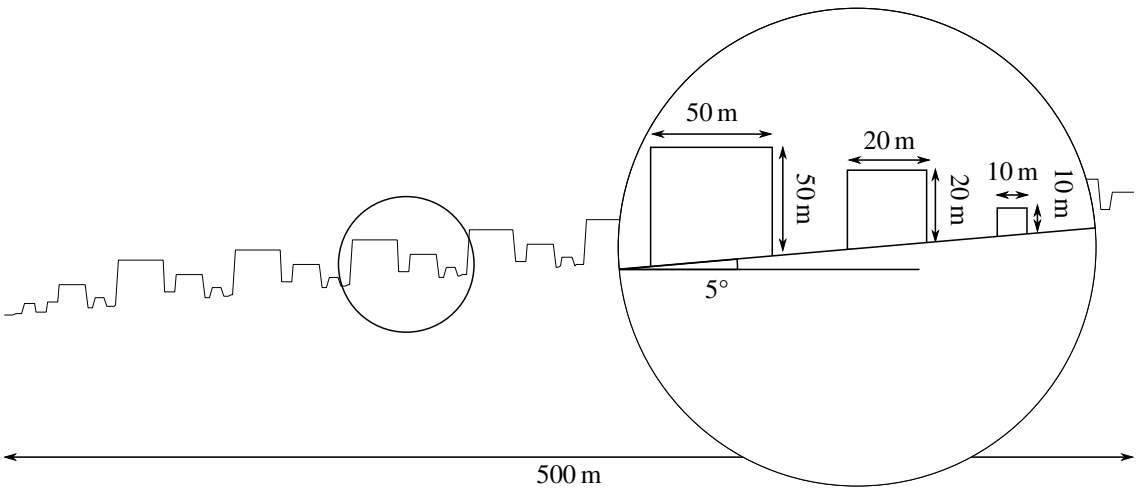

Value	2 m	5 m	7 m	10 m	15 m	25 m	50 m	75 m	100 m	250 m	500 m
Mean	0.79	2.18	2.90	3.70	4.86	6.19	7.26	7.31	7.58	9.56	14.92
Max	13.50	10.50	10.27	10.15	9.52	9.35	8.26	8.56	8.48	10.20	14.92
Min	0.00	0.00	0.00	0.00	0.00	3.10	5.26	6.69	6.43	8.64	14.92

Figure 2.16b: Terrestrial example of roughness over a rocky plane, with a high density of rocks and medium and large boulders. This could be analogous to the lava field used in *Shepard et al.* [2001]. The table shows the mean, maximum, and minimum roughness values observed along the profile.

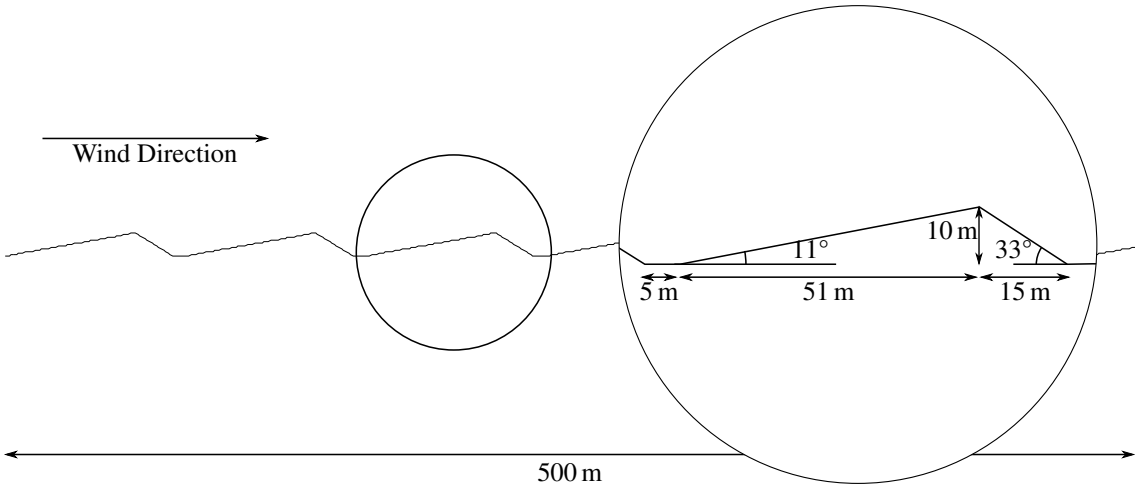

Value	2 m	5 m	7 m	10 m	15 m	25 m	50 m	75 m	100 m	250 m	500 m
Mean	0.18	0.40	0.54	0.76	1.10	1.71	2.76	3.07	3.00	3.05	3.01
Max	0.44	0.99	1.35	1.89	2.79	3.79	3.69	3.12	3.21	3.14	3.01
Min	0.00	0.00	0.07	0.25	0.48	0.93	1.98	2.99	2.75	2.95	3.01

Figure 2.16c: Terrestrial example of roughness over a dune field. In this case, the dunes are consistently spaced, small dunes. The table shows the mean, maximum, and minimum roughness values observed along the profile.

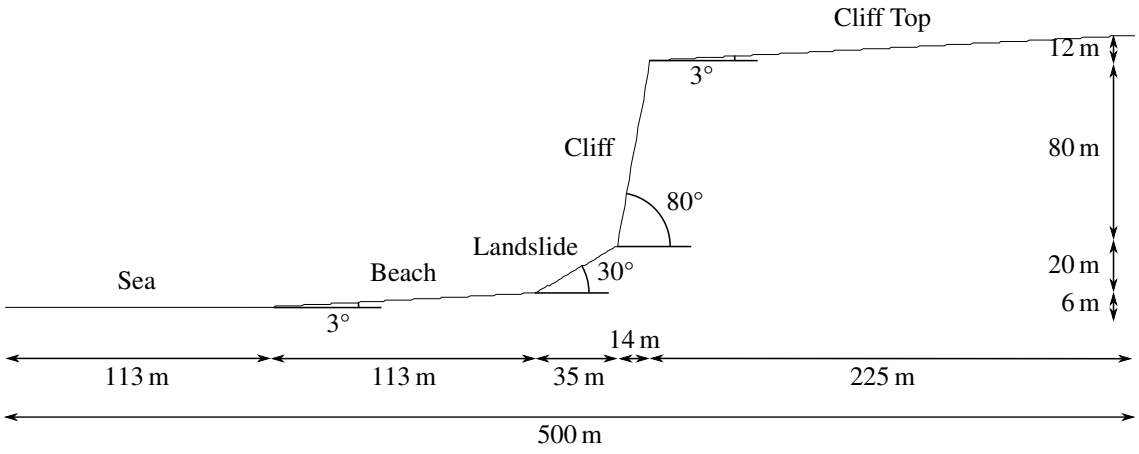

Value	2 m	5 m	7 m	10 m	15 m	25 m	50 m	75 m	100 m	250 m	500 m
Mean	0.17	0.38	0.52	0.74	1.12	1.93	4.18	6.73	9.63	37.45	53.38
Max	4.01	8.97	12.25	17.17	25.36	32.56	38.59	42.05	44.39	49.75	53.38
Min	0.00	0.00	0.00	0.00	0.00	0.00	0.00	0.00	0.00	3.80	53.38

Figure 2.16d: Terrestrial example of roughness over a cliff area, with sea, beach, landslide material, and cliff top. The table shows the mean, maximum, and minimum roughness values observed along the profile.

the Figure 2.16c produces the lowest values. This is due to the long baseline sloping terrain in the former, compared to the short baseline slopes observed in the dunes. The roughest terrain at baselines of 2 m to 75 m is observed over Figure 2.16b due to the large size and small spacing between the modelled boulders. Above these baselines the cliff schematic produces the greatest surface roughness values, which is a result of the much larger variation in topography typically observed throughout the schematic.

Finally, the peak in surface roughness values can provide an indication as to the size of the features found in a terrain. For example, Figure 2.16c shows a peak roughness value at 75 m when using the mean and at 25 m when using the maximum. These values correlate well with the entire length of individual dunes and the steepest side of the dune respectively. Similarly, the sharp increase in surface roughness values observed over 10 m to 25 m baselines when looking at the maximum in Figure 2.16d suggests that the greatest topographic variation, i.e. the cliff face, is observed at these baselines.

2.3.5 THE HURST EXPONENT AND FRACTAL DIMENSION

Early work by *Horton* [1945] and *Hack* [1957] reveals the scale-invariant nature of stream networks. Since then, this has been extended to topography [*Dodds and Rothman*, 2000; *Grohmann et al.*, 2009; *Lovejoy and Schertzer*, 2007; *Orosei et al.*, 2003; *Pelletier*, 1997; *Turcotte*, 1997], crater counting and crater depth-to-diameter scaling [*Hartmann*, 1965; *Pike*, 1974, 1977], and rock-size frequency distributions [*Golombek and Rapp*, 1997], and extends to surface roughness and slope estimates [*Shepard et al.*, 2001]. This ability for terrain to look similar at vastly different scales allows the properties of terrain at smaller scales to be predicted using the properties at much larger scales, and vice-versa, and is part of the reason scale bars are included in images [*Shepard et al.*, 2001].

The Hurst exponent, H, is a scaling parameter that represents the gradient of the line-of-best-fit between the surface roughness or slope parameter and the baseline length (Figure 2.17) [*Shepard et al.*, 2001]. H has a values between 0 and 1 for real surfaces, where 1 suggests that the surface is replicated exactly at all scales and 0 suggests no scaling law applies. It is related to the previously described roughness parameters as follows

The relationship between the RMS elevation, ξ, changes and the profile length, Δx, is

$$\xi(L) = \xi_0 \left(\frac{\Delta x}{\Delta x_0} \right)^H, \qquad [2.61]$$

where ξ_0 is the RMS elevation of the profile computed at unit scale, x_0 [*Shepard et al.*, 2001].

The relationship between RMS deviation, ν, and the baseline length is

$$\nu(\Delta x) = \nu_0 \left(\frac{\Delta x}{\Delta x_0} \right)^H, \qquad [2.62]$$

where ν_0 is the ν value at unit scale, Δx_0 [*Shepard et al.*, 2001].

The RMS slope, s_r, is related to the baseline length as

$$s_{rms}(\Delta x) = s_{rms,0}\left(\frac{\Delta x}{\Delta x_0}\right)^{1-H}, \quad [2.63]$$

where s_{r0} is the s_r value at unit scale of the data, Δx_0 [*Shepard et al.*, 2001].

The simplest method for calculating the Hurst exponent is using the variogram, a log-log plot of surface roughness against the baselines [*Shepard et al.*, 2001]. The Hurst exponent is the gradient of the line-of-best-fit, over an area of the plot where a simple linear relationship may be found. If all the data fits well onto one linear line-of-best-fit, then the terrain is referred to as fractal (Figure 2.17.a); if the data fits onto two or more linear lines of best fit then the terrain is referred to as multi-fractal (Figure 2.17.b). It is not uncommon for there to be more than one Hurst exponent value within a variogram, as it is not expected that surfaces get infinitely rougher at smaller scales, nor indefinitely larger at larger scales [*Shepard et al.*, 2001; *Orosei et al.*, 2003]. The baseline at which a sudden change in gradient occurs is known as the breakpoint, X_b, and has been shown to be an indicator of surface formation and evolution, not the Hurst exponent value itself [*Shepard et al.*, 2001; *Rosenburg et al.*, 2011]. The value of X_b indicates the scale at which competing formation and evolution processes are equal in magnitude, and also indicates the point small scale surface processes overtake those acting on larger scales. *Shepard et al.* [2001] note that a variogram can reveal more complex behaviour, such as that shown in Figure 2.17.c. Here, the plot follows a polynomial, where the maximum is thought to be related to the periodic behaviour of the surface.

2.3.6 DETRENDING AND ISOTROPY

Removing background trends from elevation data, in a process known as detrending, before surface roughness and slope are calculated, can help reveal small-scale geological processes [*Kreslavsky and Head*, 2000; *Kreslavsky et al.*, 2013; *Shepard et al.*, 2001]. Equation 2.7 suggests that the detrended surface roughness could be derived from laser altimeter pulse-widths, adding an extra depth of information to laser altimeter data. To test this, detrended surface roughness from DTM data is compared to the roughness contribution to pulse-width, using Equation 2.7, in the following science chapters.

Different methods can be used to detrend data. *Shepard et al.* [2001] suggest detrending should be carried out by subtracting a line-of-best-fit from the elevation data at the baseline, such that the mean of the data is zero. Alternatively, *Kreslavsky and Head* [1999, 2000] apply Equation 2.51 to remove trends at twice the baseline of interest in their study on MOLA elevation profile data. This removes the effect of outliers, anomalously high or low terrain, along a profile to prevent them drastically altering surface roughness and slope estimates at a location.

Detrending is not without possible disadvantages, however. By attempting to highlight fine-scale roughness, typically 10 % of the profile length, *Shepard et al.* [2001] suggest that detrending may remove large scale roughness features that may be important for the interpretation of a particular terrain. They also note that detrending may introduce a bias to the data, which can change the

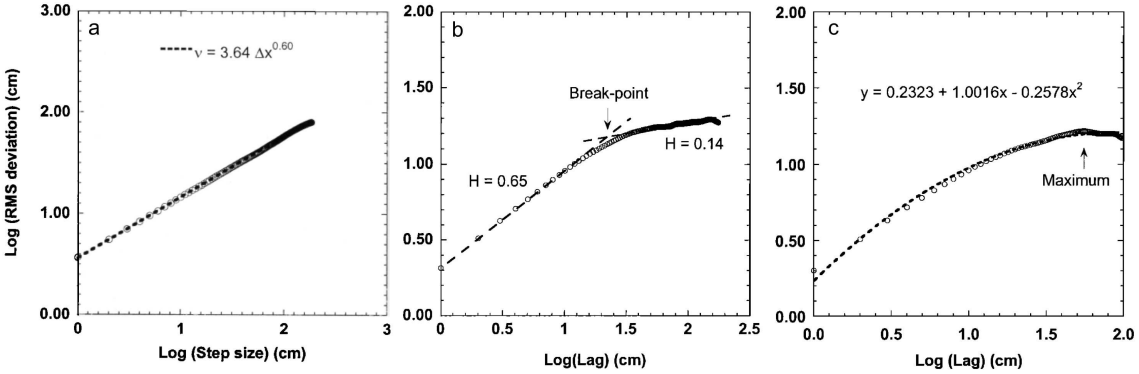

Figure 2.17: Plots showing the scaling nature of surface roughness for fractal and multi-fractal terrain [*Shepard et al.*, 2001]. (a) Fractal terrain, where RMS deviation plotted against the baseline on a log-log plot reveals a single linear relationship. (b) Multi-fractal terrain, where RMS deviation plotted against the baseline on a log-log plot reveals two linear relationships, with a clear change in gradient of the line-of-best-fit, known as the breakpoint. (c) A more complex, polynomial relationship between RMS deviation and the baseline on a log-log plot, whereby the maximum (shown) is thought to be related to periodic behaviour at this wavelength.

breakpoint, as discussed in Section 2.3.5.

Where the data allows, i.e. for 3-dimensional datasets, it is also possible to determine surface roughness and slope at different azimuths. Doing so can help determine direction dependent surface formation and evolution processes that may help in historical interpretation of a terrain. This can be particularly important in determining the direction and relative magnitude of prevailing winds in dune formation, as well as the formation of glacial and volcanic terrains [*Shepard et al.*, 2001]. Unfortunately, laser altimeter pulse-widths cannot be used in this way, as they do not record the location of high or low terrain within the pulse-footprint, instead, only revealing a measure of the distribution of terrain within the pulse-footprint.

2.3.7 EFFECTIVENESS

An effective measure of surface roughness should not only allow geologists to compare terrains, but must also be intuitive to understand. Measures such as the Power Spectrum, and the Autocorrelation length may enable quantitative comparison between terrains, but neither are intuitive [*Shepard et al.*, 2001]. Additionally, the Power Spectra has no simple relationship with other measures of surface roughness, and often appears noisy on a variogram, making it difficult to calculate any Hurst exponent or identify breakpoints [*Shepard et al.*, 2001].

Kreslavsky et al. [2013] present maps of dimensionless surface roughness to get around the fact that the IQR of s_c (Equation 2.52) is not intuitive, by setting values relative to typical values observed over the lunar highlands. In this way, researchers can compare surface roughness across the lunar surface, with only the prior knowledge that the lunar highlands are rough. This may be effective for comparing terrains on individual planets, but is unlikely to become a standardised method for comparing terrains between planets, as it may be difficult to chose a relative unit that can be applicable to all planetary terrains. Furthermore, the typical value *Kreslavsky et al.* [2013]

use for the lunar highlands may change as datasets improve in resolution and accuracy, making subsequent comparisons between datasets difficult [*Wood*, 1996, Page 15].

To make comparisons of surface roughness between planets, surface roughness must be measured using a common, easily transferable set of methods that enable simple comparisons across a variety of terrains and planets. Although these values will also be affected by changes in DTM quality, the effect can easily be reported and accounted for in error analysis.

There is also a question of stability, which is touched upon in Section 2.3.2. *Kreslavsky et al.* [2013] define a stable measure of surface roughness to be

> ...if there is a homogeneous geological unit, its roughness calculated over a large data set and over a small (but representative) subset of the same data should be similar.

This attempts to address the problem of anomalously high or low terrain (or slope) within a profile, or plane, significantly affecting the reported value of surface roughness, or slope, that is not typical to the geological unit, which is also addressed in Equation 2.51 from *Kreslavsky and Head* [1999, 2000]. This is a common occurrence for naturally occurring terrains, which typically have long-tailed frequency distributions of elevation and slope [*Kreslavsky and Head*, 1999, 2000; *Kreslavsky et al.*, 2013; *Shepard et al.*, 2001].

Similarly, stability can extend to producing maps with low noise and high visual sharpness, and characterising the topography [*Kreslavsky et al.*, 2013]. These features are less applicable to this work, as the aim here is to calibrate and develop methods for deriving surface roughness and slope from laser altimeter pulse-widths.

In practise, measures such as RMS height may be more applicable to the work outlined in this thesis, as estimates of terrain effects from laser altimeter pulse-widths are theoretically related to the variance within the pulse-footprint.

2.3.8 HOW SHOULD SURFACE ROUGHNESS AND SLOPE BE REPORTED?

In their work exploring the surface roughness of natural terrains, which attempts to set out a common scientific method to surface roughness studies, *Shepard et al.* [2001] provide an outline of how surface roughness should be reported to enable repetition and comparison of results. Of interest to this study are their suggestions that the baseline must be reported, hence the addition to the definition of surface roughness in this work, along with inaccuracies in the DTM. Additionally, any detrending should also be reported in the description of the dataset, including the methods and the baselines at which the data is detrended. Their suggestion that surface roughness is calculated at different azimuths is not applicable here, as it is not possible to derive azimuth dependent processes from laser altimeter pulse-widths.

The surface roughness estimates used in this work are the RMS height, IQR, and range, which are not only common, but also easily applied in ArcMap, the principal software environment used for the mapping elements of this work. DTM uncertainty will also be reported as the RMS-error from ground reference points, which, due to the lack of ground control data for planetary surfaces, will typically be the altitude derived from the orbiting laser altimeters. This study also works on the

principle that poor DTM data will be removed or masked out, rather than attempting to interpolate terrain to a visually realistic, but potentially incorrect alternative. This is because accurate terrain data is vital to the work, in order to be able to correctly calibrate the laser altimeter data explored in this thesis.

Finally, one process unique to this work, is deriving surface roughness and slope estimates with a weight to represent the energy distribution across the pulse-footprint, as described in Section 2.1.5. This predominantly applies to the work in Chapter 5, where we have access to accurate information of the location, geometry, and energy distribution, but is also touched upon in Chapter 3. The methods to apply this correction are described in the relevant science chapters, as the methods vary depending on data source.

3

MARS: ASSESSING MOLA PULSE-WIDTHS

The effective calibration of MOLA pulse-widths provided the original motivation for the work in this thesis: the aim being to find a consistent relationship across multiple sites that could be extrapolated to the rest of Mars to produce accurate maps of surface roughness and slope from laser altimeter pulse-width data. This chapter presents a background literature review to Mars surface roughness and slope using current datasets, followed by a description of the instruments and methods used for the work in this chapter. The results are split into three studies that explore the relationship between: MOLA pulse-widths and surface roughness using HiRISE DTMs over the final four MSL candidate landing sites; Slope-Corrected pulse-widths and surface characteristics over much rougher terrain; the roughness contribution to pulse-width and detrended surface roughness. The results suggest these pulse-widths are correlated to surface roughness over sites considered for landing and roving sites, and slope over very rough terrain. Little correlation is observed where terrain is heterogeneous over short baselines and with detrended surface roughness, which is attributed to georeferencing errors and poor pulse-width measurement.

3.1 INTRODUCTION

The insertion of Mars Global Surveyor (MGS) into orbit around Mars ended a near-20 year hiatus of successful orbital missions to the planet [*Albee et al.*, 1998]. A science goal of the Mars Orbiter Laser Altimeter (MOLA), one of five instruments on-board, was to characterise the surface at ∼100 m-scales using laser altimeter pulse-widths [*Gardner*, 1992; *Neumann et al.*, 2003a; *Smith et al.*, 2001]. Whilst it has been possible to corroborate the quality of global elevation data by comparing data at orbital crossover points, it has not possible to make quantitative comparisons to verify the quality of pulse-width data over regional scales until the advent of high-resolution, high-quality Digital Terrain Models (DTMs) from subsequent missions [*Kirk et al.*, 2008; *Kim and Muller*, 2009; *Kim et al.*, 2013]. Nor is it known the true effect of energy distribution within the pulse-footprint, which is revised from ∼170 m to ∼75 m in *Neumann et al.* [2003a] to account for the concentration of energy within the central half of the pulse-footprint. The work in this chapter attempts to address these issues by using high-resolution DTMs from the High Resolution Imaging Science Experiment (HiRISE) and the Context Camera (CTX) to produce accurate estimates of surface roughness and slope produced at different baselines, to which different versions of the MOLA pulse-widths are compared and effectively calibrated. The aim is to identify the best performing MOLA dataset and find a consistent relationship that can be extrapolated to global coverage to enable accurate and reliable comparisons to be made between different Martian terrains and with terrestrial analogues, to further our knowledge of surface formation and evolution, and identify candidate landing and roving sites.

3.2 LITERATURE REVIEW

Recent research on global Martian surface roughness use a range of datasets including (1) MOLA elevation profiles and pulse-width data [*Garvin et al.*, 1999; *Kreslavsky and Head*, 1999, 2000; *Neumann et al.*, 2003a; *Smith et al.*, 2001], (2) radar data from Mars SHAllow RADar sounder (SHARAD) and Mars Advanced Radar for Subsurface and Ionosphere Sounding (MARSIS) [*Campbell et al.*, 2013; *Grima et al.*, 2012; *Mouginot et al.*, 2009; *Picardi et al.*, 2004], and (3) thermal emission data from Thermal Emission Spectrometer (TES) and THermal EMission Imaging System (THEMIS) [*Hébrard et al.*, 2012; *Mushkin and Gillespie*, 2006], which, depending on the instrument, provide estimates of surface roughness at 10 m to 10 km baselines. Local studies have used both DTMs and high resolution surface imagery to assess the roughness, typically for landing and roving site selection [*Golombek et al.*, 1997, 1999, 2005, 2009, 2012a,b; *Grant et al.*, 2011b]. These studies typically use high-resolution images, which are not used in global comparisons due to the relatively low global coverage [*Cord et al.*, 2007; *Kim and Muller*, 2009; *Kim et al.*, 2013; *McEwen et al.*, 2010].

Garvin et al. [1999] explore the relationship between pulse-width and surface characteristics, using data from 18 orbits from early in the mission and applying minor corrections for instrument effects. They find the Northern Plains to be smoother than any desert on Earth, and conclude that

pulse-widths represent surface roughness rather than slope over most areas of Mars, mirroring a result from Shuttle Laser Altimeter (SLA)[1] pulse-widths over terrestrial dunes [*Garvin et al.*, 1998]. Using these findings, the theory proposed by *Gardner* [1992], and data from the first year's mapping, *Smith et al.* [2001] present a map of the global distribution of surface roughness from pulse-width data. This map is updated by *Neumann et al.* [2003a], who remove large amounts of saturated and cloud hitting pulses from the original Precision Experiment Data Record (PEDR) dataset, and apply large-scale slope corrections, both along- and across-track, to the pulse-width values using Equation 2.7 and a 1 km gridded MOLA elevation dataset. The result is shown in Figures 1.1a and 1.1b in Chapter 1. As part of their study, *Neumann et al.* [2003a] suggest the MOLA pulse-footprint is approximately half the original 168 m estimate given in *Smith et al.* [2001], owing to hot-spot effects, as discussed in Section 2.1.5. From this, *Neumann et al.* [2003a] propose that MOLA pulse-widths provide estimates of surface roughness at 35 m baseline rather than 100 m, which assumes the original pulse-footprint estimate.

Extensive work on calibrating these pulse-widths has yet to be conducted, but early work by *Anderson* [2003] supports the idea that MOLA pulse-width could be used in landing site selection, and later work by *Kim and Muller* [2008] and *Kim and Park* [2011] suggests there could be a correlation between these pulse-widths and surface roughness at larger scales. *Anderson* [2003] find good agreement between pulse-widths and slope using ground data from Mars Exploration Rover (MER), and geologic features as identified from Mars Orbiter Camera (MOC) images. They also observe self-affine topography from MOLA pulse-width slope estimates and longer baseline elevation profiles, suggesting that finer-scale slope can be predicted from MOLA elevation profiles. *Kim and Muller* [2008] and *Kim and Park* [2011] make quantitative comparisons between MOLA pulse-widths and surface roughness estimates from DTMs across three sites on Mars, using HiRISE and High Resolution Stereo Camera (HRSC) data. They observe weak correlations, but stress that this is only an initial result over a small number of test sites, with a best correlation observed at a 50 m baseline when using the HiRISE data.

Kreslavsky and Head [1999, 2000] present maps of surface roughness from MOLA elevation profiles at 0.6 km, 2.4 km and 19.2 km baselines (Figures A.1 and A.2). They developed Equation 2.51 to remove the effect of slopes at twice the baseline at which they are studying, to highlight smaller scale features from the background slope. Both *Kreslavsky and Head* [1999, 2000] and *Smith et al.* [2001] show a correlation between surface roughness and geologic features and terrains, however, the clearest feature in these maps is the Mars dichotomy, with the northern plains appearing much smoother than the rough southern highlands. Smaller features such as the dunes around the northern polar cap (210° E, 80° N) also show up as being rough at 0.6 km baseline in *Kreslavsky and Head* [1999, 2000], as well at pulse-footprint scales in *Neumann et al.* [2003a].

The roughest terrain is found around Olympus Mons, an area known as Lycus Sulci (215° E, 30° N) [*Kreslavsky and Head*, 1999, 2000; *Neumann et al.*, 2003a]. The formation processes of the terrain are discussed in the Section 3.8, but can be summarised by a series of extensional features

[1] SLA was a precursor to the MOLA and Ice, Cloud, and land Elevation Satellite (ICESat) missions produced from MOLA flight-spares

formed of material that has slipped from Olympus Mons. In the *Kreslavsky and Head* [1999, 2000] data, these aspect dependent roughness features could lead to a bias in the results, as this data effectively uses north-south orientated profiles and could therefore underestimate roughness in the east-west direction, whereas the surface roughness estimates from pulse-widths are independent of aspect and do not have such problems. Other notable features are Vallis Marineris (300° E, 0° N) and the chaos terrains to the east of this canyon system (270° E to 345° E, 0° N), regions of very rough terrain in both map types.

Surface roughness derived from radar using SHARAD, shown in Figures A.3 and A.4, shows good agreement with that from MOLA elevation profiles and pulse-widths, whilst *Grima et al.* [2012] observe that SHARAD reflectivity correlats well with surface slope [*Campbell et al.*, 2013]. Lycus Sulci, the northern dunes, and Vallis Marineris, appear similarly rough in both this data and MOLA data.

Finally, *Hébrard et al.* [2012] present aerodynamic roughness length maps derived from rock abundance maps (Figures A.5 to A.8). The rock abundance maps are inferred from TES, and converted to aerodynamic roughness length data using the relationship derived in *Marticorena et al.* [2006]. Like *Anderson* [2003], this data is calibrated using data from Mars landing sites, before being extended to the rest of Mars.

Other than in geological studies, how have these roughness maps been used? *Heavens et al.* [2008] use the *Neumann et al.* [2003a] and *Kreslavsky and Head* [1999, 2000] data to derive maps of aerodynamic roughness length, which are applied in climate models to study the sensitivity of climate models to surface roughness. More commonly, surface roughness data has been used to find safe landing and traverse sites for landers [*Golombek et al.*, 1999, 2005, 2012a]. Recent landing site selection has been able to use high-resolution DTMs to derive maps of local surface roughness, using techniques described in Section 2.3, but these DTM datasets are yet to achieve global coverage, calibrating MOLA pulse-widths could provide a useful tool for identifying target sites [*Golombek et al.*, 1999, 2005, 2012a; *Grant et al.*, 2011b].

3.3 MARS ORBITER LASER ALTIMETER

MOLA was one of five science instruments on-board MGS [*Smith et al.*, 2001]. The primary goal was to map the topography of the planet *at a level suitable for geophysical, geological, and atmospheric circulation studies*, as shown in Figures 3.1a and 3.1b, whilst secondary goals included improving our knowledge of the 3-dimensional structure of Mars' atmosphere, local surface characterisation, surface reflectivity, and seasonal changes in the polar environments [*Smith et al.*, 2001]. Most of these goals were completed during the mapping phase (1999 to 2001), before the laser failed after 670×10^6 pulses [*Smith et al.*, 2001]. This section describes the instrument, with a schematic and outline of the instrument shown in Figure 3.2 and Table 3.1 respectively. The background theory of laser ranging is discussed in Section 2.1.

The instrument operated mainly at nadir pointing angles, collecting data directly beneath the orbit path of MGS; but was occasionally forced to operate at other angles to accommodate for

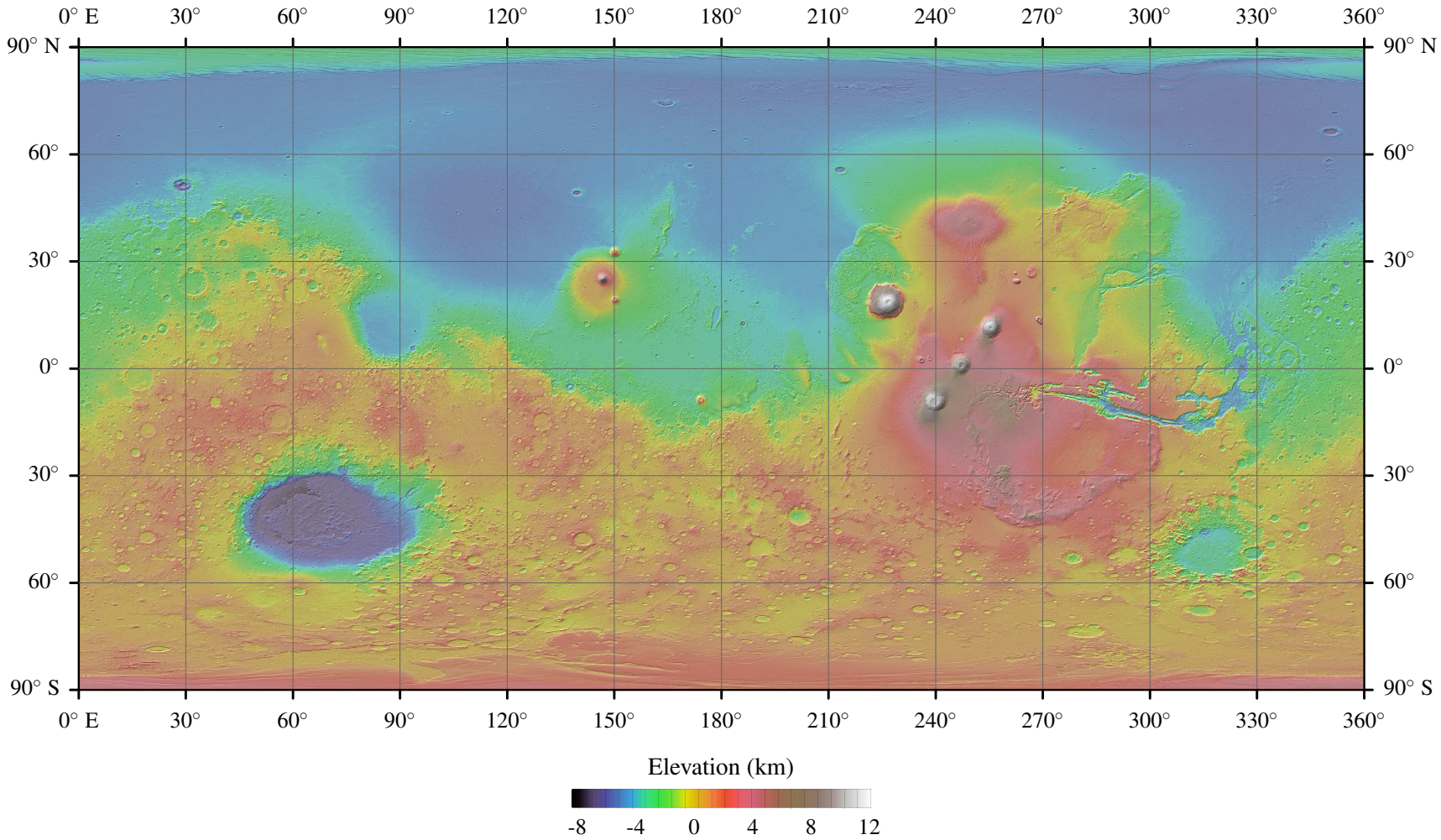

Figure 3.1a: Map of Mars topography from MOLA [*Smith et al.*, 2001]. This data is the gridded version of the dataset, with a resolution of 463 m per pixel. Some areas, particularly around the equator, are heavily interpolated due to the 4 km average inter-orbit spacing at the equator [*Smith et al.*, 2001].

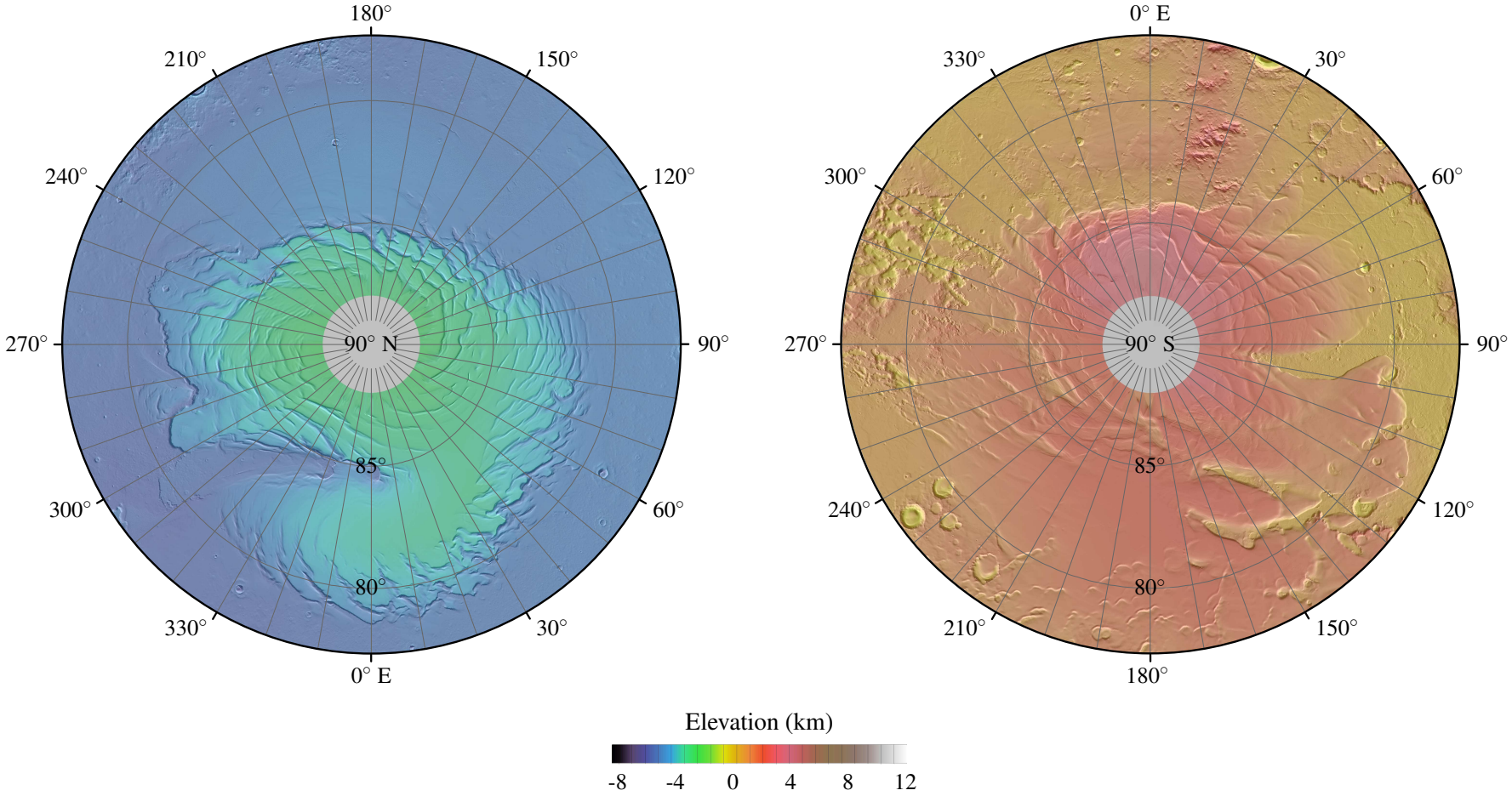

Figure 3.1b: Map of Mars polar topography from MOLA [*Smith et al.*, 2001]. This data is the gridded version of the dataset, with a resolution of 463 m per pixel.

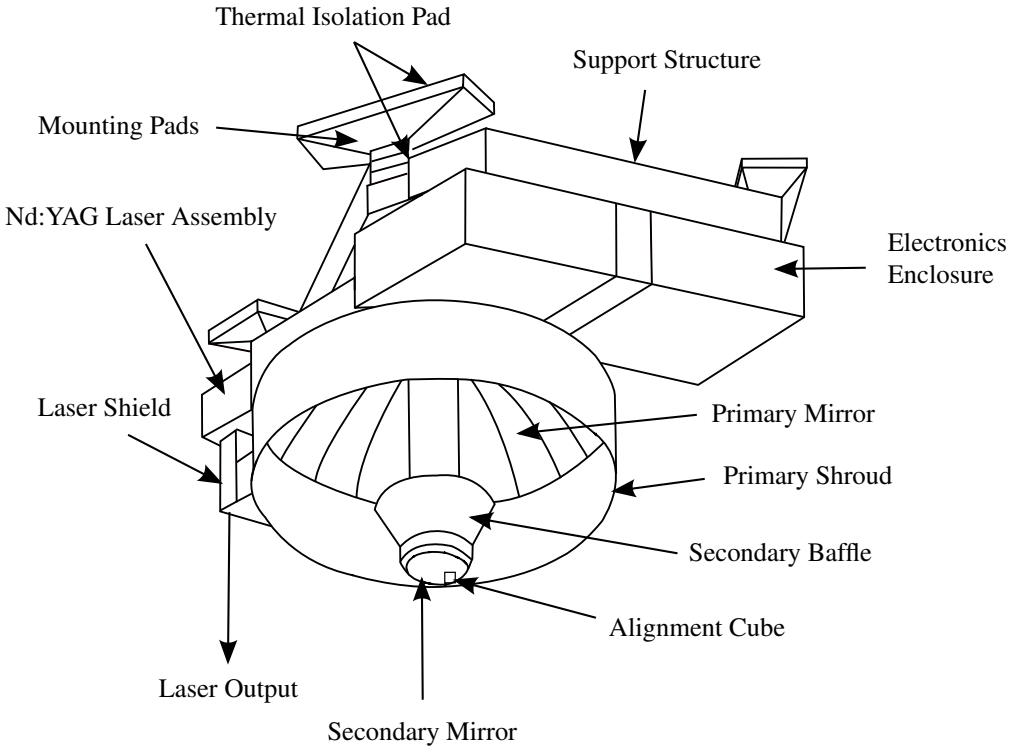

Figure 3.2: Schematic of the MOLA instrument that forms part of the MGS science payload, adapted from *Abshire et al.* [2000]. Table 3.1 gives an overview of instrument performance.

instruments [*Smith et al.*, 2001]. Figure 2.1 shows some planned orbits (Top), and the actual orbits with elevation data over Eberswalde Crater (Bottom). For regional and global studies, the MOLA gridded elevation dataset is particularly useful, however, with a typical inter-orbit spacing at the equator of 4 km, studying localised areas should include high-resolution elevation datasets, such as those discussed in Section 3.4, as the interpolated terrain is not reliable [*Smith et al.*, 2001].

The MOLA elevation dataset remains the highest resolution, and most reliably georeferenced, global elevation dataset available over Mars (Figures 3.1a and 3.1b) [*Gwinner et al.*, 2009; *Kirk et al.*, 2008; *Neumann et al.*, 2003a]. To make an elevation measurement: a pulse is fired towards the target surface (Figure 3.3a), which triggered the start of the ranging timing unit. The timing unit stopped when the echo-profile surpassed a threshold that was controlled, and continuously adjusted, by on-board software that used the received energy of previous pulses and background noise to estimate a sensible threshold [*Abshire et al.*, 2000; *Smith et al.*, 2001]. To minimise noise from backscattered solar photons, a range gate between 20 km to 80 km of the expected elevation was used, which was reduced to the minimum when terrain was correctly identified in previous pulses [*Smith et al.*, 2001]. The 2.5 ns timing resolution of the instrument resulted in a theoretical elevation accuracy of 0.38 m on smooth level surfaces, which in practise was $<$1 m and $\sim$10 m over slopes of 30° [*Abshire et al.*, 2000; *Smith et al.*, 2001]. A combination of this level of elevation accuracy and a horizontal accuracy of $<$100 m means that the MOLA elevation dataset is commonly used as a basemap to which other Mars datasets are co-registered [*Gwinner et al.*, 2009, 2010; *Kim and Muller*, 2009; *Kim et al.*, 2013; *Kirk et al.*, 2008; *Neumann et al.*, 2003a].

Stopping the laser ranging unit automatically triggered the start of the pulse-width timer, which

Table 3.1: Characteristics of the MOLA instrument, from *Smith et al.* [2001].

Element	Parameter	Specification
MOLA	Mass	23.8 kg
	Power consumption	34.2 W
Transmitter	Laser type	diode pumped, Q-switched, Cr:Nd:YAG
	Wavelength	1064 nm
	Pulse rate	10 Hz
	Energy	48 mJ pulse^{-1}
	Laser divergence	420 µrad
	Pulse length	8 ns
Receiver	Mirror	50 cm parabolic
	Detector	silicon avalanche photodiode
	Field of view	850 µrad
Electronics	Microprocessor	80C86
	TIU frequency	99.996 MHz
	Filter channel widths	20 ns, 60 ns, 180 ns and 540 ns
	Data rate	618 bit s^{-1} continuous
Resolution	Maximum ranging distance	787 km
	Range resolution	37.5 cm
	Vertical accuracy	1 m
	Surface spot size	168 m (75 m in *Neumann et al.* [2003a])
	Along-track pulse spacing	300 m
	Across-track pulse spacing	4 km

Table 3.2: MOLA filter channel characteristics from *Smith et al.* [2001].

Characteristic	1	2	3	4
Description	Smooth	Moderate	Rough	Clouds
Channel Width (ns)	20	60	180	540
Terrain Height Variation	3	9	27	81
Surface Slope (°)	1.0	2.9	8.6	24.2

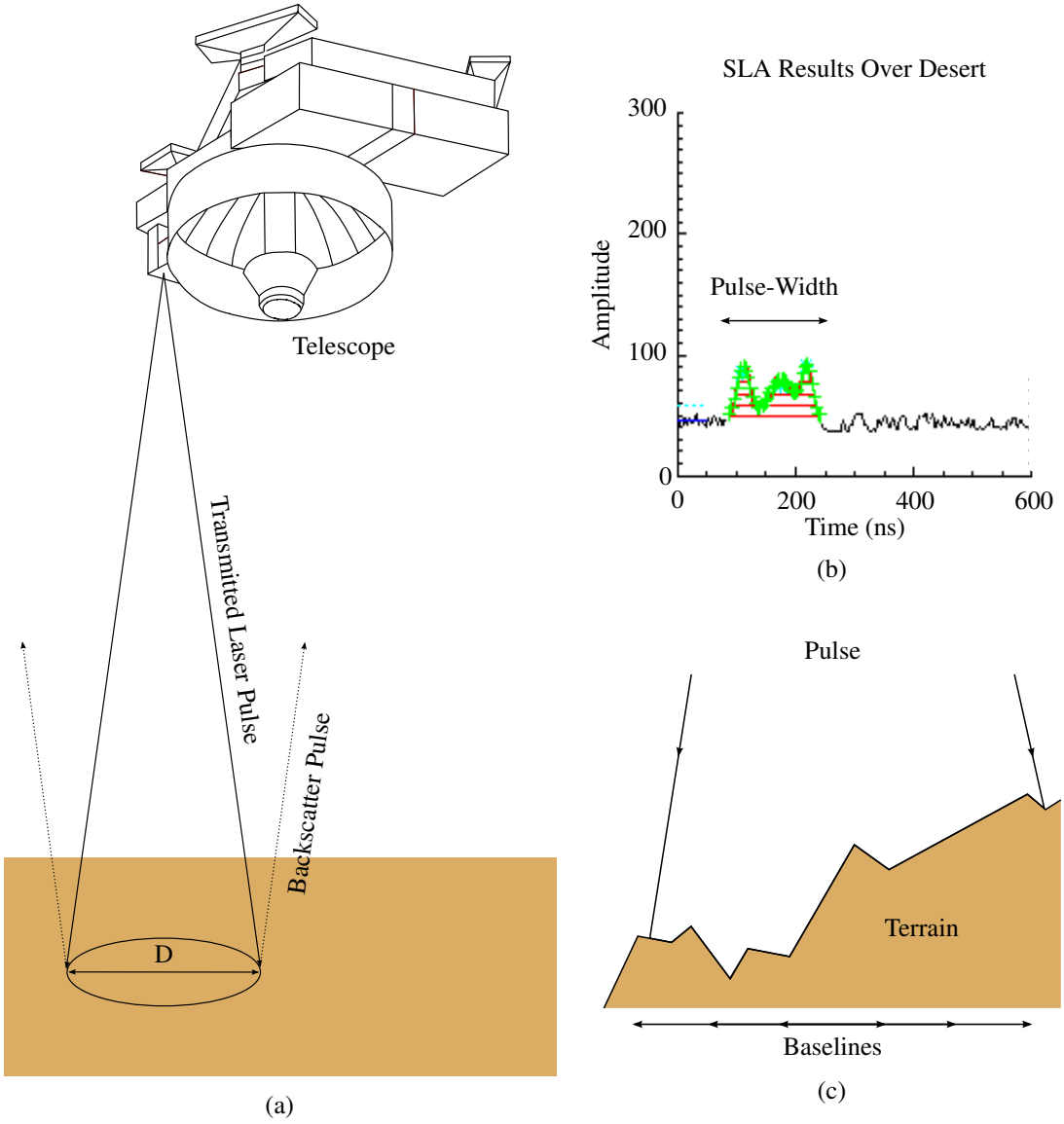

Figure 3.3: Schematic of MOLA pulse divergence over terrain (a), an example SLA echo-profile over terrestrial desert terrain (b), and how different divergence angles determine the scale of roughness features the pulse-widths respond (c).

stopped when the echo-profile dropped back below the threshold, as shown in Figure 3.3b. Unlike the Earth-orbiting SLA, which included an on-board signal digitiser, MOLA returned only the pulse-width and not the echo-profile (Figure 3.3b) [*Garvin et al.*, 1998]. An estimate of the Full Width Half Maximum (FWHM) pulse-width was calculated from the received energy and the threshold pulse-width and provided the PEDR dataset.

To increase detection probability, received pulses were amplified and the pulse-width was matched to one of four filters that best fitted surface or atmospheric properties, as outlined in Table 3.2. However, the pulse-width channel did not have to match the channel that recorded the ranging measurement, which used the filter that exceeded the detection threshold and had the shortest impulse-response width (Equation 2.5) [*Smith et al.*, 2001].

The original MOLA data is stored in PEDR files, and includes the threshold and FWHM pulse-

Table 3.3: Criteria for excluded pulses during production of the Slope-Corrected MOLA pulse-width dataset from the PEDR [*Neumann et al.*, 2003a].

Criteria	Value
Off-Nadir Angle (°)	≤2
Valid Altitude Flag	0
Energy Counts	≤255
Pulse-Width Counts	≤63

width estimates, the latter are used to estimate surface roughness in *Smith et al.* [2001]. A second version of the pulse-widths, known as Slope-Corrected pulse-widths, is presented in *Neumann et al.* [2003a] and presented in Figures 1.1a and 1.1b. These pulse-widths use a version of the MOLA gridded elevation dataset to make 1 km along- and across-track slope corrections to the PEDR pulse-widths to derive estimates of roughness from background slope, as in Equation 2.7. Cloud hitting pulses, from which *Neumann et al.* [2003b] present a two-year Martian cloud study, returns that saturated the receiver, and large off-nadir pulses are also removed to improve dataset quality (Table 3.3). Of the remaining pulse-widths, *Neumann* [2011] states that they

> ... are generally values that are attenuated by some amount of dust and scattering in the atmosphere, which may introduce forward-scattering dispersion of pulses but that didn't seem to matter unless the pulses were very weak (energy down around 10).

As *Neumann et al.* [2003a] already remove low energy echo-pulses, the effect of forward scattering is minimised in the Slope-Corrected dataset. Further identification of affected pulses is not possible as the corresponding atmospheric dust concentrations are not known, but as the atmosphere is very thin (4 mbar to 6 mbar), this effect is assumed negligible and path extension due to forward scattering is thought to be a few centimetres [*Abshire et al.*, 2000].

Finally, *Smith et al.* [2001] assume the PEDR dataset to estimate surface roughness at ∼100 m baseline, whilst *Neumann* [2011] assume 90 % of the energy to be concentrated within half the radius of the original pulse-footprint estimate and therefore reduces the surface roughness baseline to 35 m. To be able to test these estimates of baselines at which MOLA pulse-widths estimate surface roughness (Figure 3.3c), the pulse-widths are compared against surface characteristics from high-resolution DTMs, which are discussed in the following section.

3.4 DIGITAL TERRAIN MODELS

The high-resolution DTMs used in this chapter are derived from stereo-photogrammetry. This section introduces the cameras and an overview of the resulting datasets. Of the three camera systems introduced here, only data from HiRISE and CTX are compared to the MOLA pulse-widths; the HRSC instrument is used during co-registration, which is described in Section 3.6.

3.4.1 HIGH RESOLUTION IMAGING SCIENCE EXPERIMENT CAMERA

The HiRISE instrument is one of six scientific instruments on-board the Mars Reconnaissance Orbiter (MRO), which has been operational since 2006 [*HiRISE*, No Date.; *Zurek and Smrekar*, 2007; *McEwen et al.*, 2007, 2010]. As of February 2014, over 31 000 images were available, each capturing the surface at unprecedented resolution (0.25 m pixel^{-1} to 0.30 m pixel^{-1}), but at the expense of spatial coverage: typical image size is 5 km to 6 km by 25 km to 30 km [*McEwen et al.*, 2007, 2010; *HiRISE*, No Date.; *Zurek and Smrekar*, 2007]. The low spatial coverage of individual images means that each image must be of high scientific value, which requires careful planning, with each image classified into one or more of 18 science themes, and a special emphasis on candidate landing sites [*McEwen et al.*, 2007, 2010]. To date, these images have enabled scientists to study (1) seasonal changes such as recurring slope linea [*McEwen et al.*, 2011], (2) bedrock stratigraphy and mineral deposits [*Noe Dobrea et al.*, 2010; *Rice et al.*, 2011; *Thomson et al.*, 2011], and (3) the geological characterisation of landing sites and identify potential hazards for landers and rovers [*Grant et al.*, 2011b; *Golombek et al.*, 2012a].

HiRISE images are produced from 14 separate Charge Coupled Devices (CCDs), with greyscale images produced using 10 adjacent CCDs and colour images produced over a region occupying the central two, as shown in Figure 3.4 [*McEwen et al.*, 2007, 2010]. As the viewing angle relative to MRO is fixed, off-nadir viewing angles for stereo-pairs are produced by spacecraft roll, as shown in Figure 3.5 [*McEwen et al.*, 2007, 2010]. This means that images must be acquired during different orbits [*McEwen et al.*, 2007, 2010]. To minimise the differences between images due to seasonal effects, such as frost deposition, and atmospheric effects, such as dust storms and clouds, stereo-images are typically taken within 2 months of each other [*McEwen et al.*, 2010, 2011]. The HiRISE team aim for a 15° difference in viewing angle between stereo-pairs, from which 1 m pixel^{-1} DTMs with 0.20 m vertical precision can be produced [*Kirk et al.*, 2008; *Kim and Muller*, 2009; *Kim et al.*, 2013; *McEwen et al.*, 2010]. Significant visual differences in images pairs is one reason for poor stereo-matching in the DTM production process, as discussed in Section 2.2.2.3, so if images cannot be acquired within this timeframe, the science team wait until the second image can be acquired at similar sub-solar latitudes and illumination conditions [*McEwen et al.*, 2010].

The aim during the Primary Science Phase (PSP) was to image ∼1 % of the Martian surface using ∼12 000 images; in practise however, just over 9000 images were acquired, covering ∼0.55 % of the surface in unique coverage: ∼0.60 % of the surface would have been covered if there was no repeat coverage for errors, seasonal changes, or stereo [*McEwen et al.*, 2007, 2010]. The decision to acquire less images was taken to suppress engineering concerns, but resulted in larger images and a greater volume of data than originally planned [*McEwen et al.*, 2010]. Of the PSP images, ∼21 % (960 pairs) are one of a stereo-pair [*McEwen et al.*, 2010]. A similar proportion exists today, with >3600 pairs acquired during the PSP and Extended Science Phases (ESPs), which cover ∼0.24 % of the surface with unique HiRISE stereo-pairs (3.51×10^5 km^2) Table 3.4 [*HiRISE*, No Date.]. However, producing high-quality HiRISE DTMs is not an automatic process and requires heavy processing and human input. As a result, only 170 DTMs are freely available via *HiRISE* [No

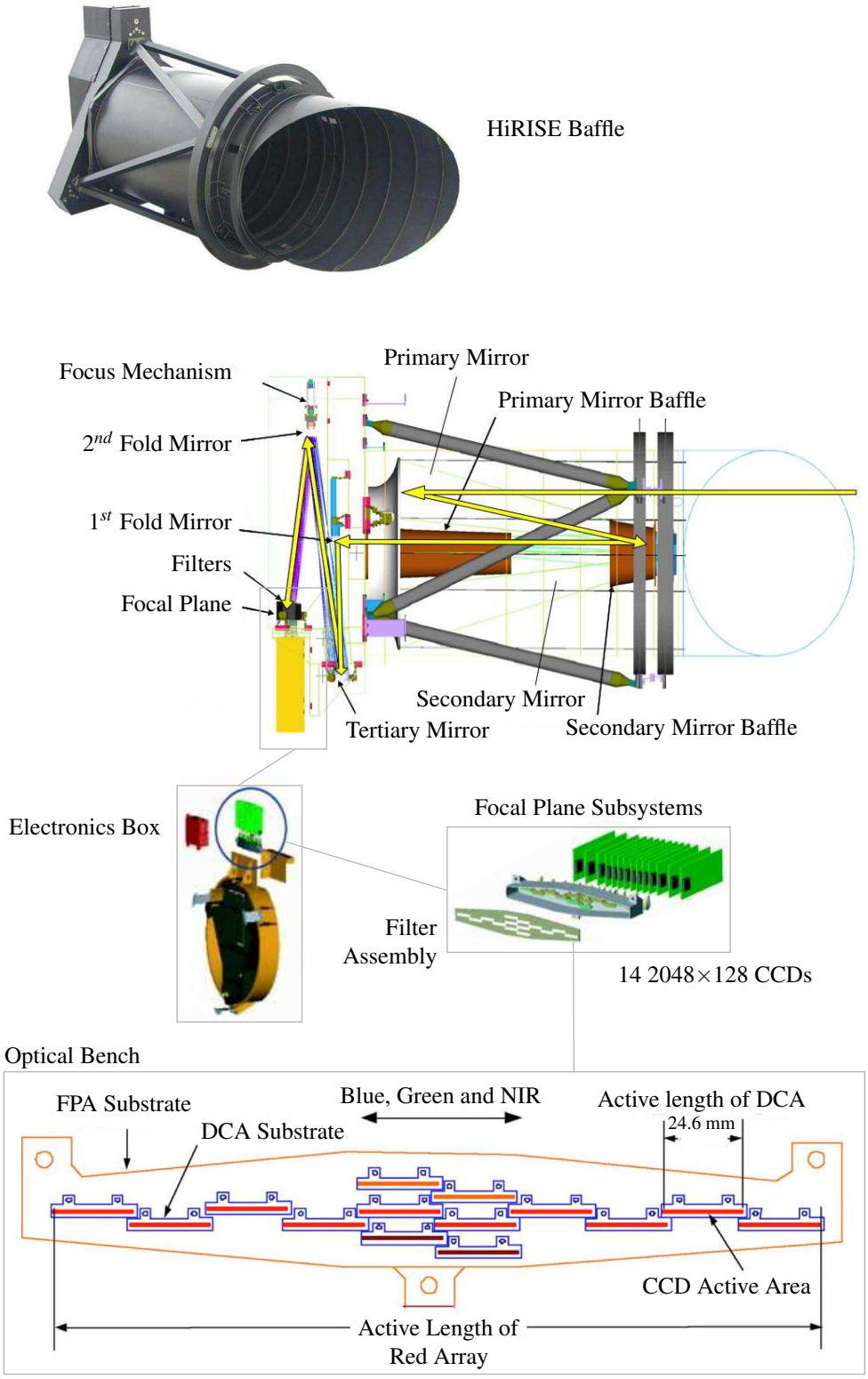

Figure 3.4: Schematic of the HiRISE instrument, adapted from *Deardorff* [No Date.]. Top: image of the HiRISE baffle. Middle: schematic of the internal structure of the HiRISE instrument. Bottom: schematic of the electronics and the CCD setup for the red, blue, green, and Near-infrared (NIR) channels.

Table 3.4: Characteristics of the MRO spacecraft and the HiRISE and CTX instruments [*Malin et al.*, 2007; *McEwen et al.*, 2007; *Zurek and Smrekar*, 2007; *Kirk et al.*, 2008; *McEwen et al.*, 2010; *Kim et al.*, 2013]. † coverage uses a sinusoidal projection and data from *Planetary Data System* [No Date.].

Element	Parameter	Specification
MRO	Orbit	Near Polar 255 km × 320 km
	Orbit Length (Time)	112 min (∼3 pm)
	Ground Speed	3.2 km s^{-1}
	Mass	∼1100 kg
HiRISE	Mass	65 kg
	Power Consumption	60 W
	Resolution	0.25 m $pixel^{-1}$ to 0.3 m $pixel^{-1}$
	Max Image Size	20 000 pixels × 63 780 pixels
	Image Size	5 km to 6 km swathe by 25 km to 30 km
	CCDs	10 Red, 2 Blue, Green, and NIR
	CCD Width	2048 pixels
	Max Image Size	3.5 GB in 6 s (28 Gbit)
	FOV	1.14°
	Mirror	0.5 m
	Focal Length	12 m
	F-Stop	24
	Image Coverage	1.54 % (2.24×10^6 km^2)
	Stereo-Angle	15° to 20°
	Stereo Coverage	0.24 % (3.51×10^5 km^2)
	DTM Resolution	1 m (0.25 m vertical accuracy)
	DTM Coverage	0.01 % (1.58×10^4 km^2)
CTX	Power Consumption	5 W idle, 7 W imaging
	Resolution	6 m $pixel^{-1}$ to 7 m $pixel^{-1}$
	CCD Width (Band-Pass)	5064 pixels (500 nm to 700 nm)
	Max Image Size	256 MB (2 Gbit)
	FOV	5.7°
	Image Size	∼30 km × ≥40 km
	Focal Length	350 mm
	F-Stop	3.25
	Image Coverage	84.21 % (1.22×10^8 km^2)
	Stereo-Angle	15° to 20°
	Stereo Coverage	11.79 % (1.71×10^7 km^2)
	DTM Resolution	18 m to 20 m

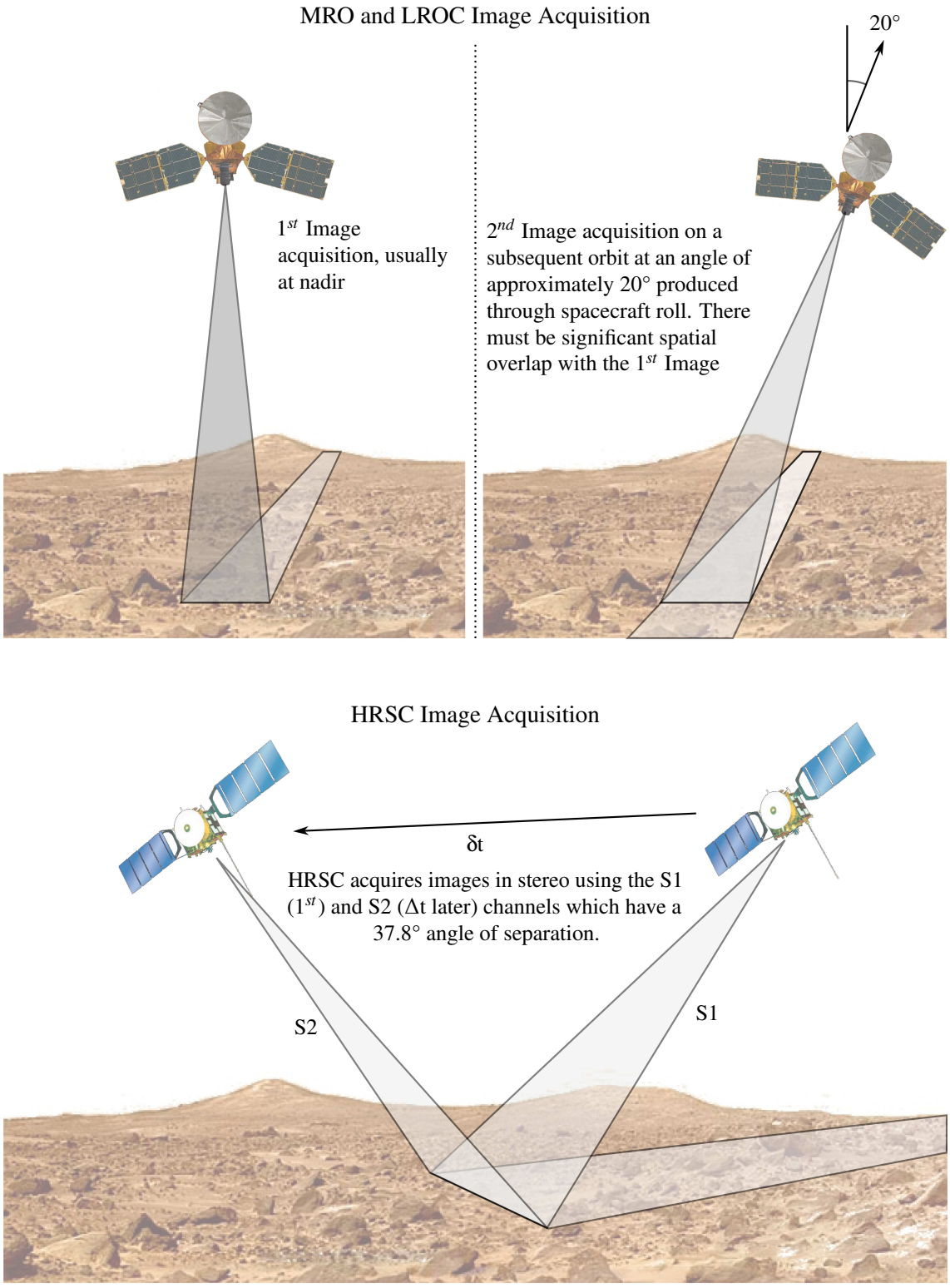

Figure 3.5: Schematic of stereo-image acquisition by MRO imagers and HRSC. Stereo-images from the MRO imagers, HiRISE and CTX, are acquired by spacecraft roll (top), whereas HRSC is a dedicated stereo-imaging instrument that acquires images through forward and backward viewing angles (bottom). The former results in images taken at during different orbits, and careful planning is required to minimise image acquisition delay that could otherwise result in atmospheric and seasonal differences, such as dust storms and frost deposition, that can affect stereo-image matching.

Date.], which are typically produced using SOftCopy Exploitation Toolkit (SOCET SET®) and Integrated Software for Imagers and Spectrometers Version 3 (ISIS3) software, as outlined in *Hare* [2010].

To produce high-resolution images and accommodate for MRO's fast ground speed (3.2 km s^{-1}), HiRISE uses Time Delay Integration to increase the Signal to Noise Ratio (SNR) by imaging each area up to 128 times with each CCD, hence the CCD depth of 128 pixels (Figure 3.4) [*McEwen et al.*, 2007]. The image repeat rate is dependent on the target surface characteristics: bright surfaces, such as the polar caps, require less imaging, especially in high contrast features such as *spider* terrain, which appears as the seasonal frost retreats [*Kieffer et al.*, 2006; *McEwen et al.*, 2007].

A negative aspect of the HiRISE dataset is its poor georeferencing. From experience, errors in HiRISE data georeferencing are typically on the scale of 100's of metres, but can be as large as several kilometres. As a result, it is important to co-register HiRISE data to other, lower resolution but correctly georeferenced datasets, especially when used with other data.

3.4.2 CONTEXT CAMERA

MRO's CTX instrument is designed to produce regional context images for HiRISE and other instruments on-board [*Malin et al.*, 2007] The 6 m $pixel^{-1}$ to 7 m $pixel^{-1}$ was carefully chosen after reviewing $\leq$7 m $pixel^{-1}$ MOC images, which revealed fine-scale geology that was not present in lower resolution images from previous orbiters [*Malin et al.*, 2007]. A schematic of the instrument is shown in Figure 3.6, along with images of the instrument with and without the baffle. The characteristics are outlined in Table 3.4.

By sacrificing very-high-resolution for spatial coverage, the CTX instrument has less emphasis on fine-scale characterisation of a site, and instead focusses on the wider geological and geomorphological context of the surface, as well as meteorological and seasonal events [*Malin et al.*, 2007; *McEwen et al.*, 2007]. Image width is $\sim$30 km from a 5.7° FOV compared to HiRISE's 1.14°, which lies at the centre of the CTX swathe [*Malin et al.*, 2007; *McEwen et al.*, 2007]. This allows for a quick characterisation of candidate landing sites as the wide swathe of the instrument means a 20 km wide landing ellipse, such as those for Mars Science Laboratory (MSL), can be contained within a single image [*Malin et al.*, 2007; *Grotzinger et al.*, 2012]. Image length is determined by the buffer size, which is 256 MB, once this is full the image is transferred to the spacecraft memory before being transmitted to Earth [*Malin et al.*, 2007].

Initially, the instrument was allocated 12 % of the data transfer during the PSP, which would cover 9 % of the Martian surface in unique coverage [*Malin et al.*, 2007]. As of 2010 this had increased to 50 % of the planet being imaged [*Malin Space Science Systems*, 2010]. Today, 55 133 images are available via the Planetary Data System (PDS) (February 2014), which cover 84.21 % of the surface. Importantly for this work, 11.79 % of these images form part of a stereo-pair, defined as images with at least 50 % overlapping spatial coverage and a difference in viewing angle of $>$15°, when using the image footprints from *Planetary Data System* [No Date.].

The same spacecraft roll that enables HiRISE to acquire stereo-images is also used for CTX, with the same plan to use roll angles of 15° or more for accurate DTM production (Figure 3.5). DTMs can be produced at 18 m pixel^{-1} to 20 m pixel^{-1}, much lower than the 1 m pixel^{-1} DTMs from HiRISE, but much larger (∼20 times) in spatial extent [*Kim and Muller*, 2009; *Kim et al.*, 2013]. A similar production chain using ISIS3 and SOCET SET® is typically used to produce these DTMs, however there is no public repository. Therefore, the CTX DTMs used in this work are made specifically duefor this project. The methods used to produce DTMs from both HiRISE and CTX are outlined in Section 3.6.1.

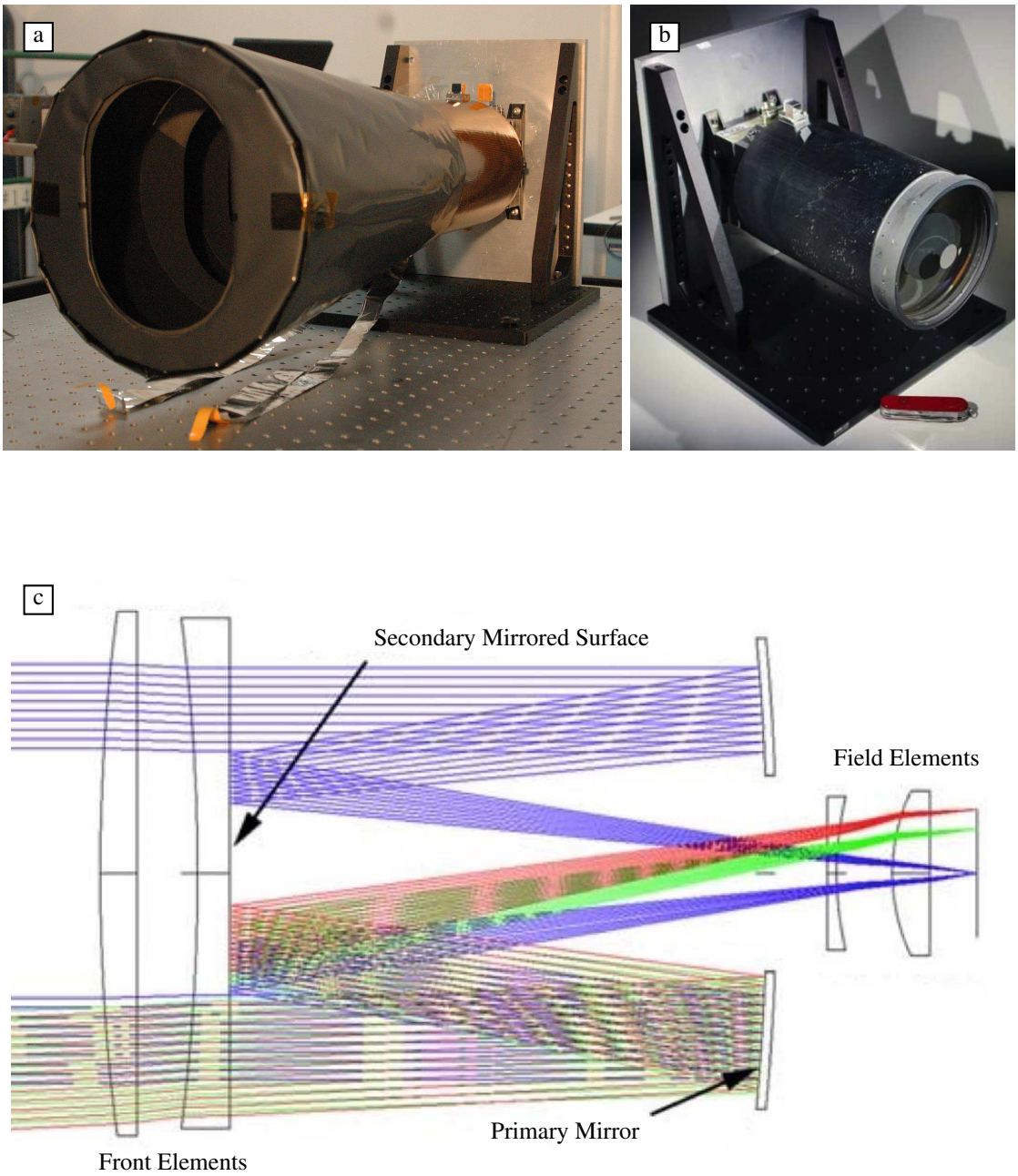

Figure 3.6: Images and schematic of the CTX instrument [*Malin Space Science Systems*, 2010]. (a) image of CTX with the baffle and (b) without (Right) the baffle. (c) schematic of the instrument and light path to the detector elements.

3.4.3 HIGH RESOLUTION STEREO CAMERA

The HRSC instrument, part of the ESA Mars Express (MEX) mission payload, has been operational since 2004, preceding the imaging instruments discussed above [*Albertz et al.*, 2005]. An image and schematic of the instrument is shown in Figure 3.7, which shows the forward and backward viewing angles for the two panchromatic and stereo channels. The characteristics of the instrument are outlined in Table 3.5.

The pushbroom instrument has nine channels, each having its own CCD, and is designed for mapping and photogrammetric analysis of the Martian surface [*Neukum et al.*, 2004]. *Gwinner et al.* [2010] report that HRSC image coverage was at 79.3 % of the surface in 2010, which has since increased to 96.51 % for all image resolutions (Table 3.5) [*Planetary Data System*, No Date.]. The camera's larger pixel size, compared to the CTX and HiRISE instruments, means that fine-scale geology cannot be observed, like it can in the other instruments. Instead, the instrument focusses the broad regional context and mapping the surface in 3-dimensions, filling in the inter-orbit gaps, at higher resolution, in the MOLA elevation data [*Albertz et al.*, 2005; *Gwinner et al.*, 2010].

Current processed DTM coverage is at 36.75 % [*Planetary Data System*, No Date.]. HRSC

Table 3.5: Characteristics of the HRSC instrument [*Neukum et al.*, 2004; *Gwinner et al.*, 2010; *Kim et al.*, 2013]. † represents coverage using a sinusoidal projection, and shapefiles from *Planetary Data System* [No Date.] available in June 2014.

Element	Parameter	Specification
MEX	Orbit	250 km × 10 100 km
	Orbit Type	Near-Polar
	Orbiter Mass	133 kg
HRSC	Mass	65 kg
	Power Consumption	45.7 W
	Resolution	12 m pixel^{-1}
	CCD Width	5184 pixels
	DTM Resolution	≥50 m (25 m in *Kim et al.* [2013])
	FOV	11.9° (8.6″)
	Image Swathe	∼60 km
	Image Length	25 km to 30 km
	CCDs	2 Stereo, 2 Panchromatic, Nadir, Red, Blue, Green, and NIR
	Stereo-Angle	37.8°
	Focal Length	175 mm
	F-Stop	5.6
	Image Coverage†	96.5 % (1.40×10^8 km^2)
	DTM Coverage†	40.48 % (5.87×10^7 km^2)

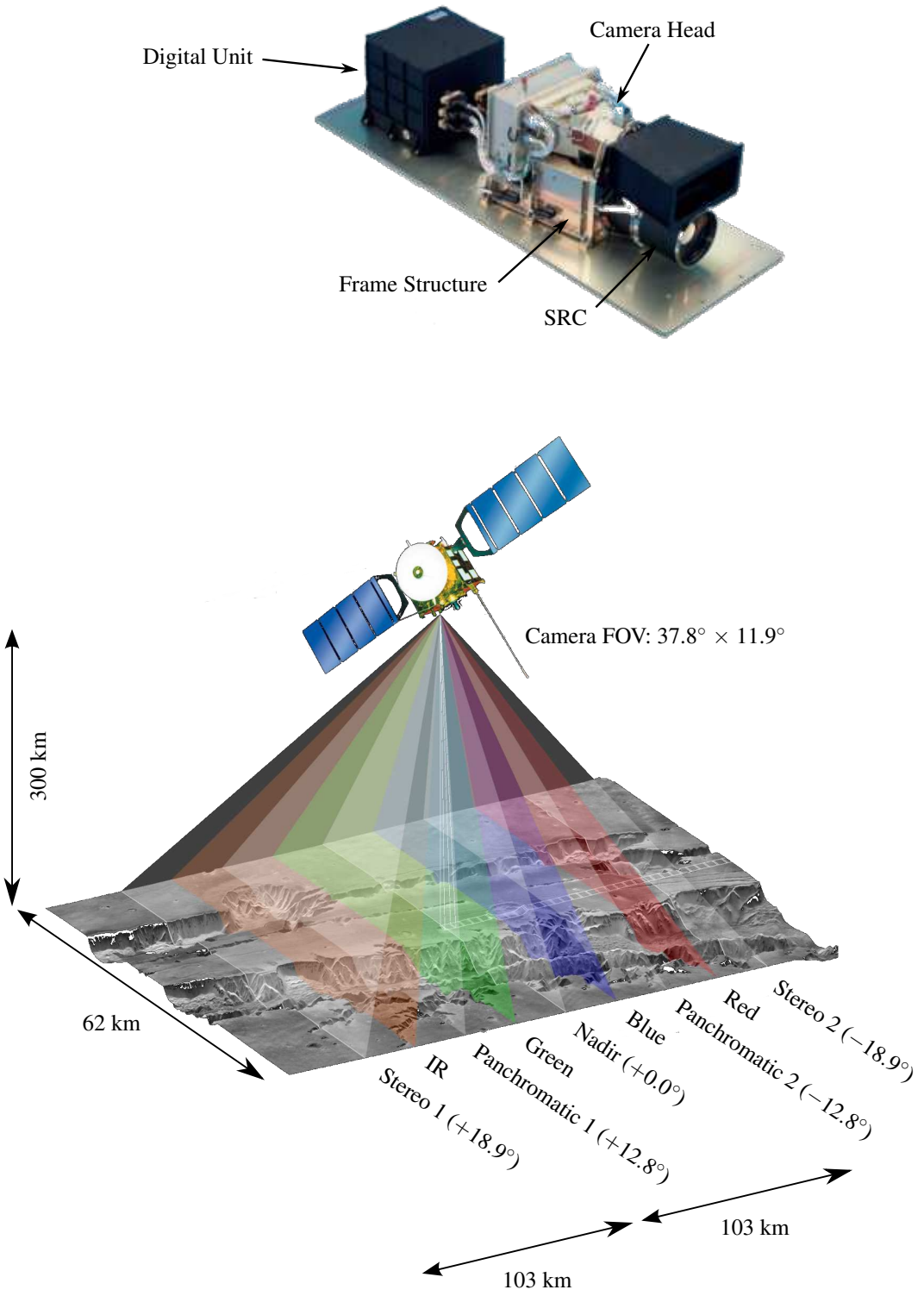

Figure 3.7: An image and schematic of the HRSC instrument on-board MEX. The viewing angle of the nadir, panchromatic and stereo channels are shown, as is the configuration of each of the colour channels. SRC refers to the Super Resolution Channel, which images the surface at 2.3 m pixel^{-1} [*Neukum et al.*, 2004].

DTMs are produced in an automatic processing chain, which places special emphasis on co-registration of the dataset to the global MOLA DTM to within 100 m, to provide data quickly rather than fine-scale geology [*Scholten et al.*, 2005; *Gwinner et al.*, 2010]. This is a major strength of the instrument, as despite the poorer image resolution of 12 m pixel^{-1} compared to CTX ($<$7 m pixel^{-1}) and HiRISE ($\sim$0.25 m pixel^{-1}), HRSC is able to provide high-quality datasets that can be used as a basemap for co-registration of CTX and HiRISE data [*Malin et al.*, 2007; *McEwen et al.*, 2007; *Gwinner et al.*, 2010]. The DTMs produce data for broader region context and fill the inter-orbit gaps from MOLA profile data [*Gwinner et al.*, 2010; *Smith et al.*, 2001].

Two of these channels are dedicated stereo-image channels that view the surface at ±18°, and another pair with viewing angles of ±12.8° [*Gwinner et al.*, 2010]. These channels are used with nadir channel nadir channel images to produce DTMs at $\geq$50 m pixel^{-1} [*Gwinner et al.*, 2010; *Neukum et al.*, 2004]. [*Kim et al.*, 2013] have been able to produce DTMs at 25 m pixel^{-1}, however, the quality is shown to be poor in slope maps, which highlight pits and spikes. The setup enables stereo-images to be acquired near-simultaneously, meaning that surface and atmospheric properties remain as similar as possible between the two images, whilst also having a fixed viewing angle between the images, which aids stereo-matching. Stereo-matching uses the approximate locations of pixels in corresponding quasi-epipolar-rectified images[2], known by the fixed camera geometry and timing, which is then refined to sub-pixel matching using an adaptive least-squares window-based matching scheme [*Scholten et al.*, 2005]. Matching points are chosen based on how many times they have been matched across the five channels, which introduces redundancy to improve stereo-matching quality [*Scholten et al.*, 2005]. Matching errors do occur however, especially over featureless terrain and sometimes due to compression and downlink artefacts [*Scholten et al.*, 2005].

3.5 MARS COORDINATE SYSTEMS

Different aerographic coordinate systems have been used, slowly evolving as each iteration of a new Mars coordinate system uses higher accuracy data from subsequent missions [*Duxbury et al.*, 2002; *Seidelmann et al.*, 2002]. Earlier recommendations to use only planetographic latitudes have since been scrapped; the commonly used datasets today follow the guidelines from the International Astronomical Union (IAU)2000, which allows planetocentric latitude [*Davies et al.*, 1980; *Duxbury et al.*, 2002; *Seidelmann et al.*, 2002]. Table 3.6 outlines the coordinate systems employed by the data used in this chapter [*Bennett et al.*, 2011].

Most of the datasets used in this work use the IAU2000 coordinate frame and planetocentric latitudes to define the latitude and longitude. This system is already defined in ArcMap and therefore easy to implement, reducing the chance of error in coordinate system definitions. The exception is the HRSC DA4 DTMs, which uses a spherical map projection system for latitude and longitude definition. As a reference surface, the datasets used in this chapter use the aeroid, an equipotential surface derived from MOLA data and available in the Mission Experiment Gridded

[2]The term *quasi*-epipolar-rectified refers to the fact that this is a pushbroom camera, and therefore does not have epipolar lines like frame-camera systems.

Table 3.6: List of Mars instruments and data products and the coordinate systems used [*Bennett et al.*, 2011; *Rossi*, 2008]. Table 2.2 outlines the IAU2000 ellipsoidal reference systems. Mars Digital Image Mosaic (MDIM) 2.1 is used only by Viking. † R=3396.0 km. Note that the HRSC .DT4 data is not used in this work, but included for completeness.

Instrument	Dataset	Map System	Reference Surface	Reference Latitude
HiRISE	DTM	IAU2000	Aeroid	Planetocentric
HRSC	DTM (DT4)	Spherical†	Sphere	Planetocentric
HRSC	DTM (DA4)	Spherical†	Aeroid	Planetocentric
Viking	MDIM2.1	IAU2000	-	Planetocentric
MOLA	PEDR	IAU2000	Aeroid	Planetocentric
MOLA	MEGDR	IAU2000	Aeroid	Planetocentric

Data Record (MEGDR) (Table 3.6).

During the data preparation process described below, all data is reprojected into a common projection reference frame to best display the data for each of the study regions.

3.6 METHODS

The methods used to produce and co-register HiRISE and CTX DTMs, extract MOLA data, and produce surface roughness and slope maps from the DTMs for the work in Sections 3.7 and 3.8 are outlined below. This is followed by a description of detrending data, which is required in Section 3.9. Finally, the methods to extract the surface roughness and slope values, and compare them to the MOLA pulse-widths are described.

3.6.1 HIRISE AND CTX DTM PRODUCTION

The HiRISE DTMs were downloaded from the public archive at *HiRISE* [No Date.], whilst the CTX DTMs were produced specifically for this project. Processing of HiRISE stereo-pairs closely follows the method outlined in *Kirk et al.* [2008], who discuss the development of the methods that use a combination of ISIS3 and SOCET SET®; a similar processing chain is employed to produce CTX DTMs. Both processing chains are outlined below and presented in Figure 3.8; the command line processes are presented in *United States Geological Survey* [2009].

Identify images Acquisition of stereo-pairs is carefully built in to the MRO mission plan, as it requires off-nadir viewing angles that affects other instruments on-board. HiRISE images are tagged as stereo-pairs and available from *HiRISE* [No Date.] [*McEwen et al.*, 2007, 2010]. The same tagging information is not available for CTX stereo-pairs, which are identified as images with significant overlap and $\geq 15°$ difference in viewing angle as in Figure 3.5.

Preprocessing ISIS3 is used for the preprocessing of the raw images from HiRISE and PDS format CTX images. This step includes image format conversion and adding Spacecraft

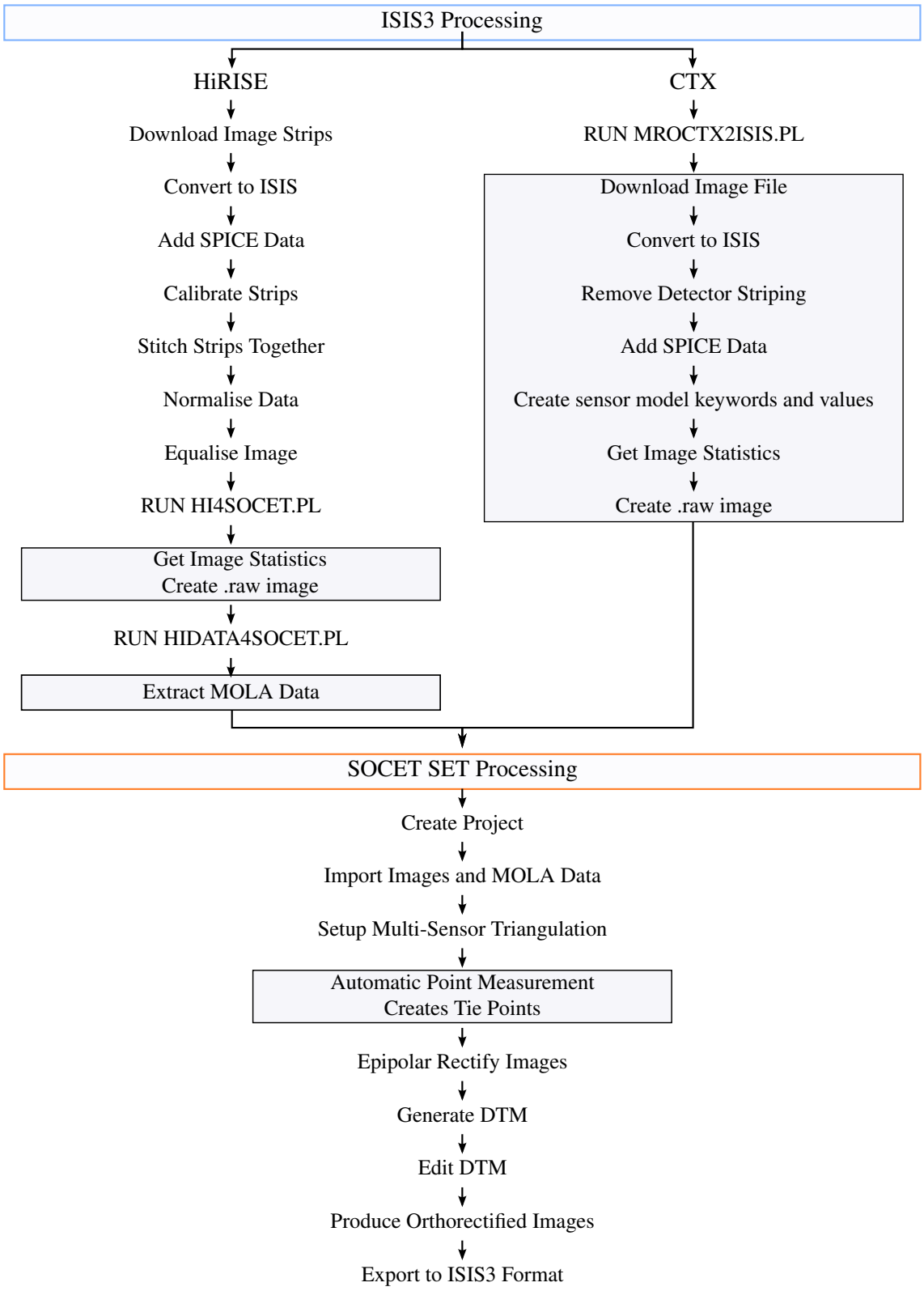

Figure 3.8: Flow diagram of the CTX and HiRISE DTM processing chains using ISIS3 and SOCET SET®, from *United States Geological Survey* [2009]. Grey boxes are processes that are run within the PERL (.pl) scripts.

and Planetary ephemerides, Instrument C-matrix and Event kernels (SPICE) data to add georeferencing information to the data. Raw HiRISE images are provided in 20 image strips, two per CCD, which are stitched together and equalised across the 10 CCD image strips that form a singe image; CTX images require a correction for a striping effect that can occur across an image [*United States Geological Survey*, 2009]. Finally, image statistics files and 8 bit .raw images are created, in preparation for SOCET SET® processing. MOLA DTM data from the Region-Of-Interest (ROI), including a large buffer zone, is extracted from the global dataset, which is used as a seed to improve matching accuracy and efficiency by providing constraints on the disparities [*Kim and Muller*, 2009; *Kim et al.*, 2013; *Kirk et al.*, 2008].

SOCET SET® Setup In SOCET SET®, a project file is created that provides an indication of the geolocation and elevation, and the geographic coordinate system to be used by the project. The image files and MOLA DTM data are imported into this project. Multi-Sensor Triangulation (MST) is performed on the images, which applies bundle-adjustment to improve co-registration between the images, and between the images and the ground-truth MOLA DTM data, by improving estimates of different parameters, such as camera pointing and position [*United States Geological Survey*, 2009]. The MST setup file defines limits as to how much these parameters are allowed to change during bundle-adjustment, with the improved estimates defined as the minimum sum-of-weighted and squared-errors for the assessment of the tie-points. These tie-points are found either automatically or manually and should ideally be evenly spread, in groups of three, across the width and length of the image to provide the best chance of high-quality stereo-matching. The errors for the tie-points are then assessed for the image as a whole, and if the Root-Mean-Square (RMS) error for the combined tie-points is less than 0.6 pixels one can move on to the next step. Otherwise, tie-points with a large RMS error (>2 pixels) should be removed and the result reassessed in an iterative process until the total RMS error is less than 0.6 pixels.

DTM production Before making the DTM, the images are epipolar rectified. A seed DTM is produced using these images and the Next-Generation Automatic Terrain Extraction (NGATE) process, which uses a combination of feature- and local-based matching, as described in Section 2.2.2.2 on Page 64. The Adaptive Automatic Terrain Extraction (AATE) matching strategy is then applied, using the NGATE strategy DTM as a seed, with the effect of smoothing the initial DTM result for a more reliable DTM product [*BAE Systems*, 2007; *Zhang and Miller*, 1997]. In areas where matching is poor, the final DTM may need editing, which can be completed in SOCET SET® using tools to smooth, fill, and interpolate surfaces within a polygon. In the CTX DTMs produced for Section 3.8 this is not carried out, instead, areas of poor matching are masked out. HiRISE DTMs, available from *HiRISE* [No Date.] and typically produced by the United States Geological Survey (USGS), may have been edited to remove small errors, such as pits and spikes. From experience, errors such as these typically small in area, and, where editing has been applied, the terrain appears

uncharacteristically smooth in a hillshaded image produced from the DTM. These areas are also removed for this work.

Othorectified Images Finally, orthorectified images are produced using the original images as input, and the final DTM from the AATE process to correct image distortion for terrain and viewing angle effects.

3.6.2 DTM CO-REGISTRATION AND QUALITY CONTROL

To effectively calibrate the MOLA pulse-widths, the DTMs, from which the surface characteristics estimates are produced, and MOLA data must be co-registered to ensure that the correct data is being extracted and compared. The methods are outlined below, and the estimated errors are presented in the following section.

ArcMap An ArcMap project was setup for each study site in each project, using a *Sinusoidal* projected coordinate system and the IAU2000 geographic coordinate system [*Snyder*, 1987].

Co-registration Data for each site were loaded into the relevant ArcMap project and the *Add Control Points* tool was used to manually co-register data using a bottom-up, pyramid scheme, like that described in *Kim and Muller* [2009]. This scheme uses the lowest resolution dataset as a basemap, to which successively higher resolution datasets are co-registered. In this case, the MOLA elevation dataset was used as a basemap, and the HRSC data added, followed by the CTX or HiRISE data.

Basemap Subsets of the global MOLA DTM (463 m pixel^{-1}), extracted with a large buffer zone around each site, were used as basemaps to which the HRSC elevation data was compared.

Intermediate Datasets Any HRSC data, DTM files ending in .DA4, and nadir images, ending in .ND4, over the ROI were downloaded from *Planetary Data System* [2014a]. The co-registration of HRSC DTMs to MOLA was verified by comparing elevations at MOLA PEDR locations, described below. Elevations were also compared using the MOLA PEDR data. Errors were observed, which are attributed to cloud hitting pulses as the MOLA elevations lay significantly above the HRSC surface. Once these pulses were removed, the data revealed good agreement between the elevations, with minor deviations existing due to the challenges of DTM production from stereo-imagery, such as the pits and spikes discussed in Chapter 2, and the size of the MOLA pulse-footprint. Two of the sites used in Section 3.8 require the Viking MDIM, which has been co-registered to the MOLA data, due to a lack of HRSC DTM coverage. To check the quality of Viking image georeferencing, hillshaded images were produced from the MOLA gridded elevation data, and visual inspections made to ensure correct coregistration. The *Hillshade* tool in the *Spatial Analyst* toolbox produces an image of the surface assuming only differences in illumination due to surface slope and aspect. Identifying co-registration errors was challenging due to the differences in resolution, and the large areas of interpolated terrain in the MOLA data, meaning the resulting hillshaded

images could look very different in regions far away from the MOLA orbit tracks used to make the DTM (Figure 2.1).

High-Resolution Data The HRSC nadir images, which cover the same location as the DTM, and Viking MDIM were then used to co-register the higher resolution CTX and HiRISE images. For each image, a minimum of 10, evenly distributed, tie-points were used to georeference the image to the lower resolution data. In Section 3.7, where there are multiple overlapping HiRISE images, co-registered HiRISE images were used to co-register subsequent images where they overlapped, always checking with the underlying HRSC images to ensure poor co-registration did not propagate throughout the HiRISE data. The same transforms used to co-register the high-resolution images to the lower resolution images were then applied to the high-resolution DTM data. The high-resolution DTM elevations were then compared to both the HRSC DTM (where available) and MOLA DTM and PEDR elevations values at MOLA pulse locations to ensure 3-dimensional accuracy.

Mosaicing Over the MSL sites with overlapping HiRISE DTMs, the DTMs were mosaiced together to form a single dataset using the *Mosaic to New Raster* tool in ArcMap 10.1, with the *blend* option used to merge DTM heights where they overlapped. This enabled more MOLA points to be used as MOLA data near the edges of a DTM were excluded if it was within the largest baseline of surface roughness or slope from the edge (i.e. the largest baseline for the MSL study is 1200 m, so data within 600 m of the mosaic DTM boundary was removed, otherwise surface roughness estimates at this baseline would include null values).

3.6.3 GEOREFERENCING AND ELEVATION ERRORS

Comparisons of DTM heights reveal no significant errors, but smaller errors can exist, especially as height checks are completed only at MOLA PEDR pulse locations: to ensure comparisons include real MOLA data. Hillshaded images were produced from the DTMs to highlight the errors in the DTM production process, such as pits and spikes due to incorrect or poor stereo-matching, and extensive areas of interpolated terrain and poorly blended terrain from mosaicing. Some errors were observed at the overlapping regions for Section 3.7 and some CTX DTMs contained extensive regions of interpolated terrain identified by triangular patterns in the hillshaded image, both were excluded from the study by applying a mask.

Table 3.7 presents the horizontal, and vertical precision and accuracy estimates for the datasets described above. The horizontal errors for MOLA are based on the estimates of MGS positioning data and the instrument timing properties, whereas the other horizontal accuracy estimates are measured relative to the MOLA estimate. *Archinal et al.* [2003] observe typical horizontal errors of $<$1 pixel (250 m), with the largest errors up to 4 pixels (1 km), when comparing measurements of offsets between the Viking MDIM and the MOLA elevation dataset using over 37 000 control points. Through co-registration of HRSC DTMs to the MOLA elevation dataset, *Gwinner et al.* [2010] show that horizontal offsets can be reduced to $<$100 m. The CTX and HiRISE estimates are derived from an estimate of the manual georeferencing processes, described above, compared to

Table 3.7: Co-registration errors of Mars datasets [*Gwinner et al.*, 2010; *Kirk et al.*, 2001; *Neumann et al.*, 2003a]. † represents datasets and values that are georeferenced to MOLA. ‡ represents datasets and values that are georeferenced to HRSC. Viking MDIM dataset is an image mosaic and therefore has no vertical values. HiRISE and CTX Vertical Accuracy values are standard deviation values from the MOLA PEDR values, after cloud hitting MOLA pulses are removed.

Dataset	Horizontal Accuracy (m)	Vertical Precision (m)	Vertical Accuracy (m)
MOLA	<100	0.38	1
Viking†	250 to 10^3	-	-
HRSC†	56 to 62	12.5	<4
CTX‡	12.5 to 25	1.32	30.5 to 50.1
HiRISE‡	12.5 to 25	0.22	12.8

the HRSC imaging data, with expected errors on the order of 1 to 2 HRSC pixels [*Gwinner et al.*, 2010].

The vertical precision errors presented in Table 3.7 are derived from theoretical estimates using the timing resolution of the MOLA instrument and Equation 2.28 for the remaining stereo-derived datasets, based on the pixel size, camera baseline, and instrument altitude [*Kim and Muller*, 2008; *Kirk et al.*, 2008].

The vertical accuracy are equal to the standard deviation of differences in elevation between these datasets and the MOLA PEDR data, for all MOLA pulses over the high-resolution DTM area. *Gwinner et al.* [2010] note that this error is <4 m when using HRSC elevation data, after bundle-adjustment. HiRISE and CTX data both produce much larger errors, which could be due to the rough terrain used in these studies, which results in large topographic variation within the MOLA pulse-footprint. The leading edge timing system of MOLA results in the highest elevations being recorded, whilst the centre of the pulse, the value extracted from the CTX DTM, could be in an area of lower elevation. When only the smooth terrain of Lycus Sulci 2, as described in Section 3.8, the standard deviation is reduced to 30.5 m after cloud hitting pulses are removed.

3.6.4 MOLA DATA COLLECTION

The MOLA data is provided from two sources: the original PEDR data (Version L), and the Slope-Corrected pulse-width dataset provided by G. Neumann in October 2011 [*Neumann et al.*, 2003a].

MOLA PEDR data was extracted over a large ROI using the *pedr2tab* program to extract data from individual data files, available from *Planetary Data System* [2014d] and *Planetary Data System* [2014c] respectively. The *PEDR2TAB.PRM* preference file determines which data is printed in the output file; selecting the 5th option means the *Sigma_optical* pulse-width value is included, along with the latitude, longitude, and aeroid elevation, amongst others. This pulse-width value includes corrections for filter characteristics and threshold settings, and is thought to provide an estimate of the surface characteristics within the pulse-footprint, as given in Equation 2.5.

The output is printed in a text file, which was mapped in the relevant ArcMap 10.1 project using the *Add XY Data* function, selecting the Mars IAU2000 geographic projection system to map the data. These data were reprojected into the Sinusoidal Projection used in the ArcMap 10.1 project by exporting the data to a *Shapefile* and using the *Project* (Feature) tool. ArcMap has the ability to project datasets into different projection systems *on-the-fly*, however this slows data viewing and can cause issues for data extraction. It is therefore best practise to project data into the projection system employed by the project before analysis.

A similar method was used to extract the Slope-Corrected pulse-width data, which is provided in a similar file structure to the PEDR data. A simple bash script was used to search through these files and extract pulses that lie within the same ROI used for the PEDR data. The Slope-Corrected data includes only the latitude, longitude, and the Slope-Corrected pulse-width value, which was mapped in the relevant ArcMap 10.1 project using the methods outlined above.

As described above, only MOLA data within half the largest baseline, 600 m, of the DTM data boundary were used in this work, to ensure that the same number of pulses were used for each comparison between pulse-widths and surface characteristics, for each MOLA pulse-width dataset separately. If this was not applied, part of the pulse-footprint of pulses within half the baseline of the boundary may contain null-data values. This would introduce some inconsistency and bias in the surface roughness and slope values across the baselines at these locations, so best practise is to exclude them.

3.6.5 SURFACE ROUGHNESS AND SLOPE MAP PRODUCTION

The surface roughness and slope values used to calibrate the pulse-width data were extracted from maps produced at different baselines from the co-registered DTMs and mosaics.

3.6.5.1 SURFACE ROUGHNESS MAPS

Surface roughness maps were produced using RMS height, as shown in Equation 2.46 in Section 2.3, as the pulse-widths reported in the PEDR and Slope-Corrected datasets are theoretically related to the RMS total and terrain pulse-width as in Equations 2.5 and 2.7 [*Neumann et al.*, 2003a; *Smith et al.*, 2001]. The maps of surface roughness distribution in *Smith et al.* [2001] and *Neumann et al.* [2003a], which are shown in Figures 1.1a and 1.1b, are scaled to this measure of surface roughness.

The ArcMap 10.1 *Focal Statistics* tool, which calculates different statistics within various window sizes and shapes, was used to produce the roughness maps. Here, the *STD* (standard deviation), which applies the same formula as RMS height, option and circular window diameters ranging from 10 m to 1200 m, equivalent to the baseline, were selected. Section 3.7 explores baselines from 10 m to 1200 m, whilst in Section 3.8 baselines from 40 m to 600 m are used due to differences in DTM resolution between HiRISE (1 m pixel^{-1}) and CTX (18 m pixel^{-1}). These baselines cover both the lower and upper limits of the current pulse-footprint estimates (70 m to 168 m) as well as the 35 m to 100 m surface roughness baselines estimates derived from these pulse-footprint estimates due to the energy concentration respectively [*Neumann et al.*, 2003a;

Smith et al., 2001].

By using a circular window the assumption is that the pulse-footprint is circular, which may not be the case under high tilt angles, hence the removal of pulse-widths taken at $\geq 2°$ tilt in *Neumann et al.* [2003a]. The exact geometry of the pulse-footprint was not recorded in the PEDR dataset, however, tilt angles of 20° result in pulse-footprint stretching of 3.6 m along the direction of tilt, significantly smaller than the georeferencing errors expected across the datasets.

From HiRISE data, the baselines used are: 10 m, 20 m, 35 m, 50 m, 70 m, 100 m, 150 m, 200 m, 300 m, 600 m, 1000 m and 1200 m. For CTX data, the baselines used are: 40 m, 60 m, 75 m, 100 m, 150 m, 200 m, 300 m, 600 m and 1000 m.

3.6.5.2 SLOPE MAPS

Slope maps were produced using the *Slope* tool in ArcMap 10.1, which defines slope as described in Section 2.3.3 and Equations 2.56 to 2.58.

As mentioned in Section 2.3.3, there are two methods to produce slope maps at different baselines. (1) Resample the original DTM data to the required baseline, producing a new DTM. The *Slope* tool is applied to the new DTM to produce a slope map at the required baseline. (2) Produce a slope map from the original DTM and use the *Focal Statistics* tool to produce slope maps at each baseline by applying the *MEAN* option and circular windows of diameter equal to the desired baseline. Both estimates use Equations 2.56 to 2.58 to produce slope estimates. Background work for Section 3.8 found that the slope outputs are very similar using theses methods, and as more work had been completed using (1), this method is used for slope map production throughout Sections 3.7 and 3.8. The resampling technique used cubic convolution to fit a smooth curve through the 16 nearest cells, and is generally deemed a better resampling method as it produces a continuous result and reduces the effect of errors by using more pixels to estimate an interpolated elevation [*Environmental Systems Research Institute*, 2001].

3.6.6 DETRENDING AND HOT-SPOTTING

Detrending data is compared to roughness contribution to pulse-width, as described in Equation 2.7, in Section 3.9. In ArcMap, high-resolution DTM data was extracted from each pulse-footprint in the Slope-Corrected pulse-width dataset over Eberswalde Crater, Mawrth Vallis, and Aureum Chaos for each pulse separately. The pulse-footprint was modelled using the *Buffer* tool, to convert the point data to a circular polygon with a diameter of 75 m (Figure 3.9). The Shapefile containing this polygon data was then split into individual pulse-footprint shapefiles, and a simple ArcPy Python script was written to apply the *Extract by Polygon* tool to each pulse-footprint, creating a small DTM for each pulse-footprint. These DTMs were converted to text files by self-sampling to produce a table of $X\ Y\ Z$ values for each cell.

For each pulse-footprint, a plane was fitted in MATLAB using linear regression. The maximum slope of this plane was found using Equations 2.59 and 2.60. Detrended elevations were found by removing the plane-of-best fit elevations from the original elevation values. Detrended surface

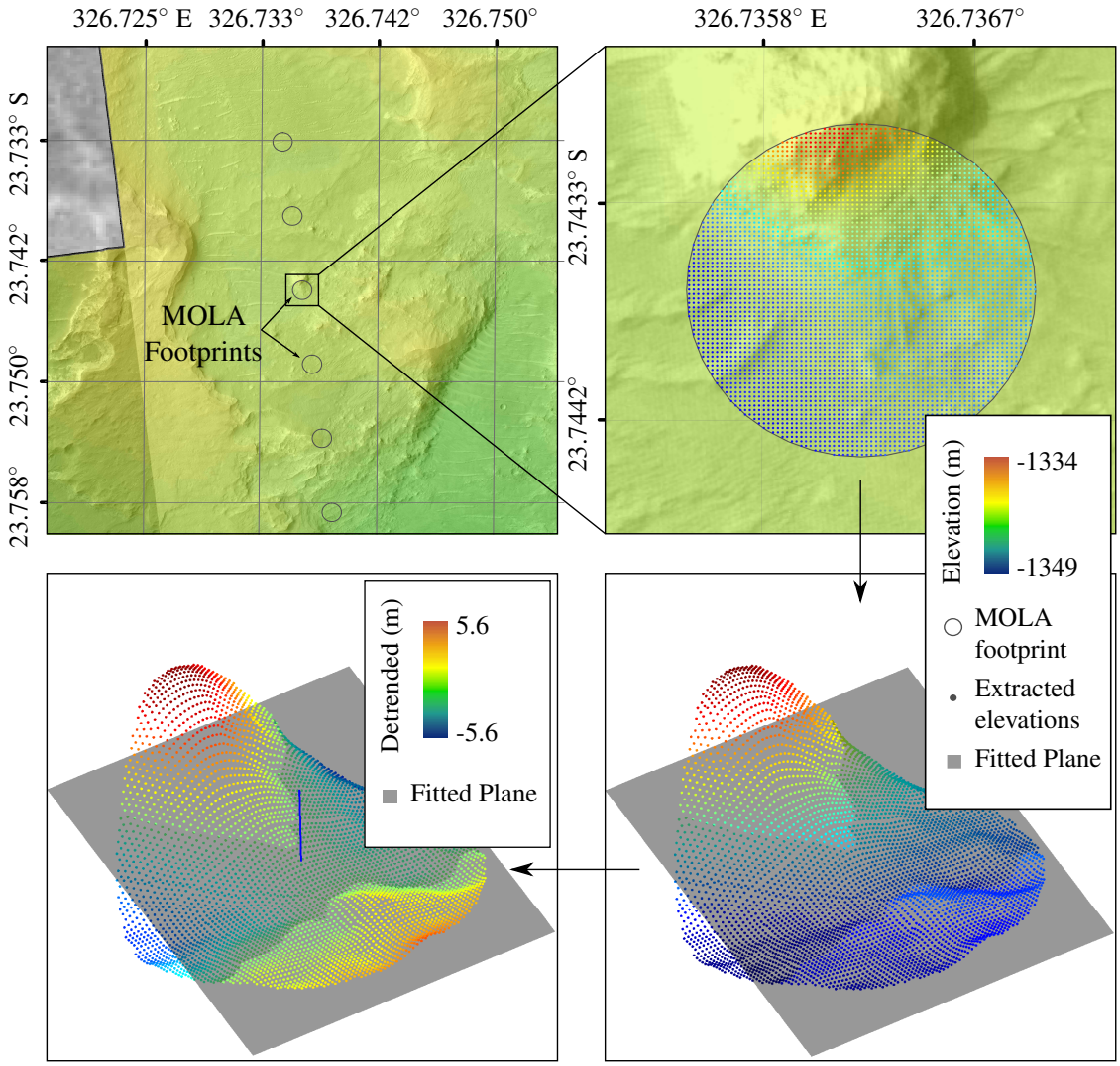

Figure 3.9: Maps and plots showing how detrended elevation data is found from extracted DTM data and a fitted plane. This example is for a pulse-footprint over Eberswalde Crater. A plane is fitted to extracted elevation data (Bottom Right), which is then subtracted from the elevation data to reveal detrended elevation (Bottom Left). The slope is found by calculating the maximum slope of a plane, using Equation 2.60. The detrended roughness is found by calculating the RMS height from these detrended elevations. To explore the effect of energy distribution across the pulse-footprint, a Gaussian filter is applied to the detrended elevations, before the RMS height is calculated.

roughness values were found by applying the RMS height (Equation 2.46) to the detrended elevation values. The aim of fitting the slope is to remove the slope contribution effect described in Equation 2.7 and Figure 2.2, and not to replicate the surface itself, hence the use of a linear, rather than polynomial, plane [*Wood*, 1996].

The pulse-width values were corrected for pulse-footprint-scale slope using Equation 2.7 to find the roughness contribution, σ_t, to the total received pulse-width. σ_ξ is plotted against the detrended surface roughness values, and a linear line-of-best-fit applied to find the relationship and R-squared value.

To replicate the effect of *hot-spotting*, which is discussed in Section 2.1.5, a Gaussian filter was applied to the detrended elevations before the detrended surface roughness is calculated. The full

equation is given in Equation 2.20, but can be simplified to

$$f(x,\mu,\sigma) = a_G e^{\frac{(\chi-\mu)^2}{2\sigma^2}}. \quad [3.1]$$

Here, a_G is the Peak amplitude of the Gaussian distribution, σ is the standard deviation of the distribution, χ is the distance from the mean, μ, defined at the centre of the pulse-footprint. Different standard deviations were used to replicate how energy distribution across each MOLA pulse may have occurred. The effect of applying this filter is to decrease the influence of detrended elevation values at the edge of the pulse-footprint, and reduces the overall detrended surface roughness value at a location.

3.6.7 DATA EXTRACTION AND COMPARISON

The surface roughness and slope map values, for each baseline, were extracted at the MOLA PEDR and Slope-Corrected pulse locations using the *Extract Multi-Values to Points* tool in ArcMap 10.1. This stores the values of surface roughness and slope in the Shapefiles produced in Section 3.6.4, with each baseline and map type[3] stored in a separate column. The Shapefiles were exported to text files for analysis in MATLAB.

Pulse-width values are plotted against surface roughness and slope for each of the baselines, surface characteristic, and pulse-width dataset separately. A linear line-of-best-fit is derived using linear regression analysis, and the R-squared value is found and used as a measure of the goodness-of-fit. Other goodness of fit methods were considered, but as the R-squared is familiar and provides a good indication as to the influence of a particular variable on a result, it was deemed a useful method. The resulting fit was also tested for significance using p-value of 0.05, which tests the distribution of residuals about the line-of-best-fit. These residuals will produce a Gaussian distribution about the line-of-best-fit, which are then *Studentised* by dividing by an estimate of the standard deviation from the line-of-best-fit. The standard *Student t-test* is performed to check for significance. This process was conducted in MATLAB using the *fitlm* tool, available in version 2014a and later.

For each site and surface characteristic, the plot with the highest R-squared value is selected. This is assumed to give an indication of the baseline at which the pulse-widths respond. The aim being to find a common baseline across each of the sites for each surface characteristic, which will validate the dataset and produce a reliable relationship that can be extrapolated to other regions across Mars.

[3] surface roughness or slope

3.7 MOLA PULSE-WIDTHS OVER THE MSL CANDIDATE LANDING SITES

3.7.1 INTRODUCTION

The starting assumption is that MOLA pulse-widths estimates surface roughness at baselines applicable for landing and roving site selection [*Smith et al.*, 2001; *Neumann et al.*, 2003a]. This first project tests this hypothesis by comparing the different MOLA pulse-width datasets to surface roughness estimates at different baselines from high-resolution HiRISE DTMs, which can estimate surface roughness at the small baselines required [*Kirk et al.*, 2008]. By doing so, the pulse-width dataset(s) will effectively be calibrated, enabling (1) the identification of candidate landing and roving sites for future missions [*Grant et al.*, 2011b; *Golombek et al.*, 2012a], (2) quantitative comparison of terrains [*Kreslavsky and Head*, 2000], and (3) a reliable surface roughness map for atmospheric studies [*Heavens et al.*, 2008]. To find the best quality MOLA pulse-widths, both the PEDR version L and Slope-Corrected pulse-width dataset, from *Neumann et al.* [2003a], are used. Additionally, *Kreslavsky* [2012] suggests that the Trigger 1 channel, discussed in Section 3.3, is the most reliable MOLA receiver channel, this dataset was extracted from the PEDR dataset to test this hypothesis. The work in this section is also presented in *Poole et al.* [2014b], which presents the results and conclusions, but not the specific site descriptions.

3.7.2 DESCRIPTION OF THE STUDY SITES

The small spatial extent of individual HiRISE DTMs, which are each up to $\sim$6 km $\times$ 30 km, and the large MOLA inter-orbit spacing, which averages $\sim$4 km at the equator, means that only regions with extensive HiRISE stereo coverage can be used, to ensure enough MOLA data is used for a significant relationship to be derived [*McEwen et al.*, 2007, 2010].

After reviewing the distribution and spatial coverage of the available DTMs, shown in Figure 3.10, the final four candidate MSL landing sites - from which Gale Crater was selected - were chosen for this work [*Grant et al.*, 2011b; *McEwen et al.*, 2007; *Planetary Data System*, No Date.; *HiRISE*, No Date.]. These four sites, which are described below, were found to be the only sites with multiple overlapping or adjacent ($<$1 km inter-DTM spacing) DTMs or stereo-pairs [*McEwen et al.*, 2007; *Planetary Data System*, No Date.; *HiRISE*, No Date.]. The DTMs were produced as part of an extensive mapping campaign for the final MSL landing site selection process described in *Grant et al.* [2011b]. The identification numbers of the DTMs used for each site are provided in Table B.1 on Page 326.

3.7.2.1 EBERSWALDE CRATER (24° S, 327° E)

Eberswalde Crater lies within the Erythraeum region, to the north of the much larger Holden Crater, also one of the final four candidate landing sites, and is discussed below and illustrated in Figure 3.10.

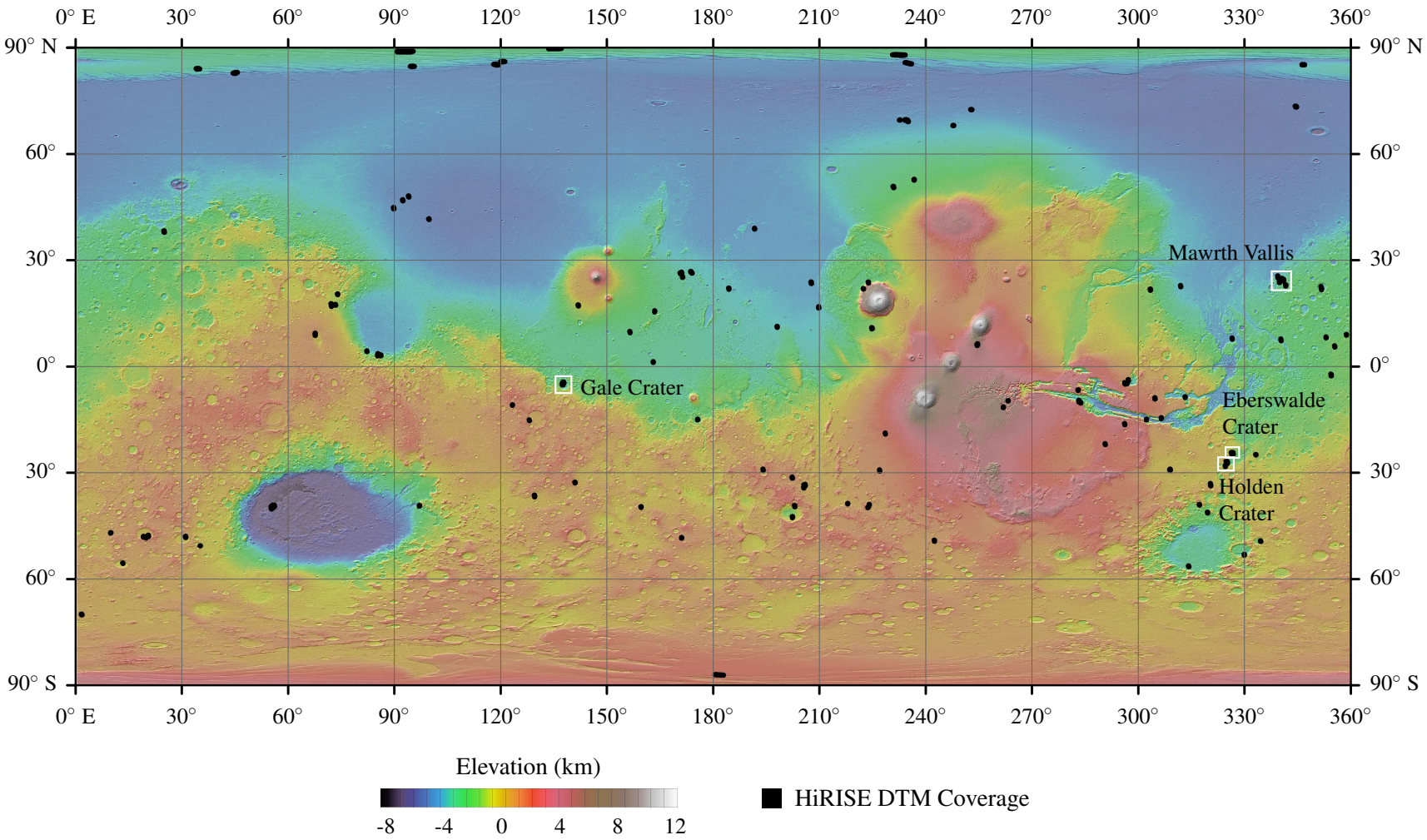

Figure 3.10: Map of freely available HiRISE DTM and final four MSL candidate landing site locations [*HiRISE*, No Date.]. Black regions represent location, not coverage, which is much smaller. The background is the MOLA gridded elevation model [*Smith et al.*, 2001].

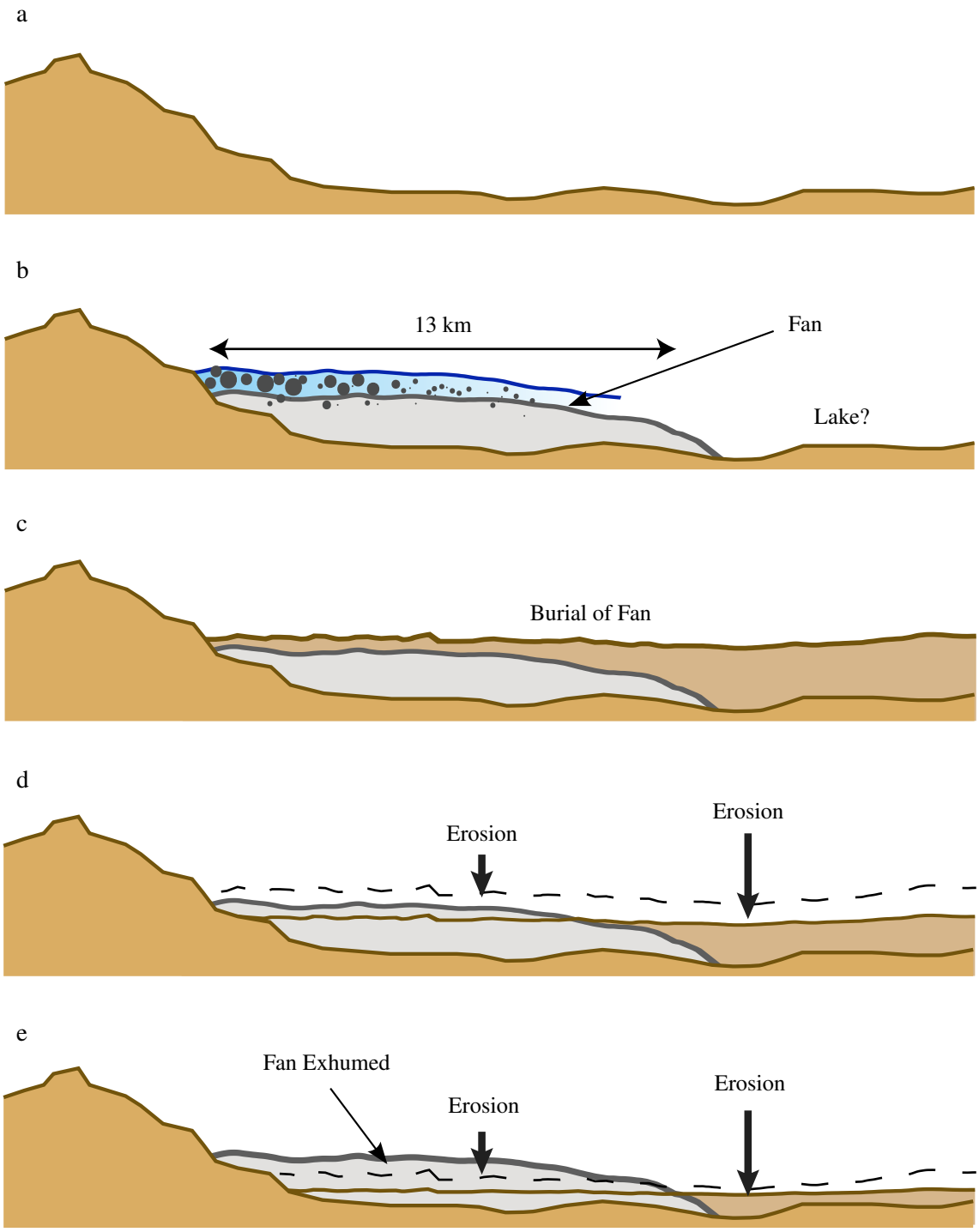

Figure 3.11: Schematic of the possible formation processes behind the creation of the interpreted Eberswalde Crater fan-shaped deposit [*Golombek et al.*, 2012a; *Pondrelli et al.*, 2008; *Rice et al.*, 2013, 2011; *Wood*, 2006]. (a) a simple crater forms. (b) fluvial activity transports material into the crater from the crater walls and beyond, possibly into a lake. The material is deposited as a fan-shaped material, in several lobes associated with different periods of activity. (c) the fan-shaped deposit is buried, lithifying the deposit. (d) the lithified deposit is exposed through aeolian erosion. (e) the lithified deposit is more erosion resistant than the burying material, and is therefore exhumed on the surface. The fan-shaped deposit at Holden Crater, which extends twice as far into its crater, appears to be in a less exhumed state than that at Eberswalde Crater, possibly between stages (d) and (e).

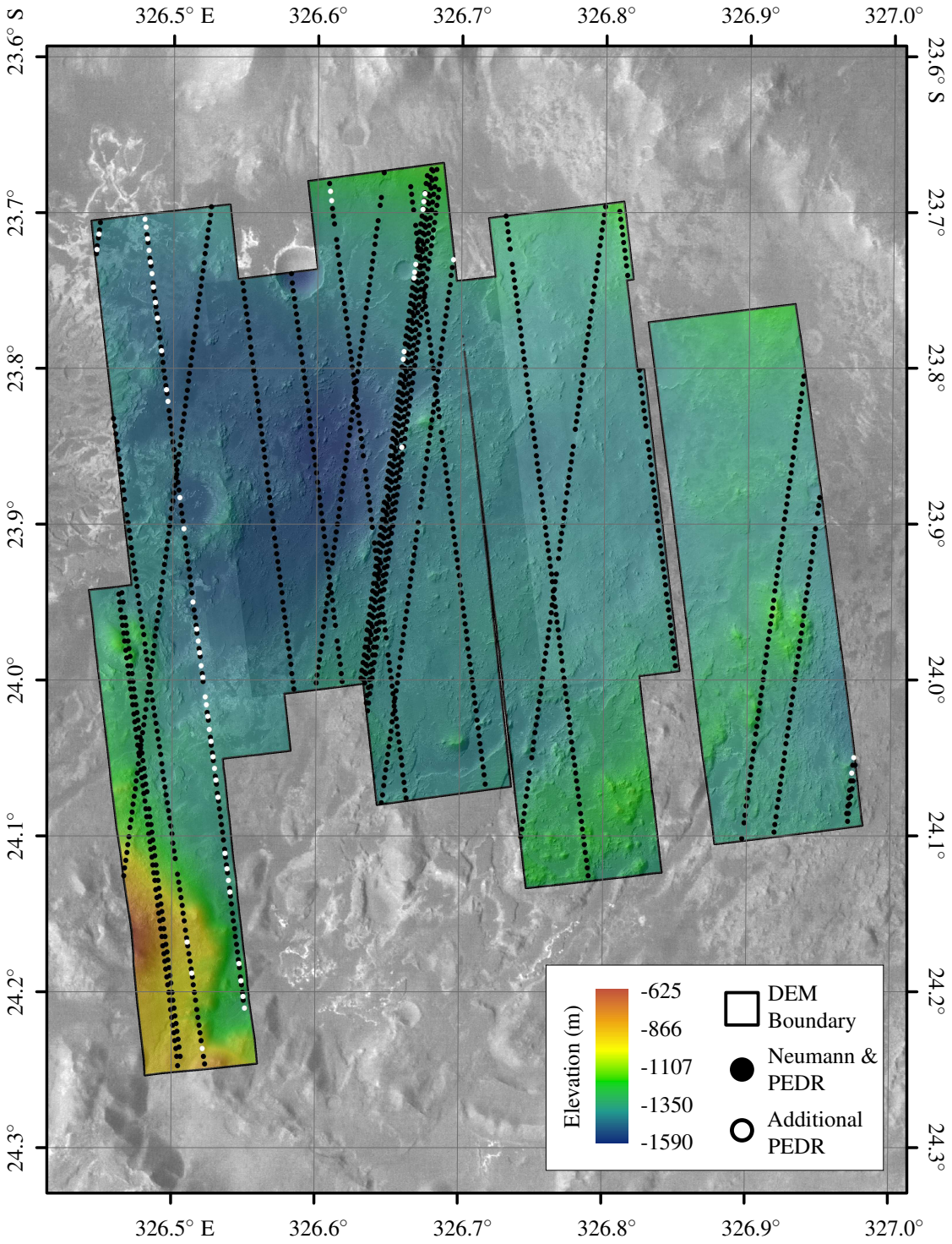

Figure 3.12: Map of the Eberswalde Crater study area, with HiRISE DTM coverage shown in colour and the MOLA pulse locations shown in black and white. The HiRISE DTMs have the corresponding orthorectified images shown on top, with 50 % transparency to highlight surface detail. Black MOLA pulse locations are those in the Slope-Corrected dataset from *Neumann et al.* [2003a]; black and white together show the original MOLA PEDR data, such that the white locations show the data that was removed from the PEDR data for the Slope-Corrected dataset. Background image is from HRSC.

The primary focus of this site would have been to explore the role of hydrological activity in surface evolution by studying crater stratigraphy, geomorphology, mineralogy, and possible evidence for climatic change [*Golombek et al.*, 2012a; *Pondrelli et al.*, 2008; *Rice et al.*, 2013, 2011; *Wood*, 2006]. Several input channels appear to flow into the crater, the largest of which terminates in what appears to be a layered, fan-shaped deposit formed during several periods of activity interpreted from several lobes within the deposit [*Rice et al.*, 2013; *Wood*, 2006; *Pondrelli et al.*, 2008; *Rice et al.*, 2011; *Golombek et al.*, 2012a]. Metre-scale boulders strewn across the crater floor and within the fan-shaped deposit suggest the outflow may have been strong. The channels may not have been simultaneously active, but *Wood* [2006] proposes evidence of lacustrine deposits on the crater floor, which suggests the presence of a lake within the closed system. Clays detected on the crater floor, which appear particularly abundant at the base of the largest deltaic system, also suggest that this fluvial activity may have been prolonged, potentially several hundred thousand years [*Golombek et al.*, 2012a].

Material for these layered deltaic systems appear to have been transported from the west via a complex valley network [*Rice et al.*, 2013, 2011]. Today, the potential deltaic system sits inverted on the crater floor, with the possible evolution processes illustrated in Figure 3.11. *Rice et al.* [2013, 2011] suggests that these deposits were buried sometime after the final fluvial episode. This may have been followed by lithification, hardening of the deposited material, which was later exhumed after the more friable burial material was eroded through wind erosion processes. The area covered by the HiRISE DTMs is shown in Figure 3.12, includes part of this deposit, as well a section of crater wall material, where the greatest change in topography within the DTM boundary is observed, and some smaller craters within the crater. Smaller mounds of material, some of which appear to be shaped by aeolian processes, dot the remaining landscape, which is typically smooth.

3.7.2.2 GALE CRATER (5° S, 138° E)

Gale Crater lies along the Mars dichotomy between the northern plains and the southern highlands (Figure 3.10). The crater measures approximately 150 km in diameter, and is thought to have been formed during the late Noachian period [*Anderson and Bell*, 2010]. The target area for the rover, which landed in August 2012, was at the base of the northwestern face of the ∼5 km layered mound that dominates the centre of the crater [*Carr and Head*, 2010; *Golombek et al.*, 2012a; *Grotzinger et al.*, 2012]. The peak of this mound is higher than the crater walls that surround it, with the exposed strata forming the primary science target for MSL in the hope that it provides a record of past habitable conditions on Mars [*Golombek et al.*, 2012a; *Grotzinger et al.*, 2012; *Milliken et al.*, 2010]. Lacustrine, fluvial, aeolian, and evaporatic processes are proposed for the formation of this mound, shown schematically in Figure 3.13, which today is being eroded by aeolian processes [*Anderson and Bell*, 2010; *Milliken et al.*, 2010; *Thomson et al.*, 2011; *Golombek et al.*, 2012a; *Grotzinger et al.*, 2012; *Kite et al.*, 2013].

The upper section of the mound is covered by sediments and characterised by a series of smooth slopes; lower down, channels and inversions are distributed around the base [*Anderson and*

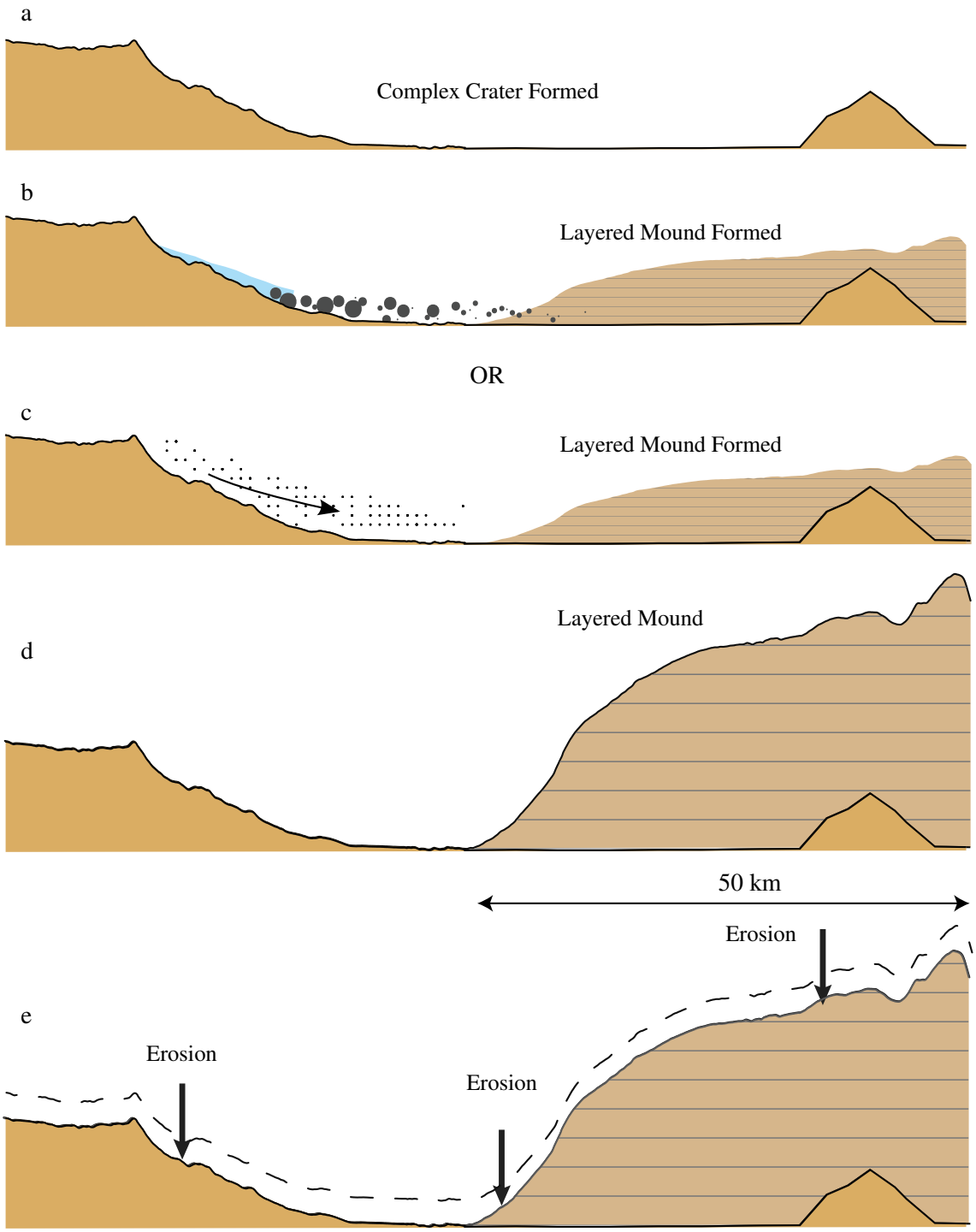

Figure 3.13: Schematic of the possible formation processes behind the creation of the Gale Crater central mound [*Anderson and Bell*, 2010; *Carr and Head*, 2010; *Golombek et al.*, 2012a; *Grotzinger et al.*, 2012; *Kite et al.*, 2013; *Milliken et al.*, 2010]. (a) a complex crater forms with a central peak. (b) one scenario, hydrological transport of material into the crater and deposited on the crater floor, with different layers representing different periods of activity. The material may have been deposited preferentially in the centre of the mound, or more consistently across the crater floor before being eroded into the shape it is today. (c) aeolian transport of material from the crater walls and beyond to the centre of the crater, again building up in layers representing periods of activity. (d) either method develops a mound that is 5 km high, higher than the surrounding crater walls. (e) Today, the terrain is being eroded by aeolian processes.

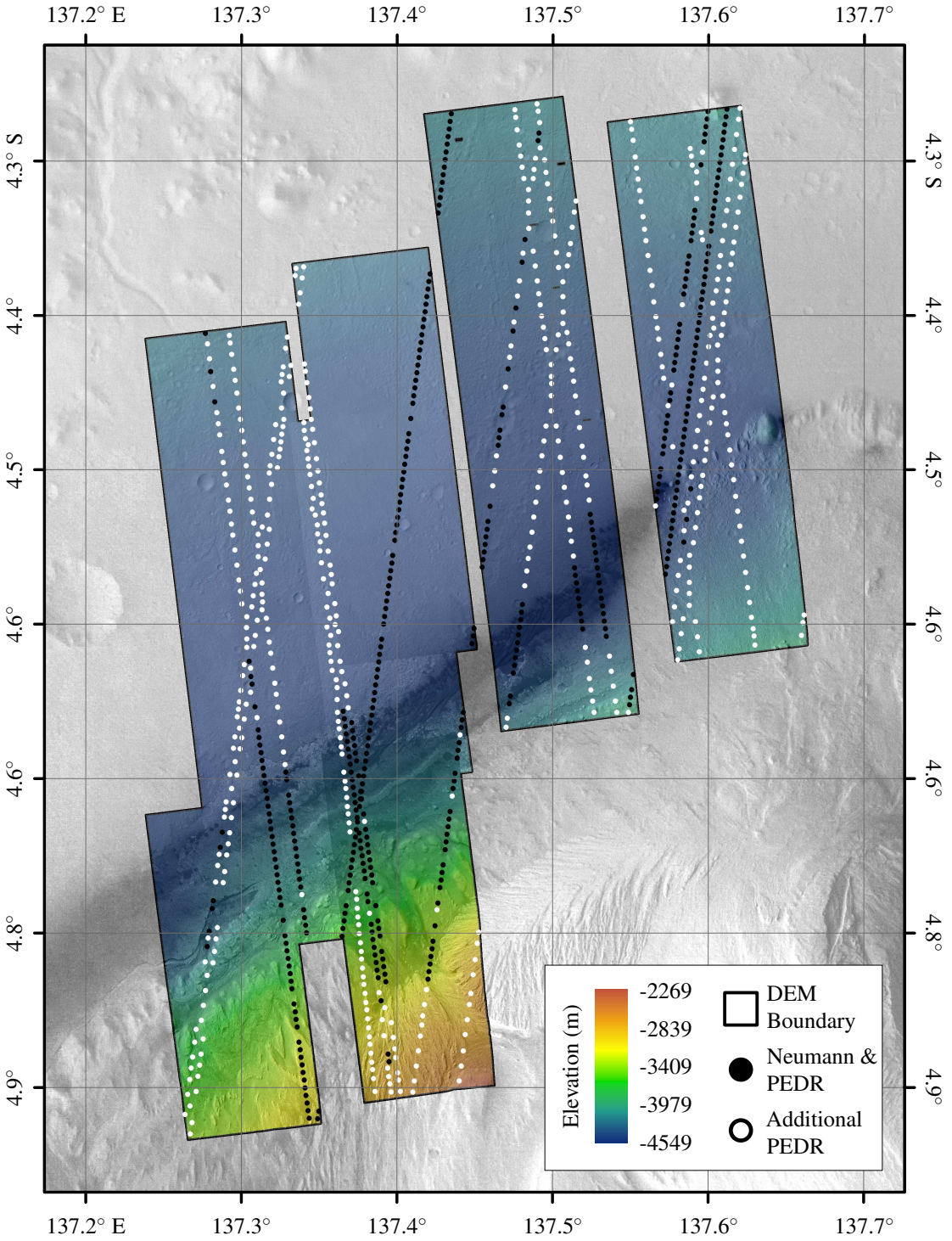

Figure 3.14: Map of the Gale Crater study area, with HiRISE DTM coverage shown in colour and the MOLA pulse locations shown in black and white. The HiRISE DTMs have the corresponding orthorectified images shown on top, with 50 % transparency to highlight surface detail. Black MOLA pulse locations are those found in the Slope-Corrected dataset from *Neumann et al.* [2003a]; black and white together show the original MOLA PEDR data, such that the white locations show the data that was removed from the PEDR data for the Slope-Corrected dataset. Background image is from HRSC.

Bell, 2010; *Golombek et al.*, 2012a; *Grotzinger et al.*, 2012]. These channels transport material to the base of the mound, but also form natural pathways for the rover to reach higher, younger, strata [*Anderson and Bell*, 2010; *Golombek et al.*, 2012a; *Grotzinger et al.*, 2012]. The transition from clay bearing strata near the base of the mound to sulphate bearing rocks further up may record the change from a relatively wet to dry conditions, although the sulphate bearing rocks may best preserve any bio-signatures, if present [*Golombek et al.*, 2012a].

Alluvial fans and dunes surround the mound, which also serve as science targets during the mission traverse [*Grotzinger et al.*, 2014; *Silvestro et al.*, 2013; *Yingst et al.*, 2013] The most noticeable roughness features over the site come from topographic changes from the crater floor to the peak of the mound, channels, and the dunes Figure 3.14. The crater floor is typically very smooth, except for a few small craters.

3.7.2.3 HOLDEN CRATER (26° S, 326° E)

Holden Crater is similar in size to Gale Crater (140 km), but the formation processes are thought to be more similar to those that shaped Eberswalde Crater (65 km), which lies immediately to the north (Figure 3.10).

The proposed landing site is located in the southwest section of the crater floor, next to what appears to be a fan-shaped deposit that would have formed the primary science target if MSL had landed here [*Grant et al.*, 2011b,a]. The material for this deposit appears to be sourced from Uzboi Vallis and extends 25 km on to the crater floor. *Pondrelli et al.* [2005] propose that it may have formed after a large body of water being held in the Uzboi Vallis breached the crater walls and flooded into the crater, transporting the crater wall material. Again, the deposit sits inverted on the surface, with a similar formation chain proposed to that outlined in Figure 3.11, except here the deposit appears less exposed, or is smaller. Large metre-scale blocks are observed across the crater support evidence for a catastrophic flooding event, which may have also transported large clasts, possibly containing rocks of varying ages, that form potential science targets for studying conditions from the crater walls and beyond [*Golombek et al.*, 2012a].

Like Eberswalde Crater, it is proposed that a crater lake may have been present, and possibly supported a habitable environment within a closed fluvial-lacustrine system [*Golombek et al.*, 2012a]. The network of channels within the broader region are thought to have formed due to precipitation during a *wet* period, which is proposed to have been followed by a significantly drier period, where aeolian erosion and depositional processes dominate [*Golombek et al.*, 2012a; *Grant et al.*, 2011a; *Pondrelli et al.*, 2005]. This drier period may then have been followed by an *icy* period where glacial abrasion and plucking eroded a previously formed deltaic system [*Pondrelli et al.*, 2005]. This is supported by the U-shape profile of Uzboi Vallis, typical of glacial valleys on Earth, and an apparent frontal moraine that could define the furthest reaches of a glacier [*Grant et al.*, 2011a; *Pondrelli et al.*, 2005]. Additionally, large aeolian bed-forms appear to be present across the crater floor, interspersed with very smooth terrain and some smaller craters [*Golombek et al.*, 2012a]. Topographic variation over this site is more gradual than those discussed above, as the

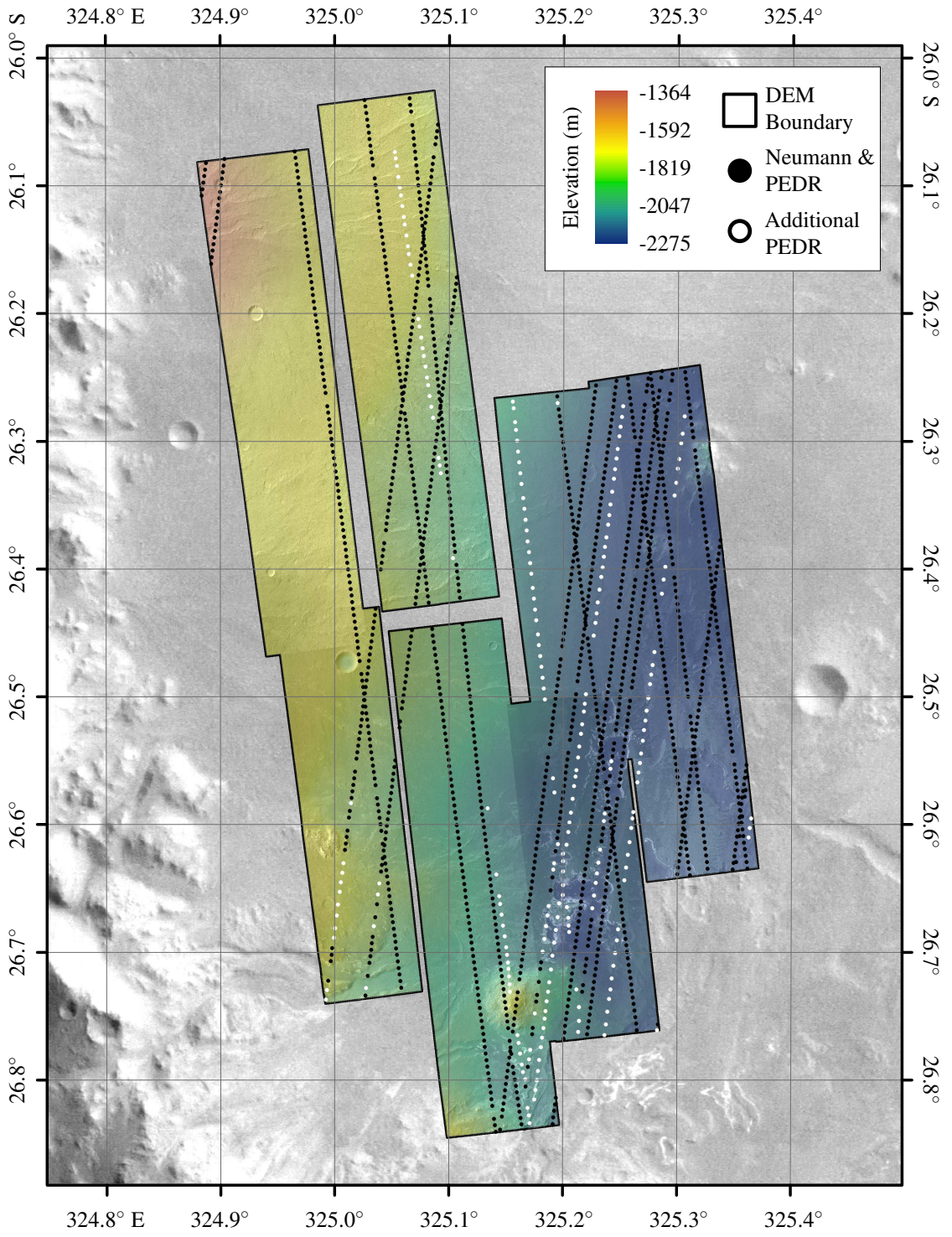

Figure 3.15: Map of the Holden Crater study area, with HiRISE DTM coverage shown in colour and the MOLA pulse locations shown in black and white. The HiRISE DTMs have the corresponding ortho-rectified images shown on top, with 50 % transparency to highlight surface detail. Black MOLA pulse locations are those found in the Slope-Corrected dataset from *Neumann et al.* [2003a]; black and white together show the original MOLA PEDR data, such that the white locations show the data that was removed from the PEDR data for the Slope-Corrected dataset. Background image is from HRSC.

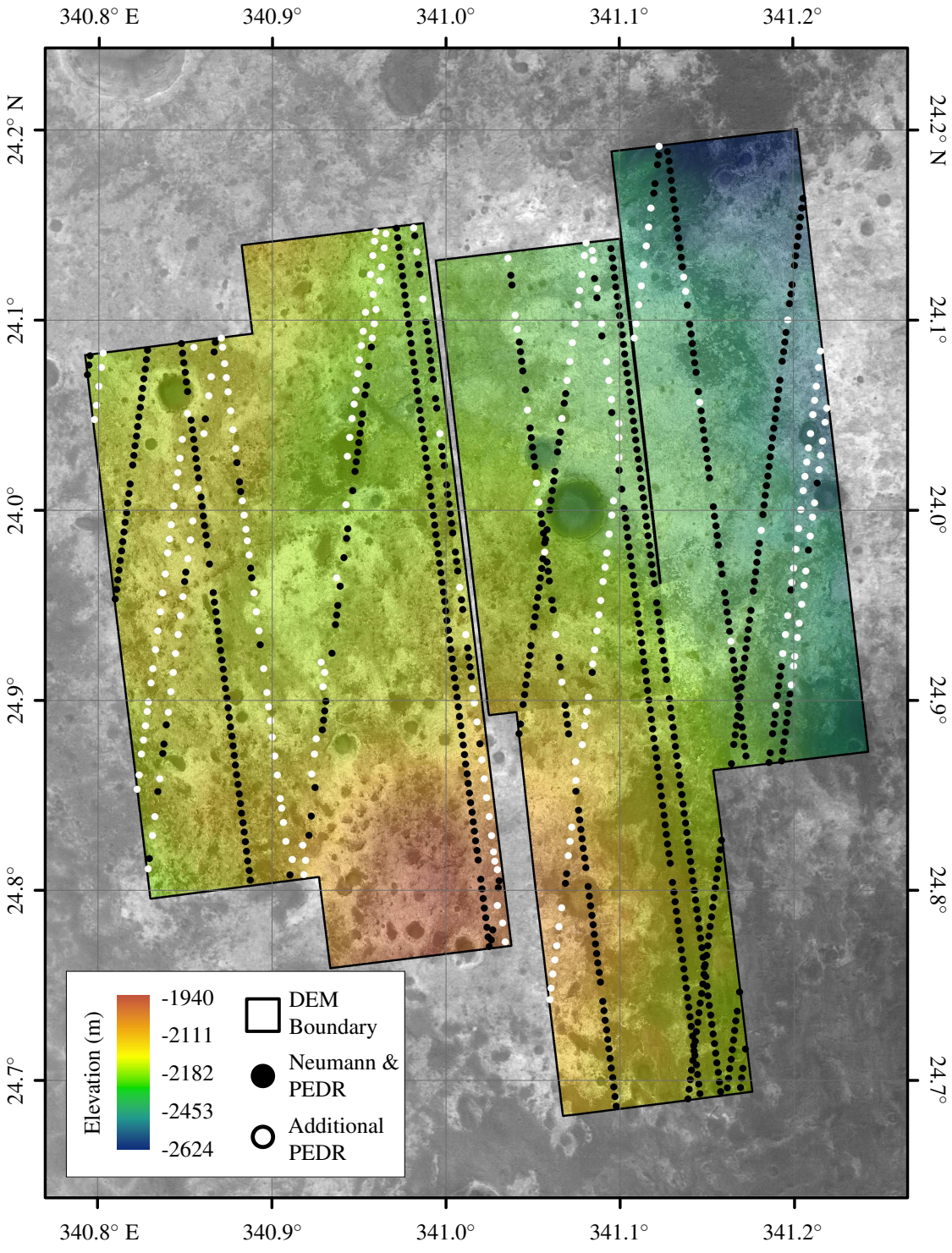

Figure 3.16: Map of the Mawrth Vallis study area, with HiRISE DTM coverage shown in colour and the MOLA pulse locations shown in black and white. The HiRISE DTMs have the corresponding ortho-rectified images shown on top, with 50 % transparency to highlight surface detail. Black MOLA pulse locations are those found in the Slope-Corrected dataset from *Neumann et al.* [2003a]; black and white together show the original MOLA PEDR data, such that the white locations show the data that was removed from the PEDR data for the Slope-Corrected dataset. Background image is from HRSC.

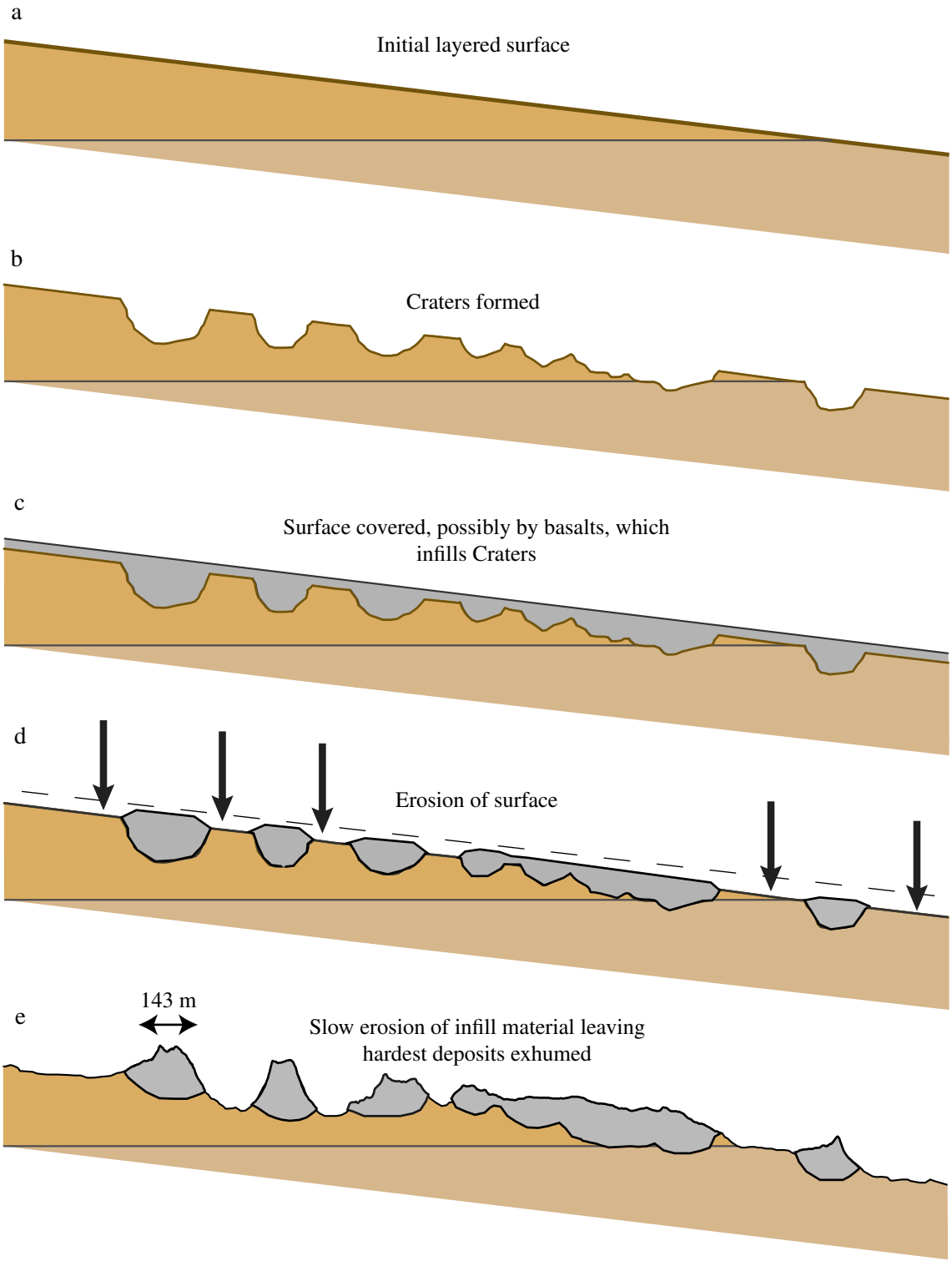

Figure 3.17: Schematic of the possible formation and evolution processes behind the formation of the Mawrth Vallis study site [*Michalski et al.*, 2010; *Noe Dobrea et al.*, 2010]. (a) smooth two layered terrain between Oyama Crater and Mawrth Vallis. (b) craters, both primary and secondary, form on the surface. (c) volcanic activity covers the surface and infills craters. (d) erosion of the surface to the bedrock, leaving behind only the thickest deposits of the volcanic material. (e) the layered bedrock is more erodible than the volcanic material, and thus erodes quicker, leaving behind the thickest volcanic deposits exhumed on the surface.

DTMs do not cover any of the crater walls. This variation is approximately −1 km over 30 km from west to east, which means that large changes in topography contribute less to the overall roughness of the terrain over this site (Figure 3.15).

3.7.2.4 MAWRTH VALLIS (22° S, 344° E)

The candidate landing site known as Mawrth Vallis is situated between Oyama crater, to the west, and Mawrth Vallis itself, to the east (Figure 3.10) [*Golombek et al.*, 2012a]. The site is the most complex to interpret, but is thought to present an opportunity to study phyllosilicate forming processes, which are thought to occur early in Mars' geologic history, and the potential for global habitability, as the conditions here could have been typical of Mars during the late Noachian period [*Golombek et al.*, 2012a].

Like Holden Crater, the topography at Mawrth Vallis varies little across the site, approximately 0.7 km from north to south over 25 km (Figure 3.16). Unlike the other candidate landing sites however, the lack of topography and features mean that it is difficult to determine the evolutionary history of the site [*Michalski et al.*, 2010]. From studies of the wider region, two distinct finely layered deposits are inferred; a thin (10's of metres) thick unit appears to overlay a much thicker unit (100's of metres) attributed to hydrothermal processes [*Noe Dobrea et al.*, 2010]. Figure 3.17 shows a schematic of these layered terrains, which are thought to have been modified by impact crater processes. This appears to have been followed by an outflow of basalts, which covered the surrounding terrains and infilled the craters and other topographic lows, forming thicker deposits than the inter-crater terrains. Aeolian erosional processes appear to have eroded through this hard volcanic layer, over large time-scales, to the more friable material beneath, leaving behind only the thickest deposits of the hard volcanic material, i.e. the infilled craters, exhumed on the surface (Figure 3.17) [*Noe Dobrea et al.*, 2010]. These deposits are now surrounded by the more easily erodible bedrock, which appears much smoother [*Noe Dobrea et al.*, 2010].

Hydrated mineral signals derived from Compact Reconnaissance Imaging Spectrometer for Mars (CRISM) data provide evidence of past aqueous activity in the region [*Noe Dobrea et al.*, 2010]. Some of these deposits sit above the layered deposits, which suggests hydrological activity at some point later in the region's past [*Noe Dobrea et al.*, 2010]. Unlike the other sites, it is the diverse chemistry of the site, rather than geomorphological features, that form the basis of any science targets [*Noe Dobrea et al.*, 2010; *Golombek et al.*, 2012a]. Therefore, the main roughness features of the site are the small craters, which appear in greater numbers here than the previous sites due to the age of the terrain, and the features interpreted as exhumed volcanic deposits. Importantly, both of these features are at much smaller scales than the large kilometre scale features found in the previously described sites.

3.7.3 RESULTS

Correlations over each of the four sites are explored separately, to investigate whether different terrains produce different relationships between surface roughness and pulse-widths. For each

site, 12 plots are produced for each of the three pulse-width datasets, one for each of surface roughness baseline to which the pulse-widths are compared. Only the best correlating plots are shown Figures 3.18 to 3.20, with the fit statistics shown in Table 3.8 for easy comparison, the full results are shown in Table C.1 in Appendix C. All results are tested for statistical significance by testing against the null-hypothesis (p-value), which finds the probability of achieving the same result by chance. The significance level of the test was set at 5 % (p-value equal to 0.05), with the results reported in the table.

The plots show pulse-widths over Eberswalde Crater to be best correlated to surface roughness estimates from HiRISE DTMs, for each of the MOLA pulse-width datasets. Using the PEDR and Slope-Corrected pulse-widths, the best correlating baseline is 150 m, whilst Trigger 1 pulse-widths produced the best correlation at 300 m baseline surface roughness (Table 3.8). Of the different pulse-width datasets, the Slope-Corrected pulse-widths produces the highest R-squared value, which suggests the removal of poor pulse-width data by *Neumann et al.* [2003a] is effective. However, R-squared values are lower than expected.

Results over Gale Crater do not follow the same pattern. Here, R-squared values are lower using the Slope-Corrected and Trigger 1 pulse-widths, compared to the PEDR pulse-widths. This is attributed to the high number of poor data within the PEDR dataset, which, by chance, is plotted in close proximity to better quality data. This produces a higher R-squared value when the low quality data is included. Shown in green in the Gale Crater plot in Figure 3.18 are a string of pulses with a consistent pulse-width value. These occur along a single orbit and are clearly erroneous as they produce very consistent pulse-width values despite varying surface roughness values, as measured

Table 3.8: Summary of results comparing MOLA pulse-widths to surface roughness over the final four MSL candidate landing sites, showing the best correlating baseline, R-squared value and number of pulses. The corresponding plots are shown in Figures 3.18 to 3.20. Where there is a dashed line for the baseline the R-squared value is considered too low (<0.1) to suggest a reliable relationship has been found. All correlations have a p-value less than 0.05.

		Region			
MOLA Dataset	Plot Property	Eberswalde	Gale	Holden	Mawrth
PEDR	R-squared	0.54	0.46	0.06	0.07
	baseline (m)	150	600	-	-
	Pulses	1410	1569	2031	1185
Trigger 1	R-squared	0.54	0.36	0.46	0.02
	baseline (m)	300	200	150	-
	Pulses	932	1271	1543	993
Slope-Corrected	R-squared	0.60	0.42	0.47	0.07
	baseline (m)	150	300	150	-
	Pulses	1157	433	1509	649

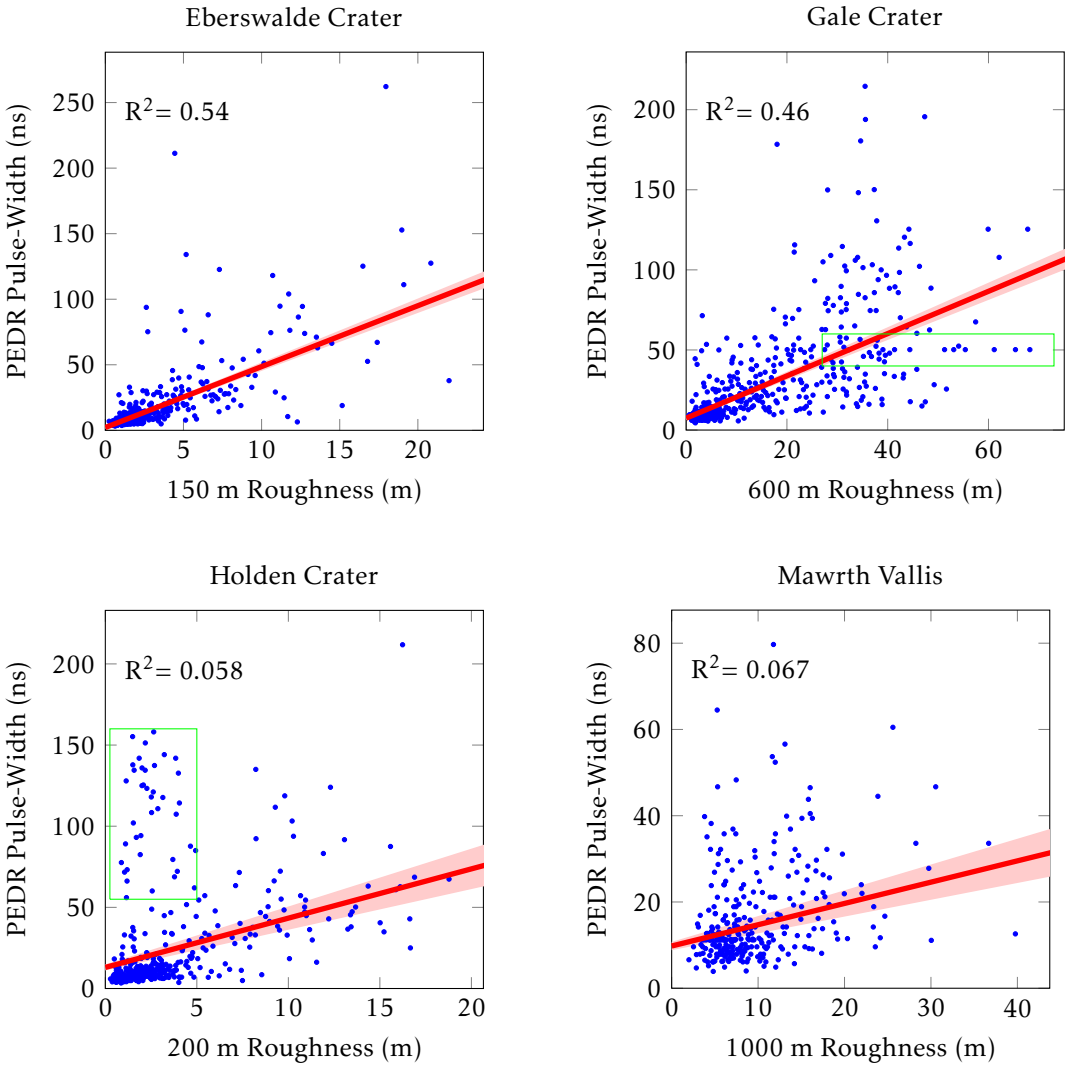

Figure 3.18: Plots showing the best correlating baseline surface roughness and MOLA PEDR pulse-widths over each of the final four MSL candidate landing sites. The highest R-squared value is shown on the plot and the baseline at which this value is found is shown along the horizontal axis. Regions of erroneous results are shown in green boxes on the Gale Crater and Holden Crater plots.

at 600 m baseline surface roughness, and a change in elevation of ∼1 km over ∼15 km producing relatively high slope values. This should produce high, but varying, pulse-width values according to the theory outlined in Section 2.1.3. The removal of this data, and other identifiable erroneous data not clearly visible from visual inspection, has caused a decrease in the observed R-squared because this data sits near other data in the plot, and has therefore decreased the density of data near the line-of-best-fit.

Unlike, Eberswalde Crater, the best correlating baselines over Gale Crater vary greatly. The highest correlation is observed at 600 m surface roughness baseline using the PEDR pulse-widths, whilst the Trigger 1 and Slope-Corrected datasets observe best correlating baselines at 200 m and 300 m respectively (Table 3.8).

The use of Trigger 1 pulse-widths does not improve R-squared values of fits compared to PEDR pulse-widths over Eberswalde Crater or Gale Crater. At the former, using Trigger 1 pulse-widths

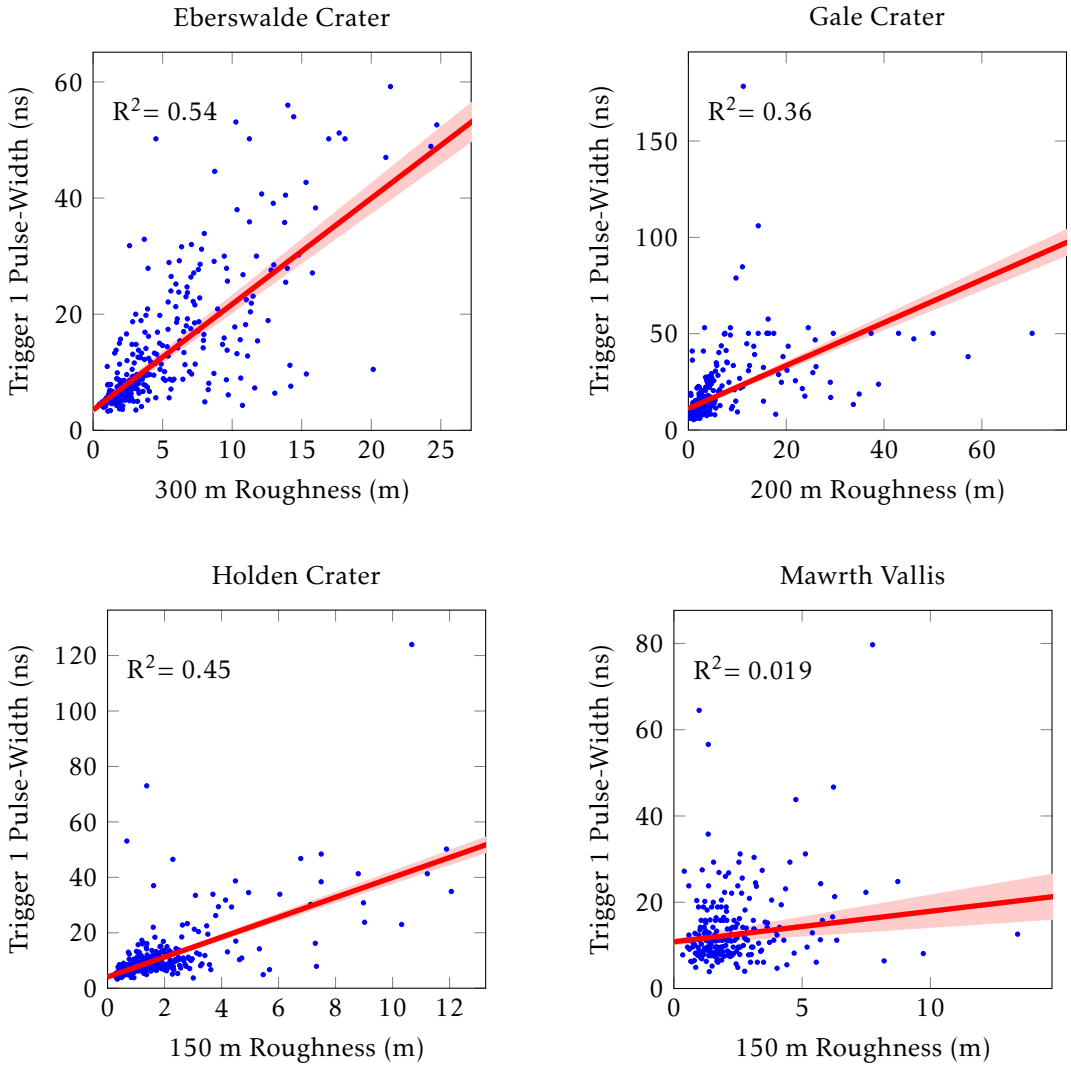

Figure 3.19: Plots showing the best correlating baseline surface roughness and MOLA Trigger 1 pulse-widths over each of the final four MSL candidate landing sites. The highest R-squared value is shown on the plot and the baseline at which this value is found is shown along the horizontal axis.

remove many pulses considered good quality in *Neumann et al.* [2003a], as shown by there being less pulses using this dataset than the Slope-Corrected pulse-width dataset in Table 3.8. At Gale Crater, 1569 pulses occur over the site in the PEDR dataset, 1271 using Trigger 1, and just 433 pulses in the Slope-Corrected dataset. This shows at least 838 pulses in the Trigger 1 data are considered poor data by *Neumann et al.* [2003a] (Table 3.8).

Contrarily, Trigger 1 pulse-widths over Holden Crater show a dramatic improvement in correlation - R-squared of 0.46 compared to 0.06 - compared to PEDR pulse-widths; the Slope-Corrected dataset performs marginally better still (R-squared of 0.47. This appears to be due to the removal of poor data, such as those highlighted in green in the Holden Crater plot in Figure 3.18. Approximately 500 fewer pulses occur in the Trigger 1 data over this site, leaving 1543 pulses in the Trigger 1 dataset, just 34 more than in the Slope-Corrected dataset (Table 3.8). The small change in the number of pulses and R-squared value when using the Slope-Corrected pulse-widths, suggests the majority of the poor data identified by *Neumann et al.* [2003a] over Holden Crater was recorded by

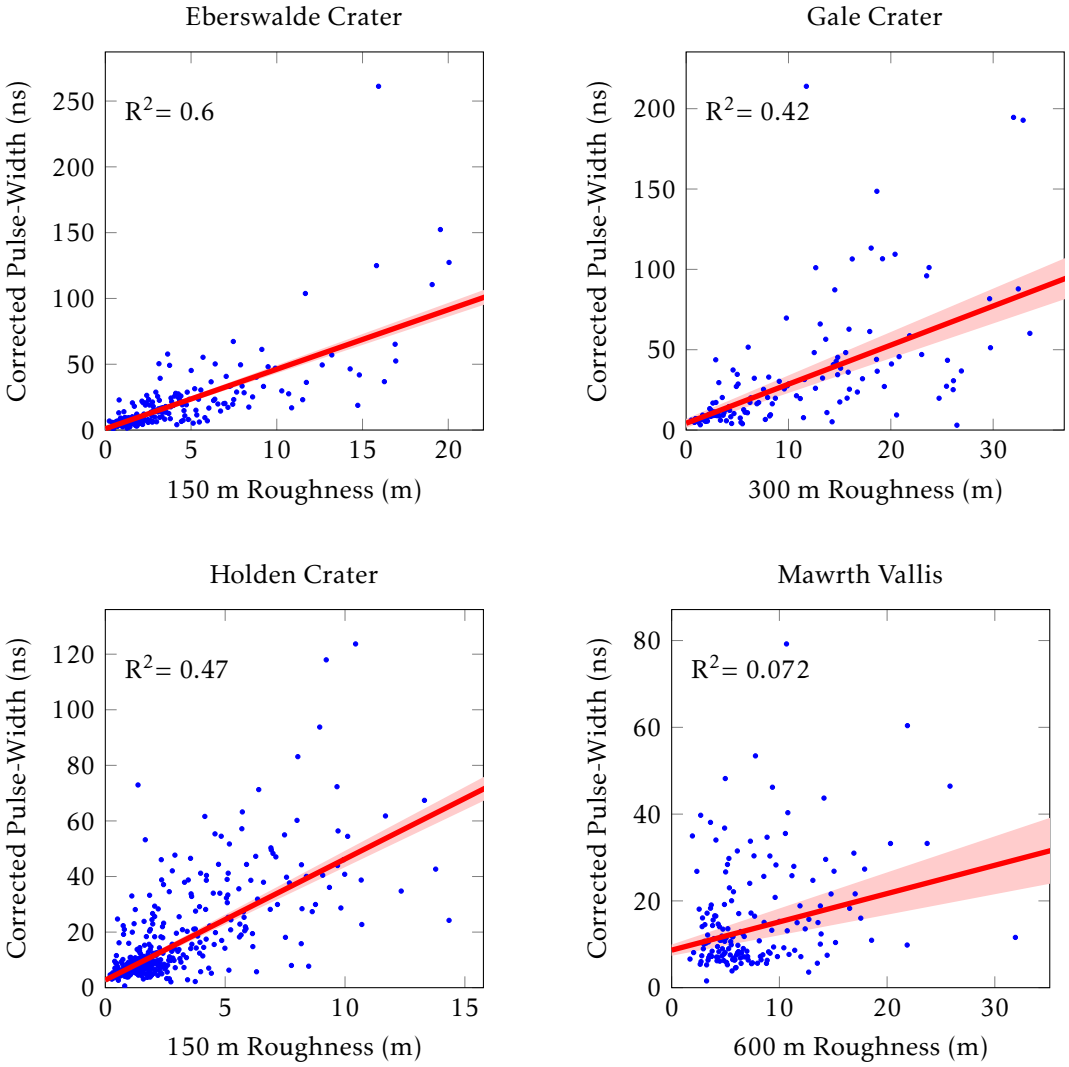

Figure 3.20: Plots showing the best correlating baseline surface roughness and MOLA Slope-Corrected pulse-widths over each of the final four MSL candidate landing sites. The highest R-squared value is shown on the plot and the baseline at which this value is found is shown along the horizontal axis.

Channels 2, 3, and 4 (Table 3.2). Furthermore, the removal of the poor data shown in Figure 3.18 compared to Figures 3.19 and 3.20, supports the hypothesis that Trigger 1 channel is the most reliable channel for Holden Crater. Like Eberswalde Crater, the best correlating plots occur at a baseline of 150 m, with no baseline selected for the PEDR pulse-width plot because of the poor correlations.

Mawrth Vallis presents some interesting results because it is the only site where surface roughness appears to have little influence on the MOLA pulse-width values. The same co-registration and DTM error checking procedures were completerd, as discussed in Section 3.6, but only poor correlations are observed. With this in mind, why would one site display such different results? To attempt to answer this question, the statistical and spatial distribution of surface roughness is investigated in Figures 3.21 to 3.25.

The surface roughness distribution in Figure 3.21 shows the distribution of 150 m baseline

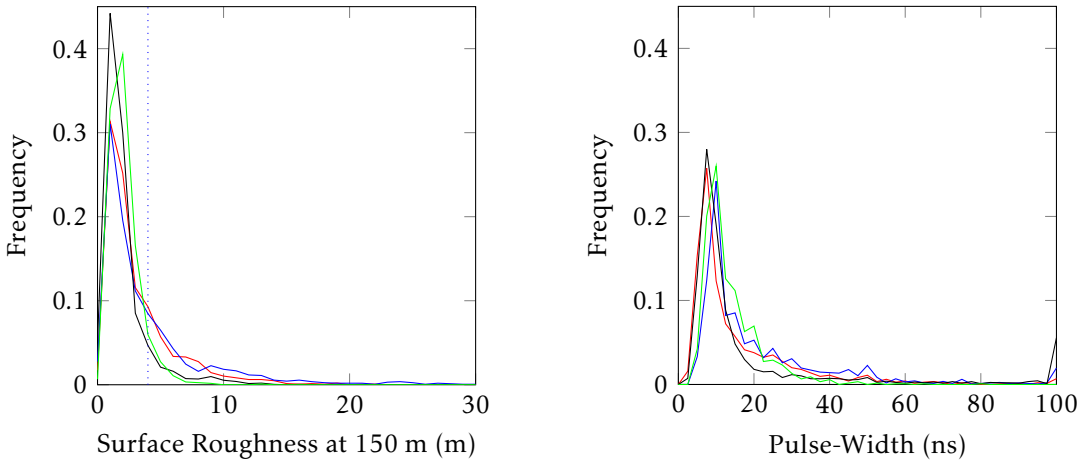

Figure 3.21: Plots of the surface roughness at 150 m and pulse-widths distribution for each site at MOLA pulse locations. Red: Eberswalde Crater; Blue: Gale Crater; Black: Holden Crater; Green: Mawrth Vallis. The 4 m roughness at 150 m threshold is shown as a vertical blue dotted line on plot (a). Above this threshold, terrain is considered part of a Rough Patch.

surface roughness: this baseline was chosen as two of the three sites where a correlation is observed using the Slope-Corrected pulse-widths revealed the highest R-squared value at this baseline (Table 3.8). The pulse-width distribution over Mawrth Vallis is similar to that at Holden Crater. Likewise, Eberswalde Crater and Gale Crater show similar distributions of surface roughness. In the pulse-width distribution plot, the distribution at Mawrth Vallis is similar to that at Gale Crater between 0.25 ns, above which the distribution closer resembles that from Holden Crater. It is clear from both of the these plots, that the distribution of surface roughness and pulse-width are not the cause of poor correlation over Mawrth Vallis, nor do these distributions allow us to predict the observed R-squared values at sites where a correlation is found.

A visual inspection of the Rough Patches identified in Figures 3.22 to 3.25 suggest the spatial extent of rough terrain may be the cause of poor results over Mawrth Vallis. Rough Patches are defined as areas of terrain where the 150 m baseline surface roughness is $\geq$4 m in Figure 3.21. This baseline is chosen as two of the three sites where a correlation is observed using the Slope-Corrected pulse-widths. The 4 m threshold is chosen because this is approximately the start of the long tail in the frequency distributions for each of the sites. The maps show that Eberswalde Crater and Gale Crater have large expanses of homogenous rough terrain, with other, smaller Rough Patches, scattered across the remaining areas of DTM coverage. The extent of rough terrain at Holden Crater is less expansive, with more evenly distributed small to medium sized areas of rough terrain. At Mawrth Vallis the spatial distribution of Rough Patches is heterogenous, with more small regions of rough terrain dotted throughout the region. Where there are relatively large regions of rough terrain, these often appear spotted due to small areas of smooth terrain within the boundary of wider Rough Patches.

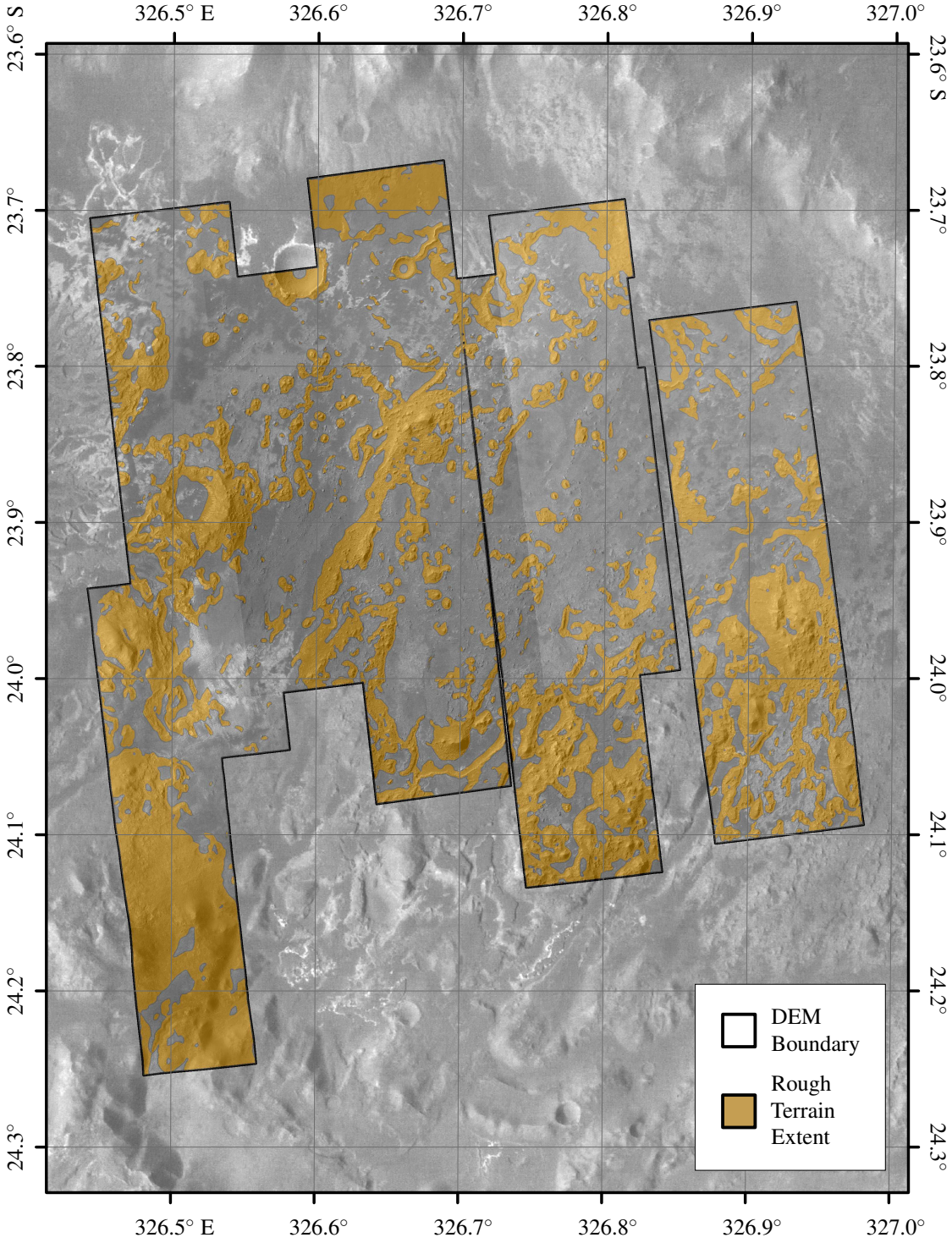

Figure 3.22: Map of the Rough Patches within the Eberswalde Crater study area, with HiRISE DTM coverage and HRSC image in the background. The areas in orange are considered *rough*, where *rough* is defined as surface roughness $\geq$4 m at 150 m baseline.

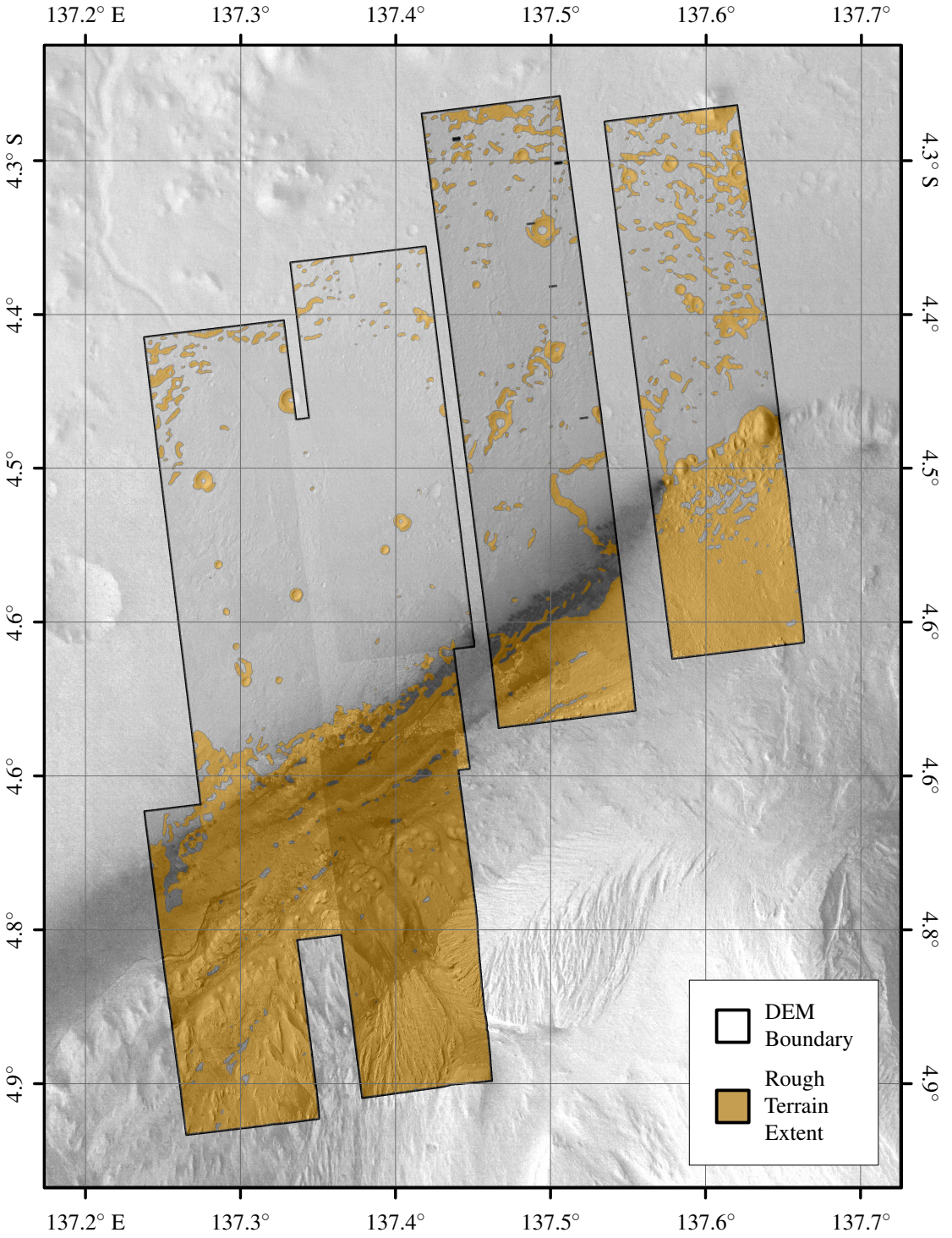

Figure 3.23: Map of the Rough Patches within the Gale Crater study area, with HiRISE DTM coverage and HRSC image in the background. The areas in orange are considered *rough*, where *rough* is defined as surface roughness $\geq$4 m at 150 m baseline.

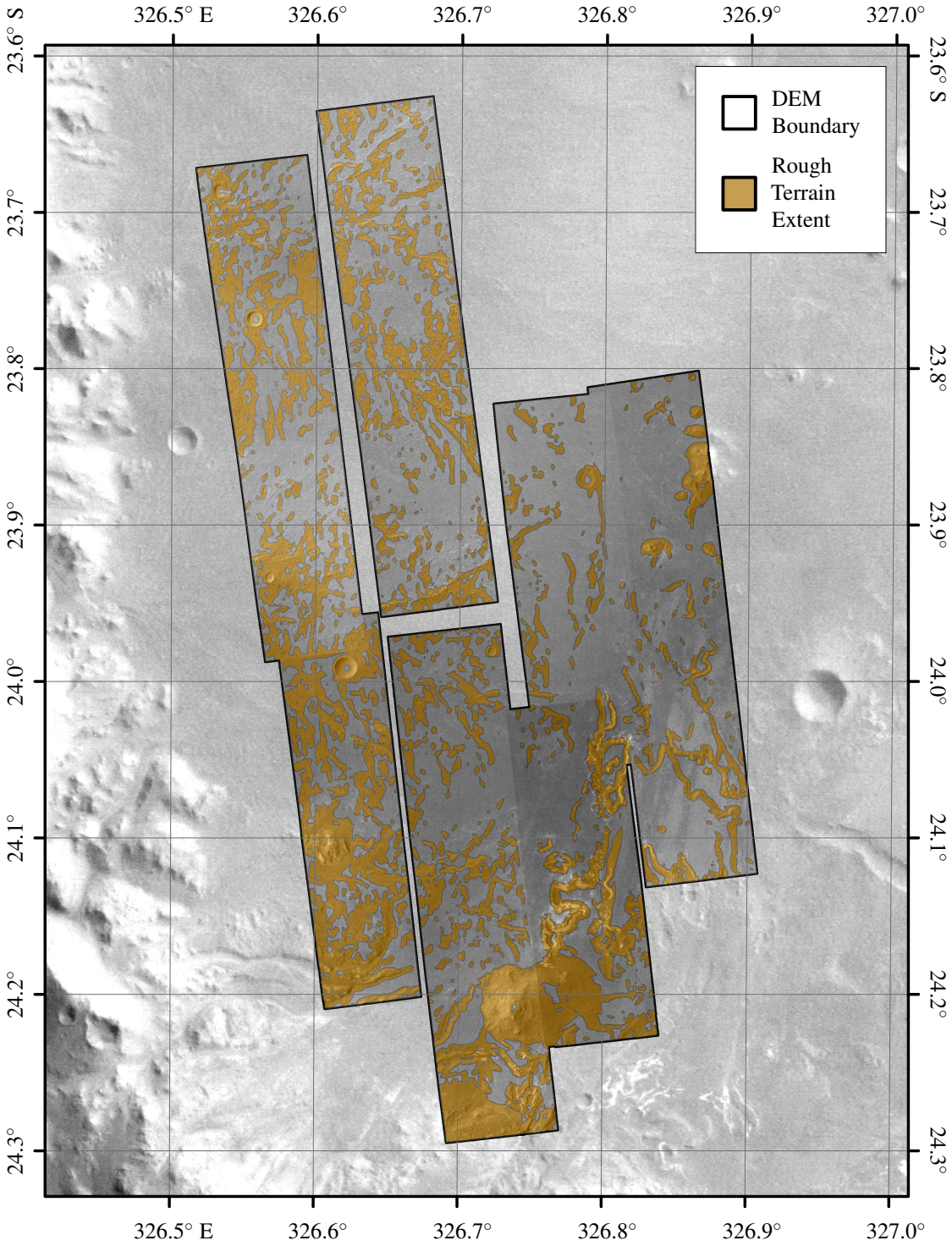

Figure 3.24: Map of the Rough Patches within the Holden Crater study area, with HiRISE DTM coverage and HRSC image in the background. The areas in orange are considered *rough*, where *rough* is defined as surface roughness $\geq$4 m at 150 m baseline.

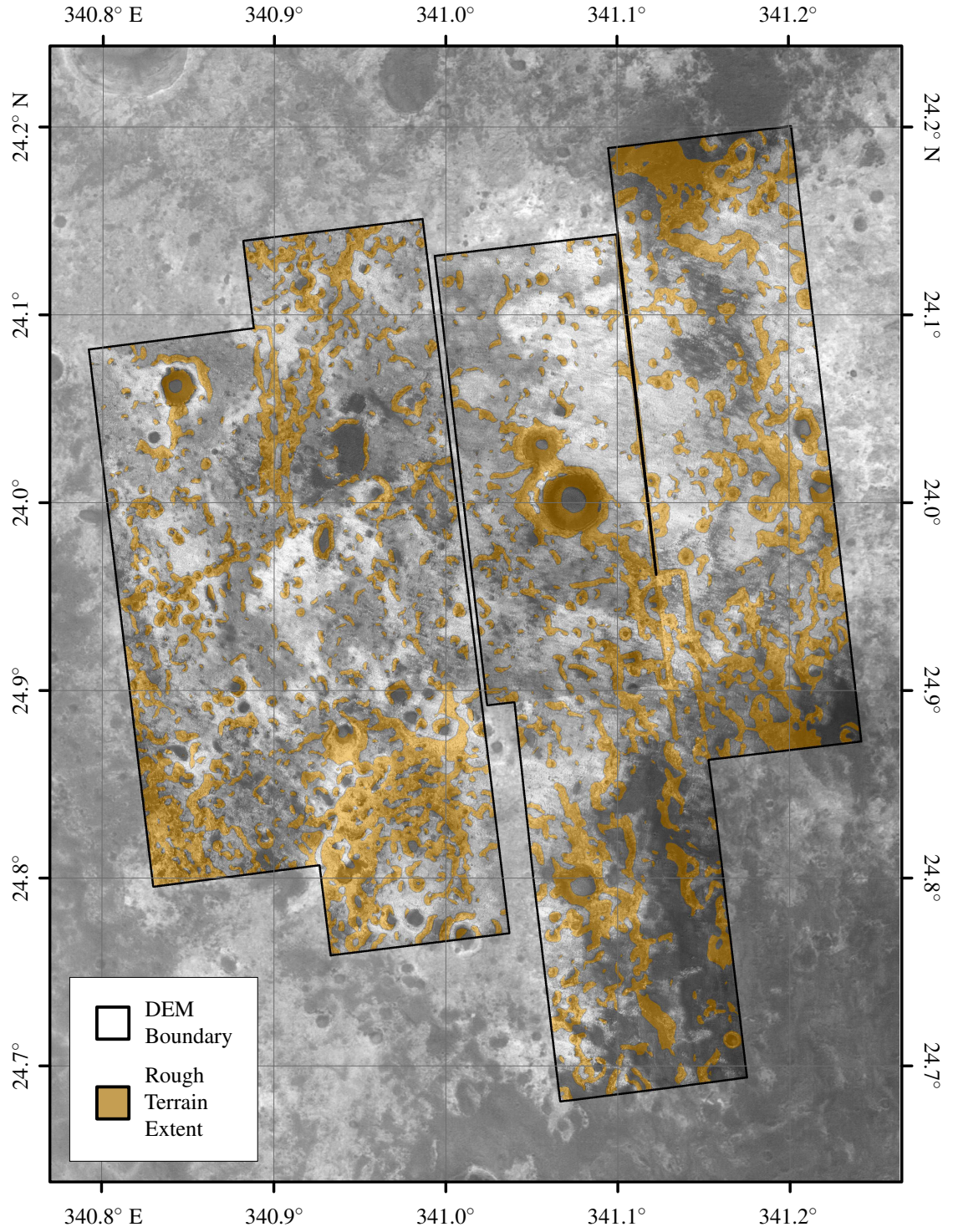

Figure 3.25: Map of the Rough Patches within the Mawrth Vallis study area, with HiRISE DTM coverage and HRSC image in the background. The areas in orange are considered *rough*, where *rough* is defined as surface roughness $\geq$4 m at 150 m baseline.

3.7.4 DISCUSSION

Geographical Information System (GIS) technology has been used to make a detailed comparison of laser altimeter pulse-widths and surface roughness estimates, using the RMS height, over areas with extensive high-resolution DTM coverage. Good correlations are observed at three of the four sites; little correlation is observed at Mawrth Vallis. The PEDR and Trigger 1 pulse-width datasets may contain a large number of poor data that show little correlation with the underlying terrain. The Slope-Corrected pulse-width dataset from *Neumann et al.* [2003a] produces the largest R-squared values at two of the sites. At Gale Crater, the PEDR pulse-width dataset produces the best correlations.

The removal of poor data from the PEDR dataset, such as cloud hitting and saturated receiver pulses, in the production of the Slope-Corrected dataset increases R-squared values at Eberswalde Crater and, most noticeably, Holden Crater, where the R-squared value of the linear fit improves from 0.06 to 0.47. The Holden Crater PEDR plot in Figure 3.18 contains a large collection of data that is not present in the equivalent Trigger 1 and Slope-Corrected plots in Figures 3.19 and 3.20 respectively. This effect is much smaller at Eberswalde Crater, where the number of pulses removed is the smallest of all the sites (Table 3.8).

Conversely, Gale Crater reveals poorer correlations between MOLA pulse-widths and surface roughness using the Slope-Corrected pulse-widths compared to the PEDR pulse-widths. This is attributed to a large number of poor data contained in the PEDR dataset, which have similar pulse-width values to the high-quality data. The higher data density around the line-of-best fit, compared to the Slope-Corrected data, results in a larger R-squared value. This is shown in Figure 3.18, where pulses such as the string of poor data, highlighted in green, sit close to the line-of-best-fit. These pulses are produced along a single orbit and could be either cloud hitting or saturated pulses, as they are not present in the Slope-Corrected dataset. Gale Crater also represents the greatest disparity in the number of pulses in the PEDR and Slope-Corrected pulse-widths, with approximately two-thirds of the PEDR data over this region removed in the production the Slope-Corrected dataset. It is for this reason that the Slope-Corrected dataset is considered more reliable, despite the smaller R-squared value of the plots shown in Figures 3.18 to 3.20.

It is clear that the generic removal of Trigger 2, 3, and 4 pulse-widths is not an effective method of identifying high-quality pulse-widths, as it often removes data at larger pulse-widths that may be good quality. This is shown when comparing the Eberswalde Crater plots in Figures 3.19 and 3.20 by the change in the vertical axis, and the reduced R-squared value when using the Trigger 1 data, whereby high pulse-width values have been removed compared to the Slope-Corrected dataset. Additionally, the number of pulses using the Trigger 1 data is smaller than the Slope-Corrected data, which shows many pulses considered good quality in *Neumann et al.* [2003a] are removed when using only the Trigger 1 data. At Eberswalde Crater there is no change in the observed R-squared value for the Trigger 1 data compared to the PEDR pulse-widths, instead there is a change of baseline at which the best correlation occurs (Table 3.8).

The principal discussion point are the results from Mawrth Vallis and why no correlation

is observed at any of the baselines for any of the pulse-width datasets (Figures 3.18 to 3.20). Figure 3.21 suggests this is not attributed to the statistical distribution of pulse-width or rough terrain. Instead, it appears to be linked to the spatial distribution of rough terrain. The three regions discussed above contain Rough Patches that are homogenous in appearance and spatially large (Figures 3.22 to 3.24); whereas at Mawrth Vallis the Rough Patches are typically small, and where they are large, appear speckled as the terrain is interspersed with smoother terrain (Figure 3.25). From this, it is interpreted that MOLA pulse-widths can only successfully determine surface roughness within the pulse-footprint where terrain is consistently rough or smooth. At Mawrth Vallis this is not the case, as the small, patchy nature of rough terrain over this region, increases the possibility of pulse-footprints overlapping both rough and smooth terrain, which could lead to complex echo-profiles. The simple threshold detection pulse-width timing system employed by the instrument, and the filtering system that matches pulse-widths to one of four channels: smooth, moderate, rough, and clouds, as described in Section 3.3, may therefore result in incorrect pulse-width measurements.

The results here suggest that MOLA pulse-widths cannot be used to reliably determine roughness for landing and roving site selection. The apparent poor sensitivity of MOLA pulse-widths to surface roughness could be a result of (1) the low intensity of reflected light, (2) atmospheric scattering along the pulse-path, and (3) scattering from the surface with the large pulse-footprint. Instead, downsampling of data may be required to produce sensible, interpretable results, but this will not overcome the issue observed at Mawrth Vallis, where no correlation is observed. Another issue is the lack of a commonly observed baseline, with a 150 m baseline observed at two sites, and 300 m at Gale Crater. This makes it difficult to extrapolate the results to the other regions of Mars. Are common baselines observed at Eberswalde Crater and Holden Crater because these sites share similar morphology, which results in similar results? Because better quality pulse-widths are found here? Or by chance?

3.8 LANDSLIDES, CHASMATA AND CHAOS

3.8.1 INTRODUCTION

To find better, more consistent, correlations, a project investigating the relationship between MOLA pulse-widths and surface characteristics over much rougher, homogeneous, terrain, than is used in Section 3.7, is presented. Rougher terrain is used as it is expected to increase the chance of pulse-footprints being over consistently rough or smooth terrain, therefore overcoming the issues interpreted to have occurred at Mawrth Vallis in the previous study. Only the Slope-Corrected pulse-width data is used, which is shown to be the most reliable dataset, predominantly due to the effective removal or poor data. The aim is (1) to gain further insights into the strengths and weaknesses of the MOLA pulse-width data, from which a new map of surface characteristics, better calibrated to more typical Martian surface properties, might be produced [*Smith et al.*, 2001; *Neumann et al.*, 2003a], and (2) to validate the method of deriving surface characteristics from laser

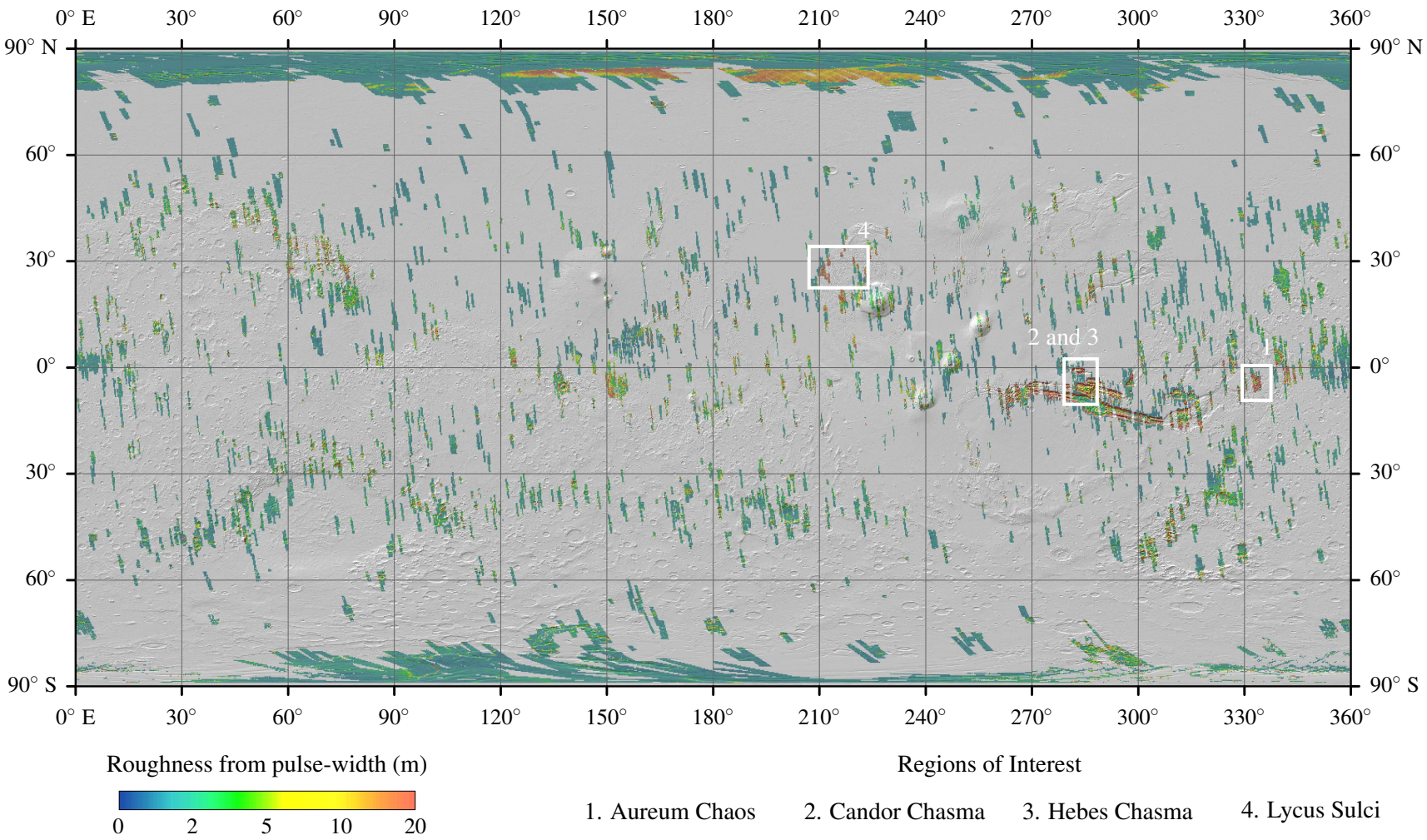

Figure 3.26: Map of Mars CTX stereo-image coverage over MOLA pulse-width surface roughness from *Neumann et al.* [2003a], shown in Figure 1.1a. The white boxes represent the study areas used in this study. Grey represents regions where no CTX stereo coverage is found.

altimeter pulse-widths, which is especially important for future laser altimeter missions.

The study uses CTX DTMs due to the low HiRISE stereo-coverage over sites not considered for landing and roving site selection [*McEwen et al.*, 2007, 2010]. Enough MOLA pulses lie within the boundary of a single CTX DTM from which to derive a mathematically significant relationship with surface characteristics [*Malin et al.*, 2007]. These DTMs were produced at lower resolution (18 m) compared to HiRISE, but it is now known that MOLA pulse-widths do not correlate to baselines as small as 35 m, as proposed by *Neumann et al.* [2003a]. Instead, it appears they correlate to roughness at much larger baselines (>150 m), which can be reliably derived from CTX DTMs [*Shepard et al.*, 2001]. In background work, HRSC DTMs were found to be too coarse over the study regions for reliable estimates of surface roughness to be derived, with only 5 pixels being within 150 m baseline calculations.

Finally, background work for Section 3.7 revealed poor correlations between MOLA pulse-widths and slope, and are therefore not reported. Here though, the greater variation in topography is expected to produce better correlations with slope, as a more significant proportion of σ_t will be derived from the slope contribution described in Equation 2.7.

3.8.2 SITE SELECTION AND CTX DTM PRODUCTION

Owing to the lack of a public archive for CTX DTM data, DTMs had to be produced specifically for this study, using the methods outlined in Section 3.6. This section describes the study site selection processes and background geomorphology of the selected sites.

To identify candidate sites, the surface roughness map from *Neumann et al.* [2003a], shown in Figures 1.1a and 1.1b at the start of this thesis, was used to highlight the roughest terrains on Mars. These terrains are cross-referenced with the surface roughness map from *Kreslavsky and Head* [2000], shown in Figures A.1 and A.2, to ensure the sites are considered rough in both datasets. The CTX image footprints from *Planetary Data System* [No Date.] were analysed to identify stereo-images in the 10 sites identified as rough. Repeat coverage is found over eight of the sites, five of which are in stereo, defined above. High-quality DTMs were produced at four of these sites, the locations of which are shown in Figure 3.26, and described below. The image identification numbers are shown in Table B.2 on Page 327.

3.8.2.1 AUREUM CHAOS (3.5° S, 332.5° E)

Aureum Chaos is an example of chaos terrain, typified by large blocky material interspersed by smoother, lower elevated terrain (Figure 3.27). This region of chaos terrain is contained within a complex basin lying to the east of Valles Marineris, and surrounded by other chaos regions, including Aurorea Chaos, Hydraotes Chaos, and Iani Chaos [*Rodriguez et al.*, 2005]. The formation of chaos terrains is likely to be very complex and is little understood, but it has been associated with early Hesperian to early Amazonian outflow activity [*Warner et al.*, 2011]. A possible chain of formation processes is shown in Figure 3.28, which is adapted from that in *Rodriguez et al.* [2005]. It appears that rocky material, which was originally part of a flat surface, has collapsed due to

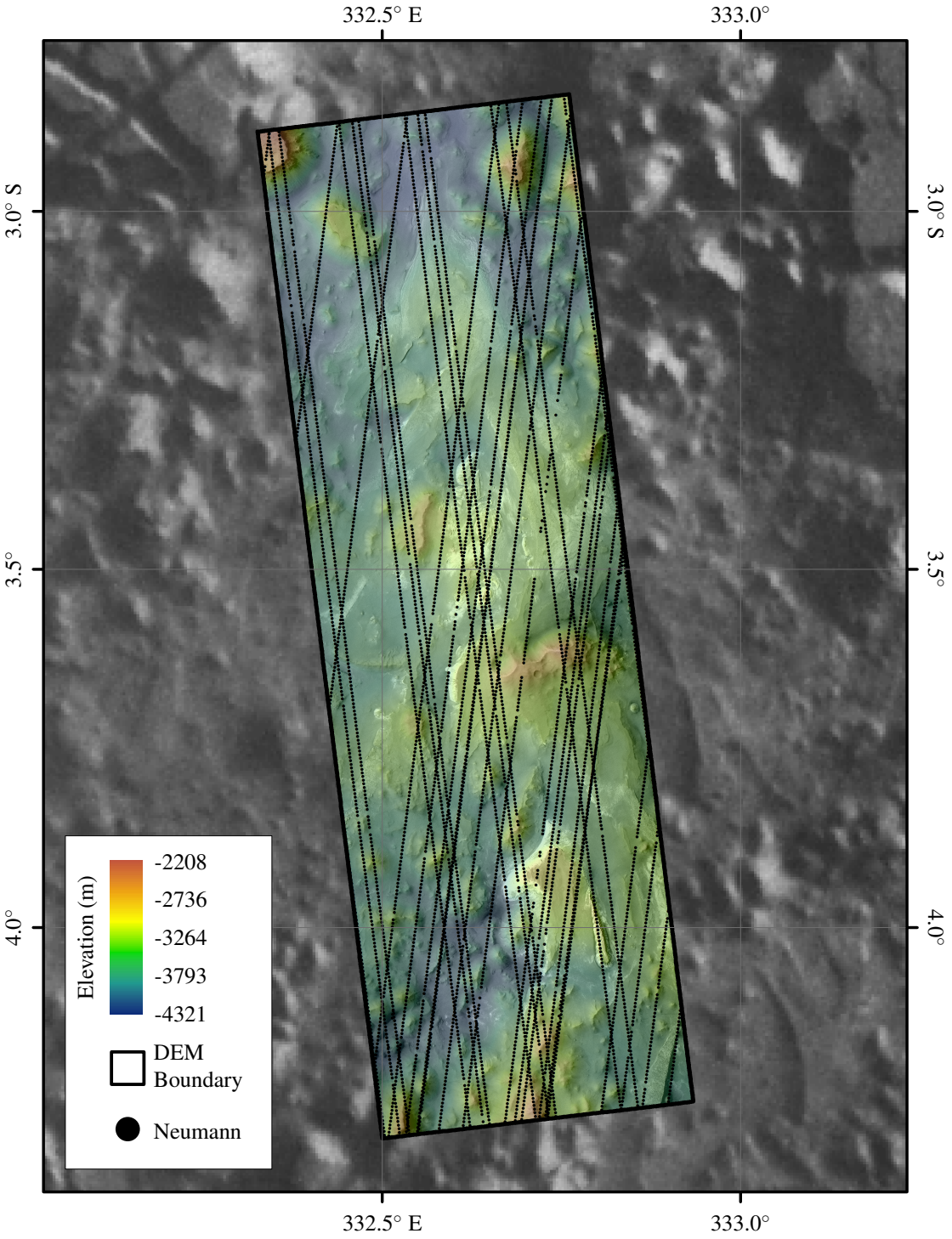

Figure 3.27: Map of Aureum Chaos study area. CTX coverage is shown in coloured topography, with Slope-Corrected MOLA pulse locations shown in black. CTX image is overlaid at 50 % transparency to highlight detail. The background image is from Viking, as there is no HRSC coverage over this region.

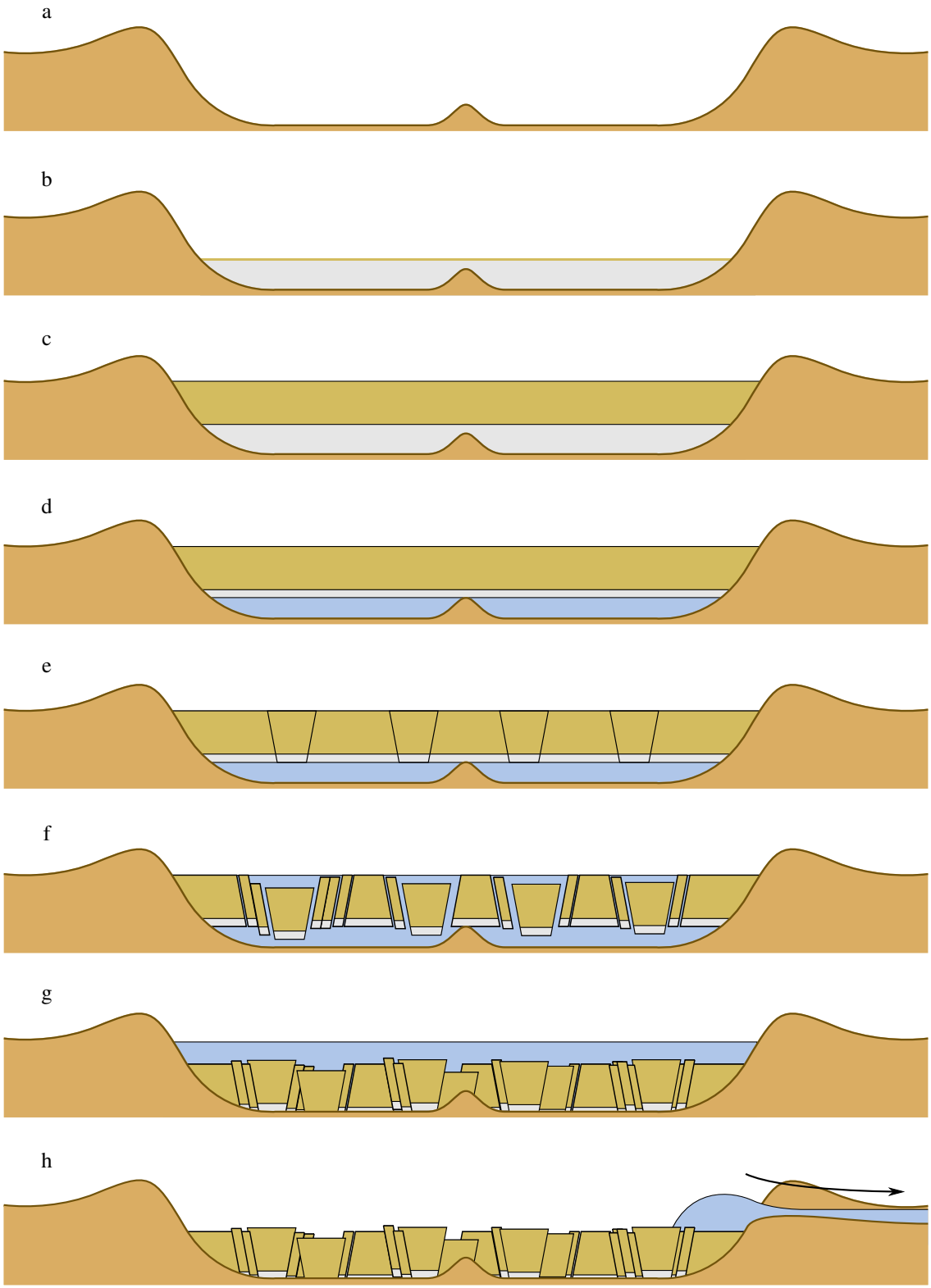

Figure 3.28: Schematic of the possible formation mechanisms of chaos terrain within Aureum Chaos [*Rodriguez et al.*, 2005]. (a) complex crater forms with central peak. (b) ice layer forms, potentially a frozen lake. (c) this ice layer is buried by dust, which forms a solid layer. (d) ice layer is melted, possibly from beneath. (e) solid layer becomes unstable, and begins crack. (f) solid layer breaks into blocks, which sink beneath the water layer. (g) water layer now sits on top of the blocks, and flows out of the crater (h) either by forging an outflow channel, or by natural elevation change.

removal of underlying material, leaving behind large blocks of hummocky terrain and flat-topped plateaus [*Rodriguez et al.*, 2005; *Warner et al.*, 2011]. Large outflow channels often appear from chaos terrains, which suggests that groundwater or ice had a significant role in the production of these terrains, as does the presence of bright hydrated minerals at some sites [*Rodriguez et al.*, 2005; *Spagnuolo et al.*, 2011; *Warner et al.*, 2011]. However, as reported in *Rodriguez et al.* [2005] and *Warner et al.* [2011], not all chaos terrains have the same morphology.

Within the ROI at Aureum Chaos, there is hummocky and flat-topped terrain, interspersed with regions apparently modified by water, with channels and depressions on the order of 1 km, as shown in Figure 3.27. The existence of bright hydrated minerals in the broader Aureum Chaos region suggests that water played a part in the long term evolution of the terrain, and not just in a short intense period of activity during the early formation period [*Spagnuolo et al.*, 2011]. Aureum Chaos also presents evidence of multiple collapse episodes, shown by several overlapping collapse basins [*Rodriguez et al.*, 2005]. In CTX images, the depressions appear smooth, with little deposited material. Rough terrain occurs where there are slopes from the hummocks and channels.

3.8.2.2 CANDOR CHASMA (5.5° S, 283.5° E)

Candor Chasma is one of the largest chasma feeding into the Valles Marineris system. There are competing theories as to how these chasmata may have formed, but the linearity of Valles Marineris and the surrounding chasmata points to tectonic formation processes, with recent work by *Andrews-Hanna* [2012a,b,c] suggesting that these features formed mainly due to vertical subsidence with some horizontal extension. This is attributed to volcanic loading of Tharsis directly over the crustal dichotomy, which may then have caused differential subsidence and extension to form the chasmata [*Golabek et al.*, 2011; *Smith et al.*, 1999]. Crater counts suggest that the Valles Marineris system formed during the Hesperian, as some canyon floors have an apparent age of 3.5 Ga, and also suggests no major refreshing events have occurred since this time [*Quantin et al.*, 2004].

The ROI is the boundary of one DTM located in the west of Candor Chasma, within which a series of roughness features, associated with different geologic processes, are observed Figure 3.29. These include steep chasma walls with landslide deposits at the base, and fine textured material across the floor (Figure 3.30) [*Murchie et al.*, 2009]. The landslides in the wide Valles Marineris system have a wide range of ages, from 3.5 Ga to 50 Ma from crater counts presented in *Quantin et al.* [2004]. All have similar features and may have a common repeating triggering mechanism. In Candor Chasma, the age of these landslides is put at $>$1.6 Ga [*Quantin et al.*, 2004].

The fine textured streaky material suggests wind erosion of friable material on the floor of the depression. This friable material is associated with the interior layered deposits that may have formed in the presence of water sometime before the landslide episodes, but after the formation of the chasmata [*Quantin et al.*, 2004]. *Murchie et al.* [2009] suggest these deposits formed as a result of modification of the dust and sand found on the chasma floor by groundwater upwelling at the surface, rather than standing water on the surface. A large layered mound dominates the centre of the chasma, which rises over 2 km from the floor, approximately half the scale of the chasma walls

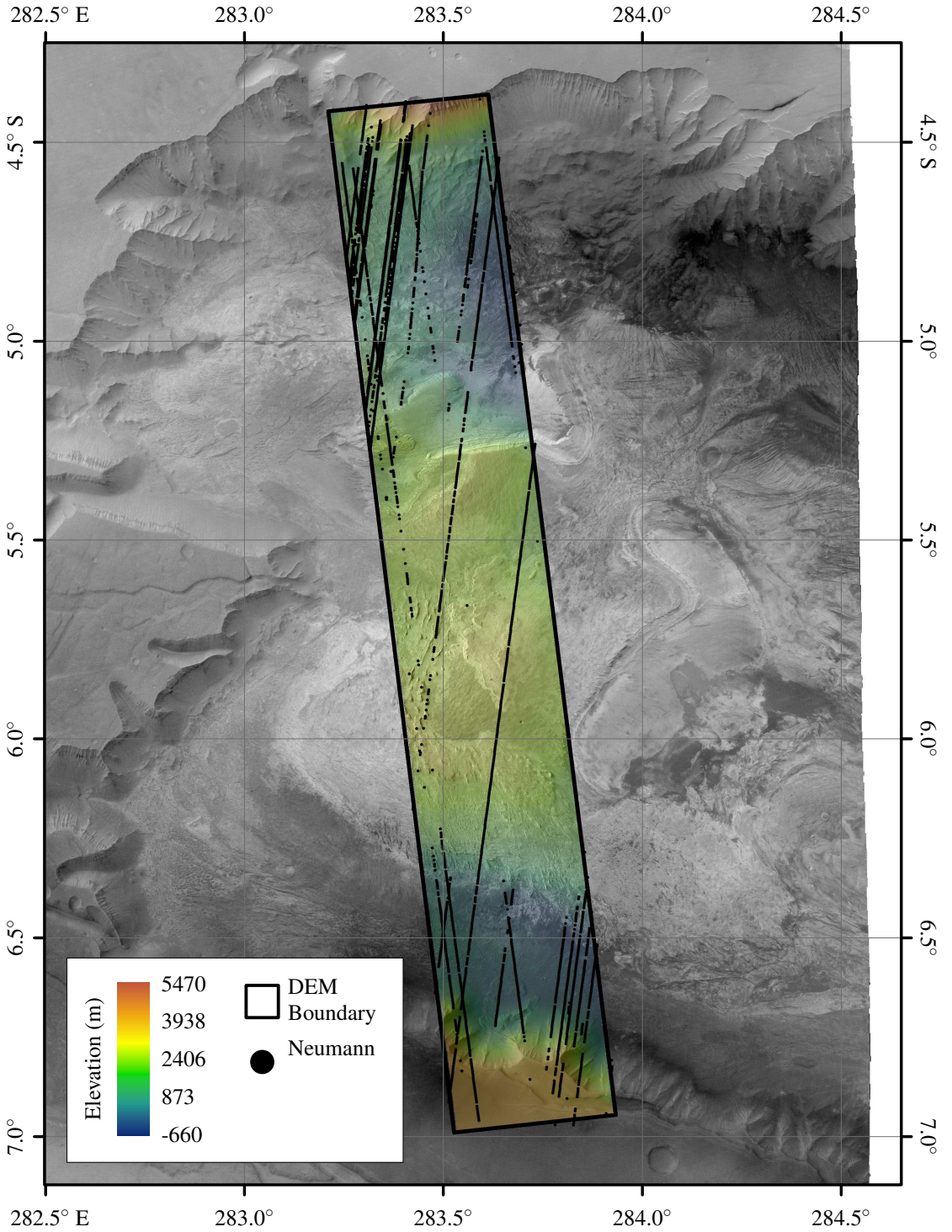

Figure 3.29: Map of the Candor Chasma study area. CTX coverage is shown in coloured topography, with Slope-Corrected MOLA pulse locations shown in black. CTX image is overlaid at 50 % transparency to highlight detail. Background image is from HRSC.

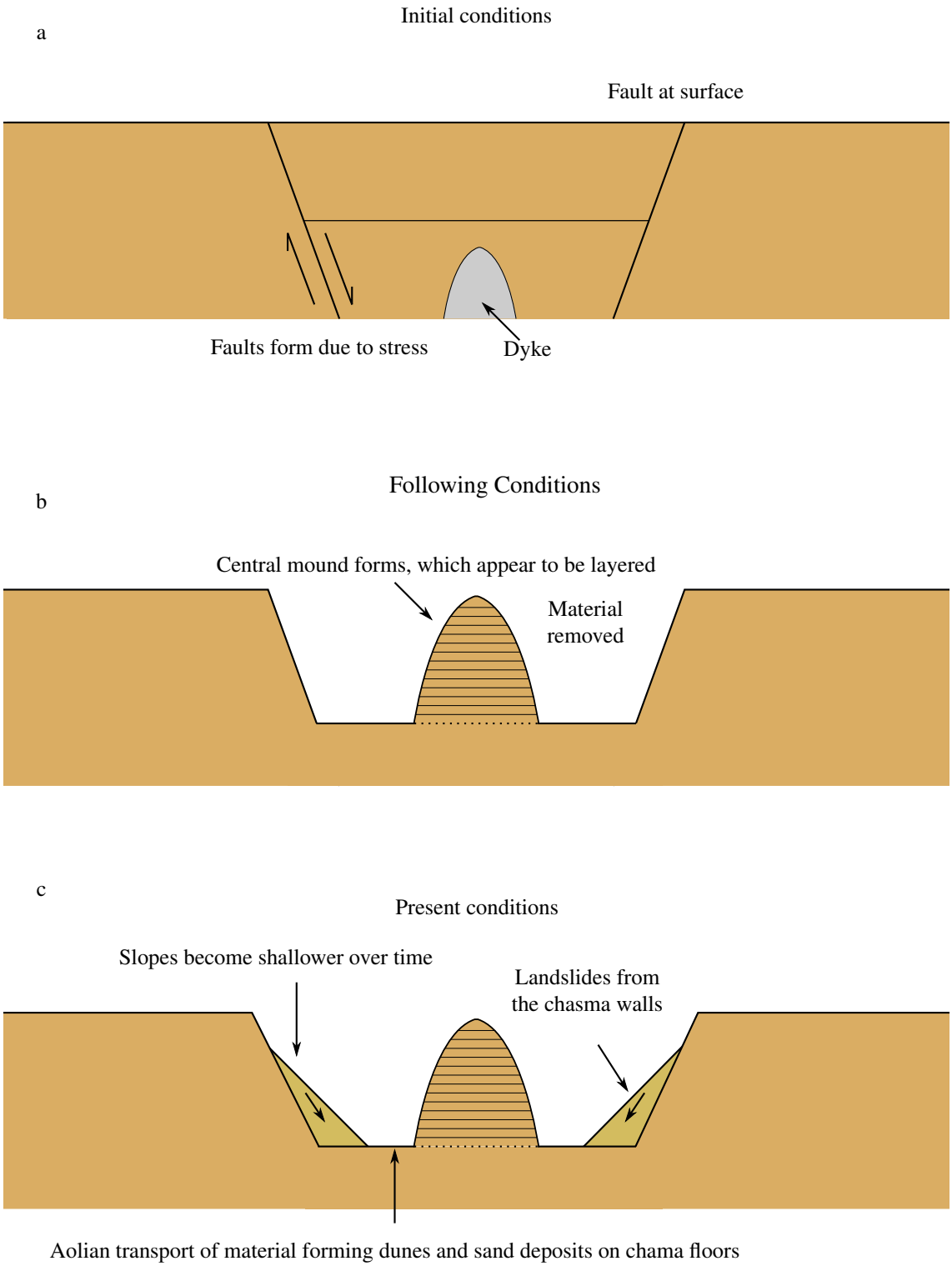

Figure 3.30: Schematic of possible Candor Chasma and Hebes Chasma formation processes. (a) dyke intrusion causes faults to develop through to the surface. (b) material is removed and what remains is a central mound which appears to be layered surrounded by chasma floors and steep chasma walls. (c) today's conditions. Over time material is transported from the chasma walls in the form of landslides, reducing the slope. Dunes also form through aeolian transport of fine grained material, and material is transported from the central mound.

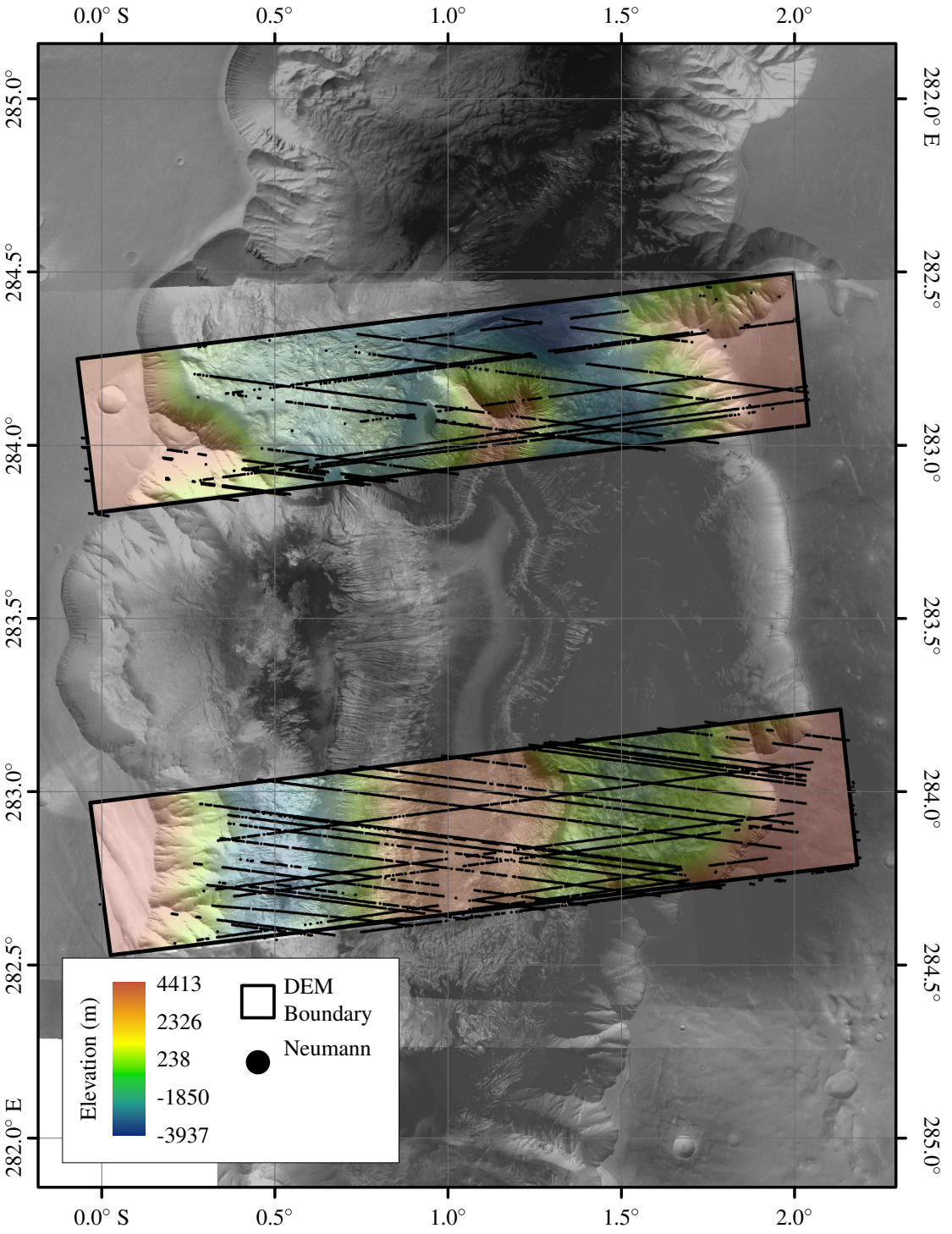

Figure 3.31: Map of the Hebes Chasma study area. CTX coverage is shown in coloured topography, with Slope-Corrected MOLA pulse locations shown in black. CTX image is overlaid at 50 % transparency to highlight detail. Background image is from HRSC.

shown in Figure 3.30. The formation mechanism is unknown, but is possibly related to deposition of wind blown material [*Fueten et al.*, 2014]. Compared to the chasma walls, the slopes of this mound are significantly shallower, and do not have landslide deposits at the base.

3.8.2.3 HEBES CHASMA (1.0° S, 283.5° E)

Hebes Chasma is an isolated depression north of the main Valles Marineris system and, like Candor Chasma, it contains a large layered mound in the centre of the depression [*Andrews-Hanna*, 2012a,b,c]. This mound is 5 km high, approximately the same scale as the chasma walls [*Andrews-Hanna*, 2012a,b,c]. The fact that this system appears isolated makes this chasma of special interest, with several formation mechanisms having been proposed for the evolution of the chasma to its present day appearance, such as erosion, collapse, and tectonic rifting followed by infilling by layered deposits as discussed above [*Andrews-Hanna*, 2012a,b,c; *Jackson et al.*, 2011].

Today, the top of the central mound, known as Hebes Mensa, contains incisions and inverted channels that may have formed due to groundwater focussing by the pressure exerted by the central mound [*Grindrod and Balme*, 2010]. Deposits of this size are not common in other chasmata in the region as they are more open, and thus have larger erosive and transport properties [*Fueten et al.*, 2008]. Furthermore, the slopes of the central mound are much steeper than the gently rising, smaller, mound found at Candor Chasma. Similarly to Candor Chasma, the processes that formed and modified the terrain have left behind rough terrain in the form of landslide deposits, hummocky terrain, and channels, all of which are observed in the two DTMs produced over this region. The age of the landslides based on crater counts has been found to be between $>$1 Ga to 200 Ma [*Quantin et al.*, 2004].

3.8.2.4 LYCUS SULCI (28.1° N, 215.5° E)

The majority of the terrain contained within the three DTMs produced over this region is very similar, differing only in apparent age. The ROI's lie to the northwest of Olympus Mons, within two of the aureole lobes that surround the massive shield volcano, in an area known as Lycus Sulci [*McGovern et al.*, 2004; *Griswold et al.*, 2008]. The three DTMs are labelled as Lycus Sulci 1, Lycus Sulci 2, and Lycus Sulci 3, which are ordered by chronology of processing, with the resulting data shown in Figures 3.32 to 3.34 respectively.

The ridged terrain that characterises this region of Mars is unique and appears to be formed by material sliding from the outer flanks of Olympus Mons. When a shield volcano, such as Olympus Mons, reaches a certain size, the stresses within it change from compressional to extensional, and if the volcano lies on mechanically weak layers of sediments or ice, as postulated by *Helgason* [1999], then basal escarpments and decollements (detachment zones) may develop, as observed in Lycus Sulci Figure 3.35. *McGovern et al.* [2004] show that these lobes are composed of landslide material derived from the flanks of Olympus Mons and, despite a low slope and fall height, stretch out up to 700 km from the headwalls that now form the basal scarp surrounding the volcano [*De Blasio*, 2011]. These landslides have been compared to subaqueous volcanoes on Earth, such as those in Hawaii,

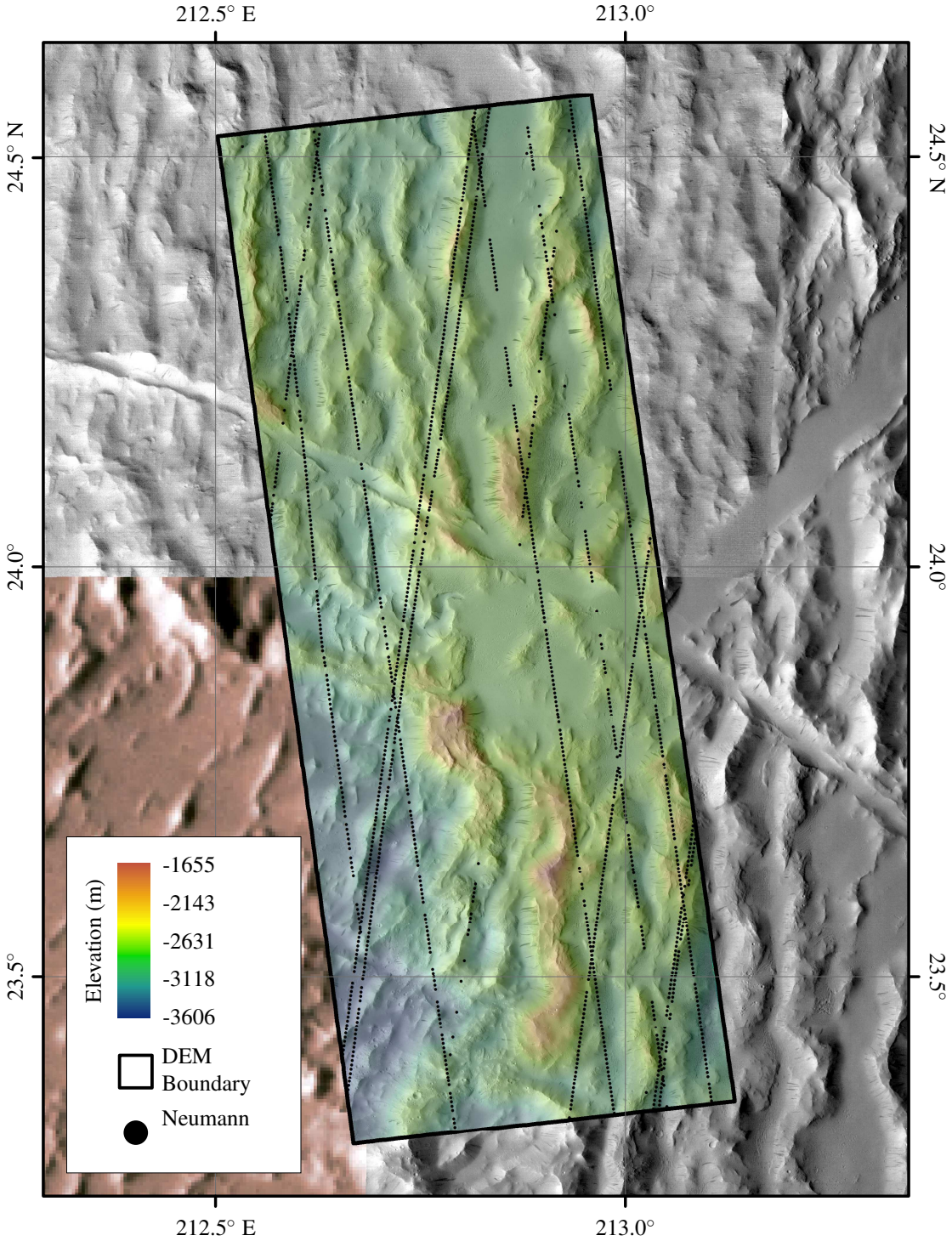

Figure 3.32: Map of the Lycus area 1 study area. CTX coverage is shown in coloured topography, with Slope-Corrected MOLA pulse locations shown in black. CTX image is overlaid at 50 % transparency to highlight detail. Background image is mainly HRSC, with region from Viking shown in colour to highlight HRSC coverage.

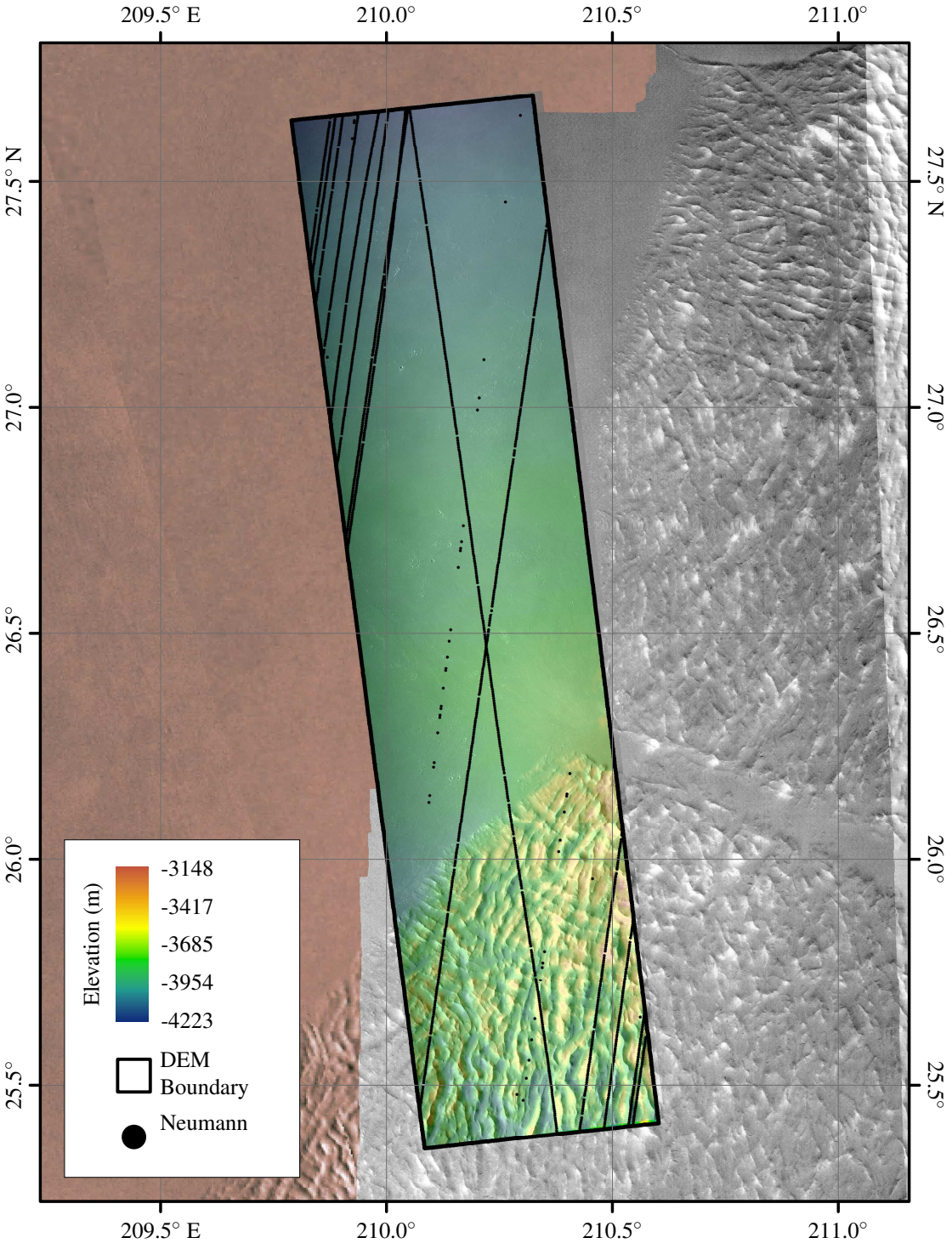

Figure 3.33: Map of the Lycus area 2 study area. CTX coverage is shown in coloured topography, with Slope-Corrected MOLA pulse locations shown in black. CTX image is overlaid at 50 % transparency to highlight detail. Background image is mainly HRSC, with region from Viking shown in colour to highlight HRSC coverage.

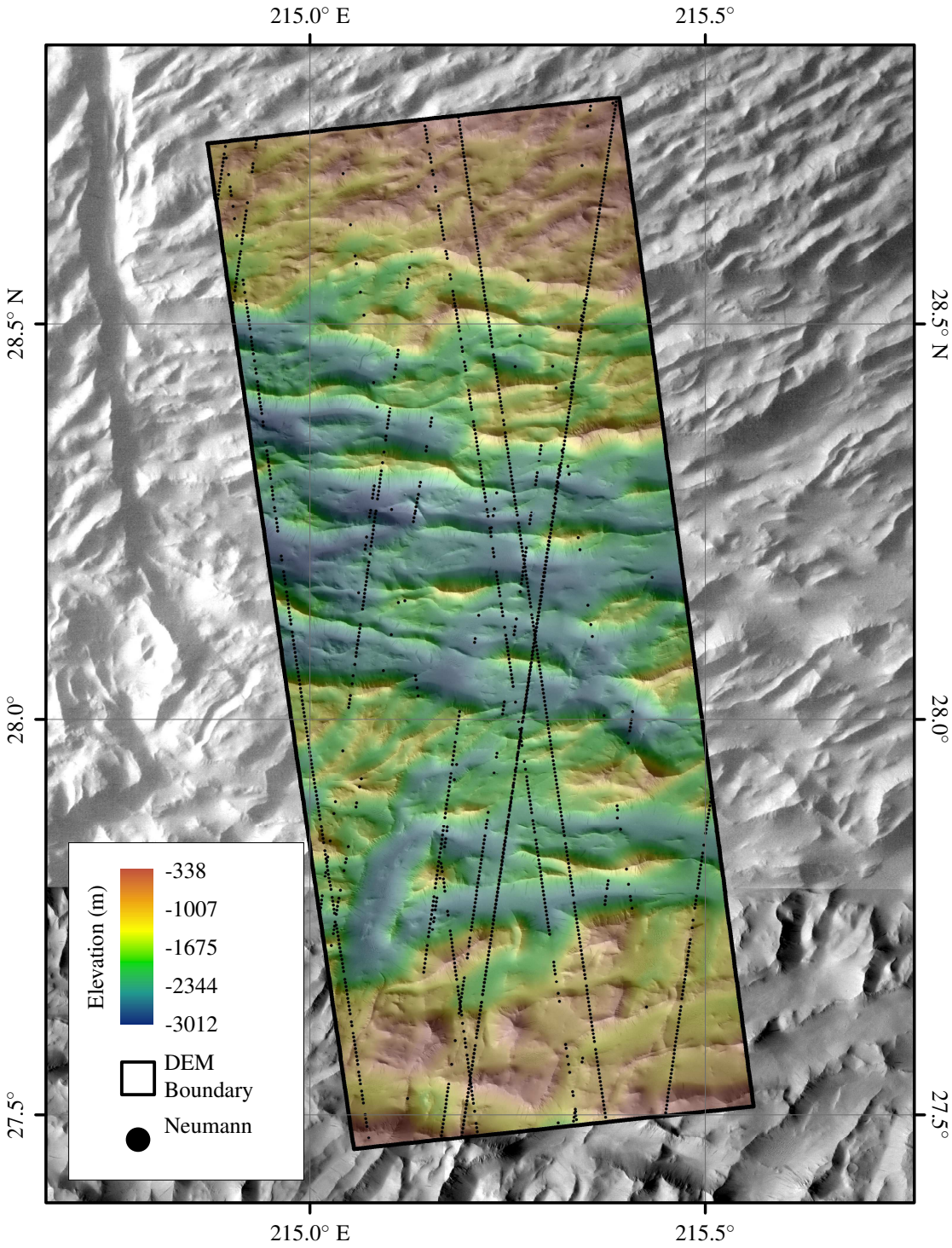

Figure 3.34: Map of the Lycus area 3 study area. CTX coverage is shown in coloured topography, with Slope-Corrected MOLA pulse locations shown in black. CTX image is overlaid at 50 % transparency to highlight detail. Background image is from HRSC.

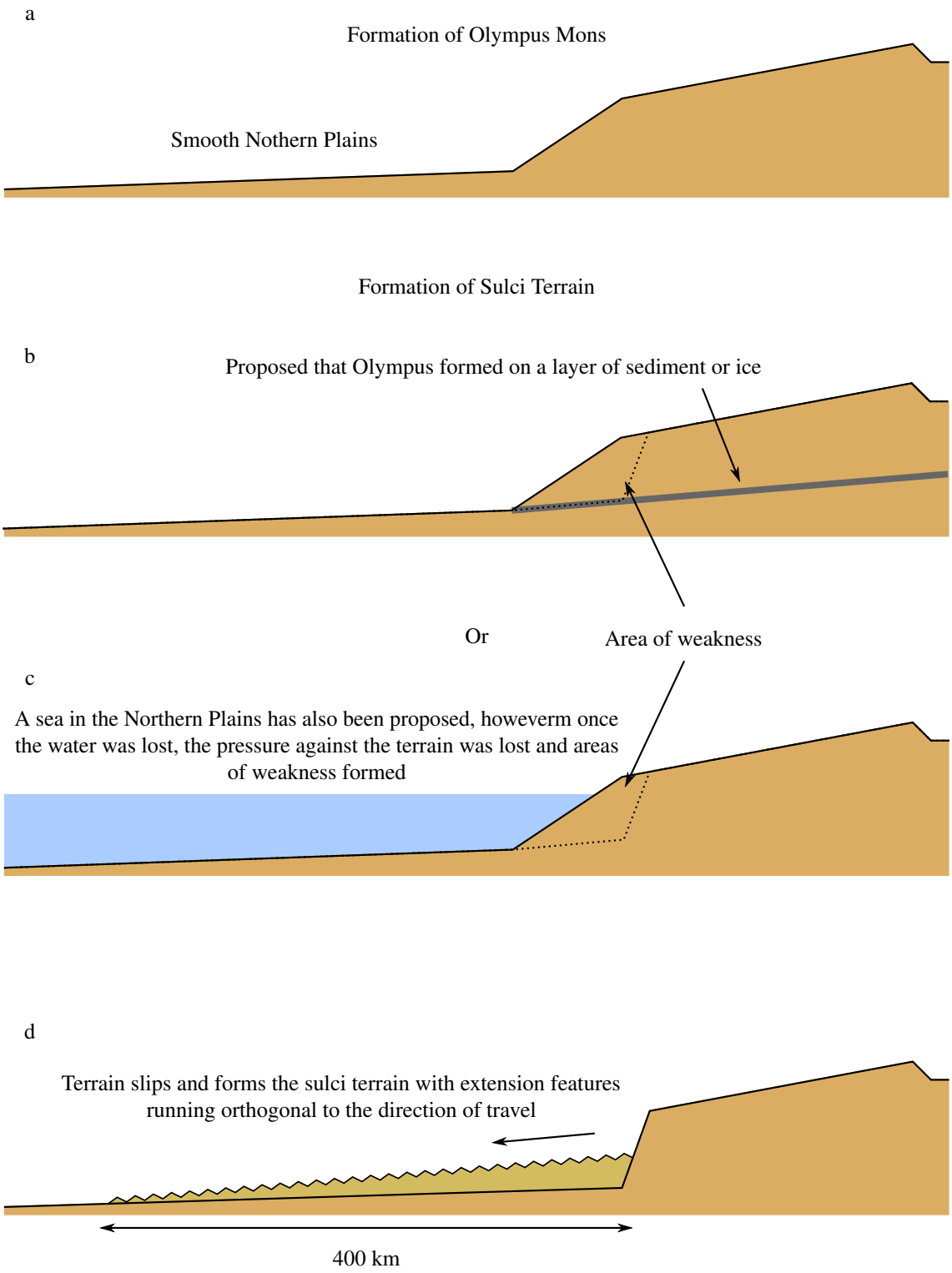

Figure 3.35: Schematic of possible Lycus Sulci formation mechanisms. (a) Olympus Mons forms on the Mars dichotomy between the Tharsis and the northern lowlands. (b) Olympus formed on a layer of ice or sediment, which is not stable over long periods. (c) Northern plains which puts pressure on the walls surrounding Olympus Mons. The ocean is then lost, removing the pressure on the walls removed, areas of weakness formed. (d) areas of weakness break away from Olympus Mons and form Lycus Sulci terrain with extensional features running orthogonal to direction of travel. Furthest reaches of the landslides are 400 km, and there are several periods of activity, with the oldest lying beneath newer slips.

and recent work by *De Blasio* [2011] shows that the great distance these lobes extended may be a result of hydroplaning [*McGovern et al.*, 2004]. It is also suggested that Olympus Mons lies on a layer of clays, formed from sediment eroded from the Tharsis rise and deposited downslope, hence the preferential mass movement away from Tharsis [*McGovern and Morgan*, 2009].

Today, the region appears as rough terrain, defined by a series of ridges and furrows running circumferential to Olympus Mons (Figures 3.32 to 3.34). A groove runs through Lycus Sulci 3, which, due to its linearity, is attributed to tectonic processes (Figure 3.34). Lycis Sulci 1 and 3 are located in the northwest lobe, which lies superimposed on the western lobe, which is where the Lycus Sulci 2 DTM is located. Part of the Lycus Sulci 2 DTM lies within the northern plains beyond the outer edge of the Olympus Mons aureole. This terrain is very smooth, with small craters ($<$1 km) and deposits from an outflow channel being of interest from a roughness perspective (Figure 3.33). Lava flows are present on all the aureole lobes, which has led to the suggestion that lava flows continued from Olympus Mons even after aureole emplacement, and may explain the apparent higher infilling of the furrows in the western lobe compared to the material superimposing it [*Griswold et al.*, 2008].

The greatest variation in topography of ridges and furrows are observed at Lycus Sulci 1 and Lycus Sulci 3, possibly due to their younger relative age meaning that there is less time for erosion, but also because Lycus Sulci 2 lies furthest from Olympus Mons. Here, the material has travelled furthest, and is therefore more likely to have spread evenly across the surface rather than maintain its ridged structure as it slipped from the its source.

3.8.3 RESULTS

The results are divided into two sections: *Regional* and *Lycus Sulci*. The first explores the regions as a whole, whilst the latter explores how the distribution of roughness features affects the observed correlations. Again, only the best correlating plots are shown, with the full results are shown in Tables C.2 and C.3 in Appendix C.

3.8.3.1 REGIONAL RESULTS

In contrast to the MSL candidate landing sites, MOLA Slope-Corrected pulse-widths show good correlation with both surface roughness and slope, although at very different baselines (Table 3.9). The best correlating slope plots are shown in Figure 3.36. The best correlating surface roughness plots appear very similar and are therefore not shown. The R-squared values of the best correlating plots are similar to those observed in the previous work, once the outlying R-squared values are removed. Unlike the MSL study, all sites show good correlations between surface characteristics and pulse-widths, and the best correlating baselines converge to similar lengths for each of the surface characteristics (Table 3.9).

The observed R-squared values for each regions are $\geq$0.4, with Lycus Sulci revealing the best correlations and Hebes Chasma the worst. The Lycus Sulci 2 results are discussed in detail in the following section, but readers should note that the distribution of surface roughness and slope values

Table 3.9: The highest R-squared values observed for comparisons made between Slope-Corrected MOLA pulse-widths and surface characteristics over rough terrain, for each region and the combined data. Also shown is each of the Lycus Sulci DTMs, with the Lycus Sulci 2 region split into rough and smooth terrain to highlight effects of a wide distribution of surface roughness. All R-squared values have a p-value <0.05.

		Slope		Roughness	
Area	Pulses	R-squared	baseline (m)	R-squared	baseline (m)
All Sites	21 017	0.55	75	0.57	300
Aureum	5690	0.52	75	0.56	300
Candor	2763	0.53	75	0.60	300
Hebes	7079	0.46	100	0.48	300
Lycus	5485	0.68	75	0.70	400
Lycus 1	1739	0.54	75	0.60	400
Lycus 2	2216	0.74	75	0.79	400
- Smooth	1605	0.06	100	0.11	300
- Rough	611	0.47	100	0.56	400
Lycus 3	1530	0.50	75	0.52	400

at this site are very different to other sites, which may be the cause of the larger R-squared values. Instead, observing the Lycus Sulci 1 and 3 results in Table 3.9 reveals this terrain to produce similar R-squared values to the other terrains used here, with R-squared values between 0.46 and 0.54. The results from Aureum Chaos suggest that using the Viking MDIM as a basemap to co-register CTX data, rather than the higher resolution HRSC nadir images, has not had an impact R-squared values: using the lower resolution Viking data may result in larger co-registration errors.

The R-squared values for the slope plots shown in Figure 3.36 are between 0.02 and 0.07 smaller than their surface roughness equivalent. These differences are not considered significant as the baselines for the best correlating slope plots are in-line with the latest estimates of MOLA pulse-footprint [*Neumann et al.*, 2003a], whilst the best correlations observed using surface roughness are very large. This suggests that MOLA pulse-widths are actually correlated to slope over rough terrain, as it seems unlikely that MOLA pulses diverge to 300 m to 400 m, as suggested in Table 3.9.

The consistency in the baselines at which the highest R-squared values are found when the pulse-widths are compared to both surface roughness and slope suggests that using rougher terrain, with a wider distribution of roughness, has enabled more reliable relationships to be found. This consistency means the data can be combined into a single dataset to provide a general picture of how pulse-widths relate to surface characteristics (Figure 3.36). The best correlating baselines in the previous study vary significantly, meaning that deriving a general relationship is not appropriate as only two of the four MSL candidate landing sites share a common baseline, whilst Gale Crater reveals the best correlation at a much larger baseline and Mawrth Vallis show little correlation at any

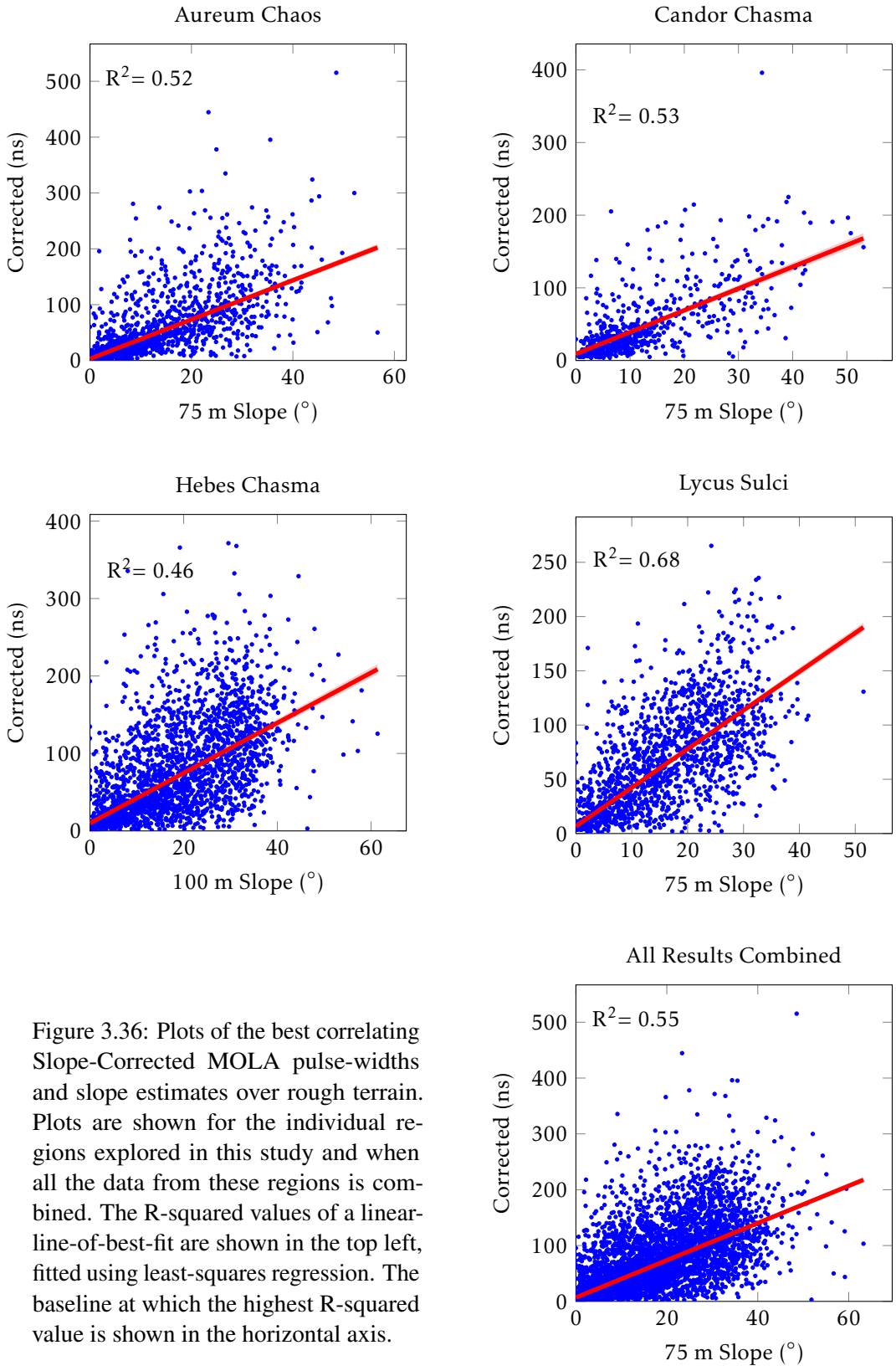

Figure 3.36: Plots of the best correlating Slope-Corrected MOLA pulse-widths and slope estimates over rough terrain. Plots are shown for the individual regions explored in this study and when all the data from these regions is combined. The R-squared values of a linear-line-of-best-fit are shown in the top left, fitted using least-squares regression. The baseline at which the highest R-squared value is shown in the horizontal axis.

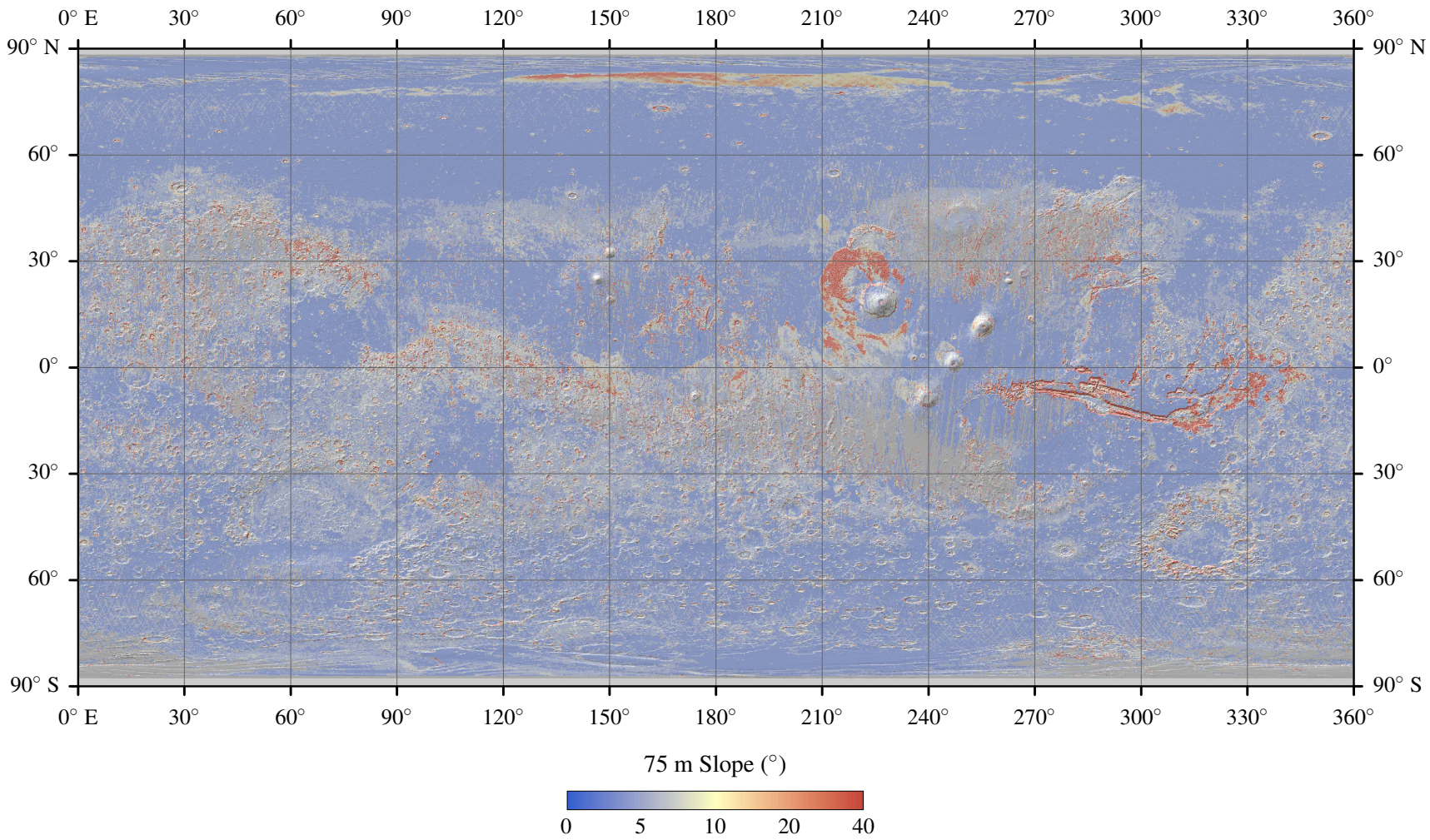

Figure 3.37: Map of the distribution of Mars slopes using the Slope-Corrected pulse-widths from *Neumann et al.* [2003a]. The data is calibrated using the relationship derived using all the data in Equation 3.2. Grey area shows where MOLA Slope-Corrected pulse-width data is missing.

baseline. Here, the combined results reveal a relationship in-line with the regional results, which suggests that a general relationship that can be applied to more typical, i.e. rougher, Martian terrain than that considered for landing and roving sites. The relationships between MOLA pulse-widths and surface characteristics, as derived from linear regression, are

$$\text{Surface Slope (75 m)} = (0.30 \times \text{MOLA pulse-width (ns)}) - 1.99, \quad [3.2]$$

$$\text{Surface Roughness (300 m)} = (0.41 \times \text{MOLA pulse-width (ns)}) - 2.65. \quad [3.3]$$

The slope relationship is applied in Figure 3.37 to provide an indication of the global distribution of slopes from pulse-width values. The slope values have been resampled using bilinear interpolation to 0.125 pixel degree^{-1}. This uses the same pulse-width data that is used to produce the surface roughness map shown in Figures 1.1a and 1.1b, but here it is scaled to 75 m slope by calibration, rather than by theoretical calibration to surface roughness using Equation 2.7 [*Neumann et al.*, 2003a].

3.8.3.2 LYCUS SULCI RESULTS

The dichotomy of rough and smooth terrains within the boundary of the Lycus Sulci 2 DTM presents a unique situation to explore how MOLA pulse-widths compare to surface characteristics over different terrains, as shown in Figure 3.38. The smooth region is defined as the expansive smooth terrain in Figure 3.33, whilst the rough terrain is the remaining part confined to the south in the same figure. Figure 3.39 shows the resulting plots for the rough and smooth terrain.

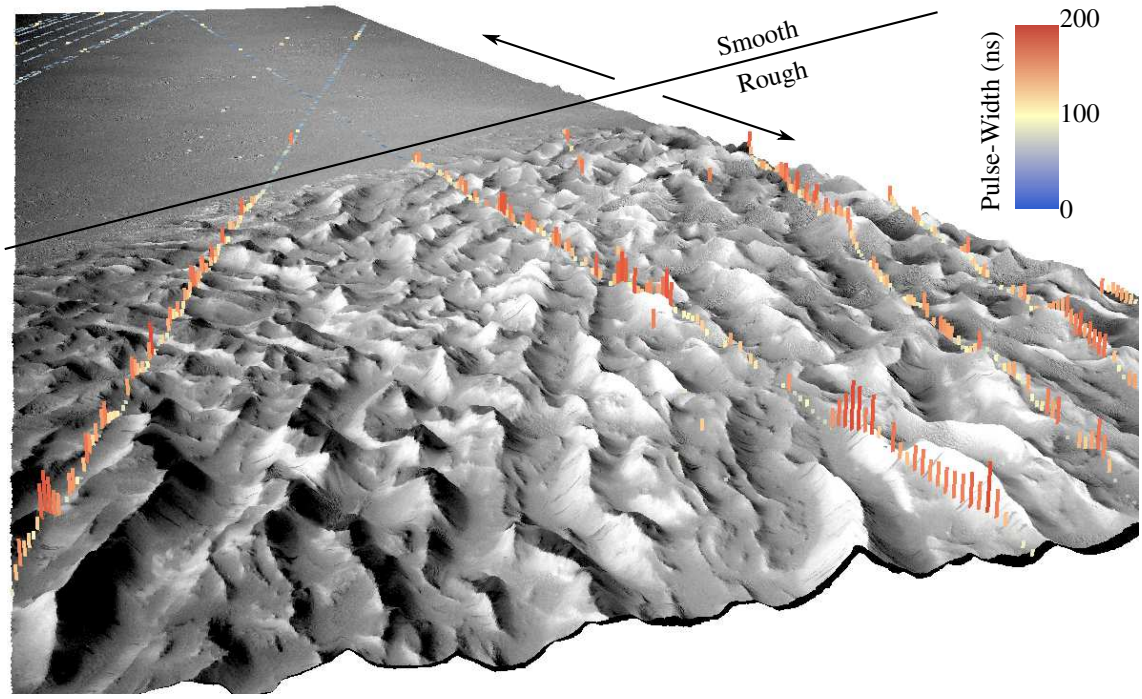

Figure 3.38: Map of the rough and smooth regions of the Lycus Sulci 2 DTM with MOLA pulse-widths overlaid. Pulse-width values are represented by both colour and height, with large red bars representing large pulse-widths and smaller pulse-widths represented by small blue bars.

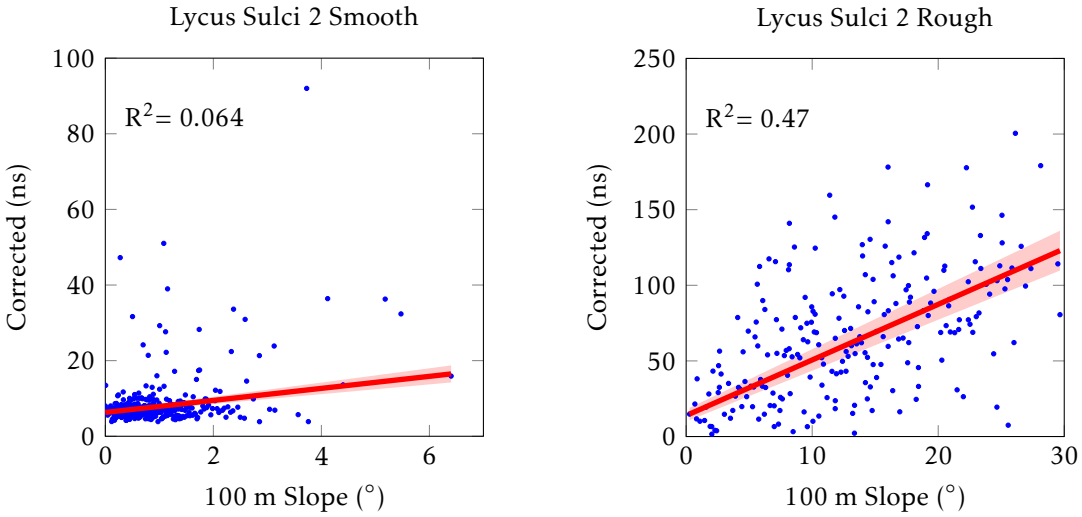

Figure 3.39: Lycus Sulci results for each of the DTMs in the region, in particular exploring the difference between the rough and smooth regions of Olympus 2. The R-squared values are shown on each of the plots, with the fit being a linear-line-of-best-fit. The baseline at which the highest R-squared value is found along the horizontal axis.

Figure 3.38 shows an oblique view of the Lycus Sulci 2 DTM, with the general location of the boundary between the rough and smooth terrains. At the top of this figure, pulse-widths are generally low, with some larger pulse-width values observed at some of the rough features, such as small craters, but also due to noise within the data. The pulse-widths over the rough terrain appear to show good agreement with the individual roughness features, with pulse-widths appearing greatest at the peaks or steep slopes of the ridged terrain.

The plots suggest that when only a narrow distribution of slope and surface roughness is used, poor correlations exist. Using a wider distribution of roughness and slope appear to help produce stronger correlations. When these rough and smooth data are combined however, the observed R-squared is greater than when the rough terrain is used alone (Table 3.9). This behaviour appears to be linked to the distribution of surface characteristics used to find a correlation, with a narrow distribution producing a poorer R-squared fit because of the way R-squared is measured. When these plots are combined, the high concentration of data over low slopes help improve the R-squared value compared to when only the data over rough terrain is used.

3.8.4 DISCUSSION

By using rougher, more homogeneous, terrain it appears that a better understanding of the relationship between MOLA pulse-widths and surface characteristics has been achieved. The R-squared values are similar to those found over the MSL candidate sites used in the previous section, once the outliers of Mawrth Vallis and the Lycus Sulci 2 DTM areas are removed, as shown in Tables 3.8 and 3.9 on Pages 131 and 156, respectively. The baselines at which the best correlations are observed converges to 75 m to 100 m using slope and 300 m to 400 m using surface roughness. However, there is still significant deviation from the line-of-best-fit, such that the resampled data

presented in Figure 3.37 produces a more interpretable result as to the global distribution of slope.

The focal discussion point is the baselines at which the highest R-squared values are observed for the two surface characteristics. The consistent baselines found across the sites allows the data to be combined to derive a more typical relationship between MOLA Slope-Corrected pulse-widths and surface characteristics, rather than region specific relationships. The combined data shows the best correlations at 300 m for surface roughness and 75 m for slope. This is interpreted to mean that MOLAs pulse-widths are correlated to slope over rough terrain, for two reasons: (1) the 75 m baseline is in-line with the latest estimates of MOLA pulse-footprint after hot-spotting effects are accounted for [*Neumann et al.*, 2003a]; (2) it seems unlikely that 300 m baseline surface roughness information is contained within pulse-widths, instead, slopes at ∼75 m may strongly influence surface roughness estimates at ∼300 m baseline over these terrains. As the slope relationship is not observed over MSL sites, this suggests that slope cannot be measured from MOLA pulse-widths over smoother terrains.

Although more consistent baselines are found here and all sites reveal a correlation, the R-squared values are not much improved due to large variations from the line-of-best-fit. The source of these variations but could be a result of the pulse-width sampling methods or atmospheric effects on the pulse [*Neumann et al.*, 2003a; *Smith et al.*, 2001]. These atmospheric effects are described in Section 2.1.4, with *Neumann* [2011] adding that many of the pulse-widths within the Slope-Corrected dataset are subject to scattering by dust, which will affect the pulse-width value. In practise however, these effects will be small due to the thin atmosphere. The errors are therefore more likely to be associated with the threshold level detection system employed by the system. In this case, the pulse-width measurements produced from MOLA are not perfectly proportionate to the surface characteristics within the pulse-footprint, and depend on other factors that cannot be isolated from the pulse-width data here.

The results from Lycus Sulci 2 may be explained by how the R-squared value is calculated. The formula for calculating R-squared in MATLAB is

$$R^2 \equiv 1 - \frac{SS_{res}}{SS_{tot}} = 1 - \frac{\Sigma_i \left(y_i - f_i\right)^2}{\Sigma_i \left(y_i - \bar{y}\right)^2}, \qquad [3.4]$$

where f_i is the expected value at y_i from the linear fit, SS_{res} is the sum-of-squares residuals, and SS_{tot} is the total sum of squares. The data from the smooth terrain in this DTM has a lower SS_{res} due to the very narrow distribution of slopes producing a low deviation from the mean pulse-width,

Table 3.10: R-squared fit statistics of the rough and smooth terrains over Lycus Sulci 2.

Fit Statistic	Smooth	Rough	All
SS_{res}	2.8458×10^4	4.1028×10^5	4.5946×10^5
SS_{tot}	3.0412×10^4	7.7846×10^5	1.7807×10^6
R-squared	0.0637	0.472	0.742

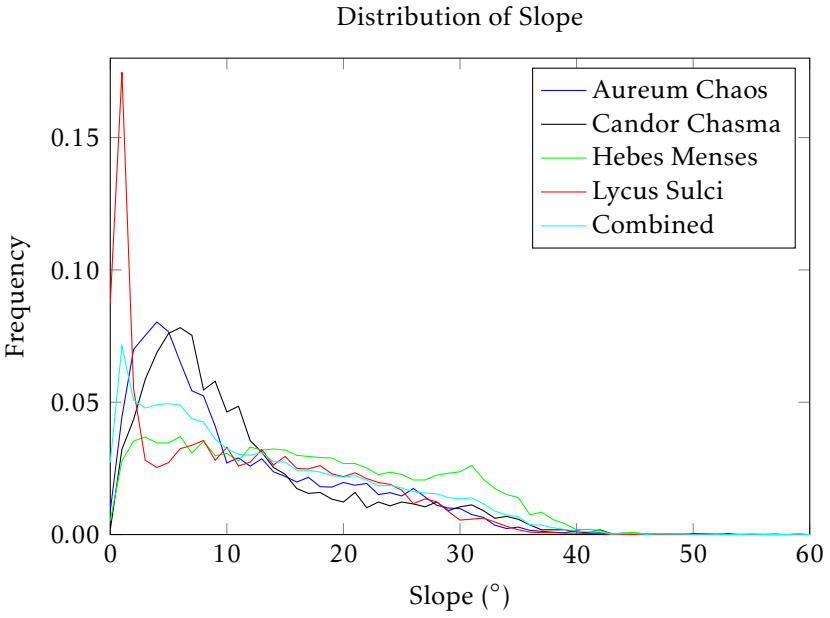

Figure 3.40: Plot of the distribution of slopes over the different sites. Lycus Sulci has a sharp peak at low slope values due to the expansive area of very flat terrain in Lycus Sulci 2. Hebes Chasma has a much wider distribution and a lower proportion of data from low sloping terrains than either Aureum Chaos or Candor Chasma, which could explain the lower R-squared value.

SS_{tot}. The natural variation in the pulse-width values from a predicted fit is proportionally large when compared to the pulse-width values, SS_{res}. These two values combine to produces very low R-squared values (Table 3.10). The data from the rough terrain has a larger SS_{res} value, but has a significantly wider distribution of slopes and therefore a greater deviation from the mean pulse-width, as shown in the SS_{tot} in Table 3.10. The deviation from the fitted line at higher slope values due to natural variability will be proportionally smaller when compared to the deviation from the mean pulse-width value, so long as the deviation from fit increases at a slower rate than the deviation from the mean pulse-width value.

Pulse-widths over the smooth terrain have a lower variability than data from equivalent slopes over the rough terrain, probably due to the consistency of the terrain reducing the effect of co-registration errors. Thus, when the data are combined there is only a small increase in SS_{res}, compared to that over the rough terrain, but a significant increase is observed in SS_{tot} due to the inclusion of the two very differently distributed pulse-width populations, which results in a higher R-squared value. This is an example where statistics can suggest a result that is significantly different to that observed. In practise, the results from the regions as a whole, or from Lycus Sulci 1 and Lycus Sulci 3 are more typical and reliable in terms of how well MOLA pulse-widths compare to surface characteristics.

There appears to be no correlation between the type of terrain and the observed correlations. Instead, the R-squared values appear to be dependent on the distribution of the surface roughness and slope over the terrains (Figure 3.40). The lowest R-squared values are observed at Hebes Chasma, which is also where the widest distribution of slope is found, with more data over very rough terrain and less over smooth terrain. At other sites, there is a concentration of data near the origin of the plots, which, although subject to the some natural variation, has less variation than pulse-widths over rougher, more sloping, terrain. However, it must be noted that visually, there does appear to be more variation from the line-of-best fit in the Hebes Chasma plot in Figure 3.36.

The question is whether a reduction in the R-squared value, from 0.53 over Candor Chasma, which is visually closest in appearance to the Hebes Chasma DTM, to 0.46 is significant? The answer is probably not, as Candor Chasma has more smooth, flat, terrain that typically produces pulse-widths with low variation that helps increase the R-squared value here, as described above.

A discussion point is also raised concerning resolution of the DTMs. The resolutions of the DTMs discussed above are the sampling resolutions of the DTM, rather than the resolution of the features that can be identified within the dataset. When exploring the resolution of features that can be derived from the Global Lunar Digital Terrain Model 100 m topographic model (GLD100), derived from stereo-photogrammetry, *Kreslavsky* [2014] suggest the resolution of features that can be derived from the 100 m pixel^{-1} dataset is approximately 6 pixels. Craters as small as 200 m in diameter can be identified, but the slope statistics are more likely representative of the interpolation algorithm than real statistics, depending on the terrain used. Assuming the same is true here, features at a minimum scale of $\sim$108 m can be derived using the 18 m pixel^{-1} CTX DTMs used here. However, as the terrain is consistently rough, and areas of poor matching have been removed, this effect will be minimised, such that slopes at the baselines using two or more pixels ($>$40 m) are thought to be reliable. This is further backed up by the best correlating baselines occurring at a similar baseline to that suggested by *Neumann et al.* [2003a]. The surface roughness element to this work is thought to be unaffected, as the baselines observed in the previous section, using much higher resolution DTMs, are $\geq$150 m, which should also be able to be resolved using the CTX data, under the assumptions by *Kreslavsky* [2014].

The final point is that the *Neumann et al.* [2003a] dataset has already been corrected for 1 km baseline slopes from the MOLA gridded elevation dataset. This means that a portion of the *Sigma_optical* pulse-width value has been removed to highlight roughness and slope from a longer baseline background slope. One could argue that this slope should be added back to the pulse-widths, however the slope values at this baseline are typically much smaller ($\ll$10 % than slope values and therefore have only a minor effect on the final pulse-width value, to the exponential relationship between surface slope and pulse-width value. At baselines of 1 km, the MOLA gridded elevation dataset is heavily interpolated, and therefore slopes are defined by the interpolation algorithm rather than direct measurement, which produces a much smoother dataset. As a result, the pulse-widths remained as they were given by *Neumann* [2011], as making such small changes to the dataset is not thought to improve the observed correlations significantly enough to produce very reliable estimates of surface characteristics, and may instead introduce another source of error to the data.

It now appears that MOLA pulse-widths can be used to explore the global distribution of local slopes at a baseline of 75 m, which adds credence to the suggestion by *Neumann et al.* [2003a] that a more realistic estimate of the MOLA pulse-footprint is half that given in *Smith et al.* [2001]. However, the maximum R-squared values remain small, which suggests that deriving surface characteristics from pulse-width estimates produces far from perfect results. Instead, MOLA pulse-width data should only be used to provide an indication of the mean slopes in a larger area to reduce the effect of the natural variation, such as that given in Figure 3.37.

3.9 CAN DETRENDED SURFACE ROUGHNESS BE EXTRACTED FROM MOLA PULSE-WIDTHS?

3.9.1 INTRODUCTION

MOLA pulse-widths show good correlations with pulse-footprint-scale slope over rough terrain. By applying the slope-correction assumption suggested by *Gardner* [1992], in Equation 2.7, it may be possible to separate the contributions from slope and surface roughness. The detrended roughness contribution to Slope-Corrected MOLA pulse-widths is compared against detrended surface roughness to test whether this assumption holds true. Furthermore, the effect of the energy distribution across the pulse-footprint, as discussed in Section 2.1.5, is tested by applying Gaussian filters with different standard deviations to the detrended elevations during the calculation of detrended surface roughness.

This study re-examines datasets from Eberswalde Crater and Mawrth Vallis, to explore if observed R-squared values can be improved, particularly at Mawrth Vallis. CTX data over Aureum Chaos data is also used, as good correlations are observed against slope at this region, which suggests a good chance of extracting detrended roughness is over this type of terrain. Unfortunately, the post spacing in CTX DTMs may inhibit this, as only $\sim$12 pixels lie within the 75 m MOLA pulse-footprint, compared to $\sim$4000 for the HiRISE DTMs. As already discussed in the previous section, *Kreslavsky* [2014] suggest that only features $\geq$108 m can be derived from the CTX DTMs, thus the 75 m pulse-footprint of the instrument may be too small to be able to derive detrended surface roughness.

If detrended surface roughness can be extracted from the dataset, or if better correlations are observed over Mawrth Vallis by removing the effect of pulse-footprint-scale slopes, then this correction could be applied to other regions of Mars using estimates of pulse-footprint-scale slopes from HRSC DTMs, which have good coverage at 50 m pixel^{-1}. Detrended roughness from slope could then be used to reveal potential science, identify candidate landing and roving sites, and make comparisons of fine-scale geology, as was the original aim of the MOLA pulse-width dataset [*Kreslavsky and Head*, 1999, 2000; *Smith et al.*, 2001]. Finally, this form of roughness could also be the source of the deviations from the line-of-best-fit observed in previous studies, and could improve results at other sites.

3.9.2 RESULTS

Example extracted pulses are shown in Figure 3.41, whilst Figure 3.42 shows plots of the roughness contribution to the received pulse-width using Equation 2.7 for each of the three sites are shown in Figure 3.42. In addition, a plot from Eberswalde Crater where a Gaussian filter has been applied to explore the effect of energy distribution across the pulse-footprint is also shown.

The plots clearly show little or no correlation between detrended surface roughness and σ_ξ across all sites. For the data over Mawrth Vallis, this presents no change, but over Eberswalde Crater and Aureum Chaos this represents a significant reduction in observed R-squared values

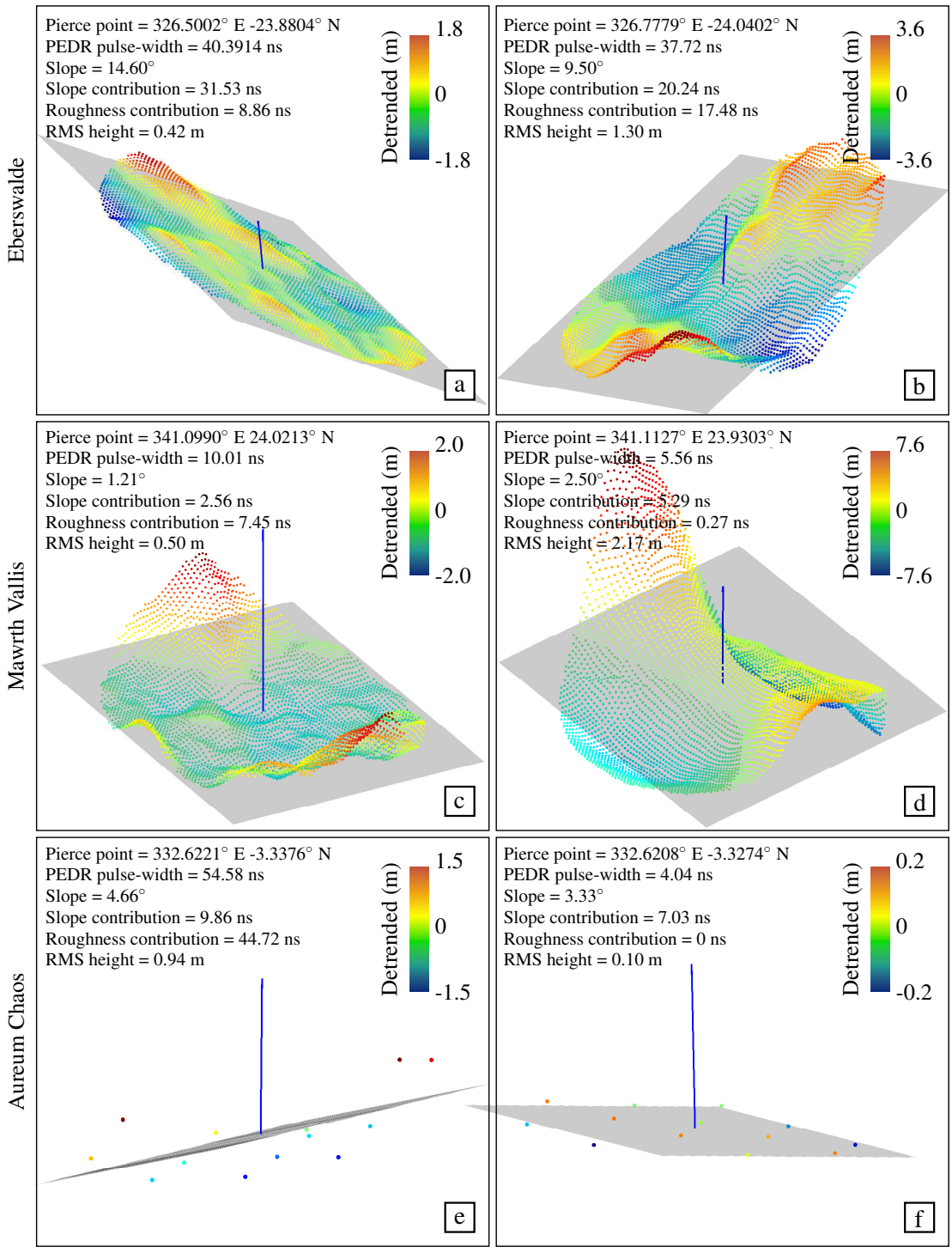

Figure 3.41: Plot examples of planes fitted to data within MOLA pulse-footprints and the resulting detrended elevation data and fit statistics over Eberswalde Crater, Mawrth Vallis, and Aureum Chaos. The number of data used to fit the planes over Eberswalde Crater and Mawrth Vallis are ∼4000, whilst only ∼12 are used over Aureum Chaos. Poor correlations are observed at all sites, these plots are to show the potential difficulties of some terrains and DTM resolutions. In Figure 3.42, the roughness contribution is plotted against the RMS height.

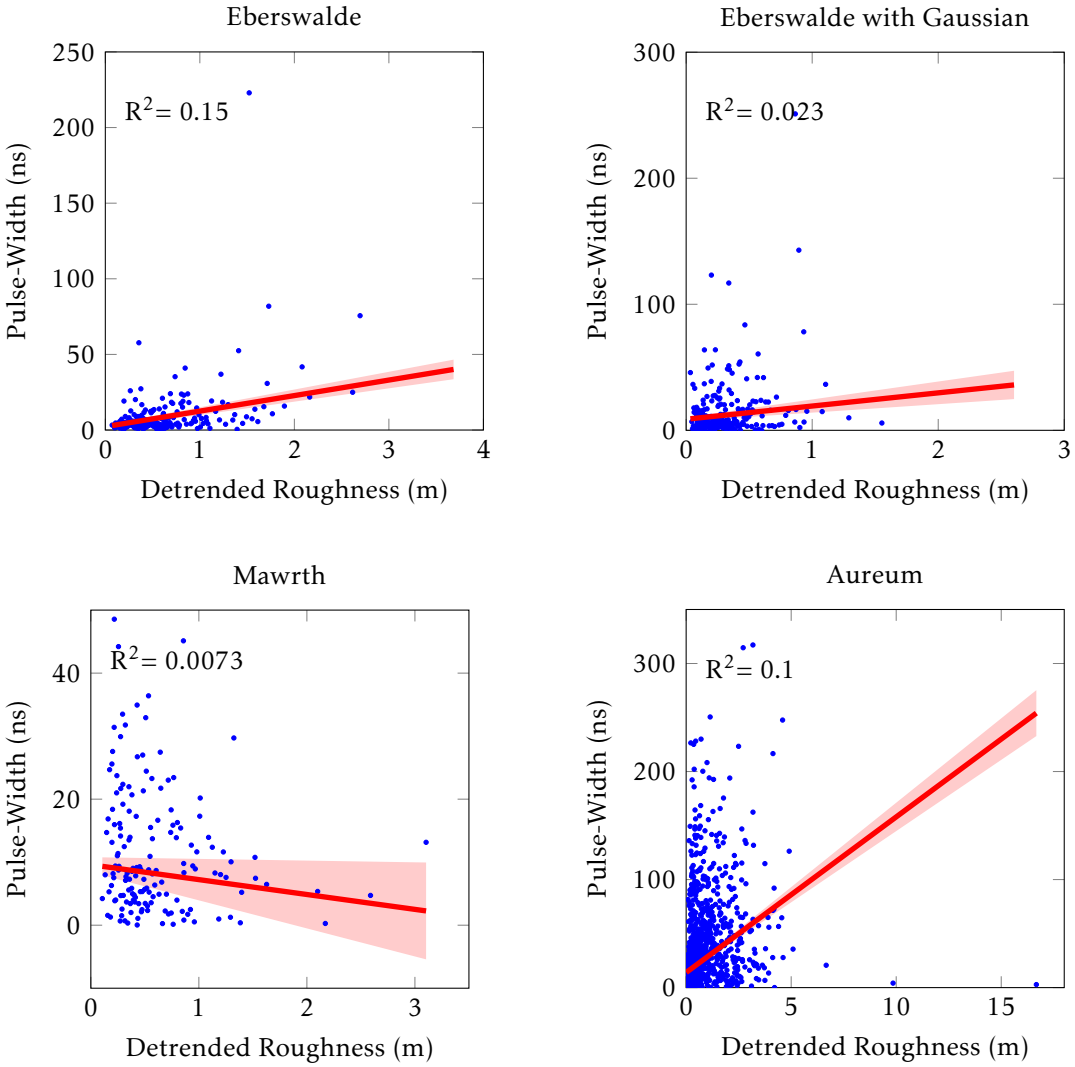

Figure 3.42: Plots of σ_ξ against detrended surface roughness as measured from DTMs over Eberswalde Crater, Mawrth Vallis, and Aureum Chaos. A Gaussian filter is applied to the RMS height calculation to account for the energy distribution across the pulse-footprint over Eberswalde Crater. In this case, the Gaussian distribution has a standard deviation of 20 m: other values were used, but with no significant change in observed R-squared. The Slope-Corrected pulse-width values have had the effect of 1 km slopes added, before the 75 m baseline slope effect is removed.

when pulse-widths are compared to surface roughness, down from 0.60 and 0.56 respectively. The largest R-squared value is observed over Eberswalde Crater, but the low R-squared value suggests that detrended surface roughness cannot be extracted from the pulse-width dataset. The results are not improved when a Gaussian filter is applied, hence it was not applied to the other sites. The standard deviation of the Gaussian applied to this plot is 20 m, others were also tried but no significant change in the R-squared values is observed.

The plot from Aureum Chaos appears visually different from the equivalent Eberswalde Crater plot. This could be a result of the CTX DTM resolution being too low and producing poor estimates of pulse-width, as similar plots were observed in background work when using the HRSC DTMs.

Figure 3.41 shows some specific examples of detrended elevation data and the resulting slope

corrections. The top plots, from Eberswalde Crater, show moderately good agreement with theory, whereby roughness contributions to pulse-width are expected over rougher terrain. The middle plots, from Mawrth Vallis, show poor agreement, but also highlight the potential for georeferencing errors to have a significant effect on results, which is discussed below. Finally, the bottom plots show the relatively low number of points from pulses over CTX data, with (f) showing an example plot where the slope contribution is greater than the pulse-width value.

3.9.3 DISCUSSION

The results suggest that detrended surface roughness cannot be extracted from the MOLA pulse-width dataset. Additionally, attempting to account for the energy distribution across the pulse-footprint does not improve the result. The reason for these particularly poor results remains unclear, but one or more of the following factors are thought to be cause

Poor Pulse-Width Estimates This has already been mentioned previously, but this effect would be more pronounced here, as the SNR is reduced after the removal of the instrument effects, which are known, and slope effects, which have been modelled. This could be due to a fault in the methods employed by the instrument, such as the threshold pulse-width timing system, or background noise, or the method of applying a slope correction uses an oversimplified model that does not adequately model real-world behaviour (Equation 2.7) [*Neumann et al.*, 2003a].

Atmospheric and Dust Effects Forward scattering by dust will cause an increase in path length of some photons within a pulse, which will increase the pulse-width and make the surface appear rougher. Small, regional, and even global dust storms are regular events on Mars, so some pulses will certainly be affected by dust. However, the filter system employed by MOLA helps identify cloud-hitting and noisy pulses that could be strongly affected by dust. These pulses are removed by *Neumann et al.* [2003a] and the path extension due to atmospheric effects is expected to be on the order of centimetres, too small for MOLA to resolve *Abshire et al.* [2000]; *Basu et al.* [2006]; *Leovy* [2001].

Co-registration Errors The co-registration errors discussed in Section 3.6.3 are likely to have a greater effect in this study than previous work over the MSL candidate landing sites and rough terrain. Despite strenuous efforts to ensure correct geolocation of all the data products used, some co-registration errors will remain (Table 3.7). This can result in a mismatch in location of the relative datasets, resulting in incorrect extraction of surface roughness, slope, and DTM heights from within the pulse-footprint.

This error may not present itself in the previous work because the variation in topography in and around the general location of a pulse-footprint may remain similar at the baselines explored here. This may also explain the low variance in pulse-widths values over the very flat, smooth terrain of Lycus Sulci 2, which will produce similar slope and surface roughness values across large areas due to its consistency. However, this work explores the deviations

from slopes specific to that location, meaning that small co-registration errors can result in very different detrended surface roughness values. This is particularly evident in Figure 3.41d, where a small change in location (to the left or right) would result in a much steeper slope, with the ridge being nearer the edge of the pulse region rather than through the middle.

3.10 MARS CHAPTER SUMMARY

The work in this chapter set out to explore the relationship between MOLA pulse-widths and surface characteristics using GIS technology and high-resolution DTMs.

Comparing different versions of the pulse-width dataset to surface characteristics derived from HiRISE DTMs over the final four MSL candidate landing sites reveals mixed correlations. Pulse-width are compared to surface roughness at different baselines to provide an indication to the size of the pulse-footprint and extent of energy distribution effects. The Slope-Corrected pulse-width dataset developed by *Neumann et al.* [2003a] is thought to be the most reliable pulse-width dataset due to the efficient removal of poor data and the fact that this dataset produces the best correlations at two of the three sites that reveal good correlations (R-squared $\geq$0.4). Pulse-widths over Mawrth Vallis reveal poor correlations when compared to surface roughness, which is attributed to the spatial distribution of surface roughness, which is highly variable over short baselines and errors in co-registration and pulse-width estimates. Furthermore, where good correlations are observed, the baselines vary greatly, from 150 m to 300 m.

Comparing to the Slope-Corrected MOLA pulse-width dataset to surface characteristics over very rough terrain reveals a consistent relationship that could be extrapolated to other, more typical, Martian terrains. Similar R-squared values are observed as above, but the pulse-width are found to be correlated to slope as well as surface roughness. The best correlating slope baseline is 75 m, whereas for surface roughness this is 300 m. As the latest estimates of the pulse-footprint is thought to be $\sim$75 m, this suggests that Slope-Corrected pulse-widths are correlated to pulse-footprint-scale slope rather than much larger baseline surface roughness.

Comparing the roughness contribution to pulse-width to the detrended surface roughness derived from DTM data over Eberswalde Crater, Mawrth Vallis, and Aureum Chaos reveals poor correlations. Attempting to account for the energy distribution across the pulse-footprint does not improve the result, instead the observed R-squared values decrease. The cause of the much poorer R-squared values is associated with the natural variation in pulse-width value and co-registration errors having greater influence. This is attributed to the modelling-out of instrument and slope effects, and detrended surface roughness estimates changing on very short baselines, respectively. Alternatively, it may not be possible to derive detrended surface roughness from laser altimeter pulse-widths.

The overarching conclusion to the work in this chapter is that, on a global level, MOLA pulse-widths can provide an indication of the pulse-footprint-scale slopes in a local area. Resampling data to a much lower resolution is required to create sensible, interpretable results, and removes the effect of the natural variability of the dataset to enable regional comparisons of the distribution of

slope. The source of this variability is unclear, but could be a result of atmospheric and dust effects on the pulse, pulse-width timing methods, and co-registration errors.

4

The Moon: Assessing LOLA Pulse-Widths

The primary aims of the LOLA instrument is to produce a high-resolution map of the lunar surface and measure pulse-widths to determine pulse-footprint-scale slopes for future lander missions using the theory outlined in Equation 2.7. Comparisons between laser altimeter pulse-widths and surface characteristics are expected to yield higher R-squared values than observed previously because the LOLA instrument is a more recent planetary lidar instrument, and the laser altimeter and DTM datasets are better co-registered. In total, 19 regions are highlighted as locations where good correlations could be observed based on results in the previous chapter, generally defined as consistently rough or sloping terrain. Very poor correlations are observed using the regional data. However, visual comparisons between LOLA pulse-widths and surface features suggested that data from individual orbits behaved differently, with some orbits showing good correlations with these features. Some orbits present larger R-squared values than those observed using MOLA data, suggesting that surface characteristics can be derived from laser altimeter pulse-widths, at finer scales than can be derived from individual laser altimeter pulses. However, less than 14 % of the orbits showed similar correlations to those observed in the previous work, with the remaining orbits containing very poor pulse-width data, which is attributed to instrument setup. This suggests that global estimates of slope and surface roughness cannot be derived reliably over the lunar surface from pulse-width data, unless there is some future improvement in the quality of the LOLA pulse-width data.

4.1 INTRODUCTION

The relationship between Lunar Orbiter Laser Altimeter (LOLA) pulse-widths and surface characteristics over different terrains on the Moon are explored to test whether surface characteristics can be derived from laser altimeter pulse-widths more reliably than using Mars Orbiter Laser Altimeter (MOLA) data [*Smith et al.*, 2010a,b; *Zuber et al.*, 2009]. These pulse-widths are compared to surface roughness and slope estimates derived from high-resolution Digital Terrain Models (DTMs) (2 m pixel^{-1}) from Lunar Reconnaissance Orbiter Camera - Narrow Angle Camera (LROC-NAC) stereo-pairs [*Mattson et al.*, 2012, 2010; *Robinson et al.*, 2010; *Smith et al.*, 2010a,b; *Tran et al.*, 2010; *Zuber et al.*, 2009]. The aim is to calibrate the pulse-widths at sites where high-resolution topographic information is available, to derive a relationship that can be extrapolated to the regions of the lunar surface that lack high-resolution DTM coverage. This data can then be used to make quantitative comparisons in geology, to highlight differences in the type and magnitude of surface formation and evolution processes, and identify candidate landing and roving sites [*Crawford et al.*, 2012; *Fisackerly*, 2012; *Kreslavsky and Head*, 1999, 2000; *Neumann et al.*, 2003a; *Rosenburg et al.*, 2011; *Spudis*, 1999].

The overarching hypothesis of this thesis has yet to be proved conclusively using MOLA pulse-width data, used for the work in the previous chapter. The results in that chapter influence the site selection process in this chapter, which is described in Section 4.6.2. Where roughness features within the terrain are small and heterogeneous, very poor correlations are observed; however, where the terrain is homogeneous and rough, better correlations are observed, albeit with a maximum R-squared value of $\leq$0.6. The improved co-registration and georeferencing of the datasets, smaller pulse-footprint, and the negligible atmospheric effects experienced by a pulse fired at the Moon, suggest better correlations might be attained using the lunar data [*Robinson et al.*, 2010; *Smith et al.*, 2010a,b; *Zuber et al.*, 2009].

In addition to producing a calibrated pulse-width dataset that can be used to explore the global distribution of slopes and surface roughness on the Moon, this work also aims to provide evidence as to whether this method should be employed on future laser altimeter instruments, such as the BepiColombo Laser Altimeter (BELA) and the Ganymede Laser Altimeter (GALA) [*Hussmann et al.*, 2013; *Thomas et al.*, 2007]. This would be particularly important for presently unexplored terrains, providing fine-scale 3-dimensional information of terrain for which we do not have high-resolution DTMs.

The following section explores the current literature regarding the global distribution of surface characteristics, followed by an introduction to the instruments and methods employed.

4.2 LITERATURE REVIEW

The earliest investigations of lunar topographic roughness, such as *Briggs* [1960] and *Hughes* [1960], use radar reflectance data to determine surface roughness. Comparisons between the radar datasets and slopes at the limb of the Moon, which are derived optically, show good agreement

where slopes are greater than 3° [*Fujinami et al.*, 1954; *Hughes*, 1960].

Campbell et al. [2009] also use Earth based radar (12.6 cm and 70 cm) to explore decimetre- and metre-scale rock abundance over the Marius Hills and Mons Rümker. They infer high roughness values, derived from high Circular Polarisation Ratio (CPR)[1] over the Marius Hills at both wavelengths. They associate this with the original volcanic eruption processes that formed the domes, which produced blocky material that is covered by only a few metres of lunar regolith. The surface of Mons Rümker on the other hand, appears to have a typically low rock abundance, instead being rich in fine-grained material, with the exception of a radar bright region using the 70 cm wavelength, associated with a thinner mantling cover over rougher terrain [*Campbell et al.*, 2009].

Orbiting radar is used by *Spudis et al.* [2010] to show that much of the northern polar region produces CPR values that are typical of the rest of the lunar surface (0.1), with fresh impact craters showing increased values of up to 1. High CPR values are also observed in the centre of older craters, which are found to correlate with the modelled permanently shadowed regions and the potential locations for ice, as identified in data from Lunar Prospector Neutron Spectrometer (LPNS) and, later, Lunar Exploration Neutron Detector (LEND), which is on-board Lunar Reconnaissance Orbiter (LRO) [*Mitrofanov et al.*, 2010]. Results from the latter are thought to suggest cometary impacts and hydrogen implantation from the solar wind as sources for the observed buried hydrogen deposits near the south pole, as well as other unknown sources [*Mitrofanov et al.*, 2010].

Yokota et al. [2008] use stereo-derived DTMs from Apollo mapping images to explore km baseline surface roughness of the lunar highlands within $1° \times 1°$ cells, across three regions. They explore RMS deviation, ν, as defined in Equation 2.47, calculated in a north-south azimuth at baselines of 0.3 km to 3.0 km. They observe fractal terrain, with different Hurst exponents across each of the regions, but conclude that studying the terrain over larger baselines is required for more extensive analysis.

The first use of laser altimeter derived lunar roughness is from Clementine lidar data [*Smith et al.*, 1997]. Here, mean values of surface roughness are produced within $30° \times 25°$ cells, where surface roughness is measured by fitting the local along- and across-track slopes to a covariance model originally developed to filter topographic data at 10 km to 100 km baselines [*Smith et al.*, 1997]. Roughness is found to correlate well with both topography and age, with variance over the lunar maria found to be less than 0.5 km, whereas over the lunar highlands, variance is over 2 km. Later, *Yokota et al.* [2014] use SELenological and ENgineering Explorer "KAGUYA" (SELENE) laser altimeter and stereo-photogrammetry data to derive roughness, defined as median differential slope, at baselines of 0.15 km to 100 km. They observe roughness over all highland terrains falls between baselines of 3 km to 30 km, whilst pre-Nectarian surfaces reveal peak roughness at 20 km to 30 km, which correlate well with crater density. Peak roughness for Nectarian surfaces is shown to be 6 km to 9 km, which is thought to be caused by secondary impact craters from basin forming processes.

[1] The CPR is defined as the the ratio between power reflected in the same sense of circular polarisation as the transmitted wave and the power reflected in the opposite sense of circular polarisation [*Campbell et al.*, 2009]. The maximum value on the Moon is ~2, with strong correlations observed between it and roughness due to scattering at or beneath a target surface [*Campbell et al.*, 2009].

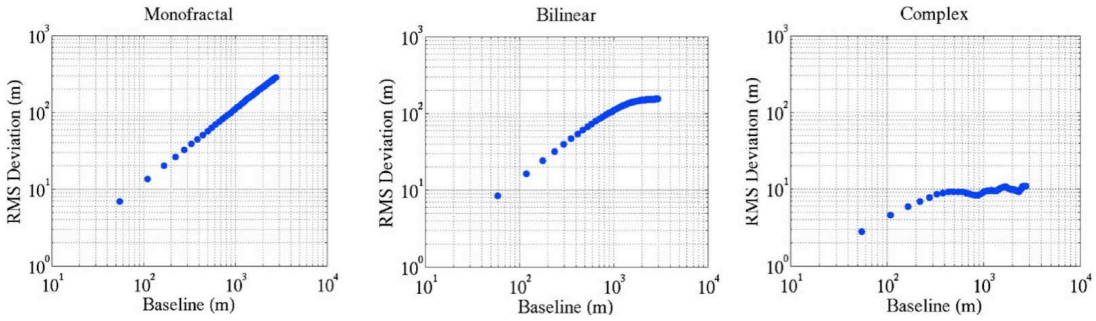

Figure 4.1: Plots of scaling behaviours of surface roughness from different terrains on the Moon, from *Rosenburg et al.* [2011]. The highlands exhibit fractal and multi-fractal behaviour (left and centre), whilst the mare exhibit more complex behaviour, with breakpoints occurring at much smaller baselines (right).

High density laser altimeter data from LOLA has enabled much finer-scale surface roughness to be derived globally [*Kreslavsky et al.*, 2013; *Rosenburg et al.*, 2011; *Smith et al.*, 2010a,b; *Zuber et al.*, 2009]. These studies make use of the novel five-spot pulse design of the instrument, discussed in Section 4.3, and the along-track elevation data, to produce surface roughness estimates at a wide range of baselines. *Rosenburg et al.* [2011] produce maps of surface roughness, using the median differential slope and RMS slope, at 17 m to 2.7 km baselines. They use both the different elevation measurements within each spot, as well as longer baseline measurements taken from pulses and inter-pulse spacing. Very different surface roughness properties exist between the nearside lunar mare and the lunar highlands, but by using the median differential slope, finer differences are revealed within these two terrain types. Using this tool, *Rosenburg et al.* [2011] are able to characterise ejecta around large basins and young craters, and make quantitative comparisons to explore the relationship between the ages of mare surfaces and surface roughness (Figure 4.1). Over the lunar highlands, terrain appears fractal, with any breakpoints occurring at $\sim$1 km (Figure 4.1). The mare exhibit more complex behaviour however, with terrain appearing to change from fractal-like to complex behaviours at small baselines, which suggests that understanding surface roughness at finer baselines could further our understanding of the evolutionary processes (Figure 4.1). Younger mare surfaces are rough at smaller baselines and become rougher at longer baselines.

Kreslavsky et al. [2013] use LOLA elevation data to explore the global distribution of surface roughness on the Moon, using the Inter-Quartile-Range (IQR) of profile curvature at baselines of 115 m to 1.8 km (Figures 4.2a and 4.2b). They observe poor correlations between hectometre and kilometre baseline surface roughness, attributed to differences in surface processes between these two scales and the time-scales of modification. Regolith accumulation and modification, as well as recent (1 Ga to 2 Ga) impact events are associated with hectometre baseline surface roughness, whereas large baseline geological processes influence kilometre baseline surface roughness. Like *Rosenburg et al.* [2011], the evolution of surface roughness is explored, with young impact craters appearing as rough terrain, which decreases with age.

Both *Rosenburg et al.* [2011] and *Kreslavsky et al.* [2013] reveal the potential usefulness of

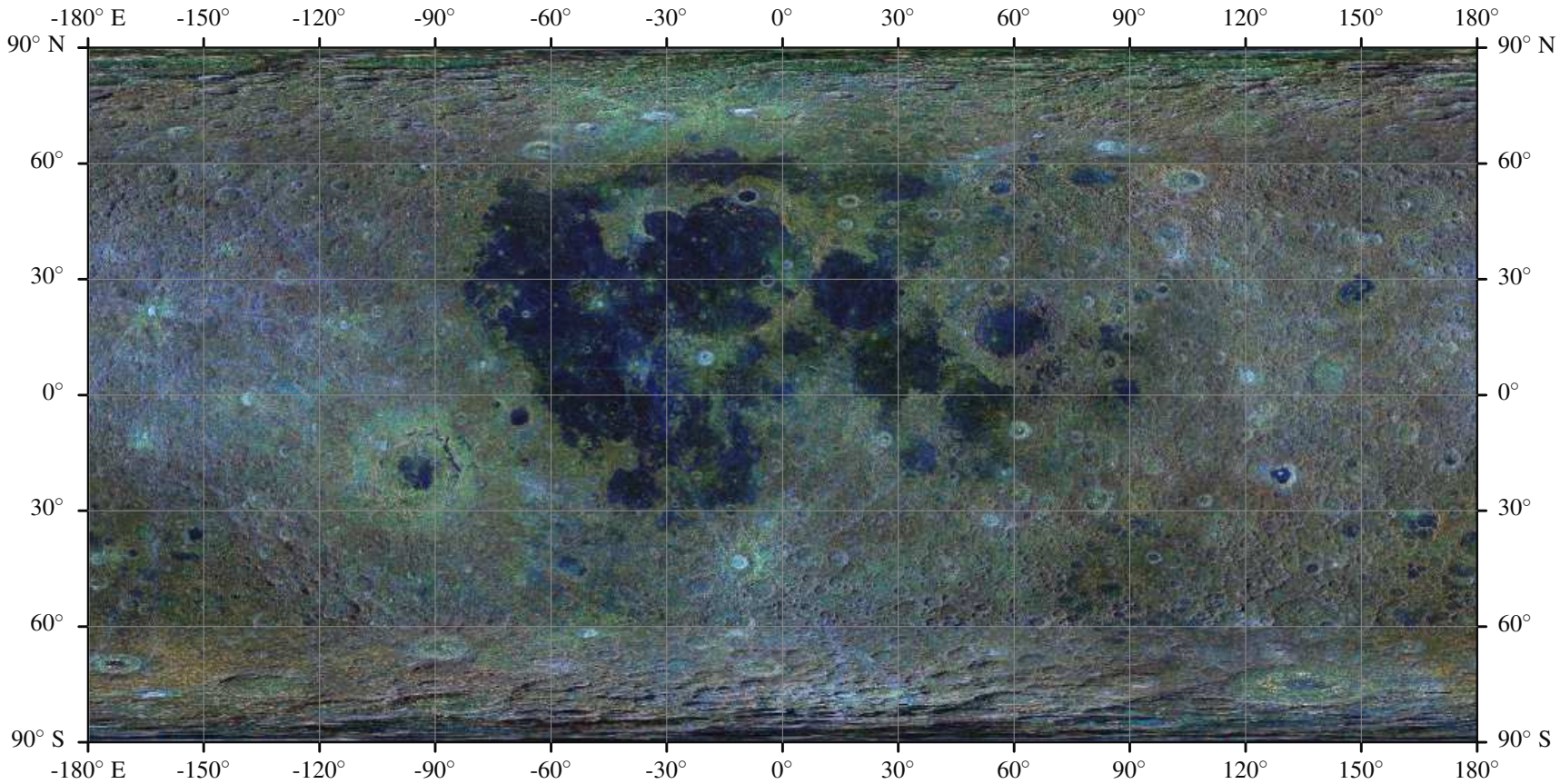

Figure 4.2a: Map of lunar surface roughness at 1.8 km, 0.96 km and 0.48 km in red, green and blue respectively, adapted from *Kreslavsky et al.* [2013]. Higher intensity colours represents rougher terrain, with bright areas representing rough terrain on all baselines.

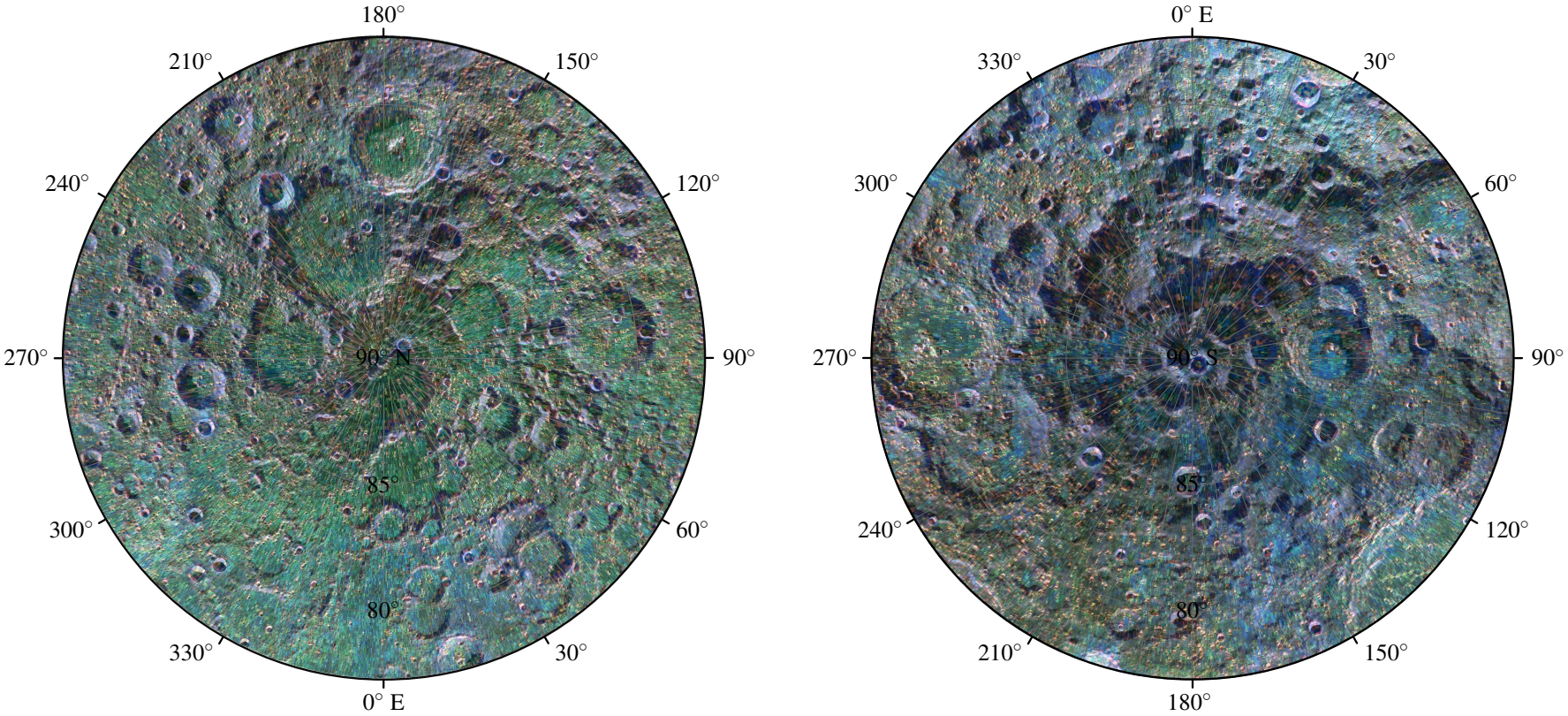

Figure 4.2b: Map of lunar polar surface roughness at 1.8 km, 0.96 km and 0.48 km in red, green and blue respectively, adapted from *Kreslavsky et al.* [2013]. Higher intensity colours represents rougher terrain, with bright areas representing rough terrain on all baselines.

surface roughness in geological mapping. This is especially true for revealing new impact features, as well as previously poorly understood contacts between volcanic plain units and their relative chronology. By measuring surface roughness from pulse-widths, LOLA is able to further reduce the minimum baseline at which the global distribution of surface roughness can be measured on the Moon, to lander and rover scales [*Neumann et al.*, 2008; *Smith et al.*, 2010b]. *Smith et al.* [2010b] derive surface roughness values between 0.4 m to 1.6 m over 5 m baselines from LOLA pulse-widths, using Equation 2.7. It is assumed that 50 % of the energy from the laser falls within the central 2.5 m area within the pulse-footprint, but it is not known how this affects the echo profile: both *Smith et al.* [2010b] and *Neumann et al.* [2008] assume that surface roughness from LOLA pulse-widths relates to 5 m baseline roughness. The map in *Smith et al.* [2010b] shows the near-side to be significantly smoother than the far-side highlands, as well as increased roughness around impact features such as crater rims, basin rings, central peaks, and ejecta blankets. In a preliminary study, *Neumann et al.* [2008] observe good agreement between roughness from pulse-widths and slopes measured from elevations within the five-spot pulse, when studying along a profile across Tycho Crater. However, as with the MOLA data, these pulse-widths have not yet been calibrated to surface characteristics from high-resolution DTMs, which is the aim of the work in this chapter. The following section discusses the specifics of the LOLA instrument.

In addition to LOLA, there have been a number of successful missions to the Moon that have included laser altimeter instruments, including Clementine, mentioned above, SELENE, and the Apollo orbiters [*Araki et al.*, 2009; *Neumann*, 2001]. The Apollo 15, 16, and 17 missions each carried laser altimeters to determine the range, however, coverage is relatively low, and the geolocation accuracy of the dataset is poor (30 km) [*Neumann*, 2001]. The Clementine lidar instrument was tasked with producing a global DTM of the Moon [*Smith et al.*, 1997]. Coverage of the far side of the Moon was greatly improved, however, poor calibration, as well as issues regarding instrument heating, low Signal to Noise Ratio (SNR), and quantisation effects meant that only ∼72 000 of the 600 000 pulses produced successful range measurements, and the final result has since been shown to be vertically offset by 3 km when compared to ground-based radar [*Margot et al.*, 1999; *Neumann*, 2001; *Smith et al.*, 1997]. Finally, the Laser Altimeter (LALT) on-board SELENE began mapping the surface in 2007. The instrument operated at 1 Hz, which results in a 1.6 km along-track pulse spacing [*Araki et al.*, 2009]. Within 4 months the instrument had acquired over 6×10^6 pulses over the surface, and produced the highest-resolution global DTM of the Moon, until the dataset was superseded by the LOLA dataset [*Araki et al.*, 2009; *Smith et al.*, 1997, 2010b]. Unfortunately, these instruments did not record the pulse-width of the echo pulse, meaning that data from these instruments cannot be used in this work.

4.3 LUNAR ORBITER LASER ALTIMETER

The LRO spacecraft was launched with LOLA on-board in June 2009 and has so far collected data from over 21 000 orbits, as available from the *Planetary Data System* [2014b] in August 2014 [*Chin et al.*, 2007; *Planetary Data System*, 2014b; *Smith et al.*, 2010a,b; *Zuber et al.*, 2009]. In the first

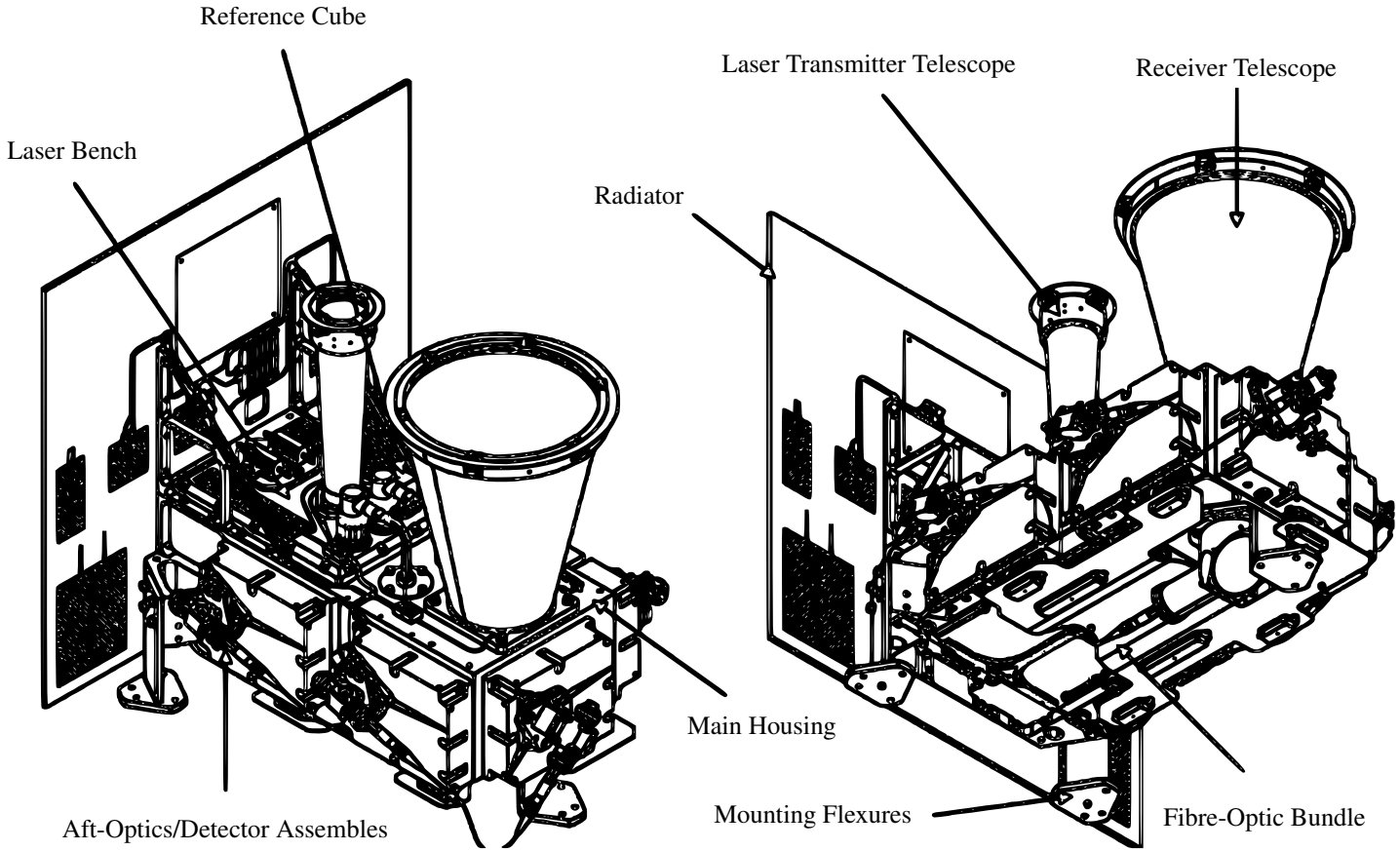

Figure 4.3: Schematic of the LOLA instrument redrawn from *Ramos-Izquierdo et al.* [2009].

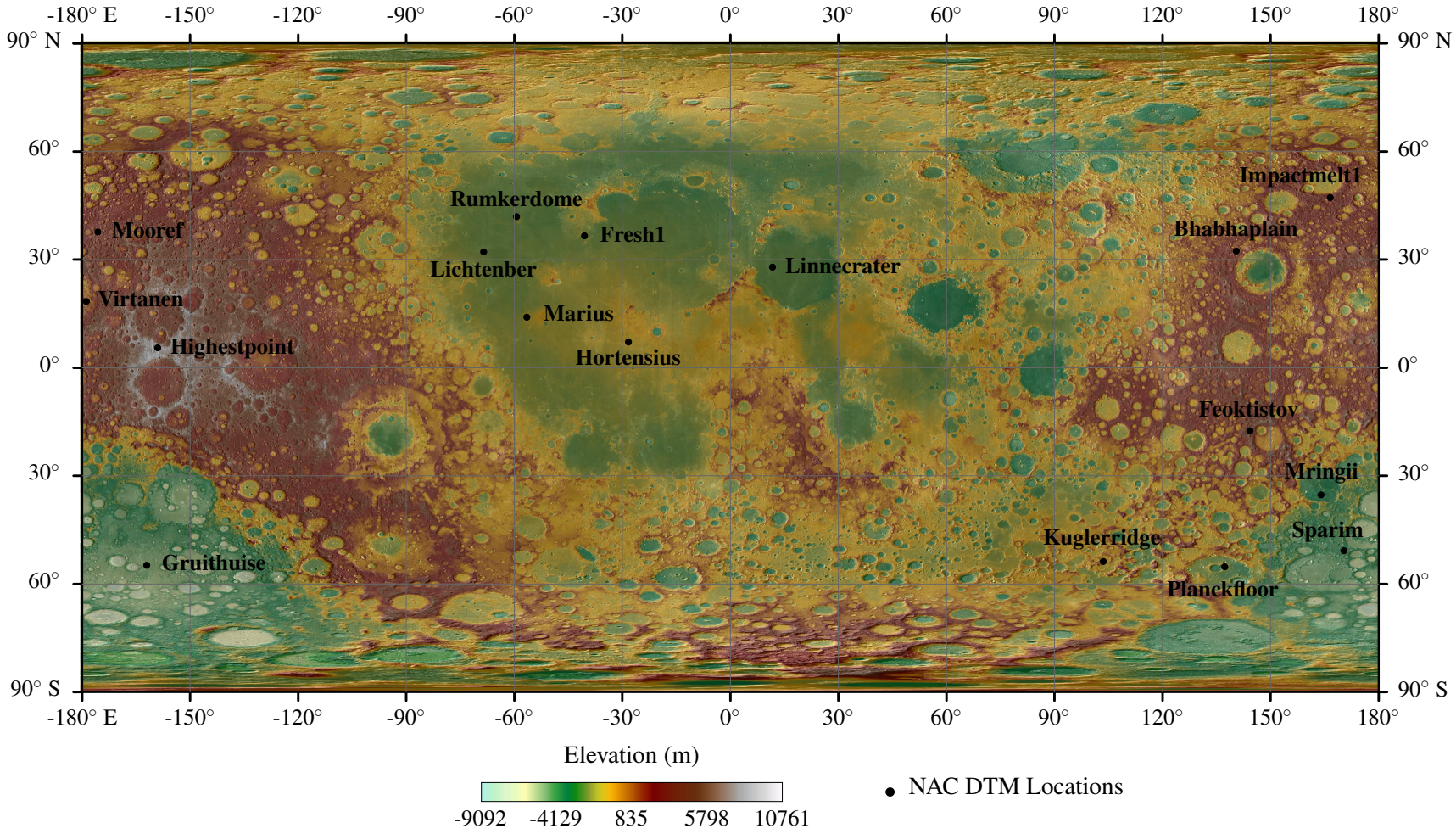

Figure 4.4a: Map of lunar elevation from LOLA from 6.5×10^9 laser altimeter pulses taken between 2009 and 2013, with the LROC-NAC DTM locations also shown.

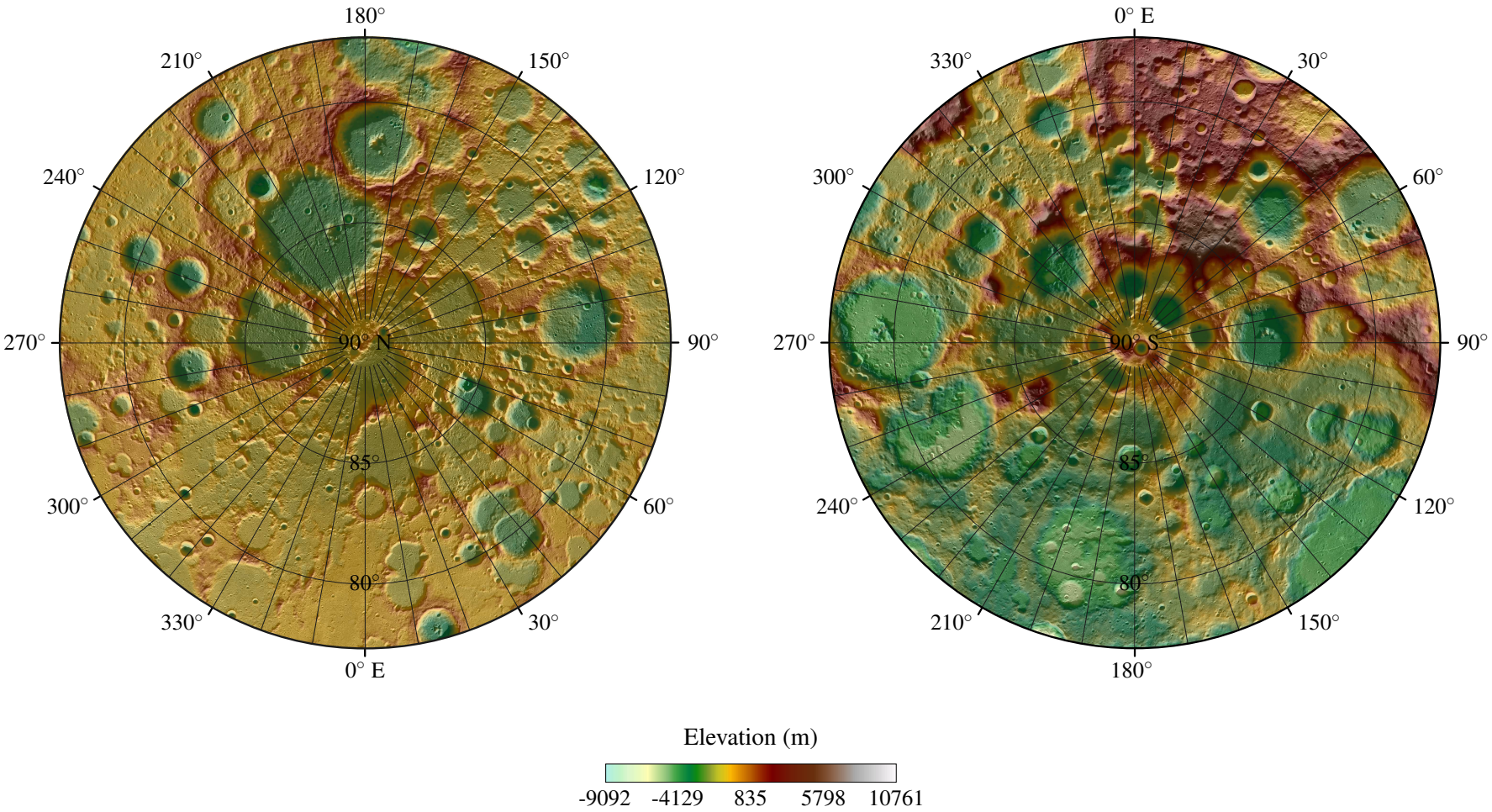

Figure 4.4b: Map of lunar polar elevation from LOLA using data from *Smith et al.* [2010a].

year of mapping, the LOLA instrument collected over 2×10^9 elevation measurements to produce the highest resolution global topographic map of the Moon to date, which is continuously being updated today [*Smith et al.*, 2010b]. A schematic of the instrument is shown in Figure 4.3 and the specific characteristics of the instrument are outlined in Table 4.1. The resulting global DTMs, derived from over 6.5×10^9 pulses (2009 to 2013) is shown in Figures 4.4a and 4.4b [*Planetary Data System*, 2014e; *Ramos-Izquierdo et al.*, 2009].

Prior to the mission, georeferencing errors of lunar data was on the order of a kilometre, to several kilometres on the far-side, and inter-pulse spacing of data from previous laser altimeter instruments was $\geq$150 m [*Araki et al.*, 2009; *Smith et al.*, 2010a]. LOLA was designed to fulfil the requirements set out by NASA's Lunar Exploration Program, which required 30 m along-track spacing, metre-scale ranging, and estimates of both bi-directional slope and surface roughness [*Smith et al.*, 2010a]. Thus, the primary aims of the instrument are to (1) map the topography of the Moon at significantly higher resolutions than the previous missions, (2) produce a precise geodetic framework for current and future mission data to be co-registered, and (3) precisely identify and characterise candidate landing and roving sites, with the eventual aim to put humans back on the Moon (Figure 4.5) [*Araki et al.*, 2009; *Chin et al.*, 2007; *Smith et al.*, 2010a,b; *Zuber et al.*, 2009]. The higher resolution elevation is also used in conjunction with gravity data to improve the lunar gravity field model and better understand the interior structure and geological evolution of the Moon [*Williams et al.*, 2014; *Zuber et al.*, 2013].

Additionally, the instrument gathers elevation data to identify Permanently Shadowed Regions (PNRs) near the poles, which could harbour ice deposits: important for both understanding lunar history, and candidate locations of proposed lunar bases [*Chin et al.*, 2007; *Gladstone et al.*, 2010; *Smith et al.*, 2010b]. Like MOLA, LOLA also uses a 1064 nm light (Table 4.1) [*Smith et al.*, 2001, 2010a]. The instrument is designed to detect changes in surface albedo over these PNRs to determine significant volumes of water ice within the PNRs around the poles [*Smith et al.*, 2010a]. Analysis of LOLA profiles over the South Pole, for slopes $<10°$, reveals 1064 nm surface albedo of 0.20 to 0.37 for non-PNRs and 0.25 to 0.42 for PNRs [*Lucey et al.*, 2014]. These differences are predominantly attributed to frost [*Lucey et al.*, 2014].

The instrument features a novel five-spot pulse design to increase the spatial density of pulses and derive small baseline slopes and surface roughness using the elevation values from individual spots within the pulse (Figure 4.5) [*Smith et al.*, 2010a,b]. The five-spot laser pulse is derived from a single pulse from one of the two on-board lasers, and is split by a diffractive optical element [*Smith et al.*, 2010b]. Each spot is thought to have a divergence of 100 µm, resulting in a pulse-footprint diameter of $\sim$5 m at the surface, with a typical spacecraft altitude of 50 km [*Smith et al.*, 2010b]. The data receiving rate is typically 140 pulses s^{-1}, with the exception of when the instrument passes the terminus to the night side of the Moon, where only two of the five transmitted spots are received [*Smith et al.*, 2010b]. This is caused by a fault in instrument design, and is commonly known as the LOLA anomaly [*Smith et al.*, 2010b]. Subsequent testing using the LOLA engineering unit revealed that the cooler temperatures on the night side causes contraction of LOLA's thermal blanket, which is attached to the laser transmitter [*Smith et al.*, 2010b]. This contraction pulls the

Table 4.1: The characteristics of LOLA from *Chin et al.* [2007] and *Smith et al.* [2010a,b].

Element	Parameter	Specification
LOLA	Mass	15.3 kg
	Power consumption	39.6 W
	Mapping Orbit	50 km
Transmitter	Laser type	Cr:Nd:YAG, cross-Porro resonator, TEM00, TEC cooled
	Wavelength	(1064.3 ± 0.1) nm
	Pulse rate	28 Hz
	Energy	laser 1: 2.7 mJ pulse^{-1} laser 2: 3.2 mJ pulse^{-1}
	Beam Splitting	>13 % total beam
	Laser divergence	(100 ± 10) µrad
	Transmitted Pulse width	5 ns to 6 ns
Receiver	Mirror	14 cm parabolic
	Detector	silicon avalanche photodiode
	Field of view	(400 ± 20) µrad
	Detector Efficiency	40 %
Electronics	Timing Resolution	>0.5 ns
Resolution	Ranging distance	20 km to 70 km
	Range resolution	5 spots, 25 m spacing
	Vertical accuracy	10 cm
	Surface spot size	5 m
	Along-track pulse spacing	18 m
	Across-track pulse spacing	1.8 km (as of 2010)

transmitter out of alignment with the receiver and reduces the received data rate to 80 pulses s^{-1} to 90 pulses s^{-1} [*Smith et al.*, 2010b]. Example orbits are shown in the top right of Figure 4.5, with the central two orbits showing only 2 of the 5 spots being returned.

To achieve the sub-50 m level horizontal precision suggested by the Lunar Exploration Program as a requirement for topographic data useful for landing and roving site selection, LOLA employs an on-board laser ranging experiment [*Smith et al.*, 2010b; *Zuber et al.*, 2009]. The laser measures the Time-Of-Flight (TOF) between Earth-based ground stations and LRO to determine the location of LRO to sub-metre accuracy, which improves the accuracy of the resulting elevation dataset [*Smith et al.*, 2010b]. *Smith et al.* [2010b] suggest that LOLA spot geolocation is known to within 10 m so that the data is useful for local, regional, and global studies (Table 4.1).

Like MOLA, the instrument does not record the full echo-profile, instead recording the start and stop time of the received pulse when above an automatically set threshold, from which roughness

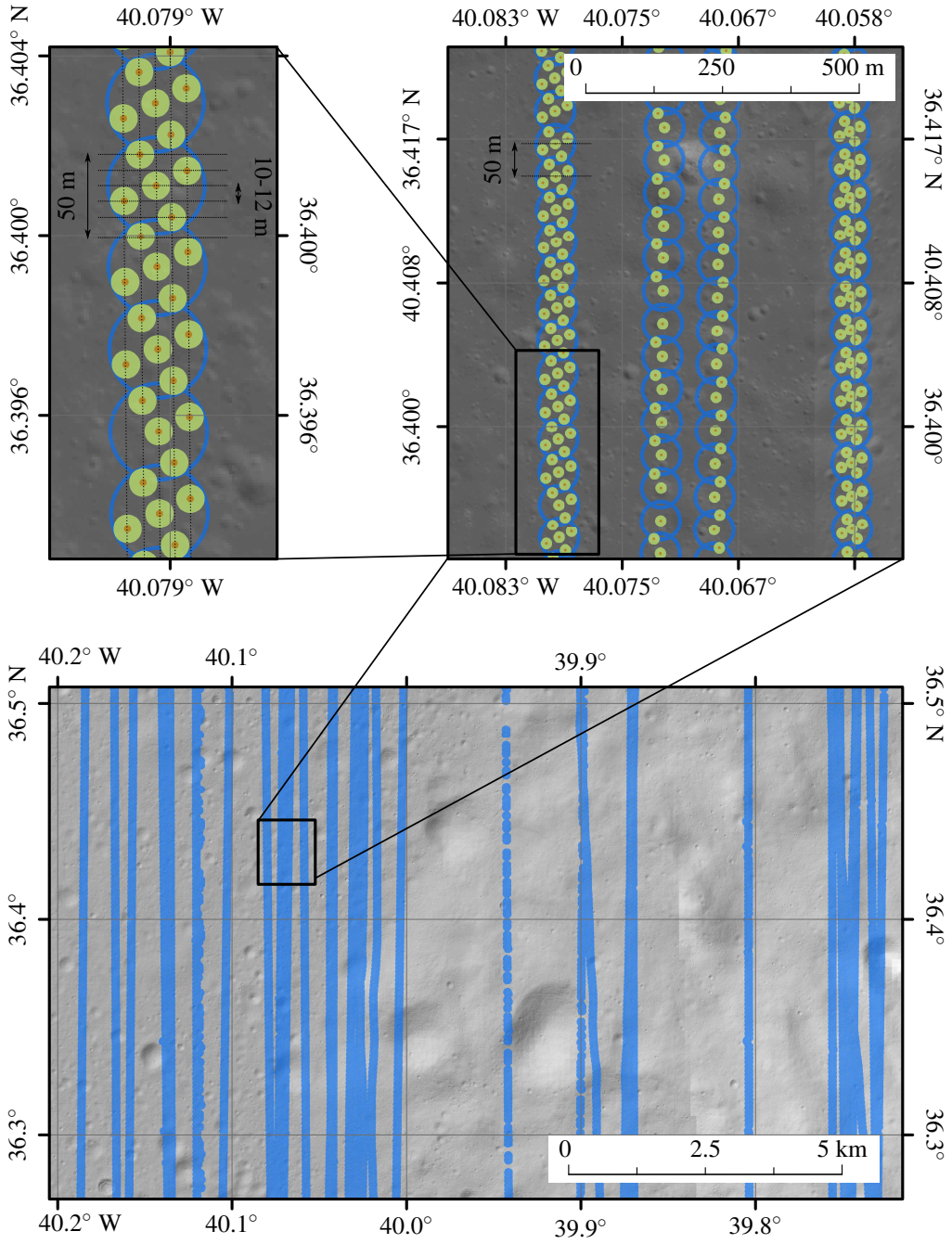

Figure 4.5: Schematic of the LOLA orbit spacing and pulse-footprint spacing. Bottom: shows the spacing between orbits over Mons Gruithuisen Delta. Top: LOLA pulse-footprint location with individual pulse positioning and spacing within each pulse.

as small as 1 m can be theoretically resolved [*Smith et al.*, 2010b]. This time-spread can be related to Root-Mean-Square (RMS) roughness within the pulse-footprint, with 50 % of the incident laser energy focussing on the central 2.5 m region of the spot [*Smith et al.*, 2010b]. At the start of the mission, apparent changes in surface reflectivity, associated with link margin and sensor alignment, caused problems with the calibration of the pulse-widths, but this is thought to have been resolved in later versions of the dataset [*Neumann et al.*, 2008; *Smith et al.*, 2010b].

4.4 DIGITAL TERRAIN MODELS

The pulse-widths in this work are compared to surface characteristics from a single data source: LROC-NAC DTMs derived from stereo-photogrammetry [*Robinson et al.*, 2010; *Tran et al.*, 2010]. The instrument and data specifications are described below.

4.4.1 LUNAR RECONNAISSANCE ORBITER CAMERA - NARROW ANGLE CAMERA

The Lunar Reconnaissance Orbiter Camera (LROC) system is also on-board LRO and consists of two cameras: the Lunar Reconnaissance Orbiter Camera - Wide Angle Camera (LROC-WAC) and Lunar Reconnaissance Orbiter Camera - Narrow Angle Camera (LROC-NAC) [*Chin et al.*, 2007; *Robinson et al.*, 2010]. The LROC-WAC camera is designed to produce global image coverage at 100 m pixel^{-1} and to provide regional context for the much higher resolution LROC-NAC images [*Chin et al.*, 2007; *Robinson et al.*, 2010]. LROC-NAC aims to address one of the primary LRO requirements, which is to resolve metre-scale features from images of the surface, surpassing the detail of earlier datasets, such as those from Apollo, Clementine, and Lunar Orbiter [*Robinson et al.*, 2010]. The images enable detailed characterisation of sites of scientific interest, such as candidate landing sites for future manned missions [*Chin et al.*, 2007; *Robinson et al.*, 2010]. From the 0.5 m pixel^{-1} images, DTMs with a resolution of 2 m pixel^{-1} can be produced from stereo-pairs acquired by spacecraft roll. An overview is provided in Table 4.2 and a schematic of the instrument is shown in Figure 4.6.

The instrument is a linear pushbroom camera that produces panchromatic images from two overlapping 5000 pixel Charge Coupled Devices (CCDs) (Figure 4.6 and Table 4.2). LRO operates at a 50 km mapping orbit, which, due to the 700 mm focal length telescope and a pixel Field Of View (FOV) of 10 µrad, results in 5 km swath images, with 0.5 m pixel^{-1} resolution [*Chin et al.*,

Table 4.2: The key characteristics of the LROC-NAC camera [*Robinson et al.*, 2010].

Parameter	LROC-NAC Left	LROC-NAC Right
FOV	2.8502°	2.8412°
Pixel FOV	10.0042 µrad	9.9764 µrad
Image Res.	0.5 m pixel^{-1}	0.5 m pixel^{-1}
Max Image Size	2.49 km × 26.1 km	2.48 km × 26.1 km
F-Stop	3.577	3.590
Focal Length	(699.62 ± 0.08) mm	(701.57 ± 0.09) mm
Primary Mirror Diameter	198 mm	198 mm
SNR (mare at 70° incidence angle)	>42	>42
Peak Power	9.3 W	
Average Power	6.4 W	
Mass	16.4 kg	

Front View

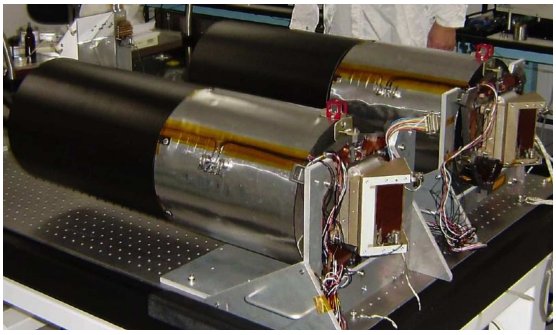

Left and Right NAC together

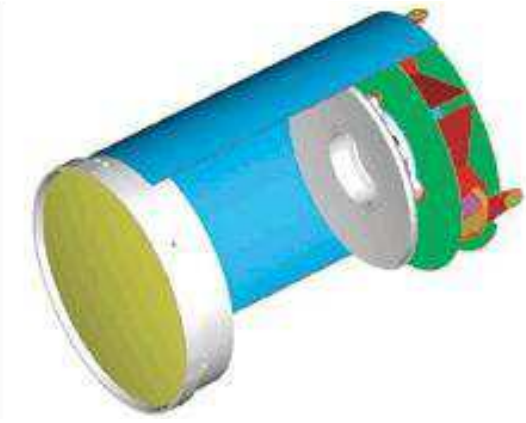

Internal Strucure

With Baffle

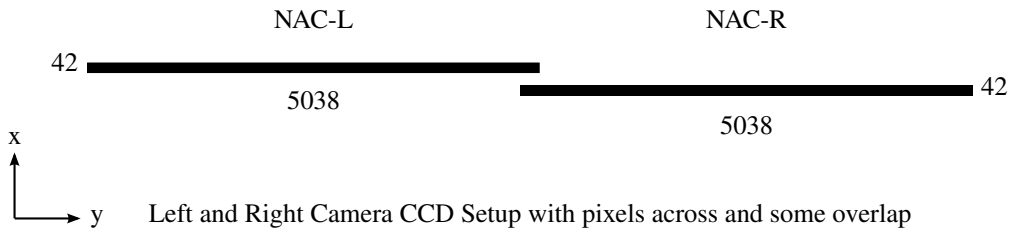

Left and Right Camera CCD Setup with pixels across and some overlap

Figure 4.6: Schematic of the LOLA instrument redrawn from [*Robinson et al.*, 2010].

2007; *Robinson et al.*, 2010]. Each CCD has a FOV of 2.85° for a full swath of 5.7°, with a small overlap of the CCDs (∼135 pixels) due to the left CCD being off-pointed in relation to the right, by ∼2.85° [*Chin et al.*, 2007; *Robinson et al.*, 2010]. The maximum length of full resolution images is 25 km, although the images can be binned to lower resolution to produce images 104 km long [*Chin et al.*, 2007; *Robinson et al.*, 2010].

To reduce costs, the electronics of the camera are based on the Context Camera (CTX) instrument, described in the previous chapter, with some modification, such as increasing the maximum pixel rate to 7.5 Mpixel s^{-1}, from 2 Mpixel s^{-1} [*Robinson et al.*, 2010]. The general design process also began with CTX, although this had to be scrapped due to the more extreme thermal ranges experienced by LRO and the need for reduced pixel FOV required for higher resolution [*Robinson et al.*, 2010].

In addition to the instruments primary objectives, LROC-NAC aims to achieve the following

objectives [*Robinson et al.*, 2010]

1. Produce high-resolution maps of permanently shadowed regions of the poles
2. Acquire stereo-images of potential landing sites for DTM production
3. Produce high-resolution maps of different geologic units to analyse their physical properties and the variability of the regolith
4. Repeat high-resolution mapping of Apollo era images to infer the impact rate

The DTMs from LROC-NAC stereo-pairs are produced at a minimum of $2\,\mathrm{m\,pixel^{-1}}$. Four of the six research groups producing these products use a combination of Integrated Software for Imagers and Spectrometers Version 3 (ISIS3) and SOftCopy Exploitation Toolkit (SOCET SET®), similar to the High Resolution Imaging Science Experiment (HiRISE) processing chain [*Kirk et al.*, 2008; *Tran et al.*, 2010]. To acquire stereo-pairs, LRO rolls during the acquisition of one of the two images to create a different viewing angle, with a recommended 12° minimum difference in viewing angle between the images, but 24° being typical [*Tran et al.*, 2010]. The vertical error in the DTMs is thought to be <1 m for the higher-resolution images, whilst for $2\,\mathrm{m\,pixel^{-1}}$ images the error is thought to be $\sim$3 m [*Tran et al.*, 2010]. The vertical precision of the DTMs is aided by the LOLA bore-sight being aligned to LROC-NAC, meaning that imaging and altimetry data is collected synchronously [*Mattson et al.*, 2010].

4.5 THE MOON'S COORDINATE SYSTEMS

The selenographic coordinate system employed by the LRO data is the International Astronomical Union (IAU)2000 Moon sphere, using planetocentric latitudes, as shown in Table 4.3 and defined in Table 2.2 on Page 74 [*LRO Project and LGCWG*, 2008]. The LOLA elevations are measured in relation to this reference sphere, which has a radius of 1737.4 km: more precisely, the selenoid equatorial radius of the Moon is 1738.1 km, and the polar radius is 1737.1 km [*LRO Project and LGCWG*, 2008; *Smith et al.*, 2010b]. This reference frame is chosen due to the requirement that data from this mission must be compatible with data from the earlier Clementine mission [*LRO Project and LGCWG*, 2008]. As one of the mission aims is to create a precise geodetic grid, it is expected that an improved reference frame will be created from the data, which will then be accepted by the international community sometime after the primary mission phase [*LRO Project and LGCWG*, 2008; *Seidelmann et al.*, 2002; *Smith et al.*, 2010b].

Table 4.3: Selenographic coordinate systems used by datasets in this chapter [*Bennett et al.*, 2011].

Instrument	Dataset	Map System	Elevation Reference	Latitude Reference
LOLA	RDR	IAU2000	Sphere	Planetocentric
LROC-NAC	DTM	IAU2000	Sphere	Planetocentric

4.6 METHODS

The methods employed to compare LOLA pulse-widths to surface characteristics, which are similar to those used in Chapter 3, are outlined below. The section begins by describing the DTM production process, site selection, and quality control, before moving on to LOLA data collection and comparison with surface characteristics.

4.6.1 DTM PRODUCTION

The DTMs used in this chapter are all freely available from *Planetary Data System* [2014b], which, at the time of the work (February 2013), provided 78 DTMs for download. As discussed in Section 4.4.1, most of the Research Groups producing LROC-NAC DTMs use a processing chain that includes ISIS3 and SOCET SET®, which is outlined in Figure 4.7 [*Tran et al.*, 2010]. This chain is similar to that used to produce HiRISE and CTX DTMs, as shown in Figure 3.8, whereby raw LROC-NAC images are downloaded and processed in ISIS3, before DTM processing in SOCET SET®. However, different parameters to account for the different camera type.

For each image in the stereo-pair, processing of the LROC-NAC images includes (1) downloading the Level 1 processed left and right CCD images, (2) adding Spacecraft and Planetary ephemerides, Instrument C-matrix and Event kernels (SPICE) data to each image, (3) calibrating each CCD image; applying a photogrammetric correction to the images to ensure they appear radiometrically similar, and finally (4) the left and right CCD images are stitched together [*Tran et al.*, 2010].

Other methods of producing these DTMs include using a combination of Orbital Mapper and Leica Photogrammetry Suite 9.3 software, as well as in-house systems that have been developed at NASA Ames Research Center and Deutsches Zentrum für Luft- und Raumfahrt (DLR) (*German Aerospace Center*) [*Tran et al.*, 2010].

4.6.2 SITE SELECTION

The results using MOLA data in Chapter 3 suggest that calibrating laser altimeter pulse-widths over homogeneously rough or sloping terrain increases the probability of a correlation between laser altimeter pulse-widths and surface characteristics being observed. To identify these sites, each of the 78 DTMs available via *Planetary Data System* [2014b] were viewed to ascertain whether the underlying topography was rough and/or highly variable. DTM and image data, which includes 0.60 and 2 m pixel^{-1} stereo-pair images, and a 2 m pixel^{-1} DTM, slope map, hillshaded image, and colour hillshaded image, were downloaded for the 34 DTMs, spread over 19 regions, that met these criteria.

For each region where these data are located, an ArcMap 10.1 project was set up and the data loaded for viewing and quality control, which is described below. This quality control process forms the final part of the site selection process, with only those sites that contain large regions of good quality DTM data selected for use.

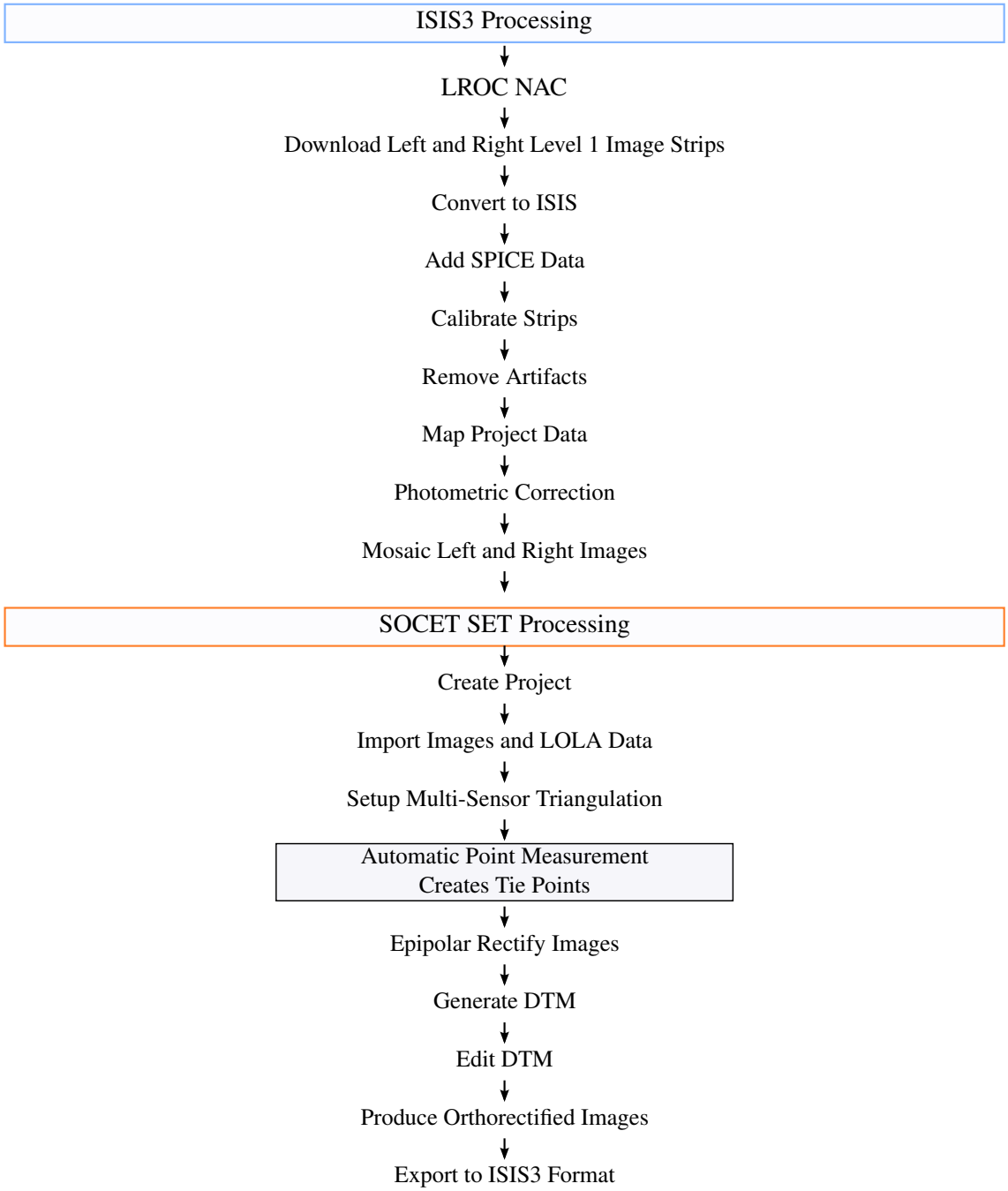

Figure 4.7: Flow diagram of the LROC-NAC DTM production process using ISIS3 and SOCET SET®. The figure is similar to that in Figure 3.8, with minor changes to the ISIS3 processing changes due to a different camera setup.

Unlike the work using HiRISE DTMs in Chapter 3, it is not a requirement that sites must have multiple overlapping or adjacent DTMs. Despite HiRISE and LROC-NAC having very similar image sizes, a significantly greater number of laser altimeter pulses lie over the LROC-NAC DTMs because of the greater data density. This increased data density is due to the five-spot design, greater pulse-rate, and a smaller inter-orbit spacing (1.8 km as of 2010), relative to the MOLA data characteristics [*Smith et al.*, 2001, 2010b].[2] This means that even a single LROC-NAC DTM contains enough data to derive mathematically significant relationships, thus enabling more sites to be explored in this work.

4.6.3 DTM QUALITY CONTROL

After loading the data into ArcMap, the DTMs were checked for errors that could result in poor correlations between LOLA pulse-widths and surface roughness and slope. Hillshaded images were made from the DTMs and used to identify pits, spikes, and heavily interpolated areas that are common in areas of poor stereo-matching, as discussed in Section 2.2. The original hillshaded images were discarded to ensure consistency with the methods applied in Chapter 3 and to ensure all hillshaded images are produced similarly. As in Section 3.6, areas that appear to be poorly matched terrain were masked from the study, unless the total amount of poorly matched terrain covered $\geq$50 % of the DTM coverage, in which case the DTM was removed from the study. From the 19 regions that contained one or more DTMs that were considered suitable for the study, 16 were found to have high-quality data that could be used to produce surface roughness and slope maps for comparison with LOLA pulse-widths. These sites are shown in Figure 4.4a.

For those sites that have multiple overlapping LROC-NAC DTMs, a DTM mosaic was produced. This enables more pulses to be used, as pulses that lay within half the maximum baseline of the boundary of the DTM coverage area are removed from the study. Like in Chapter 3, the *Mosaic to New Raster* tool in ArcMap 10.1 was used, with the *blend* option used to merge DTM heights where they overlapped. A hillshaded image was produced from the mosaic, to highlight potential errors in the mosaicing process: if there are even slight differences in DTM heights, where the DTMs overlap, linear triangular features features would be produced that are easily identified. However, these were typically not observed, perhaps due to the LOLA LROC-NAC alignment discussed above, resulting in highly accurate co-registration of imaging and laser altimeter data. Where these errors were observed, the overlap areas are masked out so inconsistent elevation data did not influence the results.

For each ArcMap project, the projection information used is the same as the LROC-NAC data, which uses an equirectangular projection with the central meridian at 180°. If only a single DTM existed over a region, then the projection used by the project is the same as the dataset; if there is a mosaic, then the mosaic is made using a projection employed by one of the original DTMs, which is then used by the project. This does not influence the results, as reprojection errors are well below

[2] Comparing the number of MOLA and LOLA pulses over a 6 km $\times$ 25 km DTM at the equator: MOLA could have 167 pulses, assuming all pulses could be used from 2 orbit tracks overlapping the DTM area; LOLA could have 7500 pulses, assuming all pulses could be used from 3 orbit tracks overlapping the DTM area.

the resolution of the DTM, as discussed in Section 2.2.5, but increases the speed of viewing data, as ArcMap 10.1 does not have to reproject data on the fly.

4.6.4 LOLA DATA COLLECTION

The LOLA data were downloaded from the *Planetary Data System* [2014b] using the LOLA RDR QUERY tool, which enables the user to select data within a user defined Region-Of-Interest (ROI). Pulses within each of the 16 ROIs, including a generous buffer zone, were downloaded in CSV and Shapefile format, and imported into the relevant ArcMap 10.1 project file. This was completed in February 2013 using Release Number 12 of the LOLA data. Comma-separated values (CSV) files are available in three formats: Frame Per Row, where data from all five spots in each pulse are contained within a single row; Point Per Row, where data from only one spot is contained within a row; and elevation data only. The Frame Per Row CSV files were used, which contain: pulse time, longitude, latitude, Moon's radius at that location, pulse-width, transmitted energy, noise, threshold, gain, and other parameters, for each spot. Each spot was mapped by importing the CSV file into ArcMap, using the *Add XY Data* function and using the IAU2000 Moon sphere as a geographic coordinate system (Table 2.2), as the locations are provided in latitude and longitude. The LOLA data were then reprojected by exporting the data to a *Shapefile*, which was then used as an input data source for the *Project* (Feature) tool to produce a new Shapefile projected into the Projected coordinate system used by the project. Spots within 30 m of the boundary of the DTM, or mosaic, were excluded from the study using a mask produced from the DTM boundary. The maximum baseline used is 60 m, therefore, surface roughness and slope estimates closer than 30 m to the boundary would not have a full search-window of data from which to calculate these surface characteristics at the largest baseline. If these pulses were to remain, null-values within the search window would be filled with the elevation value of the centre pixel, for which the surface roughness or slope is calculated, which would introduce a bias to the results. Pulse-width are not corrected using Equation 2.5, as all the factors in this equation, except for the contribution from the terrain within the pulse-footprint (σ_t), are expected to be very similar for all pulse-footprints, therefore the only factor expected to change is the terrain contribution.

4.6.5 GEOREFERENCING AND ELEVATION ERRORS

As LOLA and LROC-NAC data are acquired simultaneously, there is not thought to be a measurable difference between the co-registration of the two datasets. A visual inspection of the LROC-WAC GLD100 dataset, comparing it to elevation and image data from LOLA and LROC-NAC respectively, found offsets in surface features in image data and the profile of craters from off-nadir LOLA viewing angles, as shown in Figure 4.8 [*Scholten et al.*, 2012]. Figure 4.8a and b show the apparent location of pulse-footprints over sloping and flat terrain from nadir and off-nadir pointing orbits. In nadir-pointing orbits, the slope of terrain is irrelevant in the location of pulses, whilst for off-nadir orbits, pulse location shifts towards the spacecraft for rising terrain compared to flat terrain and away from the spacecraft for low terrain. Using this, one can check the georeferencing

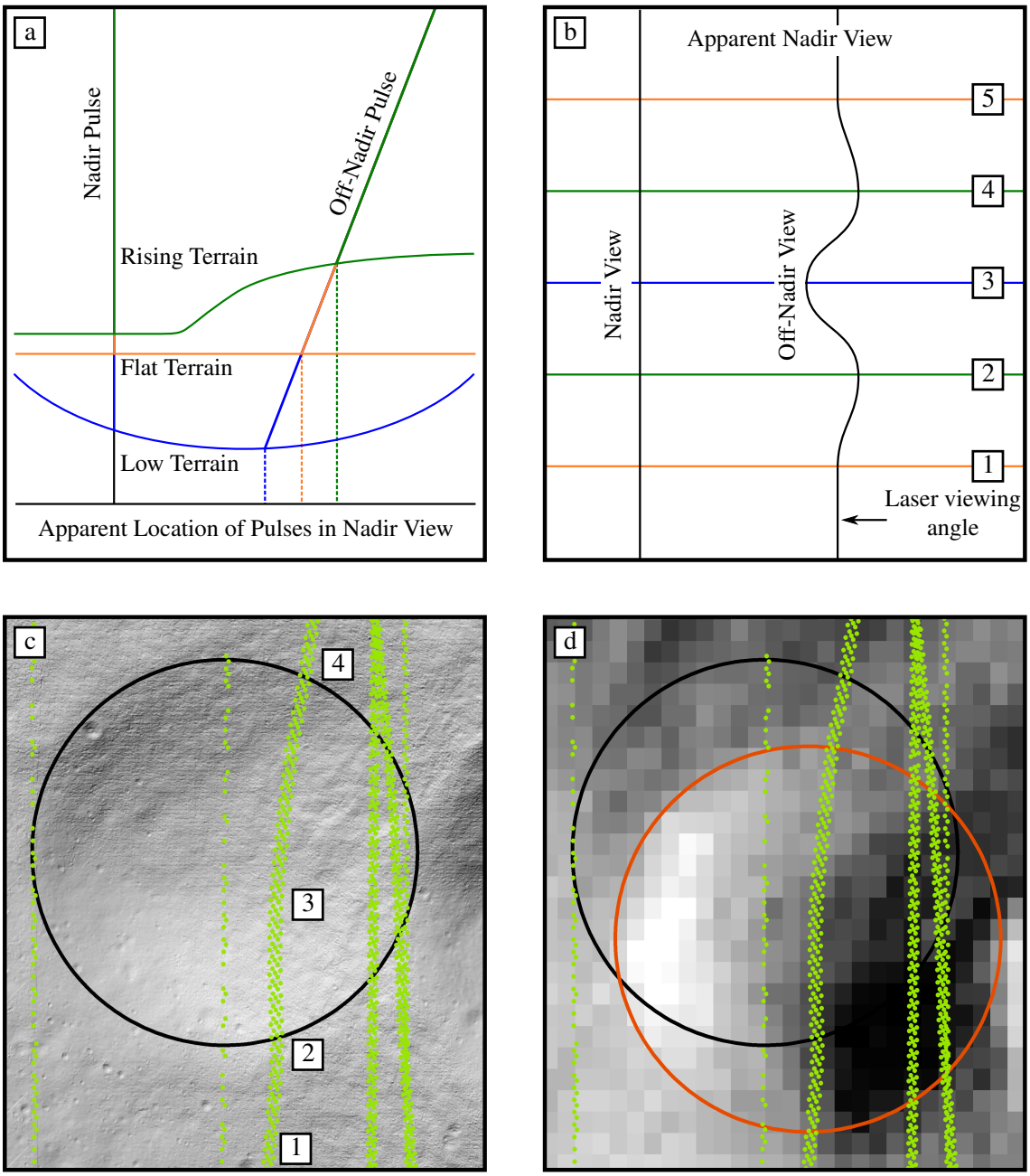

Figure 4.8: Schematic showing the co-registration checking procedure for LOLA data to LROC-NAC images. (a) shows the apparent position of pulses due to rising, flat, and low terrains from nadir and off-nadir viewing angles. Rising terrain results in a shift towards the spacecraft location in nadir view, compared to flat terrain, in off-nadir viewing angles. Lowering of terrain results in a shift away from the spacecraft compared to flat terrain. In nadir view, there is no shift in the apparent position of the pulses in an orbit. (b) shows how (a) appears in nadir view, with numbers corresponding to different features around a crater. (c) and (d) shows real LOLA data over an area in Mons Gruithuisen Delta using LROC-NAC and LROC-WAC respectively. The former shows good correlation in the shift of pulse locations as the orbit passes over a crater, shifting towards the spacecraft as the terrain rises in elevation (1) - flat terrain - to (2) - crater rim - , and (3) - crater floor - to (4) - crater rim. The pulse location shifts away from the spacecraft when the terrain decreases in elevation from the crater rim (2) to the crater floor (3). In (d), the orbit is offset with the crater features shown in the Global Lunar Digital Terrain Model 100 m topographic model (GLD100) LROC-WAC global mosaic, with the crater appearing different due to different lighting conditions. The black circle in (c) and (d), defines the crater from LROC-NAC data, whilst the orange circle in (d) defines the crater from the GLD100 LROC-WAC data.

of orbits to LROC-NAC data as an off-nadir orbit passes over a crater, as shown in Figure 4.8c and d. In Figure 4.8c, the deviations in the off-nadir orbit correlate well with these effects on pulse location, with the pulse locations shifting towards the spacecraft (right) from positions (1) and (2) as the orbit passes from flat terrain to the crater rim, as expected. This also occurs between positions (3) and (4) as the orbit passes from the crater floor to the crater rim. Whereas the position of the pulses shifts away from the spacecraft (left) when terrain decreases in elevation, as the orbit passes from the crater rim to the crater floor, as occurs between position (2) to (3). In Figure 4.8d the orbit is offset in relation to the underlying LROC-WAC GLD100 image, which appears different due to different lighting conditions. This difference may occur due to the bundle adjustment of imaging data to produce the GLD100 global mosaic, as of February 2013, and may not be present in the original LROC-WAC images.

The LROC-NAC DTM elevations are compared to those within the LOLA dataset for each of the pulses over Mons Gruithuisen Delta, a site that is described in Section 4.8. The observed correlation between LOLA and LROC-NAC DTM elevations is found to be very strong, with an R-squared value of 0.998. This strong correlation, and the fact that the laser altimeter and LROC-NAC image data are acquired simultaneously, suggests that these datasets are better co-registered than the Mars data used in the previous chapter.

4.6.6 SURFACE ROUGHNESS AND SLOPE MAP PRODUCTION

Like the previous chapter, laser altimeter pulse-widths are compared to surface roughness and slope values derived from maps derived from high-resolution topography data. The maps were produced using the same methods as in Chapter 3, the only difference being the baselines used here are much smaller due to the smaller pulse-footprint of LOLA, compared to MOLA. An upper baseline of 60 m was used in both map types, which was chosen as surface roughness and slope at baselines equal or larger than this can be derived from the elevation data alone. Therefore if pulse-widths corresponded to surface characteristics at these scales, it would provide surface roughness information at scales that can already be derived from elevation data [*Smith et al.*, 2010b].

4.6.6.1 SURFACE ROUGHNESS MAPS

Surface roughness maps were produced using the *Focal Statistics* tool, with the *STD* option and a circular window, with the radius equal to half the baseline of study. This effectively calculates the RMS height, as in Equation 2.46 in Section 2.3, within a circular pulse-footprint. The minimum baseline calculated was 6 m: any smaller there would be too few DTM pixels from which to calculate surface roughness. However, it must be noted that noise within the elevation values at smaller baselines will have a greater effect due to the small number of elevation values from which RMS height is calculated [*Shepard et al.*, 2001].

Some orbits are taken at high tilt angles, especially when LROC-NAC is acquiring stereo pairs, which may cause distortion of the pulse-footprint. The pointing-angles are recorded in the data, and therefore these pulses can be removed if they appear to produce poor results, however, due to the

relatively low orbiting altitude of LRO compared to Mars Global Surveyor (MGS), and therefore the much smaller pulse-footprint, this effect is expected to be much smaller.

4.6.6.2 SLOPE MAPS

Slope maps were produced using the *Slope* tool in ArcMap, which defines slope using Equations 2.56 to 2.58. Like Chapter 3, the *Slope* tool was applied to resampled elevation data, where the resampling resolution is equal to the baseline required. The baselines used here range from 2 m pixel^{-1} to 60 m pixel^{-1}. Again, noise within the elevation dataset will have a greater influence at smaller baselines. However, the removal of areas of poor elevation data will help reduce this effect. It is important to attempt to explore the correlation between LOLA pulse-widths and slope at these smaller baselines because the MOLA study showed those pulse-widths to be correlated to pulse-footprint-scale slopes, and *Smith et al.* [2010b] suggest that the hot-spotting effect within the pulse-footprint may result in the central 2.5 m diameter area of the pulse-footprint having the greatest influence on pulse-width.

Depending upon the best correlating baselines observed for slope, detrended roughness may be explored. However, if this baseline is close to the expected pulse-footprint (5 m), then detrended roughness will not be explored, as the surface roughness estimates at baselines close to the resolution of the elevation dataset may be unreliable, as shown in Section 3.9 [*Shepard et al.*, 2001].

4.6.7 DATA EXTRACTION AND COMPARISON

For each of the 16 regions, surface roughness and slope values were extracted from the maps for each baseline at the location of each spot within the LOLA pulse using the *Extract Multi-Values to Points* tool in ArcMap 10.1. This tool exports the map values to new columns within the projected Shapefile produced in Section 4.6.4, which were then exported to a text file for processing in MATLAB. The pulse-widths are then plotted against each baseline for each of the two surface characteristics, with the best baseline for each characteristic chosen on the basis of having the greatest R-squared value when a linear line-of-best-fit is applied using a linear regression fit in the *fit* tool in MATLAB. To test the significance of the fit, the fit is tested against the null-hypothesis to ensure a meaningful result.

Although not exact, this may provide an indication of the feature size and type that LOLA pulse-widths respond to, thus calibrating the pulse-width values to underlying terrain. The aim is to find commonly occurring baselines, like in Section 3.8, which can be used to validate the method of deriving surface characteristics from pulse-widths, and calibrate the LOLA pulse-width dataset.

4.7 REGIONAL RESULTS

4.7.1 INTRODUCTION

A starting assumptions is that LOLA pulse-widths behave similarly to MOLA, in that separate regions may behave differently depending on a number of factors, including the size, spatial distribution, and variation of terrain within a ROI. Therefore, each of the 16 regions, shown in Figure 4.4a, are explored individually to identify sites where the best correlations could be observed when the pulse-widths are compared to both surface roughness and slope. Ideally, all sites would produce strong correlations at similar baselines and relationships with the surface characteristics. These relationships could then be extrapolated to other regions of the Moon that have LOLA coverage, but not high-resolution DTM coverage, to identify candidate landing and roving sites, and differences in surface ages and formation processes, in addition to further development of the surface roughness and slope maps presented in *Kreslavsky et al.* [2013] and *Rosenburg et al.* [2011].

4.7.2 RESULTS

In practise, all the regional results show very poor correlations, similar to those observed over Mawrth Vallis (R-squared <0.1). The regional results for LOLA comparisons to both surface roughness and slope for pulses taken over the Mons Gruithuisen Delta ROI are shown in Figure 4.9 and Table 4.4. Furthermore, removal of data greater than 3 standard deviations from the mean does little to improve the results, increasing the R-squared values by only ≤ 0.02. The remaining plots are not shown, as they all appear similar to that from Mons Gruithuisen Delta, or worse. It is clear that the correlations are much poorer than expected, and are not better than the MOLAs results.

The results in Table 4.4 show LOLA pulse-widths over the Impactmelt1 DTM produce the best

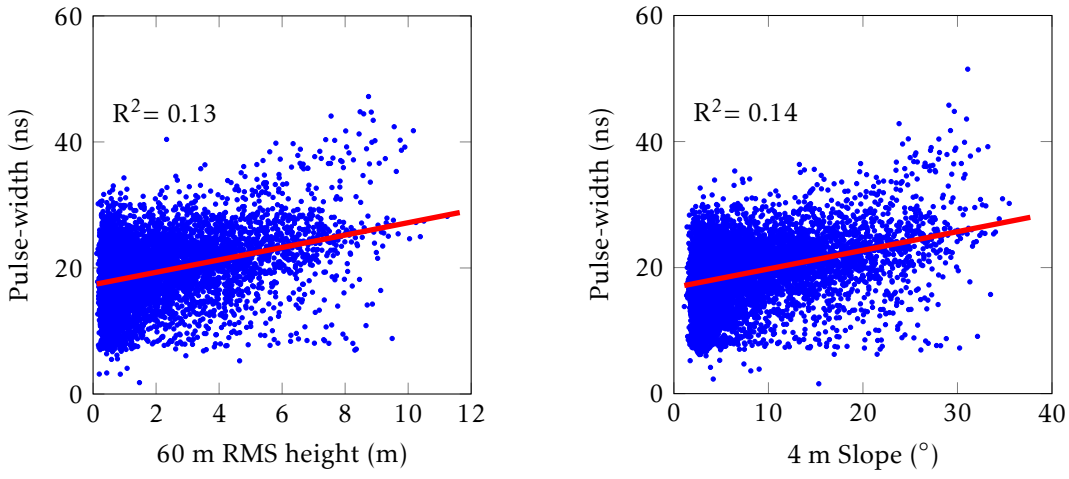

Figure 4.9: Plots of regional results comparing LOLA pulse-widths to surface roughness and slope over Mons Gruithuisen Delta. All other regions in this study showed similar, or poorer, correlations.

Table 4.4: The best R-squared values observed over each of sites used in the LOLA study. These are the best correlations observed for both slope and surface roughness.

Area	R-squared	Surface Characteristic	Baseline (m)
Bhabhaplain	0.016	Surface Roughness	60
Feoktistov	0.029	Slope	50
Fresh1	0.099	Slope	50
Gruithuise	0.135	Slope	50
Highestpoint	0.041	Surface Roughness	30
Hortensius	0.070	Slope	30
Impactmelt1	0.234	Surface Roughness	60
Lichtenber	0.050	Slope	30
Linnecrater	0.070	Slope	50
Marius	0.063	Surface Roughness	60
Mooref	0.148	Surface Roughness	60
Mringii	0.041	Slope	50
Planckfloor	0.021	Surface Roughness	60
Rumkerdome	0.025	Slope	60
Sparim	0.073	Surface Roughness	50
Virtanen	0.020	Surface Roughness	50

correlations, however, with an R-squared of 0.234, the correlation is much weaker than the sites where a correlation is observed over Mars. The baselines at which the best correlations are observed are also much greater than the expected pulse-footprint ($\sim 10\times$) and are equivalent to the best correlations being observed at 0.75 km to 1.7 km using MOLA data. However, as the correlations are typically very poor, this result, although mathematically significant, is not thought to produce an accurate picture of the relationship between LOLA pulse-widths and surface characteristics.

A visual inspection of the LOLA pulse-width values, mapped by location and pulse-width values for individual spots within each pulse, reveals very different behaviour, as shown in Figure 4.10. Instead of being split by region, like the MOLA results, correlations appear to be dependent on data from individual orbits, with some orbits revealing changes in pulse-width values that appear to correlate spatially with underlying surface features, whilst many orbits do not. Figure 4.10 shows a selection of different behaviours observed when the LOLA pulse-widths are mapped like this. Many orbits appear to contain pulse-widths that are constant along large sections of an orbit, such as those shown in Figure 4.10a and c, whilst some others have pulse-widths of certain spots within the pulse that appear similar, as in Figure 4.10b. Finally, Figure 4.10d appears to show an example of one orbit that contains pulse-widths that change with underlying topography. Here, the pulse-widths in the highlighted orbit appear to increase as the orbit passes over the crater walls, which is expected due to the increase in slope (Equation 2.7), whilst the pulse-widths are smooth, flatter terrain are smaller.

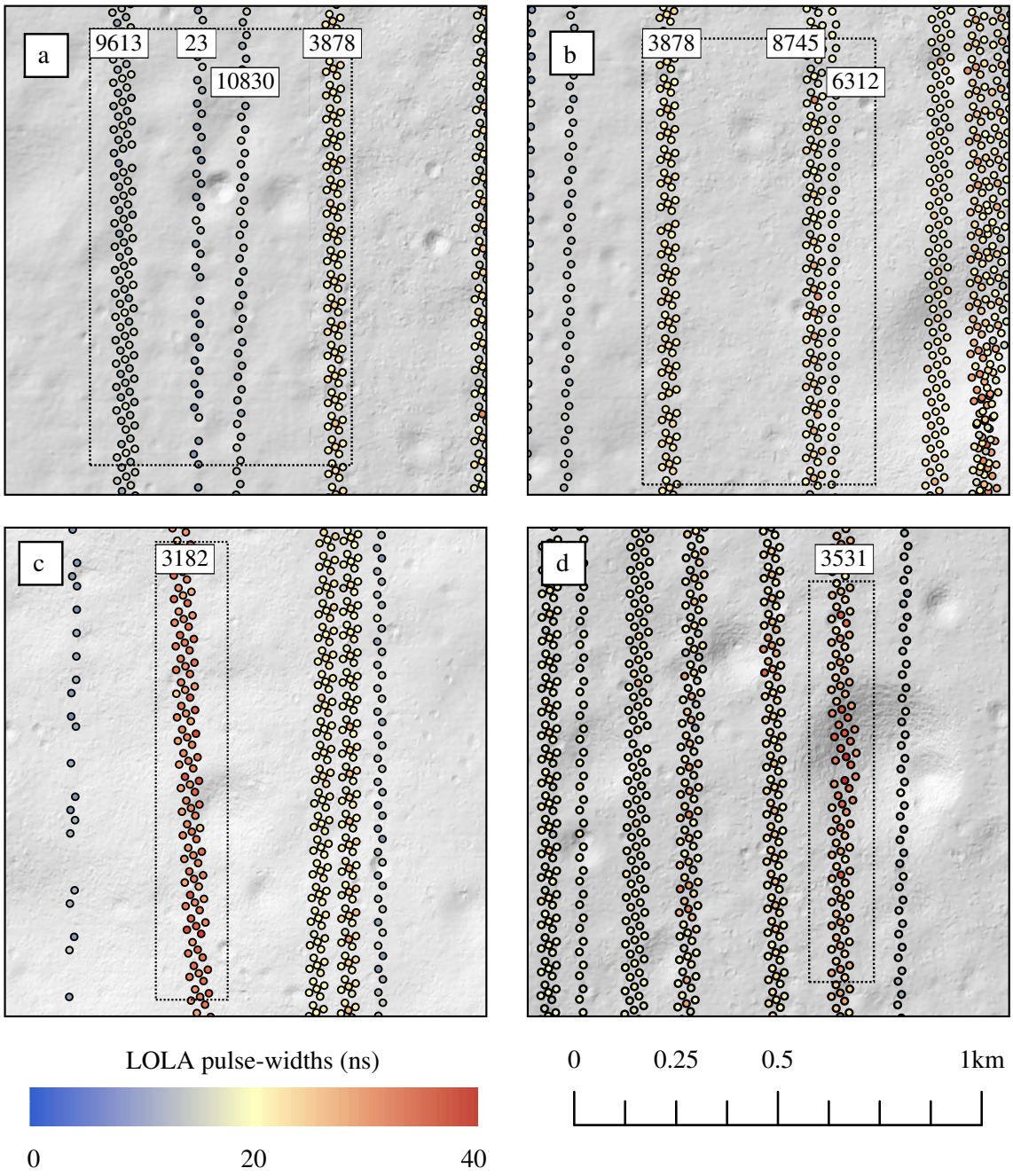

Figure 4.10: Maps of the different behaviours observed using LOLA pulse-widths from individual orbits over Mons Gruithuisen Delta. a) Four orbits that appear not to change with the underlying terrain, each having their own behaviour, with the three left orbits appearing to have small pulse-width values over the entire orbits. The right orbit (3878) shows each spot within this section of the orbit containing the same pulse-width value in each pulse. b) Orbit 8745 contains pulse-width values that change, but do not appear to change with the underlying terrain. c) Shows an example of an orbit that appears to contains only high pulse-width values along an entire orbit. d) An orbit that does appear to change with underlying terrain, with increasing pulse-widths as the orbit passes over a crater, where the slope increases causing increasing pulse-width values (Section 2.1.3), before decreasing again when the spots are over smoother terrain.

4.7.3 DISCUSSION

It is clear that on a regional basis, LOLA pulse-widths do not show strong correlations with surface characteristics. As a result, the relationships derived here cannot be extrapolated to other regions of the Moon to identify candidate landing sites or surface age. The observed correlations are much poorer than typically observed using MOLA data, as used in the previous chapter, and the baselines at which the best correlations are observed can already be reliably derived from the elevation data from individual spots within each pulse. There are no obvious differences in the factors that may affect the observed correlations, such as transmitted pulse-width or energy, and gain, etc. as setting different tolerances for these parameters does not improve the observed R-squared values. This is also true for the off-nadir pointing angles, which is also shown not to affect the results.

These poor results may be caused by the saturation or surface reflectance effects that plagued the mission in its early stages, or the LOLA anomaly may cause additional problems in pulse-width estimation that have not been detected previously [*Neumann et al.*, 2008; *Smith et al.*, 2010b]. Another possibility is that the combination of smaller pulse-footprint and larger DTM pixel size, compared to HiRISE, inhibits strong relationships being found, with noise within the DTM datasets having more of an effect at baselines close to the original resolution of the DTM. Unfortunately, extensive regions of higher-resolution DTM data ($<2\,\mathrm{m\,pixel^{-1}}$) do not exist and are limited to small areas around current landing sites, which are not used due to the low number of LOLA data that exist within the DTM boundaries.

Figure 4.10 appears to show that individual orbits may behave differently, however. This avenue is explored further in the following section, which compares pulse-widths from individual orbits to both surface roughness and slope. The hope is that individual orbits show stronger correlations than are observed here. Ideally, data from only a few orbits causes the poor correlations observed in regional data, and that these poor orbits can be identified and removed for better regional results. Additionally, the cause of these poor orbits, which produce good elevation estimates, could be identified and any extrapolation from the calibrated areas could exclude these orbits for a more reliable map roughness and/or slope from pulse-width data.

4.8 ORBIT RESULTS: WITH A CASE STUDY ON MONS GRUITHUISEN DELTA

4.8.1 INTRODUCTION

Exploring the relationship between LOLA pulse-widths and surface characteristics on an orbit-by-orbit basis, as suggested by Figure 4.10, may yield improved R-squared values compared to the regional results shown in Figure 4.9 and Table 4.4. Data from individual orbits are explored from each of the sites explored in the previous section, with a case study highlighting the effects on orbits over Mons Gruithuisen Delta, which exhibits behaviours that are observed throughout other regions used in this work (Figure 4.4a).

The same data used above are used here, with the orbit number provided in the original LOLA CSV file used to identify data in individual orbits. The primary aim of the work is to identify how each orbit performs, with the hope that only a small number of orbits cause the poor regional results and that poor orbits share common patterns in telemetry data, such as excessive noise and gain, or pulses acquired at a particular time in the mission. These poor orbits can then be identified and removed, and only pulse-width data from higher-quality orbits is used to extrapolate surface roughness estimates to other regions of the Moon where high-resolution DTM coverage does not exist.

Failing this, the aim of the work is to distinguish whether surface characteristics can be derived in a small number of orbits, ideally with better correlations than those observed using MOLA pulse-width data. This will help demonstrate that extracting surface characteristics from laser altimeter pulse-widths is viable in determining global surface roughness and slope estimates from laser altimeter pulse-width data, and a useful implementation for future missions such as BELA, on-board BepiColombo, and GALA, on-board the JUpiter ICy moons Explorer (JUICE) [*Hussmann et al.*, 2013; *Thomas et al.*, 2007].

The following section provides a description of the Mons Gruithuisen Delta region, followed by an overview of the results from all orbits and the best correlating orbits from all sites, as well as an overview of specific orbit results over Mons Gruithuisen Delta. Finally, a discussion on the orbit results, concentrating on those from the case study site.

4.8.2 DESCRIPTION OF MONS GRUITHUISEN DELTA

Mons Gruithuisen Delta is a lunar dome located at 39.6° W 36.2° N, as shown in Figure 4.11. It is one of three lunar domes found around the Gruithuisen Crater (Delta, Gamma, and Northwest), and all of which are classified as nonmare volcanic domes. The nomenclature derives from the nearby Gruithuisen crater. Lunar domes appear similar to the low relief shield volcanoes found on Earth and are typically thought to be produced through the eruption of low viscosity lava from a central magma chamber over relatively long time-periods [*Lena et al.*, 2013]. These volcanic processes have both terrestrial and Martian analogues, such as the shield volcanoes in Iceland and Olympus Mons respectively [*Lena et al.*, 2013]. Figure 4.12 shows a schematic of these *extrusive* processes. Lunar domes may also be formed *intrusively*, whereby the magma never reaches the surface, but instead penetrates rock layers and, under high pressures, forces the rock above, upwards [*Lena et al.*, 2013].

The majority of lunar domes are of very low relief. However, the lunar domes in the Gruithuisen region are of much higher relief, suggesting that they have a very different composition, in particular a high Si and low FeO and TiO_2 content [*Lena et al.*, 2013; *Wilson and Head*, 2003]. *Wilson and Head* [2003] suggest the Gruithuisen domes are an unusual mixture of mare and highland terrain, formed by magma significantly more viscous than mare basalts about 3.70 Ga to 3.85 Ga, with a very slow rise speed of $\sim 7 \times 10^{-5}\,\mathrm{m\,s^{-1}}$ and effusion rates of $6\,\mathrm{m^3\,s^{-1}}$ to $50\,\mathrm{m^3\,s^{-1}}$. This is also shown by the very different spectral signatures, which are also known as *red spots* [*Glotch et al.*,

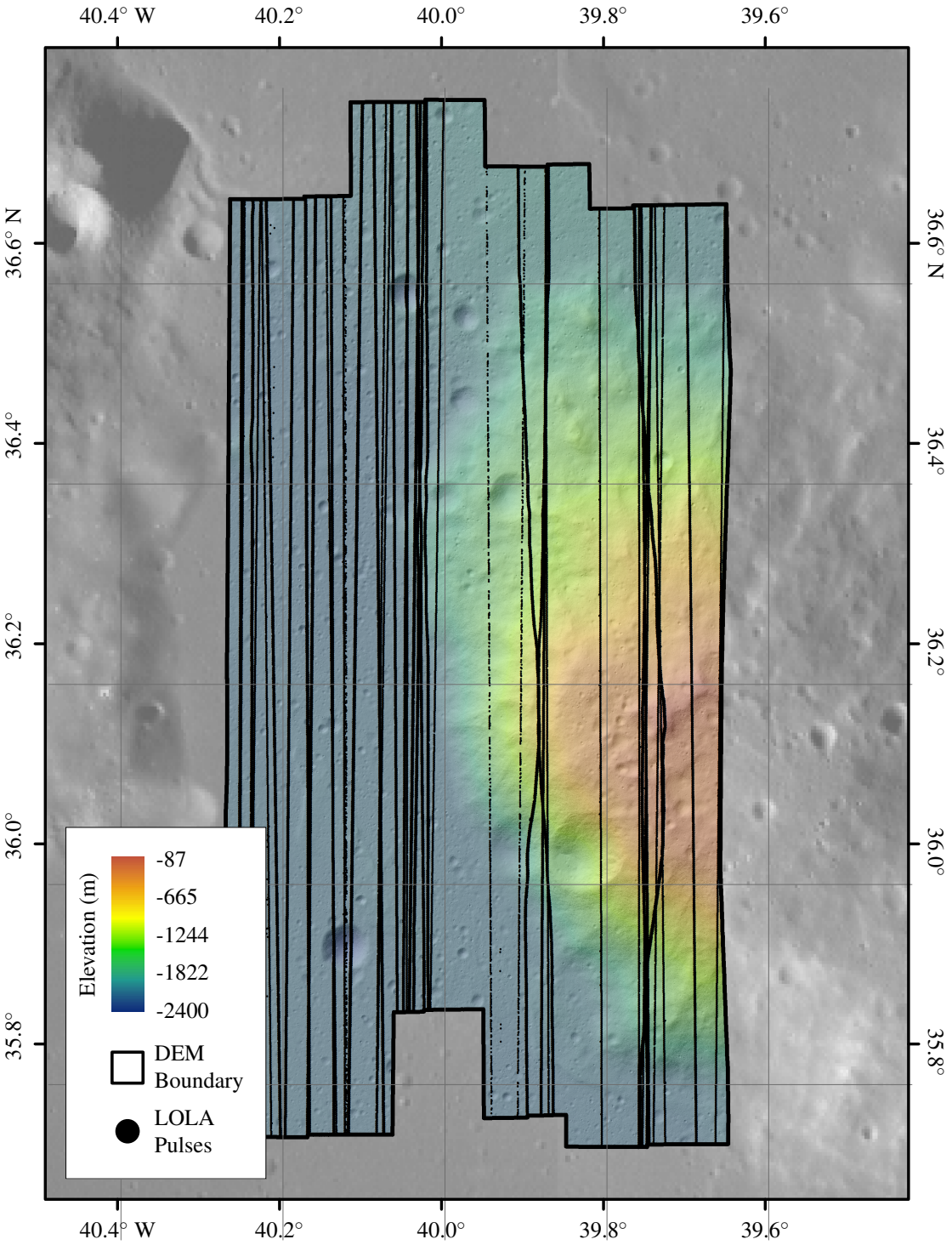

Figure 4.11: Map of the Mons Gruithuisen Delta study site. DTM coverage is shown in colour, which represents elevation of the surface. LOLA locations are shown in black. The background image is from the LROC-WAC global image mosaic.

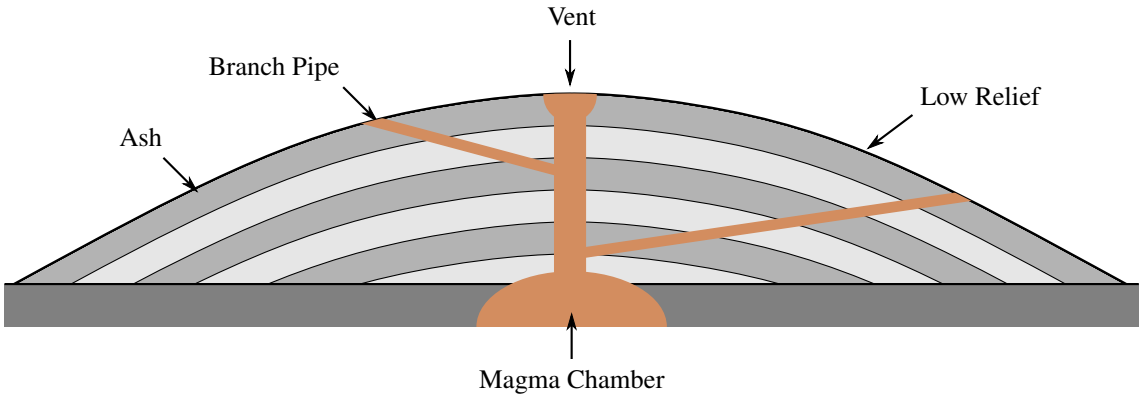

Figure 4.12: Schematic of the possible Mons Gruithuisen Delta formation processes [*Lena et al.*, 2013]. Most lunar domes are thought to be similar to shield volcanoes on Earth, with high viscosity lava forming low relief slopes. The extrusive formation processes take place over long periods of time, with thin layers, which spreads out, slowly stacking up to form a volcanic edifice. The Gruithuisen domes, as well some of the surrounding domes, are thought to be produced from lower viscosity lava with a high Si content, hence have a steeper volcanic edifice, but the overall processes remain the same.

2010]. The formation period is thought to be on the scale of decades, formed from narrow, long dikes (50 m by 15 km), on a flat surface.

The dome itself is approximately 20 km wide and 30 km long, with a topographic rise of 2 km above the surrounding terrain and a mean slope of 8.5° (Figure 4.11) [*Lena et al.*, 2013; *Wilson and Head*, 2003]. The ROI for this study covers only the western most part of the dome, which features a large variations in topography, and heavily cratered terrain. This results in a wide range of surface roughness and slope values to compare to the LOLA pulse-widths over the terrain.

4.8.3 RESULTS

The results are split into three subsections for analysis: all orbits, the best correlating orbits, and select orbits over Mons Gruithuisen Delta.

4.8.3.1 ALL ORBITS

Plots showing the distribution of R-squared values for fits applied to data from individual orbits, and baselines at which these best correlations are observed, for both slope and surface roughness, are shown in Figure 4.13. Only the plots with a p-value of <0.05 when the fit is tested against the null-hypothesis are shown, which typically removes orbits with very few data. The full results are presented in Tables C.4 and C.5 in Appendix C.

From the R-squared distribution plots it is clear that pulse-width data in most orbits show very poor correlations when compared to both surface roughness and slope. Approximately 95 % of the orbits reveal R-squared values of less than 0.4 for both surface characteristics: a threshold chosen as the low limit of when a correlation is observed for individual sites in Chapter 3. Similar distributions are observed for both surface roughness and slope.

One orbit shows very high R-squared values, 1.000 for slope and 0.992 for surface roughness.

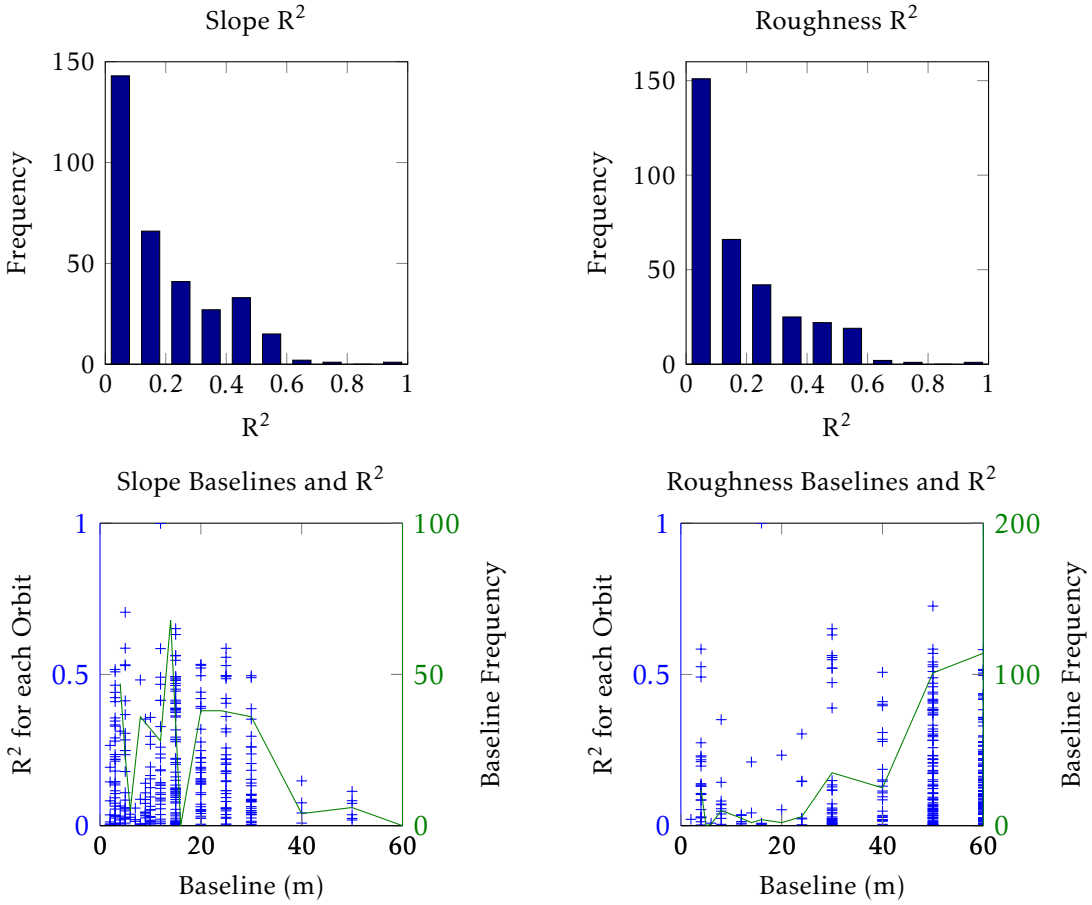

Figure 4.13: Plots of the correlations observed for individual LOLA orbit over all 16 regional sites, using only results that have p-value <0.05 when tested against the null hypothesis. Top plots show the R-squared values of the plots comparing LOLA pulse-widths to slope (left) and surface roughness (right). Bottom plots show the highest R-squared values against the baseline at which these values are found, while the right axis shows a histogram of the frequency of these baselines.

The results for this orbit are considered significant when tested against the null hypothesis, however only 3 data points are used in this calculation, which could suggest this orbit is not representative of other orbits.

The distribution of best correlating baselines show different distributions for slope and surface roughness. Here, the best correlations typically occur at much smaller baselines for slope than those observed using surface roughness, which mirrors the results over the rough terrain using MOLA pulse-widths, as shown in Section 3.8. However, there is little correlation observed when comparing the best correlating slope baselines to the best correlating baselines for surface roughness. This is in contrast to the MOLA results over very rough terrain (Section 3.8), where the best correlations for slope occurred at between 75 m to 100 m, and for surface roughness at 300 m to 400 m.

The results show that the primary aim of this section of work, to identify poor orbits that could be removed from the main dataset to produce better correlated for regional results, is not feasible due to the high proportion of poor data. Instead, a small number of select, well correlating, orbits will be explored in the following section, to determine whether these orbits share a common fit gradient and best correlation baseline.

4.8.3.2 SELECT ORBITS

To explore whether the second aim of the project can be achieved, to determine whether some orbits show strong correlations that could support the hypothesis that surface characteristics can be derived from laser altimeter pulse-widths, this section explores the better correlating plots.

Figure 4.14 shows data from orbits that have a best correlating plot with an R-squared >0.4, chosen because this is the typical R-squared values for sites that showed a correlation using MOLA pulse-width data. From the 329 orbits that are considered significant, only 45 orbits have an R-squared greater than this limit. Of these 45 orbits, only 4 showed R-squared values better than those observed previously (>0.60).

These plots show that, even for better correlating plots, there is no convergence to a common baseline for either slope or surface roughness, which instead appear evenly distributed across the baselines. This shows that even if the best correlating plots could be identified from telemetry data, the data is too inconsistent for surface characteristics derived from the pulse-widths in these orbits

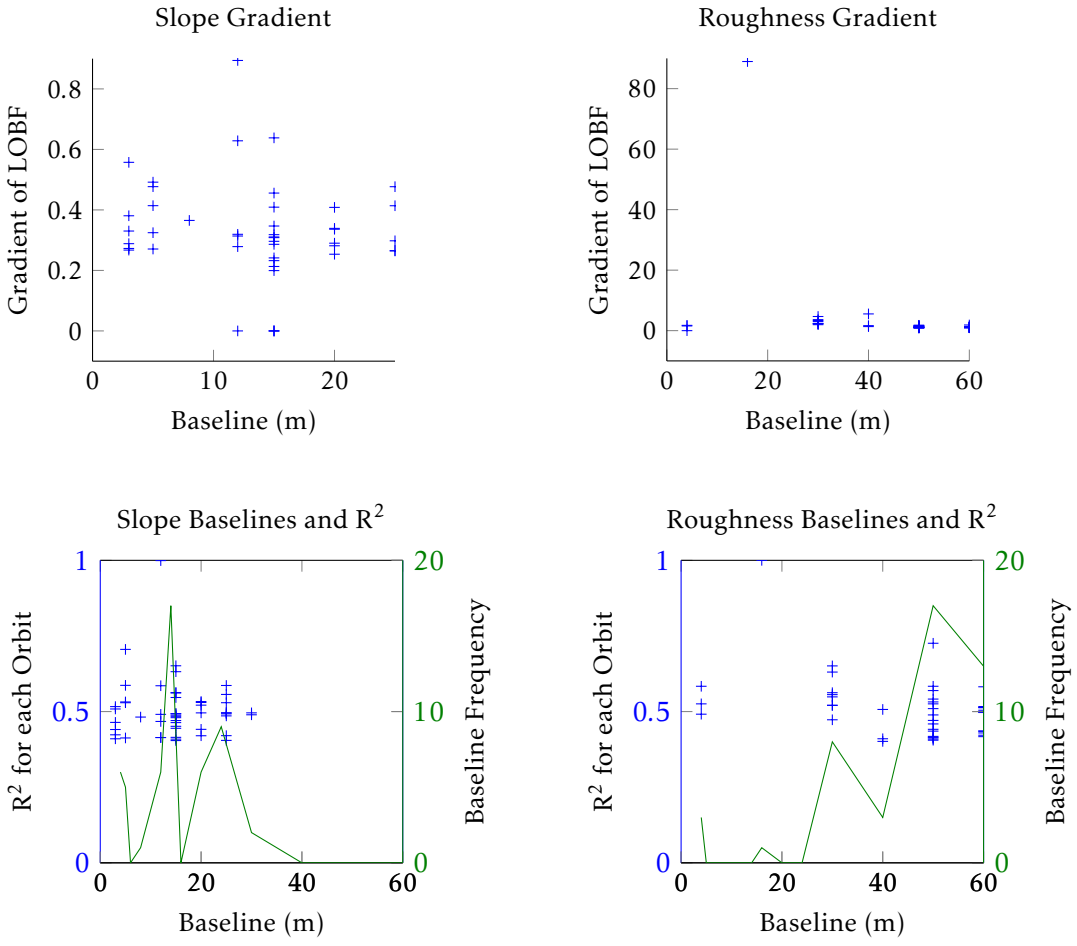

Figure 4.14: Plots of the best correlating individual LOLA orbit results from the 16 regional sites, with an R-squared value >0.4. Top plots show the gradient of the line-of-best-fit compared to the baseline at which the best correlating plot is found. Bottom plots compare the R-squared values to the baseline at which these values are found, while the right axis shows a histogram of the frequency at which these baselines occur.

to be extrapolated to the rest of the lunar surface.

The gradients of the lines-of-best fits are expected to be different due to the different best correlating baselines resulting in different estimates of the surface characteristic. To compare the gradients, one needs to compare the gradients for each baseline separately. Doing this shows that there is great variation in the line-of-best fits, showing that the data is inconsistent across different terrains, which further suggests that fine-scale roughness and slope of the lunar surface cannot be reliably derived from the LOLA pulse-widths.

The following section explores the results over Mons Gruithuisen Delta, which contains some of the highest R-squared values, as well as those that represent typical relationships with surface characteristics.

4.8.3.3 MONS GRUITHUISEN DELTA RESULTS

A selection of the slope results over Mons Gruithuisen Delta are shown in Figure 4.14 and Table 4.5. Figure 4.16 shows the orbits mapped by colour representing the highest R-squared value, when the pulse-widths in that orbit are plotted against slopes of different baselines.

Data from Orbit 3182 produce one of the best correlating plots of all the ROIs, superseded by only one orbit, which contains significantly fewer points. Originally, through visual analysis in Figure 4.10, this orbit appeared to contain only consistently high pulse-widths that showed poor correlations with underlying terrain. However, the observed R-squared values using this orbit are better than any site using MOLA pulse-widths in Chapter 3, suggesting that surface characteristics can be derived from laser altimeter pulse-widths. The smallest pulse-width values are $\sim$20 ns, rather than 0 ns, as they have not been corrected for the other contributors to pulse-width, as defined in Section 2.1.3. The best correlation occurs at 4 m baseline slopes, which is in-line with the estimates of pulse-footprint, whilst for surface roughness the best correlations occur at a baseline of 60 m.

All other plots in Figure 4.15 and Table 4.5 also exhibit the best correlations at 4 m slope baseline, whilst the surface roughness baselines occur at 50 m to 60 m. The pulse-widths follow a

Table 4.5: Surface roughness and slope baselines and R-squared values for the six best correlating orbits using LOLA data over Mons Gruithuisen Delta, as well as all the data points.

		Slope		Roughness	
Orbits	Pulses	R-squared	Baseline (m)	R-squared	Baseline (m)
All Orbits	71 290	0.14	4	0.13	60
1444	964	0.37	4	0.37	60
3182	2452	0.71	4	0.73	50
3531	2351	0.04	4	0.05	50
3879	2423	0.11	4	0.10	60
4921	963	0.57	4	0.58	60
5789	2450	0.24	4	0.26	50

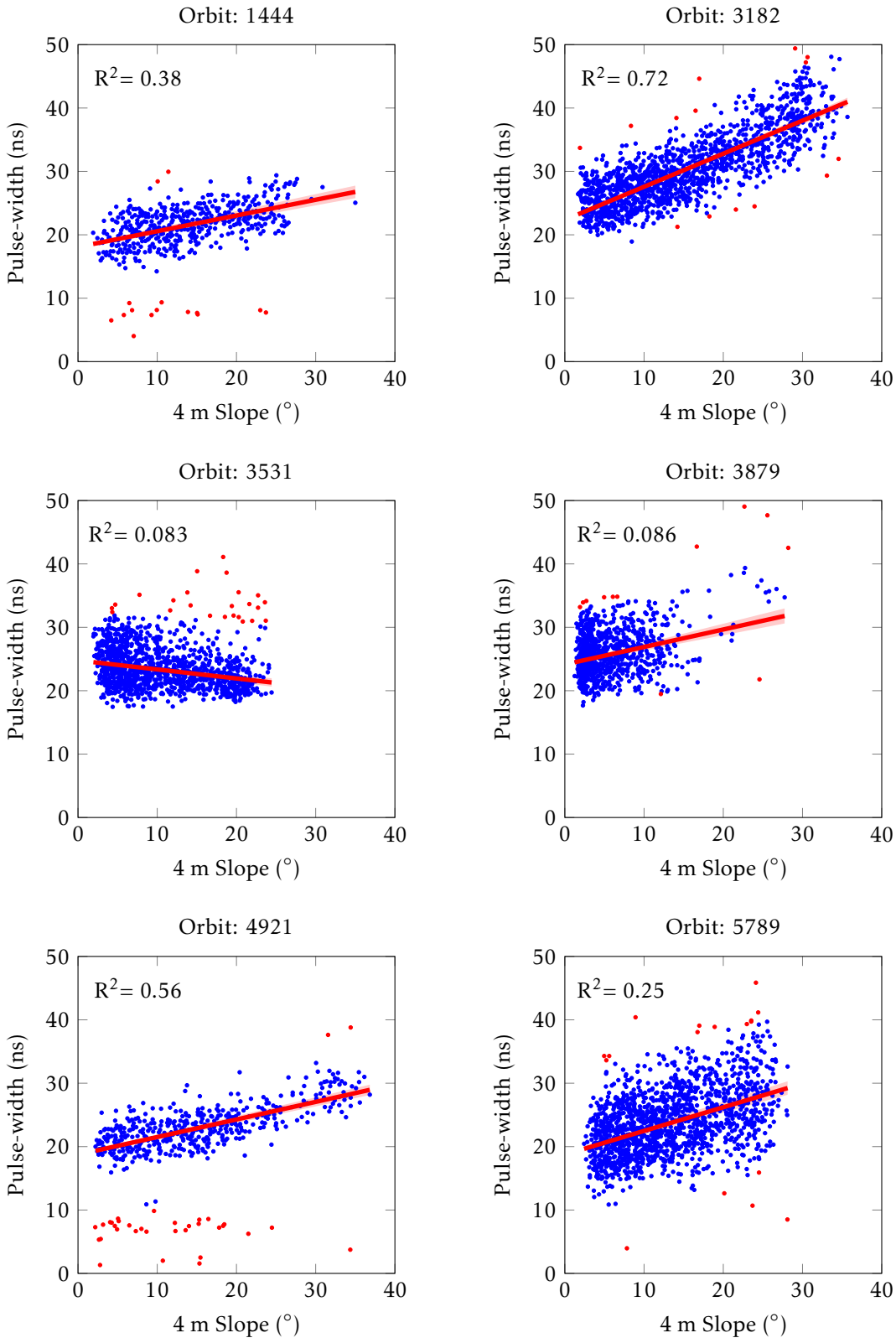

Figure 4.15: Plots comparing LOLA pulse-widths from a selection of orbits to slope over Mons Gruithuisen Delta. The baseline at which these plots are found is shown in the horizontal axis and the R-squared value is shown in the top left of each plot. Red points represent data that is excluded from the line-of-best-fit calculation, as they occur at more than 3σ away.

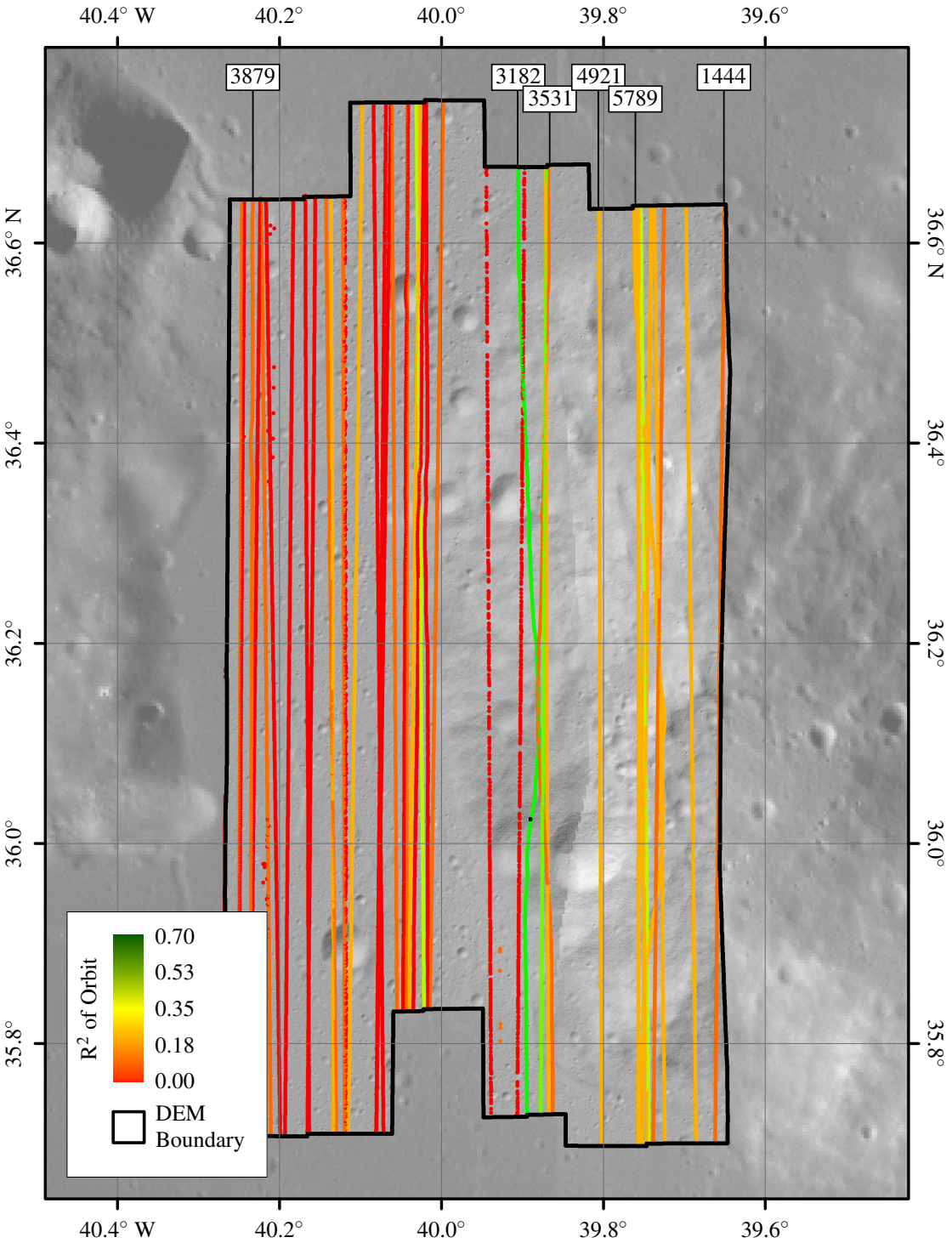

Figure 4.16: Map of the Mons Gruithuisen Delta site showing the individual orbit's R-squared value by colour. Better R-squared values are observed in the east of the image, where there is a greater variation of topography (Figure 4.11), however, calibration over this type of terrain does not always result in strong R-squared values. The image within the DTM boundary are the original LROC-NAC images, mosaicked together. The background image is the LROC-WAC global image mosaic.

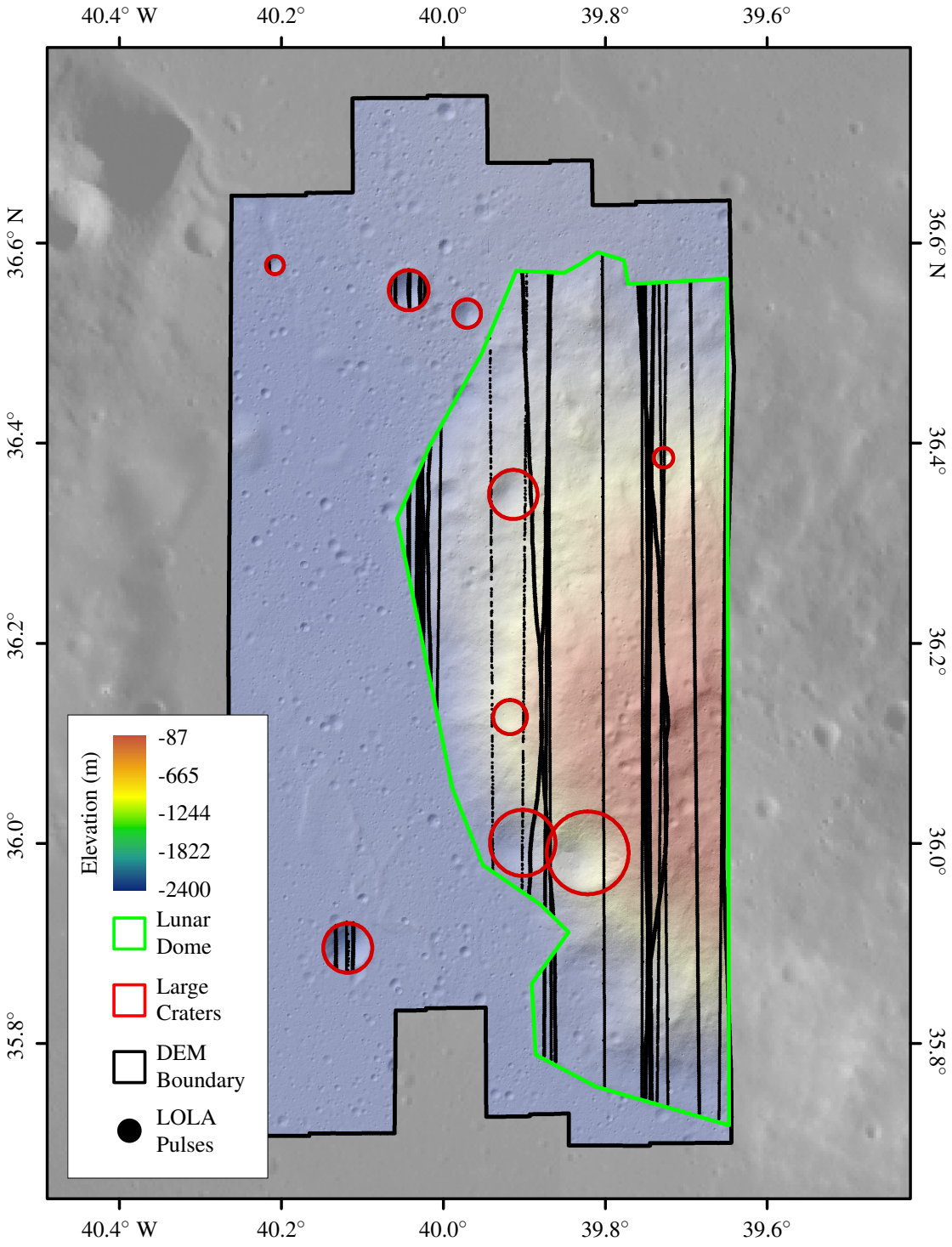

Figure 4.17: Map of the Mons Gruithuisen Delta site showing areas of large topographic variation. The points lying within the boundary of the lunar dome and the large craters in the region are shown. The image within the DTM boundary are the original LROC-NAC images, mosaicked together. The background image is the LROC-WAC global image mosaic.

Table 4.6: R-squared values for the comparisons of 4 m baseline slope and LOLA pulse-widths over the lunar dome and the crater areas of the Mons Gruithuisen Delta site, shown in Figure 4.17. This is to test whether the correlations are improved when only data over the rougher terrain of the site is used. The original R-squared values of comparisons of data from the entire orbit are also shown as a reference.

Lunar Dome			Large Craters		
Orbit	R-squared	Original R-squared	Orbit	R-squared	Original R-squared
All Orbits	0.07	0.14	All Orbits	0.15	0.14
1444	0.16	0.23	1097	0.02	0.23
1966	0.05	0.16	1271	0.19	0.16
2487	0.24	0.30	1444	0.14	0.30
2661	0.16	0.24	1966	0.04	0.24
3182	0.56	0.64	3182	0.21	0.64
3183	0.08	0.11	3183	0.04	0.11
3530	0.09	0.32	3530	0.09	0.32
3531	0.15	0.03	3531	0.00	0.02
3704	0.01	0.02	3704	0.13	0.04
4921	0.24	0.28	3878	0.22	0.28
5789	0.15	0.21	4226	0.01	0.21
5790	0.10	0.15	4921	0.24	0.15
5964	0.11	0.17	5269	0.04	0.17
6312	0.26	0.09	6312	0.06	0.09
7528	0.13	0.18	6833	0.07	0.18
8050	0.42	0.47	7528	0.06	0.47
8223	0.00	0.00	8050	0.06	0.00
8745	0.08	0.01	8223	0.01	0.01
8746	0.00	0.03	8745	0.03	0.03
9440	0.06	0.10	8746	0.01	0.10
9960	0.13	0.19	10 135	0.04	0.19
10 135	0.04	0.08	10 830	0.00	0.08
11 179	0.00	0.05			

similar pattern to the MOLA pulse-widths over rough terrain, whereby pulse-widths are correlated to slope and small baselines and surface roughness at larger ones. However, surface roughness at the baselines observed in Table 4.5 are likely to be better derived from the elevation of the spots within the pulse. Furthermore, this pattern is not observed in other regions of the Moon.

Importantly, the gradients of the lines-of-best-fit in Figure 4.15 are also very different. Direct comparisons can be made as all plots are produced using the same baseline, but the lack of common

gradient suggests that pulse-widths behave very differently on an orbit-to-orbit basis, with no observable pattern with time or the LOLA anomaly.

Correlations using data from two of the orbits, Orbit 1444 and 4921, show a significant improvement in R-squared values when data greater than 3 standard deviations from the original line-of-best fit are removed. Doing so for the latter orbit produces one of the best correlating plots of the study, in-line with R-squared values from Chapter 3. Other orbits presented poorer R-squared values, which are typical of the orbits not presented here. Removing data from more than 3 standard deviations from the line-of-best-fit for other orbits does not improve the results, which continue to show little or no correlation with underlying terrain.

Figure 4.16 shows the R-squared values of the orbits over Mons Gruithuisen Delta. There appears to be some correlation with the R-squared values of the orbits and the underlying terrain. Better correlations are observed on the eastern side of the map, where the greatest variations are observed (Figure 4.11). This may be similar to the effects observed in Section 3.8, supporting the idea that areas of greater topographic variation are required to calibrate the pulse-width data. However, using rougher or more sloping terrain does not automatically result in high R-squared values, as many of the orbits reveal R-squared values less than 0.4, and two orbits not over the roughest terrain have R-squared values greater than this.

To further explore the idea of greater topographic variation yielding improved results, LOLA pulse-widths over only the lunar dome and the larger craters within the boundary of the LROC-NAC DTM mosaic are compared to slope at 4 m. The rough terrain is shown in Figure 4.17, whilst the results are presented in Table 4.6. The craters within the boundary are relatively fresh simple craters, meaning they are bowl shaped depressions within the surface, without a distinct crater floor, meaning further classification is not possible.

The results reveal that correlations are not improved over when only the regions of greatest topographic variation are used, as shown in Table 4.6. For the results over the lunar dome, only Orbits 3531 and 6312 showed some improvement in the observed R-squared values, whereas Orbits 1271, 3704, 4921, and 8050 showed some improvement for the data over the larger craters in the area. However, using only data over rougher terrain does not improve the results as a whole and should not be considered further because (1) the improved R-squared values remain poor, (2) the number of improved results are low, and (3), perhaps most importantly, most of the orbits experience a (sometimes large) decrease in R-squared values, such as Orbit 3182, 3530, and 7528.

4.8.4 DISCUSSION

By focussing on pulse-widths in individual orbits, it is clear that some LOLA pulse-widths can reveal strong correlations when compared to surface characteristics, including fine-scale slopes. However, the majority of orbits appear to contain poor pulse-width data that shows little or no correlation with the underlying terrain. Over Mons Gruithuisen Delta, LOLA pulse-widths correlate to small scale baselines slopes, comparable to current pulse-footprint estimates, and a much larger baseline for surface roughness, similarly to MOLA over rough terrain, which suggests that LOLA

pulse-widths are actually correlated to pulse-footprint-scale slope. This pattern is not observed elsewhere however, with other orbits revealing . Detrended surface roughness cannot be compared to these pulse-widths, as the resolution of the LROC-NAC DTMs is too large for accurate estimates of surface roughness to be derived at pulse-footprint-scales.

An orbit that was assumed to contain poor pulse-width data, Orbit 3182, as it appeared to contain only high pulse-width values, actually reveals one of the best correlations. The changes to pulse-width values in this orbit are not observed in Figure 4.10 due to the colour look-up table used to display the pulse-widths, however, not all orbits that appeared to contain only high pulse-width values reveal strong correlations.

There is a noticeable difference in the spatial distribution of observed correlations, as shown in Figure 4.16. Here, orbits on the eastern edge of the Mons Gruithuisen Delta site appear to produce better correlations than those to the west. This is to be expected, as the eastern edge of the study site also exhibits the greatest range in topography, confirming the idea proposed in Chapter 3 that better correlations can be produced over the roughest terrains. However, not all orbits over the rougher terrain show strong correlations, as many of the orbits still contain poor pulse-width data, shown by the fact that most orbits in this region produce R-squared values typically around 0.35, poorer than those observed using MOLA. This is also shown when only the data over the lunar dome and the craters are used, with most orbits experiencing a decrease in the observed correlations. Instead, using rougher terrain merely improves the probability of a good correlation being observed when the pulse-width data is high quality. Finally, the LOLA anomaly and off nadir pointing angles do not affect the observed R-squared values, with the latter shown by the fact that Orbit 3182, an off-nadir pointing orbit, produces one of the best correlations.

The reason for the poor results is unclear, as there are no atmospheric effects that may cause errors in the pulse-width measurement. Co-registration errors are also not thought to be the cause, as the LOLA and LROC-NAC data appear to be well co-registered, and some orbits reveal very strong correlations. The potential errors may arise in the measurement method itself and the threshold detection system employed by LOLA.

Overall, the high R-squared values of orbits such as Orbit 3182 suggests that laser altimeter pulse-widths can be used as a strong indication of slope within the pulse-footprint of the spot. However, data in the other orbits also suggest that not all LOLA pulse-widths cannot be used to determine fine-scale slopes over the Moon.

4.9 THE MOON CHAPTER SUMMARY

Using LOLA pulse-widths can produce better correlations than those in Chapter 3, however, the dataset contains many pulse-widths that show little or no correlation with surface roughness or slope of the underlying terrain. This shows that laser altimeter pulse-widths can be used to derive surface characteristics from with the pulse-footprint, however, some improvement in methods, either instrument or processing, is required to attain consistent results.

This work has shown that the type of terrain used to calibrate the pulse-widths is important,

with rougher terrains typically producing higher, but not always strong, R-squared values. This is similar to the effect observed and discussed in Section 3.8.

By using an instrument that records the full echo-profile it may be discovered why results are poor over Mars and the Moon, and develop new methods to produce improved correlations between laser altimeter pulse-widths and surface characteristics. This is explored in the following chapter using data from one of two Earth-orbiting satellites, the Ice, Cloud, and land Elevation Satellite (ICESat) and the Shuttle Laser Altimeter (SLA).

5

EARTH: ASSESSING ICESAT PULSE-WIDTHS

The relationship between ICESat pulse-widths and surface characteristics derived from high-resolution lidar DTMs over the McMurdo Dry Valleys, Antarctica, is investigated, influenced by the findings in the previous two science chapters. The aim is to find improved correlations between laser altimeter pulse-widths and surface characteristics compared to the results in the previous chapters by developing and testing new methods made possible by the availability of full echo waveforms, as well as the methods employed by MOLA and LOLA.

ICESat data has two advantages over the previously used pulse-width datasets: (1) it is from an Earth-orbiting satellite and therefore both the pulses and DTMs are more precisely georeferenced due to GPS and INS, and (2) the resulting dataset contains the full echo-profile for each pulse, enabling different pulse-width thresholds to be tested and compared to surface roughness and slope estimates.

The results show that surface roughness and slope can be derived more reliably from laser altimeter pulse-widths when the pulse-width is calculated using the 10 % or 20 % Peak Energy threshold. When the FWHM is used, correlations are similar to those observed over Eberswalde Crater using MOLA pulse-widths, which use similar methods. Detrended surface roughness cannot be derived from pulse-width data here, despite the better co-registration, more accurate estimates of pulse-width from the full echo-profiles, and more metadata on the removal of pulses affected by atmospheric effects.

The principal recommendation for future laser altimeters is to use the full echo-profile at some stage of processing in order to achieve better correlations with surface roughness and slope.

5.1 INTRODUCTION

Ice, Cloud, and land Elevation Satellite (ICESat) full echo-profiles are used to compare laser altimeter pulse-widths to surface characteristics over the McMurdo Dry Valleys, Antarctica. Different pulse-width thresholds can be applied from these echo-profiles, which enables the testing of current and new methods to find improved, and more consistent, correlations between pulse-widths and surface characteristics compared to the results in previous chapters. Improved georeferencing of the laser altimeter data and the Digital Terrain Model (DTM) data, from which surface characteristics are derived, should improve the chances of finding a positive result, whilst comprehensive metadata provides more information regarding the atmospheric conditions when the pulse was fired, which enables different conditions to be tested and a means of effective pulse selection. To relate to Chapters 3 and 4, the work includes a study on bare-earth terrains. The additional availability of icy terrains also enables testing of relationships that could be useful for missions to the icy moons of the giant gas planets. Finally, a series of recommendations are produced for future missions to best collect fine-scale surface characteristics within the pulse-footprint.

The following section summarises current literature on Earth surface roughness and slope studies, as well as a selection of works exploring ICESat data that are relevant to the work outlined in this thesis. Section 5.3 provides an overview of the laser altimeter instrument selection process and a description of the ICESat instrument, and is followed by the study site selection process and lidar instrument and data overview. A description of Earth's coordinate systems is provided, which is relevant to this work as ICESat data needs to be converted between geographic coordinate systems. The methods are described in Section 5.7, followed by the results and a case study exploring the relationship between pulse-widths and surface characteristics over terrain that is highly variable over short baselines. The chapter concludes with a discussion and summary of results.

5.2 LITERATURE REVIEW

Atmosphere-ocean interactions can be determined from the sea-surface roughness, which is to determine the net momentum flux from the air to the oceans [*Drennan et al.*, 2010]. Another form of roughness is aerodynamic roughness length, z_0, which explores the effect of surface roughness elements on the wind speed profile and is an important parameter in modelling land-atmosphere interactions, such as the transfer of heat and momentum [*Bonan et al.*, 2002; *Borak et al.*, 2005; *Sellers et al.*, 1986]. This is not a measure of roughness itself, but is defined as the height above the zero-plane displacement height at which the logarithmic wind speed is equal to 0, and can be used to apply corrections to wind speed estimates [*World Meteorological Organization*, 2010, Part 1. Chapter 5; Part 2, Chapter 11]. A detailed understanding of wind profiles over a 1 yr period is typically required before accurate estimates of aerodynamic roughness length can be derived. However, *Marticorena et al.* [2006] reveal a relationship between this parameter and surface roughness over deserts, which can be used with radar data to derive aerodynamic roughness

length quickly over large areas of desert, a technique that has also been applied in *Hébrard et al.* [2012] over Mars.

Unlike, the previous chapters, global terrestrial surface roughness studies are not relevant to this work due to the high surface water coverage (71 %) and land vegetation coverage [*National Oceanic and Atmospheric Administration*, No Date.b]. Instead, roughness studies are conducted on more local and regional scales.

A common focus of roughness studies is that of vegetation roughness, which is used to determine the water flow through river systems, as vegetation impedes the flow of water through a system [*Augustijn et al.*, 2008; *Hwang et al.*, 2013]. Accurate river models need to take the vegetation roughness along the banks into account when predicting the effects of river restoration projects, or when predicting extreme flooding events [*Vetter et al.*, 2011].

Soil surface roughness, which is closely linked to vegetation roughness, is also explored as can help determining erosion and run-off rates [*Jester and Hancock*, 2011; *Zheng et al.*, 2013]. In the High Arctic, Synthetic Aperture Radar (SAR) is used to discover soil moisture content by modelling out estimates of surface roughness, enabling energy and greenhouse gas fluxes, and nutrient cycling to be deciphered over climatically important, yet poorly accessed, regions of Earth [*Collingwood et al.*, 2014; *Kornelsen and Coulibaly*, 2013]. However, the baselines of interest are on the order of centimetres rather than the metre-scale baselines that are of interest to this study [*Zheng et al.*, 2013].

Gupta et al. [2012] show how sea-ice roughness, which is important when trying to determine energy balance, momentum exchange, and floe size distribution, can be used to categorise sea-ice within the marginal sea-ice zone, whilst *Zwally et al.* [2002] also suggest that sea-ice roughness can be an indicator of the ice's history. Light absorption at the surface is strongly affected by sea-ice roughness: ice is predominantly forward scattering at the particle level and backward scattering when the surface is rough [*Nolin et al.*, 2002; *Pfeffer and Bretherton*, 1987; *Remy and Parouty*, 2009; *van der Veen et al.*, 2009]. Understanding this property of ice is important in the correct interpretation of satellite imagery over icy terrains [*Nolin et al.*, 2002; *Pfeffer and Bretherton*, 1987; *Remy and Parouty*, 2009; *van der Veen et al.*, 2009]. Surface roughness is shown to affect the bidirectional reflectance by *Warren et al.* [1998] in their study of sastrugi (ridges of hard snow shaped by the wind) on ice-sheets, which can be used to infer the direction of prevailing and katabatic winds, and seasonal changes in wind strength and direction [*Remy and Parouty*, 2009]. These sastrugi can cause a reduction in snow albedo, which affects the energy balance of an ice-sheet and sea-ice, similarly to the dune-like features that appear to form through blowing snow over long periods [*Remy and Parouty*, 2009; *van der Veen et al.*, 2009]. Finally, geology and thermal conditions of glacial beds may be revealed by small-scale undulations at the top of the glacier [*Bell et al.*, 1998; *van der Veen et al.*, 2009].

Comparatively few surface roughness studies have been conducted over desert terrains, with come studies using these terrains to calibrate SAR data [*Charlton and White*, 2006]. *Sud and Smith* [1985] show in their simulations that surface roughness may play a part in the rainfall over deserts. Here, the surface roughness is reduced during desertification due to the reduction of vegetation

and subsequent soil erosion -in a process comparable to increasing the albedo of an area-, which in turn causes a reduction in rainfall and further desertification. *Garvin et al.* [1998] use Shuttle Laser Altimeter (SLA) pulse-widths estimates over desert terrains to estimate the vertical roughness using Equation 2.5, finding that the roughness over the Saharan and Arabian deserts are similar to estimates of the Venusion Plains and the Northern Plains of Mars. However, these estimates have not been tested against surface characteristics from DTMs.

Shi et al. [2013] present the only published work investigating the relationship between ICESat pulse-widths and surface characteristics over non-vegetated terrains. This study uses roughness measured from the Advanced Spaceborne Thermal Emission and Reflection (ASTER) Global Digital Elevation Model (GDEM) of glaciers in the Nyainqêntangla range, Tibet, to understand the energy exchange between the atmosphere and glacier surfaces, concluding that ICESat pulse-widths are a suitable means from which to gain valuable surface information. They also observe better correlations when comparing pulse-widths and slope, compared to pulse-widths and surface roughness, as in Chapters 3 and 4 of this thesis. A drawback of the study is that it uses low resolution DTM data (30 m pixel^{-1}), which results in less precise estimates of surface roughness, as only 7 pixels to 9 pixels lie within the pulse-footprint, as well as potential errors in the slope values due to common errors from stereo-photogrammetry.

More commonly, ICESat echo-profiles are used to infer vegetation structure, such as *Harding and Carabajal* [2005] and *Lefsky et al.* [2005]. Over vegetated terrain, the profile has two prominent peaks: the first provides an estimate of the forest canopy height, and the second is a ground return. This can be used to provide an estimate of the biomass content of an area over flat terrain, defined as slopes of $<10°$ [*Hilbert and Schmullius*, 2012]. For larger slopes, the effect of pulse-width broadening due to slope effects, as in Equation 2.7, cause a blurring of the canopy and ground returns, making it more difficult to decipher canopy height reliably [*Hilbert and Schmullius*, 2012].

5.3 LASER INSTRUMENT SELECTION AND DESCRIPTION

Two Earth orbiting laser altimeter instruments provide the full echo-profile for each pulse: ICESat and SLA [*Garvin et al.*, 1998; *Schutz et al.*, 2005]. This section outlines the process of deciding which of these instruments should be used and a description of the chosen instrument, ICESat.

5.3.1 INSTRUMENT SELECTION

The instrument selection process focussed primarily on dataset coverage, and partly coincides with the site selection process, as bare-earth terrains with high-resolution DTM coverage are required to produce estimates of surface characteristics, to which the pulse-widths are compared (Figure 5.1). The minimum requirements were extensive, high-resolution DTM coverage over non-vegetated terrains that is freely available for this work.

The profiles of both ICESat and SLA are compared to explore which instrument provides the best coverage over bare-earth terrains. Figure 5.1 shows the coverage of the SLA data, which operated for 82 hrs on-board Space Shuttle *Endeavour* [*Garvin et al.*, 1998]. The dataset has very

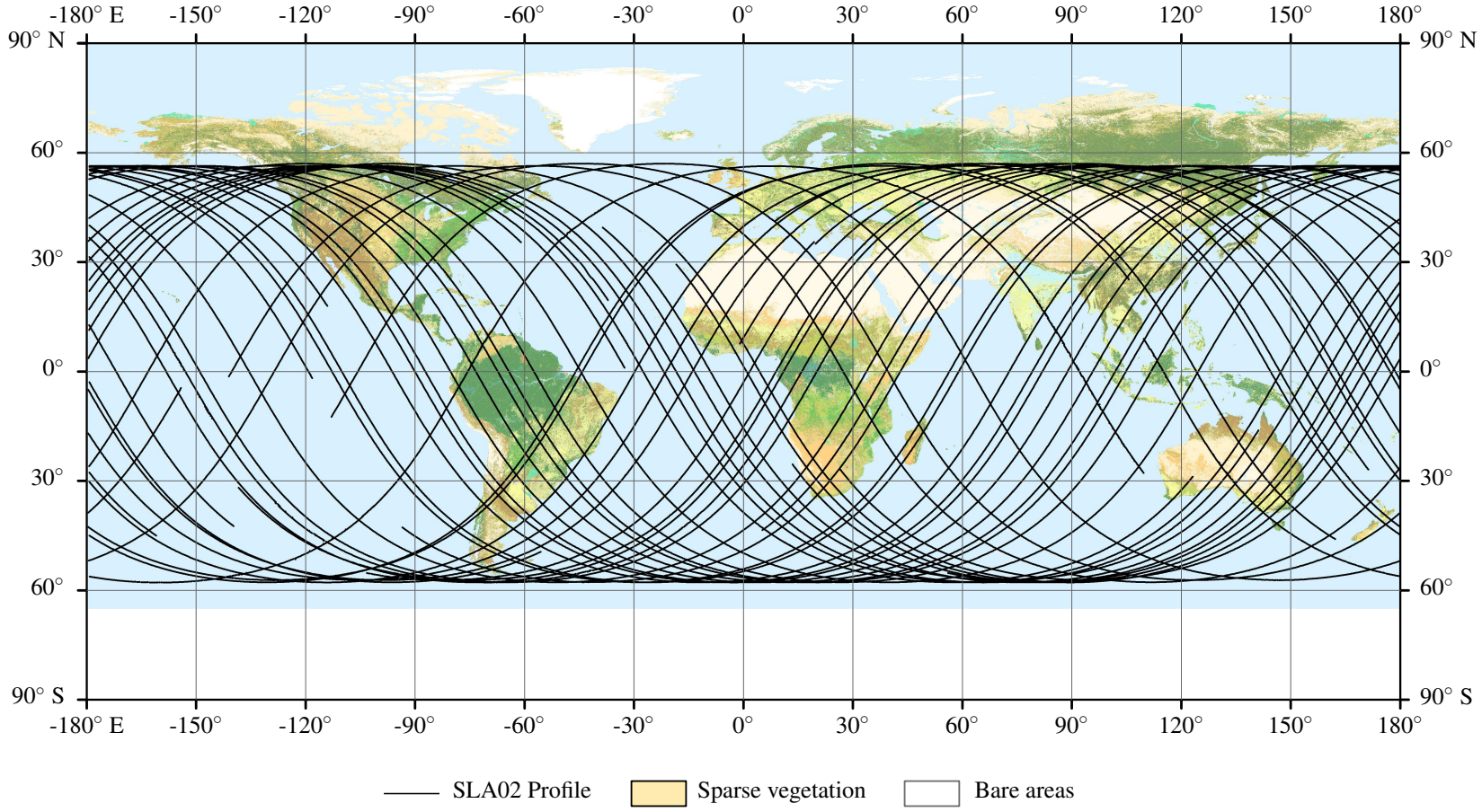

Figure 5.1: Map of SLA coverage and global land cover, highlighting the two terrains of interest for this study [*ESA*, 2011; *Garvin et al.*, 1998]. The equivalent ICESat profiles are not shown as the higher density of orbits obscures the underlying map.

low coverage, with relatively few passes over bare-earth terrains, such as the Sahara, Australia, and the deserts of the United States of America (USA) [*OpenTopography*, 2014; *United States Geological Survey*, 2014]. Furthermore, the dataset had a low pulse-rate that results in inter-footprint spacings of $\geq$600 m [*Garvin et al.*, 1998]. Within the latitudinal extents of SLA, freely-available high-resolution DTMs with significant coverage exists only over the USA, produced from lidar mapping campaigns [*OpenTopography*, 2014; *United States Geological Survey*, 2014]. The benefit of using this instrument rather than ICESat is that it is a very similar model to that employed by Mars Orbiter Laser Altimeter (MOLA), and may therefore exhibit similar behaviours that enable us to determine how the Mars results presented in Chapter 3 could be improved. On the other hand, this instrument is based on much older technology, with only a 5 ns timing resolution, and the data has large georeferencing errors of 100 m to 200 m, such that it may not provide the best conditions to derive new methods.

ICESat data has much greater spatial coverage, with a greater number of orbits that extend very close to the poles, despite orbiting on a 91 day fixed polar-orbit. This extends the range of sites that can be used in this work. A global map of the orbits is not shown due to the high density of orbits covering the underlying land coverage. The aims of ICESat require high precision geolocation of data, helped by the advent of Global Positioning Systems (GPS) and improved positioning methods, which are all discussed in the following section. Furthermore, the greater timing resolution results in more accurate estimates of pulse-width, and additional metadata is available to explore the role of energy distribution across the pulse-footprint on correlation between laser altimeter pulse-widths and surface characteristics [*Schutz et al.*, 2005].

To conclude, the ICESat instrument is used in this chapter as the provides significantly more pulses and better quality metadata to enable more accurate comparisons of pulse-widths and surface characteristics over terrestrial terrains. Atmospheric effects will play a significant role in pulse selection, therefore a higher density of pulses, more information as to the conditions in which these pulses were fired, and improved geolocation of the data, enable a better understanding of the relationship between pulse-widths and surface characteristic to be developed.

5.3.2 ICE, CLOUD, AND LAND ELEVATION SATELLITE

The primary aim of the ICESat mission was to determine seasonal and annual changes in the ice-sheet volume to enable the effect on global sea-level to be assessed [*Schutz et al.*, 2005; *Zwally et al.*, 2002]. One objective of the instrument, which was operational between 2003 and 2009, was to use laser altimetry to determine changes in ice-sheet elevation of $<$2 cm yr^{-1} over areas of 100 km $\times$ 100 km regions over $\geq$3 yrs [*Schutz et al.*, 2005; *Zwally et al.*, 2002]. The Geoscience Laser Altimeter System (GLAS) instrument was the only science instrument on-board ICESat[1], whilst a series of engineering instruments ensure high geolocation and elevation accuracy of the resulting data. A schematic of the satellite is shown in Figure 5.2 and an overview of the characteristics is provided in Table 5.1.

[1]The terms GLAS and ICESat are interchangeable, as ICESat is a single science instrument mission, but the instrument is usually referred to as ICESat

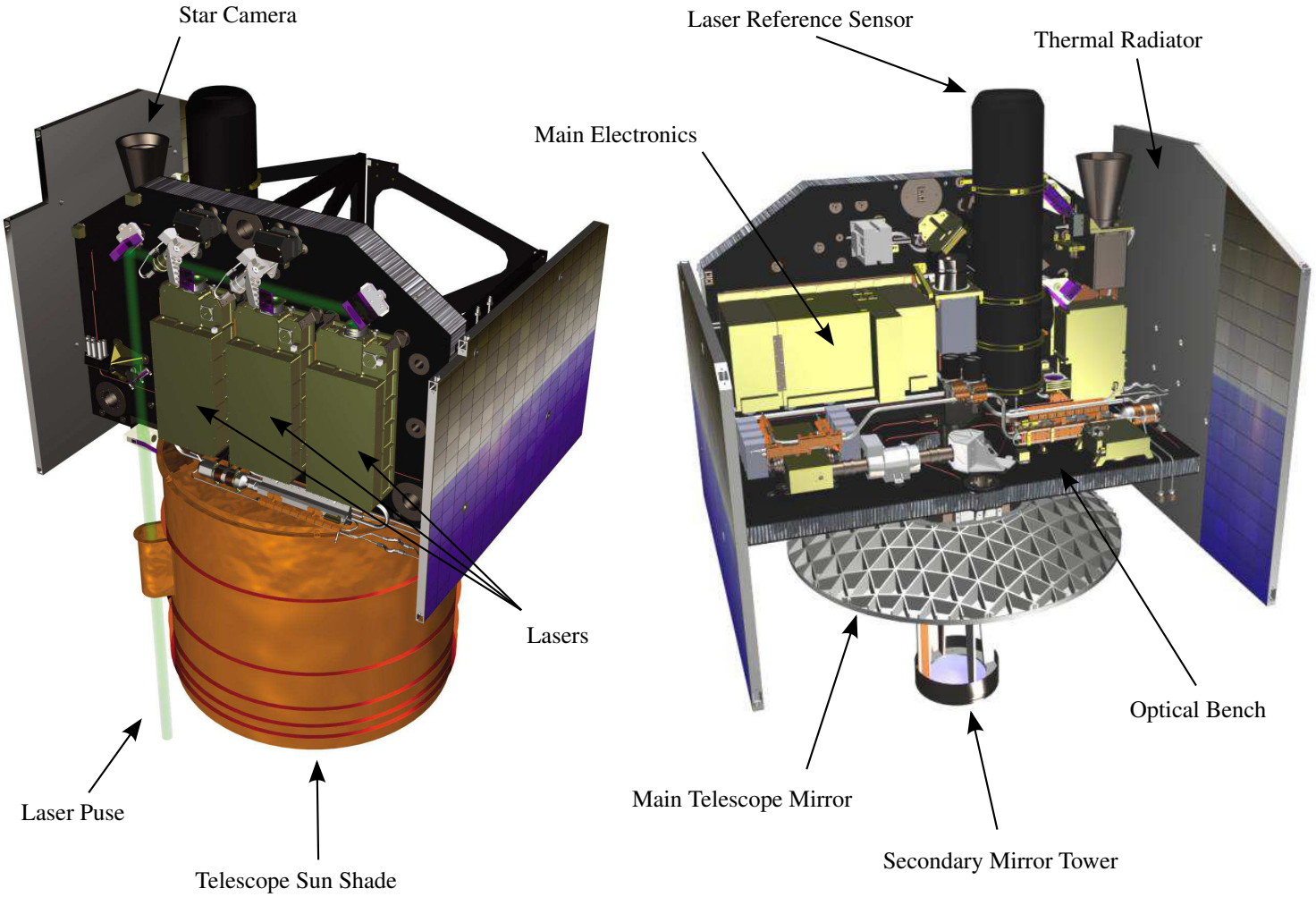

Figure 5.2: Schematic of the instruments on-board ICESat. The characteristics of the satellite are outlined in Table 5.1.

Table 5.1: The characteristics of ICESat, which carries the GLAS instrument, from *Schutz et al.* [2005] and *Zwally et al.* [2002].

Element	Parameter	Specification
ICESat	Mass	330 kg
	Power consumption	310 W
	Mapping Orbit	600 km
	Orbit Inclination	94°
	Orbit Length	91 day with 33 day sub-cycle
	Maximum Roll	±5°
Transmitter	Laser type	(3) Nd:YAG, diode pumped, Q-switched
	Wavelength	1064 nm
	Pulse Rate	40 Hz
	Energy	75 mJ pulse^{-1}
	Laser Divergence	110 µrad
	Pulse Length	4 ns to 6 ns
	Pulse Time-of-Flight	4 µm
Receiver	Mirror	1 m
	Detector	Silicon Avalanche Photodiode
	Field of view	500 µrad
	Detector Efficiency	60 %
Electronics	Timing Resolution	1 ns
Resolution	Vertical accuracy	<10 cm
	Pulse Footprint	60 m to 70 m
	Pulse Spacing	172 m

The mission used a 94° inclination orbit to achieve global coverage, especially over the world's ice-sheets and, in particular, areas of change over West Antarctica [*Schutz et al.*, 2005]. To determine seasonal and annual changes, a 91 day repeat orbit track was used with 1354 individual orbits [*Schutz et al.*, 2005; *Zwally et al.*, 2002]. The mission repeated these reference tracks to within ±1 km, performing manoeuvres regularly to overcome orbit decay to ensure a spacecraft altitude of 600 km [*Schutz et al.*, 2005]. To ensure the mission met the minimum lifetime requirement of 3 yrs, three lasers were fitted on the instrument. The lasers were designed to operate alternately, with pulse paths directed by mirrors so that path geometry remained similar [*Zwally et al.*, 2002]. The typical satellite pitch was 0.3° from nadir to mitigate the damage from specular reflection, as described in Section 2.1. Other off-nadir pointing was enabled by spacecraft roll (±5°) to produce measurements of surfaces away from the reference tracks (≤50 km) and account for orbit drift [*Schutz et al.*, 2005].

Near the poles however, the instrument pointed only at nadir to ensure repeat measurements to within ±100 m of the reference track [*Schutz et al.*, 2005].

To meet the geolocation and elevation requirements of the mission, the satellite carried two star-trackers, two GPS systems, a laser retroreflector array, and an altitude control system [*Sirota et al.*, 2005]. These systems enabled an instrument position vector and a range vector, accurate to within 1.5″ pointing accuracy, to be derived for each pulse, from which a series of georeferenced elevation values referenced to the Topex/Poseidon reference ellipsoid were produced [*Schutz et al.*, 2005; *Sirota et al.*, 2005]. These measurements also enabled highly accurate slewing for tracking of targets and reduction of pointing jitter [*Schutz et al.*, 2005]. All the instruments on-board were rigidly mounted to maintain relative pointing geometry of the instruments throughout the mission [*Schutz et al.*, 2005; *Sirota et al.*, 2005].

The higher pulse-rate of the instrument, compared to MOLA, results in a small inter-footprint spacing (∼170 m), but the pulse-footprint size is similar (Table 5.1) [*Schutz et al.*, 2005; *Smith et al.*, 2001]. The data density around the poles is higher due to the near-polar orbit of the instrument.

ICESat, unlike the laser altimeters used in the previous chapters, recorded the full echo-profile of the return energy [*Schutz et al.*, 2005]. Profile sampling began just before pulse transmission, at a sampling resolution at 1 ns (1 GHz), and ended after 4 ms (Table 5.1) [*Schutz et al.*, 2005]. The search for the expected ground return used a 1°×1° DTM, in effect, searching for the end of the profile before working backwards, such that the sample time is negative [*Schutz et al.*, 2005]. For pulses over land, 544 samples were extracted and provided in the Level 1A dataset, whilst 200 samples were provided over sea-ice and water due to the lower relief within the pulse-footprint [*Schutz et al.*, 2005]. These relate to potential elevation variations capable of being detected within the pulse-footprint of 81.6 m and 30 m, respectively, when using Equation 2.2.[2]

To accurately determine the vertical distribution of clouds and aerosols, part of the 1064 nm pulse produced from the Nd:YAG lasers was converted to 532 nm using a doubler crystal [*Schutz et al.*, 2005]. The profile from the shorter wavelength pulse was also used to correct range determination estimates from the original 1064 nm pulse and determine the optical thickness and extinction within the atmosphere [*Spinhirne et al.*, 2005]. This not only improves the range determination estimates, but also provides the means to be able to highlight pulses that were affected by atmospheric effects, either through backscatter from cloud and aerosol layers, or by broadening of the pulse-width, as discussed in Section 2.1.

In total, 15 different datasets, across 3 Levels of processing are available from ICESat. The raw science and engineering data was downlinked at Level 0, and processed into Level 1A data, across four datasets, as shown in Table 5.2. These Level 1A and Level 1B, which contain the engineering corrections, are combined to produce the Level 2 products. The work presented here uses Version 33 of the datasets, whilst at the time of writing, Version 34 is in the process of being released for each of the laser campaigns [*National Snow and Ice Data Center*, 2014b]. Table 5.2

[2]Over land, where 544 samples are taken, this relates to a maximum pulse-width of 544 ns. When this time is applied in Equation 2.2 to determine the distance light can travel in this time is 81.6 m. Similarly over the sea-ice and water, where 200 samples are taken, the maximum distance is 30.0 m.

Table 5.2: The different Hierarchical Data Format (HDF) 5 datasets available from ICESat data, with the typical file size, the number of orbits per file, and the number of files produced per day [*National Snow and Ice Data Center*, 2014b].

Product	Level	Description	File Size (MB)	Orbits/File	Files/Day
GLAH01	L1A	Global Altimetry Data	9	1/4	56
GLAH02	L1A	Global Atmosphere Data	671	2	7
GLAH03	L1A	Global Engineering Data	19	2	7
GLAH04	L1A	Global Laser Pointing Data	2 to 386	2	4
GLAH05	L1B	Global Waveform-based Range Corrections Data	25	1/4	56
GLAH06	L1B	Global Elevation Data	7	1/4	56
GLAH07	L1B	Global Elevation Data	827	2	7
GLAH08	L2	Global Planetary Boundary Layer and Elevated Aerosol Layer Heights	7	14	1
GLAH09	L2	Global Cloud Heights for Multi-layer Clouds	82	14	1
GLAH10	L2	Global Aerosol Vertical Structure Data	289	14	1
GLAH11	L2	Global Thin Cloud and Aerosol Optical Depths Data	13	14	1
GLAH12	L2	Antarctic and Greenland Ice Sheet Altimetry Data	104	14	1
GLAH13	L2	Sea Ice Altimetry Data	107	14	1
GLAH14	L2	Global Land Surface Altimetry Data	209	14	1
GLAH15	L2	Ocean Altimetry Data	279	14	1

shows the number of orbits per file, and the number of file produced per day for each dataset. Although a dataset sub-setter is available via *National Snow and Ice Data Center* [2014b], for larger regions, it is best to download and extract data from the original files. Fortunately, the reference orbits are available via *National Snow and Ice Data Center* [2014d], which contain the latitude and longitude for pulses within each orbit. From this data, the relevant orbit(s), and file(s), over the Region-Of-Interest (ROI) were identified and downloaded via the File Transfer Protocol (FTP) site [*National Snow and Ice Data Center*, No Date.].

In this work, the HDF5 formatted data is used, which can be read into MATLAB for processing [*National Snow and Ice Data Center*, 2014b]. Of interest to this study are the (1) Geoscience Laser Altimeter HDF5 format data (GLAH)01 dataset, which contains the original echo-profile, (2) GLAH04, which contains the Laser Profile Array (LPA) data, (3) GLAH05, which contains an estimate of the Root-Mean-Square (RMS) pulse-width from a profile fitted to the original received pulse, and (4) GLAH14, which contains precise pulse-footprint location, elevation, orientation, and

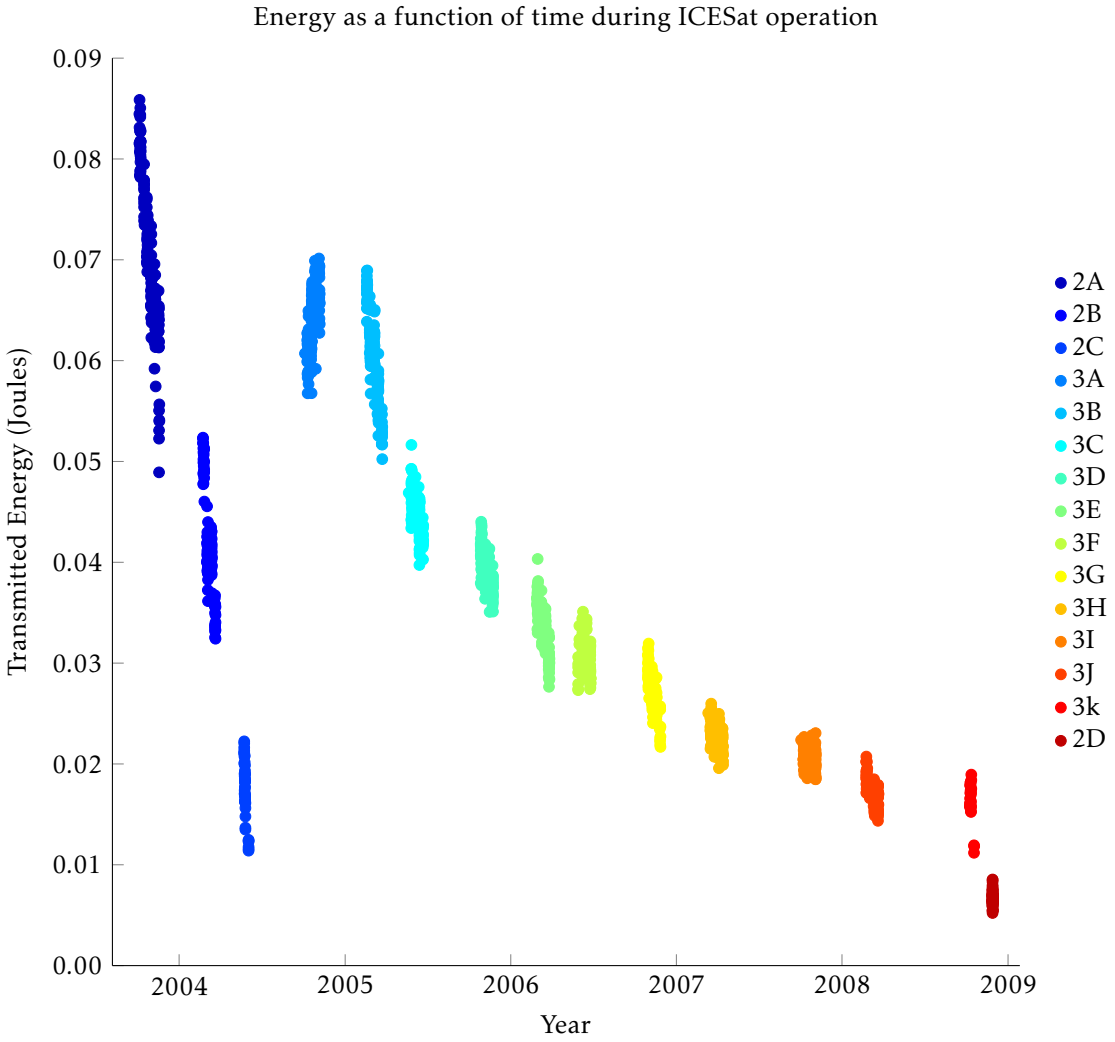

Figure 5.3: Plot of the ICESat transmitted energy per pulse, using only those pulses used in this study, as a function of time and Operational Period. Colours represent the different Operational Periods shown in the legend on the right, where the number representing the laser number, and the letters representing the Operational Period for that laser. Laser 1 is not shown as data from this laser is not used in this work.

dimensions, as well data flags, such as those that highlight potential cloud layers and scattering, from pulses collected over land (Table 5.2) [*National Snow and Ice Data Center*, 2014b].

The LPA data provides an image of the far-field pattern of the laser pulse energy. It is collected at 1 Hz and used to determine the shape and orientation of the pulse-footprint, which is determined at the region greater than e^{-2} (13.5 %) the peak energy at the centre of the pulse-footprint [*Brenner et al.*, 2011]. The image is 20 pixels $\times$ 20 pixels and each pixel images 16.5 µrad ($\sim$10 m pixel^{-1} at an altitude of 600 km), and can be used to investigate the role of energy distribution across the pulse-footprint in determining surface characteristics within the pulse-footprint [*Brenner et al.*, 2011].

Each laser was expected to last for over 1×10^9 pulses, however, Laser 1 failed after a little over a month due to manufacturing defects. These defects were thought to be present in the two remaining lasers, leading the mission team to reduce the operational period to a single 33 day

sub-cycle, three times per year, and reducing instrument capacity to 27 % to ensure the mission completed its minimum lifetime requirement [*Abshire et al.*, 2005; *Kichak*, 2003; *Schutz et al.*, 2005]. Although Laser 2 fired more than three times the number of pulses emitted by Laser 1, 417.5×10^6 pulses compared to 126.8×10^6 pulses, it too saw significant decline in energy output after a short period, which is associated with the frequency doubler and trace levels of out-gassing; subsequently, Laser 3 was operated at a lower temperature (13 °C to 16 °C), which extended the laser lifetime to 11 operational periods (Figure 5.3) [*Abshire et al.*, 2005].

5.4 DIGITAL TERRAIN MODELS

This section describes the process behind the selection of the McMurdo Dry Valleys, Antarctica, as the study site, and the a description of the Airborne Topographic Mapper (ATM), which produced the high-resolution DTMs over the region [*Csatho et al.*, 2005].

5.4.1 SITE SELECTION

The basemap in Figure 5.1 shows the global land coverage by type from European Space Agency's (ESA) GlobCover project [*Arino et al.*, 2007; *Bontemps et al.*, 2011; *ESA*, 2011]. Of interest to this study, is the 22.83 % of the land surface that is sparsely (<15 %) vegetated and bare-earth, which have spatial coverages of 8.80 % and 14.03 % respectively [*Arino et al.*, 2007; *Bontemps et al.*, 2011; *ESA*, 2011]. Additionally, 1.81 % of the surface is covered permanently by snow and ice, free from man-made objects and vegetation. These areas can be used in this work provided the conditions at the site remain stable over relatively long time periods, i.e. low snow fall and slow ice-velocities, and high-resolution DTM coverage was produced at a similar time to pulse-width data acquisition [*Bontemps et al.*, 2011]. A stable site is a fundamental requirement, as it enables the full time-series of ICESat data to be used, increasing the number of pulses that can be used and therefore increasing the probability of a statistically significant relationship to be derived between pulse-widths and surface characteristics. Finally, the study site must be an extensive region of terrain surveyed at high-resolution (1 m pixel^{-1} to 5 m pixel^{-1}), with freely available data, and lie along multiple ICESat flight paths to increase the number of pulses.

Initial searches focussed on DTMs available over the USA, due to the extensive regions of desert and the high-resolution mapping, with data available from *Planetary Data System* [2014b], *Open-Topography* [2014], and *United States Geological Survey* [2014]. However, the spatial extent of the highest resolution data is too small, or the data was not ideally positioned for multiple flight paths over the site, further affected by ICESat running at 27 % capacity, which meant that no data was acquired for many of the 1354 orbits [*Abshire et al.*, 2005]. Data at 0.1″ to 0.33″ resolution available from *United States Geological Survey* [2014] is extensive, but appears noisy over bare-earth terrain and is therefore not used.

As part of the ICESat calibration, the McMurdo Dry Valleys, Antarctica, were surveyed at high-resolution by NASA's ATM, with the data available from *United States Geological Survey* [2013] [*Csatho et al.*, 2005; *Schenk et al.*, 2004]. In total, 20 DTMs were produced, which are

shown in Figure 5.4. There are several advantages to using this data. First, the data was used for ICESat calibration and therefore produced to high standard, meaning that elevation and geolocation errors have been minimised with GPS data. Secondly, the site is situated close to the south pole, and therefore has a higher density of orbits compared to mid-latitude bare-earth sites due to the 94° ICESat orbit inclination. Finally, and possible most importantly, the local microclimate, described in Section 5.5, keeps the surface very stable and free from ice, snow, and vegetation, which enables the results from this study to remain relevant to other sites used in this thesis.

The McMurdo Dry Valleys site and dataset fits the requirements outlined at the beginning of this section. The following section discusses the ATM instrument and the resulting datasets in more detail. A characterisation of the McMurdo Dry Valleys is discussed in Section 5.5.

5.4.2 AIRBORNE TOPOGRAPHIC MAPPER

The ATM instrument is a scanning lidar developed by NASA to collect high-resolution topographic data over regions of scientific interest [*Csatho et al.*, 2005]. The instrument operation is shown schematically in Figure 2.12 on Page 69, and the characteristics are outlined in Table 5.3 [*Csatho et al.*, 2005].

The ATM is designed to measure topography, and changes in topography, over featureless icy terrains [*Manizade*, 2012]. A problem with attempting to map these terrain types is how to accurately steer the aircraft over a precisely defined flight path, so that the flight paths overlap and repeat flight paths can be flown for accurate changes in topography to be determined. In response, the Course-Deviation Indicator (CDI) system was developed [*Manizade*, 2012]. This system can guide the aircraft along straight flight paths over 100 km long, which are technically *great circles* across the Earth's surface [*Manizade*, 2012]. In cases where an Instrument Landing System (ILS) is available, this system can be used to steer the aircraft along the desired flight path.

For mapping smaller, winding flight paths, such as those required for glacier mapping, a secondary system known as Soxmap was developed [*Manizade*, 2012]. This system is also useful for filling geographical areas with parallel swathes, but only provides a visual interface of current and previous flight paths for the pilot, rather than the ability to control the aircraft itself. These systems can be used indepentently or in tandem to produce a visual navigation system for pilots to fly to a predefined flight path that produces high-quality datasets, and have become known as the Global Positioning Flight Management System (GPFMS). The typical cross-track error in the flight paths, when compared to post processing using differential GPS, is ±50 m, but this does not affect the positioning and elevation values of the resulting dataset, which instead uses all the available positioning data from GPS, differential GPS, and Inertial Navigation Systems (INS) to determine the location of each pulse [*Manizade*, 2012]. Finally, software developed at NASA, removes outlying elevation data and stitches overlapping flight paths together, ensuring that heights in overlapping areas of flight paths match through bundle block adjustment [*Csatho et al.*, 2005; *Krabill et al.*, 2002].

The ATM collected data from $\sim 1 \times 10^9$ pulses over the McMurdo Dry Valleys during a two

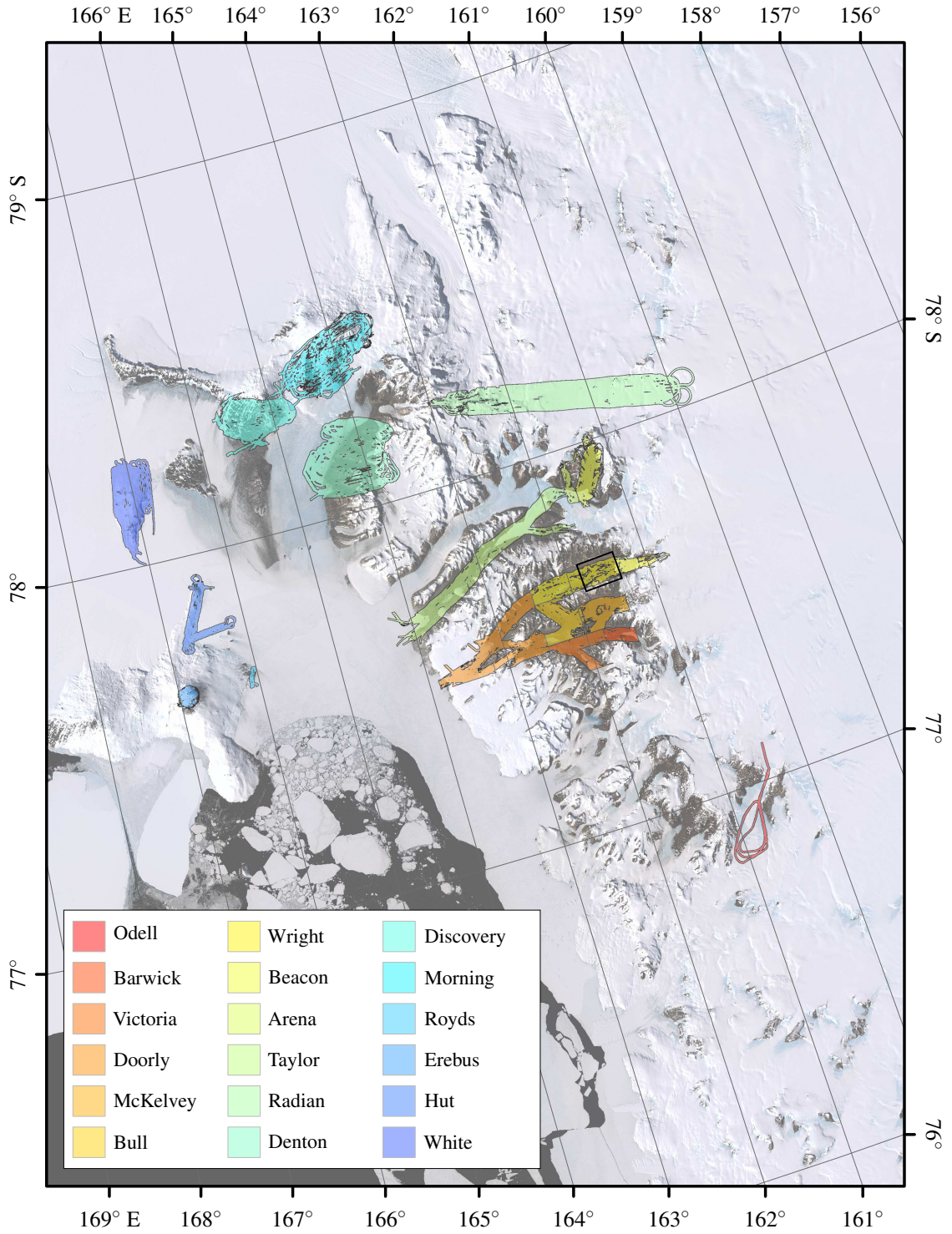

Figure 5.4: Map of ATM DTM over the McMurdo Dry Valleys, Antarctica [*Csatho et al.*, 2005].The region highlighted in black is an area known as the Labyrinth, which is described below, and used specifically in Section 5.9. A Landsat image mosaic is shown in the background. The projection system is South Pole polar stereographic projection, with the South Pole towards the top.

Table 5.3: The characteristics of the ATM instrument.

Element	Parameter	Specification
Lidar	Laser	Diode pumped Nd:YAG
	Wavelength	1064 nm
	Off-nadir Angle	15°
	Scanning Rotation Rate	20 Hz
	Laser Pulse Rate	5 kHz
	Footprint	1 m
	Laser Data Density	0.37 m^{-2}
Flight	Altitude	∼500 m
	Speed	∼50 m s^{-1}
	Aircraft	DC-8, twin-otters (DHC-6), C-130's and P-3

week period in the Antarctic summer of 2001 and 2002, producing 20 DTMs over 18 regions, and covering almost 4600 km^2 [*Csatho et al.*, 2005; *Schenk et al.*, 2004; *United States Geological Survey*, 2013]. DTMs over Odell Glacier, Radian, Denton Hills, Mount Discovery, and White Island (Figure 5.4), are available at 4 m $pixel^{-1}$, with the remaining available at 2 m $pixel^{-1}$ [*Schenk et al.*, 2004]. The DTMs are produced in reference to the World Geodetic System 1984 (WGS 84) ellipsoid, projected using the Lambert Conformal Conic, described in *Snyder* [1987], and available in Tagged Image File (.tif) format [*Schenk et al.*, 2004].

A secondary data processing phase was conducted by Ohio State University to improve elevation and geolocation accuracy, and remove outlying points [*Csatho et al.*, 2005]. A median filter, which can be fine-tuned for efficient noise removal, was applied to remove the outlying points within localised regions, with the total number of removed pulses per DTM numbering between 10^4 to 10^5 points, from a total of 10^6 pulses (∼1 %). Systematic errors, such as overlapping profiles, were corrected for by minimising the elevation differences between adjacent data points. The result is an irregular point cloud that was converted to a regular grid by interpolation using an adaptive process that automatically selected a suitable interpolation method, such as planar or higher order surfaces, based on local terrain points. Additionally, the vertical accuracy of the DTMs was compared to GPS data from geodetic GPS receivers, which provide a very accurate measurement of geolocation and elevation, (0.01 m to 0.20 m accuracy) [*Schenk et al.*, 2004]. The interpolated grid points are found to have an RMS error of 0.2 m [*Csatho et al.*, 2005]. The DTM also went through a visual inspection to remove metre-scale errors from the datasets [*Csatho et al.*, 2005].

Today, the ATM is predominantly used for operation IceBridge, which attempts to determine changes in ice-sheet mass balances and sea-ice extents over the Arctic and Antarctic, until ICESat 2 is launched, but it has also been used for coastal and ocean wave height studies [*Abdalati et al.*, 2010; *Manizade*, 2012; *Yi et al.*, 2015].

5.5 CHARACTERISTICS OF THE MCMURDO DRY VALLEYS

The McMurdo Dry Valleys are a series of ice-free valleys running for ∼50 km from the Trans Antarctic Mountains towards the coast in the Victoria Land region of Antarctica. Together they form the largest permanently snow-free region on the continent (∼4800 km^2), enabled by two conditions: (1) the Trans Antarctic Mountains block ice from the East Antarctic Ice Sheet and moisture in the atmosphere from entering the valley systems, and (2) strong katabatic winds flow down the valleys from the mountains, warming as they descend, and resulting in sublimation of ice and snow from the surface [*Doran*, 2002; *Campbell et al.*, 1998; *McMurdo Dry Valleys Long Term Ecological Research*, 2013a; *Prentice et al.*, 1998].

The valleys were formed by glacial processes, shown schematically in Figure 5.5, when the extent of the ice in the region was much greater. *Prentice et al.* [1998] propose three distinct periods of glaciation (in decreasing age): *High*, *Intermediate*, and *Low*. During the *High* and *Intermediate* phases, at least some of the ice is thought to have come from local mountain glaciers, with some contribution potentially from the East Antarctic Ice Sheet, whereas the main ice contribution during the *Low* phase is thought to be the East Antarctic Ice Sheet. Dating from the floor of Wright Valley suggests these phases occurred before (9.0 ± 1.5) Ma, with the *High* phase occurring possibly ∼34 Ma, which is thought to be a period of significant glaciation around Antarctica [*Prentice et al.*, 1998]. The climate during each of these phases is thought to be significantly warmer and wetter than today, as the erosional features appear to be formed by wet-based glaciers[3], fast flowing glaciers (m a^{-1} to m day^{-1}) that cause significant erosion of bedrock and transport significant volumes of material [*Prentice et al.*, 1998]. This has left wide, characteristically U-shaped valleys that have not been further modified by glaciation, and dotted with boulders deposited from retreating glaciers and glacial till, unsorted glacial material that has been mixed and deposited in moraines.

The proposed wet-based glaciers appear to have been replaced with cold-based glaciers[4] found at much higher elevations, which, unlike wet-based glaciers, have little or no movement and therefore were assumed to not transport significant amounts of material [*Prentice et al.*, 1998]. In a more recent study, *Hambrey and Fitzsimons* [2010] show that the cold-based glaciers found in the McMurdo Dry Valleys today, do transport sand and gravel, accumulating debris through folding and thrusting at the basal layers, and aeolian deposition upon the ice surface [*Benn and Evans*, 2010]. However, they also note that the time-scale is much slower and that the resulting landforms, such as terminal moraines, appear stable on thousand-year time-scales.

Today, several tongue shaped glaciers flow between passes in the mountains into the McMurdo Dry Valleys, such as the Commonwealth Glacier that flows into Taylor Valley, but the extremely

[3] A wet-based glacier is where the base of the ice layer in a glacier exceeds the melting point due to pressure from above, which allows the glacier to slide more freely, called *basal-sliding* [*Benn and Evans*, 2010]. Typically, this enables more entrapment of material and glacial plucking through freeze-thaw actions creating cracks in the bedrock. This embedded material then causes abrasion as it is transported by the glacier, scouring the bedrock.

[4] The glacier basal layer of a cold-based glacier does not exceed melting point, and therefore there is little or no basal-sliding. As a result, there is little or no abrasion compared to cold-based glaciers, but material can become entrapped from the substrate, where upon it can be eroded through internal forces [*Benn and Evans*, 2010; *Hambrey and Fitzsimons*, 2010].

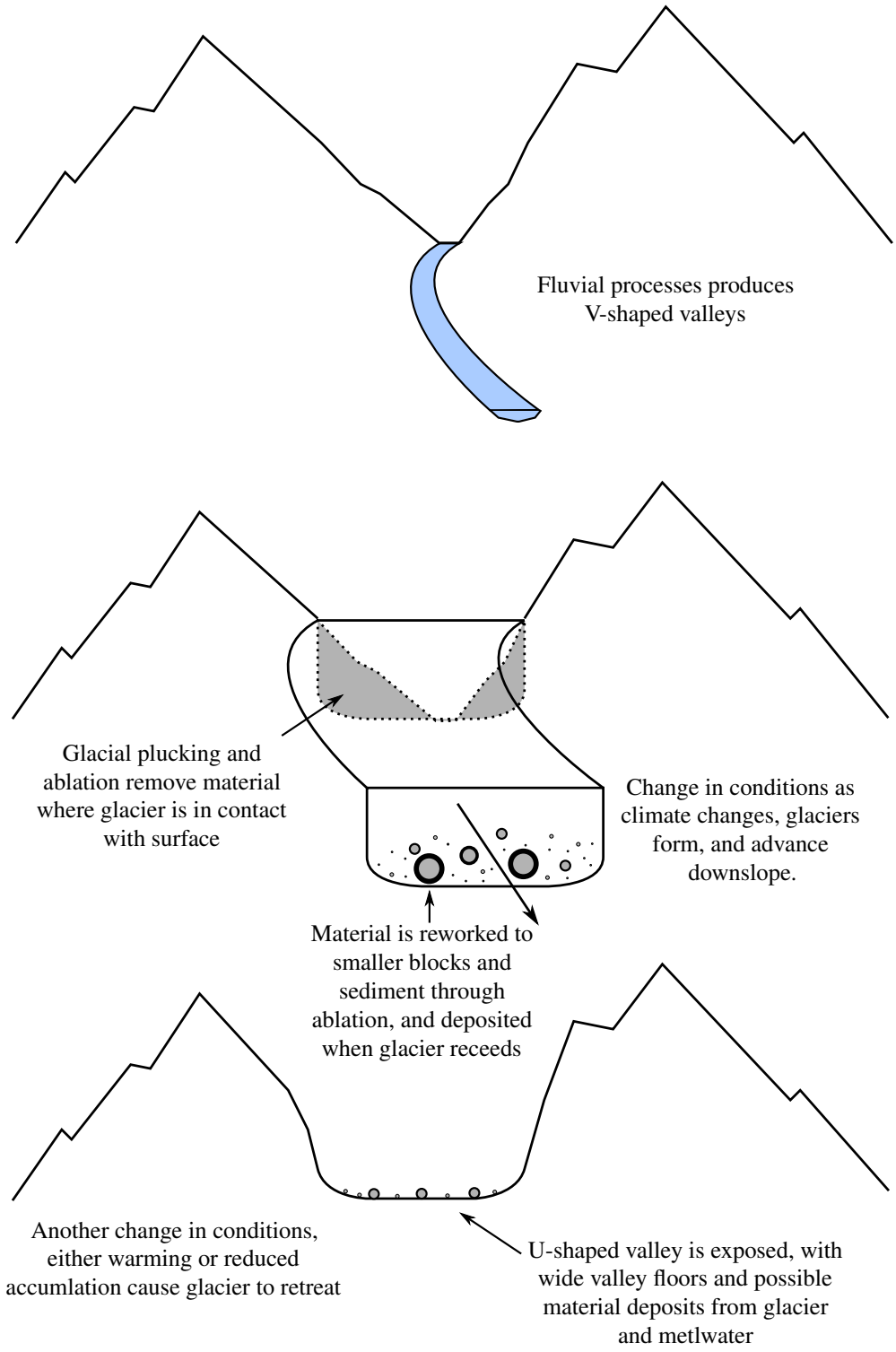

Figure 5.5: Schematic of fluvial and glacial valley morphologies. Top shows a typical fluvial cut valley, whilst middle and bottom show a glacial valley, with a characteristic U-shape. Material is cut from the bedrock through plucking and abrasion and transported down stream by the flow of ice. When the glacier recedes due to changing environmental conditions, the transported material is deposited on the valley floor, and the terminal moraine shows the maximum extent of the glacier.

arid air causes rapid sublimation of any ice that breaks away [*Doran*, 2002; *Fountain et al.*, 2009; *Prentice et al.*, 1998]. The low temperatures (−18 °C), low humidity, and limited precipitation (<100 mm water-equivalent), caused by a rain-shadow effect from the Trans Antarctic Mountains, make this a hyper-arid cold polar desert [*Fountain et al.*, 2009; *Marchant and Head*, 2007]. The primary source of water in the valleys is from glacial summer meltwater, which is generally low in volume, from ice and snow deposits higher up the valley walls [*Doran*, 2002; *Doran et al.*, 2010; *Marchant and Head*, 2007].

Downslope winds are funnelled by the valley system towards the coast, with speeds typically up to 38 m s^{-1} [*Doran*, 2002]. Two downslope winds are observed, particularly during the winter months [*Speirs et al.*, 2010, 2012]. Katabatic winds are most common, and form as air at high elevations cools by radiating heat, thus causing it to become denser and flow downslope under gravity. Another downslope wind observed in the McMurdo Dry Valleys are polar foehn winds, which are different as they originate at low elevations on the windward side of a topographic high. The air cools adiabatically by orographic lifting, i.e. being forced up a topographic slope, and deposits precipitation on the windward side of the mountain. Thus, when the wind passes over the topographic high and descends, it is much drier. In both cases, the descending air warms adiabatically and increases the air temperatures on the valley floors. *Speirs et al.* [2010] observe changes of >40 °C by foehn winds, which warm more than it cooled due to a lower moisture content relative to the windward side [*Speirs et al.*, 2010].

Precipitation on the valley floors is effectively doubled as the winds transport snow from higher up the valley, however, they also act to erode and sublimate any snow deposited on the valley floors, keeping the overall snow cover low *Fountain et al.* [2009]. These winds also shape the terrains by picking up grains of sand and dirt and effectively sandblasting the large boulders and rocks strewn across the valley floors into interesting shapes [*Doran et al.*, 2010]. Such features are known as ventifacts and can be used to indicate paleo-wind direction, with the ridges and groves lying parallel to the prevailing wind direction.

The combination of these conditions makes this region a Mars analogue site. Of particular interest is the potential for life in these extreme environments, with endolithic photosynthetic bacteria found in the interior of rocks, which is relatively moist, and anaerobic bacteria living in the ice of Taylor Glacier, living off iron and sulphur [*Doran et al.*, 1994, 2010; *Prentice et al.*, 1998]. Planetary scientists are also exploring the analogues for surface processes, such as the recurring slope lineae and *swiss cheese* terrain, which occur in the mid-latitudes and polar caps of Mars respectively [*Doran et al.*, 2010; *Levy*, 2012; *MacClune*, 2003; *Marchant and Head*, 2007].

The permanently dry conditions and ancient, slowly evolving landscape that is free of vegetation, make this region an ideal calibration site, enabling pulses from the entire ICESat time-series to be used. The DTMs over the site mainly cover the valley floors, with Hut, Odell, Radian, and White being the only significantly ice covered regions. The snow and ice covered peaks of the mountains and valley walls are also not covered, such that the DTMs cover the areas of least change. The wealth of ICESat data over the site mean that different atmospheric conditions can be tested, which should indicate the best conditions to successfully derive surface characteristics.

5.6 EARTH'S COORDINATE SYSTEMS

Two Earth reference systems are employed in the data used in this chapter, Topex/Poseidon and WGS 84, which are described in Table 2.2. The Topex/Poseidon system is used by ICESat, whilst the WGS 84 system is used by the McMurdo Dry Valley DTMs [*Schenk et al.*, 2004; *Schutz*, 2001]. Unlike the Martian datasets used in Chapter 3, the reference surfaces in both datasets are in relation to reference ellipsoids, rather than an equipotential surface, which for Earth is referred to as the geoid. This makes it easier to convert elevations between different coordinate systems, as different coordinate systems may employ different models of the geoid.

To ensure correct co-registration of data, the ICESat data is converted to the WGS 84 reference system using the equations set out in Section 2.2.5 in software from *Haran* [2004] that was converted to MATLAB format [*Ligas and Banasik*, 2011; *Meeus*, 1991]. The decision to convert the ICESat data, rather than the DTM data, was taken because the WGS 84 system is typically more common, and it is simpler to convert point data than the large raster datasets from ATM.

5.7 METHODS

The methods employed in this chapter, which are very different to those applied in previous chapters due to the precise knowledge of pulse-footprint location and availability of the full echo-profile, are outlined here.

5.7.1 DTM PROCESSING AND QUALITY CONTROL

The DTMs, which are available from *United States Geological Survey* [2013], were loaded into a single ArcMap 10.2 project for viewing and processing. To maximise the extent of data that can be used, they were mosaiced together to form a single, large, DTM, using the *Mosaic to New Raster* Tool. The resolution of the new DTM, which is shown in Figure 5.6, is $2\,\mathrm{m\,pixel^{-1}} \times 2\,\mathrm{m\,pixel^{-1}}$ and projected using the south polar stereographic coordinate system to better view the data. For a pulse to be used in the study, the entire pulse-footprint must lie within the boundary of the DTM data, by mosaicing the DTMs pulse-footprints that lie on the boundary of two or more DTMs can now be used.

A hillshaded image was produced from the mosaiced DTM to identify ROIs of poor quality elevation data. Rather than the pits and spikes observed as a result of poor stereo-matching, lidar may produce spikes of data due to atmospheric backscatter triggering the receiver before the ground-return. Two layers of processing had already been applied to the data to identify poor echo-returns, which explains why no areas of poor data were identified here. However, during the DTM detrending finer-scale errors, $\leq$10 cm inconsistencies in neighbouring DTM post heights, were identified in some areas. Errors at these scales are not thought to affect the results from non-detrended surface roughness comparisons.

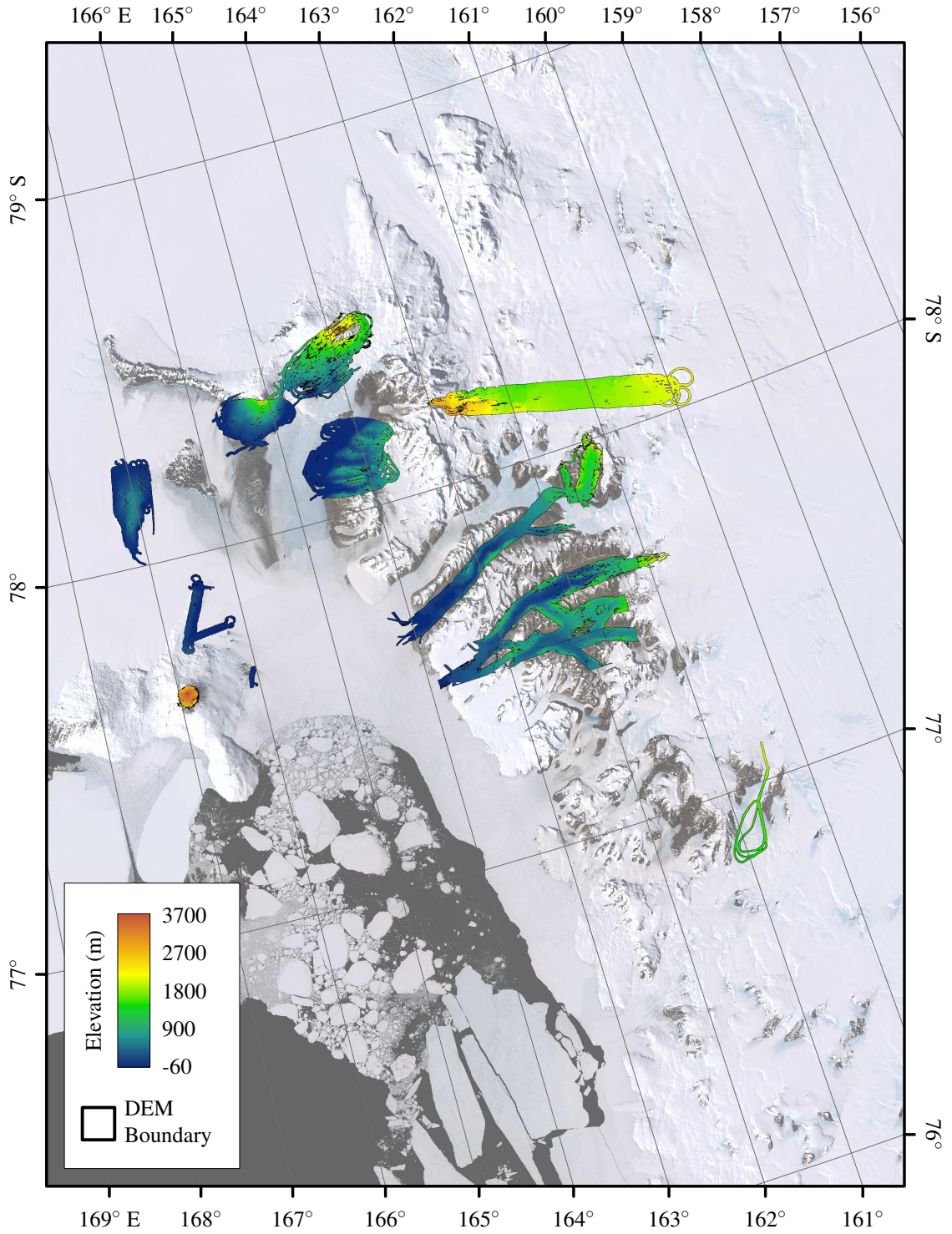

Figure 5.6: Map of ATM mosaiced DTM elevation over the McMurdo Dry Valleys, Antarctica. The individual zones are shown in Figure 5.4. A Landsat image mosaic is shown in the background. The projection system is South Pole polar stereographic projection, with the South Pole towards the top.

5.7.2 ICESAT DATA COLLECTION

To identify the orbits that may contain data over the McMurdo Dry Valleys, all ICESat reference ground-track orbits, available from *National Snow and Ice Data Center* [2014c], that appeared to contain one or more data points over a large ROI, defined approximately as the map coverage area in Figure 5.4 (and subsequent maps of the area), were identified. All GLAH01, GLAH04, GLAH05, and GLAH14 files that contain data from the identified orbits, using laser 2 and 3, were downloaded from the ICESat FTP site at *National Snow and Ice Data Center* [No Date.].

To identify the relevant data, pulses within each GLAH14 file were mapped in MATLAB to identify whether they fell within the boundary of a mask, produced from the mosaiced DTM extent minus a 70 m buffer. This mask was produced using the *Con* Tool in the *Spatial Analyst* > *Conditional* Toolbox to produce a logical raster of 0's and 1's, where 1 was a raster value and 0 was a no-data pixel. The *Raster to Polygon* Tool in the *Conversion Tools* Toolbox was then applied to produce a polygon where there is a raster value to produce a mask of the raster area. The *Buffer* tool was then used to produce a 70 m buffer either side of a line at the circumference of the raster. This buffer area was then removed from the polygon of the raster coverage using the *Erase* tool, to produce the final mask to select ICESat pulses. A 70 m buffer was used to ensure that all the pulses that lay within the boundary had pulse-footprints that lay entirely in the boundary of the DTM.

The GLAH14 files were used to identify pulses because they represent the highest level of processing, and were therefore better geolocated than the Level 1 data. These files also show metadata regarding quality of a pulse, aiding the pulse selection process. The pulse record and pulse numbers that fall within the mask were recorded. All the data for the identified pulses were extracted from the GLAH01, GLAH04, GLAH05, and GLAH14 and saved to a single MATLAB structure file, preserving the precision and file structure in the original HDF5 file, and enabling faster processing in MATLAB.

In total, 49 orbits contain data over the larger ROI, from which 624 GLAH14 files, 4254 GLAH04 files, and 34 199 GLAH01 and GLAH05 files are available. From these files, over 36 000 pulses were found to lie within the mask and have a valid return, which are mapped in Figure 5.7. Most of the data for each pulse, i.e. the received signal, elevation, location, and many warning flags, are available at the same timing resolution as the pulse-rate, meaning that pulse selection process can be completed at full resolution. However, some data is recorded at 1 Hz. As a result, the ICESat record number is recorded at 1 Hz, and the pulse number within each record is logged at 40 Hz, and therefore falls between 1 to 40.

5.7.3 CO-REGISTRATION

The altitude control system, GPS, and star-trackers on-board ICESat enable the geolocation of each pulse to be known to within a few metres [*Schutz*, 2001; *Zwally et al.*, 2002]. This is significantly better than MOLA and Lunar Orbiter Laser Altimeter (LOLA) data used in the previous chapters [*Smith et al.*, 2001, 2010b]. The geolocation was further improved by co-registering the data to the high-resolution DTM data, as noted by *Harding and Carabajal* [2005].

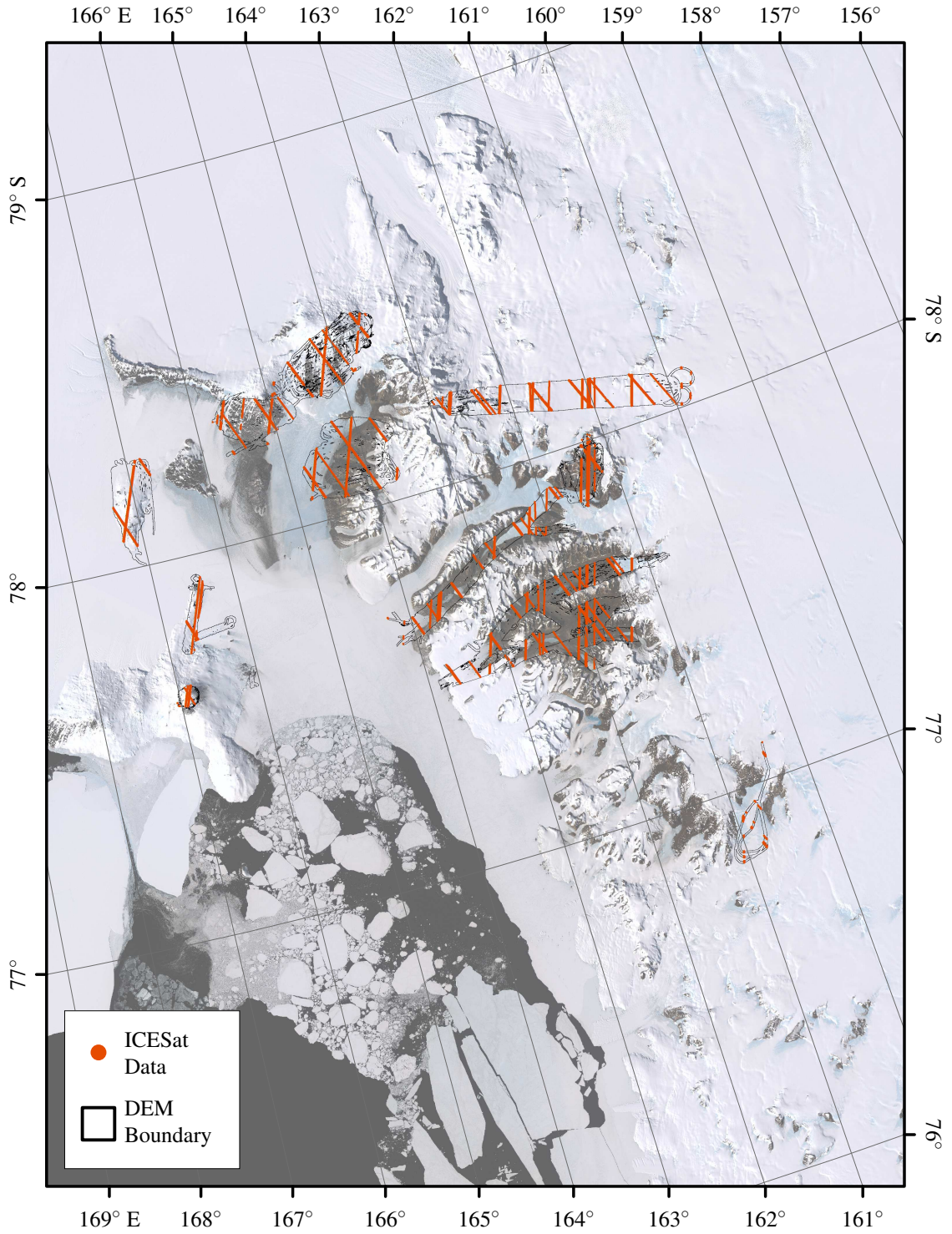

Figure 5.7: Map of ICESat laser pulse locations within the mask. A Landsat image mosaic is shown in the background.

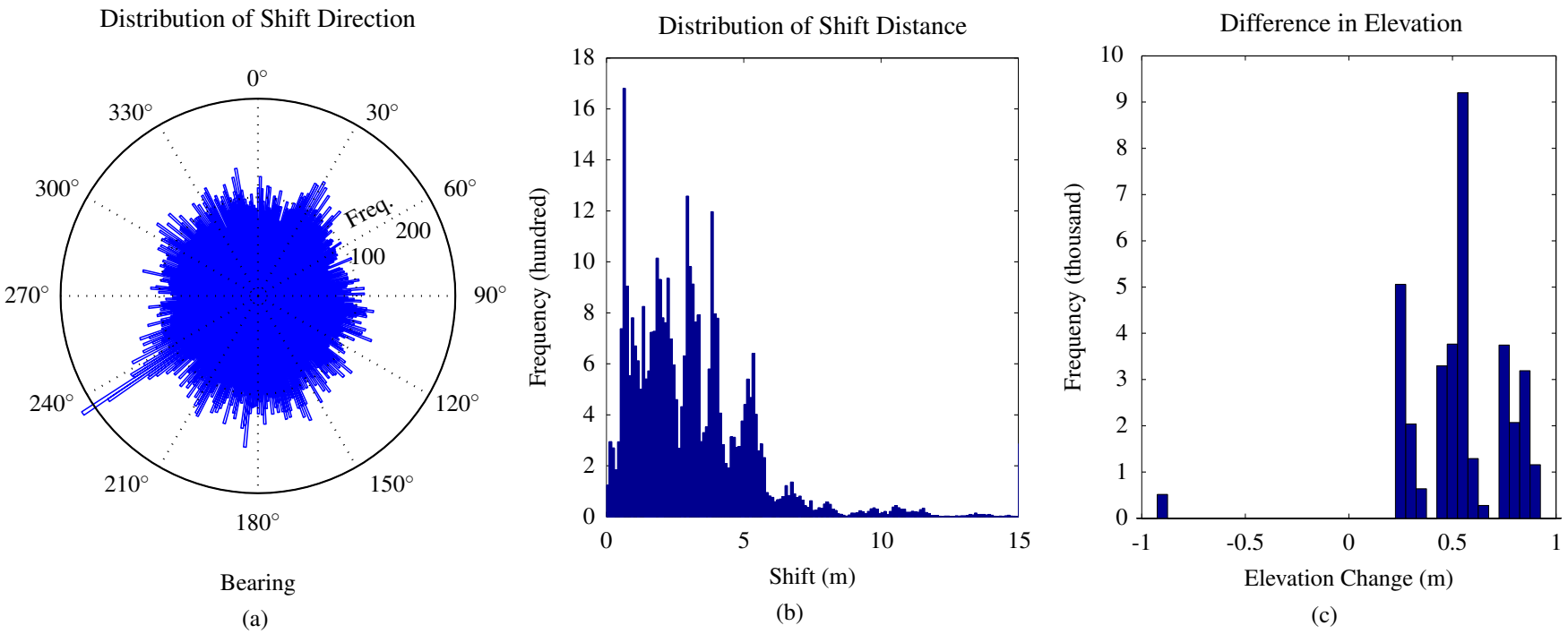

Figure 5.8: Plots showing the ICESat pulse location shift bearing, magnitude, and elevation, shown in Figures 5.9a to 5.9c. The shift magnitude continues up to 117 m, however, as only 86 pulses have a shift of >20 m, the plot focuses on shifts of less than 15 m. The difference in elevation is calculated by subtracting the new elevation from the original elevation, after the correction the difference in ellipsoid in the original GLAH14 and WGS 84. Only pulses over Mount Erebus showed a decrease in elevation.

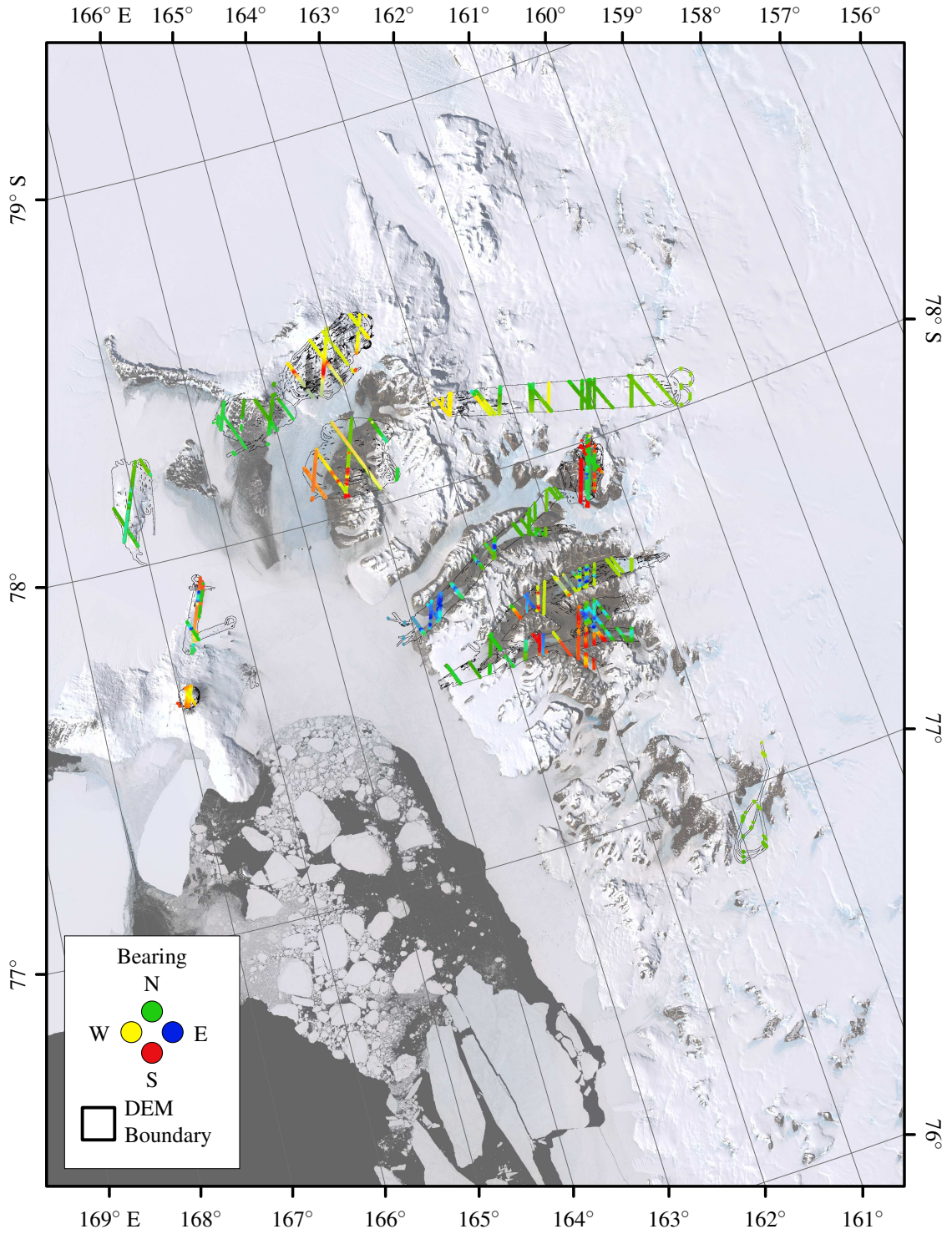

Figure 5.9a: Map of the shift direction from the original ICESat pulse-footprint location after co-registration. The ICESat elevation data is shifted to fit the DTM data. A Landsat mosaic is shown in the background.

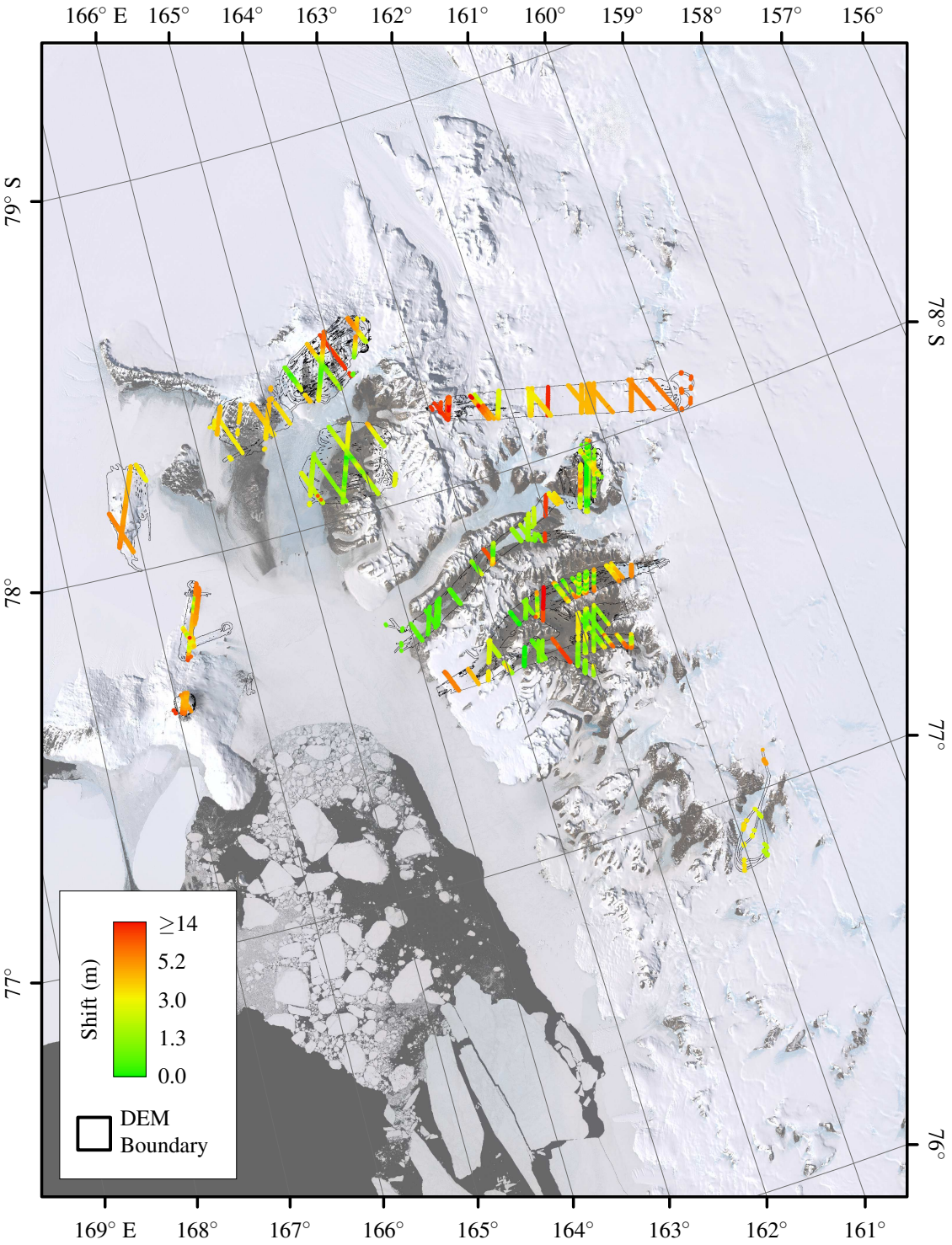

Figure 5.9b: Map of shift magnitude from the original ICESat pulse-footprint location after co-registration. The ICESat elevation data is shifted to fit the DTM data. The maximum shift was 117 m, but only 86 pulses had shifts greater than 20 m, hence the plot focussing on shifts $\leq$15 m. A Landsat mosaic is shown in the background.

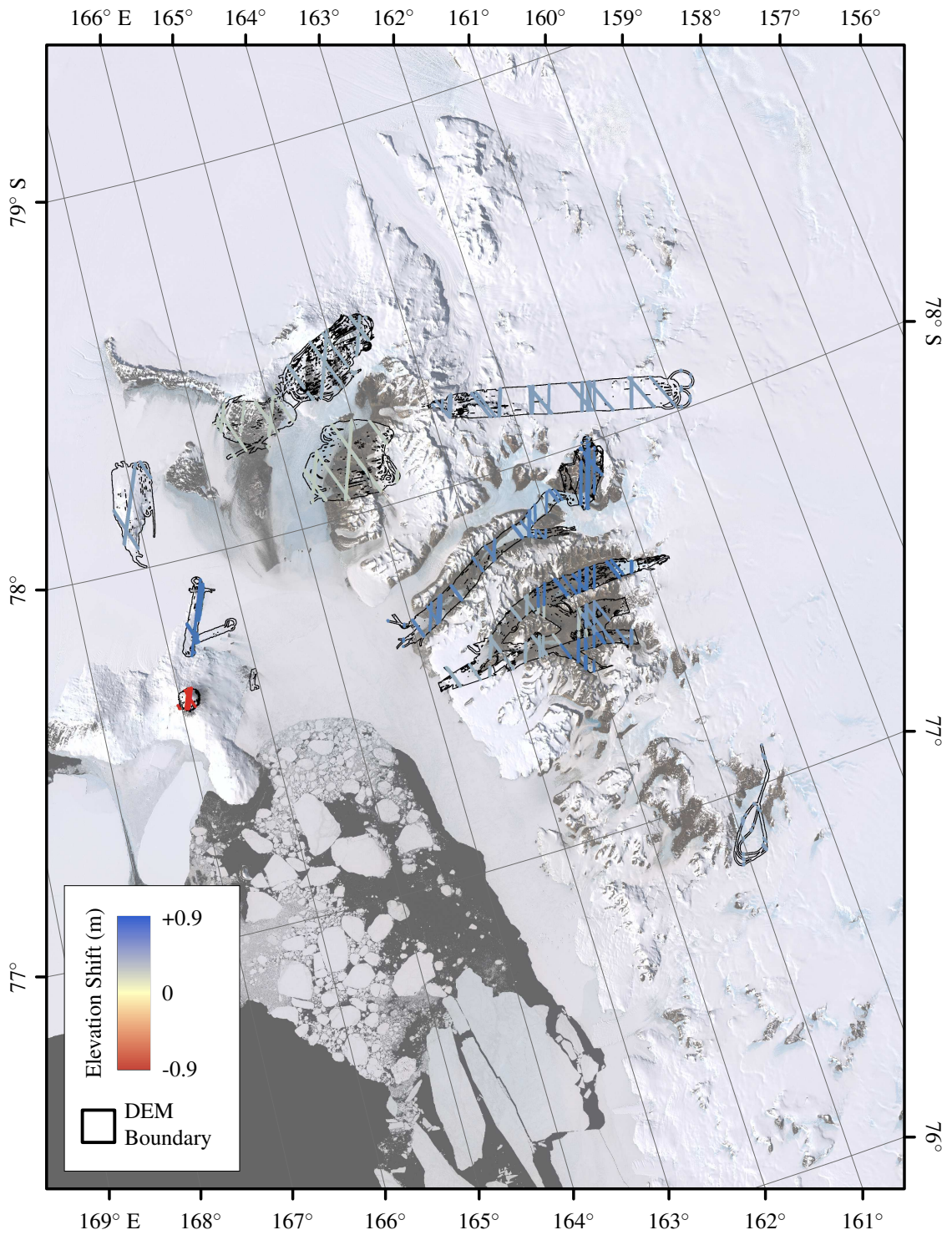

Figure 5.9c: Map of elevation change from the original ICESat pulse-footprint location after co-registration. The ICESat elevation data is shifted to fit the DTM data. The difference was found by subtracting the new elevation from the original elevation given in the GLAH14 product, once this data has been corrected for the difference in the Topex/Poseidon ellipsoid to the WGS 84 elipsoid. A Landsat mosaic is shown in the background.

Table 5.4: Fit statistics between ICESat and ATM DTMs before and after co-registration. The mean, median and mode relate to elevations extracted from within the ICESat pulse-footprints. † shows the deviation from the line-of-best-fit. ‡ shows the statistics of the line-of-best-fit.

	Original				Shifted			
Statistic	Mean	Median	Mode	Centre	Mean	Median	Mode	Centre
Mean Dev†	1.12	1.14	4.64	1.24	1.08	1.10	4.66	1.20
Max Dev†	10.75	10.48	37.17	11.33	9.60	9.49	37.17	10.61
R^2‡	1.00	1.00	1.00	1.00	1.00	1.00	1.00	1.00
RMSE‡	1.49	1.50	4.76	1.65	1.43	1.44	4.77	1.59

To improve the co-registration between the datasets, the ICESat data was shifted to fit the mosaiced DTM data, which is shown by *Schenk et al.* [2004] to be accurately geolocated when compared to GPS data. *Harding and Carabajal* [2005] observe shifts of up to 45 m are required to improve the correlations between the observed echo-profile and modelled echo-profiles derived from high-resolution DTMs. Surface matching software developed by *Lin et al.* [2010], and restored for more recent versions of MATLAB, was used to perform co-registration. Co-registration was performed for ICESat data over each of the original DTMs individually due to the size of the mosaiced DTM (>15 GB). The WGS 84 ICESat elevations are used as the ICESat elevation, and only pulses that record elevations less than the maximum elevation in the high-resolution DTMs are used in the co-registration process. This removes cloud hitting pulses that affect the quality of co-registration by producing unrealistically large shifts of several kilometres.

The co-registration algorithm uses least-squares surface matching based on a seven parameter coordinate transformation, using three rotations, three translations, and a scaling factor [*Lin et al.*, 2010; *Mills et al.*, 2003]. The software was originally developed for matching Mars DTMs, but can be applied to any elevation data and determines the new elevation values using Delaunay triangulation rather than using the elevation of the nearest DTM pixel [*Lin et al.*, 2010]. The process works iteratively. The mean absolute vertical distance is calculated at the end of each iteration, which is used to provide estimates for values of the next rotation and translation matrixes and scaling value. Differences between the two surfaces are minimised until a convergence criterion or the maximum number of iterations, set at 200, is reached [*Lin et al.*, 2010].

Most sites require the maximum 200 iterations, however, most iterations produce only small shifts of a few centimetres, and the final few iterations produce shifts at much smaller values. Further iterations would therefore not produce better results, as the pixel size of the high-resolution mosaiced DTM is 2 m × 2 m, meaning that further refinements are very unlikely to change specific pixels included in any calculation.

The shift bearing, distance, and change in elevation of the ICESat data is shown in Figure 5.8, and mapped in Figures 5.9a to 5.9c. The statistics comparing ATM and the original and newly co-registered ICESat data is shown in Table 5.4. The shift bearings in Figure 5.8a appear evenly distributed, with the exception of the peak at ∼240°. The majority of the shift magnitudes, shown

in Figures 5.8b and 5.9b, are $\leq$5 m, less than that observed in *Harding and Carabajal* [2005]. The observed changes in elevation, calculated by subtracting the new elevation from the original WGS 84 elevations, are typically between 0 m to 1 m, similar to those reported in *Schenk et al.* [2004] using GPS (Figures 5.8c and 5.9c). Only the Mount Erebus data reveals negative elevation changes, which are also in-line with some of the GPS comparisons in *Schenk et al.* [2004], but not included in their assessment due to a lack of GPS metadata, in particular the reference ellipsoid to which the GPS data is referenced. The shifts reported here suggest the elevations in the Mount Erebus DTM are too low, however, the absolute difference is similar to those reported to the other DTMs. Furthermore, differences such as this may occur more readily over areas that are both rugged and spatially small. Finally, the potential errors in elevation are not expected to influence the pulse-width discussed in this thesis as they are relatively small, and represent only a few bins of ICESat data.

5.7.4 TERRAIN TYPE

To ensure that only pulses over land are used in the analysis, pulses over the sea are removed using a mask. Likewise, a mask was applied to identify ICESat data over permanently bare-earth terrain, as part of the project set out to explore the relationship between ICESat pulse-widths and bare-terrain, which is applicable to the work in Chapters 3 and 4. In this case, a value of 1 was applied to pulses where this is true, and 0 where this is false. These values are then used in the pulse selection process, which is described in Section 5.7.9, to identify data over bare-earth (1) and ice (0). The initial masks are available from *McMurdo Dry Valleys Long Term Ecological Research* [2013b], and were modified to ensure co-registration with the Landsat mosaic. The resulting masks are shown in Figure 5.10. The ICESat data were also tagged with the area name, so comparisons between ICESat pulse-widths can be made for each DTM individually, to explore which terrains (i.e. wide valleys, steep terrain, volcanic terrain) perform best.

The ice conditions in and around the McMurdo Dry Valleys, as reported in *Pritchard et al.* [2009] and *Rignot et al.* [2011b], suggest that data over icy terrains can be used. In Figure 5.11, the icy terrains show little lateral movement, whilst Figure 5.12 shows comparatively little change in elevation over the ROI. Faster ice velocities and ice changes would imply that the terrain would have changed significantly during the lifetime of the ICESat mission and, therefore, comparisons between pulse-widths and surface characteristics would not be comparing the same terrain. The results from the icy terrains may provide important results for laser altimeters operating over the icy moons within the Solar System, such as the upcoming Ganymede Laser Altimeter (GALA) planned for the JUpiter ICy moons Explorer (JUICE) mission, to discover more about fine-scale surface characteristics and potential landing sites [*Hussmann et al.*, 2013]. However, two things to consider when using data over icy terrains are: (1) the spectral signature of ice may result in surface characteristics not being extracted from laser altimeter pulse-widths, and (2) changes in morphology due to aeolian processes may mean the terrain changes significantly.

Finally, another terrain type, highlighted in Figure 5.4 is used to provide insights into the

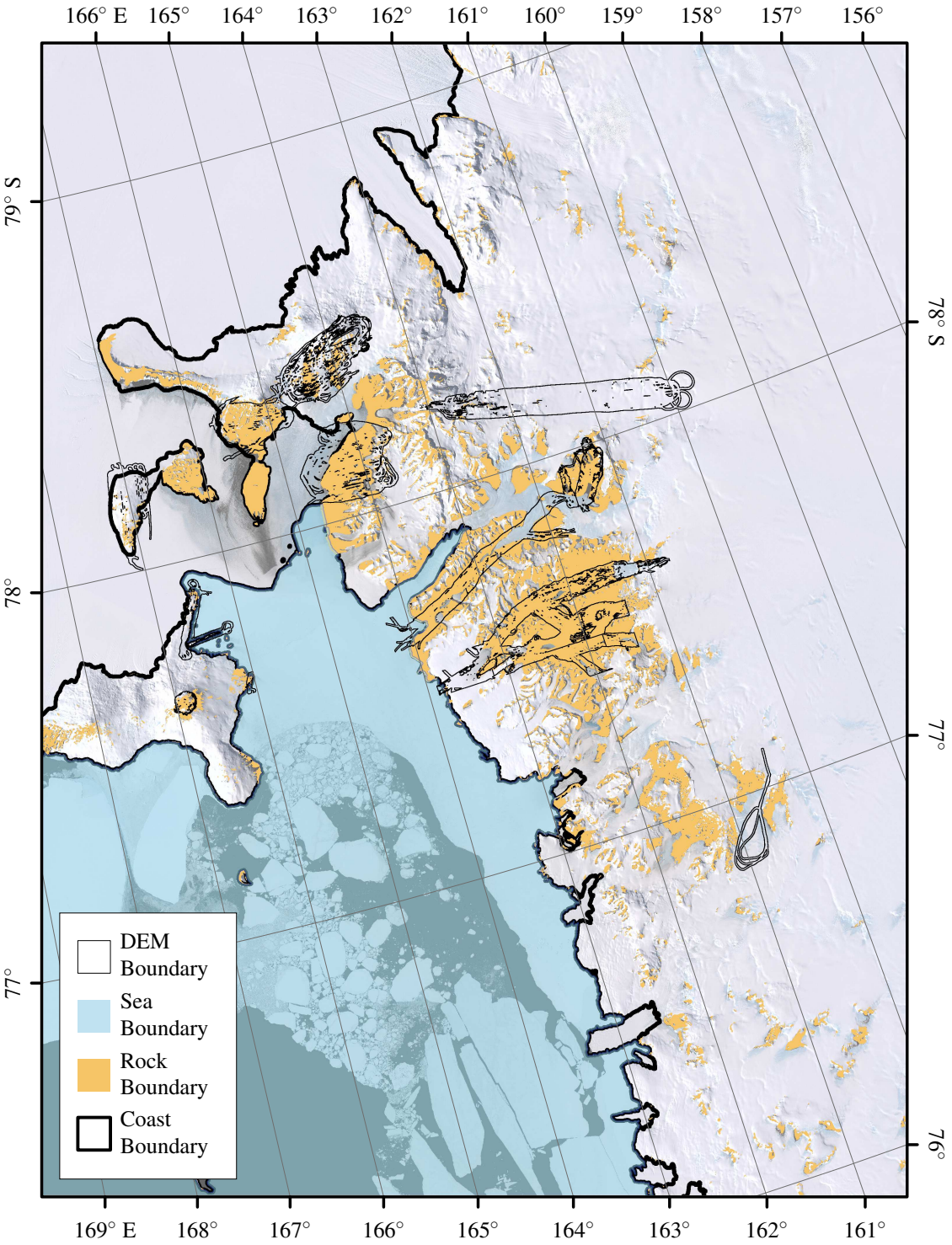

Figure 5.10: Map of the area covered by rock, sea, and ice within the ICESat study area of the McMurdo Dry Valleys. Rock and sea coverage is adapted from data at *McMurdo Dry Valleys Long Term Ecological Research* [2013b]. A Landsat mosaic is shown in the background.

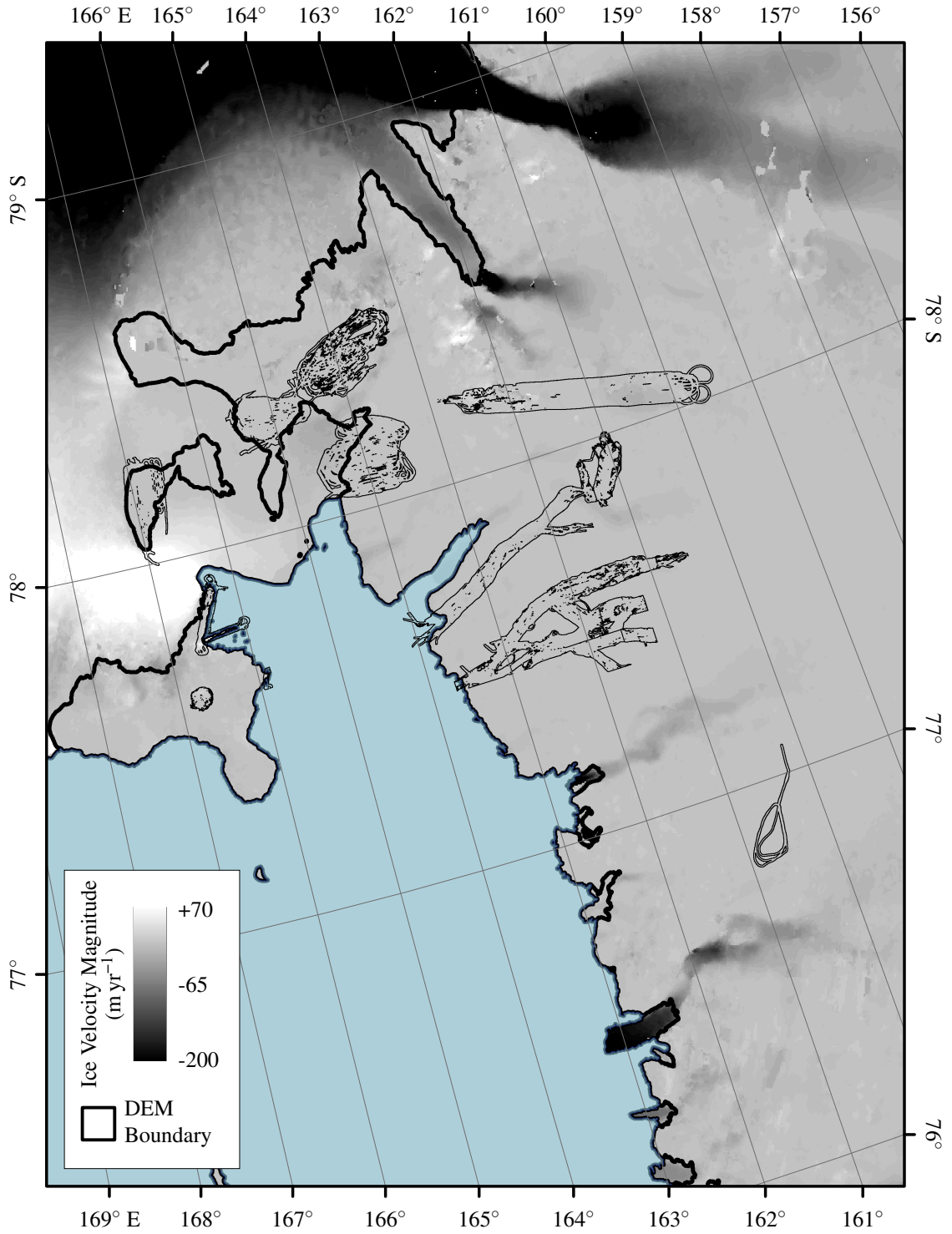

Figure 5.11: Map of ice velocity magnitude around the McMurdo Dry Valleys as reported in *Rignot et al.* [2011b], and the data available from *Rignot et al.* [2011a]. The sea mask, as shown in Figure 5.10 is applied to highlight only the ice on land and ice shelves.

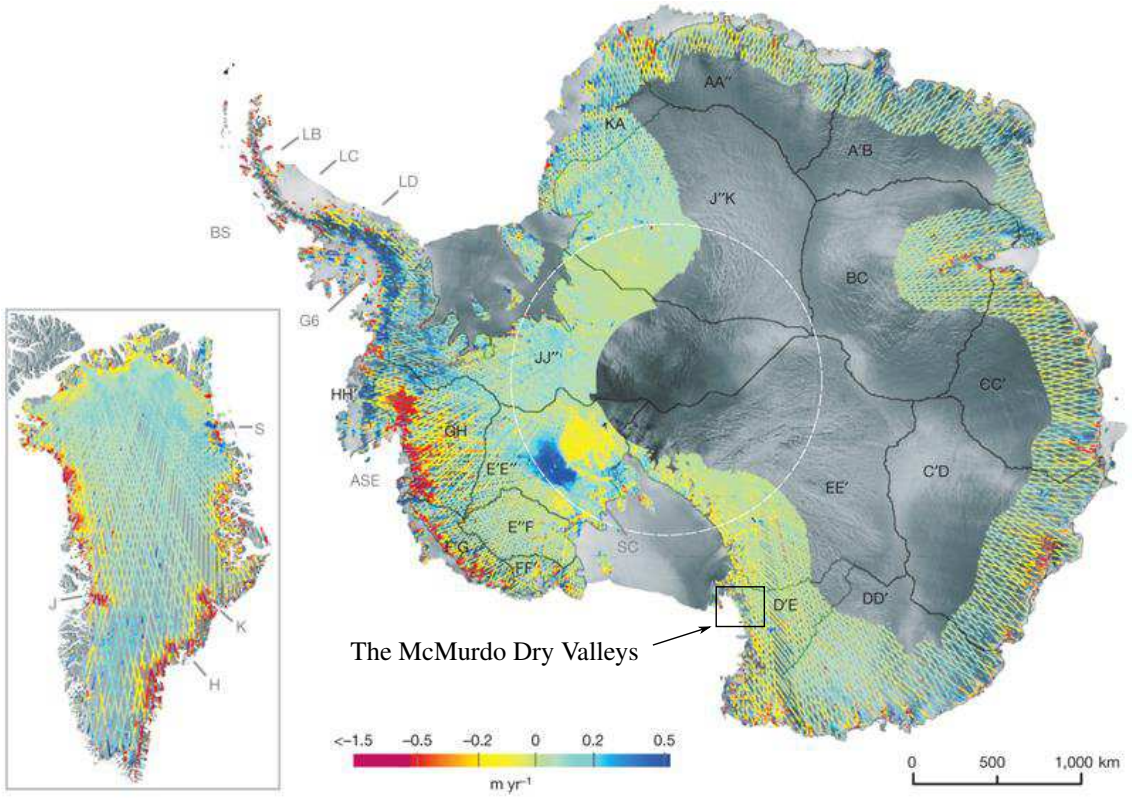

Figure 5.12: Map of elevation changes over Antarctica and Greenland [*Pritchard et al.*, 2009]. The black box represents the ROI around the McMurdo Dry Valleys.

relationship between laser altimeter pulse-widths and surface characteristics over highly variable terrain. The region is known as the Labyrinth and is described in detail in Section 5.9.

5.7.5 FITTING OF THE WAVEFORMS

By providing the full echo-profile, ICESat enables pulse-widths at different thresholds to be calculated. However, to do this, one must have reasonable estimates of the peak energy, and start and end points of the pulse return, whilst reducing the effect of noise.

One method is to apply a median filter to smooth the echo-profile. However, difficulties arise in defining a suitable window size applicable to all echoes, and identifying the start and end points of the echo-profile, as noise within the profile may cause variations in the signal before the true pulse return, which could be above the threshold used to measure the pulse-width.

The method used here is to fit the echo-profile with Gaussian distributions to form a smoothed fit. In the standard MATLAB *fit* tool, up to eight Gaussian distributions can be fitted to a signal, which sum together to form a smoothed profile, as shown in Figure 5.13. The benefits to using this method are (1) a smoothing of the effect of noise within the profile, (2) it produces a flat profile section before and after the ground echo-profile, and (3) it produces smoother increases and decreases in the profile, enabling the threshold crossing point to be easily identified.

Figure 5.13 shows the R-squared of the Gaussian profiles when they are compared to the original echo-profiles. Increasing the number of Gaussians to model the echo-profile improves the observed

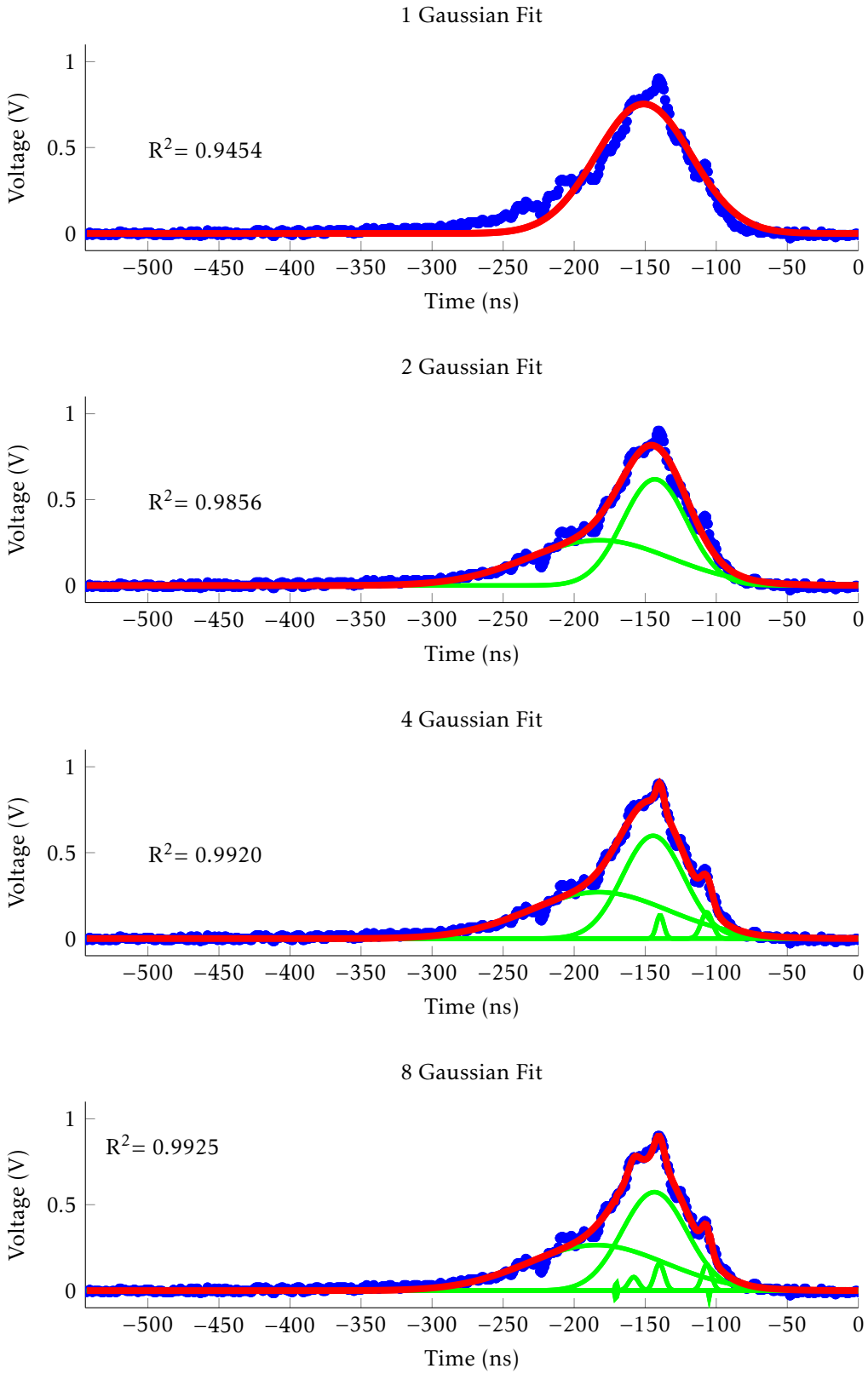

Figure 5.13: Plots comparing the different number of Gaussians required to accurately fit an example echo-profile. Final profile is shown in red, and the individual Gaussians shown in green. A minimum of two Gaussians are required in this example to produce a reasonable fit. Eight will be used throughout this work, as this provides the best fit, as many echo-profiles are more complex than that shown here. The Time is negative as ICESat searches for the end of the profile, given as 0 ns, and provides the preceding 544 samples.

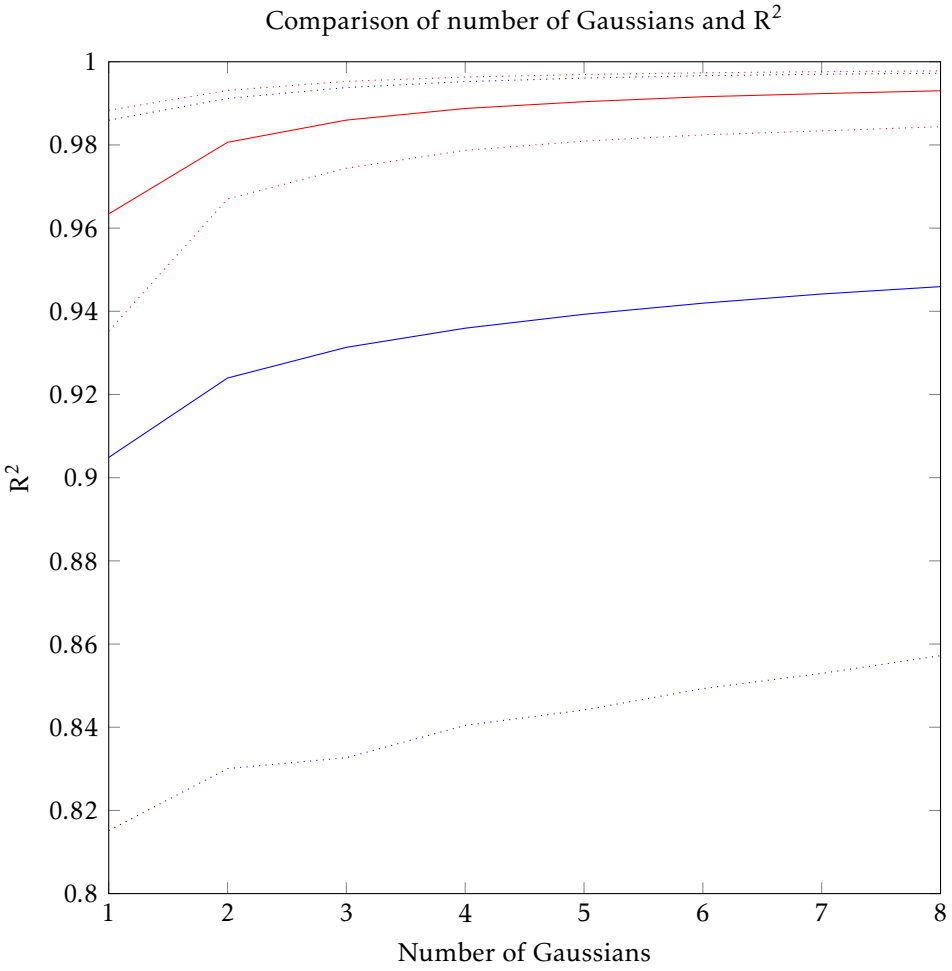

Figure 5.14: Plot comparing the mean R-squared of the fit and the number of Gaussians used for the fit for all data within the boundary of the ATM mosaiced DTM and for rock only data described in Table 5.6. Blue represents all the data within the boundary of the ATM DTMs, which includes cloud and ice data. Red represents the rock only data with the cloudy data removed. Upper and lower standard deviations are shown in the dotted lines of the same colour for each of the plots.

correlations. Figure 5.14 shows the mean R-squared values of comparisons between the original and modelled profiles for all echo-profiles used in the study. It also shows comparisons using only the pulses acquired over bare-earth terrains, with cloud-hitting pulses removed. Both show that increasing the number of Gaussians not only increases the mean R-squared values, but decreases the standard deviation of the R-squared values, such that 83 % of the fits have an R-squared of $\geq$0.98 using the latter criteria. Increasing the number of Gaussians beyond MATLAB's maximum of eight would increase the R-squared values, however, each additional Gaussian would provide less of an improvement than the previous one. One must also remember that the aim of modelling the returns with Gaussians is not to reproduce the original profiles, but to smooth out noise. There will come a point where additional Gaussians start to repeat noise patterns within the profiles, rather than reducing its effects. In conclusion, eight Gaussians are deemed a suitable number in order to provide an accurate, smoothed profile for pulse-width estimates, and is significantly better than is available from MOLA and LOLA (Figure 5.14).

The comparison of original and smoothed profiles is also a method of identifying poor data. Data that is affected by cloud, or is strongly affected by noise produces poorer R-squared values than echo-profiles that provide a clean ground return. A threshold for the minimum R-squared value can be used to identify poor data, which is described in Section 5.7.9.

5.7.6 CALCULATING PULSE-WIDTHS

Pulse-widths were calculated from the modelled eight Gaussian fitted profiles at different thresholds, which are: Full Width Half Maximum (FWHM), Standard Deviation, and 5 %, 10 %, and 20 % Peak Energy. Examples of the different thresholds are shown in Figure 5.15, using the same echo-profile shown in Figure 5.13. Lower thresholds are not used as it becomes difficult to distinguish between noise remaining in the profile, such as possible multiple scattering effects causing broadening of the profile, and the true ground return. This broadening effect results in some profiles appearing to have very wide pulse-widths ($\sim$500 ns), however a visual inspection of the profile often appeared much narrower.

The start and stop point of the pulse-width are calculated as the first and last point in time that the smoothed profile is above the desired threshold. Another option would be to interpolate between the values immediately above and below the threshold to find a more accurate time at which the threshold is crossed. However, as the pulse-widths are on the order of 100's of nanoseconds, interpolation would only change the pulse-width values by $<$1 %.

An estimate of the pulse-width is provided in the GLAH05 datasets for each pulse. These estimates are produced using the methods in *Brenner et al.* [2011]. The original signal is smoothed using increasingly wide Gaussian filters, starting at a 4 ns standard deviation, until a received signal is found; if a signal is not found then this is recorded in the *no signal* flag. The start and end of the pulse is defined as the first and last region of the return signal that are greater than the noise signal plus the standard deviation of the noise, after which the peaks of the smoothed profile are identified. Gaussians are then fitted to these peaks, with the smallest Gaussians removed or combined with neighbours, as are the Gaussians that are closer together than the limit defined in the accompanying ANC07 dataset. A standard fit uses two Gaussians, whilst an alternate, more complex, fit uses six. The standard deviation of the combined Gaussian is then used as the RMS received optical pulse-width pulse-width in the GLAH05 datasets [*Brenner et al.*, 2011].

Comparisons between the different measures of pulse-width developed here and the GLAH05 pulse-widths are shown in Figure 5.16. These plots show the standard deviation pulse-width to produce the most similar pulse-widths to those in the GLAH05 dataset, which is expected as they are produced by similar means. The 10 % and 20 % peak plots show the best correlations, whilst the FWHM show the poorest. The FWHM pulse-widths appear to be typically twice the size of those in the GLAH05 dataset, whereas the 10 % and 20 % are 3 to 5 times larger. By using a wide variety of thresholds the aim is to identify best practise for future laser altimeter instruments, as well as explore whether the observed correlations using MOLA and LOLA pulse-widths are limited by using the FWHM as an estimate of pulse-width.

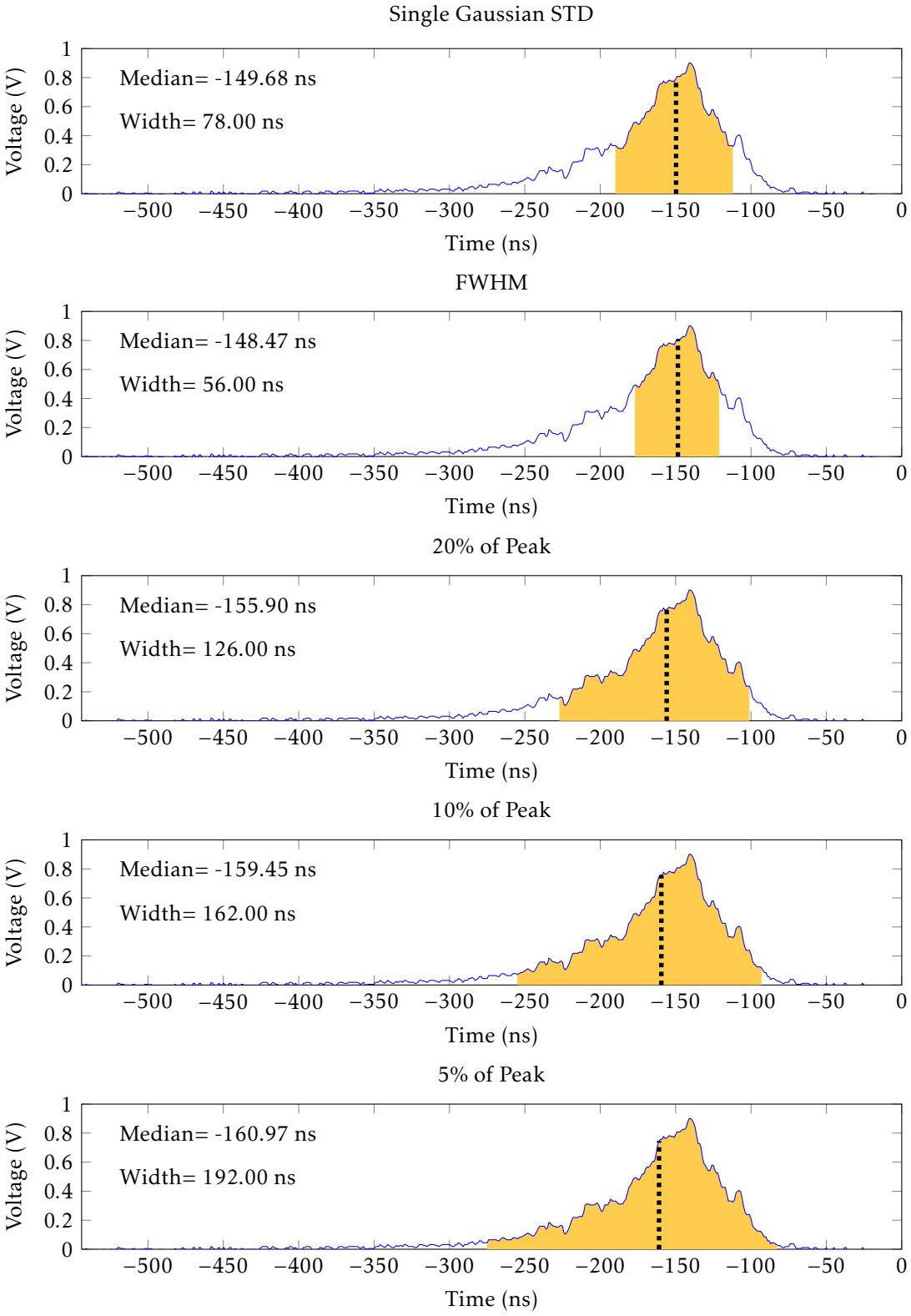

Figure 5.15: Plot examples of the pulse-width calculated at different thresholds. The dotted line is the mean pulse-width within the threshold, which is defined as the area in yellow. The time values pass from −544 ns to 0 ns as 0 ns represents the time the recording of the return pulse is stopped. Blue shows the original echo-profile. ICESat Record: 120 717 966, Pulse: 19.

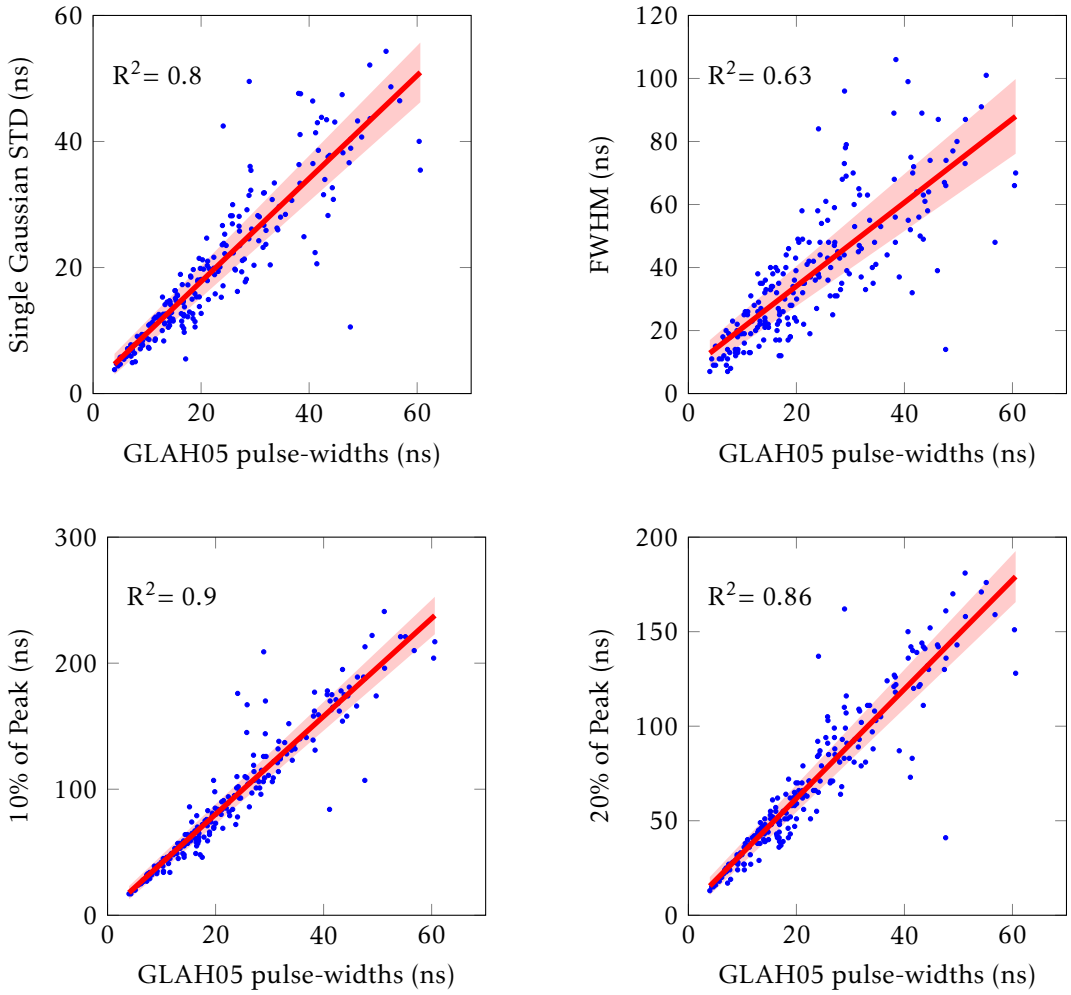

Figure 5.16: Plots comparing pulse-widths given in GLAH05 to those calculated using different thresholds. Threshold is shown in the vertical axis. Linear-line-of-best fit is shown with standard deviation.

Detrended pulse-widths were calculated using the different pulse-width thresholds, and by applying the slope correction that is described in Equation 2.7. The beam divergence angle is 110 µrad, and the transmitted pulse-width is given as 6 ns, as there is only a very small variation of 4 ns to 6 ns. The impulse response time is unknown, but is assumed to remain constant for all pulses, and is therefore not required.

5.7.7 DATA EXTRACTION

DTM data was extracted from within each pulse-footprint boundary, which totalled over 36 000 pulses. This was completed for both the shifted and non-shifted data described in Section 5.7.3. These data were saved and assigned to the ICESat data file in MATLAB, so that all data was available and easily accessible.

Contained within the ICESat GLAH14 dataset is the mean major-axis of each set of 40 pulse-footprints (*d_tpmajoraxis_avg*) and the eccentricity (*d_tpeccentricity_avg*), from which the mean minor-axis was calculated. These data are derived from the LPA image, which are available at 1 Hz,

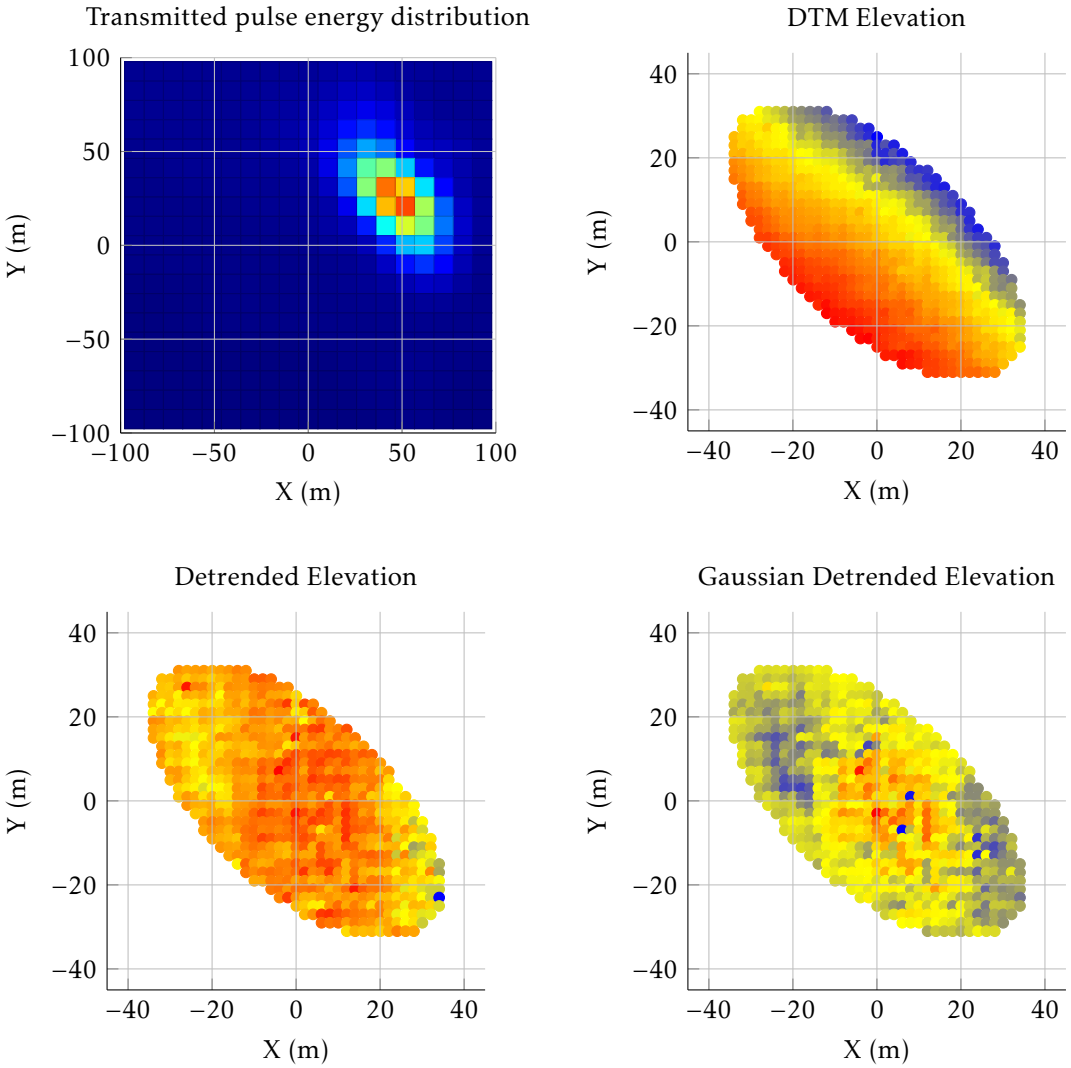

Figure 5.17: Plots showing the process of extracting pulse-footprint DTM data and finding detrended elevations, with and without the energy distribution. The pulse-footprint is defined as an elliptical area where the energy is greater than or equal to e^{-2} relative to the peak energy. The DTM elevation plot has a range of 9.85 m. The detrended elevations have a range of 2.42 m, produced by removing a plane-of-best-fit, and the bottom right plot shows the detrended elevations accounting for the energy distribution, with a range of 1.44 m. In all plots, blue represents low energy/elevation, and red high energy/elevations. This example uses the same pulse as presented in Figure 5.15, Record: 120 717 966, Pulse: 19.

shown in Figure 5.17. The pulse-footprint is defined as the elliptical area where the transmitted energy is equal or greater than e^{-2} relative to the peak energy at the centre of the pulse-footprint. The *d_beamAzimuth* value, also within the GLAH14 dataset but available at 40 Hz, provides an estimate of the azimuth, eastwards from north, from which the pulse is travelling, relative to an observer standing within the pulse-footprint. Another angle, *d_beamCoelv*, provides the angle between the horizon and the pulse, such that a vector can be calculated of the pulse flight path. Here, only the *d_beamAzimuth* value was used, which also provides an estimate for the orientation of the pulse-footprint: the major axis of the pulse-footprint will also align with the observer azimuth.

In MATLAB, a text file was made that contains the pulse-footprint: centroid latitude, centroid

longitude, major-axis, minor-axis, eccentricity, and orientation. This text file was then used with the *Table To Ellipse* tool in ArcMap 10.2 to produce a shapefile of ellipses for all the pulse-footprints over the McMurdo Dry Valleys. This shapefile was then split into individual shapefiles for each pulse-footprint and converted from a line polygon defining the edge of the pulse-footprint to a filled polygon that represents a mask of the pulse-footprint. A basic Python 2.7 script, used in the ArcMap environment, was then used to apply the *Extract By Mask* tool to each pulse-footprint shapefile. This tool extracts the DTM values within the area defined by the shapefile, which were then exported to individual text files for each pulse, and read and saved to the dataset file in MATLAB, as shown in Figure 5.17.

5.7.8 SURFACE ROUGHNESS AND SLOPE CALCULATION

The extracted DTM values, rather than maps of surface roughness and slope produced at different baselines, were used to calculate surface characteristics. The RMS height (Equation 2.46), range, and the Inter-Quartile-Range (IQR) were calculated from the extracted elevation heights directly. Slope was calculated as the maximum slope of a linear plane fitted to the extracted DTM values, as in Figure 3.9. The 3-dimensional data was plotted and a linear-plane-of-best-fit, of the form given in Equation 2.59, was fitted to data. From this equation, Equation 2.60 was derived and used to calculate the maximum slope of the plane. Detrended surface roughness was calculated for the RMS height, IQR, and range, from the detrended heights, which were calculated as the original elevations minus the height of a fitted plane. These forms of roughness represent the roughness from the background slope.

As the energy distribution of the transmitted energy is known for each set of pulse records, a new slope can also be derived by applying an energy weight to the fitting of the plane, using the energy at each point in the pulse-footprint as the weight. The energy at each point was calculated using cubic interpolation from the lower resolution energy distribution image, as shown in Figure 5.17. The different roughness values can also be calculated whilst accounting for this energy distribution, for the original and detrended roughness values. Where the energy distribution was accounted for by the weighting, the roughness type is tagged with *Gaussian*, which was used as a approximation for how the energy is distributed across the pulse-footprint.

RMS height, range, IQR, slope, and their detrended equivalents, are plotted against each of the methods of pulse-width estimation to attempt to identify which, and how well, planetary surface characteristics can best be estimated from orbiting laser altimeter pulse-widths. This study also verifies and assesses the quality of the methods employed by previous studies, which use only a crude estimate of the FWHM pulse-width, and suggests improved methods for future instruments [*Neumann et al.*, 2003a; *Smith et al.*, 2001, 2010b].

5.7.9 PULSE SELECTION

The wealth of metadata within the ICESat datasets enable the identification of pulses affected by atmospheric effects to be identified and removed. Of particular importance are the *atm_char_flag*

Table 5.5: Values assigned to three atmospheric condition flags within the GLAH14 ICESat data product [*Palm et al.*, 2011]. These flags are used in the pulse selection process, as shown in Table 5.6. * refers to the likely presence of clouds not found using the cloud search algorithm, instead highlighted by the integrated signal parameter (*i_FRir_intsig*), and the cloud top height (*i_Frir_cldtop*) is set to 10 km.

Value	*FRir_qa_flg*	*atm_char_flag*	*cld1_mswf_flg*
0	Possible	Clear	<0.010
1	↓	High Cloud Low Optical Depth	0.010 to 0.030
2		High Cloud High Optical Depth	0.030 to 0.060
3		Mid Cloud Low Optical Depth	0.060 to 0.100
4		Mid Cloud High Optical Depth	0.100 to 0.150
5		Low Cloud Low Optical Depth	0.150 to 0.225
6		Low Cloud High Optical Depth	0.225 to 0.300
7		Blowing Snow Low Optical Depth	0.300 to 0.400
8		Blowing Snow High Optical Depth	0.400 to 0.500
9		Not Tested	0.500 to 0.670
10		Insufficient	0.670 to 0.900
11			0.900 to 1.200
12	Likely		1.200 to 1.600
13	*i_FRir_intsig**		1.600 to 2.000
14	Low Clouds		>2.000
15	No Clouds		Invalid

Table 5.6: The typical number of pulses removed as a result of different factors, and the number of pulses remaining within the data assuming removal in order from top to bottom. The superscript number signifies the level of pulse-width removal the criteria are used for, with all criteria used in the previous level also applied. Each level can be applied to the three different terrain types, bare-earth (*bare*), all land (*land*), and ice only (*ice*), with the results shown in Tables 5.7a to 5.7c.

Criteria	Value	Pulses	Pulses Remaining		
Total Pulses	-	36 231		36 231	
Invalid GLAH05 Pulse-Width [1]	10^{308}	10		36 228	
Excessive Shift[1]	≥20 m	147		36 082	
Poor Elevation Match[1]	≥20 m	1907		34 330	
Poor Profile Fit (R-squared)[1]	≤0.95	6284		29 879	
Terrain			Bare	Land	Ice
			7952	28 796	16 440
FRir_qa_flg Flag[1]	0 to 14	17 219	4201	13 326	9125
atm_char_flag Flag[2]	1 to 11	19 114	2673	7270	4597
cld1_mswf_flg Flag[3]	1 to 15	33 302	204	577	373

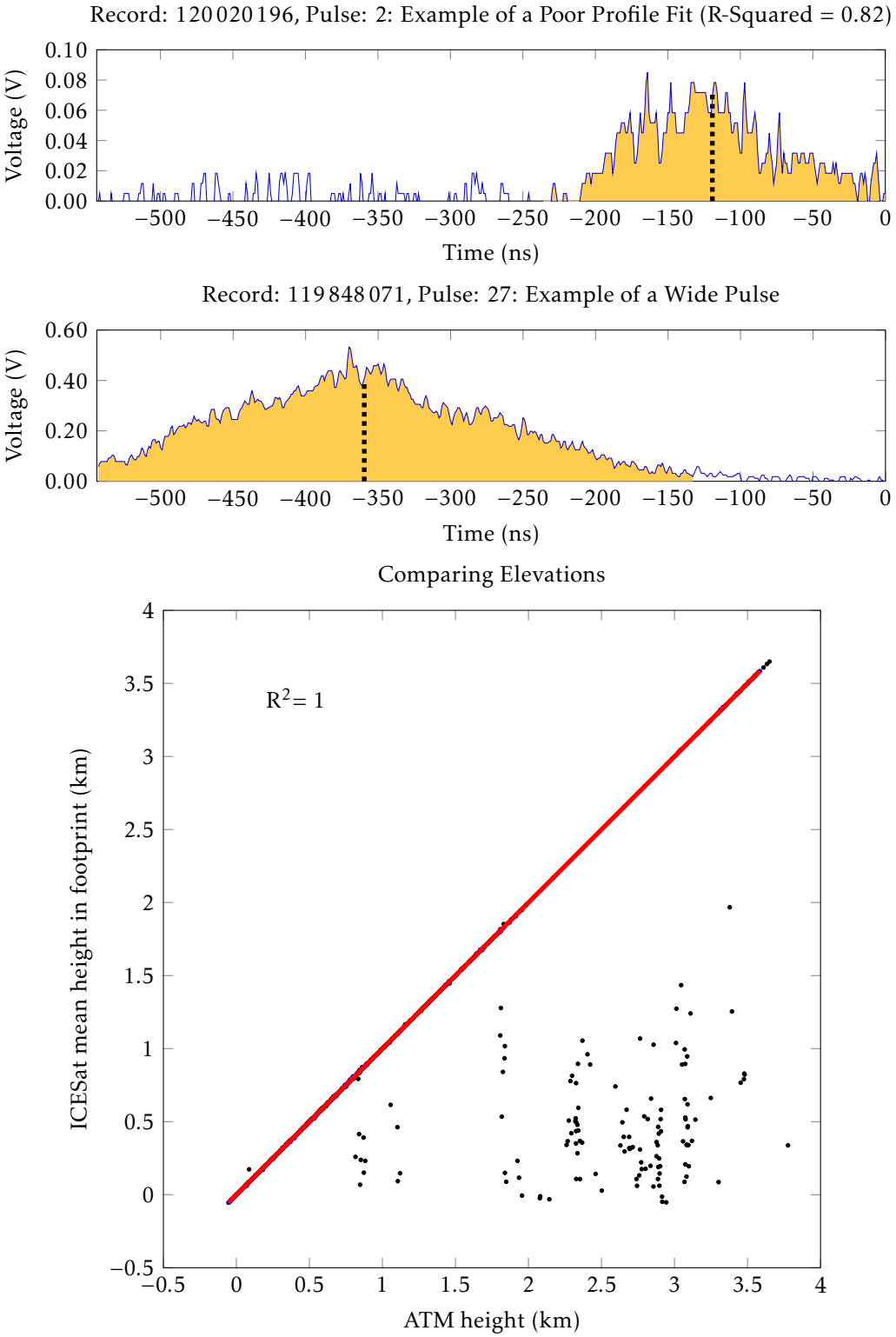

Figure 5.18: Plots showing a poorly fitted echo-profile, an echo-profile that is too wide, and a plot comparing ICESat and ATM DTM elevations. The top plot shows a low energy return pulse (peak energy ∼0.08 V compared to ∼0.50 V in the middle plot). The low signal to noise ratio results in a poor profile fit. The middle plot shows a return signal that is too wide, with the left side of the plot not showing the start of the echo-profile. In the bottom plot, the red line is the line-of-best-fit, using the blue data, where the *FRir_qa_flg*, *atm_char_flag*, and the *cld1_mswf_flg* data are removed, and black shows these removed data.

(1 Hz), *cld1_mswf_flg* (1 Hz), and *FRir_qa_flg* (40 Hz) data flags provided in the GLAH14 dataset, which are presented in Table 5.5.

The *FRir_qa_flg* is used to indicate the presence of clouds, detected using cloud search algorithms [*Palm et al.*, 2011]. The cloud search algorithms are described in *Palm et al.* [2011] (Section 3.3.2), the basic function is to search for clouds within windows of 250 m to 20 km above the surface using ever-finer time-averaged profiles, depending upon detection. Dense clouds have an optical depth greater than 2, which completely blocks the transmitted pulse, whilst thinner clouds cause forward scattering, which causes distortions to the echo-profile [*Brenner et al.*, 2011]. The *FRir_qa_flg* flag is given a value of 0 to 12 to indicate the presence of clouds identified using the cloud search algorithms, with higher numbers representing a stronger signal, a value of 13 or 14 to indicate clouds detected by other parameters, with the latter indicating low clouds ($<$150 m), and 15 if no clouds are detected.

The *atm_char_flag* is used to indicate optical depth of the atmosphere. A value of 0 indicates clear conditions and other values ranging from 1 to 9 used to indicate combinations of high ($>$5 km), medium (2 km to 5 km), and low ($<$2 km) cloud heights and blowing snow or fog, with different optical depths, such that 1 indicates high cloud with a low optical depth, and 2 indicates high cloud with a high optical depth. A value of 10 is given for insufficient data.

The final flag used here, *cld1_mswf_flg* flag, indicates scattering of the pulse, as shown in Table 5.5. This flag uses the 532 nm data to derive the optical depth of the atmosphere at 1 Hz, and is given a value of between 0 and 15. Optically thick cloud typically produces an invalid flag due to extinction of the signal. Unlike the previous flags, this data is available only at 1 Hz, so the same flag value is given to all pulse within each record (group of 40 pulses).

Table 5.6 highlights the different criteria, and the threshold values, applied during pulse selection. The final three criteria, which are the atmospheric flags discussed above, apply ever stricter limits on the atmospheric conditions allowed, shown by the increasing number of pulses affected. Forward scattering affects almost 92 % of pulses, whilst only 53 % and 48 % are affected by clouds and blowing snow, as highlighted in the *atm_char_flag* and *FRir_qa_flg* flags respectively.

The final column in Table 5.6 explores the number of pulses remaining after each of the criteria are applied. This highlights the number of pulses remaining after each criteria is applied and the degree of overlap between the criteria. The split at the terrain row shows the number of pulses remaining over only bare-earth terrains, all terrains, and only icy terrains, with the results shown in Tables 5.7a to 5.7c. These three sets of pulses were used to explore the relationships between pulse-widths and surface characteristics over natural terrestrial planetary terrains, such as those explored in Chapters 3 and 4, and those over all land surfaces, including ice, which could be applicable to planetary laser altimeter instruments operating over icy moons.

Figure 5.18 shows an example of a poorly fitted echo-profile and another of a pulse that is too wide. The first example is likely to result from atmospheric effects, due to the low Signal to Noise Ratio (SNR). The latter suggest poor identification of the pulse end, meaning the start of the echo-profile is not within the 544 ns time-frame. The bottom plot shows a comparison of the ATM and ICESat elevations. The black data represents data that is removed using the atmospheric flags

described above.

5.8 RESULTS

This section presents the results, comparing surface characteristics to the estimates of pulse-width derived from the echo-profile.

5.8.1 COMPARING PULSE-WIDTHS TO SURFACE ROUGHNESS AND SLOPE

Example plots comparing ICESat pulse-widths using the 10 % Peak Energy threshold to the four measures of surface roughness are shown in Figure 5.19. These plots use the Level 1 pulse criteria over bare-earth, as defined in Table 5.6. The R-squared of these plots, and other measures of pulse-width, compared to each of the surface characteristics are shown in Tables 5.7a to 5.7c, using bare-earth, all land, and icy surfaces respectively. The pulse-widths are plotted against surface characteristics with and without the weighting for the energy distribution across the pulse-footprint. The cell colour in the tables represents the R-squared to enable easy comparison between R-squared values within each table, with red representing poor R-squared values (0.35) and green representing high R-squared values (0.85). All results are considered statistically significant to a p-value $\ll 0.05$ when tested using the Student T-test.

The R-squared values in Table 5.7a show the 10 % Peak Energy threshold to perform consistently amongst the best indicator for each of the surface characteristics studied, for each of the three criteria for pulse selection. R-squared values between 0.71 and 0.78 are observed for most measures. Of the different measures, each of the measures of RMS height, inter-quartile range, and slope produce broadly similar R-squared values with some variation dependent on the criteria for pulse selection. The range produces poorer results, particularly using the strictest criteria, Level 3. Using Level 3 criteria, it is noticeable that accounting for the energy distribution across the pulse-footprint improves the correlations when comparing pulse-widths to RMS height and inter-quartile range estimates. These results are mirrored in the 20 % Peak Energy pulse-width estimates, albeit with marginally lower R-squared values.

The largest changes in observed R-squared values across the different criteria are observed using the 5 % thresholds. For this measure of pulse-width, some of the poorest correlations are observed when using the Level 1 criteria, whilst when using Level 2 and 3 criteria, these pulse-widths perform similarly to the 10 % and 20 % thresholds.

The FWHM pulse-width is consistently the worst performing indicator of surface characteristics, with R-squared values between 0.46 and 0.66, and decreasing R-squared values with tighter controls on pulse selection when comparing the same surface characteristics across the different criteria. Finally, the pulse-width estimates within the GLAH05 datasets, derived from the standard deviation of the combined Gaussians fitted to the echo-profile, typically show better correlations compared to FWHM estimates, but consistently poorer correlations compared to the 10 % threshold estimates, especially using the strictest criteria.

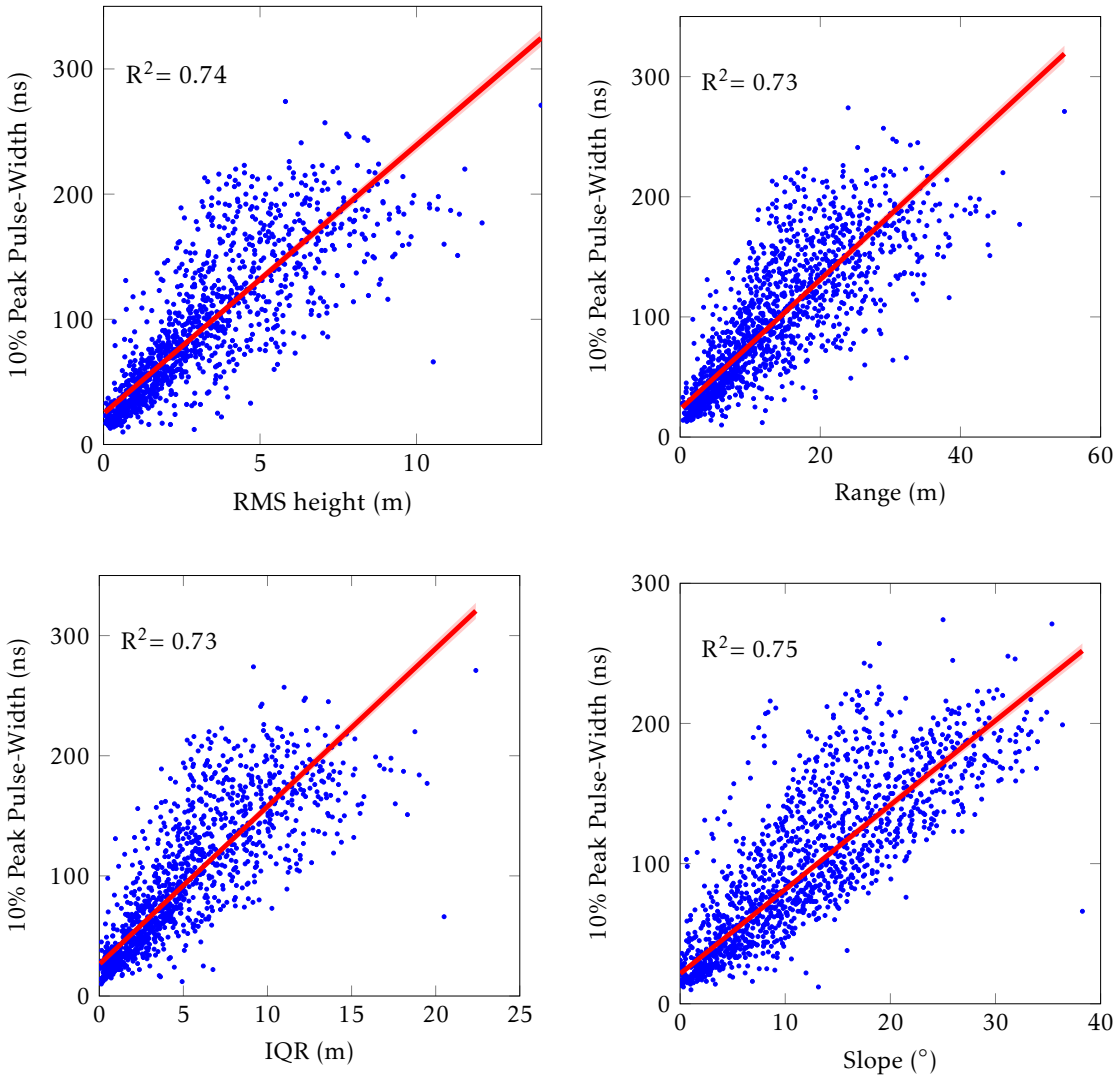

Figure 5.19: Plots comparing FWHM pulse-width values to different surface characteristics derived from within the pulse-footprint. The plot uses the Level 1 criteria defined in Table 5.6, over bare-earth terrain. The surface characteristic is shown in the horizontal axis. Red shows the linear line of best fit, and the R-squared of the fit is shown on each plot.

Table 5.7b shows the R-squared values of comparisons between the different ICESat pulse-widths to the surface characteristics, for each of the different pulse selection criteria, over all terrains within the McMurdo Dry Valleys study area. Using all terrain surfaces, rather than just bare-earth terrain, results in approximately three times more pulses than are shown in Table 5.7a. Across the three criteria, the 10 % Peak Energy pulse-width threshold measurement typically performs the best, with the 20 % Peak Energy threshold again performing very similarly. The R-squared values when using these two estimates of pulse-width are improved compared to their equivalents in Table 5.7a, with a maximum observed R-squared of 0.81. Using the Level 3 criteria, decreases in R-squared values are generally observed compared to the previous table for the RMS height and inter-quartile range measures of surface roughness.

The next best performing estimate of pulse-width is that given in the GLAH05 dataset, which produces R-squared values between 0.02 and 0.06 lower using the Level 1 and 2 criteria. Like the

Table 5.7a: Bare-Earth terrains: R-squared value of a linear fit between different ICESat pulse-widths and surface roughness and slope properties over bare-earth terrain in the McMurdo Dry Valleys, Antarctica, as measured from the ATM DTMs elevation as in Figure 5.19, with the three different criteria for which pulses are removed. The three main columns refer to the pulse removal criteria defined in Table 5.6, and the number of pulses remaining are shown in parentheses in each header.

	Level 1 Criteria (4201)					Level 2 Criteria (2673)					Level 3 Criteria (204)				
Measure of Surface Roughness	GLAH05†	FWHM‡	5 % Peak‡	10 % Peak‡	20 % Peak‡	GLAH05†	FWHM‡	5 % Peak‡	10 % Peak‡	20 % Peak‡	GLAH05†	FWHM‡	5 % Peak‡	10 % Peak‡	20 % Peak‡
RMS height	0.68	0.63	0.61	0.73	0.72	0.70	0.63	0.73	0.75	0.74	0.58	0.55	0.65	0.66	0.63
RMS height Gaussian	0.71	0.66	0.64	0.76	0.76	0.73	0.66	0.77	0.78	0.77	0.63	0.60	0.70	0.72	0.69
IQR	0.67	0.64	0.60	0.72	0.73	0.69	0.65	0.72	0.75	0.75	0.58	0.59	0.65	0.66	0.65
IQR Gaussian	0.67	0.64	0.61	0.73	0.73	0.70	0.66	0.75	0.76	0.76	0.67	0.65	0.74	0.77	0.77
Range	0.68	0.61	0.61	0.72	0.72	0.69	0.61	0.73	0.74	0.72	0.56	0.50	0.63	0.63	0.59
Range Gaussia	0.67	0.61	0.60	0.71	0.70	0.69	0.61	0.72	0.73	0.71	0.49	0.46	0.56	0.55	0.51
Slope	0.69	0.66	0.64	0.75	0.75	0.66	0.64	0.72	0.73	0.72	0.73	0.63	0.79	0.78	0.75
Slope Gaussian	0.69	0.66	0.64	0.75	0.75	0.66	0.64	0.72	0.73	0.72	0.72	0.63	0.78	0.78	0.74

Table 5.7b: All Terrains: R-squared value of a linear fit between different ICESat pulse-widths and surface roughness and slope properties over all terrain in the McMurdo Dry Valleys, Antarctica, as measured from the ATM DTMs elevation as in Figure 5.19, with the three different criteria for which pulses are removed. The three main columns refer to the pulse removal criteria defined in Table 5.6, and the number of pulses remaining are shown in parentheses in each header.

	Level 1 Criteria (13 327)					Level 2 Criteria (7271)					Level 3 Criteria (578)				
Measure of Surface Roughness	GLAH05†	FWHM‡	5 % Peak‡	10 % Peak‡	20 % Peak‡	GLAH05†	FWHM‡	5 % Peak‡	10 % Peak‡	20 % Peak‡	GLAH05†	FWHM‡	5 % Peak‡	10 % Peak‡	20 % Peak‡
RMS height	0.73	0.69	0.61	0.77	0.77	0.74	0.68	0.73	0.79	0.78	0.55	0.55	0.54	0.64	0.63
RMS height Gaussian	0.75	0.71	0.63	0.79	0.79	0.76	0.70	0.76	0.81	0.80	0.53	0.54	0.53	0.63	0.63
IQR	0.72	0.69	0.60	0.76	0.77	0.73	0.69	0.73	0.78	0.78	0.54	0.56	0.53	0.64	0.64
IQR Gaussian	0.72	0.69	0.61	0.76	0.77	0.74	0.70	0.75	0.79	0.79	0.52	0.54	0.52	0.63	0.64
Range	0.73	0.68	0.61	0.77	0.77	0.74	0.68	0.73	0.79	0.77	0.57	0.55	0.55	0.65	0.64
Range Gaussian	0.72	0.66	0.60	0.75	0.75	0.72	0.66	0.71	0.76	0.75	0.45	0.46	0.45	0.53	0.53
Slope	0.75	0.72	0.64	0.80	0.80	0.73	0.70	0.74	0.79	0.78	0.73	0.66	0.67	0.79	0.77
Slope Gaussian	0.75	0.72	0.64	0.80	0.80	0.73	0.70	0.74	0.79	0.78	0.73	0.66	0.67	0.79	0.77

Table 5.7c: Icy terrains: R-squared value of a linear fit between different ICESat pulse-widths and surface roughness and slope properties over icy terrain in the McMurdo Dry Valleys, Antarctica, as measured from the ATM DTMs elevation as in Figure 5.19, with the three different criteria for which pulses are removed. The three main columns refer to the pulse removal criteria defined in Table 5.6, and the number of pulses remaining are shown in parentheses in each header.

	Level 1 Criteria (9126)					Level 2 Criteria (4598)					Level 3 Criteria (374)				
Measure of Surface Roughness	GLAH05†	FWHM‡	5 % Peak‡	10 % Peak‡	20 % Peak‡	GLAH05†	FWHM‡	5 % Peak‡	10 % Peak‡	20 % Peak‡	GLAH05†	FWHM‡	5 % Peak‡	10 % Peak‡	20 % Peak‡
RMS height	0.70	0.65	0.53	0.74	0.75	0.70	0.64	0.65	0.75	0.74	0.48	0.49	0.42	0.60	0.60
RMS height Gaussian	0.71	0.67	0.54	0.75	0.76	0.71	0.65	0.67	0.76	0.75	0.45	0.47	0.41	0.58	0.58
IQR	0.69	0.65	0.52	0.73	0.74	0.69	0.64	0.65	0.74	0.74	0.47	0.49	0.41	0.59	0.59
IQR Gaussian	0.68	0.65	0.52	0.72	0.74	0.69	0.65	0.66	0.75	0.75	0.42	0.45	0.39	0.56	0.57
Range	0.70	0.66	0.53	0.74	0.75	0.71	0.65	0.66	0.75	0.74	0.51	0.51	0.44	0.63	0.63
Range Gaussian	0.67	0.61	0.50	0.69	0.70	0.67	0.60	0.62	0.71	0.70	0.39	0.42	0.36	0.51	0.52
Slope	0.72	0.69	0.56	0.77	0.77	0.72	0.68	0.68	0.78	0.77	0.65	0.61	0.52	0.74	0.73
Slope Gaussian	0.72	0.69	0.56	0.77	0.77	0.72	0.68	0.68	0.78	0.76	0.66	0.61	0.52	0.75	0.73

Table 5.7d: High fit: R-squared value of a linear fit between different ICESat pulse-widths and surface roughness and slope properties over all terrain in the McMurdo Dry Valleys, Antarctica, as measured from the ATM DTMs elevation as in Figure 5.19, with the three different criteria for which pulses are removed, and stricter profile fitting criteria (R-squared 0.99). The three main columns refer to the pulse removal criteria defined in Table 5.6, and the number of pulses remaining are shown in parentheses in each header. The R-squared value for the profile fit, as shown in Table 5.6, is increased from 0.95 to 0.99.

	Level 1 Criteria (10 895)					Level 2 Criteria (6190)					Level 3 Criteria (475)				
Measure of Surface Roughness	GLAH05†	FWHM‡	5 % Peak‡	10 % Peak‡	20 % Peak‡	GLAH05†	FWHM‡	5 % Peak‡	10 % Peak‡	20 % Peak‡	GLAH05†	FWHM‡	5 % Peak‡	10 % Peak‡	20 % Peak‡
RMS height	0.72	0.65	0.75	0.76	0.74	0.73	0.65	0.77	0.77	0.75	0.72	0.62	0.73	0.73	0.72
RMS height Gaussian	0.75	0.68	0.78	0.78	0.77	0.76	0.68	0.80	0.80	0.78	0.77	0.67	0.78	0.78	0.77
IQR	0.71	0.65	0.74	0.75	0.74	0.72	0.65	0.76	0.76	0.75	0.72	0.65	0.74	0.74	0.73
IQR Gaussian	0.73	0.68	0.76	0.77	0.76	0.74	0.68	0.79	0.78	0.77	0.80	0.72	0.81	0.83	0.83
Range	0.72	0.65	0.75	0.75	0.74	0.73	0.65	0.76	0.76	0.74	0.70	0.59	0.72	0.71	0.69
Range Gaussian	0.71	0.63	0.73	0.73	0.71	0.72	0.62	0.74	0.74	0.71	0.64	0.56	0.65	0.65	0.63
Slope	0.73	0.68	0.78	0.77	0.76	0.72	0.67	0.78	0.77	0.75	0.75	0.65	0.75	0.76	0.75
Slope Gaussian	0.73	0.68	0.77	0.77	0.76	0.71	0.67	0.77	0.77	0.75	0.74	0.65	0.75	0.75	0.74

10 % and 20 % pulse-widths, using the strictest criteria results in a decrease of R-squared values compared to the equivalents in the previous table.

The 5 % Peak Energy threshold pulse-widths show very little change when using the Level 1 and 2 criteria compared to the R-squared values in Table 5.7a. These pulse-widths produce the poorest results using the first set of criteria and perform similarly to the GLAH05 pulse-widths in the second criteria. However, the R-squared values using the strictest criteria are significantly lower compared to the previous table (0.08 to 0.22) and together with the FWHM pulse-widths, which also produce mixed results, produce the poorest correlations using these criteria. Similar to the 10 % Peak Energy, 20 % Peak Energy, and GLAH05 pulse-widths, R-squared values for the FWHM pulse-widths are improved compared to bare-earth results using the first two criteria and decreased using the strictest criteria, and by similar magnitudes.

The final terrain type explored is the icy terrains, shown in Table 5.7c. Approximately two-thirds of the total pulses used in Table 5.7b are over icy surfaces, as shown in Figure 5.10. Like the previous two tables, the 10 % and 20 % Peak Energy pulse-widths show the best correlations, the latter with marginally higher values using Level 1 criteria, and marginally poorer correlations in the Level 2 criteria. The R-squared values themselves lie approximately between their equivalent in the previous two tables using these criteria levels. However, using the Level 3 criteria, R-squared values are further reduced compared to Table 5.7b. The behaviour is also reflected in the three remaining measures of pulse-width, where R-squared values lie between the equivalent comparisons in the previous tables using the first two criteria, and poorer estimates in the final criteria.

The 10 % Peak Energy threshold estimate of pulse-width consistently produces the best R-squared values, closely followed by the 20 % Peak Energy threshold estimates. The worst performing estimates are the FWHM and the 5 % Peak Energy threshold estimates of pulse-width. Between these are the pulse-widths given in the GLAH05 dataset, which always outperform the FWHM estimates, and are only outperformed by the 5 % measures when using the Level 2 and 3 criteria over bare-earth terrains. With these findings in mind, the remainder of these results will focus on the 10 % and 20 % Peak Energy thresholds of pulse-width estimate.

Like the results in the previous two chapters, slope produces strong correlations between 10 % and 20 % Peak Energy threshold pulse-widths with R-squared values consistently greater than 0.7 across all terrains and criteria thresholds. Accounting for the energy distribution across the pulse-footprint in calculating slope has very little effect on the resulting correlations, unlike some of the surface roughness estimates, where it can have a significant effect. The poorest correlations are observed using the range estimates with the energy distribution weight applied. Without this weighting, the range estimates produce similar R-squared values to those produced using other estimates of surface roughness. The best correlations, when using surface roughness estimates, are typically observed using RMS height, occasionally eclipsed by IQR. Both of these estimates show slight improvements in correlations when accounting for the energy distribution, except when using the Level 3 criteria in Table 5.7b and Table 5.7c, using all terrains and icy terrains respectively.

With the exception of the strictest criteria level, using all the terrains over the McMurdo Dry Valleys produces the best correlations. Here, R-squared values are consistently close to 0.8, the

Table 5.8: The coefficients for a linear line-of-best-fit for comparisons between surface characteristics and 10 % Peak Energy estimate of pulse-width using Level 1 criteria. The equation is in the form Pulse-Width (ns) $= (a \times$ Surface Characteristic (m)$) + b$.

	Bare-Earth Terrains		All Terrains		Icy Terrains	
Roughness	a	b	a	b	a	c
RMS height (m)	15.38	34.29	18.55	26.56	21.53	23.40
RMS height Gaussian (m)	28.89	32.13	33.98	25.70	39.04	22.93
IQR (m)	9.40	35.61	11.49	27.15	13.44	23.76
IQR Gaussian (m)	26.08	35.33	31.55	27.30	36.45	24.19
Range (m)	3.90	32.71	4.62	25.71	5.29	22.83
Range Gaussian (m)	11.02	32.28	12.84	25.56	14.32	23.09
Slope (°)	4.22	33.43	4.98	25.84	5.53	23.27
Slope Gaussian (°)	4.21	33.49	4.97	25.87	5.52	23.29

highest observed across the three science chapters in this thesis, when using the 10 % and 20 % Peak Energy threshold pulse-width estimates. This is followed by the icy terrains, with the exception of the Level 3 criteria, where the poorest correlations are observed. The bare-earth terrains, on the other hand, produce the best correlations when using the Level 3 criteria level.

When using the 10 % and 20 % Peak Energy pulse-widths, the Level 1 and 2 criteria pulse selection produce the best correlations over each of the three terrain types individually. With the exception of slope estimates, R-squared values using the Level 3 criteria are consistently lower, in some cases by over 0.2.

Finally, Table 5.7d explores the effect of imposing stricter criteria on the profile fit. The comparisons in this table use echo-profile fits that have an R-squared value of 0.99, using all terrains. The primary effect is to increase the observed R-squared values for the 5 % Peak Energy threshold pulse-widths, particularly in the Level 1 and 3 criteria levels, compared to Table 5.7b. These pulse-widths perform similarly to the 10 % and 20 % Peak Energy pulse-widths, which experience lower R-squared values compared to the previous tables. Unlike the previous tables, Level 3 R-squared values are similar to those observed in the Level 1 and 2 criteria. Using these pulse-widths, accounting for the energy distribution across the pulse-footprint appears to produce better correlations when using the RMS height and IQR.

The variation in R-squared values for each of the different pulse-widths estimates, across each of the three criteria in Table 5.7d is typically smaller than those observed in previous tables, with only the comparisons between the different pulse-widths and range showing lower R-squared values in the Level 3 pulse-width criteria. This is in contrast to the previous tables where, as mentioned, the R-squared values in the Level 3 criteria are typically much lower for all surface characteristics than their equivalents using lower criteria thresholds.

Finally, the coefficients for the line-of-best-fit comparing surface characters and 10 % Peak Energy threshold pulse-width estimates are shown in Table 5.8. The 10 % threshold is used as it

typically provides the highest R-squared values, as well as performing consistently well. It is clear that there are subtle variations in the coefficients for the line-of-best-fit, which could be a result of surface reflectance.

5.8.2 HOW DO DIFFERENT ZONES COMPARE?

By mapping the R-squared values for each area individually it is possible to determine whether there are significant differences in the observed R-squared values across the different DTMs used in this work, similar to the previous studies in Chapters 3 and 4. This helps identify the strengths and weaknesses of the method, but may be subject to the same problems with the distribution of slope and surface roughness that affected the results over Lycus Sulci, in Section 3.8. The results are presented in Table 5.9 and Figure 5.20, and compare RMS height to 10 % Peak Energy threshold pulse-widths, selected using criteria Level 1 over the three terrain types, as defined in Table 5.6.

These results show significant variation in R-squared values across the zones, from 0.37 to 0.86

Table 5.9: Fit statistics between ICESat 10 % Peak Energy pulse-widths and ATM DTMs surface roughness and slope for each zone, as in Figure 5.20.

	Bare-Earth		All		Ice		Maximum	
DTM	ξ	θ	ξ	θ	ξ	θ	ξ (m)	θ (°)
Odell	-	-	0.37	0.36	0.37	0.36	0.92	2.78
Barwick	0.48	0.70	0.68	0.80	0.85	0.84	4.87	17.58
Vicotria	0.85	0.79	0.84	0.80	0.83	0.84	9.07	25.21
Doorly	0.81	0.81	0.84	0.84	0.83	0.83	11.95	31.80
McKelvey	0.84	0.73	0.83	0.72	0.79	0.68	6.34	26.77
Bull	0.86	0.86	0.86	0.86	0.83	0.85	3.81	14.82
Wright	0.74	0.66	0.81	0.77	0.80	0.78	10.34	35.75
Beacon	0.76	0.74	0.76	0.73	0.73	0.70	10.71	35.73
Arena	-	-	-	-	-	-	-	-
Taylor	0.82	0.83	0.80	0.81	0.70	0.70	13.75	40.31
Radian	0.70	0.55	0.72	0.73	0.72	0.73	8.73	25.28
Denton	0.71	0.75	0.77	0.80	0.77	0.81	10.47	29.91
Discovery	0.69	0.65	0.72	0.67	0.74	0.68	9.53	34.00
Morning	0.71	0.77	0.71	0.73	0.70	0.70	11.87	31.67
Royds	-	-	-	-	-	-	-	-
Erebus	0.53	0.48	0.56	0.46	0.57	0.38	9.62	30.64
Hut Point	-	-	0.56	0.63	0.56	0.63	28.64	50.92
White	0.53	0.73	0.68	0.71	0.68	0.70	10.82	33.35

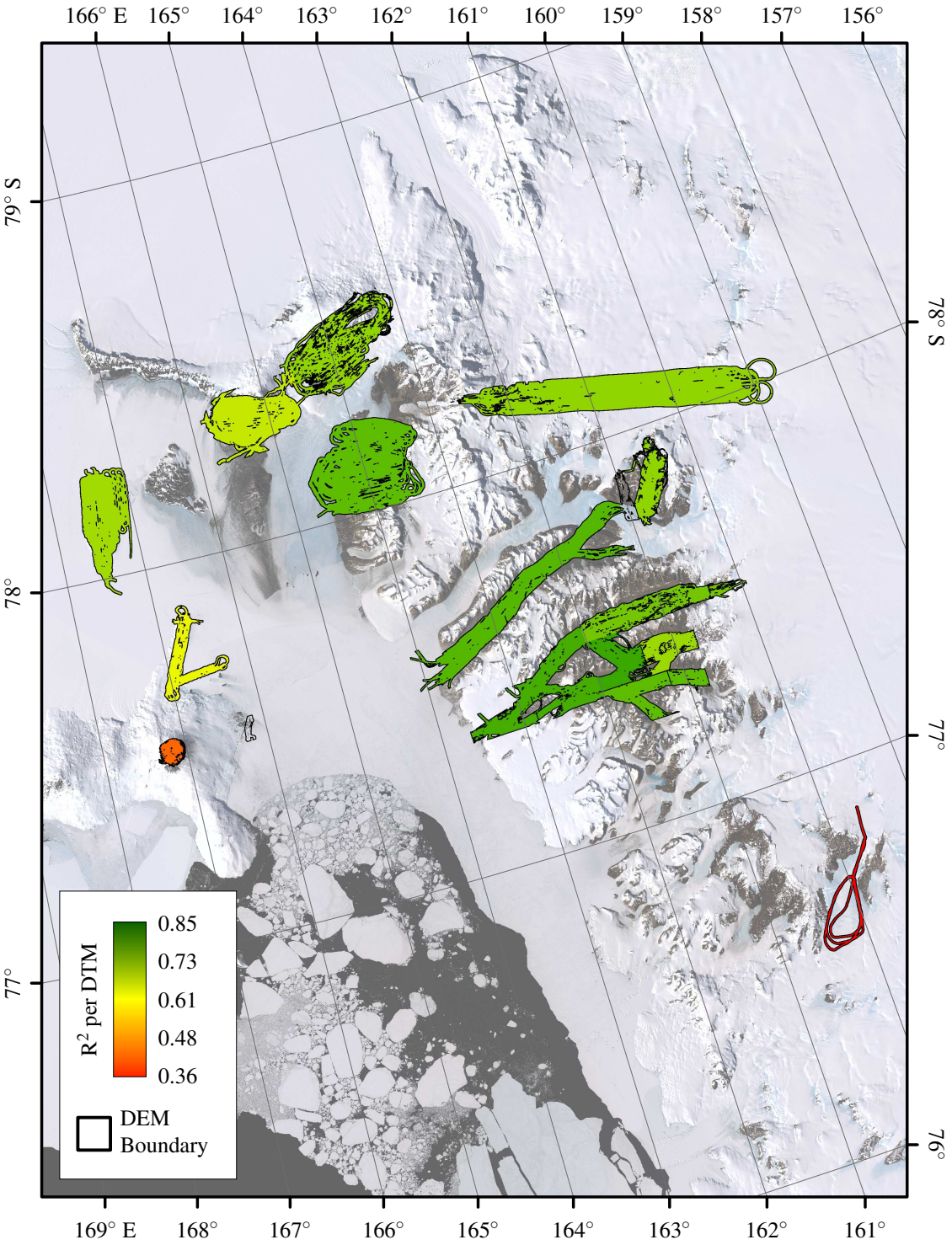

Figure 5.20: Map of R-squared value for each area, when comparing 10 % Peak Energy pulse-widths and slope. Data is presented in Table 5.9. A Landsat mosaic is shown in the background.

over Odell and Bull respectively. Arena and Royds contain no data for any of the terrain types[5], whilst Odell and Hut Point only contain data over ice, meaning that the *All* column and the *Ice* column contain the same number of pulses and the same R-squared values.

R-squared values over Odell are the poorest of all the sites, followed by those from Erebus (Table 5.9 and Figure 5.20). Odell has a much smaller range in surface roughness and slope values than any of the other sites, 0.92 m and 2.78°, which could cause the poor results, as discussed in Section 3.8 (Table 5.9). Other than Odell, there does not appear to be a correlation between the distribution of surface characteristics and the observed R-squared values, suggesting that there is a lower limit of distribution of surface roughness or slope, above which the R-squared value is dependent on other properties. The poor results over Erebus are not explained by the distribution of surface roughness or slope, and instead could be a result of poor co-registration of the datasets. Both Erebus, Hut Point, and Erebus are also the smallest DTMs used in the work, so the results could also be a result of the size of the region studied. The low number of data over Erebus, 42 to 51 for bare-earth and icy terrains respectively, means that removing data over this region for Tables 5.7a to 5.7d will have very little impact of the observed R-squared values, and is therefore not carried out.

Figure 5.20 shows that the major valleys and areas of greatest topographic variation to be where the best correlations are found, when the 10 % Peak Energy threshold pulse-widths are compared to slope. Flatter terrains, such as the terrains in the left of Figure 5.20 and Odell in the lower right, typically produce lower R-squared values.

5.8.3 How do Different Operational Periods Compare?

By comparing data across the different Operational Periods, which are described in Section 5.3.2, the data may reveal whether there is a change in the observed correlations with changes in energy output for each laser and for different periods individually, as shown in Figure 5.3 on Page 224. This could highlight whether low energy outputs or significant changes in energy outputs affects the observed correlations.

The results, which are shown in Table 5.10, show Laser 3 produces the best correlations, with the poorest correlations observed during Operational Period 2B. However, there is no correlation between the mean transmitted energy, or the energy change during an Operational Period, and the observed R-squared value of the fit. There are also significant changes in the gradient of the line-of-best fit between these operational periods, although there is a string of consistent gradients for Operational Periods 3E to 3H, with 3C and 3D also showing similar gradients.

5.8.4 Finding Detrended Roughness from Pulse-Widths

The results in Section 5.8.1 show the strongest correlations observed in this thesis, especially those observed using slope. ICESat data may therefore present the best opportunity to explore the

[5]Here, most data is removed to effects from clouds, leaving too few data points for a significant relationship to be found.

Table 5.10: Fit statistics between ICESat and ATM DTMs surface roughness for each Operational Period. The letters in the Operational Periods correspond to the 33 day sub-cycle.

Op. Period	Num. Points	R-squared	Gradient	Mean Energy (J)	Energy Change (J)
2A	981	0.69	25.40	0.070	0.045
2B	348	0.57	24.18	0.042	0.026
2C	326	0.62	15.15	0.017	0.014
3A	740	0.85	21.32	0.064	0.019
3B	684	0.89	18.57	0.060	0.025
3C	393	0.91	26.46	0.045	0.013
3D	828	0.90	24.36	0.040	0.012
3E	150	0.89	32.63	0.027	0.013
3F	1562	0.85	29.11	0.023	0.008
3G	1448	0.84	29.51	0.021	0.010
3H	862	0.83	29.27	0.017	0.008
3I	320	0.86	35.28	0.016	0.009

relationship between the roughness contribution to pulse-widths and detrended surface roughness, as presented in Equation 2.7. As well the different measures of pulse-width derived from the echo-profiles, improved georeferencing and co-registration of datasets is thought to limit the effect of errors that may have hampered previous results, whilst the large pulse-footprint and high-resolution data enable accurate estimates of detrended surface roughness to be derived.

Different estimates of pulse-width are compared to slope in Figure 5.21, which also shows the predicted pulse-width due to slope and instrument effects in green, derived using Equation 2.7. According to this equation, the difference between the measured pulse-width and the theoretical pulse-width is a result of detrended surface roughness, i.e. roughness from the background slope. It is clear from these plots that only the 10 % and 20 % Peak Energy pulse-width thresholds, and therefore the 5 % threshold, which are even wider, produce pulse-width estimates greater than the predicted pulse-width using all except roughness.

In Table 5.11, the detrended surface roughness contribution to the pulse-widths are compared to detrended surface roughness, for each of the three selection criteria. The observed R-squared values show that very poor correlations are observed between the roughness contribution to pulse-widths, as outlined in Equation 2.7, and detrended surface roughness, with the best correlations observed using Level 2 GLAH05 and detrended Range (0.18). Typically, however, the R-squared values range from 0.10 to 0.15 for all pulse-width estimates except for FWHM pulse-widths, which are poorer when using the Level 1 and Level 2 selection criteria.

5.9 REPLICATING THE MAWRTH VALLIS RESULTS

Table 5.11: Detrended Roughness: R-squared value of a linear fit between different ICESat pulse-widths and detrended surface roughness, as measured from the ATM DTMs elevation as in Figure 5.19, with different criteria for which pulses are removed due to atmospheric effects. The three main columns refer to the pulse removal criteria defined in Table 5.6, and the number of pulses remaining are shown in parentheses in each header.

	Level 1 Criteria (13 327)					Level 2 Criteria (7271)					Level 3 Criteria (578)				
Measure of Surface Roughness	GLAH05†	FWHM‡	5 % Peak‡	10 % Peak‡	20 % Peak‡	GLAH05†	FWHM‡	5 % Peak‡	10 % Peak‡	20 % Peak‡	GLAH05†	FWHM‡	5 % Peak‡	10 % Peak‡	20 % Peak‡
RMS height detrended (m)	0.12	0.08	0.13	0.14	0.14	0.16	0.06	0.12	0.12	0.12	0.11	0.13	0.08	0.12	0.10
RMS height detrended Gaussian (m)	0.11	0.08	0.14	0.14	0.14	0.15	0.06	0.13	0.12	0.12	0.10	0.13	0.10	0.13	0.11
IQR detrended (m)	0.11	0.08	0.13	0.14	0.14	0.16	0.06	0.12	0.12	0.12	0.11	0.16	0.07	0.10	0.09
IQR detrended Gaussian (m)	0.11	0.07	0.13	0.14	0.14	0.15	0.06	0.13	0.13	0.12	0.12	0.16	0.12	0.15	0.13
Range detrended (m)	0.13	0.09	0.14	0.15	0.15	0.18	0.06	0.13	0.13	0.13	0.07	0.11	0.10	0.13	0.10
Range detrended Gaussian (m)	0.10	0.08	0.15	0.15	0.15	0.15	0.07	0.15	0.14	0.13	0.01	0.10	0.11	0.12	0.08

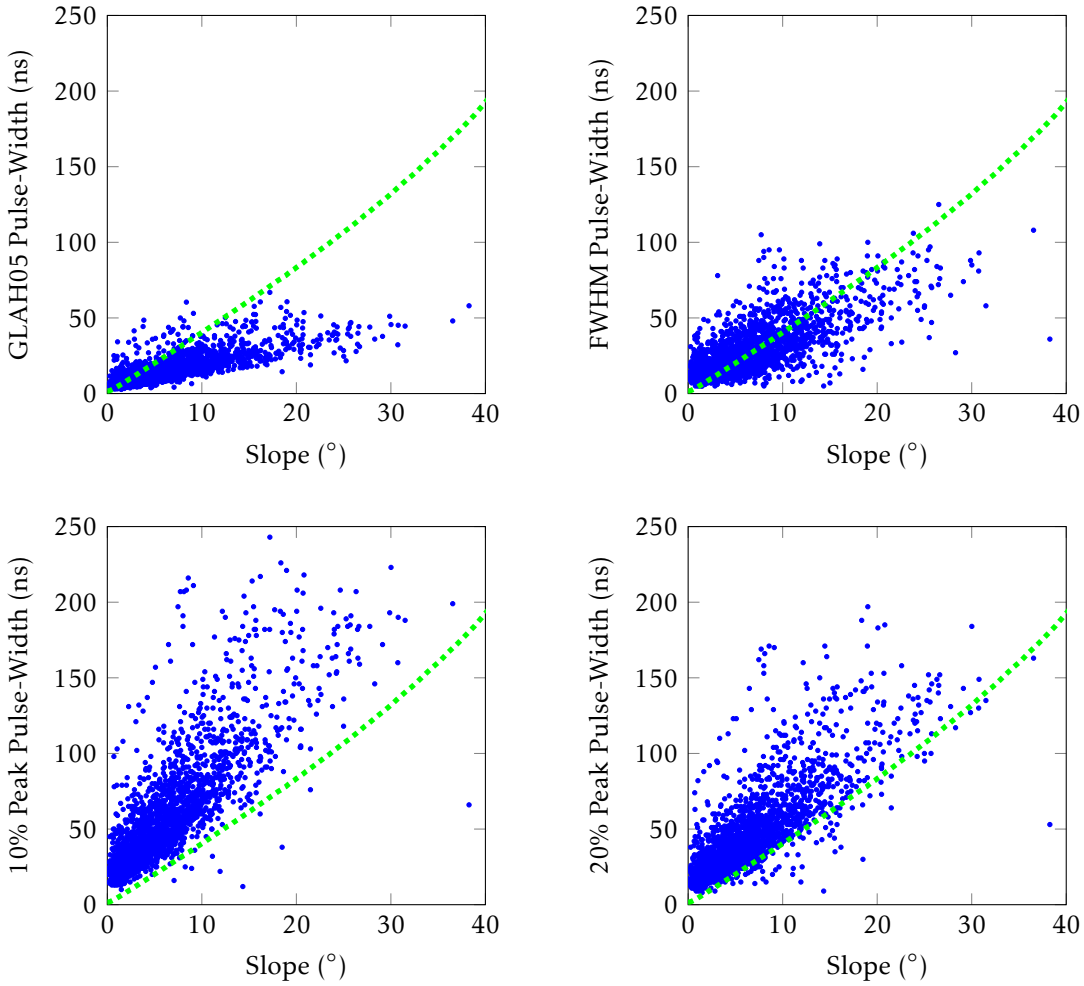

Figure 5.21: Plots comparing the different pulse-width thresholds to slope, and the theoretical slope contribution in Equation 2.7. Slope is compared to: GLAH05, FWHM, 10 % Peak Energy, and 20 % Peak Energy pulse-widths. Green are theoretically estimated pulse-width using all but the roughness contribution to pulse-width in Equation 2.7, and blue shows the estimated pulse-widths.

5.9.1 INTRODUCTION

One area of Wright Valley, known as the Labyrinth, shown in Figure 5.22, appears closest in appearance to Mawrth Vallis, an area of Mars that presented very poor results in Chapter 3. The roughness of both terrains appears heterogeneous and highly variable over short baselines. Pulse-widths from the Labyrinth terrain, which is highlighted in Figure 5.4, are selected and compared to the different measures of surface roughness and slope in an attempt to discover whether the results observed over the Martian site are replicated. If poor correlations are observed again here, this would suggest that surface roughness over these types of terrains cannot be derived from laser altimeter pulse-widths, however, if the opposite is true, this would suggest that the problem lies with the poor georeferencing and pulse-width estimation methods employed by MOLA.

The terrain covers an area approximately 50 km × 20 km, where a network of bedrock channels, some of which have a positive gradient, emerge from the margin of Wright Upper Glacier, part of the East Antarctic Ice Sheet [*Lewis et al.*, 2006]. Channel formation is ascribed to fast-flowing

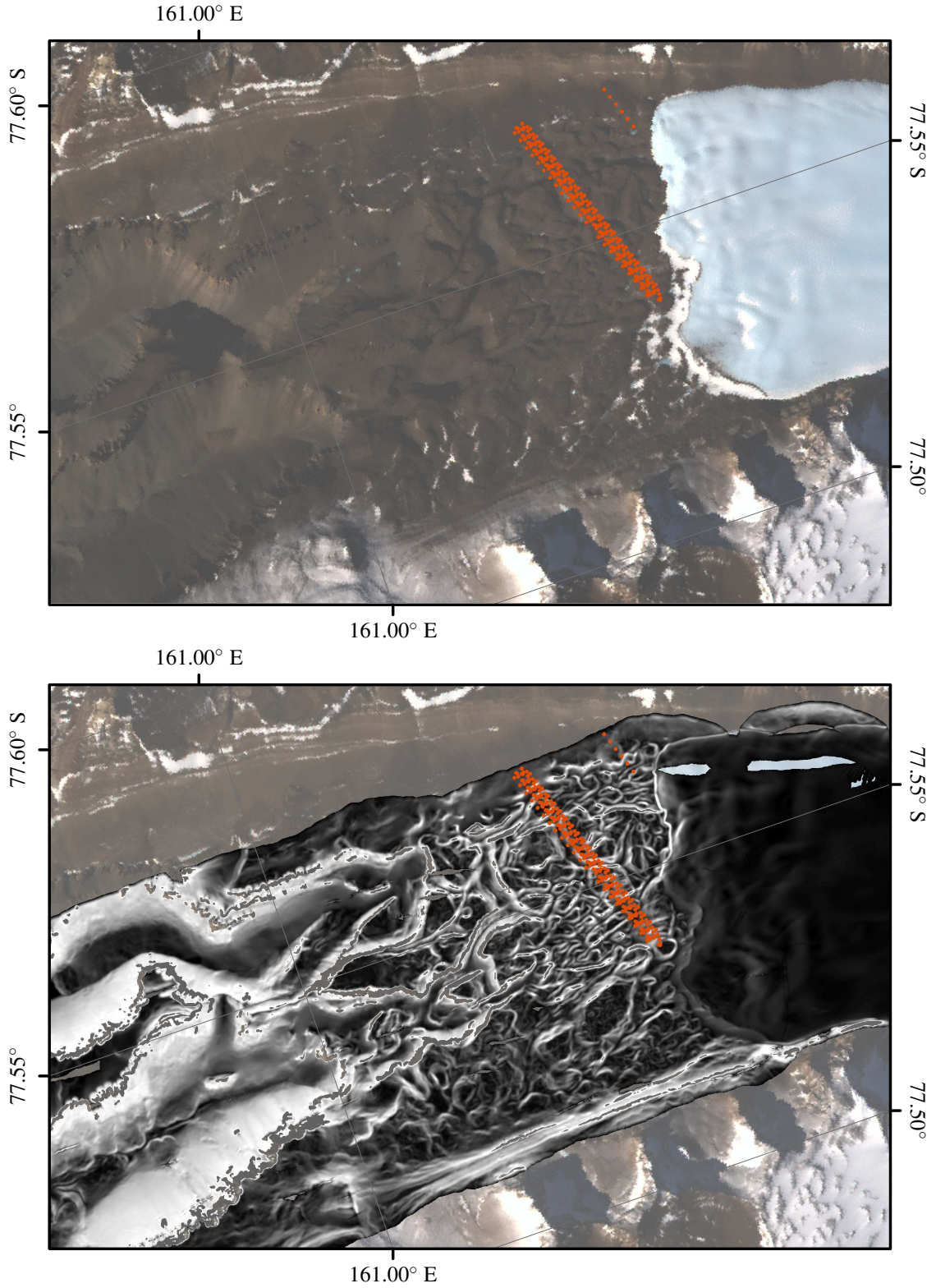

Figure 5.22: Maps of the Labyrinth terrain (top) and its roughness characteristics (bottom). ICESat pulse locations are shown in orange, and the roughness characteristics are shown in white to black (0 m to 12 m for 70 m baseline RMS height. A Landsat mosaic is shown in the background, slope map in bottom image is produced using the *slope* tool in ArcMap 10.1 and the ATM DTM at the original DTM resolution of 2 m pixel^{-1}.

subglacial meltwater, sourced from episodic drainage of subglacial lakes, with positive downstream elevation changes allowed as water is forced through a closed channel system between the bedrock and the glacier [*Lewis et al.*, 2006]. Channel modification is thought to occur by hydraulic plucking and abrasion from bed-load and suspended load [*Lewis et al.*, 2006]. The criss-crossing nature of the channels results in a series of peaks and troughs that is a terrestrial analogue for the spatial distribution of roughness observed at Mawrth Vallis. The roughness elements are typically larger than those observed at Mawrth Vallis, up to 600 m wide and 250 m deep, but smaller, and less homogeneous, than those observed at any of the other Mars sites [*Lewis et al.*, 2006].

Each of the different measures of pulse-width are compared to the original and energy weighted measures of surface roughness and slope used in the previous section. The pulse selection uses only the Level 1 criteria described above, with an echo-profile fit R-squared of 0.95, and only pulses over the bare-earth terrain used, as shown in Figure 5.22.

5.9.2 RESULTS

Once pulses affected by atmospheric effects have been removed, 145 useable pulses are found over the terrain. The results are presented in Table 5.12, for each of the different pulse-width and surface characteristic measures.

There are three points of interest raised from the results presented. The first is the results comparing the pulse-widths to slope are typically much poorer than those compared to the different measures of surface roughness. In Tables 5.7a to 5.7d, R-squared values are typically similar to those using the RMS height, whereas over the Labyrinth terrain, the R-squared values over slope are between 0.14 and 0.26 smaller for four of the five measures of pulse-width. This suggests that, like the Mars study, only consistent slopes can be used to calibrate pulse-width data, as some areas may have low slope but high roughness due to the spatial distribution terrain across the pulse-footprint.

Another point is that the GLAH05 pulse-widths consistently produces the largest R-squared values, which is not observed previously. The 10 % Peak Energy threshold produces the next best correlations, followed by 5 % and 20 % Peak Energy thresholds.

Finally, and possibly most importantly, FWHM pulse-widths show significantly poorer R-squared values than observed using other estimates of pulse-width. For the different estimates of surface roughness, the R-squared values are approximately 0.4 lower than the highest R-squared values using the GLAH05 values, but can be up to 0.51 smaller; slope results are also smaller, but with a smaller difference due to the consistently poor results when comparing to this surface characteristic. The differences between the R-squared values using the FWHM pulse-widths and the best performing pulse-width are much larger than observed previously using Level 1 and 2 criteria in Tables 5.7a to 5.7d. The pulse-widths derived by MOLA are also estimates of the FWHM profile, derived from the total energy received and the pulse-width at an automatically derived threshold setting. In this case, R-squared values are between 0.4 to 0.6 lower over Mawrth Vallis than the other sites, however, this results in R-squared values over the Mawrth Vallis terrain of <0.1, compared to <0.4 using a similar pulse-width estimate over the Labyrinth terrain. There could be

a link between this pulse-width estimate and measuring surface characteristics over this type of highly variable terrain. Better correlations may observed over the Labyrinth terrain because the data is better co-registered, more accurate estimates of FWHM pulse-widths can be derived from the full echo-profile, and there are greater variations in topography observed over the Labyrinth terrain than Mawrth Vallis, which has been shown previously to result in larger R-squared values.

Due to the low number of original data over the Labyrinth, 305 pulses, Level 3 criteria could not be applied. Using Level 2 criteria, smaller R-squared values are observed ($\sim$0.2 smaller) for all pulse-width estimates except for FWHM, where smaller reductions of $\sim$0.07 are observed.

5.10 DISCUSSION

By using full echo-profile data to derive pulse-widths, high-quality high-resolution DTM data, and well georeferenced and co-registered datasets, the work in this chapter shows surface characteristics can be derived from orbiting laser altimeter pulse-widths.

The best correlating pulse-widths are the 10 % and 20 % Peak Energy thresholds, rather than the FWHM estimates, which are used by laser altimeters over Mars and the Moon. The upper limit of R-squared values of 0.66 using bare-earth terrains over the McMurdo Dry Valleys could suggest that FWHM pulse-widths do not correlate well with surface characteristics, in contrast to the concept outlined in Equation 2.5. The R-squared value correlates well with that observed at Eberswalde Crater in Table 3.8 on Page 131, where the R-squared value is found to be 0.60. A slightly larger R-squared value could be observed here because of improved georeferencing and more accurate estimates of pulse-width from the full echo-profile.

R-squared values increase when using the icy terrains, as shown in Table 5.7c, as well as when using All terrains, as shown in Table 5.7c. The FWHM pulse-width estimates produce an R-squared

Table 5.12: R-squared values of a linear fit of different estimates of pulse-width compared to different estimates of surface roughness and slope over the Labyrinth terrain. The terrain is similar in appearance to Mawrth Vallis, whereby there is high variation in roughness over short baselines, and is used to attempt to find the causes of the poor data over the Martian terrain. In total, 145 pulses are used here, using the Level 1 criteria defined in Table 5.6.

Surface Characteristic	GLAH05†	FWHM‡	5 % Peak‡	10 % Peak‡	20 % Peak‡
RMS height	0.73	0.29	0.71	0.65	0.56
RMS height Gaussian	0.80	0.32	0.79	0.74	0.63
Range	0.70	0.40	0.69	0.68	0.61
Range Gaussian	0.75	0.33	0.76	0.72	0.63
IQR	0.70	0.19	0.70	0.61	0.49
IQR Gaussian	0.74	0.30	0.72	0.67	0.55
Slope	0.48	0.39	0.54	0.58	0.51
Slope Gaussian	0.47	0.41	0.54	0.59	0.53

value of 0.70 under these conditions, which is in-line with some individual orbit results presented in Chapter 4. This suggests that using highly reflective surfaces can produce higher R-squared values. However, it still performs consistently poorer than the other pulse-width estimates explored here, which approach R-squared values of 0.8.

Lower threshold pulse-widths derived from the full echo-profile appear to produce better R-squared values. Using a percentage threshold rather than an absolute value helps reduce the effect of low signal returns. Using the 8-Gaussian fit to the profile also appears to remove the effects of background signal noise, producing a smooth line from which pulse-width estimates can be derived. Increasing the number of Gaussian fits beyond this is unlikely to improve the quality of the fit with the original data, as in Figure 5.14.

The best correlations are observed when the pulse-widths are compared to slope and RMS height, however, the difference between the R-squared values using these measures and IQR and range are small, typically less than 0.05. When comparing 10 % and 20 % Peak Energy pulse-widths to slope and RMS height, R-squared values can be $\geq$0.8, significantly better than observed using MOLA and LOLA pulse-widths. Furthermore, the R-squared values are consistently high and do not vary with the transmitted energy. Accounting for the energy distribution across the pulse-footprint improves R-squared values by up to 0.04, which could be significant, however, typical improvements are 0.01, and no improvements are observed when slope was measured in this way. The slight improvement in R-squared values suggests the energy distribution has a measurable difference in the resulting estimate of surface roughness, but it is difficult to convert this into an interpretable dataset when laser altimeter pulse-widths are used to map surface roughness. One method is to find the relationship between the measure of surface roughness and the measure accounting for the energy distribution across the pulse-footprint, however, this may introduce another source of uncertainty and variation within the data. Using RMS height as an example, the linear relationship between the RMS height and RMS height Gaussian (as in Tables 5.7a to 5.7d) over bare-earth terrains is

$$\text{RMS Height} = (1.81 \times \text{RMS Height Gaussian}) - 0.03, \qquad [5.1]$$

which has an R-squared of 0.97. From such an example, it may be possible to determine the roughness at the baseline of the pulse-footprint, removing the effect of the energy weighting applied. One must assume that a similar relationship exists on other planetary bodies however.

The best pulse selection criteria appears to be Level 1 and 2. Level 3 R-squared values are consistently much poorer. There are small differences between the Level 1 and 2 criteria R-squared values, but there is no consistent pattern across the different terrains or surface characteristic used. As the differences in R-squared values between equivalent pulse-width and surface characteristic measures are $<$0.03 for these selection criteria, it is not thought significant which one is best. Instead, using Level 1 criteria is preferred as it offers more pulse data.

Increasing the profile fit limit to an R-squared of 0.99 has little effect on the observed R-squared values for all except the 5 % Peak Energy pulse-width estimates and the Level 3 criteria correlations.

R-squared values for the 5 % Peak Energy pulse-width estimates increase to match that of the 10 % and 20 % Peak Energy pulse-widths, whilst the Level 3 criteria R-squared values are in-line with Level 1 and 2 criteria R-squared values in the case of the latter. Imposing a stricter lower limit for the profile fit will remove pulses that contain more noise or natural variation within the signal. This is particularly important for the lowest threshold limits, which may be triggered by noise, hence the improvement in R-squared values for the 5 % thresholds.

The very slow ice velocities observed in the ROI means that pulse-widths can be compared to estimates of surface characteristics from all terrains. The initial assessment explored only bare-earth terrains, as this is closely linked to the work completed in the previous science chapters. The largest R-squared values are observed using data from all terrains, followed by the icy terrain data, and, finally, the bare-earth data. The higher R-squared values observed using icy terrains rather than bare-earth terrains could be a result of the difference in reflectance of these surfaces: the icy terrains, which are bright and, unlike alpine glaciers, are not debris covered, have a mean reflectance of 0.54, whereas the bare-earth terrains have a mean reflectance of 0.38. Higher relative received energy pulses are likely to improve the quality of the pulse-width measurement, as this typically increases the Peak Energy and the respective thresholds used for pulse-width estimation here, however it is unclear why this does not translate to the transmitted energy.

Like the work in previous chapters, the distribution of surface roughness and slope affects the quality of the calibration, as observed over Odell Glacier in Table 5.9 and Figure 5.20. Poor R-squared values are also observed over Erebus, but this may be a result of poor co-registration of the DTM rather than the distribution of surface characteristics within the pulse-footprint, as shown by the large shift in elevation in this DTM. There is a loose correlation between the types of terrains producing the best correlations: the large valleys, with large distributions of surface roughness and slope appear to produce the best correlations, whilst flatter terrains, such as Hut Point, White Island, and Radian Glacier appear to show lower correlations.

Table 5.11 suggests that detrended surface roughness cannot be derived from pulse-width data using the assumption described in *Neumann et al.* [2003a] and outlined in Equation 2.7. This assumption appears to be over-simplified and not suitable for real-world applications. In reality, the distribution of topography across a pulse-footprint may result in a low slope value, but a high surface roughness value, which may have the same surface roughness value as highly sloping smooth terrain. Using only highly sloping terrains, as defined from the DTM data, decreases the R-squared values so that no correlation, rather than weak correlation, is observed.

Finally, the Labyrinth terrain offers the opportunity to determine whether the results at Mawrth Vallis will always occur, or if they are a result of the MOLA instrument setup and co-registration errors. The results suggest that, where the distribution of surface roughness and slope is highly variable over short baselines comparable to the pulse-footprint, as observed at Mawrth Vallis and the Labyrinth terrain, using the FWHM as a measure of pulse-width will result in poor correlations when compared to surface characteristics. Over the non-Labyrinth bare-earth terrains, the R-squared value when comparing the FWHM and 10 % Peak Energy pulse-widths is 0.84, whereas over the Labyrinth the R-squared value is 0.54. This suggests that the profile of the pulses over the Labyrinth

is typically very different to those over other bare-earth terrains. The mean profile of echo-profiles over these terrains appear very similar to each other, but there could be a clue in that there is a wider distribution of pulse-widths for FWHM relative to 10 % Peak Energy pulse-widths. The R-squared values observed using the FWHM pulse-width estimates over the Labyrinth terrain may be better than those observed over Mawrth Vallis due to (1) improved georeferencing and co-registration of datasets, (2) more accurate estimates of the FWHM pulse-width, and (3) slightly larger roughness features at the Earth analogue site, which results in a slightly wider distribution of surface characteristics and therefore a greater chance of better correlations being observed.

5.11 EARTH CHAPTER SUMMARY

The results using ICESat full echo-profiles show that surface characteristics can be derived from orbiting laser altimeter pulse-widths. However, the method of estimating the pulse-widths affects the resulting correlations with surface characteristics, with the 10 % Peak Energy pulse-widths performing best, closely followed by 20 % Peak Energy thresholds.

Like in previous chapters, very strong correlations are observed when these pulse-widths are compared to slope, with RMS height also performing very well. Range and IQR are more inconsistent, but strong correlations can be observed using some combinations.

Using pulses over an area known as the Labyrinth, the work shows that poor correlations are observed over Mawrth Vallis in Chapter 3 due to the method of estimating pulse-width. FWHM pulse-widths, which are predicted by MOLA using an automatic threshold detection system and the total received energy, performed significantly poorer than other estimates of pulse-width, whilst comparisons with the different pulse-widths and slope also performed consistently poorly. FWHM pulse-widths perform consistently poorer than other measures throughout the work, however, they performed especially poorly under these conditions, leading to the suggestion that highly variable surface roughness and slope over baselines comparable to that of the pulse-footprint may result in an echo-profile that is very different in appearance to other bare-earth terrains, and one where the FWHM does not correlate with surface characteristics. This could be a result of the distribution of elevations within the pulse-footprint resulting in a laser altimeter echo-profile that is very different in shape at the higher intensity returns, where the FWHM pulse-width will be effective, compared to the lower intensity returns as the intensity rises and falls, where lower threshold pulse-width estimates are effective.

The hypothesis put forward by *Gardner* [1992] that detrended surface roughness can be derived from the pulse-width by a simple model of the effects of slope on pulse-widths is shown not to work efficiently here, with R-squared values <0.2. This suggests that Equation 2.7 over-simplifies the effect of slope on pulse-width values.

6

Concluding Remarks and Future Work

This chapter summarises: the concluding remarks from the three science chapters; the principal recommendations for future laser altimeter instruments; the contributions the work in this thesis has made to science; suggestions for future work.

The principal conclusion is that surface characteristics can be derived from the pulse-width of orbiting laser altimeter instruments.

The principal recommendations for future planetary laser altimeter instruments are outlined, using the lessons learnt from the work in this thesis. The primary recommendation is to use the full echo-profile to calculate laser altimeter pulse-widths at 10 % Peak Energy thresholds.

The contributions made to science are outlined, along with a list of current and future peer-reviewed journal and conference papers to come from the work presented in this thesis.

Finally, the chapter outlines potential for future work related to the work outlined in this thesis, including current and future datasets, and laboratory work.

6.1 THESIS OVERVIEW

The work in this thesis set out to explore the relationship between planetary laser altimeter pulse-widths and surface characteristics within the pulse-footprint, testing the hypothesis put forward by *Gardner* [1992], in Equation 2.5 on Page 50, by comparing surface roughness and slope estimates from high-resolution Digital Terrain Models (DTMs) to pulse-width data collected over Mars, the Moon, and Earth. The research is motivated by the fact that global maps of surface roughness produced in *Neumann et al.* [2003a] and *Smith et al.* [2001] from Mars Orbiter Laser Altimeter (MOLA) pulse-widths use a theoretical relationship that had not been calibrated over extensive areas, with previous results not showing conclusive proof of a useful relationship [*Gardner*, 1992; *Kim and Muller*, 2008; *Kim and Park*, 2011; *Saiger et al.*, 2007]. Furthermore, the research set out to explore whether detrended surface roughness can be derived from the pulse-widths, using a basic assumption of the effects of slope on the total received pulse-width, as proposed by *Neumann et al.* [2003a].

6.1.1 MARS

Data from MOLA is compared to surface roughness and slope estimates from High Resolution Imaging Science Experiment (HiRISE) and Context Camera (CTX) DTMs, at $1\,\mathrm{m\,pixel^{-1}}$ and $18\,\mathrm{m\,pixel^{-1}}$ respectively.

A Slope-Corrected version of the MOLA pulse-width dataset provides the highest correlations, which removes erroneous data and makes 1 km slope corrections. The highest correlations are observed over Eberswalde Crater, where roughness features are large and homogeneous. Where roughness is heterogeneous and small, poor correlations are observed. Over very rough terrain, pulse-widths appear correlated to pulse-footprint-scale slopes. Finally, it appears that detrended surface roughness cannot be derived from the dataset.

The poor correlations generally observed are thought to be due to poor estimates of pulse-width, which are derived from the estimates of the pulse-width above an automatically set threshold and the total energy received. However, the work in Chapter 5, which uses full echo-profiles in Ice, Cloud, and land Elevation Satellite (ICESat) data, therefore enabling different pulse-width thresholds to be tested, shows that Full Width Half Maximum (FWHM) pulse-widths perform poorer than other, lower threshold estimates, when compared to surface characteristics. Poor co-registration of datasets, due to large differences in resolution between datasets, is also likely to play a part, particularly over Mawrth Vallis, and for detrended pulse-widths, which are likely to be more susceptible to co-registration errors.

6.1.2 THE MOON

Data from Lunar Orbiter Laser Altimeter (LOLA) are compared to surface characteristics of underlying terrain derived from high-resolution, $2\,\mathrm{m\,pixel^{-1}}$, DTMs from Lunar Reconnaissance Orbiter Camera - Narrow Angle Camera (LROC-NAC) over 16 regions across the lunar surface. It

was expected that by using a combination of a more recent laser altimeter instrument and better co-registered datasets, that greater correlations would be observed.

Instead, poor correlations are observed over the individual regions, whilst a visual inspection suggests that pulse-width data in individual orbits behaves differently. Many orbits reveal little or no correlation with underlying surface features and only 45 of the 329 orbits with significant results reveal R-squared values greater than or equal to the sites showing some correlation over Mars (R-squared $>$0.4). However, some orbits reveal very strong correlations when pulse-widths are compared to slope, leading to the suggestion that surface characteristics can be reliably derived from laser altimeter pulse-widths, assuming high data quality. Like the Mars study, rougher, topographically variable terrain typically produces better correlations.

6.1.3 EARTH

To explore whether better correlations can be found when comparing surface characteristics to laser altimeter pulse-widths, full echo-profiles from ICESat are compared to high-resolution DTMs over the McMurdo Dry Valleys, Antarctica, derived from the Airborne Topographic Mapper (ATM). The terrain covers both bare-earth and icy terrains, which links with the work carried out in previous chapters and provides data relevant to future laser altimeter instruments, such as the Ganymede Laser Altimeter (GALA) [*Hussmann et al.*, 2013]. The data are well co-registered and using full echo-profiles enables different pulse-width thresholds to be tested to find larger R-squared values. Finally, an area known as the Labyrinth also provides an opportunity to repeat the Mawrth Vallis study, as this terrain appears morphologically similar in the spatial distribution of roughness and slope.

The results show surface roughness and slope can be derived more reliably by using different thresholds for measuring pulse-widths. Using a 10 % Peak Energy threshold produces the best correlations between laser altimeter pulse-widths and surface characteristics. The pulse-widths are also selected based on three criteria, defined by different atmospheric conditions relating to when the pulses were fired: cloud (Level 1), fog and blowing snow conditions (Level 2), and forward-scattering (Level 3). The best R-squared values are observed using Level 1 and 2 criteria. Level 3 selection criteria performs poorer, except when tighter controls on fitting the echo-profile are employed, which could be a result of pulses less affected by background noise being used. Better correlations are observed using the icy terrains than the bare-earth terrains, possibly due to higher reflectance from icy surfaces resulting in a more accurate echo-profile.

When using the FWHM pulse-width threshold, as used by MOLA, over the Labyrinth terrain, poor results are again observed. Using different thresholds produces much better correlations, leading to the suggestion that surface roughness over heterogeneous terrain cannot be derived using FWHM pulse-widths. Interestingly, R-squared values using slope also produces poor correlations for all pulse-width estimates, which could suggest that only regions of consistent slope can be interpreted and that surface roughness estimates using other measures are more reliable or consistent.

Again, detrended surface roughness is compared to the surface roughness contribution to the

received pulse-width, as defined in Equation 2.7, to explore whether the assumption by *Neumann et al.* [2003a] holds true. This is shown not to be the case and suggests that the results found over Mars in a similar study are not solely a result of poor georeferencing, but are more likely because Equation 2.7 over-simplifies the effects of roughness on the received pulse-width.

6.1.4 OVERALL

The work has shown that surface roughness and slope can be derived from laser altimeter pulse-widths. However, the FWHM method proposed by *Gardner* [1992], and employed by MOLA and LOLA, has been shown to perform poorly even under ideal conditions. Instead, surface characteristics are best derived from pulse-widths measured at the 10 % (preferred) or 20 % Peak Energy threshold crossing. These pulse-widths perform consistently well when ICESat data is used and cloud hitting pulses are removed, with R-squared values $\sim$0.8, whilst imposing stricter atmospheric criteria on pulse selection does not improve correlations significantly, and reduces data coverage. Where roughness and slope are heterogeneous at baselines similar to the pulse-footprint, pulse-widths are better correlated to RMS height, rather than slope.

Finally, it appears that: (1) photon and speckle noise, (2) multiplication noise by the detector, (3) detector thermal noise, (4) and quantisation noise, as predicted by *Gardner* [1992], introduce some natural variation within the observed echo, which reduces the correlations between these pulse-widths and underlying surface characteristics.

6.2 RECOMMENDATIONS FOR FUTURE INSTRUMENTS

The principal recommendations for future laser altimeter instruments are

- Record the full echo-profile at high-resolution ($\leq$1 ns), to enable more accurate estimates of pulse-width to be derived.
- Smooth the received echo efficiently to remove the effects of background noise in the received echo-profile, from which the pulse-width is derived. Here, the smoothing technique used fits up to eight Gaussians to the received echo to produce a smooth profile, from which the location of the threshold cross can be identified.
- Use 10 %, or 20 %, Peak Energy threshold, rather than the FWHM proposed by *Gardner* [1992], as an estimate of the pulse-widths as these are shown to correlate consistently well with surface roughness over all terrain types. These pulse-widths also correlate to slope estimates, except where terrain is heterogeneous at baselines similar to the pulse-footprint.

The following are not necessary in producing a good pulse-width dataset, but are preferred in producing extra information that can benefit data quality

- The full echo-profile does not have to be permanently recorded in the dataset, but it can provide another means to identify poor data and explore different thresholds.

- Recording and accounting for the energy distribution across the pulse-footprint does improve the observed correlations with underlying terrain, which can be reliably translated to roughness without this energy effect, as shown in Equation 5.1. However, the improvement is not considered significant and is only recommended if instrument setup and data transmission, storage, and processing rates allow.

- If a high-resolution stereo-imaging instrument is also part of the spacecraft payload, using a similar set up as LOLA, in that the bore-sight for the laser altimeter was in-line with the imaging instrument view, benefited the instrument in being able to produce accurate DTMs that can be used to calibrate the pulse-width data.

6.3 CONTRIBUTIONS TO SCIENCE

The work in this thesis benefits past and current datasets, which have culminated in a set of recommendations for future instruments, outlined above. Furthermore, work from this thesis has been presented in peer-reviewed journals and at major conferences.

6.3.1 THESIS CONTRIBUTIONS

- The testing of different pulse-width thresholds has lead to the identification of a more suitable pulse-width threshold to be used to infer surface characteristics within the pulse-footprint. Surface characteristics over bare-earth terrains on Earth are best derived from laser altimeter pulse-widths measured from the 10 % Peak Energy threshold. This result is expected to be extrapolated to planetary terrains, as pulses affected by atmospheric effects are removed in the study, as described below. The FWHM method of estimating pulse-widths, which is used by MOLA and LOLA, is revealed to produce the poorest correlations with surface characteristics when compared to the Standard Deviation of Gaussians, and 5 %, 10 % and 20 % Peak Energy thresholds [*Smith et al.*, 2001, 2010b]. However, to accurately measure pulse-widths using the recommended threshold, the full echo-profile must be recorded and processed for effective background noise removal.

- The method used to measure surface characteristics does not significantly impact upon the observed correlations between laser altimeter pulse-widths and surface characteristics, which varies very little, however RMS height performs consistently well. A maximum R-squared value of 0.81 is observed in Chapter 5, although typical values are $>$0.72. Using the Range as a measure of surface roughness tends to produce poorer correlations, especially when the strictest criteria for pulse selection are applied. The results can be further improved by applying a weighting to the surface roughness calculation to reduce the impact of the energy distribution across the laser altimeter pulse-footprint, however, as the R-squared value typically improve by only 0.01 to 0.02, this step is not a requirement for future instruments.

- Topographic variation can also be compared to slope within the pulse-footprints, which,

when compared to laser altimeter pulse-widths over consistently rough or smooth terrain, are shown to produce some of the highest correlations, with a maximum R-squared 0f 0.8 observed inChapter 5. Unlike above, applying a weighting to reduce the effects of transmitted energy across the laser altimeter pulse-footprints does not improve the results.

- It is found that applying the strictest criteria in pulse selection, which remove pulses affected by atmospheric effects, is not required to produce the best correlations, instead, removing only cloud hitting pulses is required.

- Deriving surface characteristics from laser altimeter pulse-widths is found to work best over high-reflectance surfaces, which is associated with the higher energy return in the echo-profile and the higher Signal to Noise Ratio (SNR).

- Over terrain with short baseline slopes and roughness features, estimates of slope show poor correlations with all pulse-width estimates, as do correlations between pulse-width using the FWHM method and all measures of surface characteristics used here. For this reason, the relationship between RMS height and 10 % Peak Energy pulse-widths is thought to be most consistent across all bare-earth terrains.

- Detrended roughness cannot be derived from the pulse-width data using the assumption made in Equation 2.7, which is thought to be over-simplifying the effects of detrended roughness on the echo-profile.

- Finally, when combined together, the contributions of this thesis help aid the development of future laser altimeter instruments, which will help improve data quality for future missions and lead to a greater understanding of terrains that have so far not been fully explored with high-resolution mapping, such as the BepiColombo Laser Altimeter (BELA) and GALA instruments.

6.3.2 JOURNAL PAPERS

The following paper has been produced from the work outlined above

W. Poole, J.-P. Muller, S. Gupta, and P. M. Grindrod. Calibrating Mars Orbiter Laser Altimeter pulse widths at Mars Science Laboratory candidate landing sites. *Planetary and Space Science*, 99:118–127, September 2014b. doi:10.1016/j.pss.2014.05.012

6.3.3 CONFERENCE PROCEEDINGS

The work presented here has been presented at the following conferences

W. D. Poole, J.-P. Muller, and S. Gupta. On the Calibration of MOLA Pulse-Width Surface Roughness Estimates Using High-Resolution DTMs. In *43rd Lunar and Planetary Science Conference*, Houston, Tx, March 2012b. URL: http://www.lpi.usra.edu/meetings/lpsc2012/pdf/1854.pdf

W. D. Poole, J.-P. Muller, and S. Gupta. On the calibration of Mars Orbiter Laser Altimeter surface roughness estimates using high-resolution DTMs . In *European Geosciences Union General Assembly*, 2012a. URL: http://meetingorganizer.copernicus.org/EGU2012/EGU2012-4305.pdf

W. D. Poole, J.-P. Muller, and S. Gupta. Mars Orbiter Laser Altimetry Pulse-Widths an Indicator of Surface Roughness at Gale Crater [EPSC2012-554-1]. In *European Planetary Science Congress*, Vienna, Austria, 2012c. URL: http://meetingorganizer.copernicus.org/EPSC2012/EPSC2012-554-1.pdf

W. D. Poole, J.-P. Muller, and S. Gupta. How Reliable are Surface Roughness Estimates from Planetary Laser Altimeter Pulse-Widths? An Assessment Using MOLA and LOLA Pulse-Width Data. In *44th Lunar and Planetary Science Conference*, Houston, USA, March 2013a. URL: http://www.lpi.usra.edu/meetings/lpsc2013/pdf/1511.pdf

W. D. Poole and J.-P. Muller. On an assessment of surface roughness estimates from lunar laser altimetry pulse-widths for the Moon from LOLA using LROC narrow-angle stereo DTMs. In *European Geosciences Union General Assembly*, Vienna, Austria, April 2013. URL: http://meetingorganizer.copernicus.org/EGU2013/EGU2013-12757.pdf

W. D. Poole, J.-P. Muller, S. Gupta, and P. M. Grindrod. Surface roughness from MOLA backscatter pulse-widths. In *European Planetary Science Congress*, London, UK, September 2013b. URL: http://meetingorganizer.copernicus.org/EPSC2013/EPSC2013-321.pdf

W. D. Poole, J.-P. Muller, and P. M. Grindrod. Footprint Scale Surface Roughness from ICESat Pulse-Widths: Lessons Learnt for Future Planetary Laser Altimeters. In *45th Lunar and Planetary Science Conference*, Houston, Tx, March 2014a. URL: http://www.hou.usra.edu/meetings/lpsc2014/pdf/1150.pdf

6.4 FUTURE WORK

The primary conclusion from the work presented in this thesis is that planetary surface characteristics within the pulse-footprint of an orbiting laser altimeter can be derived from an estimate of the pulse-width of the echo-profile. This opens the door to future research using these data, to maximise the quality and volume of data that can be harvested from this datasource.

6.4.1 CURRENT DATASETS

Chapter 3 suggests that little more can be derived from the MOLA pulse-width dataset, however, the LOLA dataset may yet prove to be a valuable resource. Some orbits show strong correlations between the pulse-width and pulse-footprint-scale slopes, which fulfils one of the science goals of the instrument: aiding the identification of candidate landing and roving sites [*Smith et al.*, 2010a,b]. Future work using this dataset will have to focus on either recalibrating the poor-quality pulse-width data observed in many orbits, or producing a method to identify high-quality orbits, as LROC-NAC data coverage is too low to be able to calibrate each orbit. Assuming either of these are

completed, the result could either be a global map of pulse-footprint-scale slopes over the Moon, or, if there is a low proportion of high-quality orbits, a map of pulse-footprint-scale slopes over the poles only, where the concentration of orbits is high. As the target landing sites for future lunar missions are the lunar poles, this latter option would still provide a useful dataset. If a global map of fine-scale slopes could be derived, this would provide data at a significantly smaller baseline than used previously, which could reveal further information on surface dating, and the processes that helped in the formation and evolution of the surface, similar to the work presented in *Kreslavsky et al.* [2013] and *Rosenburg et al.* [2011].

ICESat echo-profile data has been used to determine the distribution of vegetation, however this work has shown that these profiles can also be used to determine surface roughness and slope within the pulse-footprint over bare-earth and icy terrains [*Harding and Carabajal*, 2005]. Estimates of slope assuming no surface roughness, and surface roughness assuming no slope, were provided in the datasets until they were removed after a report identified that these may be unreliable [*Brenner et al.*, 2011]. The work here shows that using 10 % Peak Energy threshold, rather than the standard deviation of fitted Gaussians, provides a better estimate of these surface characteristics within the pulse-footprint. Recalculating the surface roughness and slope over bare-earth terrains using this new measure of pulse-width will produce a useful dataset that could be used to explore seasonal and annual changes in ice sheet, glacier, and sea ice roughness, which could lead to a better understanding of the energy balance in a climatically sensitive environment.

The current Mercury Laser Altimeter (MLA) mission provides data on the pulse-width as a result of terrain within the pulse-footprint, in a similar approach as MOLA and LOLA [*Cavanaugh et al.*, 2007; *Zuber et al.*, 2008, 2012]. Using this dataset, new information could be revealed about fine-scale surface features, especially in permanently shadowed regions. However, high-resolution DTMs are not yet available, meaning that calibration is not possible. Estimates could be produced using the relationships derived in this work.

6.4.2 FUTURE MISSIONS

Planned planetary laser altimeter instruments include GALA and BELA, visiting Ganymede and Mercury respectively.

BELA will form part of the Mercury Planetary Orbiter (MPO) payload, which is the ESA component to the BepiColombo mission to Mercury and expected to launch in July 2016 and arrive in 2024 [*ESA*, 2014a]. The pulse-footprint is expected to be 20 m to 50 m, with a 2 ns timing resolution enabling surface roughness and slope estimates from pulse-width estimates [*Universität Bern*, No Date.]. Importantly, BELA can record the full echo-profile, enabling methods like those developed in this thesis to be applied, for a more accurate estimate of the surface characteristics within the pulse-footprint [*Universität Bern*, No Date.]. This is particularly important, given the high noise levels over the day-side of Mercury [*Universität Bern*, No Date.]. Data from BELA could also be compared and cross-calibrated to that from MLA for greater coverage and quality.

GALA also plans to explore surface roughness and slope, over Ganymede, however this

instrument is still in the early stages of development, with the launch not due until 2022 and arrival at Jupiter in 2030 [*ESA*, 2014b; *Hussmann et al.*, 2013].

6.4.3 SINGLE PHOTON DETECTION

The future of laser altimetry and 3-d terrain mapping may lie in the use of single-photon counting lidar systems. An advantage of these systems is that the detection levels are sensitive enough to detect just a single photon within a reflected pulse to record a positive ground return [*Vacek et al.*, 2011, 2015]. This results in less power required for the transmitted pulse, which makes the system smaller and more efficient, and the possibility to split the transmitted beam into a series of spots, which can be arranged in an array so that the lidar becomes a 3-d imager, such as the Sigma Space photon counting system [*Degnan et al.*, 2008]. Flying altitudes for lidar systems can then be increased, whilst post-spacing of the resulting datasets remains the same, with datasets of 8 points m^{-2} to 12 points m^{-2} achieved at flying altitudes of over 7 km, and scanning methods. Furthermore, ground returns can also be recorded in dense fog, vegetated terrains, and water in a single pulse due to the single photon sensitivity [*Degnan et al.*, 2008; *Gwenzi and Lefsky*, 2014]. Finally, *Degnan et al.* [2008] report that this technology can be successfully scaled to orbital distances to map planetary surfaces, which could produce datasets on the few metre scales with a single laser altimeter using a few Watts of power.

The disadvantage of this system is that it does not produce a waveform, meaning that the surface roughness from pulse-width cannot be applied. However, the higher data density capabilities of the system may result in surface roughness being calculated between data points, similar to the 5-spot LOLA pulse design described in Chapter 4.

One such instrument that will put this technology into action is the ICESat-2 mission, as the new mission objectives are to include the determination of vegetation height [*Herzfeld et al.*, 2014; *Moussavi et al.*, 2014]. The transmitted pulse will have an energy of 25 µJ to 100 µJ, 6 beams across three tracks that are separated by 3.3 km, and a pulse-rate of 10 kHz to produce a much denser elevation dataset [*Moussavi et al.*, 2014]. The multi-beam approach and the photon counting system will produce a point-cloud of elevation measurements, which should prove better at the determination of canopy height within the pulse-footprint [*Gwenzi and Lefsky*, 2014; *Herzfeld et al.*, 2014; *Moussavi et al.*, 2014]. A challenge is to then extract the forest canopy height, which can appear fuzzy in the point-cloud, as the number of expected return photons can range from 0 to 10 over vegetated areas due to the low reflectivity of soil and vegetation [*Moussavi et al.*, 2014].

6.4.4 LABORATORY AND FIELD WORK

All laser altimeters are calibrated before flight to ensure correct alignment and transmitted power is as expected, however, a further step could also could be to replicate the returns over different terrain types and morphologies. This could explore the effects of surface reflectance, moisture, materials, and morphology on the resulting pulse-width. Clearly, the pulse-width in laboratory or small-scale field testing will be much smaller, so terrain features need to be scaled accordingly,

and the timing resolution of the instrument will need to be significantly greater to measure small differences in elevation ($\sim$1 mm). A range of conditions could be replicated to change the amount of received energy either through greater target surface distances or atmospheric conditions.

REFERENCES

W. Abdalati, H. J. Zwally, R. Bindschadler, B. Csatho, S. L. Farrell, H. A. Fricker, D. Harding, R. Kwok, M. Lefsky, T. Markus, A. Marshak, T. Neumann *et al.* The ICESat-2 Laser Altimetry Mission. *Proceedings of the IEEE*, 98(5):735–751, May 2010. doi:10.1109/JPROC.2009.2034765.

J. B. Abshire, X. Sun, and R. S. Afzal. Mars Orbiter Laser Altimeter: Receiver Model and Performance Analysis. *Applied Optics*, 39(15):2449–2460, 2000. doi:10.1364/AO.39.002449.

J. B. Abshire, X. Sun, H. Riris, J. M. Sirota, J. F. McGarry, S. Palm, D. Yi, and P. Liiva. Geoscience Laser Altimeter System (GLAS) on the ICESat Mission: On-orbit measurement performance. *Geophysical Research Letters*, 32(21):L21S02, 2005. doi:10.1029/2005GL024028.

T. Acharya and A. K. Ray. *Image Processing*. Principles and Applications. John Wiley & Sons, Inc., Hoboken, NJ, USA, September 2005. ISBN 9780471719984. doi:10.1002/0471745790.

O. Aharonson, M. T. Zuber, G. A. Neumann, and J. W. Head III. Mars: Northern hemisphere slopes and slope distributions. *Geophysical Research Letters*, 25(24):4413–4416, December 1998. doi:10.1029/1998GL900057.

O. Aharonson, M. T. Zuber, and D. H. Rothman. Statistics of Mars' topography from the Mars Orbiter Laser Altimeter: Slopes, correlations, and physical Models. *Journal of Geophysical Research*, 106(E10):23723–23735, October 2001. doi:10.1029/2000JE001403.

A. L. Albee, F. D. Palluconi, and R. E. Arvidson. Mars Global Surveyor Mission: Overview and Status. *Science*, 279(5357):1671–1672, March 1998. doi:10.1126/science.279.5357.1671.

J. Albertz, M. Attwenger, J. Barrett, S. Casley, P. Dorninger, E. Dorrer, H. Ebner, S. Gehrke, B. Giese, K. Gwinner, C. Heipke, E. Howington-Kraus *et al.* HRSC on Mars Express - Photogrammetric and cartographic research. *Photogrammetric Engineering and Remote Sensing*, 71(10):1153–1166, October 2005. URL: http://www.asprs.org/a/publications/pers/2005journal/october/2005_oct_1153-1166.pdf.

American Society for Photogrammetry and Remote Sensing Lidar Committee. ASPRS Guidelines: Vertical Accuracy Reporting for Lidar Data. Technical report, American Society for Photogrammetry and Remote Sensing, May 2004a. URL: http://www.asprs.org/a/society/committees/lidar/Downloads/Vertical_Accuracy_Reporting_for_Lidar_Data.pdf.

American Society for Photogrammetry and Remote Sensing Lidar Committee. ASPRS LIDAR GUIDELINES: Horizontal Accuracy Reporting. Technical report, American Society for Photogrammetry and Remote Sensing, 2004b. URL: http://www.asprs.org/a/society/committees/standards/Horizontal_Accuracy_Reporting_for_Lidar_Data.pdf.

F. S. Anderson. Analysis of MOLA data for the Mars Exploration Rover landing sites. *Journal of Geophysical Research*, 108(E12):8084, 2003. doi:10.1029/2003JE002125.

R. B. Anderson and J. F. Bell III. Geologic mapping and characterization of Gale Crater and implications for its potential as a Mars Science Laboratory landing site. *MARS*, 2010. doi:10.1555/mars.2010.0004.

J. C. Andrews-Hanna. The formation of Valles Marineris: 1. Tectonic architecture and the relative roles of extension and subsidence. *Journal of Geophysical Research*, 117(E3):E03006, March 2012a. doi:10.1029/2011JE003953.

J. C. Andrews-Hanna. The formation of Valles Marineris: 2. Stress focusing along the buried dichotomy boundary. *Journal of Geophysical Research*, 117(E4):E04009, April 2012b. doi:10.1029/2011JE003954.

J. C. Andrews-Hanna. The formation of Valles Marineris: 3. Trough formation through superisostasy, stress, sedimentation, and subsidence. *Journal of Geophysical Research*, 117(E6): E06002, June 2012c. doi:10.1029/2012JE004059.

H. Araki, S. Tazawa, H. Noda, Y. Ishihara, S. Goossens, S. Sasaki, N. Kawano, I. Kamiya, H. Otake, J. Oberst, and C. Shum. Lunar Global Shape and Polar Topography Derived from Kaguya-LALT Laser Altimetry. *Science*, 323(5916):897–900, 2009. doi:10.1126/science.1164146.

B. A. Archinal, R. L. Kirk, T. C. Duxbury, E. M. Lee, R. Sucharski, and D. Cook. Mars Digital Image Model 2.1 Control Network. In *Lunar and Planetary Science XXXIV*, January 2003. URL: http://www.lpi.usra.edu/meetings/lpsc2003/pdf/1485.pdf.

O. Arino, D. Gross, F. Ranera, M. Leroy, P. Bicheron, C. Brockman, P. Defourny, C. Vancutsem, F. Achard, L. Durieux, L. Bourg, J. Latham *et al.* GlobCover: ESA service for global land cover from MERIS. In *2007 IEEE International Geoscience and Remote Sensing Symposium*, pages 2412–2415. IEEE, 2007. ISBN 978-1-4244-1211-2. doi:10.1109/IGARSS.2007.4423328.

D. C. M. Augustijn, F. Huthoff, and E. H. van Velzen. Comparison of vegetation roughness descriptions. In *th International Conference on Fluvial Hydraulics, River Flow*, Çeşme. Izmir, Turkey, September 2008. URL: http://doc.utwente.nl/60441/.

BAE Systems. Next-Generation Automatic Terrain Extraction (NGATE). Technical report, BAE Systems, 2007. URL: http://www.socetgxp.com/docs/education/white_papers/wp_ngate.pdf.

E. P. Baltsavias. A comparison between photogrammetry and laser scanning. *ISPRS Journal of Photogrammetry and Remote Sensing*, 54(2-3):83–94, July 1999. doi:10.1016/S0924-2716(99)00014-3.

S. Basu, J. Wilson, M. Richardson, and A. Ingersoll. Simulation of spontaneous and variable global dust storms with the GFDL Mars GCM. *Journal of Geophysical Research*, 111(E9):E09004, 2006. doi:10.1029/2005JE002660.

R. E. Bell, D. D. Blankenship, C. A. Finn, D. L. Morse, T. A. Scambos, J. M. Brozena, and S. M. Hodge. Influence of subglacial geology on the onset of a West Antarctic ice stream from aerogeophysical observations. *Nature*, 394(6688):58–62, 1998. doi:10.1038/27883.

P. L. Bender, D. G. Currie, R. H. Dicke, D. H. Eckhardt, J. E. Faller, W. M. Kaula, J. D. Mulholland, H. H. Plotkin, S. K. Poultney, E. C. Silverberg, D. T. Wilkinson, J. G. Williams *et al.* The Lunar Laser Ranging Experiment. *Science*, 182(4109):229–238, October 1973. doi:10.1126/science.182.4109.229.

D. Benn and D. J. A. Evans. *Glaciers and Glaciation*. Hodder Education, 2nd edition, 2010. ISBN 978-0-340-90579-1.

K. Bennett, D. Scholes, J. Wang, and F. Zhou. Orbital Data Explorer User's Manual: COORDINATE SYSTEM? Planetary Data System. November 2011, *Webpage*. URL: http://ode.rsl.wustl.edu/moon/pagehelp/quickstartguide/index.html?coordinate_system.htm. Date of Last Access: 15-06-2015.

G. B. Bonan, K. W. Oleson, M. Vertenstein, S. Levis, X. B. Zeng, Y. J. Dai, R. E. Dickinson, and Z. L. Yang. The land surface climatology of the community land model coupled to the NCAR community climate model. *Journal of Climate*, 15(22):3123–3149, November 2002. doi:10.1175/1520-0442(2002)015<3123:TLSCOT>2.0.CO;2.

S. Bontemps, P. Defourny, E. Van Bogaert, O. Arino, V. Kalogirou, and J. R. Perez. GLOBCOVER 2009: Products Description and Validation Report. Technical report, UCLouvain & ESA Team, February 2011. URL: http://due.esrin.esa.int/globcover/LandCover2009/GLOBCOVER2009_Validation_Report_2.2.pdf.

J. S. Borak, M. F. Jasinski, and R. D. Crago. Time series vegetation aerodynamic roughness fields estimated from modis observations. *Agricultural and Forest Meteorology*, 135(1-4):252–268, 2005. doi:10.1016/j.agrformet.2005.12.006.

A. C. Brenner, H. J. Zwally, C. R. Bentley, B. M. Csathó, D. J. Harding, M. A. Hofton, J.-B. Minster, L. Roberts, J. L. Saba, R. H. Thomas, and D. Yi. Derivation of Range and Range Distributions From Laser Pulse Waveform Analysis for Surface Elevations, Roughness, Slope, and Vegetation Heights. Technical report, Geoscience Laser Altimeter System (GLAS), November 2011. URL: http://www.csr.utexas.edu/glas/pdf/WFAtbd_v5_02011Sept.pdf.

C. Brenner. Aerial Laser Scanning. In *International Summer School "Digital Recording and 3D Modeling"*, pages 1–244, Aghios Nikolaos, Crete, Greece, April 2006. URL: http://www.ikg.uni-hannover.de/fileadmin/ikg/staff/publications/sonstige_Beitraege/Brenner_tutorialSommerSchool2006.pdf.

B. H. Briggs. Roughness of the Moon as a Radar Reflector. *Nature*, 187(4736):490–490, August 1960. doi:10.1038/187490a0.

B. A. Campbell, B. R. Hawke, and D. B. Campbell. Surface morphology of domes in the Marius Hills and Mons Rümker regions of the Moon from Earth-based radar data. *Journal of Geophysical Research*, 114(E1):E01001, January 2009. doi:10.1029/2008JE003253.

B. A. Campbell, N. E. Putzig, L. M. Carter, G. A. Morgan, R. J. Phillips, and J. J. Plaut. Roughness and near-surface density of Mars from SHARAD radar echoes. *Journal of Geophysical Research*, 118(3):436–450, 2013. doi:10.1002/jgre.20050.

I. B. Campbell, G. G. C. Claridge, D. I. Campbell, and M. R. Balks. The Soil Environment of the Mcmurdo Dry Valleys, Antarctica. In *Ecosystem Dynamics in a Polar Desert: the Mcmurdo Dry Valleys, Antarctica*, pages 297–322. American Geophysical Union, Washington, D. C., 1998. ISBN 9780875908991. doi:10.1029/AR072p0297.

M. H. Carr and J. W. Head III. Geologic history of Mars. *Earth and Planetary Science Letters*, 294 (3-4):185–203, June 2010. doi:10.1016/j.epsl.2009.06.042.

J. F. Cavanaugh, J. C. Smith, X. Sun, A. E. Bartels, L. Ramos-Izquierdo, D. J. Krebs, J. F. McGarry, R. Trunzo, A. M. Novo-Gradac, J. L. Britt, J. Karsh, R. B. Katz *et al.* The Mercury Laser Altimeter instrument for the MESSENGER mission. *Space Science Reviews*, 131(1-4):451–479, August 2007. doi:10.1007/s11214-007-9273-4.

M. B. Charlton and K. White. Sensitivity of radar backscatter to desert surface roughness. *International Journal of Remote Sensing*, 27(8):1641–1659, 2006. doi:10.1080/01431160500491740.

A. F. Cheng, R. W. Farquhar, and A. G. Santo. NEAR Overview . *Johns Hopkins APL Technical Digest*, 19(2), 1998. URL: http://www.jhuapl.edu/techdigest/TD/td1902/cheng.pdf.

G. Chin, S. Brylow, M. Foote, J. Garvin, J. Kasper, J. Keller, M. Litvak, I. Mitrofanov, D. Paige, K. Raney, M. Robinson, A. Sanin *et al.* Lunar reconnaissance orbiter overview: The instrument suite and mission. *Space Science Reviews*, 129(4):391–419, April 2007. doi:10.1007/s11214-007-9153-y.

T. D. Cole, M. T. Boies, A. S. El-Dinary, A. Cheng, M. T. Zuber, and D. E. Smith. The Near-Earth Asteroid Rendezvous Laser Altimeter. In *The Near Earth Asteroid Rendezvous Mission*, pages 217–253. Springer Netherlands, Dordrecht, 1997. ISBN 978-94-010-6189-6. doi:10.1007/978-94-011-5200-6_5.

A. Collingwood, P. Treitz, and F. Charbonneau. Surface roughness estimation from RADARSAT-2 data in a High Arctic environment. *International Journal of Applied Earth Observation and Geoinformation*, 27(PART A):70–80, April 2014. doi:10.1016/j.jag.2013.08.010.

A. Cord, D. Baratoux, N. Mangold, P. Martin, P. Pinet, R. Greeley, F. Costard, P. Masson, B. Foing, and G. Neukum. Surface roughness and geological mapping at subhectometer scale from the High Resolution Stereo Camera onboard Mars Express. *Icarus*, 191(1):38–51, November 2007. doi:10.1016/j.icarus.2007.04.029.

I. A. Crawford, M. Anand, C. S. Cockell, H. Falcke, D. A. Green, R. Jaumann, and M. A. Wieczorek. Back to the Moon: The scientific rationale for resuming lunar surface exploration. *Planetary and Space Science*, 74(1):3–14, 2012. doi:10.1016/j.pss.2012.06.002.

B. Csatho, T. Schenk, W. Krabill, T. Wilson, W. Lyons, G. McKenzie, C. Hallam, S. Manizade, and T. Paulsen. Airborne Laser Scanning for High-Resolution Mapping of Antarctica. *Eos, Transactions American Geophysical Union*, 86(25):237–238, June 2005. doi:10.1029/2005EO250002.

M. E. Davies, V. K. Abalakin, C. A. Cross, R. L. Duncombe, H. Masursky, B. Morando, T. C. Owen, P. K. Seidelmann, A. T. Sinclair, G. A. Wilkins, and Y. S. Tjuflin. Report of the IAU working group on cartographic coordinates and rotational elements of the planets and satellites. *Celestial Mechanics and Dynamical Astronomy*, 22(3):205–230, October 1980. doi:10.1007/BF01229508.

F. V. De Blasio. The aureole of Olympus Mons (Mars) as the compound deposit of submarine landslides. *Earth and Planetary Science Letters*, 312(1-2):126–139, December 2011. doi:10.1016/j.epsl.2011.09.019.

G. Deardorff. HiRISE Instrument. High Resolution Imaging Science Experiment. No Date., *Webpage*. URL: http://hirise.lpl.arizona.edu/HiRISE/instrument.html. Date of Last Access: 15-06-2015.

J. Degnan, R. Machan, E. Leventhal, D. Lawrence, G. Jodor, and C. Field. Inflight performance of a second-generation photon-counting 3D imaging lidar. In M. D. Turner and G. W. Kamerman, editors, *SPIE Defense and Security Symposium*, pages 695007–695007–9. SPIE, May 2008. doi:10.1117/12.784759.

K. DeVenecia, S. Walker, and B. Zhang. New approaches to generating and processing high resolution elevation data with imagery. In *Photogrammetric Week*, pages 297–308, Heidelberg, Germany, 2007. Photogrammetric Week. URL: http://www.ifp.uni-stuttgart.de/publications/phowo07/330DeVenecia.pdf.

P. S. Dodds and D. H. Rothman. Scaling, Universality, and Geomorphology. *Annual Review of Earth and Planetary Sciences*, 28(1):571–610, May 2000. doi:10.1146/annurev.earth.28.1.571.

P. T. Doran. Valley floor climate observations from the McMurdo dry valleys, Antarctica, 1986–2000. *Journal of Geophysical Research*, 107(D24):ACL 13.1–ACL 13.12, 2002. doi:10.1029/2001JD002045.

P. T. Doran, R. A. Wharton Jr., and W. B. Lyons. Paleolimnology of the McMurdo Dry Valleys, Antarctica. *Journal of Paleolimnology*, 10(2):85–114, 1994. doi:10.1007/BF00682507.

P. T. Doran, W. B. Lyons, and D. M. McKnight. *Life in Antarctic Deserts and other Cold Dry Environments*. Astrobiological Analogs. Cambridge University Press, Cambridge, 2010. ISBN 9780521889193. doi:10.1017/CBO9780511712258.

W. M. Drennan, P. K. Taylor, and M. J. Yelland. Parameterizing the Sea Surface Roughness. *dx.doi.org*, 35(5):835–848, February 2010. doi:10.1175/JPO2704.1.

D. P. Duda, J. D. Spinhirne, and E. W. Eloranta. Atmospheric multiple scattering effects on GLAS altimetry. I. Calculations of single pulse bias. *IEEE Transactions on Geoscience and Remote Sensing*, 39(1):92–101, 2001. doi:10.1109/36.898668.

T. C. Duxbury, R. L. Kirk, B. A. Archinal, and G. A. Neumann. Mars Geodesy/Cartography Working Group recommendations on Mars cartographic constants and coordinate systems. In *International Society for Photogrammetry and Remote Sensing*, pages 743–748, 2002. URL: http://www.isprs.org/proceedings/XXXIV/part4/pdfpapers/521.pdf.

Environmental Systems Research Institute. ESRI: Spatial Analyst: Advanced GIS Spatial Analysis Using Raster and Vector Data. Technical report, December 2001. URL: http://www.esri.com/library/whitepapers/pdfs/arcgis_spatial_analyst.pdf.

Environmental Systems Research Institute. ESRI: How Slope works. Earth Science Research Institute. 2012, *Webpage*. URL: http://resources.arcgis.com/en/help/main/10.1/index.html. Date of Last Access: 15-06-2015.

P. W. Epperlein. *Semiconductor Laser Engineering, Reliability and Diagnostics*. A Practical Approach to High Power and Single Mode Devices. John Wiley & Sons, January 2013. ISBN 9781119990338. doi:10.1002/9781118481882.

ESA. GlobCover. European Space Agency. 2011, *Webpage*. URL: http://due.esrin.esa.int/globcover/. Date of Last Access: 15-06-2015.

ESA. BepiColombo. European Space Agency. 2014a, *Webpage*. URL: http://sci.esa.int/bepicolombo/. Date of Last Access: 15-06-2015.

ESA. ESA chooses instruments for its Jupiter icy moons explorer. European Space Agency. March 2014b, *Webpage*. URL: http://sci.esa.int/juice/51417-esa-chooses-instruments-for-its-jupiter-icy-moons-explorer/. Date of Last Access: 15-06-2015.

R. P. Feynman, R. B. Leighton, and M. Sands. *The Feynman Lectures on Physics: Definitive Edition*, volume 1 of *Volume I*. Pearson Addison Wesley, 2006. ISBN 0-8053-9046-4.

R. Fisackerly. Destination Moon: The European lunar lander: Opening a new era for exploration. ESA Bulletin, 2012. URL: http://esamultimedia.esa.int/multimedia/publications/ESA-Bulletin-150/.

A. G. Fountain, T. H. Nylen, A. Monaghan, H. J. Basagic, and D. Bromwich. Snow in the McMurdo Dry Valleys, Antarctica. *International Journal of Climatology*, 30(5):633–642, 2009. doi:10.1002/joc.1933.

C. M. R. Fowler. *The Solid Earth: An Introduction to Global Geophysics*. Cambridge University Press, 2nd edition, 2005.

F. Fueten, R. Stesky, P. MacKinnon, E. Hauber, T. Zegers, K. Gwinner, F. Scholten, and G. Neukum. Stratigraphy and structure of interior layered deposits in west Candor Chasma, Mars, from High Resolution Stereo Camera (HRSC) stereo imagery and derived elevations. *Journal of Geophysical Research*, 113(E10):E10008, October 2008. doi:10.1029/2007JE003053.

F. Fueten, J. Flahaut, R. Stesky, E. Hauber, and A. P. Rossi. Stratigraphy and mineralogy of Candor Mensa, West Candor Chasma, Mars: Insights into the geologic history of Valles Marineris. *Journal of Geophysical Research*, 119(2):331–354, February 2014. doi:10.1002/2013JE004557.

T. Fujii and T. Fukuchi. Laser remote sensing. Taylor and Francis, 2005. ISBN 978-0-8247-4256-0. URL: http://www.crcpress.com/product/isbn/9780824742560.

S. Fujinami, T. Ina, and S. Kawai. On the Profile of the Moon's Silhouette, as Observed in the Partial Eclipse of February 14th 1953. *Publications of the Astronomical Society of Japan*, 6(2): 67–75, 1954. URL: http://adsabs.harvard.edu/abs/1954PASJ....6...67F.

C. S. Gardner. Target signatures for laser altimeters: an analysis. *Applied Optics*, 21(3):448, 1982. doi:10.1364/AO.21.000448.

C. S. Gardner. Ranging Performance of Satellite Laser Altimeters. *IEEE Transactions on Geoscience and Remote Sensing*, 30(5):1061–1072, September 1992. doi:10.1109/36.175341.

J. Garvin, J. Bufton, J. Blair, D. Harding, S. Luthcke, J. Frawley, and D. Rowlands. Observations of the Earth's topography from the Shuttle Laser Altimeter (SLA): Laser-pulse Echo-recovery measurements of terrestrial surfaces. *Physics and Chemistry of the Earth*, 23(9-10):1053–1068, 1998. doi:10.1016/S0079-1946(98)00145-1.

J. B. Garvin, J. J. Frawley, and J. B. Abshire. Vertical roughness of Mars from the Mars Orbiter Laser Altimeter. *Geophysical Research Letters*, 26(3):381–384, February 1999. doi:10.1029/1998GL900309.

D. Gatziolis and H.-E. Andersen. A Guide to LIDAR Data Acquisition and Processing for the Forests of the Pacific Northwest. Technical Report PNW-GTR-768, USDA, July 2008. URL: http://www.fs.fed.us/pnw/pubs/pnw_gtr768.pdf.

G. R. Gladstone, S. A. Stern, K. D. Retherford, R. K. Black, D. C. Slater, M. W. Davis, M. H. Versteeg, K. B. Persson, J. W. Parker, D. E. Kaufmann, A. F. Egan, T. K. Greathouse *et al.* LAMP: The Lyman Alpha Mapping Project on NASA's Lunar Reconnaissance Orbiter Mission. *Space Science Reviews*, 150(1-4):161–181, January 2010. doi:10.1007/s11214-009-9578-6.

T. D. Glotch, P. G. Lucey, J. L. Bandfield, B. T. Greenhagen, I. R. Thomas, R. C. Elphic, N. Bowles, M. B. Wyatt, C. C. Allen, K. D. Hanna, and D. A. Paige. Highly Silicic Compositions on the Moon. *Science*, 329(5998):1510–1513, September 2010. doi:10.1126/science.1192148.

G. J. Golabek, T. Keller, T. V. Gerya, G. Zhu, P. J. Tackley, and J. A. D. Connolly. Origin of the martian dichotomy and Tharsis from a giant impact causing massive magmatism. *Icarus*, 215(1): 346–357, September 2011. doi:10.1016/j.icarus.2011.06.012.

M. Golombek and D. Rapp. Size-frequency distributions of rocks on Mars and Earth analog sites: Implications for future landed missions. *Journal of Geophysical Research*, 102(E2):4117–4129, February 1997. doi:10.1029/96JE03319.

M. Golombek, J. Grant, A. R. Vasavada, J. Grotzinger, M. Watkins, D. Kipp, E. N. Dobrea, J. Griffes, and T. Parker. Final Four Landing Sites for the Mars Science Laboratory. In *40th Lunar and Planetary Science Conference*, March 2009. URL: http://www.lpi.usra.edu/meetings/lpsc2009/pdf/1404.pdf.

M. Golombek, J. Grant, D. Kipp, A. Vasavada, R. Kirk, R. Fergason, P. Bellutta, F. Calef, K. Larsen, Y. Katayama, A. Huertas, R. Beyer *et al.* Selection of the Mars Science Laboratory Landing Site. *Space Science Reviews*, 170(1-4):641–737, September 2012a. doi:10.1007/s11214-012-9916-y.

M. Golombek, A. Huertas, D. Kipp, and F. Calef. Detection and Characterization of Rocks and Rock Size-Frequency Distributions at the Final Four Mars Science Laboratory Landing Sites. *MARS*, 7:1–22, August 2012b. doi:10.1555/mars.2012.0001.

M. P. Golombek, R. A. Cook, T. Economou, W. M. Folkner, A. F. C. Haldemann, P. H. Kallemeyn, J. M. Knudsen, R. M. Manning, H. J. Moore, T. J. Parker, R. Rieder, J. T. Schofield *et al.* Overview of the Mars Pathfinder Mission and Assessment of Landing Site Predictions. *Science*, 278(5344):1743–1748, December 1997. doi:10.1126/science.278.5344.1743.

M. P. Golombek, H. J. Moore, A. F. C. Haldemann, T. J. Parker, and J. T. Schofield. Assessment of Mars Pathfinder landing site predictions. *Journal of Geophysical Research*, 104(E4):8585–8594, April 1999. doi:10.1029/1998JE900015.

M. P. Golombek, R. E. Arvidson, J. F. Bell, P. R. Christensen, J. A. Crisp, L. S. Crumpler, B. L. Ehlmann, R. L. Fergason, J. A. Grant, R. Greeley, A. F. C. Haldemann, D. M. Kass *et al.* Assessment of Mars Exploration Rover landing site predictions. *Nature*, 436(7047):44–48, July 2005. doi:10.1038/nature03600.

J. A. Grant, R. P. Irwin III, S. A. Wilson, D. Buczkowski, and K. Siebach. A lake in Uzboi Vallis and implications for Late Noachian–Early Hesperian climate on Mars. *Icarus*, 212(1):110–122, March 2011a. doi:10.1016/j.icarus.2010.11.024.

J. A. Grant, M. P. Golombek, J. P. Grotzinger, S. A. Wilson, M. M. Watkins, A. R. Vasavada, J. L. Griffes, and T. J. Parker. The science process for selecting the landing site for the 2011 Mars Science Laboratory. *Planetary and Space Science*, 59(11-12):1114–1127, September 2011b. doi:10.1016/j.pss.2010.06.016.

E. Grayzeck. Earth Fact Sheet. NASA. July 2013, *Webpage*. URL: http://nssdc.gsfc.nasa.gov/planetary/factsheet/earthfact.html. Date of Last Access: 15-06-2015.

J. S. Greenfeld. An operator-based matching system. *Photogrammetric Engineering and Remote Sensing*, 1991. URL: http://cat.inist.fr/?aModele=afficheN&cpsidt=19779862.

C. Grima, W. Kofman, A. Herique, R. Orosei, and R. Seu. Quantitative analysis of Mars surface radar reflectivity at 20MHz. *Icarus*, 220(1):84–99, July 2012. doi:10.1016/j.icarus.2012.04.017.

P. M. Grindrod and M. R. Balme. Groundwater processes in Hebes Chasma, Mars. *Geophysical Research Letters*, 37(13):L13202, July 2010. doi:10.1029/2010GL044122.

J. Griswold, M. H. Bulmer, D. Beller, and P. J. McGovern. An Examination of Olympus Mons Aureoles. In *Lunar and Planetary Science XXXIX*, Houton, USA, March 2008. URL: http://www.lpi.usra.edu/meetings/lpsc2008/pdf/2239.pdf.

C. H. Grohmann, M. J. Smith, and C. Riccomini. Surface roughness of topography: A multi-scale analysis of landform elements in midland valley, Scotland. In *Proceedings of Geomorphometry*, Zurich, Switzerland, September 2009. URL: http://geomorphometry.org/system/files/grohmann2009geomorphometry.pdf.

J. P. Grotzinger, D. Y. Sumner, L. C. Kah, K. Stack, S. Gupta, L. Edgar, D. Rubin, K. Lewis, J. Schieber, N. Mangold, R. Milliken, P. G. Conrad *et al.* A Habitable Fluvio-Lacustrine Environment at Yellowknife Bay, Gale Crater, Mars. *Science*, 343(6169):1242777–1242777, January 2014. doi:10.1126/science.1242777.

J. P. Grotzinger, J. A. Crisp, A. R. Vasavada, R. C. Anderson, C. J. Baker, R. Barry, D. F. Blake, P. Conrad, K. S. Edgett, B. Ferdowski, R. Gellert, J. B. Gilbert *et al.* Mars Science Laboratory Mission and Science Investigation. *Space Science Reviews*, 170(1-4):5–56, September 2012. doi:10.1007/s11214-012-9892-2.

A. W. Gruen and E. P. Baltsavias. Adaptive Least Squares Correlation With Geometrical Constraints. In O. D. Faugeras and R. B. Kelley, editors, *1985 International Technical Symposium/Europe*, pages 72–82. SPIE, June 1986. doi:10.1117/12.952246.

M. Gupta, D. G. Barber, R. K. Scharien, and D. Isleifson. Detection and classification of surface roughness in an Arctic marginal sea ice zone. *Hydrological Processes*, 28(3):599–609, November 2012. doi:10.1002/hyp.9593.

D. Gwenzi and M. A. Lefsky. Prospects of photon counting lidar for savanna ecosystem structural studies. *ISPRS - International Archives of the Photogrammetry, Remote Sensing and Spatial Information Sciences*, XL-1:141–147, 2014. doi:10.5194/isprsarchives-XL-1-141-2014.

K. Gwinner, F. Scholten, F. Preusker, S. Elgner, T. Roatsch, M. Spiegel, R. Schmidt, J. Oberst, R. Jaumann, and C. Heipke. Topography of Mars from global mapping by HRSC high-resolution digital terrain models and orthoimages: Characteristics and performance. *Earth and Planetary Science Letters*, 294(3-4):506–519, June 2010. doi:10.1016/j.epsl.2009.11.007.

K. Gwinner, F. Scholten, M. Spiegel, R. Schmidt, B. Giese, J. Oberst, C. Heipke, R. Jaumann, and G. Neukum. Derivation and validation of high-resolution digital terrain models from Mars Express HRSC-Data. *Photogrammetric Engineering and Remote Sensing*, 75(9):1127–1142, September 2009. URL: http://www.asprs.org/a/publications/pers/2009journal/september/2009_sep_1127-1142.pdf.

J. T. Hack. Studies of longitudinal stream profiles in Virginia and Maryland. Technical Report Paper 294-B, U.S. Department of Interior, 1957. URL: http://pubs.usgs.gov/pp/0294b/report.pdf.

M. J. Hambrey and S. J. Fitzsimons. Development of sediment-landform associations at cold glacier margins, Dry Valleys, Antarctica. *Sedimentology*, 57(3):857–882, February 2010. doi:10.1111/j.1365-3091.2009.01123.x.

T. Haran. Software: convert_ellipsoid.pro. December 2004, *Webpage*. URL: ftp://sidads.colorado.edu/pub/DATASETS/icesat/tools/idl/ellipsoid/convert_ellipsoid.pro. Date of Last Access: 15-06-2015.

D. J. Harding and C. C. Carabajal. ICESat waveform measurements of within-footprint topographic relief and vegetation vertical structure. *Geophysical Research Letters*, 32(21):L21S10, 2005. doi:10.1029/2005GL023471.

T. M. Hare. SOCET SET for HiRISE Tutorial. United States Geological Survey. January 2010, *Webpage*. URL: http://webgis.wr.usgs.gov/pigwad/tutorials/socetset/SocetSet4HiRISE.htm. Date of Last Access: 15-06-2015.

W. K. Hartmann. Terrestrial and lunar flux of large meteorites in the last two billion years. *Icarus*, 4(2):157–165, May 1965. doi:10.1016/0019-1035(65)90057-6.

H. Hasegawa, K. Matsuo, M. Koarai, N. Watanabe, H. Masaharu, and Y. Fukushima. DEM accuracy and the base to height (B/H) ratio of stereo images. *International Archives of Photogrammetry and Remote Sensing*, XXXIII(Part B4), 2000. URL: http://www.isprs.org/proceedings/XXXIII/congress/part4/356_XXXIII-part4.pdf.

N. G. Heavens, M. I. Richardson, and A. D. Toigo. Two aerodynamic roughness maps derived from Mars Orbiter Laser Altimeter (MOLA) data and their effects on boundary layer properties in a Mars general circulation model (GCM). *Journal of Geophysical Research*, 113(E2):E02014, February 2008. doi:10.1029/2007JE002991.

E. Hébrard, C. Listowski, P. Coll, B. Marticorena, G. Bergametti, A. Määttänen, F. Montmessin, and F. Forget. An aerodynamic roughness length map derived from extended Martian rock abundance data. *Journal of Geophysical Research*, 117(E4):E04008, 2012. doi:10.1029/2011JE003942.

J. Helgason. Formation of Olympus Mons and the aureole-escarpment problem on Mars. *Geology*, 27(3):231–234, 1999. doi:10.1130/0091-7613(1999)027<0231:FOOMAT>2.3.CO;2.

U. C. Herzfeld, B. W. McDonald, B. F. Wallin, T. A. Neumann, T. Markus, A. Brenner, and C. Field. Algorithm for Detection of Ground and Canopy Cover in Micropulse Photon-Counting Lidar Altimeter Data in Preparation for the ICESat-2 Mission. *IEEE Transactions on Geoscience and Remote Sensing*, 52(4):2109–2125, April 2014. doi:10.1109/TGRS.2013.2258350.

C. Hilbert and C. Schmullius. Influence of Surface Topography on ICESat/GLAS Forest Height Estimation and Waveform Shape. *Remote Sensing*, 4(8):2210–2235, August 2012. doi:10.3390/rs4082210.

HiRISE. High Resolution Imaging Science Experiment - University of Arizona. No Date., *Webpage*. URL: http://hirise.lpl.arizona.edu/. Date of Last Access: 15-06-2015.

R. J. Hogan. Fast approximate calculation of multiply scattered lidar returns. *Applied Optics*, 45 (23):5984–5992, 2006. doi:10.1364/AO.45.005984.

R. E. Horton. Erosional Development of Streams and their Drainage Basins; Hydrological Approach to Quantitative Morphology. *Geological Society of America Bulletin*, 56(3):275–370, March 1945. doi:10.1130/0016-7606(1945)56[275:EDOSAT]2.0.CO;2.

V. A. Hughes. Roughness of the moon as a radar reflector. *Nature*, 186(4728):873–874, June 1960. doi:10.1038/186873a0.

H. Hussmann, K. Lingenauber, H. Michaelis, M. Kobayashi, N. Thomas, L. Lara, H. Araki, T. Behnke, K. Gwinner, N. Namiki, H. Noda, J. Oberst *et al.* The Ganymede Laser Altimeter (GALA) as part of the JUICE payload: instrument, science objectives and expected performance. In *European Planetary Science Congress*, September 2013. URL: http://meetingorganizer.copernicus.org/EPSC2013/EPSC2013-428.pdf.

P. A. Hwang, D. M. Burrage, D. W. Wang, and J. C. Wesson. Ocean Surface Roughness Spectrum in High Wind Condition for Microwave Backscatter and Emission Computations. *Journal of Atmospheric and Oceanic Technology*, 30(9):2168–2188, September 2013. doi:10.1175/JTECH-D-12-00239.1.

A. B. Ivanov and J. J. Lorre. Analysis of Mars Orbiter Camera Stereo Pairs. *Lunar and Planetary Institute Science XXXIII*, 2002. URL: http://www.lpi.usra.edu/meetings/lpsc2002/pdf/1845.pdf.

M. P. A. Jackson, J. B. Adams, T. P. Dooley, A. R. Gillespie, and D. R. Montgomery. Modeling the collapse of Hebes Chasma, Valles Marineris, Mars. *Geological Society of America Bulletin*, 123 (7-8):1596–1627, 2011. doi:10.1130/B30307.1.

P. L. Jester and D. W. Hancock III. The Algorithm Theoretical Basis Document for Level 1A Processing. Technical report, Geoscience Laser Altimter System (GLAS), September 2011. URL: http://www.csr.utexas.edu/glas/pdf/L1A_ATBD_09_2011.pdf.

R. A. Kichak. Independent GLAS Anomoly Review Board Executive Summary. Technical report, NASA, Goddard Space Flight Cent., Greenbelt, Md., November 2003. URL: http://misspiggy.gsfc.nasa.gov/tva/meldoc/photonicsdocs/IGARBreport.pdf.

H. H. Kieffer, P. R. Christensen, and T. N. Titus. CO_2 jets formed by sublimation beneath translucent slab ice in Mars' seasonal south polar ice cap. *Nature*, 442(7104):793–796, August 2006. doi:10.1038/nature04945.

J. R. Kim and J.-P. Muller. Very high resolution stereo DTM extraction and its application to surface roughness estimation over Martian surface. In *The International Archives of the Photogrammetry, Remote Sensing and Spatial Information Sciences*, Beijing, China, July 2008. URL: http://www.isprs.org/proceedings/XXXVII/congress/4_pdf/176.pdf.

J. R. Kim and J.-P. Muller. Multi-resolution topographic data extraction from Martian stereo imagery. *Planetary and Space Science*, 57(14-15):2095–2112, December 2009. doi:10.1016/j.pss.2009.09.024.

J. R. Kim and J. G. Park. Topographic Local Roughness Extraction and Calibration Over Martian Surface by Very High Resolution Stereo Analysis and Multi Sensor Data Fusion. In *ISPRS - International Archives of the Photogrammetry, Remote Sensing and Spatial Information Sciences*, pages 131–136, Guilin, China, October 2011. doi:10.5194/isprsarchives-XXXVIII-4-W25-131-2011.

J. R. Kim, S.-Y. Lin, J.-P. Muller, N. H. Warner, and S. Gupta. Multi-resolution digital terrain models and their potential for Mars landing site assessments. *Planetary and Space Science*, 85: 89–105, September 2013. doi:10.1016/j.pss.2013.06.001.

T. Kim. A study on the epipolarity of linear pushbroom images. *Photogrammetric Engineering and Remote Sensing*, 2000. URL: http://www.asprs.org/a/publications/pers/2000journal/august/2000_aug_961-966.pdf.

R. L. Kirk, B. A. Archinal, and E. M. Lee. Global Digital Image Mosaics of Mars: Assessment of Geodetic Accuracy. In *Lunar and Planetary Science XXXII*, January 2001. URL: http://www.lpi.usra.edu/meetings/lpsc2001/pdf/1856.pdf.

R. L. Kirk, E. Howington-Kraus, M. R. Rosiek, J. A. Anderson, B. A. Archinal, K. J. Becker, D. A. Cook, D. M. Galuszka, P. E. Geissler, T. M. Hare, I. M. Holmberg, Keszthelyi, L. P. *et al.* Ultrahigh resolution topographic mapping of Mars with MRO HiRISE stereo images: Meter-scale slopes of candidate Phoenix landing sites. *Journal of Geophysical Research*, 113 (E3):E00A24, March 2008. doi:10.1029/2007JE003000.

E. S. Kite, K. W. Lewis, M. P. Lamb, C. E. Newman, and M. I. Richardson. Growth and form of the mound in Gale Crater, Mars: Slope wind enhanced erosion and transport. *Geology*, 41(5): 543–546, May 2013. doi:10.1130/G33909.1.

K. C. Kornelsen and P. Coulibaly. Advances in soil moisture retrieval from synthetic aperture radar and hydrological applications. *Journal of Hydrology*, 476:460–489, 2013. doi:10.1016/j.jhydrol.2012.10.044.

W. B. Krabill, W. Abdalati, E. B. Frederick, S. S. Manizade, C. F. Martin, J. G. Sonntag, R. N. Swift, R. H. Thomas, and J. G. Yungel. Aircraft laser altimetry measurement of elevation changes of the greenland ice sheet: technique and accuracy assessment. *Journal of Geodynamics*, 34(3-4): 357–376, October 2002. doi:10.1016/S0264-3707(02)00040-6.

M. A. Kreslavsky and J. W. Head III. Kilometer-scale slopes on Mars and their correlation with geologic units: Initial results from Mars Orbiter Laser Altimeter (MOLA) data. *Journal of Geophysical Research*, 104(E9):21911–21924, September 1999. doi:10.1029/1999JE001051.

M. A. Kreslavsky. Personal Communication: Highest quality MOLA received pulse channel. March 2012.

M. A. Kreslavsky. Personal Communication: Reviewer Comments of Poole et al. [2014b]. August 2014.

M. A. Kreslavsky and J. W. Head III. Kilometer-scale roughness of Mars: Results from MOLA data analysis. *Journal of Geophysical Research*, 105(E11):26695–26711, November 2000. doi:10.1029/2000JE001259.

M. A. Kreslavsky, J. W. Head, G. A. Neumann, M. A. Rosenburg, O. Aharonson, D. E. Smith, and M. T. Zuber. Lunar topographic roughness maps from Lunar Orbiter Laser Altimeter (LOLA) data: Scale dependence and correlation with geologic features and units. *Icarus*, 226:52–66, 2013. doi:10.1016/j.icarus.2013.04.027.

R. Kwok, G. F. Cunningham, H. J. Zwally, and D. Yi. ICESat over Arctic sea ice: Interpretation of altimetric and reflectivity profiles. *Journal of Geophysical Research*, 111(C6):C06006, 2006. doi:10.1029/2005JC003175.

R. Kwok, G. F. Cunningham, H. J. Zwally, and D. Yi. Ice, Cloud, and land Elevation Satellite (ICESat) over Arctic sea ice: Retrieval of freeboard. *Journal of Geophysical Research*, 112(C12): C12013, December 2007. doi:10.1029/2006JC003978.

Laser Check. Angle Resolved Laser Scatter Surface Roughness Measurements. 2015, *Webpage*. URL: http://www.surface-finish.net/Technology/technology.html. Date of Last Access: 15-06-2015.

F. Leberl, A. Irschara, T. Pock, P. Meixner, M. Gruber, S. Scholz, and A. Wiechert. Point Clouds: Lidar versus 3D Vision. *Photogrammetric Engineering and Remote Sensing*, 76(10):1123–1134, October 2010. URL: http://www.icg.tugraz.at/publications/pdf/laservs3dvision.pdf.

M. A. Lefsky, D. J. Harding, M. Keller, W. B. Cohen, C. C. Carabajal, F. Del Bom Espirito Santo, M. O. Hunter, and R. de Oliveira Jr. Estimates of forest canopy height and aboveground biomass using ICESat. *Geophysical Research Letters*, 32(22):L22S02, 2005. doi:10.1029/2005GL023971.

R. Lena, C. Wöhler, J. Phillips, and M. T. Chiocchetta. *Lunar Domes: Properties and Formation Processes*. Springer Praxis Books, 2013. doi:10.1007/978-88-470-2637-7.

C. B. Leovy. Weather and climate on Mars. *Journal of Geophysical Research*, 412(6843):245–249, July 2001. doi:10.1038/35084192.

J. Levy. Hydrological characteristics of recurrent slope lineae on Mars: Evidence for liquid flow through regolith and comparisons with Antarctic terrestrial analogs. *Icarus*, 219(1):1–4, May 2012. doi:10.1016/j.icarus.2012.02.016.

A. R. Lewis, D. R. Marchant, D. E. Kowalewski, S. L. Baldwin, and L. E. Webb. The age and origin of the Labyrinth, western Dry Valleys, Antarctica: Evidence for extensive middle Miocene subglacial floods and freshwater discharge to the Southern Ocean. *Geology*, 34(7):513, 2006. doi:10.1130/G22145.1.

M. Ligas and P. Banasik. Conversion between Cartesian and geodetic coordinates on a rotational ellipsoid by solving a system of nonlinear equations. *Geodesy and Cartography*, 60(2):145–159, January 2011. doi:10.2478/v10277-012-0013-x.

T. M. Lillesand, R. W. Kiefer, and J. W. Chipman. Remote Sensing and Image Interpretation. John Wiley & Sons, Inc, 2008. ISBN 978-0-470-05245-7. URL: http://www.worldcat.org/title/remote-sensing-and-image-interpretation/oclc/144219714.

S.-Y. Lin, J.-P. Muller, J. P. Mills, and P. E. Miller. An assessment of surface matching for the automated co-registration of MOLA, HRSC and HiRISE DTMs. *Earth and Planetary Science Letters*, 294(3-4):520–533, June 2010. doi:10.1016/j.epsl.2009.12.040.

X. Liu. Airborne LiDAR for DEM generation: some critical issues. *Progress in Physical Geography*, 32(1):31–49, February 2008. doi:10.1177/0309133308089496.

S. Lovejoy and D. Schertzer. Scaling and multifractal fields in the solid earth and topography. *Nonlinear Processes in Geophysics*, 14:465–502, August 2007. doi:10.5194/npg-14-465-2007.

LRO Project and LGCWG. A Standardized Lunar Coordinate System for the Lunar Reconnaissance Orbiter and Lunar Datasets. Technical report, October 2008. URL: http://lunar.gsfc.nasa.gov/library/LunCoordWhitePaper-10-08.pdf.

P. G. Lucey, G. A. Neumann, M. A. Riner, E. Mazarico, D. E. Smith, M. T. Zuber, D. A. Paige, D. B. Bussey, J. T. Cahill, A. McGovern, P. Isaacson, L. M. Corley *et al.* The global albedo of the Moon at 1064 nm from LOLA. *Journal of Geophysical Research*, 119(7):1665–1679, July 2014. doi:10.1002/2013JE004592.

K. L. MacClune. Glaciers of the McMurdo dry valleys: Terrestrial analog for Martian polar sublimation. *Journal of Geophysical Research*, 108(E4):5031, 2003. doi:10.1029/2002JE001878.

M. C. Malin, J. F. Bell, B. A. Cantor, M. A. Caplinger, R. T. Clancy, K. S. Edgett, L. Edwards, R. M. Haberle, S. W. Lee, and M. A. Ravine. Context Camera Investigation on board the Mars Reconnaissance Orbiter. *Journal of Geophysical Research*, 112:E05S04, May 2007. doi:10.1029/2006JE002808.

Malin Space Science Systems. Mars Reconnaissance Orbiter (MRO) Context Camera (CTX). Marlin Space Science Systems. 2010, *Webpage*. URL: http://www.msss.com/all_projects/mro-ctx.php. Date of Last Access: 15-06-2015.

Malin Space Science Systems. Mars Global Surveyor Mission Plan 6. Mapping Phase. Marlin Space Science Systems. No Date., *Webpage*. URL: http://www.msss.com/mars/global_surveyor/mgs_msn_plan/section6/section6.html. Date of Last Access: 15-06-2015.

S. Manizade. Trajectory Maps - ATM. NASA Goddard Space Flight Center/Wallops Flight Facility. 2012, *Webpage*. URL: http://atm.wff.nasa.gov. Date of Last Access: 15-06-2015.

D. R. Marchant and J. W. Head III. Antarctic dry valleys: Microclimate zonation, variable geomorphic processes, and implications for assessing climate change on Mars. *Icarus*, 192(1):187–222, December 2007. doi:10.1016/j.icarus.2007.06.018.

J.-L. Margot, D. B. Campbell, R. F. Jurgens, and M. A. Slade. The topography of Tycho Crater. *Journal of Geophysical Research*, 104(E5):11875, May 1999. doi:10.1029/1998JE900047.

B. Marticorena, M. Kardous, G. Bergametti, Y. Callot, P. Chazette, H. Khatteli, S. Le Hegarat-Mascle, M. Maille, J.-L. Rajot, D. Vidal-Madjar, and M. Zribi. Surface and aerodynamic roughness in arid and semiarid areas and their relation to radar backscatter coefficient. *Journal of Geophysical Research*, 111(F3):F03017, 2006. doi:10.1029/2006JF000462.

S. Mattson, B. Archinal, R. Beyer, K. Edmundson, B. Gaskell, I. Haase, E. Howington-Kraus, R. Li, N. Mastrodemos, A. McEwen, Z. Moratto, J. Oberst *et al.* High Resolution Topography from LROC-NAC Geometric Stereo Images. In *Annual Meeting of the Lunar Exploration Analysis Group*, 2010. ISBN http://ntrs.nasa.gov/search.jsp?R=20110012558. URL: http://www.lpi.usra.edu/meetings/leag2010/pdf/3066.pdf.

S. Mattson, A. S. McEwen, M. S. Robinson, E. Speyerer, B. Archinal, and the LROC team. Exploring the Moon with LROC-NAC Stereo Anaglyphs. In *European Planetary Science Congress*, September 2012. URL: http://meetingorganizer.copernicus.org/EPSC2012/EPSC2012-486-2.pdf.

A. S. McEwen, E. M. Eliason, J. W. Bergstrom, N. T. Bridges, C. J. Hansen, W. A. Delamere, J. A. Grant, V. C. Gulick, K. E. Herkenhoff, L. Keszthelyi, R. L. Kirk, M. T. Mellon *et al.* Mars Reconnaissance Orbiter's High Resolution Imaging Science Experiment (HiRISE). *Journal of Geophysical Research*, 112(E5):E05S02, May 2007. doi:10.1029/2005JE002605.

A. S. McEwen, M. E. Banks, N. Baugh, K. Becker, A. Boyd, J. W. Bergstrom, R. A. Beyer, E. Bortolini, N. T. Bridges, S. Byrne, B. Castalia, F. C. Chuang *et al.* The High Resolution Imaging Science Experiment (HiRISE) during MRO's Primary Science Phase (PSP). *Icarus*, 205(1):2–37, January 2010. doi:10.1016/j.icarus.2009.04.023.

A. S. McEwen, L. Ojha, C. M. Dundas, S. S. Mattson, S. Byrne, J. J. Wray, S. C. Cull, S. L. Murchie, N. Thomas, and V. C. Gulick. Seasonal Flows on Warm Martian Slopes. *Science*, 333: 740–743, August 2011. doi:10.1126/science.1204816.

P. J. McGovern, J. R. Smith, J. K. Morgan, and M. H. Bulmer. Olympus Mons aureole deposits: New evidence for a flank failure origin. *Journal of Geophysical Research*, 109(E8):E08008, August 2004. doi:10.1029/2004JE002258.

P. J. McGovern and J. K. Morgan. Volcanic spreading and lateral variations in the structure of Olympus Mons, Mars. *Geology*, 37(2):139–142, February 2009. doi:10.1130/G25180A.1.

McMurdo Dry Valleys Long Term Ecological Research. McMurdo Dry Valleys: Long Term Ecological Research. McMurdo Dry Valleys Long Term Ecological Research. November 2013a, *Webpage*. URL: http://www.mcmlter.org. Date of Last Access: 15-06-2015.

McMurdo Dry Valleys Long Term Ecological Research. Mapping Services/GIS. 2013b, *Webpage*. URL: http://www.mcmlter.org/mapping.htm. Date of Last Access: 15-06-2015.

J. H. Meeus. *Astronomical algorithms*. Willmann-Bell, Incorporated, Richmond, Virginia, USA, 1st edition, December 1991. ISBN 978-0943396354.

X. Meng, N. Currit, and K. Zhao. Ground Filtering Algorithms for Airborne LiDAR Data: A Review of Critical Issues. *Remote Sensing*, 2(3):833–860, March 2010. doi:10.3390/rs2030833.

J. R. Michalski, J.-P. Bibring, F. Poulet, D. Loizeau, N. Mangold, E. N. Dobrea, J. L. Bishop, J. J. Wray, N. K. McKeown, M. Parente, E. Hauber, F. Altieri *et al.* The Mawrth Vallis Region of Mars: A Potential Landing Site for the Mars Science Laboratory (MSL) Mission. *Astrobiology*, 10(7):687–703, September 2010. doi:10.1089/ast.2010.0491.

R. E. Milliken, J. P. Grotzinger, and B. J. Thomson. Paleoclimate of Mars as captured by the stratigraphic record in Gale Crater. *Geophysical Research Letters*, 37(4):L04201, February 2010. doi:10.1029/2009GL041870.

J. P. Mills, S. J. Buckley, and H. L. Mitchell. Synergistic fusion of GPS and photogrammetrically generated elevation models. *Photogrammetric Engineering Remote Sensing*, 69(4):341–349, April 2003. doi:10.14358/PERS.69.4.341.

I. G. Mitrofanov, A. B. Sanin, W. V. Boynton, G. Chin, J. B. Garvin, D. Golovin, L. G. Evans, K. Harshman, A. S. Kozyrev, M. L. Litvak, A. Malakhov, E. Mazarico *et al.* Hydrogen Mapping of the Lunar South Pole Using the LRO Neutron Detector Experiment LEND. *Science*, 330 (6003):483–486, October 2010. doi:10.1126/science.1185696.

J. Mouginot, W. Kofman, A. Safaeinili, C. Grima, A. Herique, and J. Plaut. MARSIS surface reflectivity of the south residual cap of Mars. *Icarus*, 201(2):454–459, June 2009. doi:10.1016/j.icarus.2009.01.009.

M. S. Moussavi, W. Abdalati, T. Scambos, and A. Neuenschwander. Applicability of an automatic surface detection approach to micro-pulse photon-counting lidar altimetry data: implications for canopy height retrieval from future ICESat-2 data. *International Journal of Remote Sensing*, 35 (13):5263–5279, June 2014. doi:10.1080/01431161.2014.939780.

S. Murchie, L. Roach, F. Seelos, R. Milliken, J. Mustard, R. Arvidson, S. Wiseman, K. Lichtenberg, J. Andrews-Hanna, J. Bishop, J.-P. Bibring, M. Parente *et al.* Evidence for the origin of layered deposits in Candor Chasma, Mars, from mineral composition and hydrologic modeling. *Journal of Geophysical Research*, 114(E2), February 2009. doi:10.1029/2009JE003343.

A. Mushkin and A. R. Gillespie. Mapping sub-pixel surface roughness on Mars using high-resolution satellite image data. *Geophysical Research Letters*, 33(18):L18204, 2006. doi:10.1029/2006GL027095.

National Oceanic and Atmospheric Administration. Atmospheric Remote Sensing: Instruments: Lidar Primer. Earth System Research Laboratory Chemical Sciences Division, US Department of Commerce. No Date.a, *Webpage*. URL: http://www.esrl.noaa.gov/csd/groups/csd3/instruments/lidar/. Date of Last Access: 15-06-2015.

National Oceanic and Atmospheric Administration. National Oceanic and Atmospheric Administration: Ocean. National Oceanic and Atmospheric Administration. No Date.b, *Webpage*. URL: http://www.noaa.gov/ocean.html. Date of Last Access: 15-06-2015.

National Snow and Ice Data Center. ICESat: Frequently Asked Questions. National Snow and Ice Data Center. 2014a, *Webpage*. URL: http://nsidc.org/data/icesat/faq.html. Date of Last Access: 15-06-2015.

National Snow and Ice Data Center. ICESat / GLAS Data Dictionaries. National Snow and Ice Data Center. 2014b, *Webpage*. URL: http://nsidc.org/data/icesat/data-dictionaries-landing-page.html. Date of Last Access: 15-06-2015.

National Snow and Ice Data Center. ICESat Reference Orbit Ground Tracks. National Snow and Ice Data Center. 2014c, *Webpage*. URL: http://nsidc.org/data/icesat/orbit_grnd_trck.html. Date of Last Access: 15-06-2015.

National Snow and Ice Data Center. ICESat Tools. National Snow and Ice Data Center. 2014d, *Webpage*. URL: http://nsidc.org/data/icesat/tools.html. Date of Last Access: 15-06-2015.

National Snow and Ice Data Center. ICESat/GLAS Data Directory. National Snow and Ice Data Center. No Date., *Webpage*. URL: n4ftl01u.ecs.nasa.gov/SAN/GLAS. Date of Last Access: 15-06-2015.

G. Neukum, R. Jaumann, and the HRSC Co-Investigator Team. HRSC: the High Resolution Stereo Camera of Mars Express. Technical report, ESA, August 2004. URL: http://sci.esa.int/science-e/www/object/doc.cfm?fobjectid=34967.

G. A. Neumann. Some Aspects of Processing Extraterrestrial LIDAR Data: Clementine, NEAR, MOLA. *International Archives of Photogrammetry and Remote Sensing*, XXXIV-3/W4:73–80, October 2001. URL: http://www.isprs.org/proceedings/XXXIV/3-W4/pdf/Neumann.pdf.

G. A. Neumann, J. B. Abshire, O. Aharonson, J. B. Garvin, X. Sun, and M. T. Zuber. Mars Orbiter Laser Altimeter pulse width measurements and footprint-scale roughness. *Geophysical Research Letters*, 30(11):1561, 2003a. doi:10.1029/2003GL017048.

G. A. Neumann, D. E. Smith, M. T. Zuber, E. Mazarico, M. H. Torrence, J. F. Cavanaugh, X. Sun, F. G. Lemoine, and O. Aharonson. Preliminary Measurement of Meter-scale Roughness on the Moon from Lunar Orbiter Laser Altimeter (LOLA) Pulse Spreading. In *Eos, Transactions American Geophysical Union*, December 2009. URL: http://abstractsearch.agu.org/meetings/2009/FM/sections/U/sessions/U31A/abstracts/U31A-0001.html.

G. A. Neumann. Personal Communication: Discussion on MOLA pulse-width data processing. October 2011.

G. A. Neumann, D. E. Smith, and M. T. Zuber. Two Mars years of clouds detected by the Mars Orbiter Laser Altimeter. *Journal of Geophysical Research*, 108(E4):5023, 2003b. doi:10.1029/2002JE001849.

G. A. Neumann, M. H. Torrence, E. M. Mazarico, J. Cavanaugh, X. Sun, D. E. Smith, M. T. Zuber, and the LOLA Science Team. Meter-Scale Roughness on the Moon from Lunar Orbiter Laser Altimeter (LOLA) Pulse Spreading: Implications for Exploration. In *Annual Meeting of the Lunar Exploration Analysis Group*, 2008. URL: http://www.lpi.usra.edu/meetings/leag2009/presentations/Day-2%20PM/03-15_Neumann.pdf.

E. Z. Noe Dobrea, J. L. Bishop, N. K. McKeown, R. Fu, C. M. Rossi, J. R. Michalski, C. Heinlein, V. Hanus, F. Poulet, R. J. F. Mustard, S. Murchie, A. S. McEwen *et al.* Mineralogy and stratigraphy of phyllosilicate-bearing and dark mantling units in the greater Mawrth Vallis/west Arabia Terra area: Constraints on geological origin. *Journal of Geophysical Research*, 115(E7): E00D19, July 2010. doi:10.1029/2009JE003351.

A. W. Nolin, F. M. Fetterer, and T. A. Scambos. Surface roughness characterizations of sea ice and ice sheets: case studies with MISR data. *IEEE Transactions on Geoscience and Remote Sensing*, 40(7):1605–1615, July 2002. doi:10.1109/TGRS.2002.801581.

M. Okutomi and T. Kanade. A locally adaptive window for signal matching. *International Journal of Computer Vision*, 7(2):143–162, January 1992. doi:10.1007/BF00128133.

Olympus. Knowledge: Surface Roughness. *Webpage*. URL: https://www.olympus-ims.com/en/knowledge/metrology/roughness/. Date of Last Access: 15-06-2015.

OpenTopography. OpenTopography: A Portal to High-Resolution Topography Data and Tools. 2014, *Webpage*. URL: http://www.opentopography.org. Date of Last Access: 15-06-2015.

R. Orosei, R. Bianchi, A. Coradini, S. Espinasse, C. Federico, A. Ferriccioni, and A. I. Gavrishin. Self-affine behavior of Martian topography at kilometer scale from Mars Orbiter Laser Altimeter data. *Journal of Geophysical Research*, 108(E4):8023, 2003. doi:10.1029/2002JE001883.

M. N. Ott, D. B. Coyle, D. B. Coyle, J. S. Canham, and H. W. Leidecker. Qualification and issues with space flight laser systems and components. *Proceedings of SPIE*, 6100:490–504, February 2006. doi:10.1117/12.674042.

G. P. Otto and T. Chau. 'Region-growing' algorithm for matching of terrain images. *Image and Vision Computing*, 7(2):83–94, May 1989. doi:10.1016/0262-8856(89)90001-2.

S. P. Palm, W. D. Hartmann, D. L. Hlavka, E. J. Welton, and J. D. Spinhirne. GLAS Atmospheric Data Products. Technical report, Geoscience Laser Altimeter System (GLAS), May 2011. URL: http://www.csr.utexas.edu/glas/pdf/glasatmos.atbdv5.0.pdf.

J. D. Pelletier. Why is topography fractal? *arxiv:physics*, May 1997. URL: http://arxiv.org/pdf/physics/9705033v1.pdf.

W. T. Pfeffer and C. S. Bretherton. The effect of crevasses on the solar heating of a glacier surface. In *The Physical Basis of Ice Sheet Modelling*, Proceedings of the Vancouver Symposium, August 1987. IAHS Publ. URL: ftp://luna.atmos.washington.edu/pub/breth/papers/1987/pfeffer-breth-crevasse.pdf.

G. Picardi, D. Biccari, R. Seu, and J. Plaut. MARSIS: Mars advanced radar for subsurface and ionosphere sounding. Technical report, ESA, August 2004. URL: http://www.esa.int/esapub/sp/sp1240/sp1240web.pdf.

R. J. Pike. Depth/diameter relations of fresh lunar craters: Revision from spacecraft data. *Geophysical Research Letters*, 1(7):291–294, 1974. doi:10.1029/GL001i007p00291.

R. J. Pike. Apparent depth/apparent diameter relation for lunar craters. *Proceeding of Lunar and Planetary Science Conference 8th*, 1977. URL: http://adsabs.harvard.edu/full/1977LPSC....8.3427P.

Planetary Data System. PDS Imaging Node Home Page. Planetary Data System. 2014a, *Webpage*. URL: http://pds.nasa.gov. Date of Last Access: 15-06-2015.

Planetary Data System. PDS Geosciences Node: Lunar Orbital Data Explorer. Planetary Data System. June 2014b, *Webpage*. URL: http://ode.rsl.wustl.edu/moon. Date of Last Access: 15-06-2015.

Planetary Data System. MOLA PEDR Data. Planetary Data System. October 2014c, *Webpage*. URL: http://pds-geosciences.wustl.edu/missions/mgs/pedr.html. Date of Last Access: 15-06-2015.

Planetary Data System. MOLA PEDR Software. Planetary Data System. October 2014d, *Webpage*. URL: http://pds-geosciences.wustl.edu/missions/mgs/molasoftware.html. Date of Last Access: 15-06-2015.

Planetary Data System. LRO: LOLA. Planetary Data System. June 2014e, *Webpage*. URL: http://geo.pds.nasa.gov/missions/lro/lola.htm. Date of Last Access: 15-06-2015.

Planetary Data System. Product Coverage Shapefiles for Mars. Planetary Data System. No Date., *Webpage*. URL: http://ode.rsl.wustl.edu/mars/coverage/ODE_Mars_shapefile.html. Date of Last Access: 15-06-2015.

M. Pondrelli, A Baliva, S. Di Lorenzo, L. Marinangeli, and A. P. Rossi. Complex evolution of paleolacustrine systems on Mars: An example from the Holden crater. *Journal of Geophysical Research*, 110(E4), April 2005. doi:10.1029/2004JE002335.

M. Pondrelli, A. P. Rossi, L. Marinangeli, E. Hauber, K. Gwinner, A. Baliva, and S. Di Lorenzo. Evolution and depositional environments of the Eberswalde fan delta, Mars. *Icarus*, 197(2):429–451, October 2008. doi:10.1016/j.icarus.2008.05.018.

W. D. Poole and J.-P. Muller. On an assessment of surface roughness estimates from lunar laser altimetry pulse-widths for the Moon from LOLA using LROC narrow-angle stereo DTMs. In *European Geosciences Union General Assembly*, Vienna, Austria, April 2013. URL: http://meetingorganizer.copernicus.org/EGU2013/EGU2013-12757.pdf.

W. D. Poole, J.-P. Muller, and S. Gupta. On the calibration of Mars Orbiter Laser Altimeter surface roughness estimates using high-resolution DTMs . In *European Geosciences Union General Assembly*, 2012a. URL: http://meetingorganizer.copernicus.org/EGU2012/EGU2012-4305.pdf.

W. D. Poole, J.-P. Muller, and S. Gupta. On the Calibration of MOLA Pulse-Width Surface Roughness Estimates Using High-Resolution DTMs. In *43rd Lunar and Planetary Science Conference*, Houston, Tx, March 2012b. URL: http://www.lpi.usra.edu/meetings/lpsc2012/pdf/1854.pdf.

W. D. Poole, J.-P. Muller, and S. Gupta. Mars Orbiter Laser Altimetry Pulse-Widths an Indicator of Surface Roughness at Gale Crater [EPSC2012-554-1]. In *European Planetary Science Congress*, Vienna, Austria, 2012c. URL: http://meetingorganizer.copernicus.org/EPSC2012/EPSC2012-554-1.pdf.

W. D. Poole, J.-P. Muller, and S. Gupta. How Reliable are Surface Roughness Estimates from Planetary Laser Altimeter Pulse-Widths? An Assessment Using MOLA and LOLA Pulse-Width Data. In *44th Lunar and Planetary Science Conference*, Houston, USA, March 2013a. URL: http://www.lpi.usra.edu/meetings/lpsc2013/pdf/1511.pdf.

W. D. Poole, J.-P. Muller, S. Gupta, and P. M. Grindrod. Surface roughness from MOLA backscatter pulse-widths. In *European Planetary Science Congress*, London, UK, September 2013b. URL: http://meetingorganizer.copernicus.org/EPSC2013/EPSC2013-321.pdf.

W. D. Poole, J.-P. Muller, and P. M. Grindrod. Footprint Scale Surface Roughness from ICESat Pulse-Widths: Lessons Learnt for Future Planetary Laser Altimeters. In *45th Lunar and Planetary Science Conference*, Houston, Tx, March 2014a. URL: http://www.hou.usra.edu/meetings/lpsc2014/pdf/1150.pdf.

W. Poole, J.-P. Muller, S. Gupta, and P. M. Grindrod. Calibrating Mars Orbiter Laser Altimeter pulse widths at Mars Science Laboratory candidate landing sites. *Planetary and Space Science*, 99:118–127, September 2014b. doi:10.1016/j.pss.2014.05.012.

M. L. Prentice, J. L. Kleman, and A. P. Stroeven. The Composite Glacial Erosional Landscape of the Northern Mcmurdo Dry Valleys: Implications for Antarctic Tertiary Glacial History. In *Ecosystem Dynamics in a Polar Desert: the Mcmurdo Dry Valleys, Antarctica*, pages 1–38. American Geophysical Union, Washington, D. C., 1998. ISBN 9780875908991. doi:10.1029/AR072p0001.

H. D. Pritchard, R. J. Arthern, D. G. Vaughan, and L. A. Edwards. Extensive dynamic thinning on the margins of the Greenland and Antarctic ice sheets. *Nature*, 461(7266):971–975, September 2009. doi:10.1038/nature08471.

C. Quantin, P. Allemand, N. Mangold, and C. Delacourt. Ages of Valles Marineris (Mars) landslides and implications for canyon history. *Icarus*, 172(2):555–572, December 2004. doi:10.1016/j.icarus.2004.06.013.

L. Ramos-Izquierdo, V. S. Scott III, J. Connelly, S. Schmidt, W. Mamakos, J. Guzek, C. Peters, P. Liiva, M. Rodriguez, J. Cavanaugh, and H. Riris. Optical system design and integration of the lunar orbiter laser altimeter. *Applied Optics*, 48(16):3035–3049, 2009. doi:10.1364/AO.48.003035.

F. Remy and S. Parouty. Antarctic Ice Sheet and Radar Altimetry: A Review. *Remote Sensing*, 1 (4):1212–1239, December 2009. doi:10.3390/rs1041212.

M. S. Rice, S. Gupta, J. F. Bell, and N. H. Warner. Influence of fault-controlled topography on fluvio-deltaic sedimentary systems in Eberswalde crater, Mars. *Geophysical Research Letters*, 38(L16):L16203, 2011. doi:10.1029/2011GL048149.

M. S. Rice, J. F. Bell III, S. Gupta, N. H. Warner, K. Goddard, and R. B. Anderson. A detailed geologic characterization of Eberswalde crater, Mars. *MARS*, 8:15–57, May 2013. doi:10.1555/mars.2013.0002.

E. Rignot, J. Mouginot, and B. Scheuchl. *MEaSUREs InSAR-Based Antarctica Ice Velocity Map*. Science, Boulder, Colorado USA: National Snow and Ice Data Center, 2011a. doi:10.5067/MEASURES/CRYOSPHERE/nsidc-0484.001.

E. Rignot, J. Mouginot, and B. Scheuchl. Ice Flow of the Antarctic Ice Sheet. *Science*, 333(6048): 1427–1430, September 2011b. doi:10.1126/science.1208336.

M. S. Robinson, S. M. Brylow, M. Tschimmel, D. Humm, S. J. Lawrence, P. C. Thomas, B. W. Denevi, E. Bowman-Cisneros, J. Zerr, M. A. Ravine, M. A. Caplinger, F. T. Ghaemi *et al.* Lunar Reconnaissance Orbiter Camera (LROC) Instrument Overview. *Space Science Reviews*, 150 (1-4):81–124, March 2010. doi:10.1007/s11214-010-9634-2.

J. A. P. Rodriguez, S. Sasaki, R. O. Kuzmin, J. M. Dohm, K. L. Tanaka, H. Miyamoto, K. Kurita, G. Komatsu, A. G. Fairen, and J. C. Ferris. Outflow channel sources, reactivation, and chaos formation, Xanthe Terra, Mars. *Icarus*, 175(1):36–57, May 2005. doi:10.1016/j.icarus.2004.10.025.

M. A. Rosenburg, O. Aharonson, J. W. Head, M. A. Kreslavsky, E. Mazarico, G. A. Neumann, D. E. Smith, M. H. Torrence, and M. T. Zuber. Global surface slopes and roughness of the Moon from the Lunar Orbiter Laser Altimeter. *Journal of Geophysical Research*, 116(E2):E02001, February 2011. doi:10.1029/2010JE003716.

A. P. Rossi. HRSC Map and Reference Issues. In *Mars Express Workshop*, May 2008. URL: http://pds-geosciences.wustl.edu/workshops/MEX_WORKSHOP_May08_presentations/4_HRSC_level4_map_projection_small.pdf.

P. Saiger, J. Oberst, and M. Wählisch. Calibration of the MOLA Laser Pulse Spread for Interpretations of Surface Roughness . In *ISPRS - International Archives of the Photogrammetry, Remote Sensing and Spatial Information Sciences*, March 2007. URL: http://www.dlr.de/pf/Portaldata/6/Resources/dokumente/isprs_2007/Saiger_ISPRS_2007.pdf.

D. Scharstein and R. Szeliski. A taxonomy and evaluation of dense two-frame stereo correspondence algorithms. *International Journal of Computer Vision*, 47(1-3):7–42, 2002. doi:10.1023/A:1014573219977.

T. Schenk, B. M. Csathó, Y. Ahn, S. W. Shin, and K. I. Huh. DEM Generation from the Antarctic LIDAR Data. Technical report, Geoscience Laser Altimeter System (GLAS), September 2004. URL: http://usarc.usgs.gov/lidar/lidar_pdfs/Site_reports_v5.pdf.

F. Scholten, K. Gwinner, T. Roatsch, K. D. Matz, M. Wählisch, B. Giese, J. Oberst, R. Jaumann, G. Neukum, and the HRSC Co-Investigator Team. Mars Express HRSC Data Processing-Methods and Operational Aspects. In *ASPRS*, page 1143, 2005. URL: http://www.asprs.org/a/publications/pers/2005journal/october/2005_oct_1129-1142.pdf.

F. Scholten, J. Oberst, K. D. Matz, T. Roatsch, M. Wählisch, E. J. Speyerer, and M. S. Robinson. GLD100: The near-global lunar 100 m raster DTM from LROC WAC stereo image data. *Journal of Geophysical Research*, 117(E12):E00H17, December 2012. doi:10.1029/2011JE003926.

B. E. Schutz, H. J. Zwally, C. A. Shuman, D. Hancock, and J. P. DiMarzio. Overview of the ICESat Mission. *Geophysical Research Letters*, 32(L21):L21S01, November 2005. doi:10.1029/2005GL024009.

B. E. Schutz. Laser Altimetry and Lidar from ICESat/GLAS. In *Geoscience and Remote Sensing Symposium IGARSS, IEEE International*, pages 1016–1019, Sydney, NSW, July 2001. IEEE. ISBN 0-7803-7031-7. doi:10.1109/IGARSS.2001.976732.

P. K. Seidelmann, V. K. Abalakin, and M. Bursa. Report of the IAU/IAG working group on cartographic coordinates and rotational elements of the planets and satellites: 2000. *Celestial Mechanics and Dynamical Astronomy*, 82(1):83–110, 2002. doi:10.1023/A:1013939327465.

G. Seiz, S. Tjemkes, and P. Watts. Multiview Cloud-Top Height and Wind Retrieval with Photogrammetric Methods: Application to Meteosat-8HRV Observations. *Journal of Applied Meteorology and Climatology*, 46(8):1182–1195, August 2007. doi:10.1175/JAM2532.1.

P. J. Sellers, Y. Mintz, Y. C. Sud, and A. Dalcher. A Simple Biosphere Model (SIB) for Use Within General-Circulation Models. *Journal of the Atmospheric Sciences*, 43(6):505–531, March 1986. doi:10.1175/1520-0469(1986)043<0505:ASBMFU>2.0.CO;2.

J. Shan and C. Toth. *Topographic Laser Ranging and Scanning: Principles and Processing*. CRC Press, 2009. ISBN 978-1-4200-5142-1.

M. K. Shepard, B. A. Campbell, M. H. Bulmer, T. G. Farr, L. R. Gaddis, and J. J. Plaut. The roughness of natural terrain: A planetary and remote sensing perspective. *Journal of Geophysical Research*, 106(E12):32777–32795, December 2001. doi:10.1029/2000JE001429.

J. Shi, M. Meneti, and R. Lindenbergh. Parameterization of Surface Roughness Based on ICESat/GLAS Full Waveforms: A Case Study on the Tibetan Plateau. *Journal of Hydrometeorology*, 14:1278–1292, 2013. doi:10.1175/JHM-D-12-0130.1.

A. E. Siegman. *Lasers*. University Science Books, 1986. ISBN 0935702115.

S. Silvestro, D. A. Vaz, R. C. Ewing, A. P. Rossi, L. K. Fenton, T. I. Michaels, J. Flahaut, and P. E. Geissler. Pervasive aeolian activity along rover Curiosity's traverse in Gale Crater, Mars. *Geology*, 41(4):483–486, March 2013. doi:10.1130/G34162.1.

J. M. Sirota, S. Bae, P. Millar, D. Mostofi, C. Webb, B. Schutz, and S. Luthcke. The transmitter pointing determination in the Geoscience Laser Altimeter System. *Geophysical Research Letters*, 32(22), 2005. doi:10.1029/2005GL024005.

D. E. Smith, M. T. Zuber, G. A. Neumann, and F. G. Lemoine. Topography of the moon from the Clementine lidar. *Journal of Geophysical Research*, 102(E1):1591–1611, January 1997. doi:10.1029/96JE02940.

D. E. Smith, M. T. Zuber, S. C. Solomon, R. J. Phillips, J. W. Head, J. B. Garvin, W. B. Banerdt, D. O. Muhleman, G. H. Pettengill, G. A. Neumann, r. G. Lemoine, J. B. Abshire *et al.* The Global Topography of Mars and Implications for Surface Evolution. *Science*, 284:1495–1503, May 1999. doi:10.1126/science.284.5419.1495.

D. E. Smith, M. T. Zuber, H. V. Frey, J. B. Garvin, J. W. Head, D. O. Muhleman, G. H. Pettengill, R. J. Phillips, S. C. Solomon, H. J. Zwally, W. B. Banerdt, T. C. Duxbury *et al.* Mars Orbiter Laser Altimeter: Experiment summary after the first year of global mapping of Mars. *Journal of Geophysical Research*, 106(E10):23689–23722, October 2001. doi:10.1029/2000JE001364.

D. E. Smith, M. T. Zuber, G. B. Jackson, J. F. Cavanaugh, G. A. Neumann, H. Riris, X. Sun, R. S. Zellar, C. Coltharp, J. Connelly, R. B. Katz, I. Kleyner *et al.* The Lunar Orbiter Laser Altimeter Investigation on the Lunar Reconnaissance Orbiter Mission. *Space Science Reviews*, 150(1-4): 209–241, January 2010a. doi:10.1007/s11214-009-9512-y.

D. E. Smith, M. T. Zuber, G. A. Neumann, F. G. Lemoine, E. Mazarico, M. H. Torrence, J. F. McGarry, D. D. Rowlands, J. W. Head III, T. H. Duxbury, O. Aharonson, P. G. Lucey *et al.* Initial observations from the Lunar Orbiter Laser Altimeter (LOLA). *Geophysical Research Letters*, 37 (L18):L18204, September 2010b. doi:10.1029/2010GL043751.

J. Snyder. Map Projections: A Working Manual. Technical Report 1395, U.S Geological Survey, 1987. URL: http://pubs.er.usgs.gov/djvu/PP/PP_1395.pdf.

S. C. Solomon, R. L. McNutt, R. E. Gold, M. H. Acuna, D. N. Baker, W. V. Boynton, C. R. Chapman, A. F. Cheng, G. Gloeckler, J. W. Head, S. M. Krimigis, W. E. McClintock *et al.* The MESSENGER mission to Mercury: scientific objectives and implementation. *Planetary and Space Science*, 49(14-15):1445–1465, December 2001. doi:10.1016/S0032-0633(01)00085-X.

M. G. Spagnuolo, A. P. Rossi, E. Hauber, and S. van Gasselt. Recent tectonics and subsidence on Mars: Hints from Aureum Chaos. *Earth and Planetary Science Letters*, 312(1-2):13–21, December 2011. doi:10.1016/j.epsl.2011.09.052.

J. C. Speirs, D. F. Steinhoff, H. A. McGowan, D. H. Bromwich, and A. J. Monaghan. Foehn Winds in the McMurdo Dry Valleys, Antarctica: The Origin of Extreme Warming Events. *Journal of Climate*, 23(13):3577–3598, July 2010. doi:10.1175/2010JCLI3382.1.

J. C. Speirs, H. A. McGowan, D. F. Steinhoff, and D. H. Bromwich. Regional climate variability driven by foehn winds in the McMurdo Dry Valleys, Antarctica. *International Journal of Climatology*, 33(4):945–958, April 2012. doi:10.1002/joc.3481.

J. D. Spinhirne, S. P. Palm, W. D. Hart, D. L. Hlavka, and E. J. Welton. Cloud and aerosol measurements from GLAS: Overview and initial results. *Geophysical Research Letters*, 32(22): L22S03, November 2005. doi:10.1029/2005GL023507.

P. D. Spudis, D. B. J. Bussey, S. M. Baloga, B. J. Butler, D. Carl, L. M. Carter, M. Chakraborty, R. C. Elphic, J. J. Gillis Davis, J. N. Goswami, E. Heggy, M. Hillyard *et al.* Initial results for the north pole of the Moon from Mini-SAR, Chandrayaan-1 mission. *Geophysical Research Letters*, 37(6), March 2010. doi:10.1029/2009GL042259.

P. D. Spudis. The Case For Renewed Human Exploration Of The Moon. *Earth, Moon, and Planets*, 87(3):159–171, 1999. doi:10.1023/A:1013186823933.

Y. C. Sud and W. E. Smith. The influence of surface roughness of deserts on the July circulation. *Boundary-Layer Meteorology*, 33(1):15–49, September 1985. doi:10.1007/BF00137034.

O. Svelto. Principles of lasers. Springer, Boston, MA, 2010. ISBN 978-1-4419-1301-2. doi:10.1007/978-1-4419-1302-9.

N. Thomas, T. Spohn, J. P. Barriot, W. Benz, G. Beutler, U. Christensen, V. Dehant, C. Fallnich, D. Giardini, O. Groussin, K. Gunderson, E. Hauber *et al.* The BepiColombo Laser Altimeter (BELA): Concept and baseline design. *Planetary and Space Science*, 55(10):1398–1413, July 2007. doi:10.1016/j.pss.2007.03.003.

G. W. Thompson and D. F. Maune. Issues and Answers in Quality Control of LIDAR DEMs. Technical report, March 2002. URL: http://www.ncfloodmaps.com/pubdocs/qc_lidar_dems.pdf.

B. J. Thomson, B. J. Thomson, N. T. Bridges, N. T. Bridges, R. Milliken, R. Milliken, A. Baldridge, A. Baldridge, S. J. Hook, S. J. Hook, J. K. Crowley, J. K. Crowley *et al.* Constraints on the origin and evolution of the layered mound in Gale Crater, Mars using Mars Reconnaissance Orbiter data. *Icarus*, 214(2):413–432, August 2011. doi:10.1016/j.icarus.2011.05.002.

C. K. Toth and D. A. Grejner-Brzezinska. Complimentarity of LIDAR and Stereo Imagery for Enhanced Surface Extraction . *International Archives of Photogrammetry and Remote Sensing*, XXXIII(Part B3):897–904, 2000. URL: http://www.isprs.org/proceedings/xxxiii/congress/part3/897_XXXIII-part3.pdf.

T. Tran, M. Rosiek, and E. Howington-Kraus. Generating digital terrain models using LROC NAC images. In *ISPRS Technical Commission IV*, Orlando, Florida, 2010. URL: http://www.isprs.org/proceedings/XXXVIII/part4/files/TRAN-2.PDF.

D. L. Turcotte. *Fractals and chaos in geology and geophysics*. Cambridge University Press, Cambridge, UK, 2nd edition, 1997. ISBN 9780521567336.

United States Geological Survey. Stereo Processing using HiRISE Stereo Imagery ISIS3 and SOCET® SET. United States Geological Survey Astrogeology Science Center, June 2009. URL: ftp://pdsimage2.wr.usgs.gov/pub/pigpen/mars/tutorials/SS4HIRISE_JUNE2009/.

United States Geological Survey. United States Antarctic Resource Center. United States Geological Survey. January 2013, *Webpage*. URL: http://usarc.usgs.gov. Date of Last Access: 15-06-2015.

United States Geological Survey. National Elevation Dataset. United States Geological Survey. 2014, *Webpage*. URL: http://ned.usgs.gov. Date of Last Access: 15-06-2015.

Universität Bern. BELA and Laser Altimetry. Planetary Imaging Group, Universität Bern. No Date., *Webpage*. URL: http://space.unibe.ch/pig/science/projects/bela-and-laser-altimetry.html. Date of Last Access: 15-06-2015.

M. Vacek, V. Michalek, and M. Peca. Photon counting altimeter and lidar for air and spaceborne applications. *SPIE Optics+ ...*, 2011. doi:10.1117/12.886454.

M. Vacek, V. Michalek, M. Peca, I. Prochazka, J. Blazej, and G. Djurovic. Single photon lidar demonstrator for asteroid rendezvous missions. In P. Tománek, D. Senderáková, and P. Páta, editors, *Photonics Prague 2014*, pages 945007–945007–11. SPIE, January 2015. doi:10.1117/12.2070323.

C. J. van der Veen, Y. Ahn, B. M. Csatho, E. Mosley-Thompson, and W. B. Krabill. Surface roughness over the northern half of the Greenland Ice Sheet from airborne laser altimetry. *Journal of Geophysical Research*, 114(F1), 2009. doi:10.1029/2008JF001067.

M. Vetter, B. Höfle, M. Hollaus, C. Gschöpf, G. Mandlburger, N. Pfeifer, and W. Wagner. VERTICAL VEGETATION STRUCTURE ANALYSIS AND HYDRAULIC ROUGHNESS DETERMINATION USING DENSE ALS POINT CLOUD DATA - A VOXEL BASED APPROACH. *ISPRS - International Archives of the Photogrammetry, Remote Sensing and Spatial Information Sciences*, XXXVIII-5/W12:265–270, 2011. doi:10.5194/isprsarchives-XXXVIII-5-W12-265-2011.

M. Wang, F. Hu, and J. Li. Epipolar resampling of linear pushbroom satellite imagery by a new epipolarity model. *ISPRS Journal of Photogrammetry and Remote Sensing*, 66(3):347–355, May 2011. doi:10.1016/j.isprsjprs.2011.01.002.

N. H. Warner, S. Gupta, J. R. Kim, J.-P. Muller, L. Le Corre, J. Morley, S.-Y. Lin, and C. McGonigle. Constraints on the origin and evolution of Iani Chaos, Mars. *Journal of Geophysical Research*, 116(E6):E06003, June 2011. doi:10.1029/2010JE003787.

S. G. Warren, R. E. Brandt, and P. O'Rawe Hinton. Effect of surface roughness on bidirectional reflectance of Antarctic snow. *Journal of Geophysical Research*, 103(E11):25789–25807, October 1998. doi:10.1029/98JE01898.

J. G. Williams, A. S. Konopliv, D. H. Boggs, R. S. Park, D.-N. Yuan, F. G. Lemoine, S. Goossens, E. Mazarico, F. Nimmo, R. C. Weber, S. W. Asmar, H. J. Melosh *et al.* Lunar interior properties from the GRAIL mission. *Journal of Geophysical Research*, 119(7):1546–1578, July 2014. doi:10.1002/2013JE004559.

L. Wilson and J. W. Head. Lunar Gruithuisen and Mairan domes: Rheology and mode of emplacement. *Journal of Geophysical Research*, 108(E2):5012, 2003. doi:10.1029/2002JE001909.

J. Wood. *The geomorphological characterisation of digital elevation models*. PhD thesis, University of Leicester, 1996. URL: http://www.soi.city.ac.uk/~jwo/phd.

L. J. Wood. Quantitative geomorphology of the Mars Eberswalde delta. *Geological Society of America Bulletin*, 118(5-6):557–566, May 2006. doi:10.1130/B25822.1.

World Meteorological Organization. *Guide to Meteorological Instruments and Methods of Observation*. World Meteorological Organization, 2010. ISBN 978-92-63-10008-5.

D. Yi, J. P. Harbeck, S. S. Manizade, N. T. Kurtz, M. Studinger, and M. Hofton. Arctic Sea Ice Freeboard Retrieval With Waveform Characteristics for NASA's Airborne Topographic Mapper (ATM) and Land, Vegetation, and Ice Sensor (LVIS). *IEEE Transactions on Geoscience and Remote Sensing*, 53(3):1403–1410, March 2015. doi:10.1109/TGRS.2014.2339737.

R. A. Yingst, L. C. Kah, M. Palucis, R. M. E. Williams, J. Garvin, J. C. Bridges, N. Bridges, R. G. Deen, J. Farmer, O. Gasnault, W. Goetz, V. E. Hamilton *et al.* Characteristics of pebble- and cobble-sized clasts along the Curiosity rover traverse from Bradbury Landing to Rocknest. *Journal of Geophysical Research*, 118(11):2361–2380, November 2013. doi:10.1002/2013JE004435.

Y. Yokota, J. Haruyama, C. Honda, T. Morota, M. Ohtake, H. Kawasaki, S. Hara, K. Hioki, and the LISM Working Group. Lunar topography: Statistical analysis of roughness on a kilometer scale. *Advances in Space Research*, 42(2):259–266, 2008. doi:10.1016/j.asr.2007.07.003.

Y. Yokota, K. Gwinner, J. Oberst, J. Haruyama, T. Matsunaga, T. Morota, H. Noda, H. Araki, M. Ohtake, S. Yamamoto, P. Gläser, Y. Ishihara *et al.* Variation of the lunar highland surface roughness at baseline 0.15-100 km and the relationship to relative age. *Geophysical Research Letters*, 41(5):1444–1451, March 2014. doi:10.1002/2013GL059091.

B. Zhang and S. Miller. Adaptive automatic terrain extraction. *Proc. SPIE , Integrating Photogrammetric Techniques with Scene Analysis and Machine Vision, III*, 3072, August 1997. doi:10.1117/12.281065.

B. Zhang, S. Miller, K. DeVenecia, and S. Walker. Automatic terrain extraction using multiple image pair and back matching. In *Proceedings of the ASPRS Annual Conference*, Reno, Nevada, 2006. URL: ftp://jetty.ecn.purdue.edu/jshan/proceedings/asprs2006/files/0180.pdf.

Z.-C. Zheng, S.-Q. He, and F.-Q. Wu. Changes of soil surface roughness under water erosion process. *Hydrological Processes*, 28(12):3919–3929, July 2013. doi:10.1002/hyp.9939.

C. L. Zitnick and T. Kanade. A cooperative algorithm for stereo matching and occlusion detection. *Pattern Analysis and Machine Intelligence, IEEE Transactions on*, 22(7):675–684, 2000. doi:10.1109/34.865184.

M. T. Zuber, D. E. Smith, S. C. Solomon, R. J. Phillips, S. J. Peale, J. W. Head III, S. A. Hauck II, R. L. McNutt Jr., J. Oberst, G. A. Neumann, F. G. Lemoine, X. Sun *et al.* Laser Altimeter Observations from MESSENGER's First Mercury Flyby. *Science*, 321(5885):77–79, July 2008. doi:10.1126/science.1159086.

M. T. Zuber, D. E. Smith, R. S. Zellar, G. A. Neumann, X. Sun, R. B. Katz, I. Kleyner, A. Matuszeski, J. F. McGarry, M. N. Ott, L. A. Ramos-Izquierdo, D. D. Rowlands *et al.* The Lunar Reconnaissance Orbiter Laser Ranging Investigation. *Space Science Reviews*, 150(1-4):63–80, May 2009. doi:10.1007/s11214-009-9511-z.

M. T. Zuber, D. E. Smith, R. J. Phillips, S. C. Solomon, G. A. Neumann, S. A. I. Hauck, S. J. Peale, O. S. Barnouin, J. W. Head, C. L. Johnson, F. G. Lemoine, E. Mazarico *et al.* Topography of the Northern Hemisphere of Mercury from MESSENGER Laser Altimetry. *Science*, 336(6078): 217–220, 2012. doi:10.1126/science.1218805.

M. T. Zuber, D. E. Smith, M. M. Watkins, S. W. Asmar, A. S. Konopliv, F. G. Lemoine, H. J. Melosh, G. A. Neumann, R. J. Phillips, S. C. Solomon, M. A. Wieczorek, J. G. Williams *et al.* Gravity Field of the Moon from the Gravity Recovery and Interior Laboratory (GRAIL) Mission. *Science*, 339(6120):668–671, 2013. doi:10.1126/science.1231507.

R. W. Zurek and S. E. Smrekar. An overview of the Mars Reconnaissance Orbiter (MRO) science mission. *Journal of Geophysical Research*, 112:E05S01, May 2007. doi:10.1029/2006JE002701.

H. J. Zwally, B. Schutz, W. Abdalati, J. Abshire, C. Bentley, A. Brenner, J. Bufton, J. Dezio, D. Hancock, D. Harding, T. Herring, B. Minster *et al.* ICESat's laser measurements of polar ice, atmosphere, ocean, and land. *Journal of Geodynamics*, 34(3-4):405–445, October 2002. doi:10.1016/S0264-3707(02)00042-X.

A

Maps

This appendix contains additional maps which are relevant to the work presented in this thesis.

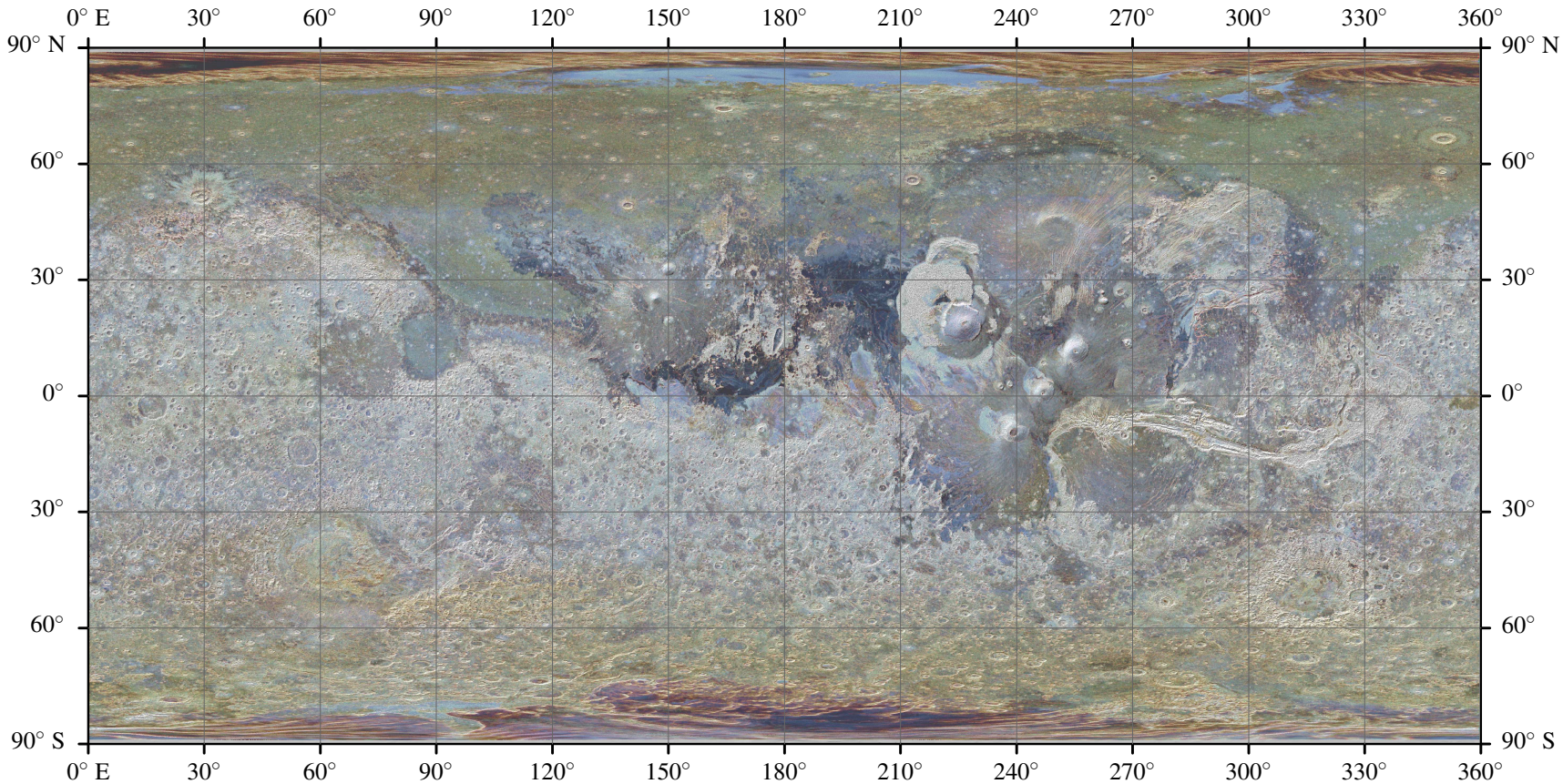

Figure A.1: Mars surface roughness map adapted from *Kreslavsky and Head* [2000] using MOLA profile data. The red, green and blue channels represent surface roughness at 0.6 km, 2.4 km and 19.2 km. Higher intensity represents rougher regions, and bright areas represent regions which are rough on all baselines.

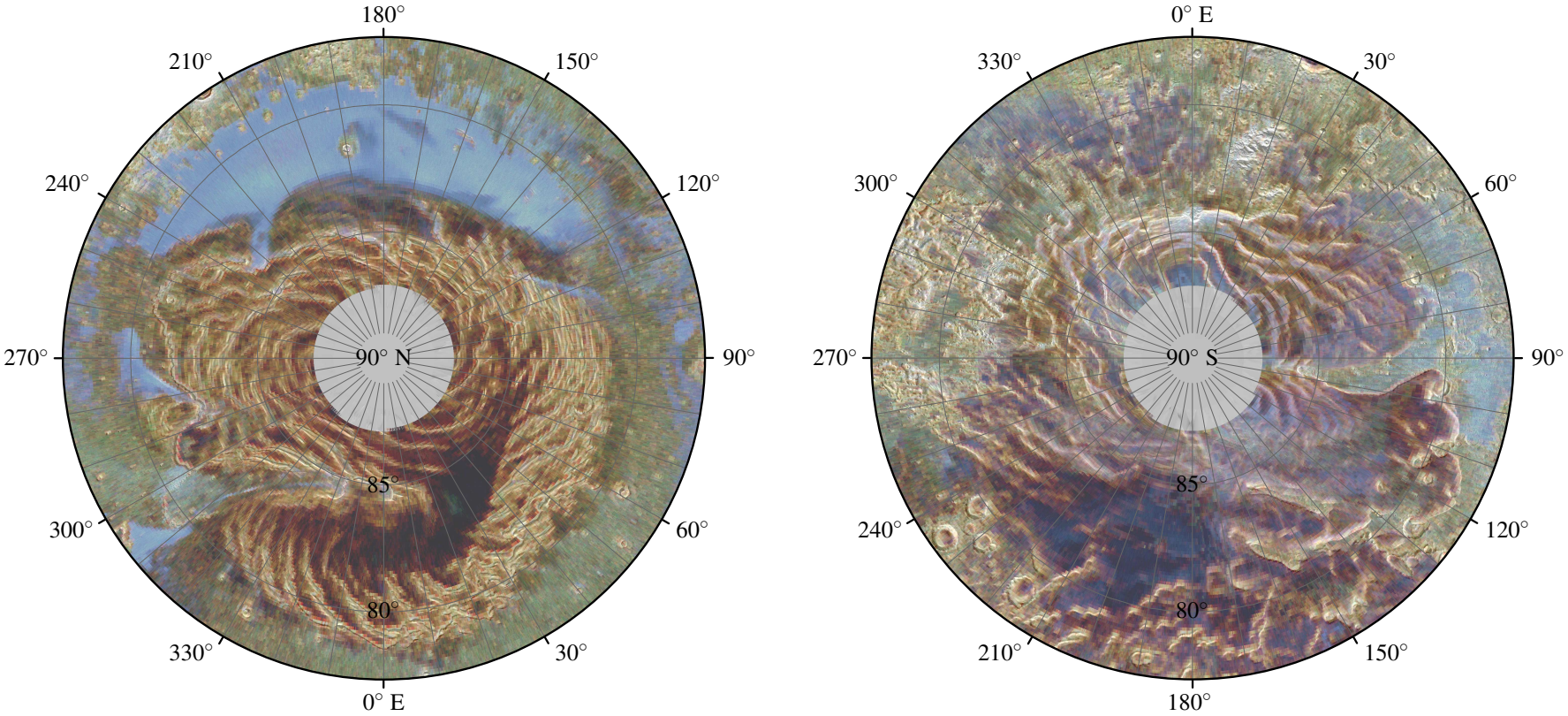

Figure A.2: Mars polar surface roughness map adapted from *Kreslavsky and Head* [2000] using MOLA profile data. The red, green and blue channels represent surface roughness at 0.6 km, 2.4 km and 19.2 km. Higher intensity represents rougher regions, and bright areas represent regions which are rough on all baselines.

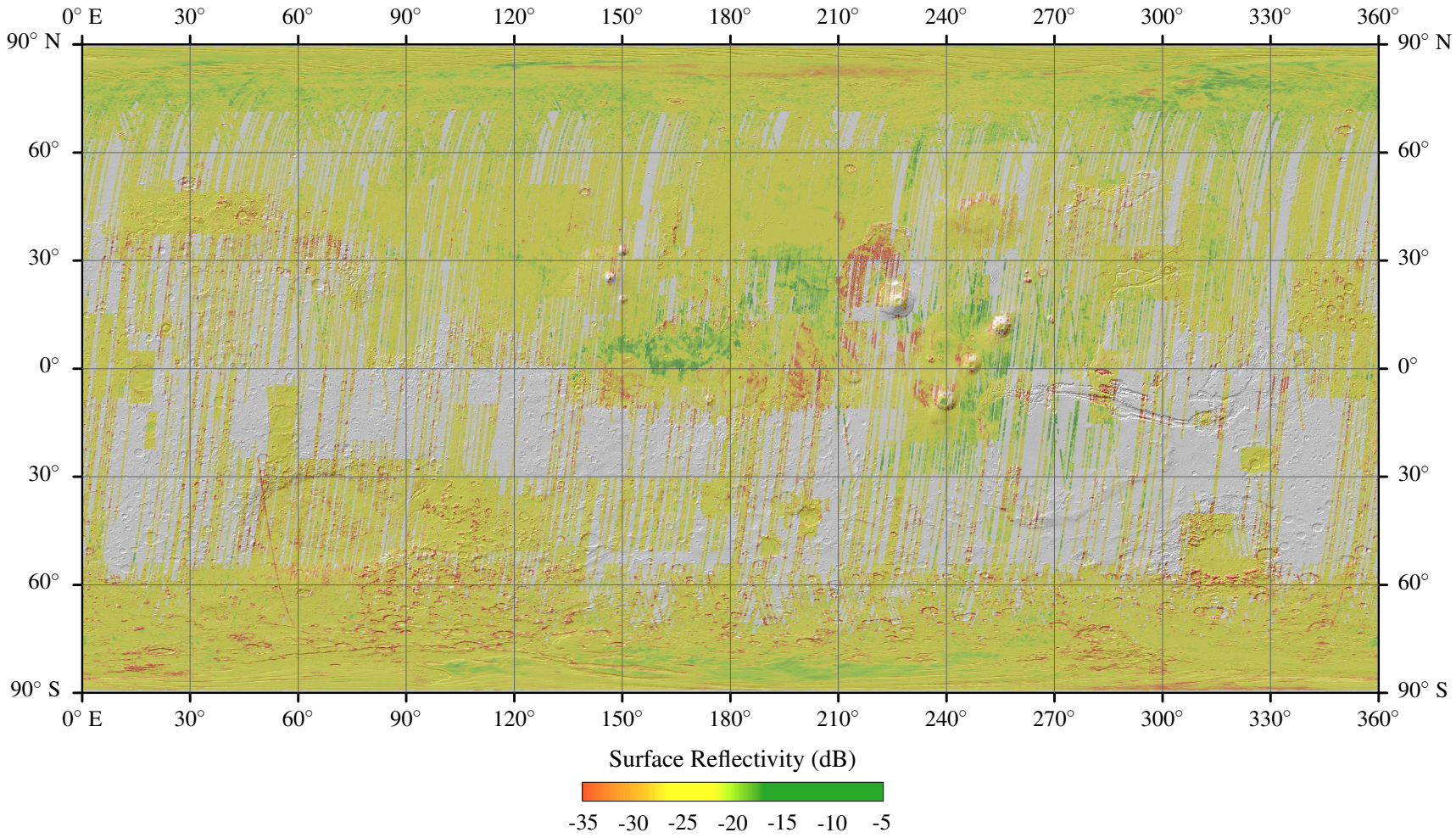

Figure A.3: Mars SHAllow RADar sounder (SHARAD) reflectance at 20 MHz map adapted from *Grima et al.* [2012]

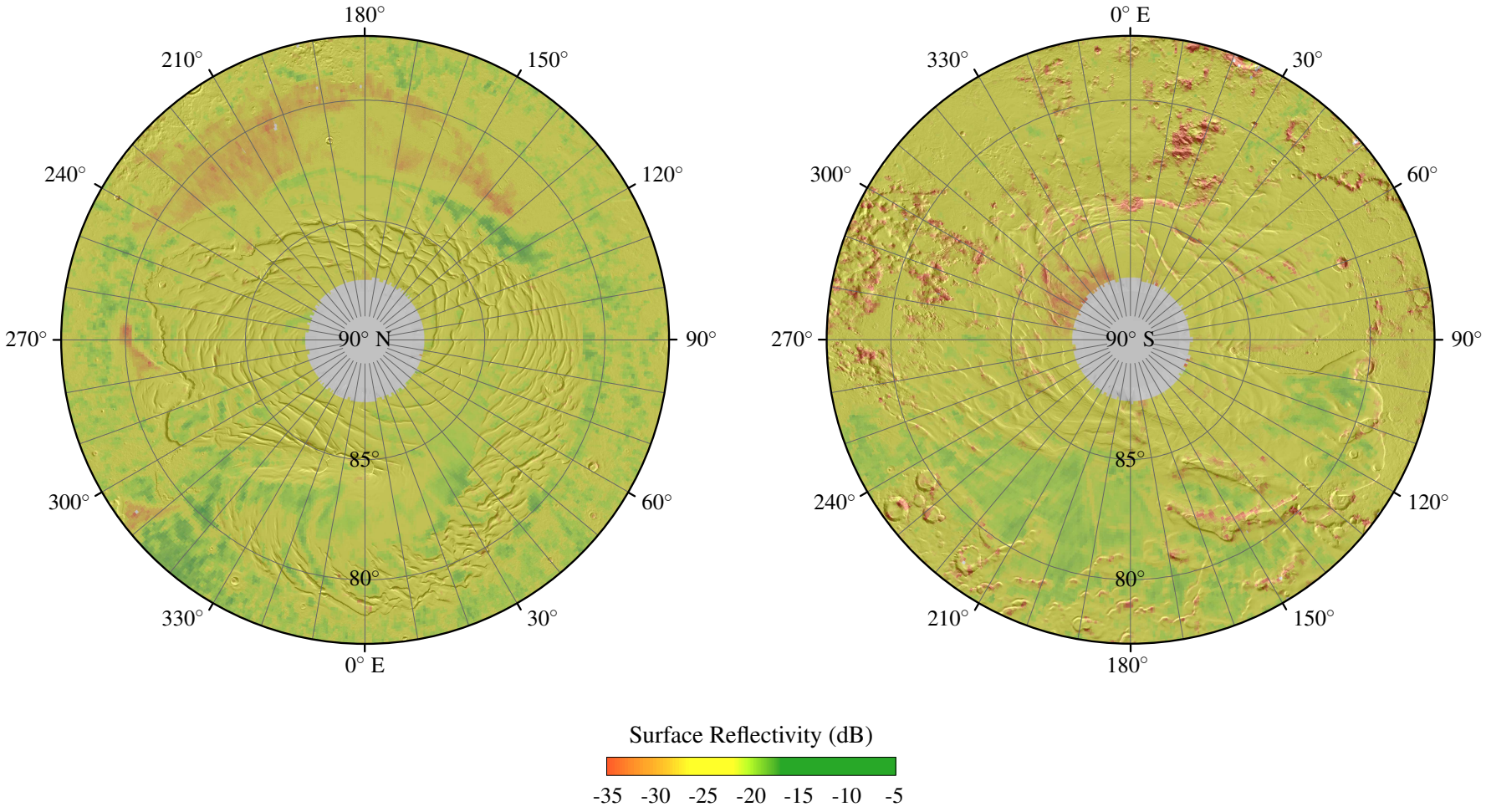

Figure A.4: SHARAD polar reflectance at 20 MHz map adapted from *Grima et al.* [2012]

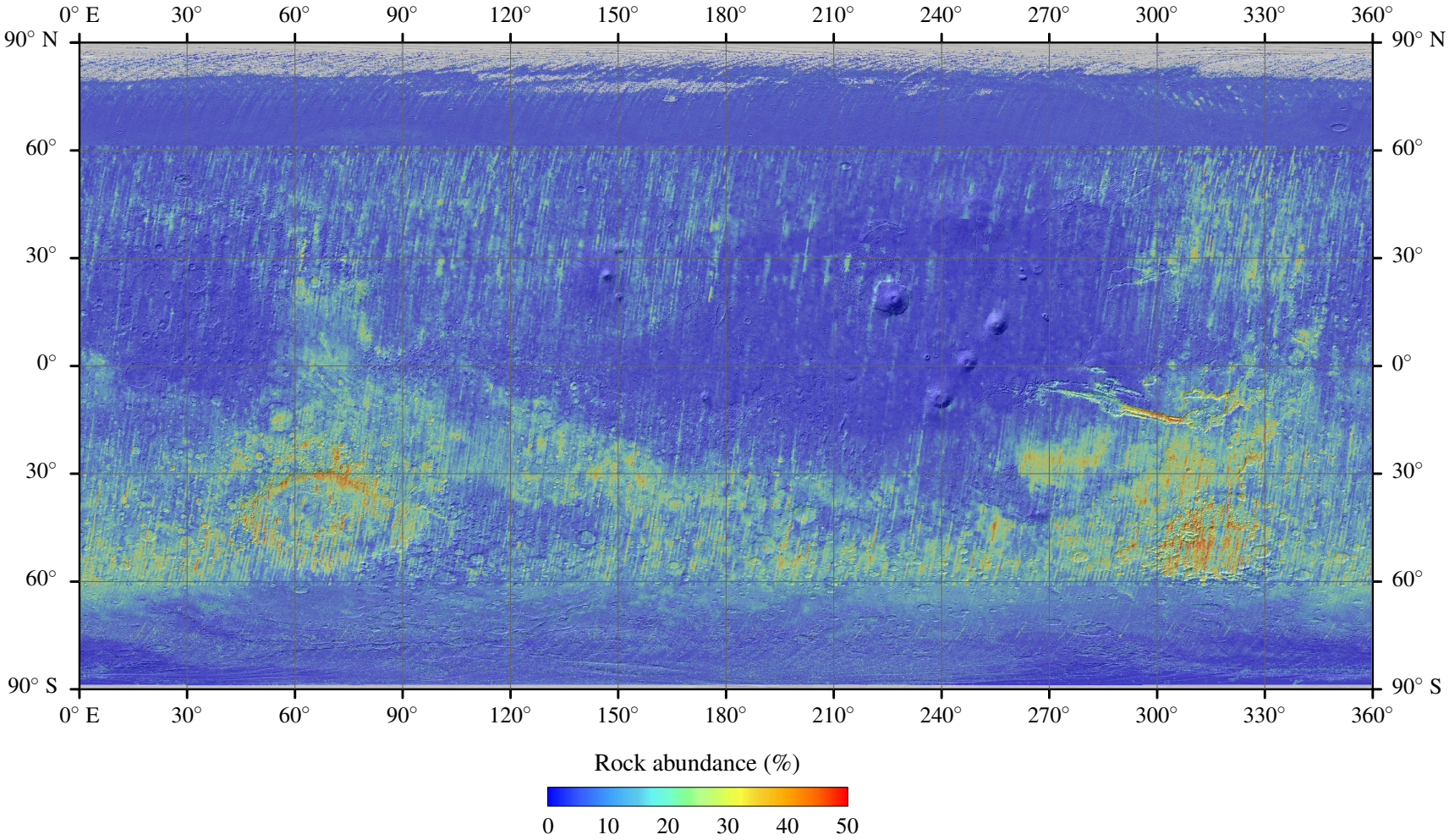

Figure A.5: Mars rock abundance derived from Thermal Emission Spectrometer (TES) data, adapted from *Hébrard et al.* [2012].

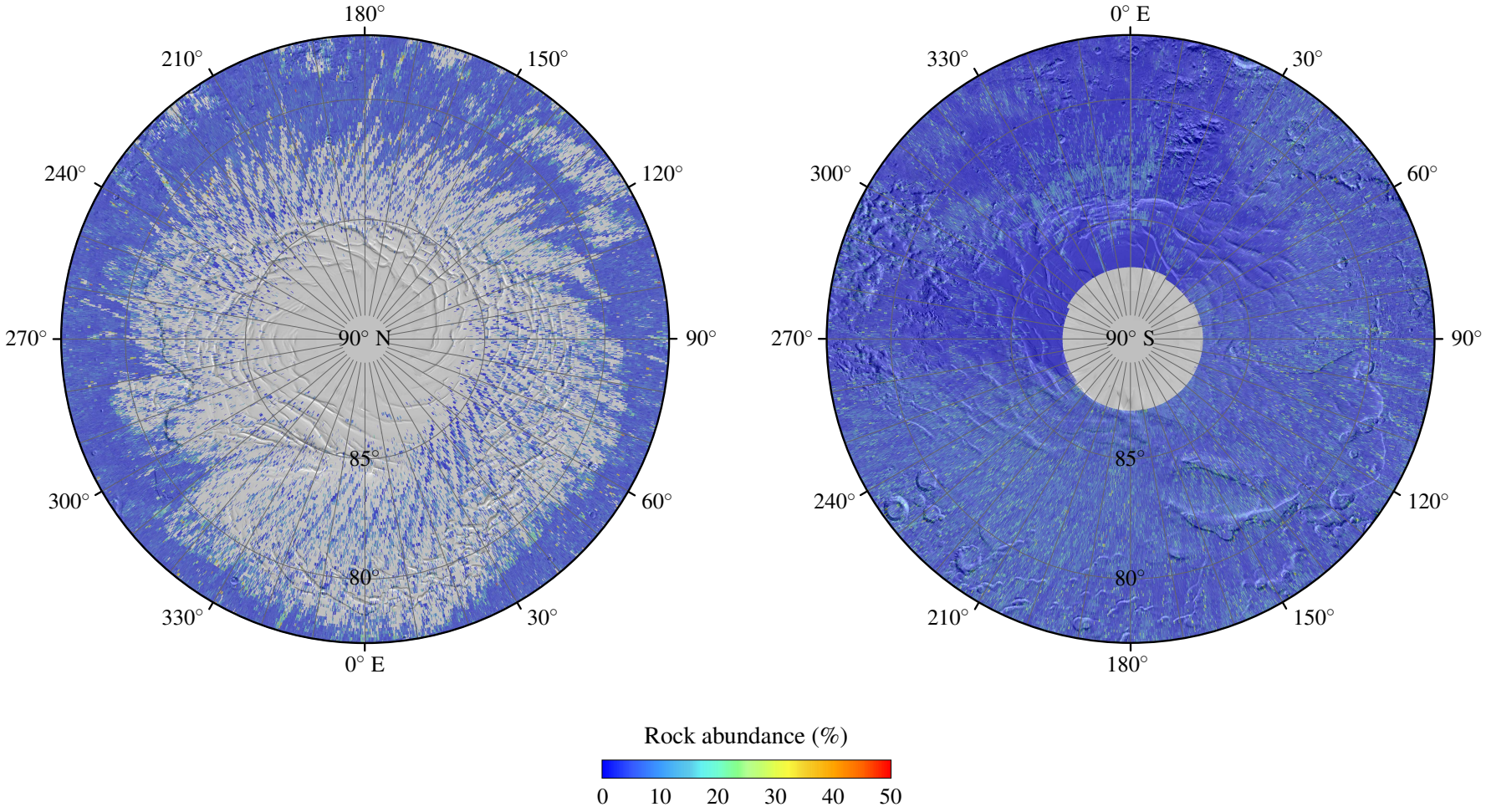

Figure A.6: Mars polar rock abundance derived from TES data, adapted from *Hébrard et al.* [2012].

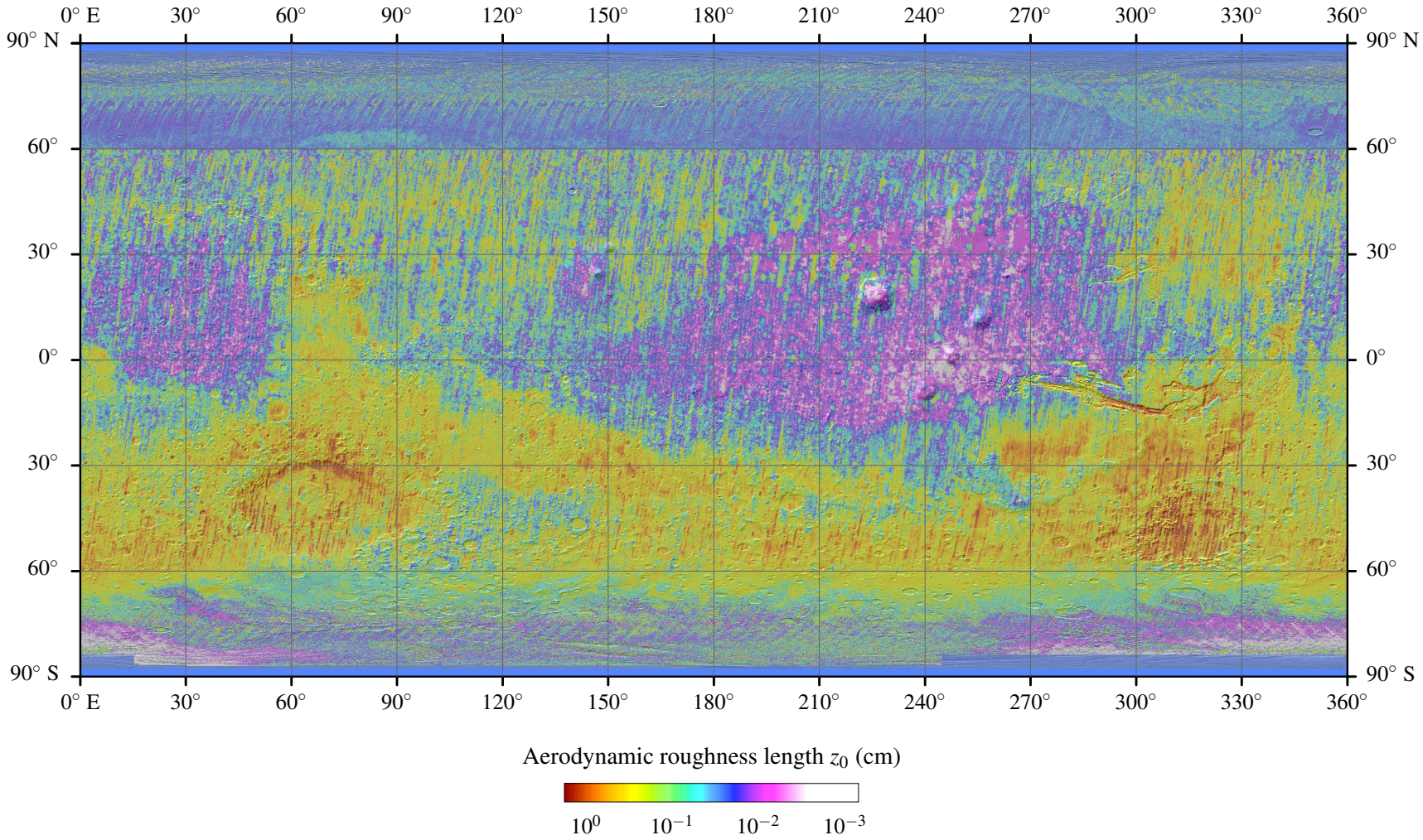

Figure A.7: Mars aerodynamic roughness length map derived from rock abundance using TES data as in Figure A.5, adapted from *Hébrard et al.* [2012].

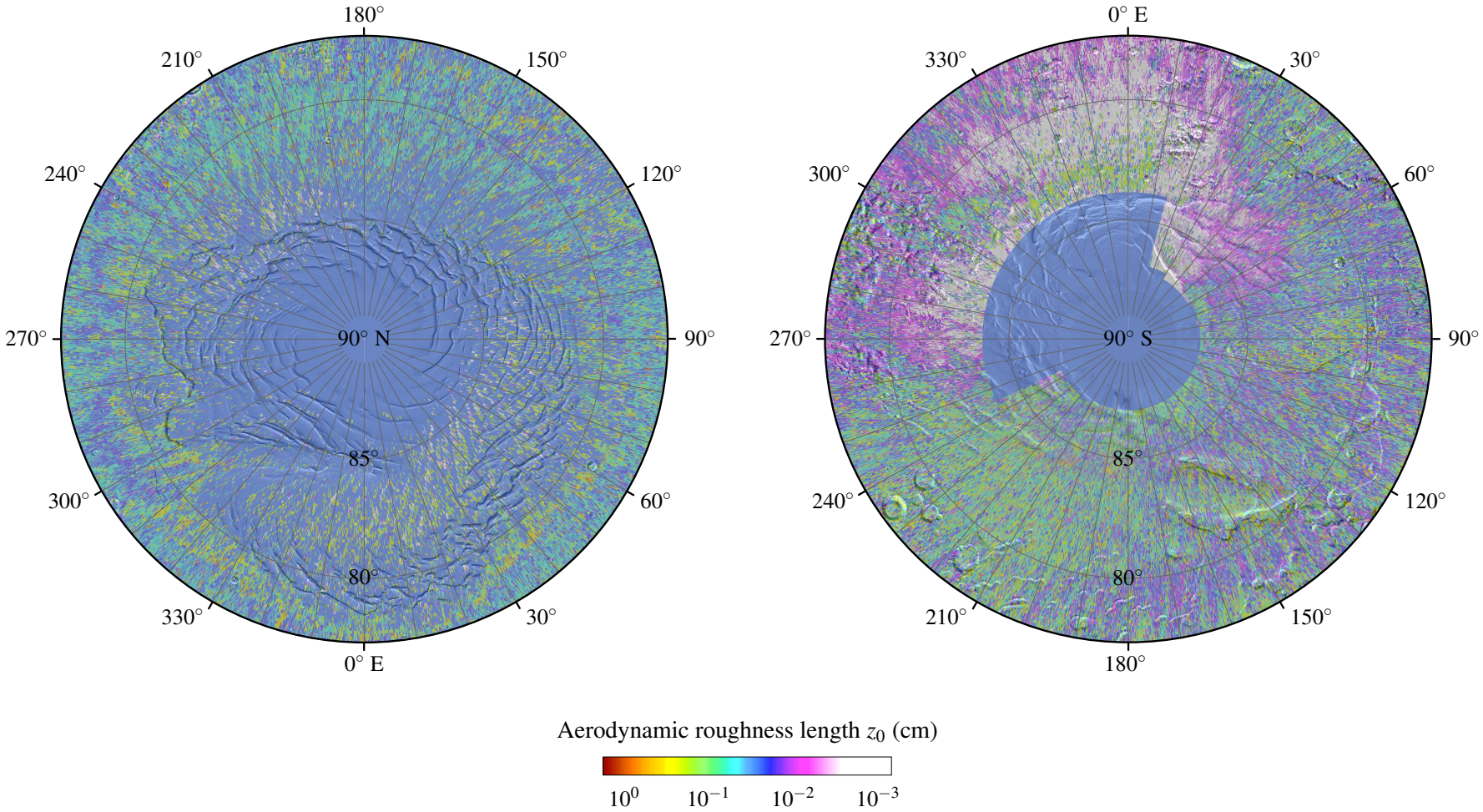

Figure A.8: Mars polar aerodynamic roughness length map derived from rock abundance using TES data as in Figure A.5, adapted from *Hébrard et al.* [2012].

B

Data Sources

This appendix contains information regarding the source of the data used in this thesis for each of the projects presented in Chapters 3 to 5.

Table B.1: The identification numbers for the HiRISE images used in Section 3.7.

Region	DTM Number
Eberswalde Crater	DTEEC_011265_1560_011331_1560_U01
	DTEEC_010052_1560_010553_1560_U01
	DTEEC_016065_1560_016210_1560_U01
	DTEEC_019190_1560_019335_1560_U01
	DTEEC_019757_1560_020034_1560_U01
	DTEEC_020324_1555_020390_1555_U01
Gale Crater	DTEEC_009505_1755_009571_1755_U01
	DTEEC_010573_1755_010639_1755_U01
	DTEEC_009650_1755_009716_1755_U01
	DTEEC_009149_1750_009294_1750_U01
	DTEEC_011417_1755_011562_1755_U01
	DTEEC_018854_1755_018920_1755_U01
Holden Crater	DTEEC_008272_1560_010474_1560_U01
	DTEEC_007191_1535_007903_1535_U01
	DTEEC_015999_1535_016276_1535_U01
	DTEEC_002088_1530_002154_1530_U01
	DTEEC_019612_1535_019678_1535_U01
	DTEEC_019823_1530_019889_1530_U01
	DTEEC_019045_1530_019322_1530_U01
Mawrth Vallis	DTEEC_002074_2025_002140_2025_U01
	DTEEC_005964_2045_011884_2045_U01
	DTEEC_010816_2040_010882_2040_U01
	DTEEC_008469_2040_008825_2040_U01
	DTEEC_006887_2050_007823_2050_U01
	DTEEC_006676_2045_007612_2045_U01
	DTEEC_015985_2040_016262_2040_U01

Table B.1 presents a list of the DTMs used in Section 3.7. The list of stereo-pairs used for Section 3.8 is shown in Table B.2.

Table B.2: The identification numbers for the CTX images used in Section 3.8.

Region	Image 1	Image 2
Aureum Chaos	G15_023963_1764_XN_03S027W	G15_024029_1764_XN_03S027W
Candor Chasma	P02_001707_1744_XN_05S076W	P05_002841_1744_XI_05S076W
Hebes Chasma	B18_016818_1790_XN_01S077W	P12_005808_1790_XI_01S077W
	P01_001509_1791_XN_00S075W	P08_003975_1790_XI_01S075W
Lycus Sulci	G17_025009_2041_XN_24N147W	P06_003371_2041_XN_24N147W
	G17_024851_2068_XI_26N149W	G19_025774_2068_XI_26N149W
	B11_013827_2083_XI_28N144W	P08_004228_2083_XN_28N144W

C

Extended Results

This appendix contains the extended results tables for each of the projects presented in Chapters 3 and 4.

Table C.1: R-squared values when surface roughness is compared to Slope-Corrected pulse-width values over the candidate Mars Science Laboratory (MSL) landing sites used in Section 3.7.

		Baseline (m)											
Area	Data Source	2	10	20	35	50	70	100	150	200	300	600	1000
Eberswalde Crater	PEDR	0.27	0.35	0.38	0.44	0.47	0.51	0.54	0.52	0.49	0.39	0.29	0.15
	Trigger 1	0.18	0.27	0.30	0.38	0.43	0.49	0.53	0.53	0.54	0.48	0.37	0.21
	Corrected	0.30	0.37	0.40	0.49	0.54	0.58	0.60	0.58	0.53	0.40	0.31	0.17
Gale Crater	PEDR	0.16	0.23	0.27	0.32	0.35	0.38	0.41	0.43	0.45	0.46	0.43	0.39
	Trigger 1	0.17	0.22	0.26	0.30	0.18	0.34	0.35	0.36	0.21	0.35	0.34	0.34
	Corrected	0.20	0.24	0.27	0.28	0.30	0.32	0.35	0.38	0.42	0.42	0.36	0.29
Holden Crater	PEDR	0.03	0.03	0.04	0.04	0.05	0.05	0.06	0.06	0.06	0.06	0.05	0.05
	Trigger 1	0.18	0.26	0.33	0.36	0.39	0.42	0.46	0.45	0.38	0.27	0.22	0.11
	Corrected	0.22	0.30	0.36	0.40	0.43	0.47	0.47	0.46	0.38	0.26	0.20	0.07
Mawrth Vallis	PEDR	0.01	0.01	0.02	0.02	0.02	0.03	0.03	0.04	0.04	0.007	0.07	0.04
	Trigger 1	0.00	0.01	0.02	0.01	0.02	0.02	0.02	0.02	0.01	0.01	0.01	0.01
	Corrected	0.01	0.02	0.03	0.03	0.03	0.03	0.03	0.04	0.05	0.07	0.07	0.05

Table C.2: R-squared values when surface roughness is compared to Slope-Corrected pulse-width values over the Rough Terrain study sites used in Section 3.8.2.

	Surface Roughness Baseline (m)								
Area	40	60	75	100	150	200	300	600	1000
Aureum Chaos	0.54	0.56	0.41	0.52	0.53	0.56	0.45	0.54	0.37
Candor Chasma	0.47	0.38	0.45	0.58	0.59	0.60	0.56	0.54	0.53
Hebes Chasma	0.36	0.28	0.33	0.44	0.46	0.48	0.47	0.47	0.47
Lycus Sulci	0.23	0.44	0.48	0.55	0.63	0.62	0.70	0.65	0.58

Table C.3: R-squared values when slope is compared to Slope-Corrected pulse-width values over the Rough Terrain study sites used in Section 3.8.2.

	Slope Baseline (m)									
Area	20	40	60	75	100	150	200	300	600	1000
Aureum Chaos	0.44	0.48	0.41	0.52	0.52	0.51	0.44	0.45	0.36	0.34
Candor Chasma	0.42	0.40	0.43	0.53	0.51	0.51	0.48	0.44	0.39	0.35
Hebes Chasma	0.37	0.32	0.33	0.45	0.46	0.45	0.44	0.40	0.40	0.39
Lycus Sulci	0.26	0.55	0.52	0.68	0.63	0.62	0.62	0.54	0.53	0.44

Table C.4: R-squared values when surface roughness is compared to LOLA pulse-width values over the Gruithuisen Mons Delta study site used in Section 4.8, with data separated by orbit.

	Baseline (m)												
Orbit	4	6	8	10	12	15	18	20	25	30	40	50	60
928	0	0	0	0	0	0.02	0	0.04	0.01	0.02	0.01	0.01	0
1097	0.09	0.09	0.09	0.1	0.09	0.09	0.09	0.08	0.09	0.09	0.09	0.09	0.09
1271	0.15	0.16	0.15	0.17	0.16	0.12	0.18	0.08	0.13	0.1	0.14	0.12	0.15
1444	0.25	0.26	0.23	0.27	0.25	0.17	0.27	0.15	0.2	0.18	0.23	0.2	0.24
1618	0	0	0	0	0	0	0	0	0	0	0	0	0
1792	0.05	0.05	0.06	0.06	0.06	0.04	0.06	0.04	0.05	0.04	0.05	0.05	0.05
1966	0.17	0.18	0.19	0.19	0.2	0.11	0.2	0.13	0.13	0.15	0.15	0.16	0.16
2487	0.33	0.34	0.36	0.36	0.38	0.24	0.37	0.25	0.27	0.29	0.3	0.32	0.32
2661	0.26	0.27	0.28	0.29	0.29	0.19	0.3	0.19	0.22	0.22	0.23	0.25	0.25
3009	0	0	0	0	0	0	0	0	0	0	0	0	0
3182	0.68	0.68	0.72	0.7	0.73	0.56	0.72	0.65	0.62	0.68	0.65	0.7	0.66
3183	0.12	0.12	0.1	0.12	0.1	0.09	0.12	0.08	0.1	0.09	0.11	0.1	0.11

Continued

	Baseline (m)												
Orbit	4	6	8	10	12	15	18	20	25	30	40	50	60
3530	0.35	0.35	0.4	0.37	0.41	0.24	0.38	0.31	0.28	0.35	0.31	0.37	0.33
3531	0.04	0.04	0.05	0.04	0.05	0.02	0.04	0.04	0.03	0.05	0.03	0.05	0.03
3704	0.02	0.02	0.02	0.02	0.02	0.02	0.02	0.02	0.02	0.02	0.02	0.02	0.02
3878	0.04	0.05	0.05	0.05	0.06	0.02	0.05	0.04	0.03	0.04	0.04	0.04	0.04
3879	0.09	0.09	0.09	0.1	0.1	0.08	0.1	0.07	0.08	0.07	0.09	0.08	0.09
4052	0.01	0.01	0.01	0.01	0.02	0.01	0.02	0.01	0.01	0.01	0.01	0.01	0.01
4226	0.28	0.28	0.29	0.29	0.3	0.26	0.3	0.24	0.27	0.26	0.27	0.27	0.28
4921	0.54	0.55	0.55	0.57	0.56	0.41	0.58	0.48	0.47	0.51	0.51	0.54	0.53
5095	0.06	0.06	0.06	0.07	0.07	0.05	0.08	0.04	0.05	0.04	0.06	0.05	0.06
5269	0.05	0.05	0.05	0.06	0.05	0.05	0.06	0.03	0.05	0.03	0.05	0.04	0.05
5442	0	0	0	0	0	0	0	0	0	0	0	0	0
5443	0.02	0.02	0.02	0.02	0.02	0.02	0.02	0.01	0.02	0.01	0.02	0.01	0.02
5789	0.22	0.23	0.25	0.24	0.26	0.17	0.24	0.17	0.19	0.19	0.21	0.21	0.21
5790	0.16	0.17	0.14	0.18	0.16	0.11	0.18	0.09	0.13	0.1	0.15	0.11	0.15
5964	0.17	0.18	0.17	0.2	0.19	0.11	0.21	0.09	0.13	0.11	0.15	0.13	0.16

Continued

	Baseline (m)												
Orbit	4	6	8	10	12	15	18	20	25	30	40	50	60
6312	0.1	0.1	0.13	0.11	0.13	0.06	0.11	0.08	0.07	0.1	0.08	0.11	0.09
6833	0	0	0	0	0	0	0	0	0	0	0	0	0
7528	0.19	0.19	0.21	0.19	0.2	0.13	0.2	0.2	0.15	0.21	0.17	0.21	0.18
8050	0.5	0.51	0.53	0.53	0.54	0.38	0.54	0.45	0.44	0.48	0.47	0.5	0.49
8223	0	0	0	0	0	0	0	0	0	0	0	0	0
8745	0.01	0.01	0.02	0.01	0.02	0.01	0.01	0.02	0.01	0.02	0.01	0.02	0.01
8746	0.03	0.03	0.04	0.03	0.04	0.04	0.03	0.04	0.04	0.04	0.04	0.04	0.04
8918	0.02	0.01	0.01	0	0.01	0.01	0	0.06	0.01	0.03	0.03	0.01	0.03
9093	0	0	0	0	0.01	0	0.01	0	0	0	0	0	0
9440	0.12	0.12	0.13	0.13	0.14	0.06	0.13	0.09	0.08	0.1	0.1	0.11	0.11
9613	0.02	0.02	0.02	0.02	0.02	0.01	0.02	0.01	0.01	0.01	0.01	0.01	0.02
9788	0.03	0.03	0.04	0.04	0.05	0.03	0.04	0.03	0.03	0.03	0.03	0.04	0.03
9960	0.22	0.23	0.23	0.24	0.25	0.13	0.25	0.11	0.16	0.15	0.19	0.18	0.2
10135	0.08	0.09	0.08	0.09	0.08	0.07	0.08	0.06	0.08	0.07	0.08	0.07	0.08
10830	0.01	0.01	0.01	0.01	0.01	0	0.01	0	0	0	0	0	0

Continued

	Baseline (m)												
Orbit	4	6	8	10	12	15	18	20	25	30	40	50	60
11179	0.06	0.06	0.09	0.07	0.09	0.03	0.08	0.04	0.04	0.06	0.05	0.06	0.05
11352	0	0	0	0	0	0	0	0	0	0	0	0	0

Table C.5: R-squared values when slope is compared to LOLA pulse-width values over the Gruithuisen Mons Delta study site used in Section 4.8, with data separated by orbit.

	Baseline (m)													
Orbit	4	6	8	10	12	15	18	20	25	30	40	50	60	
928	0	0	0	0	0	0	0	0	0.01	0	0	0.02	0	0
1097	0.07	0.09	0.09	0.08	0.09	0.08	0.08	0.08	0.08	0.09	0.08	0.09	0.09	0.09
1271	0.14	0.15	0.15	0.15	0.15	0.16	0.16	0.16	0.16	0.16	0.15	0.13	0.15	0.15
1444	0.28	0.24	0.25	0.26	0.26	0.26	0.27	0.27	0.27	0.25	0.28	0.18	0.22	0.23
1618	0	0	0	0	0	0	0	0	0	0	0	0	0	0
1792	0.04	0.04	0.05	0.04	0.04	0.05	0.04	0.05	0.05	0.05	0.04	0.04	0.04	0.05
1966	0.18	0.16	0.17	0.18	0.18	0.19	0.19	0.18	0.19	0.18	0.19	0.11	0.14	0.16
2487	0.37	0.32	0.32	0.33	0.34	0.35	0.35	0.36	0.36	0.35	0.36	0.25	0.28	0.3
2661	0.31	0.25	0.25	0.26	0.27	0.28	0.29	0.29	0.29	0.27	0.3	0.2	0.22	0.24
3009	0	0	0	0	0	0	0	0	0	0	0	0	0	0
3182	0.71	0.66	0.66	0.67	0.67	0.68	0.69	0.69	0.69	0.68	0.7	0.58	0.62	0.64
3183	0.11	0.11	0.11	0.11	0.11	0.12	0.11	0.12	0.12	0.11	0.12	0.09	0.11	0.11

Continued

	Baseline (m)													
Orbit	4	6	8	10	12	15	18	20	25	30	40	50	60	
3530	0.41	0.34	0.35	0.35	0.36	0.36	0.36	0.37	0.37	0.36	0.38	0.26	0.3	0.32
3531	0.06	0.03	0.03	0.03	0.04	0.04	0.04	0.04	0.04	0.04	0.05	0.02	0.03	0.03
3704	0.02	0.02	0.02	0.02	0.02	0.02	0.02	0.02	0.02	0.02	0.02	0.02	0.02	0.02
3878	0.04	0.04	0.05	0.05	0.05	0.05	0.05	0.05	0.05	0.05	0.05	0.03	0.03	0.04
3879	0.11	0.08	0.09	0.09	0.1	0.1	0.1	0.1	0.11	0.1	0.11	0.08	0.08	0.08
4052	0.02	0.01	0.01	0.01	0.01	0.01	0.01	0.01	0.02	0.01	0.02	0.01	0.01	0.01
4226	0.27	0.26	0.27	0.27	0.27	0.28	0.28	0.28	0.28	0.27	0.27	0.26	0.26	0.26
4921	0.55	0.51	0.52	0.53	0.53	0.54	0.54	0.55	0.55	0.54	0.56	0.42	0.47	0.5
5095	0.06	0.05	0.05	0.05	0.05	0.05	0.05	0.05	0.05	0.05	0.05	0.05	0.05	0.05
5269	0.05	0.05	0.05	0.05	0.05	0.05	0.05	0.05	0.05	0.05	0.06	0.05	0.05	0.05
5442	0	0	0	0	0	0	0	0	0	0	0	0	0	0
5443	0	0.02	0.02	0.02	0.02	0.02	0.02	0.02	0.02	0.02	0.01	0.02	0.02	0.02
5789	0.25	0.21	0.22	0.22	0.22	0.22	0.23	0.23	0.24	0.22	0.24	0.18	0.19	0.21
5790	0.18	0.16	0.16	0.17	0.17	0.18	0.18	0.18	0.18	0.17	0.18	0.12	0.14	0.15
5964	0.2	0.18	0.17	0.19	0.19	0.19	0.2	0.21	0.21	0.19	0.21	0.12	0.15	0.17

Continued

	Baseline (m)													
Orbit	4	6	8	10	12	15	18	20	25	30	40	50	60	
6312	0.09	0.1	0.11	0.1	0.11	0.11	0.11	0.11	0.11	0.11	0.1	0.06	0.07	0.09
6833	0	0	0	0	0.01	0	0	0	0	0	0	0	0	0
7528	0.19	0.18	0.19	0.19	0.19	0.19	0.19	0.19	0.19	0.19	0.19	0.14	0.17	0.18
8050	0.53	0.49	0.5	0.51	0.51	0.51	0.52	0.52	0.53	0.51	0.53	0.41	0.46	0.47
8223	0	0	0	0	0	0	0	0	0	0	0	0	0	0
8745	0.02	0.01	0.01	0.01	0.01	0.01	0.01	0.01	0.02	0.01	0.02	0.01	0.01	0.01
8746	0.03	0.03	0.03	0.03	0.03	0.03	0.03	0.03	0.03	0.03	0.03	0.04	0.03	0.03
8918	0.26	0	0	0	0	0.04	0	0	0.03	0	0.01	0.01	0.01	0
9093	0	0	0	0	0	0	0	0	0	0	0	0	0	0
9440	0.09	0.1	0.11	0.12	0.12	0.12	0.12	0.12	0.11	0.12	0.11	0.07	0.08	0.1
9613	0.01	0.02	0.02	0.02	0.02	0.02	0.01	0.01	0.01	0.02	0.01	0.01	0.02	0.02
9788	0.06	0.03	0.03	0.03	0.03	0.03	0.03	0.03	0.04	0.03	0.04	0.03	0.03	0.03
9960	0.25	0.2	0.21	0.22	0.22	0.23	0.23	0.24	0.24	0.22	0.25	0.15	0.17	0.19
10135	0.07	0.09	0.09	0.09	0.09	0.09	0.08	0.08	0.08	0.08	0.08	0.08	0.08	0.08
10830	0	0	0.01	0	0.01	0.01	0.01	0.01	0	0.01	0	0	0	0

Continued

	Baseline (m)													
Orbit	4	6	8	10	12	15	18	20	25	30	40	50	60	
11179	0.08	0.05	0.06	0.06	0.06	0.07	0.07	0.07	0.08	0.07	0.08	0.03	0.04	0.05
11352	0	0	0	0	0	0	0	0	0	0	0	0	0	0